Experimental study of unsteady flows in urbanised areas

Elisa Beteille

THÈSE DE DOCTORAT

de l'École nationale des ponts et chaussées

Experimental study of unsteady flows in urbanised areas

Étude expérimentale des écoulements instationnaires dans les zones urbanisées

École doctorale N°531, Science, Ingénierie et Environnement (SIE)

Spécialité : Mécanique des fluides

Thèse préparée au sein du Laboratoire d'Hydraulique Saint-Venant, et du Laboratoire National d'Hydraulique et Environnement d'EDF R&D

Thèse présentée et soutenue le *21 novembre 2024*, par

Élisa BETEILLE

Composition du jury:

Sandra, SOARES-FRAZÃO Prof., UCLouvain	*Rapporteur*
Nicolas, RIVIERE Prof., INSA Lyon	*Rapporteur*
Pilar, GARCÍA-NAVARRO Prof., Univ. Zaragoza	*Examinateur*
Frédéric, MOULIN Prof., IMFT, Univ. Paul Sabatier - Toulouse III	*Examinateur*
Rui, M.L. FERREIRA Ass. Prof., CERIS, Instituto Superior Técnico, Univ. de Lisboa	*Examinateur*
Sébastien, BOYAVAL ICPEF, LHSV, ENPC, Institut Polytechnique de Paris, EDF R&D	*Directeur de thèse*
Frédérique, LARRARTE DR, Univ. Gustave Eiffel and LHSV, ENPC, Institut Polytechnique de Paris, EDF R&D	*Co-directrice de thèse*
Éric, DEMAY Ing., EDF R&D	*Encadrant de thèse*

Élisa Beteille: *Experimental study of unsteady flows in urbanised areas,* Étude expérimentale des écoulements instationnaires dans les zones urbanisées, November 2024

EXPERIMENTAL STUDY OF UNSTEADY FLOWS IN URBANISED AREAS

ÉLISA BETEILLE

Thèse effectuée au sein du **Laboratoire d'Hydraulique Saint-Venant** de l'École nationale des ponts et chaussées et d'**EDF R&D**

6, quai Watier
BP 49
78401 Chatou cedex
France

Convention CIFRE EDF N° **2021/0912**

Élisa Beteille: *Experimental study of unsteady flows in urbanised areas,* Étude expérimentale des écoulements instationnaires dans les zones urbanisées, November 2024

À l'effaceur de mots du cerveau de mes 6 ans.

— **Lili**

ACKNOWLEDGEMENTS / REMERCIEMENTS

Ces trois années de doctorat sont passées à la vitesse de l'éclair, et il est déjà temps d'écrire les remerciements. Merci à tous ceux qui ont été impliqués, de près ou de loin, dans cette aventure, ainsi qu'à ceux qui m'ont soutenue et encouragée. Grâce à vous tous, ce moment est arrivé ! ☺

First, I would like to express my deepest gratitude to Sandra Soares-Frazao and Nicolas Rivière for agreeing to read and evaluate my thesis as referees. Thank you for the time you dedicated to reviewing my work and for your valuable suggestions to improve the manuscript. I have incorporated as many of your recommendations as possible into the final version! It was truly an honor to have both of you as members of the jury. I would also like to extend my sincere thanks to Frédéric Moulin for taking the role of president of the jury. Additionally, I am grateful to Pilar Garcia-Navarro and Rui M.L. Ferreira for their pertinent questions and discussions on the day of my defense. I want to thank all the jury members for your kindness and for the genuine interest you have shown in my work.

Je tiens évidemment à remercier mes encadrants, avec qui j'ai travaillé durant ces trois années de thèse : Frédérique, Sébastien et Eric. Merci pour le temps que vous avez consacré à ce sujet, pour votre soutien dans les moments difficiles, et pour vos efforts lorsque nous faisions face à des impasses !

Je souhaite également remercier particulièrement :

- Sofia, pour ta disponibilité, ta sympathie, ton écoute et ton aide. Je n'aurais pas pu rêver d'une meilleure cheffe de groupe.
- Vito, pour ton aide précieuse et l'intérêt constant que tu portes aux travaux des doctorants dans le cadre de ton projet. Merci de nous offrir l'opportunité de diffuser nos travaux à l'international et d'être toujours présent pour nous soutenir dans ce sens-là.
- L'équipe du POMPHY, pour votre aide, votre disponibilité, votre bonne humeur et votre soutien. Sans vous, le dispositif expérimental n'aurait jamais vu le jour (les fuites de la vanne me hantent encore), et les longues campagnes expérimentales auraient eu raison de moi ! Un merci particulier à Nicolas et Kévin pour avoir mis la main à la pâte, m'avoir appris à faire des joints de salle de bain et à manier un tournevis. Merci également à Clément pour ton passage quotidien dans les halls et les bonnes idées que nos discussions ont générées.
- Les développeurs de code_saturne, en particulier Martin et Thomas, pour votre aide et vos conseils sur le modèle. Il va sans dire que, sans votre soutien, les résultats numériques auraient été bien moins nombreux !!!
- Guillaume B., pour avoir pris le temps, en fin de thèse, de me transmettre ton travail sur le logiciel FUDAA, qui m'a été extrêmement utile. Merci pour ta gentillesse et ton esprit pédagogue.

Globalement, merci à tous les collègues des départements LNHE et MFEE du site de Chatou pour les nombreuses discussions à la pause-café, votre soutien et votre bonne humeur, qui rendent les journées de travail très agréables ! ☺

Ces trois années à EDF n'auraient pas été les mêmes sans vous, collègues, doctorants et stagiaires, et les afterworks qui vont avec ☺. Je pense à mon cobureau Bastien, Guillaume, JP, Fatna, Antoine, Élie, Maxime, Junjian, Proko, Fabien, Momo, Coline, Jiaze, Guilhem... J'ai sûrement oublié beaucoup de monde, mais à tous ceux qui ont été là, qui sont partis ou revenus, MERCI ! Vous êtes en grande partie responsables des beaux souvenirs que je garderai de ces trois ans. ☺

Un grand merci aussi à mon stagiaire Pablo, dont le stage s'est déroulé pendant ma troisième année de thèse, qui ne s'est pas dégonflé devant la manip et a pris en main son sujet comme un chef ! Merci à toi ☺

Merci aussi à tous les copains qui ont été présents de près ou de loin pendant ces 3 ans :

- Mes nageuses d'amour : Marion, Alys et Alice mes copines depuis toujours. Même si on est dispachées aux quatres coins de la terre maintenant, nos vacances ensembles m'ont toujours fait le plus grand bien ! Hâte des prochaines ♡.
- La bande des N7iens : Quentin (P. Et B.), Flo, Adri, Valou, Roro ! Vous me manquez fort ! Nos retrouvailles Toulousaines sont à chaque fois exceptionnelles ! Hâte d'organiser la prochaine retraite Bethmalaise...
- Le menu & parisiens associés : Belka, Nina, Mat, Juliette, Ludo, Julia, Jo, Sylvain, Annaelle, Thai, Alice, Antonin, Alix, Arthur, Mathilde, Seb, Yohanne, Jen, Cécile, Marianne, Emy et toute la bande. Merci à vous pour toutes ces soirées parisiennes endiablées, ces repas de folies, ces soirées jeux et vacances au soleil qui m'ont permis de décompresser !
- Yuyu membre éminent de la CCC (coloc d'enfer dans le 15ème) ! Merci pour tous ces souvenirs de dingues et surtout bon vent chercheur ♡.
- Luc (désormais Toulousain) merci pour tous ces moments passés à Paris, les midi muscus, les soirées sur le dancefloor et les jeux de rôles !!! RDV à Tolosa ☺.
- Les copains toulousains : Meuhmeuh et Salomé merci d'avoir pris des nouvelles régulièrement et de m'avoir encouragée ! Vous êtes les best ☺

Merci à Rose-Marie et Marc, des amis de longue date, d'avoir été là le jour J, c'était très symbolique ! Merci pour les photos et gros gros bisous à vous deux.

Merci aussi à Édouard d'avoir rendu possible le pot de thèse au JO !!!

Je vais terminer ces remerciements avec les personnes qui ont été là pour toutes les étapes importantes de ma vie, et qui, je le sais, seront aussi là pour les prochaines : **LA FAMILLE** ♡. Merci à tous d'avoir fait le déplacement depuis notre chère ville Toulousaine jusqu'à ChatouTown pour découvrir mon dernier appart étudiant, ma ville, mon lieu de travail et surtout pour m'écouter parler toute une matinée de vagues et de *je ne sais quoi*, le tout en anglais pour votre plus grand bonheur.

Un grand merci à Jacques et Gaby d'avoir toujours été là, d'avoir pris votre courage à deux mains pour venir à Chatou, m'écouter parler anglais pendant des heures sous le froid glacial de l'Île-de-France. On se souviendra d'ailleurs TOUS de ce blizzard qui nous a cueillis juste après la soutenance !

Merci aussi à mes frères et sœurs : Célia, Milan et Lila, pour m'avoir motivée, écoutée parler de choses bizarres ~~pendant ces trois ans~~ et pour m'accueillir avec toujours autant d'amour et d'enthousiasme quand je rentre à Tolosa! Vivre avec vous me manque ♡ !

Merci à mon Papa, pour m'avoir toujours encouragée, aidée et conseillée notamment durant la thèse ! Merci aussi de m'avoir permis de me remettre en jambe avec Labview, je garderai toujours dans un coin de ma tête le souvenir nostalgique de nos longues discussions sur la meilleure manière de construire les programmes ! Merci à Marie pour tes encouragements et ta joie de vivre, même sous 10 cm de neige.

Merci à ma Mounie pour tes encouragements, ton aide et ton soutien sans faille depuis toujours et, bien sûr, pendant ces trois dernières années. Rien de tout ça n'aurait été possible sans tes efforts, conseils et ta rigueur grammaticale (hihi). Ta détermination et ta force de caractère sont un exemple pour nous tous. La meilleure des mamans, ça c'est sûr !! Merci à Jean-Luc pour ta bonne humeur et ta bienveillance depuis toujours, c'est rafraîchissant et ça fait du bien !

Globalement, je ne remercierai jamais assez mes parents pour leurs efforts et sacrifices, qui m'ont permis de comprendre le monde comme je le comprends aujourd'hui. Notre famille est incroyable, merci à tous pour ces moments de retrouvailles comme on n'en fait pas deux, et pour ce soutien constant envers chacun en toutes circonstances !!! Une pensée aussi à Crys, Roti, Ari, Iago et le reste de la famille de l'autre côté de l'océan : beijos !

Enfin, merci à celui qui m'a soutenue tous les jours depuis le début de cette thèse, qui m'a vue dans mes meilleurs comme dans les pires moments, mais qui a toujours su trouver les mots pour me remotiver. Merci d'avoir été là pour me guider, m'aider à y voir plus clair, et faire en sorte que je sois dans les bonnes conditions pour aller au bout. Merci Hector pour tout l'amour que tu m'as donné ces dernières années, et pour tous ces moments que tu m'as fait vivre ! Au mental breakdown spécial fin de thèse. ♡
Muito obrigada por tudo, meu amor !

Fiouf c'était beaucoup de prénoms... promis je n'ai pas triché ! ☺

Bisous à tous et encore merci,

Eli

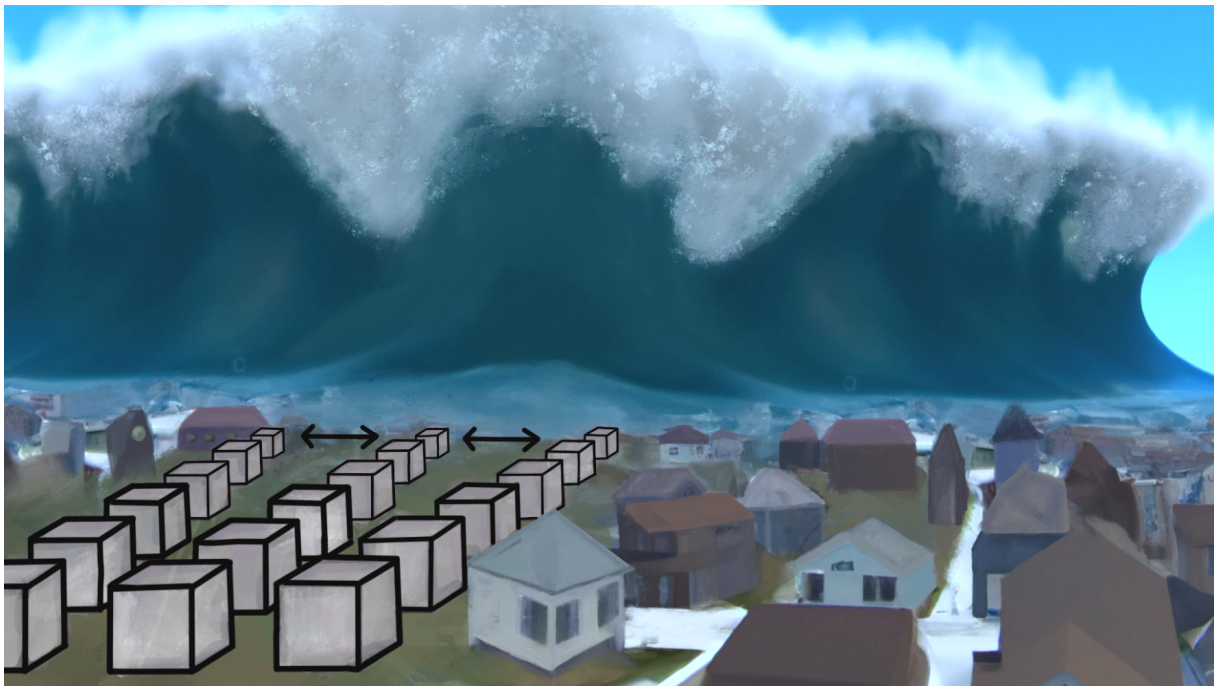

Elisa Beteille, 2024, concours MT180.

ABSTRACT

The failure of hydraulic structures can result in the propagation of flood waves across large domains containing rural and urban areas. Such events would cause rapid flooding with complex flows, leading to catastrophic consequences for downstream populations and facilities, and devastating natural environments and ecosystems. Unfortunately, climate change is expected to increase the probability of extreme weather events, and the rise of intense rainfall presents new challenges for managing hydraulic dams. Additionally, the rapid expansion of urban areas increases communities' vulnerability to flooding.

Therefore, it is crucial to accurately describe these complex phenomena and predict their evolution using numerical models. The validation and calibration of these models are performed using data from laboratory studies, as there are scarce observations and measurements from real-case event. Furthermore, the highly transient nature of these phenomena poses challenges for current metrology, contributing to a lack of precise and comprehensive data on these phenomenons within the scientific community.

To advance our understanding of the physical processes involves and validate numerical models, an experimental setup was developed at the EDF Lab Chatou in France. This setup enables the study of dam-break wave propagation through a series of obstacles representing idealised urban areas. The objective is to characterise the flow dynamics and analyse how various urban parameters, such as building spacing and number of streets, influence the flood process. Wave sensors measure water levels upstream, within, and downstream of the urban area. Additionally, a high-speed camera positioned above the flow performs Large-Scale Particle Image Velocimetry (LSPIV) measurements to calculate the instantaneous velocity field of the free surface. Moreover, the interaction between the wave and obstacles is documented using a high-speed camera along the channel and the water elevation in this area is calculated using image analysis measurements. Finally, the global impact of the urban forms on the flow is analysed through energy head calculations downstream of them.

Simultaneously, detailed numerical simulations of the observed flows are conducted using the open-source Computational Fluid Dynamics (CFD) solver code_saturne. The initial validation of the model is carried out on simple urban configurations, identifying areas for improvement. Finally, simulations of a selected number of urban forms are performed to extend the experimental dataset. Previously measured punctual tendencies of the energy head are confirmed through profile analysis, and head loss coefficients related to the studied urban parameters are extracted.

Overall, the thesis results contribute to a new dataset on unsteady flows in urbanised areas, enhancing understanding of these complex phenomena and supporting the validation of numerical models. Moreover, with improved knowledge of these phenomena, communities can develop safer urban planning strategies and optimise the design of industrial safety measures. A novel method to assess the influence of various urban parameters on the flow using the spatially averaged energy head is proposed. This method could support the calibration of simplified numerical models to account for the effects of urban areas on large-scale flood studies. This work aims to protect both property and people within a changing environmental and societal context.

keywords : dam-break flows, laboratory experiments, urban flood, free surface velocity field, particle image velocimetry, numerical modelling

RÉSUMÉ

La rupture d'un ouvrage hydraulique peut entraîner la propagation d'une vague d'inondation sur de vastes domaines comprenant à la fois des zones rurales et urbaines. Un tel événement engendrerait une inondation rapide avec des écoulements complexes qui aurait des conséquences catastrophiques pour les populations et les installations situées en aval, et détruirait les environnements naturels et les écosystèmes. Malheureusement, les changements climatiques pourraient augmenter les probabilités d'événements météorologiques extrêmes et l'augmentation des épisodes de pluies intenses pose de nouveaux défis pour la gestion des barrages hydrauliques. De plus, l'expansion rapide des zones urbaines accroît la vulnérabilité des communautés face aux inondations.

Il est donc crucial de pouvoir décrire précisément ces phénomènes complexes et d'en prédire l'évolution à l'aide de modèles numériques. La validation et la calibration de ces modèles reposent en grande partie sur des données issues d'études en laboratoire car il existe peu d'observations et de mesures de cas réels. De plus, la nature fortement transitoire des phénomènes observés pose des défis à la métrologie actuelle, entraînant un manque de données précises et complètes dans la communauté scientifique.

Pour améliorer notre connaissance des phénomènes physiques engendrés par la présence d'obstacles sur l'écoulement et valider les modèles numériques, un dispositif expérimental a été développé, sur le site EDF Lab Chatou en France. Il permet d'étudier la propagation d'une onde de submersion à travers un ensemble d'obstacles représentant des quartiers urbains simplifiés. L'objectif est de caractériser l'écoulement et d'analyser comment différents paramètres urbains, tels que l'espacement des bâtiments ou le nombre de rues, influent sur l'inondation. Des sondes acoustiques mesurent la hauteur d'eau en amont, au sein, et en aval de la zone urbaine. De plus, une caméra haute fréquence est placée au-dessus de l'écoulement et qui grâce à une analyse LSPIV (Large-Scale Particle Image Velocimetry) permet de mesurer le champ de vitesse instantané de la surface libre. L'impact entre la vague et les obstacles est documenté grâce à une caméra haute fréquence placée le long du canal, et le niveau d'eau dans cette zone est calculé à l'aide de mesures par analyse d'images. Enfin, l'impact global des formes urbaines sur l'écoulement est analysé à travers le calcul de la charge hydraulique en aval de celles-ci.

En parallèle, des simulations numériques des écoulements observés sont réalisé à l'aide du logiciel CFD (Computational Fluid Dynamics) libre code_saturne. La validation initiale du modèle est effectuée sur des configurations urbaines simples, identifiant des domaines à améliorer. Enfin, des simulations d'un nombre sélectionné de formes urbaines sont réalisées pour étendre la base de donnée expérimentale. Les tendances ponctuelles précédemment mesurées de la charge hydraulique sont confirmées par l'analyse des profils, et les coefficients de perte de charge liés aux paramètres urbains étudiés sont extraits.

Finalement, les résultats de la thèse alimentent une nouvelle base de données pour les écoulements instationnaires dans les zones urbanisées, permettant une meilleure compréhension des phénomènes mis en jeu et participant à la validation des modèles numériques. De plus, grâce à une meilleure connaissance de ces phénomènes, les collectivités pourront élaborer des stratégies d'urbanisation plus sûres et optimiser le dimensionnement des dispositifs de sécurité industrielle. Une nouvelle méthode pour évaluer l'influence de divers paramètres urbains sur l'écoulement en utilisant la charge hydraulique moyennée spatialement est proposée. Cette méthode pourrait aider la calibration de modèles numériques simplifiés pour tenir compte de l'effet des zones urbaines dans les études d'inondation grande échelle. Ce travail s'inscrit donc dans une optique de protection des biens et des personnes dans un contexte environnemental et sociétal changeant.

mots-clés : écoulements instationnaires, expériences en laboratoire, inondation urbaine, champ de vitesse de la surface libre, vélocimétrie par image de particules, modèle numérique

PUBLICATIONS

Journal Papers

Beteille, E., Larrarte, F., Boyaval, S., Demay, E. (2025). Dam-break flow over various obstacles configurations. Journal of Hydraulic Research. 2025. doi:10.1080/00221686.2025.2460020. https://doi.org/10.1080/00221686.2025.2460020

And probably a data paper coming soon... ☺

Conference Proceedings

Beteille, E., Boyaval, S., Larrarte, F., Demay, E. (2024). Experimental analysis on the influence of urban forms on unsteady urban flooding. 12th International Conference on Fluvial Hydraulics, River Flow 2024

Beteille, E., Boyaval, S., Larrarte, F., Demay, E. (2024). Experimental and Numerical Investigation of Dam Break Flow Propagation Through Various Obstacle Configurations. In: Gourbesville, P., Caignaert, G. (eds) Advances in Hydroinformatics—SimHydro 2023 Volume 1. SimHydro 2023. Springer Water. Springer, Singapore. doi:10.1007/978-981-97-4072-7_18. https://link.springer.com/chapter/10.1007/978-981-97-4072-7_18

Beteille, E., Larrarte, F., Boyaval, S., Demay, E. (2023). Providing Validation Data for Numerical Codes Dealing with Unsteady Urban Flooding. 40th IAHR World Congress : Rivers - Connecting Mountains and Coasts, Aug 2023, Vienne, Austria. pp.1456-1464, doi:0.3850/978-90-833476-1-5_iahr40wc-p0127-cd. https://doi.org/10.3850/978-90-833476-1-5_iahr40wc-p0127-cd

CONTENTS

1 INTRODUCTION 1
1.1 General context . . . 2
1.2 Industrial context . . . 4
1.3 Scope of the thesis . . . 4
1.4 Methodology . . . 5
1.5 Structure of the manuscript . . . 5
2 REVIEW OF EXPERIMENTAL INVESTIGATION OF FAST TRANSIENT URBAN FLOODING 7
2.1 Introduction . . . 8
2.2 Investigation on dam-break waves without obstacles . . . 8
2.2.1 Setup characteristics . . . 8
2.2.2 Instrumentation for dam-break flow studies . . . 11
2.3 Laboratory investigations of dam-break wave in presence of a single obstacle . . . 12
2.4 Experimental investigation of dam-break waves through idealised urban areas . . . 13
2.5 Laboratory investigations on the influence of urban forms on steady flows . . . 17
2.6 Conclusion . . . 18
3 COMPARATIVE STUDY OF NUMERICAL MODELS FOR DAM-BREAK FLOW IN URBANISED AREA 20
3.1 Introduction . . . 21
3.2 Numerical modelling of dam-break flow in urban area . . . 21
3.3 Numerical models . . . 22
3.3.1 TELEMAC-2D: Governing equations . . . 23
3.3.2 code_saturne: Governing equations . . . 24
3.4 Dam-break flow reproduction with TELEMAC-2D and code_saturne . . . 27
3.4.1 Test cases presentation . . . 27
3.4.2 Results comparison . . . 29
3.5 Additional validation of code_saturne for dam-break flow in an enclosed domain . . . 33
3.5.1 Case presentation . . . 33
3.5.2 Numerical model . . . 34
3.5.3 Comparisons between experimental and numerical results . . . 34
3.6 Conclusion . . . 37
4 EXPERIMENTAL SETUP 39
4.1 Introduction . . . 40
4.2 Sizing of the experimental setup . . . 40
4.2.1 Sizing of the gate width . . . 40
4.2.2 Selection of the flow conditions . . . 43
4.2.3 Final geometry of the experimental setup . . . 44
4.3 Metrology and calibration . . . 44
4.3.1 Wave gauge . . . 45
4.3.2 LSPIV analysis . . . 45
4.3.3 Image analysis measurement . . . 46
4.4 Acquisition system . . . 46
4.5 Repeatability . . . 47
4.5.1 Setup repeatability . . . 47
4.5.2 Opening of the gate . . . 48
4.6 Experimental protocol . . . 48
4.7 Post-processing method . . . 50
4.7.1 LSPIV post-processing . . . 50
4.7.2 IAM post-processing . . . 52
4.8 Validation of the methodology . . . 55
4.9 Conclusion . . . 56
5 PRELIMINARY EXPERIMENTAL CAMPAIGN: DAM-BREAK FLOW OVER VARIOUS OBSTACLES CONFIGURATIONS 57
5.1 Introduction . . . 58

5.2 Methodology . . . 58
5.2.1 Performed tests and configurations . . . 58
5.2.2 Repeatability . . . 61
5.3 Experimental results . . . 62
5.3.1 Free surface flow description . . . 62
5.3.2 Investigation of the flow area impacted by the obstacles . . . 65
5.3.3 Water depth description upstream and downstream of the gate . . . 67
5.3.4 Splash-up zone evolution . . . 70
5.4 Numerical methodology . . . 73
5.5 Numerical validation results . . . 75
5.5.1 Reproduction of the upstream oscillations . . . 75
5.5.2 Water depth comparison upstream and downstream of the urban area . . . 76
5.5.3 Free surface velocity comparison . . . 78
5.5.4 Turbulence model sensitivity analysis . . . 82
5.5.5 Summary . . . 86
5.6 Conclusion . . . 86
6 INFLUENCE OF URBAN FORMS ON FAST TRANSIENT FLOW 88
6.1 Introduction . . . 89
6.2 Modifications of the experimental protocol . . . 89
6.3 Repeatability of the experiments . . . 93
6.4 Urban form parameters . . . 94
6.5 Influence of the streets in the main direction of the flow . . . 94
6.5.1 Definition of thirteen urban forms . . . 94
6.5.2 Longitudinal street width impact (l_x) on the flow . . . 95
6.5.3 Longitudinal street number impact (n_x) on the flow . . . 113
6.5.4 Summary . . . 115
6.6 Influence of the streets along the cross section of the flow . . . 117
6.6.1 Definition of the idealised urban forms . . . 117
6.6.2 Cross streets impact ($n_y = 0$) on the flow . . . 118
6.6.3 Cross streets width and number impact (l_y) on the flow . . . 124
6.6.4 Summary . . . 129
6.7 Comparisons of current experiments with past experimental studies . . . 130
6.8 Conclusion . . . 132
7 MODELLING FAST TRANSIENT FLOW THROUGH VARIOUS URBAN FORMS 133
7.1 Introduction . . . 134
7.2 Numerical reproduction of selected urban forms with code_saturne . . . 134
7.3 Water depth comparisons with experimental data . . . 136
7.4 Spatialisation of the observed tendencies using 3D simulations . . . 139
7.5 Hydraulic jump investigation and recommendations for future experimental setups . . . 146
7.6 Conclusion . . . 149
8 GENERAL CONCLUSION AND PERSPECTIVES 150
8.1 Contributions and findings . . . 151
8.2 Perspectives . . . 152
8.2.1 Dam-break flow experiments . . . 152
8.2.2 Numerical aspects . . . 153

Appendix 155
A SUMMARY OF THE URBAN CONFIGURATIONS STUDIED 156
B DETAILS ABOUT THE ACQUISITION PROGRAM 161
C DETAILS ABOUT THE IMAGE ANALYSIS MEASUREMENT PROGRAM 164
D SUPPLEMENTARY DATA FROM CHAPTER 5 168
E SUPPLEMENTARY DATA FROM CHAPTER 6 176
F SUPPLEMENTARY DATA FROM CHAPTER 7 182

BIBLIOGRAPHY 188

LIST OF FIGURES

Figure 1.1 (a) Flood of La Crenze in Saint Laurent le Minier (France, 2014), *source: EPTB Fleuve Hérault* [16]; (b) Flash floods in Rhineland-Palatinate (Germany, 2021), *source: Harald Tittel/dpa via AP* [17]. 2
Figure 1.2 Devastating floods caused by the Mediterranean storm Daniel in Libya, resulting in dam-breaks and neighbourhood destruction in coastal areas (Derna in Libya, 2023), *source: Jamal Alkomaty / AP Photo / Picture alliance* [31]. 3
Figure 1.3 Methodology of the research project. 6
Figure 2.1 Schematic top view of rectangular experimental facilities for dam-break flow studies: (a) Total Dam-Break in a rectangular channel and (b) Partial Dam-Break in a rectangular channel. Blue area illustrates the water. 10
Figure 3.1 Sketch of different turbulence approaches: (a) RANS, (b) LES and (c) DNS, in relation to the modeling of the turbulent energy spectrum. 22
Figure 3.2 Illustration of the void fraction field: on the left, with a homogeneous water field; and on the right, with air bubbles trapped under the free surface. The orange line represents the actual position of the free surface, and the numbers represent the volume fraction of water in each cell. Sketch adapted from Davidson *et al.* (2015) [128]. 28
Figure 3.3 Void fraction (α) profile of a dam-break flow crossing an obstacle configuration at $t = 4$ s. 28
Figure 3.4 Schematic view of the measurement points for the comparison between TELEMAC-2D, code_saturne and experimental data. 28
Figure 3.5 Flow visualisation at $t = 10$ s without obstacles in the flow for solvers (a) TELEMAC-2D and (b) code_saturne ($\alpha \leq 0.5$). 29
Figure 3.6 Dam-break case: Water depth comparison between experiments, code_saturne and TELEMAC-2D simulations at position P1 for (a) a global view and (b) a zoomed view. 30
Figure 3.7 Dam-break case: Water depth comparison between experiments, code_saturne and TELEMAC-2D simulations at position P2 for (a) a global view and (b) a zoomed view. 30
Figure 3.8 Water depth comparison between (a) TELEMAC-2D and (b) code_saturne at $t = 5$ s. 31
Figure 3.9 Flow visualisation at $t = 10$ s with one obstacle in the flow for solvers (a) TELEMAC-2D and (b) code_saturne ($\alpha \leq 0.5$). 31
Figure 3.10 Dam-break case with one obstacle: Water depth comparison between experiments, *code_saturne* and TELEMAC-2D simulations at positions: (a) P2, upstream of the obstacle and (b) P3, downstream of the obstacle. 32
Figure 3.11 Water depth profiles obtained with TELEMAC-2D at four different time-steps. . 32
Figure 3.12 code_saturne void fraction field (α). Zoom near the obstacle for: (a) $t = 1.6$ s and (b) $t = 10$ s. The black lines centered at $x = 8.55$ m and $x = 8.75$ m corresponds respectively to the position of probes P2 and P3. 33
Figure 3.13 Sketch of the experimental setup and associated measurement points from Kocaman *et al.* (2021) [35]. 34
Figure 3.14 Water height visualisation at different time steps from code_saturne simulation. Dark blue surface corresponds to $y = 0$ m and $\alpha \leq 0.5$. 35
Figure 3.15 Comparison between (left) experimental from Kocaman *et al.* (2021) [35] and (right) water depth field from code_saturne ($\alpha = 0.5$) for $t = [0.2, 0.6]s$. 35
Figure 3.16 Comparison between (left) experimental from Kocaman *et al.* (2021) [35] and (right) water depth field from code_saturne ($\alpha = 0.5$) for $t = [0.8, 1.4]s$. 36
Figure 3.17 Water depth comparison between experimental data from Kocaman *et al.* (2021) [35] and code_saturne at different positions: (a) P1, (b) P2, (c) P3 and (d) P4. . 37
Figure 4.1 2D computational domain and water depth initial condition for case 50. 40

Figure 4.2 Water height time history upstream of the gate at position (a) P1 (4,0) m, (b) P2 (6.5,0) m and, downstream of the gate at position (c) P3 (8.35, 0) m. 41
Figure 4.3 Water depth spatial field at t = 5 s for Cases (a) 50, (b) 60, (c) 80 and, (d) 100. . 42
Figure 4.4 Top view of the flow and visual comparison between (a) h_0 = 0.25 m and (b) h_0 = 0.3 m. 43
Figure 4.5 Schematic views of the experimental setup, (a) top and (b) side sections [m]. . . . 44
Figure 4.6 Three-dimentional (3D) sketch of the experimental setup [m]. Red line highlight the gate guides at x = 6.925 m. 44
Figure 4.7 (a) Resistive wave gauge TDH250 placed upstream of the breach and, (b) Acoustic gauges Mic+35/IU/TC placed downstream of the breach. 45
Figure 4.8 High-velocity laboratory camera (FASTCAM Mini UX50). 45
Figure 4.9 (a) Spherical seeding particles used for the LSPIV analysis, (b) manual addition of the particles to the flow. 46
Figure 4.10 Acquisition card and power supply of the water height sensors. 46
Figure 4.11 Schematic diagram of the acquisition software functions. 47
Figure 4.12 Water depth variation, 95% confidence interval and standard deviation for the reference dam-break case, without obstacles, at position (a) (6.5, 0) m and (b) (8.35, 0) m. 48
Figure 4.13 (a) Seeding particles placed in the measurement area before the acquisition and, (b) image recorded of the channel bed without seeding particles for the background removal step. 50
Figure 4.14 Illustration of the background removal routine of the LSPIV analysis. 51
Figure 4.15 Illustration of the main steps of the LSPIV analysis. 51
Figure 4.16 Schematic diagram of the Image Analysis Measurement (IAM) software functions. 53
Figure 4.17 Illustration of the main steps of water height Image Analysis Measurement (IAM). 54
Figure 4.18 Sketch of the principle of the IAM technique for detecting the position on a free surface. Green lines represent the ROI position and red text the detected pixel corresponding to the detected free-surface. 54
Figure 5.1 Geometry of the urban form $2-10-2-10$ and definition of the parameters characterising urban forms in the manuscript. Grey surfaces represent the position of the obstacles, red surfaces represent the streets along the x axis, and green surfaces represent the streets along the y axis. 58
Figure 5.2 Top view of the configurations studied and probes locations, (a) $0-0-0-0$: one single obstacle of length 0.1 m, (b) $1-0-1-0$: one single obstacle of length 0.2 m,(c) $2-10-2-10$: 3x3 aligned obstacles of individual length of 0.1 m and (d) $4-0-4-0$: one single obstacle of length 0.5m. 59
Figure 5.3 Schematic views of the experimental setup, (a) top and (b) side sections. The coordinate system, the probes locations (R1 to R4, A1 to A6) and the Field Of View (FOV) for both Large-Scale Particle Image Velocimetry (LSPIV) and Image Analysis Measurement (IAM) are also illustrated. 60
Figure 5.4 Water depth variation for all studied configurations, 95% confidence interval for probes (a) R3 and (b) A1. 62
Figure 5.5 General observation of the flow pattern at t = 15 s. Red lines highlight the presence of obstacles, green dashed lines the presence of a splash-up, blue dashed lines and arrows the presence of a wake zone and yellow dashed lines a reflection zone. . . 63
Figure 5.6 Free surface velocity variation for cases $0-0-0-0$, $2-10-2-10$ and $4-0-4-0$ at 3 different time steps. Black surfaces illustrate the obstacles position. . . 64
Figure 5.7 Free surface velocity comparison between case 0 and cases $0-0-0-0$, $2-10-2-10$ and $4-0-4-0$ computed as the relative velocity difference $\frac{|V_{n_x-l_x-n_y-l_y}-V_0|}{|V_0|} \times 10^2$[%] at 3 different time steps. Black surfaces illustrate the obstacles position. . 66
Figure 5.8 Histograms of the relative velocity variation for cases $0-0-0-0$, $2-10-2-10$ and $4-0-4-0$ at (a) t = 4 s, (b) t = 9 s and (c) t = 14 s. 67
Figure 5.9 Water height time variation at positions (a) R1, (b) R2, (c) R3 and (d) R4 for cases 0, $0-0-0-0$, $1-0-1-0$, $2-10-2-10$ and $4-0-4-0$. 68
Figure 5.10 Sketch of the positions of probes for cases $0-0-0-0$, $1-0-1-0$, $2-10-2-10$, and $4-0-4-0$, along with the corresponding curve colour coding, are shown. 69

Figure 5.11 Water height time variations downstream of the gate at positions (a) A1, (b) A2, (c) A3, (d) A4, (e) A5 and (f) A6 for cases 0, $0-0-0-0$, $1-0-1-0$, $2-10-2-10$ and $4-0-4-0$. . . . 69
Figure 5.12 Snapshots of the splash-up at $t = 1.25$ s for cases $0-0-0-0$, $1-0-1-0$ and $2-10-2-10$. Red dashed line highlights obstacles edges. . . . 70
Figure 5.13 Snapshots of the splash-up at $t = 1.75$ s for cases $0-0-0-0$, $1-0-1-0$ and $2-10-2-10$. Red dashed line highlights obstacles edges. . . . 71
Figure 5.14 Snapshots of the splash-up at $t = 5$ s for cases $0-0-0-0$, $1-0-1-0$ and $2-10-2-10$. Red dashed line highlights obstacles edges. . . . 71
Figure 5.15 Sketch of the free-surface detection using the IAM technique for case $4-0-4-0$ at $t = 1.75$ s. Green lines represent the ROI position (a vertical line of 1 pixel long, see Table 5.5) and red dashed line the resulting elevation z. . . . 72
Figure 5.16 Splash-up height comparison at position A2 between wave gauge measurements (black dashed line) and IAM (cross points) for cases (a) $0-0-0-0$, (b) $1-0-1-0$ and (c) $2-10-2-10$. . . . 72
Figure 5.17 Case $2-10-2-10$: Snapshots of the simulation at $t = 8$ s. The blue surface represents water cells ($\alpha < 0.5$), and the grey surfaces represent the walls located at y > -0.35 m. . . . 73
Figure 5.18 Numerical mesh refinement along the (a) x-axis, (b) y-axis and (c) z-axis. Each black line represents the centre of an individual cell, except along the (a) x-axis, where black lines are plotted every 10 cells for enhanced clarity. . . . 74
Figure 5.19 Case $2-10-2-10$. Mesh sensitivity analysis of the water height profile at y = 0 m for (a) x = [0, 12] m and (b) x = [8, 10] m at t = 4 s. Gray rectangles represent the obstacle positions. 48M: 48 million cells mesh, 6M: 6 million cells mesh and 800K: 800 thousand cells mesh. . . . 74
Figure 5.20 Case $2-10-2-10$. Mesh sensitivity analysis of the water height variations at positions (a) R3 and (b) A1. 48M: 48 million cells mesh, 6M: 6 million cells mesh and 800K: 800 thousand cells mesh. . . . 75
Figure 5.21 Case $0-0-0-0$. Water depth variations comparison between experimental and numerical data at position R3. . . . 76
Figure 5.22 Case $0-0-0-0$. Vertical velocity profile evolution through the breach (x = -0.075 m) from the numerical model at different positions: (a) y = 0 m (b) y = 0.2 m. . . . 76
Figure 5.23 Water height comparison at position A1 between wave gauge measurements (black dashed line) and numerical model (blue line) for cases $0-0-0-0$, $1-0-1-0$, $2-10-2-10$ and $4-0-4-0$. . . . 77
Figure 5.24 Water height comparison at position A6 between wave gauge measurements (black dashed line) and numerical model (blue line) for cases $0-0-0-0$, $1-0-1-0$, $2-10-2-10$ and $4-0-4-0$. . . . 78
Figure 5.25 Case $0-0-0-0$. Surface velocity field comparison at three different time steps. V_{EXP} represents the horizontal velocity obtained from the LSPIV analysis (Section 5.3.1) and V_{NUM} refers to the vertically averaged horizontal velocity for $\alpha \leq 0.5$. Black surfaces illustrate the obstacles' positions. . . . 79
Figure 5.26 Case $2-10-2-10$. Surface velocity field comparison at three different time steps. V_{EXP} represents the horizontal velocity obtained from the LSPIV analysis (Section 5.3.1) and V_{NUM} refers to the vertically averaged horizontal velocity for $\alpha \leq 0.5$. Black surfaces illustrate the obstacles' positions. . . . 80
Figure 5.27 Case $2-10-2-10$. Surface velocity field comparison at three different time steps. V_{EXP} represents the horizontal velocity obtained from the LSPIV analysis (Section 5.3.1) and V_{NUM} refers to the vertically averaged horizontal velocity for $\alpha \leq 0.5$. Black surfaces illustrate the obstacles' positions. . . . 81
Figure 5.28 Case $2-10-2-10$. Water height at positions (a) A1 and (b) A6 between experimental data (black dashed line) and numerical models. . . . 83
Figure 5.29 Case $2-10-2-10$ without turbulence model. Surface velocity field comparison at three different time steps. V_{EXP} represents the horizontal velocity obtained from the LSPIV analysis and V_{NUM} refers to the vertically averaged horizontal velocity for $\alpha \leq 0.5$. Black surfaces illustrate the obstacles' positions. . . . 84

Figure 5.30 Case $2-10-2-10$ with $k-\epsilon$ (with linear production) turbulence model. Surface velocity field comparison at three different time steps. V_{EXP} represents the horizontal velocity obtained from the LSPIV analysis and V_{NUM} refers to the vertically averaged horizontal velocity for $\alpha \leq 0.5$. Black surfaces illustrate the obstacles' positions. . . . 84
Figure 5.31 Case $2-10-2-10$ with $k-\omega$ SST turbulence model. Surface velocity field comparison at three different time steps. V_{EXP} represents the horizontal velocity obtained from the LSPIV analysis and V_{NUM} refers to the vertically averaged horizontal velocity for $\alpha \leq 0.5$. Black surfaces illustrate the obstacles' positions. . 85
Figure 5.32 Case $2-10-2-10$ with $R_{ij}-\epsilon$ SSG turbulence model. Surface velocity field comparison at three different time steps. V_{EXP} represents the horizontal velocity obtained from the LSPIV analysis and V_{NUM} refers to the vertically averaged horizontal velocity for $\alpha \leq 0.5$. Black surfaces illustrate the obstacles' positions. . 85
Figure 6.1 Snapshot of the water transparency and free surface patterns during (a) water depth measurements and (b) LSPIV analysis during the urban forms campaign. . 90
Figure 6.2 IAM high-speed camera resolution from (a) the preliminary study for case $0-0-0-0$ and (b) the actual study for case $0-0-2-10$. . . . 91
Figure 6.3 3D schematic view of the position of the Region Of Interest (ROI) used for the IAM analysis. The blue area is an approximation of the Field Of View (FOV) of the IAM camera. . . . 92
Figure 6.4 Schematic views of the experimental setup, (a) top and (b) side sections. The coordinate system, the probes locations (R1 to R2, A1 to A6) and the Field Of View (FOV) for both Large-Scale Particle Image Velocimetry (LSPIV) and Image Analysis Measurement (IAM) are also illustrated. . . . 92
Figure 6.5 Water depth variation for all studied configurations at positions (a) R2 (135 curves) and (b) A1 (66 curves). All curves are plotted with an opacity equal to 0.3 for better readability. . . . 93
Figure 6.6 Geometry of the urban form $2-10-2-10$ and definition of the parameters characterising urban forms in the manuscript. Grey surfaces represent the positions of the obstacles, red surfaces represent the streets along the x direction, and green surfaces represent the streets along the y direction. . . . 94
Figure 6.7 Top view of the configuration $0-0-2-10$ whitout longitudinal street. . . . 95
Figure 6.8 Top view of the twelve configurations $n_x-l_x-n_y-l_y$ with three different street number (n_x) and four different street width (l_x). . . . 96
Figure 6.9 Superposition of cases (a) $n_x=1$, (b) $n_x=2$ and (c) $n_x=3$ for all street width l_x. 96
Figure 6.10 Effect of street width l_x on water depth variations for cases with $n_x=1$ at positions (a) A1, (b) A2, (c) A3, (d) A4, (e) A5 and (f) A6. . . . 97
Figure 6.11 Effect of street width l_x on water depth variations for cases with $n_x=3$ at positions (a) A1, (b) A2, (c) A3, (d) A4, (e) A5 and (f) A6. . . . 98
Figure 6.12 Effect of street width l_x on water depth variations for cases with $n_x=0$ and 2 at positions (a) A1, (b) A2, (c) A3, (d) A4, (e) A5 and (f) A6. . . . 99
Figure 6.13 Cases $n_x=3$. Evolution of the water depth profile (y = 0 m) at times (a) t = 5 s, (b) t = 10 s, (c) t = 15 s, and (d) t = 20 s. Grey rectangles represent cubes position. . . . 101
Figure 6.14 Evolution of the water depth at x = 8 and y = -0.05 m from the IAM analysis for cases (a) $n_x=1$, (b) $n_x=2$ and (c) $n_x=3$. . . . 101
Figure 6.15 Snapshots from the IAM camera of the splash-up for cases $n_x=2$ and $l_x=[0.05, 0.20]$ m at $t=8$ s. . . . 102
Figure 6.16 Zoomed view of the binarized image during IAM profile detection of image from Figure 6.15a. Green line represents the initial ROI position at x = 8.1 m. Red points represent the free surface position detected for each ROI position. . . . 103
Figure 6.17 Water depth profiles for cases $n_x=2$ at t = 8s from the IAM analysis of images in Figure 6.15. Black surface represent the cube position. . . . 103
Figure 6.18 Illustration of the reflection zone evolution and side walls influence for case 0 at 2 different times. LSPIV vectors are superposed to background LSPIV camera images. . . . 104
Figure 6.19 Free surface velocity variation for cases $n_x=1$ at 3 different time step. Black surfaces illustrate the obstacles position. . . . 105

Figure 6.20 Free surface velocity variation for cases $n_x = 0$ and 2 at 3 different time step. Black surfaces illustrate the obstacles position. . . . 106
Figure 6.21 Free surface velocity variation for cases $n_x = 3$ at 3 different time step. Black surfaces illustrate the obstacles position. . . . 107
Figure 6.22 Illustration of the hydraulic jump development, visible at $x = [8.8, 9]$ m, for case $3-10-2-10$ at 3 different time step. LSPIV vectors are superposed to background images corresponding from the LSPIV camera at the first time step of the averaged time. . . . 108
Figure 6.23 Horizontal velocity retrieved from LSPIV at positions A1, A2, A3, A4, A5 and A6 for cases (a) $1-05-2-10$ and (b) $1-20-2-10$. . . . 108
Figure 6.24 Horizontal velocity retrieved from LSPIV at positions A1, A2, A3, A4, A5 and A6 for cases (a) $3-05-2-10$ and (b) $3-20-2-10$. . . . 109
Figure 6.25 Energy head evolution for case 0 at positions A1, A2, A3, A4 , A5 and A6. . . . 109
Figure 6.26 Energy head evolution at position A1 for cases (a) $n_x = 1$ and (b) $n_x = 3$. . . . 110
Figure 6.27 Relative urban areas impact for the energy head E' at position A6 related to case 0 for cases (a) $n_x = 1$, (b) $n_x = 2$ and (c) $n_x = 3$. . . . 110
Figure 6.28 Cases $n_x = 1$. Relative urban areas impact for (a) the water depth h' and (b) the free surface velocity V' at position A6 related to case 0. . . . 111
Figure 6.29 Cases $n_x = 3$. Evolution of (a) the water depth h' and (b) the free surface velocity V' downstream of the urban area at position A6. . . . 111
Figure 6.30 Cases $n_x = 2$. Relative urban areas impact for (a) the water depth h' and (b) the free surface velocity V' at position A6 related to case 0. . . . 112
Figure 6.31 Top view of the configurations with $n_x = 0$, 1, 2 and 3 and $l_x = 0.20$ m. . . . 113
Figure 6.32 Cases $l_x = 0.05$ m. Evolution of (a) the water depth h' and (b) the free surface velocity V' downstream of the urban area at position A6. . . . 113
Figure 6.33 Cases $l_x = 0.15$ m. Evolution of (a) the water depth h' and (b) the free surface velocity V' downstream of the urban area at position A6. . . . 114
Figure 6.34 Cases $l_x = 0.05$ m. Evolution of the water depth profile (y = 0 m) at times (a) t = 5 s, (b) t = 10 s, (c) t = 15s, and (d) t = 20 s. . . . 114
Figure 6.35 Variation of street number. Time variation of the relative energy head E' related to case 0 at position A6 for cases (a) $l_x = 0.05$ m, (b) $l_x = 0.10$ m, (c) $l_x = 0.15$ and (d) $l_x = 0.20$ m. . . . 115
Figure 6.36 Temporal variation at position A6 for (a) water depth h (m), (b) velocity magnitude V_{xy} (m/s) and (c) energy head E (m) for all studied urban parameters. . . . 116
Figure 6.37 Top view of the four configurations without cross street ($n_y = 0$). . . . 117
Figure 6.38 Superposition of cases with $n_x = 3$ and $n_y = 0$ for all street width l_x. . . . 117
Figure 6.39 Top view of the four configurations with one cross street to study the influence of the streets along the y-axis. . . . 118
Figure 6.40 Water depth comparison for cases $n_y = 0$ at positions (a) A1, (b) A2, (c) A3, (d) A4, (e) A5 and (f) A6. . . . 119
Figure 6.41 Water depth comparison between cases $3-05-2-10$ and $3-05-0-0$ at positions (a) A5 and (b) A6. . . . 120
Figure 6.42 Water depth comparison between cases $3-10-2-10$ and $3-10-0-0$ at positions (a) A5 and (b) A6. . . . 120
Figure 6.43 Relative water depth h' of cases $n_y = 2$ related to cases with $n_y = 0$ at positions (a) A5 and (b) A6. . . . 121
Figure 6.44 Comparison of the water depth at position x = 8 m from the IAM analysis between $n_y = 0$ and 2 for cases (a) $l_x = 0.05$ m and (b) $l_x = 0.20$ m. . . . 121
Figure 6.45 Relative urban areas impact for the free surface velocity V' of cases with $n_y = 3$ at positions (a) A3, (b) A4, (c) A5 and (d) A6 related to cases with $n_y = 0$. . . . 121
Figure 6.46 Free surface velocity variations for cases $n_y = 0$ at 3 different time step. Black surfaces illustrate the obstacles position. . . . 122
Figure 6.47 Free surface velocity comparison between cases $n_y = 2$ and cases $n_y = 0$ at 3 different time step. Black surfaces illustrate the obstacles position for cases $n_y = 2$. White surfaces illustrate the obstacles position for cases $n_y = 0$. . . . 123
Figure 6.48 Cases $l_x = 0.10$ m. Water depth comparison for four l_y values at position (a) A1, (b) A2, (c) A3, (d) A4, (e) A5 and (f) A6. . . . 125

Figure 6.49 Cases $l_x = 0.20$ m. Water depth comparison for four l_y values at position (a) A1, (b) A2, (c) A3, (d) A4, (e) A5 and (f) A6. . . . 126
Figure 6.50 Free surface velocity variations for cases $n_y = 1$ at different time step. Black surfaces illustrate the obstacles position. . . . 127
Figure 6.51 Free surface velocity comparison between various cross street parameters and case $n_y = 0$ at 3 different time step. Black surfaces illustrate the obstacles position for cases $n_y = 1$. White surfaces illustrate the obstacles position for cases $n_y = 0$. . . 128
Figure 6.52 Relative cross street impact for the energy head E' at position A6 related to case $n_y = 0$ for cases $n_x = 3$ and $l_x = 0.1$ m at positions (a) A3, (b) A4, (c) A5 and (d) A6. . . . 129
Figure 6.53 Relative cross street impact for the energy head E' at position A6 related to case $n_y = 0$ for cases $n_x = 3$ and $l_x = 0.2$ m at positions (a) A3, (b) A4, (c) A5 and (d) A6. . . . 130
Figure 6.54 Comparison of the free-surface profile $\frac{h}{h_0}$ in central longitudinal street at $t = 5$ s between (a) case $3-05-2-10$ and (b) $4-10-4-10$ from Soares-Frazão *et al.* (2008) [53]. . . . 131
Figure 6.55 Comparison of the free-surface profile $\frac{h}{h_0}$ in central longitudinal street at $t = 10$ s between (a) case $3-05-2-10$ and (b) $4-10-4-10$ from Soares-Frazão *et al.* (2008) [53]. . . . 131
Figure 7.1 Schematic view of the studied configurations with (a) $n_x = 1$ and (b) $n_x = 3$. Each axis grey dash represents the centre of an individual cell, and each black dash is plotted every 10 cells for enhanced clarity. Position of probes A5 and A6 is also illustrated. . . . 134
Figure 7.2 Numerical mesh refinement along the (a) x-axis, (b) y-axis and (c) z-axis. Each black line represents the centre of an individual cell, except along the (a) x-axis, where black lines are plotted every 10 cells for enhanced clarity. . . . 135
Figure 7.3 Evolution of the time interval for case $3-10-2-10$. . . . 135
Figure 7.4 Case $3-15-2-10$. Water height comparison downstream of the urban area at positions (a) A5 and (b) A6 between wave gauge measurements (blue line) and the numerical model (black dashed line). . . . 136
Figure 7.5 Case $1-20-2-10$. Water height comparison downstream of the urban area at positions (a) A5 and (b) A6 between wave gauge measurements (blue line) and the numerical model (black dashed line). . . . 137
Figure 7.6 Void fraction distribution for case $1-20-2-10$ at (a) $t = 5$ s and (b) $t = 20$ s along $y = 0$. Black lines represents A5 and A6 position. . . . 137
Figure 7.7 Case $3-20-2-10$. Water height comparison downstream of the urban area at positions (a) A5 and (b) A6 between wave gauge measurements (blue line) and the numerical model (black dashed line). . . . 137
Figure 7.8 Case $1-05-2-10$. Water height comparison downstream of the urban area at positions (a) A5 and (b) A6 between wave gauge measurements (blue line) and numerical model (black dashed line). . . . 138
Figure 7.9 Void fraction distribution for case $1-05-2-10$ at $t = 9$ s along $y = 0$. Black lines represents A5 and A6 position. . . . 138
Figure 7.10 Case $3-05-2-10$. Water height comparison downstream of the urban area at positions (a) A5 and (b) A6 between wave gauge measurements (blue line) and numerical model (black dashed line). . . . 139
Figure 7.11 Case $3-10-2-10$. Water height comparison downstream of the urban area at positions (a) A5 and (b) A6 between wave gauge measurements (blue line) and numerical model (black dashed line). . . . 139
Figure 7.12 Void fraction distribution for case $3-10-2-10$ at $t = 20$ s along $y = 0$. Black lines represents A5 and A6 position. . . . 139
Figure 7.13 Water height visualisation (clear blue) at different time steps for case $3-05-2-10$ (side view). Black lines represents A5 and A6 position. Grey surfaces represents the cube. Dark blue surfaces corresponds to $y = 0$ m and $\alpha \leq 0.5$. . . . 140
Figure 7.14 Water depth profile for case $3-05-2-10$ at four different time steps. . . . 141
Figure 7.15 Water depth profile for case $3-10-2-10$ at four different time steps. . . . 141
Figure 7.16 Water depth profile for case $3-15-2-10$ at four different time steps. . . . 142
Figure 7.17 Water depth profile for case $3-20-2-10$ at four different time steps. . . . 142

Figure 7.18 Energy head E profiles along $x = 9$ m for cases with $n_x = 3$ at three different time steps. . . . 143
Figure 7.19 Energy head E profiles along $x = 9$ m for cases with $n_x = 1$ at three different time steps. . . . 144
Figure 7.20 Cases $n_x = 3$. Spatially averaged numerical energy head $\langle E \rangle$ between $-0.5 > y > 0.5$ along (a) $x = 8.6$ m, (b) $x = 8.8$ m and (c) $x = 9$ m at three different time steps. . . . 144
Figure 7.21 Street number impact on the spatially averaged numerical energy head $\langle E \rangle$ between $-0.5 > y > 0.5$ along $x = 9$m at (a) $t = 4$ s, (b) $t = 9$ s and (c) $t = 14$ s. . . . 145
Figure 7.22 Relative difference of the integrated energy head ($\sqrt{(E_{A6} - E_{A1})^2}$ / E_{A1} [-]) over sections A6 and A1 related to the street size for cases (a) $n_x = 1$ and (b) $n_x = 3$. 146
Figure 7.23 Water depth visualisation for cases (left) $3-05-2-10$ and (right) $3-20-2-10$. (Top view) at (a) $t = 4$ s, (b) $t = 9$ s and (c) $t = 14$ s for $\alpha \leq 0.5$. . . . 147
Figure 7.24 Water depth comparison for case $1-05-2-10$ with and without channel side walls at position (a) A5 and (b) A6. . . . 147
Figure 7.25 Water depth comparison for case $3-05-2-10$ with and without channel side walls at position (a) A5 and (b) A6. . . . 148
Figure 7.26 Water depth visualisation for case $1-05-2-10$ (top view) at (a) $t = 4$ s, (b) $t = 9$ s and (c) $t = 14$ s for $\alpha \leq 0.5$. . . . 148
Figure A.1 Geometry of the urban form $2-10-2-10$ and definition of the parameters characterising urban forms in the manuscript. . . . 156
Figure A.2 Top view of the configurations studied and probes locations in Chapter 5. . . . 158
Figure A.3 Top view of the configurations with various longitudinal street number/width and probes locations studied in Chapter 6. . . . 159
Figure A.4 Top view of the configurations with no lateral streets and probes locations studied in Chapter 6. . . . 160
Figure A.5 Top view of the configurations with various lateral street width and probes locations studied in Chapter 6. . . . 160
Figure B.1 Illustration of the graphical interface of the acquisition program. . . . 162
Figure C.1 Illustration of the calibration and ROI definition steps of the Image Analysis Measurement (IAM) program. . . . 164
Figure C.2 Example of impact measurement using the Image Analysis Measurement (IAM) program. . . . 165
Figure C.3 Example of profile detection using the Image Analysis Measurement (IAM) program. . . . 166
Figure D.1 Free surface velocity evolution for case 0. Black surfaces illustrate the obstacles position. . . . 169
Figure D.2 Free surface velocity evolution for case $0-0-0-0$. Black surfaces illustrate the obstacles position. . . . 170
Figure D.3 Free surface velocity evolution for case $1-0-1-0$. Black surfaces illustrate the obstacles position. . . . 171
Figure D.4 Free surface velocity evolution for case $2-10-2-10$. Black surfaces illustrate the obstacles position. . . . 172
Figure D.5 Free surface velocity evolution for case $4-0-4-0$. Black surfaces illustrate the obstacles position. . . . 173
Figure D.6 Water height comparison at position A2 between wave gauge measurements (black dashed line) and numerical model (blue line) for cases $0-0-0-0$, $1-0-1-0$, $2-10-2-10$ and $4-0-4-0$. . . . 174
Figure D.7 Water height comparison at position A3 between wave gauge measurements (black dashed line) and numerical model (blue line) for cases $0-0-0-0$ and $2-10-2-10$. . . . 174
Figure D.8 Water height comparison at position A4 between wave gauge measurements (black dashed line) and numerical model (blue line) for cases $0-0-0-0$ and $2-10-2-10$. . . . 175
Figure D.9 Water height comparison at position A5 between wave gauge measurements (black dashed line) and numerical model (blue line) for cases $0-0-0-0$, $1-0-1-0$, $2-10-2-10$ and $4-0-4-0$. . . . 175

Figure E.1 Cases $n_x = 1$. Evolution of the water depth profile (y = 0 m) at times (a) t = 5 s, (b) t = 10 s, (c) t = 15 s, and (d) t = 20 s. Grey rectangles represent cubes position. . . . 176
Figure E.2 Cases $n_x = 2$. Evolution of the water depth profile (y = 0 m) at times (a) t = 5 s, (b) t = 10 s, (c) t = 15 s, and (d) t = 20 s. Grey rectangles represent cubes position. . . . 177
Figure E.3 Cases $l_y = 0.10$ m. Evolution of the water depth profile (y = 0 m) at times (a) t = 5 s, (b) t = 10 s, (c) t = 15s, and (d) t = 20 s. . . . 177
Figure E.4 Cases $l_y = 0.15$ m. Evolution of the water depth profile (y = 0 m) at times (a) t = 5 s, (b) t = 10 s, (c) t = 15s, and (d) t = 20 s. . . . 178
Figure E.5 Cases $l_y = 0.20$ m. Evolution of the water depth profile (y = 0 m) at times (a) t = 5 s, (b) t = 10 s, (c) t = 15s, and (d) t = 20 s. . . . 178
Figure E.6 Images of the water jet at t = 1.1 s for cases $l_x = 0.05$ (b, c, d). . . . 179
Figure E.7 Images of the water jet at t = 1.1 s for cases $l_x = 0.20$. . . . 180
Figure E.8 Evolution of the water depth at x = y = 8 m from the IAM analysis for cases (a) $l_x = 0.05$ m and (b) $l_x = 0.20$ m. . . . 180
Figure E.9 Water depth comparison between cases $3-15-2-10$ and $3-15-0-0$ at positions (a) A5 and (b) A6. . . . 181
Figure E.10 Water depth comparison between cases $3-20-2-10$ and $3-20-0-0$ at positions (a) A5 and (b) A6. . . . 181
Figure E.11 Evolution of the head loss calculated between position A1 and A6 for cases (a) $n_x = 1$ and (b) $n_x = 3$. . . . 181
Figure F.1 Case $1-05-2-10$. Water height comparison at positions (a) R1, (b) R2, (c) A1, (d) A2, (e) A3 and (f) A4 between wave gauge measurements (blue line) and numerical model (black dashed line). . . . 182
Figure F.2 Case $3-05-2-10$. Water height comparison at positions (a) R1, (b) R2, (c) A1, (d) A2, (e) A3 and (f) A4 between wave gauge measurements (blue line) and numerical model (black dashed line). . . . 183
Figure F.3 Case $3-10-2-10$. Water height comparison at positions (a) R1, (b) R2, (c) A1, (d) A2, (e) A3 and (f) A4 between wave gauge measurements (blue line) and numerical model (black dashed line). . . . 184
Figure F.4 Case $3-15-2-10$. Water height comparison at positions (a) R1, (b) R2, (c) A1, (d) A2, (e) A3 and (f) A4 between wave gauge measurements (blue line) and numerical model (black dashed line). . . . 185
Figure F.5 Case $1-20-2-10$. Water height comparison at positions (a) R1, (b) R2, (c) A1, (d) A2, (e) A3 and (f) A4 between wave gauge measurements (blue line) and numerical model (black dashed line). . . . 186
Figure F.6 Case $3-20-2-10$. Water height comparison at positions (a) R1, (b) R2, (c) A1, (d) A2, (e) A3 and (f) A4 between wave gauge measurements (blue line) and numerical model (black dashed line). . . . 187

LIST OF TABLES

Table 2.1 Setup characteristics and wave scenarios in experimental investigations of dam-break flow in rectangular channels. . . . 9
Table 2.2 Experimental investigations of dam-break flow in rectangular channels. . . . 11
Table 2.3 Previous experimental studies of unsteady flow over idealised urban areas: Setup characteristics. . . . 14
Table 2.4 Previous experimental studies of unsteady flow over idealised urban areas: Cases studies. . . . 14
Table 2.5 Previous experimental studies of unsteady flow over idealised urban areas: Analysed flow variables. . . . 15
Table 2.6 Previous experimental studies on the influence of urban forms on steady flows. . 17
Table 3.1 Summary of the advantages and disadvantages of 2D and 3D models for dam-break flow over complex topography applications. . . . 23
Table 3.2 Computation time comparison between TELEMAC-2D and code_saturne. . . . 33
Table 4.1 Test cases of the gate width study . . . 41
Table 4.2 Advantages and disadvantages of different measurement techniques for fast transient flow. . . . 55
Table 5.1 Parameters characterising the configurations studied. . . . 59
Table 5.2 List of probe types and locations (m). . . . 60
Table 5.3 Summary of the parameters used for the LSPIV analysis in Fudaa-LSPIV [130]. . 60
Table 5.4 Summary of the filter parameters used for the LSPIV analysis. . . . 61
Table 5.5 Summary of the parameters used for image analysis measurement program (Appendix C). . . . 61
Table 5.6 Evolution of the splash-up size over time. . . . 65
Table 5.7 Evolution of the wake zone size over time. . . . 65
Table 5.8 Interval weight (%) of the velocity variation (%) at 3 different time steps. . . . 67
Table 5.9 Summary of the computational time for all studied urban forms. . . . 75
Table 5.10 Summary of the computational time for case $2-10-2-10$ with different turbulence models. . . . 82
Table 5.11 Case $2-10-2-10$. Interval weight (%) of the relative velocity variation (%) between experimental data and numerical model for 3 different turbulence closure models. . . . 83
Table 6.1 Summary of the parameters used for the LSPIV analysis in Fudaa-LSPIV [130]. . 90
Table 6.2 Summary of the filter parameters used for the LSPIV analysis. . . . 90
Table 6.3 Summary of the parameters used in the image analysis measurement program (Appendix C). . . . 91
Table 6.4 List of probe types and locations (m). . . . 93
Table 6.5 Number of experiments performed. . . . 93
Table 6.6 Parameters characterising urban forms to study the influence of the streets along the x-axis. . . . 95
Table 6.7 Arrival time (s) of the wake zone at position A6 for the studied urban parameters $(n_x - l_x - 2 - 10)$. . . . 112
Table 6.8 Parameter characterising urban forms : the lateral urban size L_y. . . . 113
Table 6.9 Parameters characterising urban forms to study the influence of the streets along the y-axis. . . . 118
Table 7.1 Summary of the computational time for all studied urban forms. . . . 136
Table A.1 Parameters characterising urban forms in the manuscript. . . . 157

NOMENCLATURE

Acronyms

1D	One-dimensional
2D	Two-dimensional
3D	Three-dimensional
ADV	Acoustic Doppler Velocimetry
ANRT	Association Nationale de la Recherche et de la Technologie
ASN	Autorité de Sûreté Nucléaire
AWG	Acoustic Wave Gauge
CFD	Computational Fluid Dynamics
CFL	Courant–Friedrichs–Lewy condition
CIFRE	Convention Industrielle de Formation par la Recherche
CR	Rectangular Channel with reservoir
DNS	Direct Numerical Simulation
EDF	Électricité De France
EPR	European Pressurised Reactor
EPR2	Evolutionary Power Reactor 2
FC	Floodplain channel
FEM	Finite Element Method
FG	Flap Gate
FOV	Field Of View
GRP	Ground Reference Points
HSG	Horizontal Sluice Gate
IA	Interrogation Area
IAM	Image Analysis Measurement
LES	Large Eddy Simulation
LHSV	Laboratoire d'Hydraulique Saint-Venant
LNHE	Laboratoire National d'Hydraulique et Environnement
LSPIV	Large-Scale Particle Image Velocimetry
M-CICSAM	Modified Compressive Interface Capturing Scheme for Arbitrary Meshes
MPS	Moving Particle Semi-implicit
MWG	Mechanical Wave Generator
NI	National Instrument Corporation
NVD	Normalised Variable Diagram

PDB	Partial Dam-Break
PFV4	Photron FASTCAM Viewer 4
PIV	Particule Image Velocimetry
PTV	Particule Tracking Velocimetry
PVC	Polyvinyl Chloride
R&D	Research and Development
RANS	Reynolds Averaged Navier-Stokes
ROI	Region Of Interest
RW	Rectangular Wave maker channel
RWG	Resistive Wave Gauge
SA	Search Area
SPH	Smoothed-Particle Hydrodynamic
SW	Shallow Water
TDB	Total dam-break
TDH	Transducteur De Houle
TLD	Tracking, Learning and Detection tracker
TP	Tank with Partial opening and free outflow condition
UVP	Ultrasonic Velocity Profiler
VOF	Volume-Of-Fluid
VSG	Upstream Vertical Sluice Gate
WGP	Wave Generator Pump

Greek Symbols

α	Void fraction [-]
Δt	Time interval or Time step [s]
ϵ	Turbulent kinetic dissipation rate $[m^2 s^{-3}]$
μ	Dynamic viscosity $[kg\ m^{-1} s^{-1}]$
ν_t	Turbulent eddy viscosity $[m^2 s^{-1}]$
Ω	Volume $[m^3]$
ρ	Density $[kg\ m^{-3}]$
σ	Standard deviation [m]
$\underline{\underline{\sigma}}$	Stress tensor $[kg\ m^{-1} s^{-2}]$
$\underline{\underline{\tau}}$	Viscous stress tensor $[kg\ m^{-1} s^{-2}]$

Latin Symbols

$\mathcal{F}_i$	List of faces of cell i
$\mathcal{G}$	Turbulent kinetic energy gravity production term $[m^2 s^{-3}]$
$\mathcal{P}$	Turbulent kinetic energy shear stress production term $[m^2 s^{-3}]$

$\mid \Omega_i \mid$	Volume of the i-th cell
$\mid \underline{u} \mid$	Magnitude of the depth-averaged flow velocity vector $[m\ s^{-1}]$
$\underline{\underline{I}}$	Identity tensor [-]
$\underline{F}_f$	Friction law $[m\ s^{-2}]$
$\underline{S}_f$	Outward normal vector of the face f of the cell Ω_i [-]
$\underline{u}$	Depth-averaged flow velocity vector $[m\ s^{-1}]$
ξ	Fluctuation level [pix]
C	Chézy friction coefficient $[m^{1/2}/s]$
C_γ	Drift flux factor [-]
$E' = \frac{E_{n_x - l_x - n_y - l_y}}{E_0}$	Energy head of case $n_x - l_x - n_y - l_y$ ($E_{n_x - l_x - n_y - l_y}$) related to the energy head of case 0 (E_0) [-]
$E = \frac{V_{xy}^2}{2 \times g} + h$	Energy head [m]
f_{acq}	Frequency acquisition $[s^{-1}]$
fps	Frame per second [-]
g	Gravitational acceleration $[m\ s^{-2}]$
H	Characteristic water depth [m]
h	Water depth [m]
$h' = \frac{h_{n_x - l_x - n_y - l_y}}{h_0}$	Water depth of case $n_x - l_x - n_y - l_y$ ($h_{n_x - l_x - n_y - l_y}$) related to the water depth of case 0 (h_0) [-]
h_0	Initial water depth in the reservoir [m]
h_1	Downstream water depth in the reservoir [m]
k	Turbulent kinetic energy $[m^2 s^{-2}]$
L	Length of the channel [m]
l_c	Obstacle horizontal length [m]
L_r	Reservoir length [m]
l_s	Street width [m]
L_x	Total length of the urban forms along the x-axis [m]
l_x	Width of the streets along the x-axis [m]
L_y	Total length of the urban forms along the y-axis [m]
l_y	Width of the streets along the y-axis [m]
M_k	Interfacial forces $[N\ m^{-1}]$
$n = h^{1/6}/C$	Manning coefficient $[s\ m^{-1/3}]$
n_x	Number of streets along the x-axis [-]
n_y	Number of streets along the y-axis [-]
N_{config}	Number of obstacle configurations [-]
N_{probe}	Number of probe locations [-]

p	Total pressure [Pa]
r_0^*	Normalised residual threshold [-]
$R_b = \frac{W}{\text{breach width}}$	Breach width ratio [-]
S_b	Bottom slope [-]
s_x	Splash-up length along the x-axis [m]
s_y	Splash-up length along the y-axis [m]
ST_ε	Turbulent kinetic energy dissipation rate source term [-]
ST_k	Turbulent kinetic energy source term [-]
t	Time [s]
t_{acq}	Duration of the acquisition [s]
t_{gate}	Opening time of the gate [s]
u	Velocity component along the longitudinal x-axis [$m\ s^{-1}$]
u_r	Local relative velocity [$m\ s^{-1}$]
V	Velocity [$m\ s^{-1}$]
v	Velocity component along the longitudinal y-axis [$m\ s^{-1}$]
$V' = \frac{V_{xy(n_x - l_x - n_y - l_y)}}{V_{xy(0)}}$	Horizontal velocity of case $n_x - l_x - n_y - l_y$ related to the horizontal velocity of case 0 [-]
V_c	Characteristic flow velocity [$m\ s^{-1}$]
V_0	Velocity field of the reference dam break case called 0 [$m\ s^{-1}$]
V_{xy}	Horizontal velocity component [$m\ s^{-1}$]
V_x	Velocity component in the horizontal x-direction [$m\ s^{-1}$]
V_y	Velocity component in the horizontal y-direction [$m\ s^{-1}$]
W	Facility width [m]
w	Velocity component along the vertical z-axis [$m\ s^{-1}$]
W_r	Reservoir width [m]
w_x	Wake zone length along the x-axis [m]
w_y	Wake zone length along the y-axis [m]
Z_b	Elevation of the bed topography [m]
Z_s	Free surface elevation [m]

Mathematical Conventions

$\cdot$	Scalar product
$\frac{D}{Dt}$	Lagrangian derivative
div	Divergence operator
$\underline{\nabla}$	Gradient operator
$\otimes$	Tensor product
$\sum$	Sum

$\underline{\underline{R}}$	Tensor
$\underline{U}$	Vector

Dimensionless Numbers

$\mathrm{Fr} = V/(gH)^{0.5}$	Froude number

Subscripts

$3runs$	Standard deviation between three replicates
a	Air
acq	Acquisition
avg	Averaged
EXP	Experimental
$mean$	Averaged
$n_x - l_x - n_y - l_y$	Configuration names
NUM	Numerical
w	Water
x	Longitudinal direction of the experimental setup
y	Transversal direction of the experimental setup
z	Vertical direction of the experimental setup

1

INTRODUCTION

Contents

1.1 General context 2
1.2 Industrial context 4
1.3 Scope of the thesis 4
1.4 Methodology 5
1.5 Structure of the manuscript 5

1.1 GENERAL CONTEXT

The sudden failure of hydraulic structures, such as a dam or dike break, can lead to the rapid propagation of flood waves across large domains containing urban, industrial, and natural areas (Figure 1.1) [1]. Such event poses catastrophic risks to downstream populations, causing severe damage and destroying natural environments and ecosystems (Figure 1.2) [2–4]. The consequences of dam failures on populations can vary widely. In the worst-case scenario, they can reach hundreds of victims (e.g., the Malpasset dam break in France, 1959) or even thousands (e.g., the Banqiao dam break in China, 1975), depending on the scale and location of the disaster. Moreover, due to climate change and rapid urbanisation, the probability of flash floods has increased [5, 6] and their impact can be particularly severe [7–12]. Specifically, the increase in extreme rainfall events poses new challenges for water resource management [13], while the rapid expansion of urban areas increases the vulnerability of communities to flooding [14]. Therefore, to assess and mitigate these risks, it is essential to forecast the severity of flood wave propagation, especially throughout urban areas [15].

(a) **(b)**

Figure 1.1: (a) Flood of La Crenze in Saint Laurent le Minier (France, 2014), *source: EPTB Fleuve Hérault* [16]; (b) Flash floods in Rhineland-Palatinate (Germany, 2021), *source: Harald Tittel/dpa via AP* [17].

Numerical models are valuable tools for estimating flood hazards and risks in the case of extreme transient flooding, typically following a dam-break event [18]. Such approach has become increasingly attractive and popular due to advancements in computational capabilities [19], allowing for the processing of large datasets and the solving of complex mathematical models. Numerical simulation of floods in rural environments has become common practice and typically relies on one-dimensional (1D) or two-dimensional (2D) Shallow Water (SW) equations [20]. The simplifying assumptions used in these models, such as the hydrostatic pressure distribution and zero vertical velocity usually proves legitimate in rural environments. The accuracy of these models is mainly affected by the quality of the land topography input data [21–24] and the mesh size. On the contrary, floods in urban areas may exhibit more complex flow features at the scale of buildings, as well as significant spatio-temporal variations that modellers want to take into account. Most of the urban facilities divert the flow into multiple paths around buildings, intersections and street furniture, creating three-dimensional (3D) physical phenomena within the flow that cannot be neglected to accurately model floods at human scale. Current operational flood models, developed for large-scale applications, are unable to accurately predict such processes due to simplifying assumptions. These 2D or 1D models represent the impact of facilities on global flood dynamics by applying significant safety margins which are estimated using analytical-empirical parameterisations [19, 25]. The estimates in such models could be made more realistic with a better understanding of flow behaviour within urbanized areas.

Since the beginning of the century, significant effort has been made in developing reliable urban flood models [26], whose complexity gradually increased over time. In this scope, a balance between accuracy and computing time must be made. On one hand, simplified models may omit some key information, not reproducing local inundation features. On the other hand, more sophisticated numerical approaches and models can reproduce detailed flood information but are computationally expensive. In some cases they also require high fidelity input data that can be difficult to obtain (such as building layouts and pipe networks). Therefore, large-scale urban flood models represent a challenge due to the computational cost of processing complex input data for large areas and reproducing the intricate flow paths of the complex

3D phenomenon [27, 28]. Also, urban flood models require high-quality and accurate validation datasets for their development and validation [26, 29].

The validation of numerical models is generally performed using real-case event data. In the case of extreme urban flooding, field marks or aerial imagery are scarce due to the relative rarity of such phenomena and do not capture the spatial complexity and transient features of the flow, especially in urban areas [25]. Moreover, during extreme weather events, field measurements are challenging due to safety concerns for the experimentalists, difficulty in accessing the measurement zones and the unsuitability of expensive laboratory metrology for such extreme field conditions. Consequently, the validation of numerical flood wave models crucially misses real-case event data [1], which is essential for validating the calibration parameters of urban flood models. Field data can be completed with laboratory experiments, as they enable the use of advanced measurements techniques, producing detailed data under controlled conditions [30].

Figure 1.2: Devastating floods caused by the Mediterranean storm Daniel in Libya, resulting in dam-breaks and neighbourhood destruction in coastal areas (Derna in Libya, 2023), *source: Jamal Alkomaty / AP Photo / Picture alliance* [31].

Experimental physical modelling of fast transient flow at reduced scale is thus a widely used approach to provide insights into the flow characteristics, thanks to accurate and controlled measurements [25]. Indeed, under controlled conditions, a large number of quantities of interest related to transient flow can be measured. One may list the water depth, the 2D velocity field or 3D punctual velocity, extreme pressures on the obstacles and fast image acquisition of the flow. More recently, advancements in non-intrusive measurement techniques, which do not interfere with the flow, have extended the range and the accuracy of data that can be collected from fast transient flow [32]. However, experiments involving fast transient flow through urban areas limit metrology choices, which must have a high-frequency acquisition and be adapted to non-continuous measurement areas. Consequently, transient experiments often result in the omission of relevant flow variables required to describe the complex flow processes.

In the past, a considerable number of laboratory tests on flood waves, resembling those following a dam-break, have been conducted, considering a variety of conditions and covering a wide range of flow scenarios [32]. Particularly, dam-break flow in rectangular channels (without obstacles) have been extensively investigated [33–41], providing high-quality datasets for the validation of flood models without obstacles. Additional experiments focused on characterising the flow around isolated obstacles of various shapes [34, 42–46]. More recently, laboratory experiments have been extended to characterise the flow at the urban district scale. While most experimental studies have been applied to steady flow crossing urban areas [47–52], recent experiments have been performed in fast transient flow conditions [53–56]. Yet, experimental datasets of flash floods influenced by urban forms remain particularly scarce, especially at the district level. One reason, as mentioned earlier, is that fast transient flow in the presence of obstacles may prevent the use of some types of metrology, raising challenges in characterising the local flow within urbanised areas. Numerically, local wake or water jump zones are difficult to reproduce when using simplified models.

On the other hand, complex models may lack sufficient validation data and are more expensive, making their use more difficult in an industrial framework.

1.2 INDUSTRIAL CONTEXT

Électricité de France (EDF) is a global producer, distributor and supplier of electricity. In France, EDF mainly generates electricity through nuclear power and renewable energy sources. The LNHE (Laboratoire National d'Hydraulique et Environnement), department of EDF's R&D, has been contributing to strengthening nuclear safety against the risk of external flooding for over 20 years. The MOISE project aims to address the needs of EDF's nuclear engineering by enhancing the safety of the company current and future nuclear installations against the risks of external flooding, both in France and abroad. It also involves contributing to the safety demonstration for the protections of current existing installations, as well as the design and sizing of various protection structures for new nuclear projects. The requirements related to the safety of the installations are constantly evolving, challenging EDF to improve and innovate for the implementation of new technological solutions for current and future European Pressurised Reactor (EPR) projects. In recent years, new challenges related to external flooding have emerged and are detailed below:

- Taking into account the effects of climate change in the context of sizing new reactors (EPR2).
- Extending the life of current installations beyond 60 years and implementing adaptation strategies at the territorial level.
- Developing a new alert system for river sites to enable better real-time management strategies in the event of an extreme flood.
- Developing and applying new advanced study methods to optimise numerical studies (safety, sizing of installations, characterisation of hazards) and better control uncertainties related to the characterisation of extreme phenomena.

The robustness of the protection against the risk of external flooding of nuclear installations must be demonstrated, as defined by the Autorité de Sûreté Nucléaire (ASN) guide n°13 [57]. This guide defines eleven reference flooding scenarios and provides recommendations for their evaluation. The impact of urbanised areas is considered in two of these scenarios: 'failure of a water-retaining structure' (ROR) and 'large watershed flooding' (CGB). The objective of the document is to characterise very rare extreme phenomena (with a frequency of occurrence of the order of 10^{-4}) while also conservatively covering the uncertainties (statistical or deterministic) related to the characterisation of such hazards. The operational studies performed in this work shall contribute to a summary note, acting as the external flooding safety demonstration for nuclear installations.

Overall, the MOISE project is partly dedicated to enhancing EDF Group's knowledge of extreme flood phenomena. It involves a deeper understanding of the hazards through research in numerical and experimental modelling of physical processes and continuous updates of the state of the art. In this context, the present thesis has been carried out within the project and its financial support was provided by the french ANRT (Association Nationale de la Recherche et de la Technologie) with the CIFRE Grant 2021/0912.

1.3 SCOPE OF THE THESIS

Large-scale flood studies critically misses validation data to more realistically estimate the impact of urban areas on flood extent during extreme events. The 3D local phenomena induced by intricate urban forms on the flow path have been scarcely studied in laboratory, and their numerical reproduction poses challenges to current 3D models. To support the development and validation of more reliable operational flood models, additional experimental campaigns are needed to generate novel, high-quality validation datasets of local 3D phenomena that may occur within urbanised areas during extreme flood event. More precisely, this manuscript focuses on answering the following questions:

1. *Can experimental studies contribute to providing accurate and reliable supplementary validation datasets on the influence of urban forms on unsteady flooding?*

2. *Are Computational Fluid Dynamics (CFD) models sufficiently mature to reproduce such phenomenon and to provide accurate complementary data on the flow characteristics?*

3. *Can one extract generalised trends from various idealised urban layouts and apply them to engineering flood models?*

The main goal of the present research project is to develop a novel experimental setup to reproduce transient flow in presence of obstacles. Recent and adapted measurement techniques will be used to provide high-quality datasets. Additionally, the project aims to perform a parametric analysis on the influence of urban layout on unsteady urban flooding to support the development and validation of engineering flood models. The expected outcome, in addition to the new urban flood dataset, is to improve the physical understanding of dam-break flow in presence of idealised urban areas and to identify possible correlations between urban parameters and the flow processes.

1.4 METHODOLOGY

To provide answers to the previous stakes, the employed methodology integrates both experimental and numerical approaches. The main steps are illustrated in Figure 1.3 and defined below:

- Perform a literature review on past experimental studies to present the state-of-the-art experimental setups for dam-break flow, without obstacles, through a single obstacle and for steady/unsteady flow through idealised urban layouts (Figure 1.3, task 1.1). Such primordial step will ease and guide future choices regarding experimental metrology, setup geometry, and the urban forms to be studied.
- Compare different numerical flood models and select one to reproduce the observed phenomena (Figure 1.3, tasks 2.1 and 2.2).
- Perform numerical simulations for the sizing of the experimental setup (Figure 1.3, task 1.2).
- Implement and build the experimental setup, from the sizing of the geometry to the acquisition chain, to reproduce transient flow through various urban layouts (Figure 1.3, task 1.3).
- Carry out a preliminary experimental study on simple obstacle configurations and validate the experimental setup and protocol (Figure 1.3, task 1.4).
- Develop post-processing methods and program to analyse the raw experimental data (Figure 1.3, task 1.5).
- Validate the chosen numerical approach using experimental datasets from the literature and the preliminary experimental campaign (Figure 1.3, task 2.3 and 2.4).
- Based on the preliminary campaign, conduct a second experimental campaign, focusing on various idealised urban layouts with different urban parameters (Figure 1.3, task 3.1).
- Validate the chosen numerical approach on the second experimental campaign data and extend spatially the experimental dataset (Figure 1.3, task 3.2).
- Analyse the influence of various urban parameters, conclude on the influence of urban forms on flow variables and extract generalised trends from the studied configurations (Figure 1.3, task 3.3).

1.5 STRUCTURE OF THE MANUSCRIPT

The outline of the manuscript is the following:

First, Chapter 2 summarises past experimental studies on fast transient flows without obstacles or through different idealised urban forms. Different aspects, such as the setup geometries, measurement techniques and previously studied obstacle configurations, are discussed.

Then, two different numerical models are presented in Chapter 3. Both of them are compared to dam-break flow experiments. As a result, one of them is selected for the sizing of the experimental setup and the other for reproducing future experiments.

Next, the experimental setup designed to study repeatable unsteady dam-break flows through idealised urban areas is presented in Chapter 4. Following the sizing of the setup, the final geometry, measurement techniques and post-processing methods are described.

The preliminary experimental campaign is conducted in Chapter 5. Four simple obstacle configurations are studied to challenge the experimental protocol developed. Then, the obtained dataset is used to validate the selected numerical approach.

Taking into account the feedback from the previous campaign, the obstacle configurations are extended in Chapter 6 to 21 urban forms based on 4 urban parameters. The influence of the obstacle configurations on the flow is mostly studied downstream of the urban areas using water depth measurements, free surface velocity analysis and energy head calculations.

Finally, Chapter 7 numerically reproduces a selection of the urban forms studied experimentally. The simulations are used to spatially extend the experimental data, verify previously observed punctual tendencies and extract head loss coefficients.

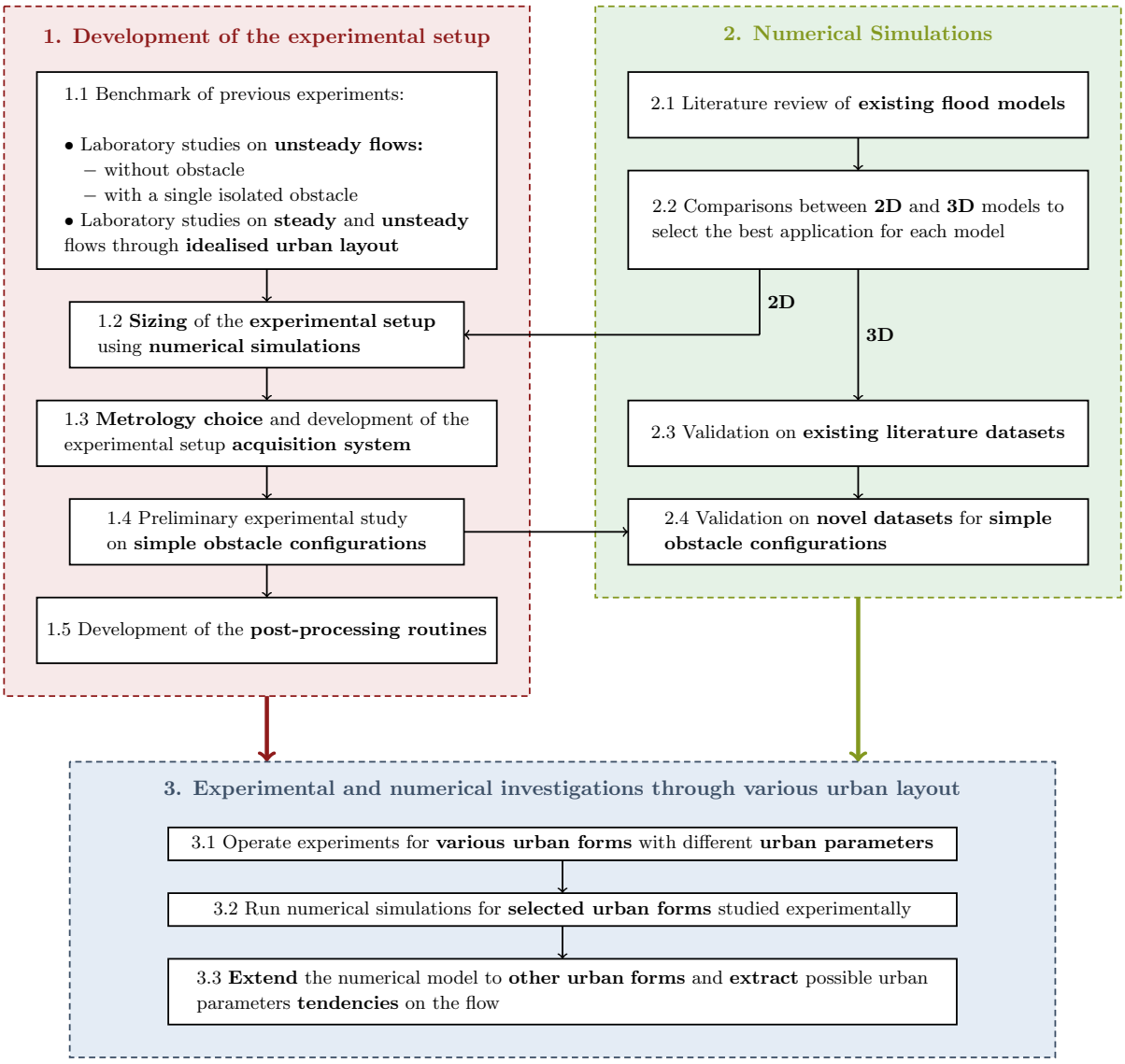

Figure 1.3: Methodology of the research project.

2

REVIEW OF EXPERIMENTAL INVESTIGATION OF FAST TRANSIENT URBAN FLOODING

Summary :
This chapter presents a literature review of past experimental studies on fast transient flows without obstacles or through different idealised urban forms. It describes the different setup geometries to generate dam-break waves and measurement techniques adapted to fast-transient flows are listed. Their advantages and disadvantages are also discussed. Additionally, existing experiments of fast transient flows in the presence of a single obstacle or urban forms are summarised, as well as their respective findings. Conclusions from this chapter form the basis for the sizing of the experimental setup, the selection of the metrology, and the studied urban parameters.

Contents

2.1 Introduction **8**
2.2 Investigation on dam-break waves without obstacles **8**
2.2.1 Setup characteristics 8
2.2.2 Instrumentation for dam-break flow studies 11
2.3 Laboratory investigations of dam-break wave in presence of a single obstacle **12**
2.4 Experimental investigation of dam-break waves through idealised urban areas **13**
2.5 Laboratory investigations on the influence of urban forms on steady flows **17**
2.6 Conclusion **18**

2.1 INTRODUCTION

Dam-break wave propagation in urbanised areas is a typical extreme flood with unsteady and rapidly varying flow, leading to complex three-dimensional physical phenomena. Besides providing valuable information of the flow, laboratory investigations are mandatory for the validation of numerical flood wave models, which crucially misses real-case event data. Over the last decade, improvements in instrumentation and monitoring for experimental studies have increased the types of data that can be collected for fast transient flow [32]. However, adding obstacles into the flow creates complex physical phenomena that prevents the use of advanced measurement techniques employed in basic dam-break flow studies. Consequently, experimental datasets of fast transient flow through various obstacle configurations are scarcely available.

This chapter presents a literature review of previous experimental studies on dam-break flow without obstacles, through a single obstacle and for unsteady and steady flows through idealised urban layouts. It provides a state-of-the-art overview of various experimental setups, metrology, and urban configurations used in the past. This review may benefit researchers who are setting up new experimental setups with advanced measurement methods, as well as those conducting numerical validation.

The chapter is organised as follows: Section 2.2 offers an overview of fundamental investigations on dam-break waves, detailing the various setup geometries and metrology employed. Section 2.3 briefly comments on experimental studies involving dam-break flow in the presence of a single obstacle. Section 2.4 provides a literature review of investigations of dam-break waves through idealised urban areas. Finally, Section 2.5 completes the previous sections with additional studies on the influence of urban forms in steady flow conditions.

2.2 INVESTIGATION ON DAM-BREAK WAVES WITHOUT OBSTACLES

Dam-break flow experiments have been studied extensively from the early 1900s to the present day. Those conducted at the beginning of the previous century were mostly qualitative [58–60]. Over this period, various test conditions, measuring techniques and experimental setups have been employed. The first datasets related to dam-break flow were mainly used to verify analytical Ritter's [61] and Stoker's [62] solutions of dam-break flow problem or numerical models of dam-break wave. This section focuses on experimental studies of dam-break flow without obstacles. First, the different channel geometries and the opening systems are discussed, followed by an analysis of the various measurement methods employed.

2.2.1 *Setup characteristics*

Channels with different sizes [63, 64], slopes [65, 66], or opening systems [67] have been used in the past to study dam-break flow. The most popular setup consists of horizontal rectangular channels with a gate that retains the water while the reservoir is filled. Table 2.1 references previous studies performed in rectangular channels with various tank sizes, shapes, slopes and opening systems. Note that this review does not list all existing experimental studies but still highlights the main trends used.

2.2.1.1 *Setup geometry*

The first part of Table 2.1 defines for all studies the different length and width of the channel and the reservoir as well as the slope of the setup. Each configuration presents its own advantages and disadvantages. For example, experiments conducted in long channels (longer than 10 meters) [39, 63, 65, 68, 69] allows for a better observation of the dam-break wave propagation and evolution. On the other hand, shorter channels (shorter than 5 meters) [64, 66, 70, 71] are generally easier to build and faster to operate. For most experimental setups, the outlets boundaries are open so that the dam-break wave does not reflect at the end of the channel. Still, some studies used closed outlet boundaries [35] to study the reflection of the wave with the walls. The slope of the channel is also a studied parameter. While most experimental setups are horizontal, some have a constant slope [69, 72] or even a variable slope [39, 65, 66]. Additionally, most of the experimental setups are performed with uniform coating to control the roughness of the bed. Although common materials used are cement, wood, and PVC, some studies use artificial grass [65] or different coatings to vary the roughness [68] of the bed. Finally, even though this review is limited to rectangular channels, some studies have performed dam-break experiments in

channels with different cross sections [73–76]. Exploring all these different types of setup characteristics is very important for developing accurate numerical models in different idealised channel geometries.

Table 2.1: Setup characteristics and wave scenarios in experimental investigations of dam-break flow in rectangular channels.

Reference	**Setup Characteristics**[1]				**Dam-break type**[2]			
	L [m]	W [m]	L_r [m]	S_b	Type[3]	Gate[4]	h_0 [m]	h_1 [m]
Lauber et Hager (1998) [39, 77]	14	0.5	3.5	0.5 - 0	TDB	VSG	0.3	0
Yang *et al.* (2010) [63]	18.1	1.6	10	0	PDB	N.A.	0.4	0.12
Aleixo *et al.* (2011) [70]	3	0.25	3	0	TDB	VSG*	0.4 - 0.325	0
LaRocque *et al.* (2013) [72]	3.94	0.18	3.37	0.93 %	TDB	VSG	0.35 - 0.25	0
Liu *et al.* (2017) [78]	5	0.4	1.5	0	TDB	VSG	0.2 - 0.16	0.04 - 0
Cordero *et al.* (2018) [66]	4	3	1	12° - 0	PDB	VSG	0.2 - 0.1	0
Liu *et al.* (2018) [79]	9.63	1	8.37	0	TDB	VSG	0.6	0.24 - 0
Stolle *et al.* (2019) [80]	8.45	1.5	21.55	0	TDB	FG	0.5 - 0.3	0
von Häfen *et al.* (2019) [67]	8.45	1.5	21.55	0	TDB	FG	0.7 - 0.3	0
Melis *et al.* (2019) [65]	11.6	0.5	N.A.	3 - 0 %	TDB	VSG	0.3 - 0.15	0
Wang *et al.* (2020) [81]	9.63	1	8.37	0	TDB	VSG	0.6 - 0.2	0.54 - 0.01
Espartel et Manica (2021) [82]	6	0.24	0.71	0	TDB	VSG	0.4 - 0.1	0.08 - 0
Kocaman *et al.* (2021) [35]	0.74	0.5	0.25	0	PDB	VSG	0.15	0.03 - 0
Nguyen-Thi *et al.* (2021) [83]	1.72	0.055	0.28	0	TDB	VSG	0.11	0.66 - 0
Takagi et Furukawa (2021) [71]	2.5	0.38	0.5	0	TDB	VSG	0.5	dry/wet
Xu *et al.* (2021) [69]	13	0.25	0.82	0.0031	TDB	N.A.	0.4	0.098 - 0
Ozmen-Cagatay *et al.* (2022) [64]	0.916	0.2	0.3	0	TDB	VSG	0.15	0
Nielsen *et al.* (2022) [68]	13	0.5	N.A.	0	TDB	N.A.	0.4	0.018

* Downward moving gate

N.A.: Not Available
[1] L: channel length; W: facility width; L_r: reservoir length; S_b: bottom slope
[2] h_0: upstream water depth; h_1: downstream water depth
[3] TDB: Total dam-break; PDB: Partial dam-break
[4] VSG: upward Vertical Sluice Gate; FG: Flap Gate

Remark : The setup characteristics listed in Table 2.1 determine the flow conditions, the access to the flow for the instrumentation and, depending on the size of the setup, the preparation time of each experiment. In fact, conducting dam-break experiments with dry bed conditions in 30-meter-long channels requires significantly more time for filling and stabilising the tank or drying the bed between experiments compared to 1-meter-long setups.

2.2.1.2 *Opening systems*

Once the reservoir is filled, the gate is opened using different mechanisms allowing the volume of water in the reservoir to propagate inside the channel. Various setups are used to generate dam-break waves in the literature and are detailed in the second part of Table 2.1. Two types of waves can be distinguished: a total and a partial dam-break wave, as illustrated in Figure 2.1.

In the case of a total dam-break [78, 80, 82, 83], a gate as large as the channel is removed to generate a "two-dimensional" (2D) dam-break wave (Figure 2.1a). In this type of study, the sides of the channel are typically made of glass to allow side observation of the flow and the use of image processing techniques. The geometry of such channels is generally narrow, allowing for excellent observation of the dam-break wave phenomenon and the use of advanced optical measurement techniques.

Partial dam-break flow [35, 63, 66], on the other hand, consist of a gate narrower than the reservoir and the downstream flooded area, as illustrated in Figure 2.1b. Such setup creates 'three dimensional' wave propagation downstream of the breach. Once the flow reaches the side walls, a reflecting wave is

generated, creating two hydraulic jumps that reunite downstream. Despite this reflection (that is hard to avoid in small scale experiments), such setup is considered similar to dam-break or dike events.

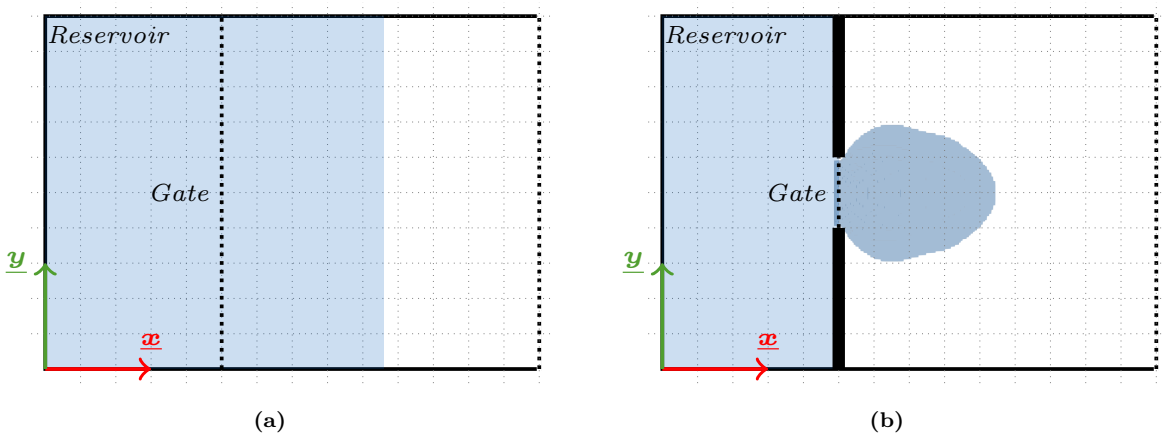

Figure 2.1: Schematic top view of rectangular experimental facilities for dam-break flow studies: (a) Total Dam-Break in a rectangular channel and (b) Partial Dam-Break in a rectangular channel. Blue area illustrates the water.

Remark : Partial dam-break setups are preferred when obstacles or specific features are added to the flooded area because larger (and longer) channels are needed to place them. For total dam-break setups, wider gates present challenges related to the height and time required to open them, as well as the waterproofing of the gate's joints.

Different types of gate opening mechanisms can be used to generate the dam-break wave. The two most used mechanisms are the upward and downward sluice gates [84]. Both methods consist of vertical moving walls and have their respective advantages and disadvantages. On one hand, an upward-moving gate [39, 67, 70] is generally easier to implement and does not interfere with the channel bed, but may not accurately replicate the dam-break process. On the other, a downward-moving gate [70] introduces a hole in the channel structure, leading to leakage issues and most existing setups do not have enough space underneath. However, the main advantage of a downward-moving gate, when working with sediments, is that it does not artificially bring sediments into the stream [85]. Note that other types of gates can be used, like horizontal sluice gate [55] or flap gate [56] that are very useful to control the flow condition downstream of the gate.

Remark : Most gates are activated using a weighted pulley system, but the pneumatic cylinder system ensures a controlled opening with a precisely measured trial start. On the other hand, pneumatic gates are generally slower than upward-lifted gates using a counterweight system.

Note : An important factor to take into account when performing dam-break flow studies is the control of the initial conditions. Given the unsteady phenomena, the repeatability of the experiments is crucial, as quantities are averaged over several trials and to enhance datasets, since not everything can be measured during the same test (e.g. imaging techniques cannot be applied when gauges are located in the field of view). To insure repeatability, monitoring the initial conditions of the test, such as the upstream water depth, the downstream bed condition, the opening time of the gate and the triggering of the various metrology devices, is mandatory. Using a leak-proof gate is also important to ensure similar bed conditions and that the initial water depth is maintained during the stabilisation of the reservoir.

2.2.2 *Instrumentation for dam-break flow studies*

Recent developments in non-intrusive measurement techniques have expanded the types of data that can be accurately collected from unsteady flow [86, 87]. Table 2.2 details the analysed flow variables and measuring techniques of previous dam-break studies listed in Table 2.1. This part of the review aims to provide information on the established instrumentation and types of data collected in these studies.

The first part of Table 2.2 details the studied parameters of each experiment. Dam-break flow investigations focus on various features of the flow, such as the roughness of the bed and the impact of the upstream water depth on the dam-break wave characteristics. In summary, some studies focused on the upstream water depth [65–67, 70, 72, 78, 80–82], the downstream conditions [35, 69, 71, 78, 79, 81–83], the slope of the channel [39, 65, 66], the viscosity of the fluid [64, 83], the roughness of the channel bed [36, 65, 68, 76] and finally, the channel cross section [74–76].

Table 2.2: Experimental investigations of dam-break flow in rectangular channels.

Reference	**Parameters studied**	**Analysed flow variables**[1]			**Measuring technique**[2]
		h	V	Other	
Lauber et Hager (1998) [39, 77]	Wave characteristics[3]	✓	✓	✗	Camera (50 fps)
Yang *et al.* (2010) [63]	Wave characteristics	✓	✓	Bottom pressure	Video camera; PIV Pressure probes
Aleixo *et al.* (2011) [70]	PTV paramameters	✓	✓	✗	Camera (100fps); PTV
LaRocque *et al.* (2013) [72]	Dam-break scenario[4]	✓	✓	✗	Acoustic wave gauges Ultrasonic velocity profilers
Liu *et al.* (2017) [78]	Dam-break scenario	✓	✗	✗	Camera (150 fps) Resistive wave gauges
Cordero *et al.* (2018) [66]	Bed slope	✓	✗	✗	Camera (100 fps)
Liu *et al.* (2018) [79]	Dam-break scenario	✓	✓	✗	Cameras (48 fps)
Stolle *et al.* (2019) [80]	Gate velocity	✓	✓	✗	Cameras (120/70 fps) Resistive wave gauges Propeller velocity flowmeter
von Häfen *et al.* (2019) [67]	Gate velocity	✓	✗	✗	Resistive wave gauges
Melis *et al.* (2019) [65]	Dam-break scenario over dense vegetation	✓	✗	✗	Cameras (30 fps)
Wang *et al.* (2020) [81]	Dam-break scenario	✓	✗	✗	Cameras (48 fps)
Espartel et Manica (2021) [82]	Dam-break scenario	✓	✗	✗	Cameras (240 fps)
Kocaman *et al.* (2021) [35]	Dam-break scenario in enclosed domain	✓	✗	✗	Camera (50 fps) Acoustic wave gauges
Nguyen-Thi *et al.* (2021) [83]	Fluid viscosity	✓	✗	✗	Camera (203 fps)
Takagi et Furukawa (2021) [71]	Gate velocity	✓	✗	Bottom pressure	Camera (2400 fps) Pressure sensors
Xu *et al.* (2021) [69]	Bed roughness	✓	✗	Shear stress	Acoustic wave gauges Shear plates
Ozmen-Cagatay *et al.* (2022) [64]	Fluid density	✓	✗	✗	Camera (60 fps)
Nielsen *et al.* (2022) [68]	Bed roughness	✓	✗	Shear stress	Acoustic wave gauges Shear plates

✓: Available
✗: Not available
[1] h: Water depth; V: Velocity
[2] PIV: Particle Image Velocimetry; PTV: Particle Tracking Velocimetry
[3] Wave characteristics: Wave velocity and depth in different setup configurations
[4] Dam-break scenario: Various initial upstream and downstream water depth scenarios

The second and third parts of Table 2.2 summarise the analysed flow variables and associated measuring techniques presented in each study. First, we can see that the water depth is always studied but the measuring techniques differs. As show in Table 2.1, most of the experiments are performed in narrow channels on total dam-break waves. Such setup allows for an easy optical access to the flow through the side wall. The water depth can then be optically measured through video cameras placed on the side walls [39, 63–66, 70, 71, 79, 81–83]. On the other hand, some studies use wave probes to measure the water depth evolution locally. This is specific for partial dam-break setups, where the water depth is not constant along the width of the setup (see Figure 2.1b). These studies often use resistive wave gauges [67, 78, 80], which are particularly fast and accurate (with a precision of about 0.1 mm) but are intrusive, potentially impacting the measurement, especially for fast transient phenomena with low water depth. Additionally, the development of faster acoustic wave gauges has enabled their application to fast transient phenomena such as dam-breaks, although they are slower and less accurate than resistive ones (with a precision about 1 mm).

The flow velocity is an additional feature that can be measured, either with punctual or field measurements. Earlier investigations have measured the front wave propagation velocity using video cameras [39, 77, 79]. Narrow and long channels are particularly suited for performing such wave propagation measurements. Others used local velocity gauges, such as Acoustic Doppler Velocimeters (ADV), which measure the three velocity components locally. However, the intrusiveness of these sensors can significantly disturb the flow, making the interpretation of results more difficult. Additionally, the variations between air environment (before the opening of the gate) and water environment (after) can lead to air bubbles being trapped on the ADV head, resulting in inaccurate values and low water depth (about 10 cm) downstream of the breach further complicates the use of such devices. More recently, optical velocity measurements, such as Particle Image Velocimetry (PIV) and Particle Tracking Velocimetry (PTV), have been applied to unsteady flow [63, 70]. Such techniques measure the velocity field by tracking the motion of groups of particles or individual particles, providing detailed information about their trajectories. Vertical velocity fields measurements can be performed using side-view cameras in total dam-break experiments [70]. In the case of non-homogeneous lateral velocity (partial dam-break experiments for example), PIV or PTV measurements can be performed on specific lateral profiles highlighted by a laser sheet. Such techniques require two perpendicular optical accesses to the flow and cannot be performed in traditional channels with non-transparent beds. Nevertheless, both measuring methods (PIV and PTV) can be applied to retrieve the velocity of the free surface, known as Large-Scale Particle Image Velocimetry (LSPIV). In this case, floating particles are added to the flow, allowing for the reconstruction of the free-surface flow trajectories. LSPIV measurements are easier to operate since they do not require laser or a second or side optical access to the flow.

Note : In steady flow conditions, time-averaging procedures such as ensemble averages can be applied to the instantaneous velocity fields acquired using optical techniques. The raw fields are first filtered to eliminate erroneous velocity vectors detected using low correlation thresholds, for example. Then, the filtered fields are averaged over the entire acquisition time. Even if most vectors in individual fields are filtered, the velocity information in the resulting time-averaged field may be complete. However, such time-averaging techniques cannot be applied to unsteady flow conditions, which limits their application in studying transient phenomena. But more recently, thanks to the development of faster video cameras, LSPIV techniques have been applied to unsteady flow conditions [88–90].

2.3 LABORATORY INVESTIGATIONS OF DAM-BREAK WAVE IN PRESENCE OF A SINGLE OBSTACLE

Experimental studies investigating dam-break waves interacting with singularities, such as isolated obstacles, have gradually increased in the literature. One of the challenges for numerical models, particularly shallow water (SW) ones, is to accurately reproduce the effects of singularities in the flow dynamics. Indeed, deviations from the hydrostatic pressure assumption are created in presence of such phenomena, which is hardly accounted for in shallow water models.

Various experimental setups with different geometries and wave generation mechanisms have been employed to study dam-break scenarios involving singularities. Most experiments involve rectangular channels with either total or partial breach openings. Also, the dam-break wave is generally generated using vertical sluice gates (see Subsection 2.2).

To assess the impact of singularities on flow dynamics, studies have investigated obstacle sizes, shapes and orientations. Some focused on the interaction of dam-break waves with vertical walls [91–93], most of the time conducted in narrow channels with total dam-break scenarios, providing detailed observations of the wave impact. Conversely, observations of flow patterns around single obstacles in wider channels with partial dam-break scenarios are more limited. The most studied shapes of obstacles include rectangular, circular and pyramidal forms [32], which can be either insubmersible (columns or pillars) [42, 44–46] or submersible (buildings) [43]. Furthermore, studies involving deformable [94, 95] or movable objects [96] have investigated damping effects and object transportation in fluid-structure interaction scenarios.

In dam-break experiments with single isolated obstacles, measurements of flow depth and velocity are typically taken at key locations, particularly around the obstacles [45]. Recent advancements in imaging techniques have facilitated measurements of free surface velocity and wave propagation. Additionally, new methods have been employed to measure hydrodynamic loads on entire obstacles or pressure impacts on structure faces [33, 97–100]. These datasets are essential for validating numerical models that assess hydrodynamic forces and other hydraulic variables, ensuring the reliability of structural assessments.

2.4 EXPERIMENTAL INVESTIGATION OF DAM-BREAK WAVES THROUGH IDEALISED URBAN AREAS

Flooding of urban areas has gained significant interest in the literature due to the high exposure of residential zones and the need to develop more accurate flood models. Table 2.3, 2.4 and 2.5 list experimental studies of dam-break flow through idealised urban areas, that are represented by one or many arrays of solid blocks with different sizes and orientations.

Table 2.3 lists the different setup characteristics of the experimental studies. Various channel types and wave generation systems have been used to reproduce unsteady flow. While some studies used regular setups resembling those used for basic dam-break studies (see section 2.2) [53, 56, 101, 102], other ones adapted river physical models [54] or floodplain channels [55] to perform dam-break experiments. The channel geometry needs to be carefully designed to avoid excessive hydrological interaction between the tank's side walls and the studied configurations. Reflected flows on the side walls may cause water to accumulate in the measurement area, leading to observed phenomena that are not directly induced by the studied configurations. On the other hand, real-case dam-break events may occur in valley environments with mountains on both sides of the flood wave and such specific flood condition also needs to be studied. One advantage of using floodplain channels [55, 103] or free outflow conditions [103] is that there are no close side walls downstream of the gate, preventing the flow reflection on the side walls. However, such setups are uncommon in hydraulic laboratories, where prismatic open channels (rectangle, trapezoid, triangle and circle cross-section) are more typical. Additionally, the length of the setup needs to be long enough to ensure that the effects of the obstacles on the downstream flow are observable. For partial dam-breaks, the breach width ratio must be carefully chosen so that the position of the reflected flow does not interferes with the studied area. Moreover, using long reservoirs allows sufficient space to place metrology upstream of the breach, that can be used to ensure the repeatability of various trials in addition to measurements downstream of the urban area. It provides valuable measurements for the numerical reproduction of the experimental flow conditions and allows for longer experiments with the same upstream flow condition. Finally, several opening systems are used. While some studies used classical opening systems generally employed for dam-break experiments (see section 2.2) [53, 101–103], other studies adopted wave maker channels [54, 104] to produce unsteady flow.

Remark : Constructing an experimental setup with a simple geometry (rectangular cross-section with homogeneous topography and bed roughness), a simple opening system (vertical sluice gate), with controlled initial bed condition (dry), and providing data of the flow conditions upstream of the gate is essential to help numerical modellers reproduce the experimental flow conditions.

Table 2.3: Previous experimental studies of unsteady flow over idealised urban areas: Setup characteristics.

Reference	Setup Characteristics[1]							
	Type[2]	L [m]	W [m]	L_r [m]	W_r [m]	S_b	R_b [-]	Gate[3]
Szydlowski *et al.* (2006) [103]	TP	6.75	3	3	3.5	0	6	VSG
Testa *et al.* (2007) [54]	RW	5	1.8	✗	✗	River topography	1	WGP
Soares-Frazão *et al.* (2008) [53]	CR	35.8	3.6	6.75	3.6	0	3.6	VSG
Kim *et al.* (2015) [55]	FC	30	30	5	50	0	30	HSG
Tomiczek *et al.* (2016) [104]	RW	45	4	✗	✗	1:10	1	MWG
Norin *et al.* (2017) [101]	CR	7	1.39	N.A.	N.A.	0	1	SG
Kusuma *et al.* (2019) [56]	CR	10	1	2	4	0	1	FG
Chumchan *et al.* (2020) [102]	CR*	0.984	0.484	0.24	0.485	0	4.84	VSG

* Closed outlet boundary

✗: Not applicable
[1] L: channel length; W: facility width; L_r: reservoir length; W_r: reservoir width; S_b: bottom slope; R_b: breach width ration (W / breach width); Gate: wave generation system
[2] TP: tank with partial opening and free outflow condition; CR: rectangular channel with reservoir; FC: floodplain channel; RW: rectangular wave maker channel
[3] VSG: upstream Vertical Sluice Gate; WGP: Wave Generator Pump; HSG: Horizontal Sluice Gate; MWG: Mechanical Wave Generator; FG: Flap Gate

Table 2.4 details the initial flow conditions and the parameters of the obstacle configurations. First, the dam-break type is defined by the initial flow water depth h_0, upstream of the breach and h_1, downstream of it. Various upstream water depths were tested, depending on the height of the setups and the opening sizes of the vertical sluice gates (the opening size of the gate should be superior to the upstream water depth to keep the free surface flow condition). The upstream flow condition defines the wave height and the emergence/submergence of the obstacles. The downstream water depth defines the bed condition as either dry ($h_1 = 0$ m) or wet ($h_1 > 0$ m). Dry bed condition ensures an exact reproduction between trials since wet bed condition may slightly vary between the trials.

Table 2.4: Previous experimental studies of unsteady flow over idealised urban areas: Cases studies.

Reference	Dam-Break Type[1]		Obstacle configurations[2]		
	h_0 [m]	h_1 [m]	Layout (n_x x n_y)	l_c [m]	l_s [m]
Szydlowski *et al.* (2006) [103]	0.21	0	5x4 streets	0.10	0.10
Testa *et al.* (2007) [54]	✗	wet	3x3 streets & associated staggered layout	0.15	0.15
Soares-Frazão *et al.* (2008) [53]	0.40	0.011	4x4 streets: aligned & oriented layout	0.3	0.1
Kim *et al.* (2015) [55]	0.3 - 0.45	0	1 anisotropic porosity layout	0.2	0.1 / 0.4
Tomiczek *et al.* (2016) [104]	✗	0	2x2 streets	0.4	0.2 - 0.4
Norin *et al.* (2017) [101]	0.225	0	1 staggered layout	0.1	0.178 / 0.18
Kusuma *et al.* (2019) [56]	0.2 - 0.3 - 0.4	0	4 (staggered) obstacle layouts	0.1	0.1
Chumchan *et al.* (2020) [102]	0.15	0	1x1 aligned obstacles	0.085	0.08 - 0.1

✗: Not applicable
[1] h_0: upstream water depth; h_1: downstream water depth
[2] n_x: number of streets along the x-axis; n_y: number of streets along the y-axis; l_c: obstacle horizontal length; l_s: street width

Remark : Particular attention should be given to control the upstream and downstream bed conditions, directly linked to the opening system (leakages at the gate impact the control of h_0 and h_1) and the filling system of the reservoir, to ensure repeatable dam-break experiments.

In the listed experiments (Table 2.4), idealised urban areas are used, composed of arrays of solid blocks arranged in different configurations and orientations. Obstacles' sizes are based on the flow conditions being studied, depending on whether they need to be emerged or submerged. Some studies consider insubmersible obstacle conditions [53], or submerged cubes [56, 101]. Also, the ratio between the obstacle length and the street width can be defined to fit realistic values (for example, the centre of Brussels [53]), while in other cases, it is chosen from a more subjective point of view, often being set to 1 and can be associated to realistic suburban districts values. The most studied urban parameters are aligned against staggered obstacle configurations [54]; orientation of the obstacles relative to the main direction of the dam-break wave [53, 102]; the initial flow conditions [55, 56]; and the street width [104]. However, none of the aforementioned unsteady experimental studies investigated the influence of specific urban parameters, such as the number or size of streets, on a basic dam-break wave in a simple geometric setup.

Table 2.5 details the parameters and quantities of interest studied. As demonstrated in Section 2.2, the main measured flow variables in dam-break experiments are the water depth (hydrographs or profiles) and the velocity. The first difference with the datasets provided by basic dam-break flow studies is in the water depth measurements. Adding obstacles into the flow creates a complex free surface near the urban form (with water jets during impact, or hollows and humps) that significantly complicates the measurements. Downstream of the breach, where the use of intrusive gauges isn't recommended or is impossible for low water depth, the discontinuity of the free surface challenges the use of acoustic gauges. Given these difficulties, some studies provide water depth profiles at selected times. Additionally, the number of punctual water depth measurements is crucial to provide a complete description of the flow inside and around the urban layout. Usually, a compromise is made between the number of probes used during the same experiment and the time allocated to perform several trials for additional positions.

Table 2.5: Previous experimental studies of unsteady flow over idealised urban areas: Analysed flow variables.

Reference	**Parameters studied**	**Analysed flow variables**[1]			
		h[2]	N_{probes}[3]	V	Other
Szydlowski *et al.* (2006) [103]	Flow characteristics	Temporal	10	✗	✗
Testa *et al.* (2007) [54]	Aligned/staggered	Temporal	10	✗	✗
Soares-Frazão *et al.* (2008) [53]	Orientation	Spatial	$\simeq 16$	Vector map*	✗
Kim *et al.* (2015) [55]	h_0	Temporal	17	✗	✗
Tomiczek *et al.* (2016) [104]	Street width	Temporal	6	✗	Forces on obstacle
Norin *et al.* (2017) [101]	Water flow rates	Temporal	2	Velocity profile	✗
Kusuma *et al.* (2019) [56]	h_0	Spatial	9	✗	✗
Chumchan *et al.* (2020) [102]	Orientation	✗	✗	✗	Flow images

* Acquisition frequency = 40 fps

✗: Not available
[1] h: Water depth; V: velocity
[2] Temporal: water depth hydrographs; Spatial: water depth profile at selected times
[3] N_{probes}: number of probe locations available

Studies focusing on velocity measurements in the presence of idealised urban areas remain scarce. Indeed, advanced optical velocity measurements, commonly performed on dam-break flow experiments with no obstacles, are complicated to execute in presence of urban layouts since setups are wider (to contain the configurations) and optical access to the flow inside the urban forms is challenging. However, Soares-Frazão *et al.* (2008) [53] performed PTV measurements to obtain the vector map of the free surface in the urban areas, highlighting the possibility of performing PTV and LSPIV measurements under such conditions.

The following provides further details regarding each experimental dam-break study in the presence of idealised urban areas:

Szydlowski *et al.* (2006) [103] studied a single urban configuration of 5x4 streets with aligned obstacles and compared the water height time history with numerical results. A splash-up was observed with a higher water level and reduced velocity upstream of the first row of obstacles, where the dam-break wave reflects against the buildings. The flow then suddenly accelerates along the longitudinal streets. Also, a recirculation zone was present downstream of each row of obstacle. Finally, a water-jet rising vertically

was observed just after the wave reflection against the first row of obstacles. The hydrostatic sensors placed to measure the water depth were not able to capture this effect.

Testa *et al.* (2007) [54] conducted experiments in a large and long outdoor channel with complex bottom topography, investigating two different city layouts: 3x3 streets with aligned obstacles and the associated staggered configuration. The experimental setup included a complex bottom topography and the dam-break wave was generated using a wave generator pump. The dataset obtained comprised water level hydrographs recorded at 10 locations using resistive gauges. During the experiments, the creation of a splash-up area upstream of the obstacle configuration was also observed. For both studied obstacle configurations, the splash-up was similar, and it was concluded that the building density in the experiment was high enough to make the city appear as a compact obstacle (i.e., an obstacle as large as the area occupied by the idealised urban configurations).

Soares-Frazão *et al.* (2008) [53] used a rectangular channel with a partial opening to produce the dam-break wave. Two idealised urban layouts with insubmersible obstacles were studied: 4x4 streets with aligned obstacles and the same layout rotated by 22.5°. Main observations indicated that the splash-up area created upstream of the configurations was no longer symmetric once the urban layout was rotated and more local reflections in the streets were observed during the initial stages of the experiment. The experimental dataset was also compared with a two-dimensional shallow-water model, particularly focusing on water-surface profiles and the free surface vector map. A numerical mesh sensitivity analysis was performed, showing that the mesh with about 10 cells over the width of the streets gives an accurate representation of the wave structure.

An anisotropic porosity area composed of arrays of buildings with unevenly spaced obstacles in the cross-flow and along-flow directions was studied by Kim *et al.* (2015) [55]. The laboratory experiments were conducted in a tank separated from the reservoir by a sliding gate with a long opening time. The water depth hydrographs were compared with different porosity models.

Tomiczek *et al.* (2016) [104] conducted wave experiments through 2x2 streets with aligned obstacles for different street widths. The experiments varied offshore wave characteristics and onshore structural configurations and the dataset included water depth measurements and extreme pressures within and around the obstacles. The experiments were conducted in a rectangular wave maker channel with a bottom planar slope emerging on a flat beach. In this study, nine obstacle configurations were investigated, including a single obstacle, at different positions from the beach. Initial observations showed that the water surface profile was nearly identical to that in front of the single obstacle configuration. Notably, they observed that narrower streets increased the peak pressures on the first row of obstacles. Additionally, ADV measurements were affected by low water levels and breaking-wave turbulence. Consequently, due to signal noise, the ADV measurements were not conclusive.

Norin *et al.* (2017) [101] conducted experiments in a rectangular channel and tested a single staggered obstacles layout across the width of the channel. The dataset was then compared to a two-dimensional shallow-water model for each set of conditions. One of the objectives of the numerical model was to study the effect of the mesh size on the results. Simulations showed that meshes using a refinement of the order of the obstacles size lead to unrealistic results, suggesting a refinement of at least 3 cells per obstacle in the flow direction axis.

Kusuma *et al.* (2019) [56] studied a single obstacle, 3 aligned obstacles, 3/2 staggered buildings and 3/2/3 staggered buildings. Observations showed that the water depth in all configurations followed the same pattern but with different magnitudes.

Finally, Chumchan *et al.* (2020) [102] studied two obstacle configurations in a small enclosed domain. The urban configurations consisted of a 1x1 street layout aligned with the main direction of the flow and then rotated by 45°. High-quality images of the flow were provided and compared qualitatively with LES numerical simulations (Ansys Fluent and XFlow).

To improve the scientific community's understanding of the impact of urban areas on unsteady urban flooding, additional experimental studies can be be performed. Particularly, the comparison of specific urban parameters under the same flow conditions may help understand specific features of the flow.

Moreover, additional efforts are needed to develop and adapt advanced optical measurement techniques, such as LSPIV, to provide insights into the complex flow patterns within the streets.

2.5 LABORATORY INVESTIGATIONS ON THE INFLUENCE OF URBAN FORMS ON STEADY FLOWS

Experimental studies of dam-break flow through urban areas are significantly challenged by the fast transient phenomena that occur, making it difficult to use advanced measurement techniques typically employed in steady flow conditions. More precisely, each instantaneous velocity field obtained from PIV and PTV techniques, is often averaged over the entire acquisition time. Additionally, the use of high-velocity laboratory cameras is not mandatory in steady flow conditions. For the reasons listed above, optical measurement techniques are commonly used for long-duration urban flooding studies.

Table 2.6 lists some experimental studies on the influence of urban forms in steady flow conditions. The type of building layout and the number of tested configurations are detailed in the first part of the table, followed by the parameters studied and the analysed flow variables. In steady flow conditions, the experiments are not averaged between different trials but during an acquisition time determined by a convergence analysis of the flow variables. Thus, the experimental time required to study a single configuration is smaller in steady flow conditions compared to dam-break flow experiments, where the same trials need to be repeated several times. Consequently, the number of tested configurations in each steady flow condition study is also greater.

Table 2.6: Previous experimental studies on the influence of urban forms on steady flows.

Reference	**Type of building layout**[1]		**Parameters studied**	**Analysed flow variables**	
	Layout (n_x x n_y)	N_{config}		h	V^2
Huang *et al.* (2014) [52]	2x3 streets	6	Blockage effect	✓	✗
Zhou *et al.* (2016) [51]	2 x [0,1,2,3,4] streets	5	Blockage effect	✗	PIV
Velickovic *et al.* (2017) [50]	4x4 streets	5	Orientation, street width, and flow discharge	✓	✗
Oukacine *et al.* (2019) [105]	6x118 streets	1	Emergence / submergence	✓	ADV & PIV
Doumic *et al.* (2021) [48]	2x2 streets & associated staggered layout	2	Emergence / submergence	✗	UVP
Li *et al.* (2021) [47]	1x2 streets	7	Urban forms	✓	LSPIV

[1] n_x: number of streets along the x direction; n_y: number of streets along the y direction; N_{config}: number of tested configurations
[2] PIV: Particle Image Velocimetry, ADV: Acoustic Doppler Velocimetry; UVP: Ultrasonic Velocity Profiler, LSPIV: Large-Scale Image Velocimetry

Among the studies, the blockage effect of the urban area on the flow was investigated [51, 52]. The influence of urban forms, street width, and orientation was also studied [47, 50], as well as the emergence or submergence of obstacles in the flow [48, 105]. The water depth was measured at different positions using both intrusive and non-intrusive gauges. Note that the challenges of acquisition frequency and non-continuous free surface encountered in unsteady flow condition are not present here, allowing experimentalists to use any type of water depth gauge. Optical velocity measurements were also performed [47, 51, 105], providing valuable velocity fields within and around the urban area.

Huang *et al.* (2014) [52] conducted an experiment to quantify the building drag resistance. A 2x3 streets layout with aligned obstacles of different sizes was studied, comparing six different blockage effects of the urban area. In this study, various water depth profiles were compared with two-dimensional simulations. A method was presented to modify the Manning's roughness coefficient to account for the blockage effect of buildings, which produced accurate results.

Zhou *et al.* (2016) [51] investigated the blockage effect in a simplified urban area through five obstacle configurations. Experiments were carried out in a rectangular recirculating channel and mean velocities were measured using a PIV measurement system. Water depths were determined using a digital image technique and tape mounted on the blocks. Results showed that water depth through the urban area

increases with larger blockage ratios and the wake zone downstream of the urban area extends with an increase in the Froude number. PIV measurements were only performed downstream of the urban area.

Then, Velickovic *et al.* (2017) [50] performed steady flow experiments in a rectangular and horizontal channel initially designed for dam-break flow [45]. To achieve steady conditions, the gate remained open and the discharge was regulated via a control system. A 4x4 streets layout was studied for different orientation and street widths. It was observed that the difference between the water depth upstream and downstream of the city increased with the discharge. Additionally, an isotropic configuration not aligned with the main flow direction resulted in a higher flow resistance compared to the same configuration aligned with it.

Oukacine *et al.* (2019) [105] performed velocity measurements inside a large area of obstacles (9x119 aligned rows of obstacles). In this study, intrusive velocity measurements with an ADV were performed in the urban area, as well as optical PIV measurements, highlighting complex three-dimensional flow patterns around the arrangement of buildings.

Doumic *et al.* (2021) [48] studied a 2x2 street layout and the associated staggered configuration. The vertical and horizontal velocity profiles were successfully measured using an intrusive ultrasonic velocity profiler.

Finally, Li *et al.* (2021) [47] studied various urban layouts experimentally and numerically to assess the influence of urban forms on flow variables. Four independent dimensionless parameters were used to define the urban forms:

- The number of streets aligned along the x and y directions,
- The conveyance porosities $\psi = \frac{n \times l}{L}$, corresponding to the ratio of the number of streets and their width over the width of the entire urban area.

Based on experimental and computational modelling, the authors analysed how flow variables (flow depths, discharge partition and velocity field) in urban flooding are influenced by the different urban parameters. They successfully performed LSPIV measurements to retrieve the 2D velocity field of the free surface around the different urban forms. The principal result of the study is the influence of a single parameter: the conveyance porosity along the main direction of the flow compared to the three others. Additionally, increasing the number of streets along the main direction of the flow increases the flow resistance.

Overall, the studies listed in Table 2.6 contribute to the understanding of flow dynamics in the urban areas under steady flow condition. The observations of these studies highlight important urban parameters that impact flow behaviour, such as the conveyance porosity along the main direction of the flow. Additionally, optical techniques, such as LSPIV, applied in steady conditions encourage their use for unsteady ones.

2.6 CONCLUSION

Based on the review of 32 experimental studies, various types of experimental setups and associated measurement techniques have been presented. The different geometries and opening systems present specific advantages and disadvantages, which are highlighted and summarised below:

- Rectangular setups with homogeneous beds are advantageous for the numerical reproduction of the experimental conditions. Additionally, such channels are commonly used in hydraulic laboratories and can be easily adapted for dam-break flow experiments by adding a gate.
- Upstream vertical sluice gates are the easiest way to generate dam-break waves. These devices can be easily added to existing rectangular channels without the need to create a discontinuity in the channel bed or side walls (to implement, for example, downstream vertical sluice gates or horizontal sluice gates). Additionally, avoiding leakages and implementing opening systems for other types of gates (such as flap gates or horizontal sluice gates) can be more difficult. Finally, using a pneumatic cylinder to open the gate allows for a repeatable opening with a precisely measured trial start.
- Two types of dam-break waves can be generated (total and partial). Even though total dam-breaks have the advantage of not creating wave reflections on the side walls, partial dam-breaks are easier

to implement (considering implementation in existing channels, gate weight, and leakage control) and allow longer incoming flow conditions.

- Glass side walls allow for an optical access to the flow and the use of optical measurement techniques.
- Wide channels are necessary to incorporate obstacle configurations into it and minimise hydrodynamic interactions between the configuration and the side walls.
- Long reservoirs have the advantage of storing a large volume of water, thereby maintaining a consistent flow rate for a longer period. Additionally, there is sufficient space to place metrology equipment inside them.
- Special attention in controlling the initial conditions of the trial is mandatory to perform repeatable dam-break experiments. In fact, leakages at the gate impact the control of the upstream water depth and the downstream bed conditions.

Moreover, various measurement techniques have been used to analyse different flow variables. In dam-break experiments, the water depth is always measured in around the obstacle configurations. Resistive wave gauges are intrusive but tend to have a high acquisition frequency. These devices are used for their robustness and accuracy. However, the intrusiveness of the sensors prevents their use in certain conditions, especially within and around urban areas due to lower water depth. Acoustic wave gauges are sometimes preferred even though their acquisition frequency and accuracy are lower than those of resistive gauges. Caution should be taken when several acoustic gauges are placed inside the channel or close to obstacles due to acoustic interference. In some conditions, the water depth is measured by observation or video tracking through optical image analysis. Another measured characteristic of the flow is the velocity and several devices and techniques are used. However, adding obstacles into the flow blocks the view and access to the sensors, making PIV measurement techniques and the use of intrusive devices challenging. Thus, LSPIV technique, mostly applied in steady flow conditions, could be advantageous for providing the complex flow paths of the free surface around the urban configuration. Also, instrumented obstacles can provide the pressure variation over time on the obstacles.

Finally, this chapter listed experimental studies on the influence of urban forms in both steady and unsteady conditions. While most experiments on unsteady flow tested a small number of configurations, Li et al. (2021) highlighted the influence of one specific urban parameter under steady flow conditions: the conveyance porosity in the main direction of the flow. Such results will guide future research to concentrate its effort on studying three main urban parameters: the number of streets in the main flow direction (n_x), the width of those streets (l_x) and the width of the urban area (L_y) perpendicular to the main direction of the flow.

3

COMPARATIVE STUDY OF NUMERICAL MODELS FOR DAM-BREAK FLOW IN URBANISED AREA

Summary :
This chapter provides an overview of numerical modelling approaches for dam-break flow in urbanised areas. A particular description is made for two numerical models used in this work. The first one resolves the 2D Shallow Water (SW) equations, TELEMAC-2D, and the second one resolves the 3D Reynolds-Averaged Navier-Stokes (RANS) equations, code_saturne. Both models are then compared to dam-break flow experiments. Following the validation results, code_saturne is selected to reproduce the future experiments, and TELEMAC-2D for the sizing of the experimental setup.

Contents

3.1 Introduction **21**
3.2 Numerical modelling of dam-break flow in urban area **21**
3.3 Numerical models **22**
3.3.1 TELEMAC-2D: Governing equations 23
3.3.2 code_saturne: Governing equations 24
3.4 Dam-break flow reproduction with TELEMAC-2D and code_saturne **27**
3.4.1 Test cases presentation 27
3.4.2 Results comparison 29
3.5 Additional validation of code_saturne for dam-break flow in an enclosed domain . . . **33**
3.5.1 Case presentation 33
3.5.2 Numerical model 34
3.5.3 Comparisons between experimental and numerical results 34
3.6 Conclusion **37**

3.1 INTRODUCTION

Numerical modelling of dam-break flow has become increasingly attractive and popular due to advancements in computational capabilities, which allow for the processing of large datasets and the solving of complex mathematical problems [19].

Laboratory experiments are mainly adopted for the validation of numerical models due to the high cost and time-consuming nature of carrying out accurate experimentation [1, 32]. In this scope, the numerical reproduction of idealised dam-break flow experiments presented in Chapter 2 will be performed to identify the strengths and weaknesses of current 'established' solvers and guide future developments.

This chapter provides a general overview of existing flood numerical models and present the two solvers used in this thesis. The content is organised as follows: Section 3.2 presents a global overview of flood inundation numerical approaches with a particular focus on three-dimensional (3D) models. Then, the two solvers used in the current study, TELEMAC-2D and code_saturne, will be presented in Section 3.3. A preliminary comparison between both solvers and a new dam-break flow experiment are presented in Section 3.4. Finally, Section 3.5 performs a comparative study of dam-break flow modelling between code_saturne and experimental data from a reference literature case [35].

3.2 NUMERICAL MODELLING OF DAM-BREAK FLOW IN URBAN AREA

Reliable prediction of flooding includes the accurate estimation of the flood extent, the spatial distribution of water depth, flow velocity and the speed of the propagating water front [106]. These hydrodynamic variables can be computed using operational numerical models, both 2D and 3D, which are a well-established approach for conducting flood risk analysis.

Experimental studies of dam-break flow are frequently employed for the validation of numerical models, with the predominant approach being two-dimensional (2D) models, used in over 50% of cases [32]. 2D numerical approaches typically rely on depth-averaged Shallow Water (SW) equations and are commonly solved using the finite volume method. Earlier in the century, the finite difference method was preferred. The 2D approach also leads to faster computations.

However, the simplifying assumption used in 2D models, namely the hydrostatic pressure distribution, is not applicable in flows with vertical accelerations or curvilinear flow paths. In real dam-break events, the land topography may include bottom singularities, and the wave path may traverse urban areas with complex layouts and various infrastructures. The effects of urban areas can be estimated in 2D models using different methods. For refined meshes, all obstacles can be explicitly included in the mesh. On the other hand, for coarser meshes, the entire urban area can be modelled using increased roughness or porosity coefficients. These methods provide satisfactory results under specific flood conditions. First, in cases of high water depth in front of obstacles, the vertical phenomena induced by the obstacles may be neglected, and 2D models with increased roughness or porosity coefficients give satisfactory results. Similarly, when the water depth is low in front of obstacles, vertical phenomena may also be neglected, and refined meshes with included obstacles provide satisfactory results. Conversely, when the water depth is on the same order as the obstacle height, 3D local phenomena may occur with coupled submergence/emergence of obstacles, which cannot be neglected. The effect of these 3D phenomena cannot be accurately taken into account by 2D shallow water models, leading to inaccurate predictions of flood variables and flood extent. Nevertheless, given their computational efficiency, significant efforts have been made over the past two decades for the development of 2D modelling approaches [26].

In order to predict local and 3D effects, such as vertical velocities and stratification around obstacles in the flow, 3D numerical methods are particularly useful. These methods are based on the Navier-Stokes equations and are coupled with the Volume-of-Fluid (VOF) method to accurately track the free surface. Note that recently, mesh-free particle methods such as Smoothed-Particle Hydrodynamics (SPH) [107–111] and Moving Particle Semi-implicit (MPS) [33] were applied to dam-break flow. These methods benefit from being mesh-free but are computationally expensive due to the need to compute interactions among neighbouring particles and are beyond the scope of this work.

Turbulence is a significant numerical stake in fluid dynamics simulations, as it characterises the random fluctuations of quantities when the flow speed or scale is large. This phenomenon is prevalent in most fluid applications and must be accounted for when simulating dam-break flow. It becomes even more important to account for in the presence of obstacles, where vortices and local recirculation areas are likely to form. The effect of turbulence can be accounted for in both 2D and 3D models; however, the following paragraph will focus on turbulence modelling in 3D models.

Turbulence modelling is widely studied, and recent advances in computational resources and models allow 3D solvers to use different approaches, summarised in Figure 3.1. These approaches vary in complexity and computational cost. The first method, called Direct Numerical Simulation (DNS) (Figure 3.1c), is the most accurate and is aimed at incompressible isothermal flows. It solves the Navier-Stokes equations with a constant mass density $\rho = 10^3\ kg.m^{-3}$ and viscosity $\mu = 10^{-6}\ kg\ m^{-1}s^{-1}$ with a view to capturing the entire turbulent energy spectrum. Yet, DNS is not often used in industrial applications due to its high computational cost. One possible solution to reduce the cost of turbulent simulations is to apply a spatial filter to control which turbulent scales are modelled and which are solved; this approach is called Large Eddy Simulation (LES) (Figure 3.1b). Here, the smallest turbulence length scales are modelled using a subgrid model, while the larger eddies are solved. This promising method is still not widely used for industrial application because it requires fine grids and thus, significant computational resources. Finally, the most popular approach involves averaging the governing equations, coupled with closure models, known as Reynolds-Averaged Navier-Stokes (RANS) simulations (Figure 3.1a).

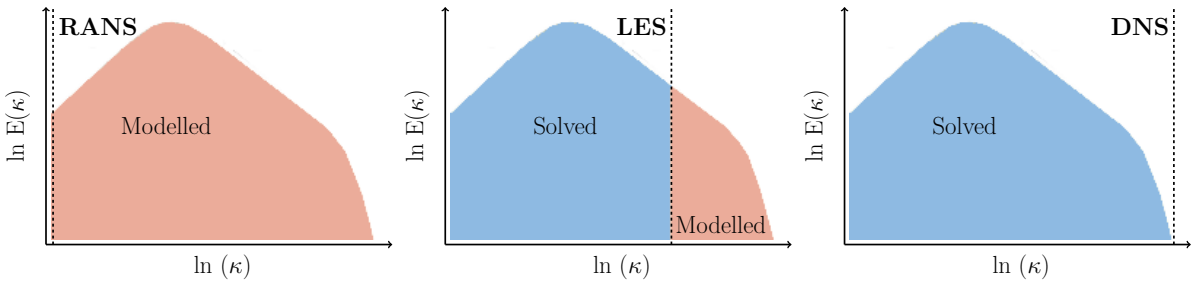

(a) RANS models **(b)** LES models **(c)** DNS models

Figure 3.1: Sketch of different turbulence approaches: (a) RANS, (b) LES and (c) DNS, in relation to the modeling of the turbulent energy spectrum.

The computational cost of 3D models is still a significant limitation for their application to dam-break scenarios, specially for large-scale domains where spatial accuracy is required [19]. 2D depth-averaged models have always been preferred, particularly for industrial applications, but the actual need for a better understanding of the effect of urban areas on large-scale flooding has fostered the application of 3D approaches in the urban flooding field. Table 3.1 provides a summary of the advantages and disadvantages of 2D and 3D models applied to dam-break flow over complex topography.

As mentioned for RANS methods, a turbulence closure model must be selected to close the equations system. The classical $k - \varepsilon$ model is the most commonly adopted [35, 112–117]. However, no systematic sensitivity analyses on turbulence model have been performed in numerical studies of dam-break flow over complex topography. Turbulence models are typically selected based on comparisons with basic dam-break cases characterised by simple geometric channels (see Section 2.2) [19].

3.3 NUMERICAL MODELS

Two numerical solvers will be used in this work, depending on the needs of the study (sizing of the experimental setup, validation with experimental dataset). The first one, named TELEMAC-2D [118], is based on the 2D SW equations, and the second is a CFD solver based on the numerical solution of 3D RANS equations for two-phase flow, named code_saturne [119].

Table 3.1: Summary of the advantages and disadvantages of 2D and 3D models for dam-break flow over complex topography applications.

Model	Advantages	Disadvantages
2D	• Easy to build and implement • Low computational cost • Robust and stable • Accessible result visualisation and tools	• Limitations due to simplifying assumptions • Model the effect of obstacles (calibration of roughness/porosity coefficients, obstacles included in the mesh)
3D	• Reproduction of 3D local effects (velocity field, stratification) • Reproduction of non-hydrostatic effects • Complete experimental data with non-measurable flow variables	• High computational cost • More complex implementation • Less validation data for 3D phenomena

3.3.1 *TELEMAC-2D: Governing equations*

The open-source TELEMAC-2D software [118] solves the Shallow Water (SW) equations, derived by Barré de Saint-Venant in 1871 [120]. The model is based on the Finite Element Method (FEM) over unstructured triangular grids. The three-dimensional Navier-Stokes equations are then averaged over the vertical axis to obtain the following SW equations:

$$\frac{\partial h}{\partial t} + \underline{u} \cdot \underline{\nabla}(h) + h\text{div}\,(\underline{u}) = 0, \tag{3.1}$$

$$\frac{\partial u}{\partial t} + \underline{u} \cdot \underline{\nabla}(u) = -g\frac{\partial Z_s}{\partial x} + F_{f,x} + \frac{1}{h}\text{div}\,(h\nu_t \underline{\nabla} u)\,, \tag{3.2}$$

$$\frac{\partial v}{\partial t} + \underline{u} \cdot \underline{\nabla}(v) = -g\frac{\partial Z_s}{\partial y} + F_{f,y} + \frac{1}{h}\text{div}\,(h\nu_t \underline{\nabla} v)\,. \tag{3.3}$$

where t is the time [s], $g = 9.81\ [m/s^2]$ the gravitational acceleration, h the water depth [m], Z_s the free surface elevation [m], $\underline{u} = (u, v)$ the depth-averaged flow velocity vector [m/s], with u being the component along the longitudinal x-axis and v being the component along the transversal y-axis and ν_t the turbulent eddy viscosity term $[m^2/s]$. The friction law $\underline{F}_f = (F_{f,x}, F_{f,y})$, with $F_{f,x}$ being the component of the friction law along the longitudinal x-axis and $F_{f,y}$ being the component along the transverse y-axis, is defined as follows:

$$\underline{F}_f = -\frac{g}{hC^2} \mid \underline{u} \mid \underline{u}, \tag{3.4}$$

where $\mid \underline{u} \mid$ is the magnitude of $\underline{u}$ [m/s] and C corresponds to the Chézy friction coefficient $[m^{1/2}/s]$.

The Manning formula is used to calculate the value of the Chézy coefficient as a function of the Manning coefficient $n = h^{1/6}/C\ [s/n^{1/3}]$:

$$\underline{F}_f = -\frac{gn^2}{h^{4/3}} \mid \underline{u} \mid \underline{u}, \tag{3.5}$$

The turbulent eddy viscosity ν_t is determined using the $k-\varepsilon$ turbulence model [121], which is averaged over the vertical to simulate the transport of turbulent quantities, where k is the turbulent kinetic energy and ε is the turbulent energy dissipation:

$$\frac{\partial k}{\partial t} + \underline{u} \cdot \underline{\nabla}(k) = \frac{1}{h}\text{div}\left[h\frac{\nu_t}{\sigma_k}\underline{\nabla} k\right] + \mathcal{P} - \varepsilon + \mathcal{P}_{kv}, \tag{3.6}$$

$$\frac{\partial \varepsilon}{\partial t} + \underline{u} \cdot \underline{\nabla}(\varepsilon) = \frac{1}{h}\text{div}\left[h\frac{\nu_t}{\sigma_\varepsilon}\underline{\nabla} \varepsilon\right] + \frac{\varepsilon}{k}\left[C_{\varepsilon 1}\mathcal{P} - C_{\varepsilon 2}\varepsilon\right] + \mathcal{P}_{\varepsilon v}, \tag{3.7}$$

where

$$\mathcal{P} = \nu_t\left(\frac{\partial u_i}{\partial x_j} + \frac{\partial u_j}{\partial x_i}\right)\frac{\partial u_i}{\partial x_j}, \tag{3.8}$$

$$\mathcal{P}_{kv} = C_k\frac{u_*^3}{h}, \mathcal{P}_{\varepsilon v} = C_\varepsilon\frac{u_*^4}{h^2}, \tag{3.9}$$

$$\text{with } C_k = \frac{1}{\sqrt{C_f}}, C_\varepsilon = 3.6\frac{C_{\varepsilon 2}\sqrt{C_\mu}}{C_f^{3/4}}, \tag{3.10}$$

$$u_* = \sqrt{\frac{C_f}{2}(u^2+v^2)}, \tag{3.11}$$

$$\sigma_k = 1, \sigma_\varepsilon = 1.3, C_\mu = 0.09, C_{\varepsilon 1} = 1.44, C_{\varepsilon 2} = 1.92. \tag{3.12}$$

3.3.2 *code_saturne: Governing equations*

The CFD open-source solver code_saturne [119] uses the finite volume method to solve the RANS equations [122]. To study non-linear free-surface wave and wave-structure interaction, code_saturne is enhanced with a Volume-of-Fluid (VOF) technique to model water-air mixture. The two fluids are defined by a concentration scalar α, defined between zero and one, called the volume fraction of one of the two phases.

So, the volume fraction of phase k in any domain Ω is define by:

$$\alpha_{\Omega,k} = \frac{\text{volume of phase 1 in } \Omega}{\text{volume of } \Omega}, \tag{3.13}$$

In the scope of this work, the fluid w corresponds to water and the fluid a to air. Their volume fractions are written as $\alpha_w = \alpha$ and $\alpha_a = 1-\alpha$. For all simulations using code_saturne in this manuscript, the different fluid densities are set to $\rho_w = 998.2\ kg/m^3$ and $\rho_a = 1.22\ kg/m^3$, while the dynamic viscosity values are $\mu_w = 1\ \times 10^{-3}\ kg\ m^{-1}s^{-1}$ and $\mu_a = 1\ \times 10^{-5}\ kg\ m^{-1}s^{-1}$.

Each fluid can be described by its governing equations:

$$\frac{\partial \alpha_k}{\partial t} + \text{div}\ (\alpha_k \underline{u}_k) = 0, \tag{3.14}$$

$$\frac{\partial (\alpha_k \rho_k)}{\partial t} + \text{div}\ (\alpha_k \rho_k \underline{u}_k) = 0, \tag{3.15}$$

$$\frac{\partial (\alpha_k \rho_k \underline{u}_k)}{\partial t} + \underline{\text{div}}\ (\alpha_k \underline{u}_k \otimes \rho_k \underline{u}_k) = -\underline{\nabla}(\alpha_k p_k) + \underline{\text{div}}\left(\alpha_k \underline{\underline{\tau_k}}\right) + \alpha_k \rho_k \underline{g} + \underline{M}_k, \tag{3.16}$$

where ρ_k is the fluid density, $\underline{u}_k$ the velocity, $\rho_k \underline{u}_k$ the momentum, τ_k the shear stress tensor and M_k the interfacial force with $M_w + M_a$ considered equal to zero. In reality, each fluid is not solved individually; instead, a mixture over a volume is used. Thus, the conservation of mass (3.15) becomes:

$$\frac{\partial \rho}{\partial t} + \text{div}\ (\rho \underline{u}) = 0, \tag{3.17}$$

where the fluid density ρ and dynamic viscosity μ are defined by the following mixture law:

$$\rho = \alpha \rho_w + (1-\alpha)\rho_a, \tag{3.18}$$

$$\mu = \alpha \mu_w + (1-\alpha)\mu_a. \tag{3.19}$$

Each fluid property is assumed to be constant and thus each phase is incompressible. Similarly, a mixture velocity is defined as a Favre-averaged over a small volume:

$$\underline{u} = \frac{\alpha \rho_w \underline{u_w} + (1-\alpha)\rho_a \underline{u_a}}{\rho}. \tag{3.20}$$

Then, for the water phase, by writing the water velocity u_w, as a function of the mixture velocity u and the local relative velocity $u_r = u_a - u_w$ and replacing it by $(u - (1-\alpha)(\rho_a/\rho)u_r)$ in the continuity equation (3.14), one obtains:

$$\frac{\partial \alpha}{\partial t} + \text{div}\ (\alpha \underline{u}) = \text{div}\left(\alpha(1-\alpha)\frac{\rho_a}{\rho} u_r\right), \tag{3.21}$$

and the mixture momentum equation becomes:

$$\frac{\partial (\rho \underline{u})}{\partial t} + \underline{\text{div}}\ (\underline{u} \otimes \rho \underline{u}) = -\underline{\text{div}}\left[\alpha(1-\alpha)\frac{\rho_w \rho_a}{\rho} \underline{u_r} \otimes \underline{u_r}\right] - \underline{\nabla} p + \underline{\text{div}}\ \underline{\underline{\tau}} + \rho \underline{g}. \tag{3.22}$$

The common assumption of phase-pressure equilibrium ($p_w \approx p_a$) within a cell volume is taken. If we compare equations 3.14 and 3.21, one additional drift velocity term appears, $\text{div}\left(\alpha(1-\alpha)\frac{\rho_a}{\rho} u_r\right)$, which disappears far from the free surface where $\alpha = 0$ or 1. A good way to close the drift velocity term is to limit the diffusion of the free surface.

The discretised version of equation 3.21 reads:

$$\mid \Omega_i \mid \frac{\alpha_i^{n+1} - \alpha_i^n}{\Delta t} + \sum_{f \in \mathcal{F}_i} \alpha_f^{n+1} \left(\underline{u}^{n+1} \cdot \underline{S}\right)_f + \sum_{f \in \mathcal{F}_i} (\alpha(1-\alpha))_f^{n+1} \left(\underline{u}_r^{n+1} \cdot \underline{S}\right)_f = 0, \tag{3.23}$$

where n denotes the time step, i the cell number, $\mid \Omega_i \mid$ the volume of the i-th cell, Δt the time step and $\mathcal{F}_i$ the list of faces of cell i. f refers to the face f between the cell Ω_i and a neighbouring cell and $\underline{S}_f$ denotes the outward normal vector of the face f of the cell Ω_i. $\left(\underline{u}^{n+1} \cdot \underline{S}\right)_f$ is the velocity flux of $\underline{u}$ through a face f and $\left(\underline{u}_r^{n+1} \cdot \underline{S}\right)_f$ the velocity flux of $\underline{u}_r$ through a face f.

In this work, the modelling choice for the flux of the drift velocity $\underline{u_r}$ is calculated following the approach described by Deshpande *et al.* (2012) [123]:

$$\left(\underline{u}_r^{n+1} \cdot \underline{S}\right)_f = min\left(C_\gamma \frac{\left(\underline{u}^{n+1} \cdot \underline{S}\right)_f}{\underline{S}_f}, \underset{f'}{max}\left[\frac{\left(\underline{u}^{n+1} \cdot \underline{S}\right)_{f'}}{\underline{S}_{f'}}\right]\right)(\underline{n} \cdot \underline{S})_f, \tag{3.24}$$

where the *max* operation is performed over the entire domain, while the *min* operation is done locally at each face f of the cell Ω_i. C_γ is the drift flux factor and $\underline{n}_f$ is the vector normal to the interface calculated as:

$$\underline{n}_f = \frac{(\nabla\alpha)_f}{|\,(\nabla\alpha)_f + \delta\,|}, \quad \text{with} \quad (\nabla\alpha)_{f_{ij}} = \frac{(\nabla\alpha)_i + (\nabla\alpha)_j}{2}, \quad \text{and} \quad \delta = \frac{10^{-8}}{\overline{|\,\Omega_i\,|}^{1/3}}. \tag{3.25}$$

with $(\nabla\alpha)_i$ retrieved as defined in Archambeau *et al.* (2004) [124].

Moreover, for a viscous Newtonian fluid the stress tensor can be written as:

$$\underline{\underline{\tau}} = \mu\left(\underline{\underline{\nabla u}} + \underline{\underline{\nabla}}^T\underline{u}\right) - \frac{2}{3}\mu \mathrm{div}\,(\underline{u})\underline{\underline{I}}. \tag{3.26}$$

Note that code_saturne belong to the *prediction-correction class of algorithms* [125] and solves the incompressible RANS equations discretised in time by an implicit Euler scheme:

$$\mathrm{div}\,(\underline{u}) = 0, \tag{3.27}$$

$$\frac{\partial\alpha}{\partial t} + \mathrm{div}\,(\alpha\underline{u}) = \mathrm{div}\left(\alpha(1-\alpha)\frac{\rho_a}{\rho}u_r\right), \tag{3.28}$$

$$\begin{aligned}\frac{\partial\left(\rho\underline{u}\right)}{\partial t} + \underline{\mathrm{div}}\,(\underline{u}\otimes\rho\underline{u}) = &-\underline{\nabla}\left(p + \frac{2}{3}\mu\mathrm{div}\,(\underline{u})\right) - \underline{\mathrm{div}}\left[\alpha(1-\alpha)\frac{\rho_w\rho_a}{\rho}\underline{u_r}\otimes\underline{u_r}\right] \\ &+ \underline{\mathrm{div}}\left[(\mu+\mu_T)\left(\underline{\underline{\nabla u}} + \underline{\underline{\nabla}}^T\underline{u}\right)\right] + \rho\underline{g}.\end{aligned} \tag{3.29}$$

The first equation is the continuity equation. The second is the transport equation for α and the last is the momentum equation. The $k-\varepsilon$ model, with linear production [126], is used, which solves two supplementary transport equations:

$$\frac{\partial(\rho k)}{\partial t} + \mathrm{div}\,(k\underline{u}\rho) - \mathrm{div}\left(\left[\mu + \frac{\mu_T}{\sigma_k}\right]\underline{\nabla}k\right) = \rho(\mathcal{P}+\mathcal{G}) - \rho\varepsilon + ST_k, \tag{3.30}$$

$$\frac{\partial(\rho\varepsilon)}{\partial t} + \mathrm{div}\,(\underline{u}\rho\varepsilon) - \mathrm{div}\left(\left[\mu + \frac{\mu_T}{\sigma_\varepsilon}\right]\underline{\nabla}\varepsilon\right) = \rho C_{\varepsilon 1}\frac{\varepsilon}{k}[\mathcal{P} + (1-C_{\varepsilon 3})\mathcal{G}] - \rho C_{\varepsilon 2}\frac{\varepsilon^2}{k} + ST_\varepsilon, \tag{3.31}$$

where:

$$\mu_T = C_\mu \rho \frac{k^2}{\varepsilon} \quad \text{with} \quad C_\mu = 0.09, \tag{3.32}$$

$$\mathcal{P} = 2\mu_T \, ||| \underline{\underline{\nabla u}} |||^2 \equiv 2\mu_T \underline{\underline{\nabla u}} : \underline{\underline{\nabla u}} \quad \text{(Frobenius norm)}, \tag{3.33}$$

$$\mathcal{G} = -\frac{\mu_T}{\sigma_T} \nabla \rho \cdot \underline{g} \quad \text{with} \quad \sigma_T = 1, \tag{3.34}$$

$$\sigma_\varepsilon = 1.3, C_{\varepsilon 1} = 1.44, C_{\varepsilon 2} = 1.92, C_{\varepsilon 3} = 1.0. \tag{3.35}$$

Equation 3.23 is solved in the final time scheme step. To compute α^{n+1}, a second-order M-CICSAM (Modified Compressive Interface Capturing Scheme for Arbitrary Meshes) scheme is used along with an NVD (Normalised Variable Diagram) scheme. A β-limiter is employed to respect the min-max principle, ensuring that the value of α stays between zero and one:

$$\alpha_f = \beta_f \alpha_f^{M-CICSAM} + (1 - \beta_f) \alpha_f^{NVD}. \tag{3.36}$$

Further details of *code_saturne* spatial and temporal discretisation may be found in its theory guide [127] and in Archambeau *et al.* (2004) [122].

Note that using the VOF module involves an additional post-processing step to retrieve the water height. Here, the water volume fraction, α is used to calculate the position of the free surface for each probe. The following method is applied: first, a control volume, Ω, of one or many cells wide and over the full height of the domain, H, is defined. The resulting water height, h, at each time step is the ratio on this column of the volume of water and its total volume, V_t, multiplied by its total height as described by equation 3.37:

$$h_{num} = \frac{\int_\Omega \alpha V_t}{\int_\Omega dV_t} \times h_m. \tag{3.37}$$

The above formula is typically employed to calculate water depth in domains characterised by a distinct separation between two phases. However, it presents limitations when applied to aerated flow, where an air-water mixture condition may be present, containing saturated cells of water, air, or a mixture of both. Integrating saturated cells may lead to an underestimation of the water height, as illustrated in Figure 3.2. For example, in this case, for the same defined control volume Ω and free surface position, the integration of the void fraction will lead to a different water height value due to the presence of air cells under the free surface in the case on the right. Figure 3.3 illustrates a void fraction profile of a dam-break flow crossing an obstacle configuration along the x-axis at $t = 4$ s. In this case, if the control volume Ω is defined at $x = 0.9$ m, air bubbles are located beneath the free surface, and thus the calculated water depth will be underestimated compared to the real numerical position of the free surface. On the other hand, if the control volume Ω is defined at $x = 1.6$ m, the water environment is homogeneous, and thus the calculated position of the free surface will match its numerical position.

3.4 DAM-BREAK FLOW REPRODUCTION WITH TELEMAC-2D AND CODE_SATURNE

3.4.1 *Test cases presentation*

The two previously presented solvers, TELEMAC-2D and code_saturne, are compared in this section to an experimental dam-break flow case, with and without the presence of a single obstacle in the flow path. The test case consists of the propagation of a partial dam-break wave in a horizontal and rectangular channel, as illustrated in Figure 3.4. An upward vertical sluice gate, located at x = 6.95 m, is used to generate the dam-break wave and three measurement points are employed to compare the water depth variation with the numerical models. The first measurement point, P1, is placed upstream of the gate (x = 6.50 m) to ensure the ability of the numerical models to reproduce the upstream hydrodynamic conditions and the effect of the gate opening on the flow dynamics. The second measurement point, P2, is placed downstream of the gate and upstream of the single obstacle (x = 8.55 m). This measurement point records the arrival time and height of the dam-break wave, as well as the effect of the obstacle

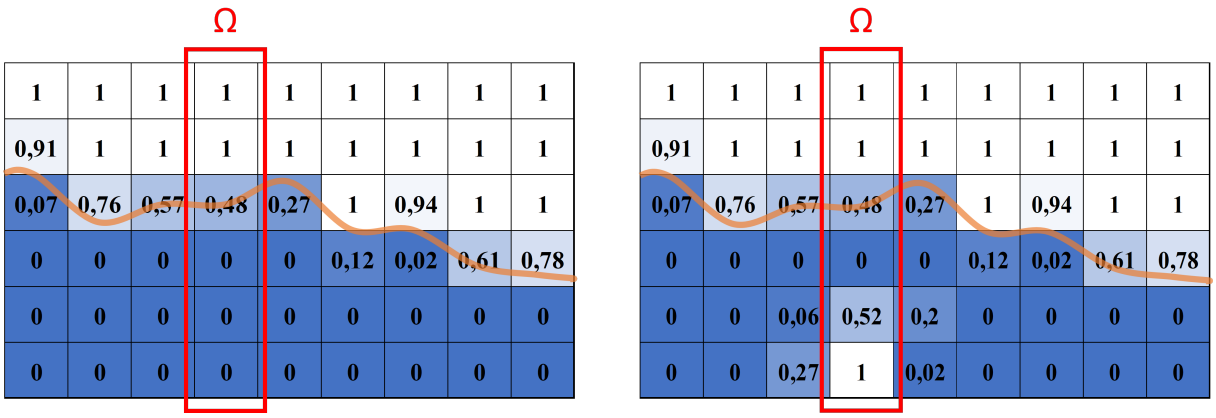

Figure 3.2: Illustration of the void fraction field: on the left, with a homogeneous water field; and on the right, with air bubbles trapped under the free surface. The orange line represents the actual position of the free surface, and the numbers represent the volume fraction of water in each cell. Sketch adapted from Davidson *et al.* (2015) [128].

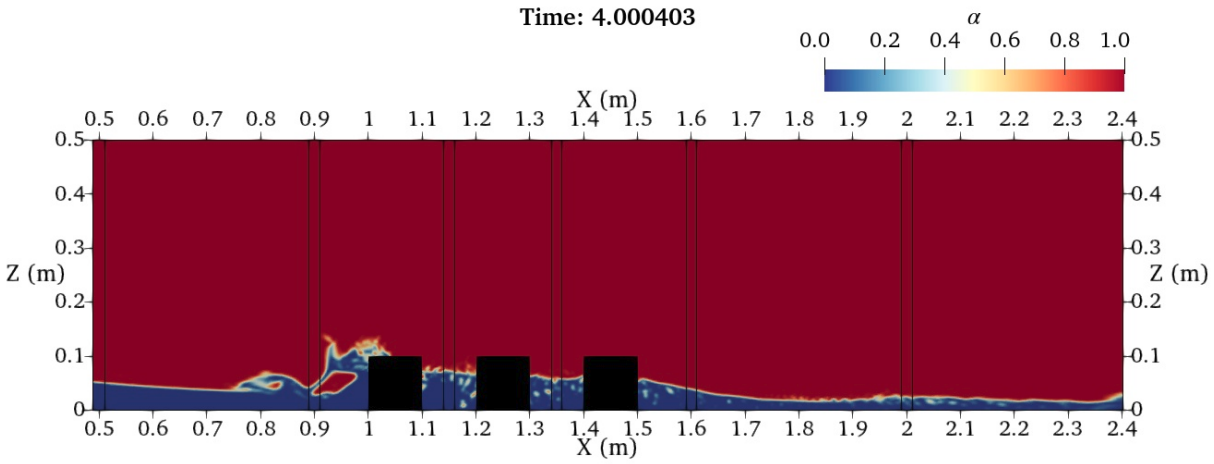

Figure 3.3: Void fraction (α) profile of a dam-break flow crossing an obstacle configuration at $t = 4$ s.

on the flow. Finally, the last measurement point, P3, is placed downstream of the obstacle (x = 8.75 m). The obstacle used is a cube with a size of 0.1 m, centered in the channel at x = 8.65 m and y = 0 m. The opening time of the gate, obtained from video tracking, is about $v_{gate} = 0.78$ m/s. The initial water depth in the reservoir was set to 0.25 m. Details about the experimental setup and measurement techniques are provided in Chapter 4 and the experimental results are extracted from the preliminary campaign presented in Chapter 5.

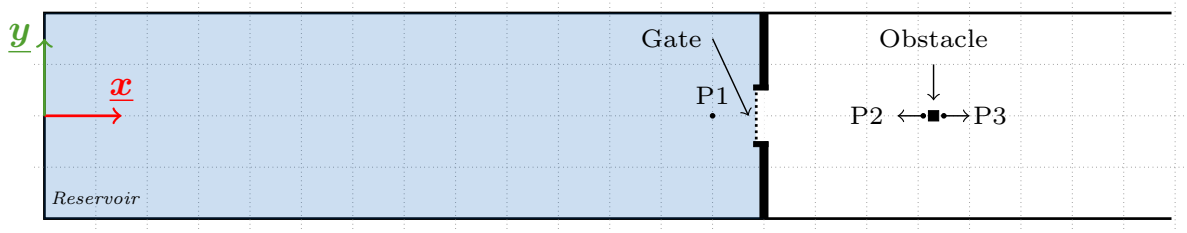

Figure 3.4: Schematic view of the measurement points for the comparison between TELEMAC-2D, code_saturne and experimental data.

The computational domain is 14 meters long and 2 meters wide for both numerical models and 0.5 meters high for code_saturne. The 2D computational domain from TELEMAC-2D is a triangular unstructured grid with a uniform average size of 0.007 m, composed of 1.4 million tetrahedral cells. The mesh was selected based on a mesh sensitivity study. Since the computational cost of the model was acceptable, the

mesh was designed to ensure good resolution around the breach to reproduce the observed phenomena in the area with homogeneous cell size on the entire domain. On the other hand, the 3D computational domain used for code_saturne is discretised using 6.1 millions hexahedral cells. After a mesh sensitivity analysis, refinements were made along the z-axis for cells of low height and in the x and y axes in areas of interest, such as the breach surroundings and the obstacle. Details about the refinement zones of the mesh from code_saturne are presented in Chapter 5, Figure 5.18.

Concerning the boundary conditions, the channel bottom and side walls were set as smooth walls and the end of the channel as a free outlet. In the code_saturne simulation, a symmetry condition was assigned to the top boundary faces. Both simulations were run during $t = 25$ s with a variable time step Δt to keep the CFL condition under unity. The effect of the gate opening is modelled in code_saturne as a rectangular moving wall with a velocity of 0.78 m/s. An initial volume of water of dimensions 6.95 $\times$ 2 $\times$ 0.25 m is defined, corresponding to the initial water depth in the reservoir.

3.4.2 *Results comparison*

The first comparison between both models is made without obstacles in the flow, as illustrated in Figure 3.5. Water depth comparisons upstream of the gate, at position P1, are illustrated in Figure 3.6. These comparisons include code_saturne's simulations with the gate opening ($code\_saturne_{gate}$), without the gate opening (*code_saturne*), the TELEMAC-2D simulation, and the experiments. Similarly, the two solvers are compared in Figure 3.7 downstream of the gate, at position P2.

(a) TELEMAC-2D.

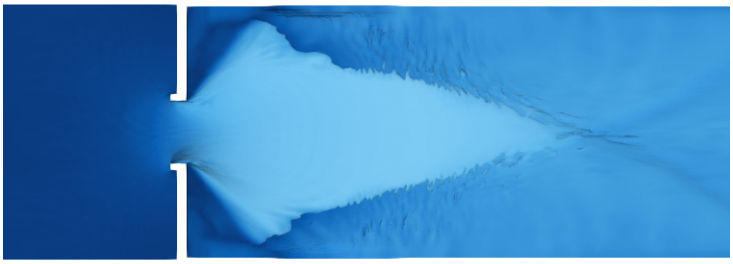

(b) code_saturne with VOF module.

Figure 3.5: Flow visualisation at $t = 10$ s without obstacles in the flow for solvers (a) TELEMAC-2D and (b) code_saturne ($\alpha \leq 0.5$).

Oscillations of the free surface are observable at position P1 (Figure 3.6), leading to variations of the gate flow rate that influence the downstream flow dynamics, making the numerical reproduction more challenging. This phenomenon is directly induced by the width of the gate and consists of primary and secondary waves, reflected on the side walls. The primary ones, with a period of approximately 7.5 seconds, are well reproduced by both numerical models (Figure 3.6a). On the other hand, the periods of the secondary waves are not all correctly predicted (Figure 3.6b). First, the SW model predicts secondary oscillations significantly shifted compared to the measurements. The 3D RANS simulation, without taking account for the gate opening, led to closer results to the expected values but the secondary oscillations are still shifted. This shift disappears when the gate opening is taken into account (blue line in Figure 3.6). This result highlights the importance of accounting for the gate opening in simulations to correctly predict the upstream hydrodynamic conditions of the experiments. As observed by Lauber *et al.* (1998) [39], the opening of the gate plays, in fact, an important role in the shape-profile of the generated wave. The instantaneous opening, which is considered in the TELEMAC-2D and code_saturne simulations, generates

a steep wavefront and a rapid decrease in water depth. In contrast, the gradual opening, considered in the code_satunrne$_{gate}$ simulation, lead to a less steep wavefront, resembling a thin film of water. The effect of the gate time-opening on the upstream water depth can be observed in Figure 3.6 with a slower emptying of the tank. While adding the vertical displacement of the gate effect in SW simulations can be difficult, the porous module of code_saturne allows its simple implementation. code_saturne was shown to be able to predict correctly the upstream experimental flow conditions.

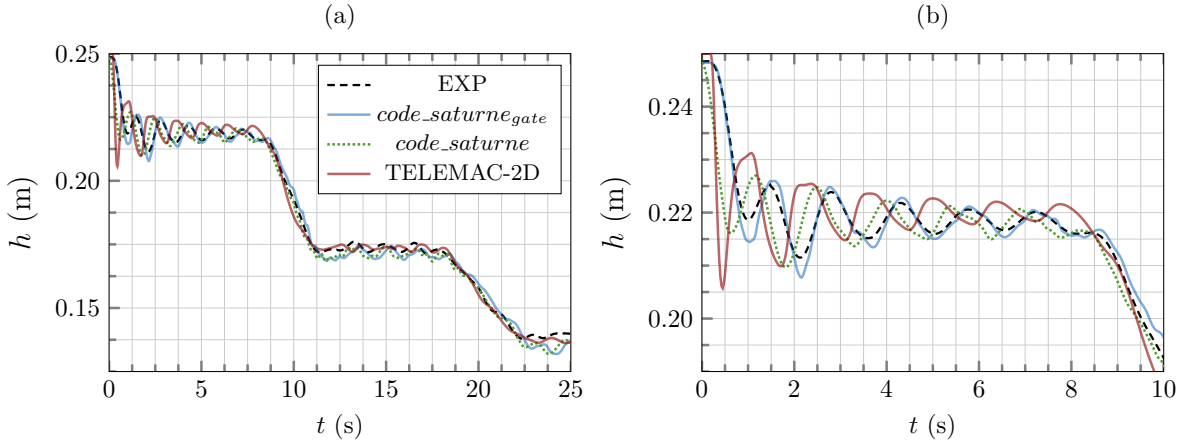

Figure 3.6: Dam-break case: Water depth comparison between experiments, code_saturne and TELEMAC-2D simulations at position P1 for (a) a global view and (b) a zoomed view.

Downstream of the gate, Figure 3.7 shows the arrival time and height of the dam-break wave at position P2. The water height estimation is slightly overestimated by the SW model (Figure 3.7a), while the RANS model closely matches the experimental data. The wave's arrival time in the SW and RANS models without the effect of the gate opening is faster and similar between the two models (Figure 3.7b). Adding the gate displacement led to a correct wave arrival time prediction by the RANS simulation.

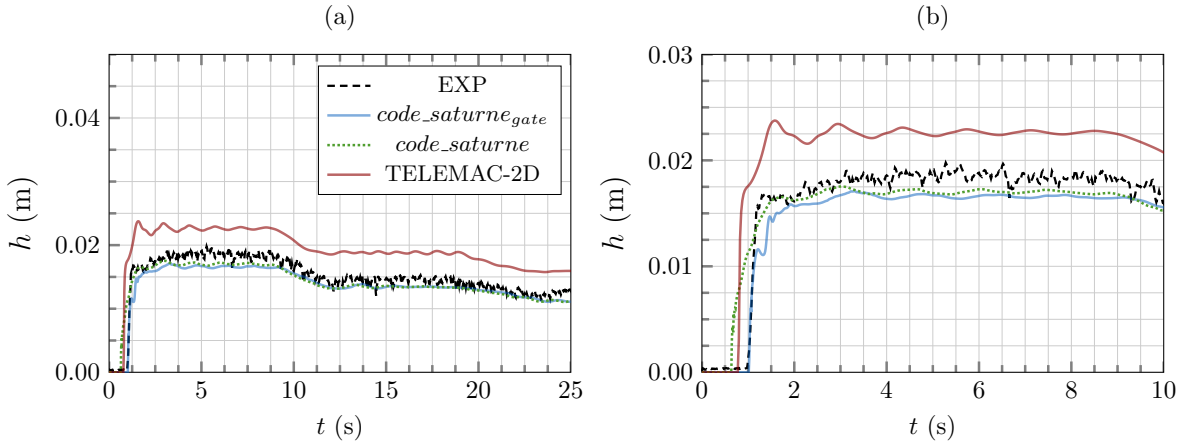

Figure 3.7: Dam-break case: Water depth comparison between experiments, code_saturne and TELEMAC-2D simulations at position P2 for (a) a global view and (b) a zoomed view.

Remark : As highlighted by Figures 3.6 and 3.7, modelling the vertical displacement of the gate in the RANS simulation is mandatory to accurately simulate the upstream hydrodynamic conditions, as well as the arrival time and shape of the dam-break wave. Therefore, from now on, all 3D simulations performed with code_saturne will account for the gate's opening. For readability, *code_saturne*$_{gate}$ will be referred as *code_saturne* in the legends.

Qualitatively, Figure 3.8 illustrates the water depth over the computational domain at $t = 5$ s. Results are similar between the two models, notably with the position of the reflection of the partial dam-break wave on the side walls at x = 7.5 m. The position of the meeting point between the two reflected waves is slightly different and is positioned further downstream in the RANS simulation.

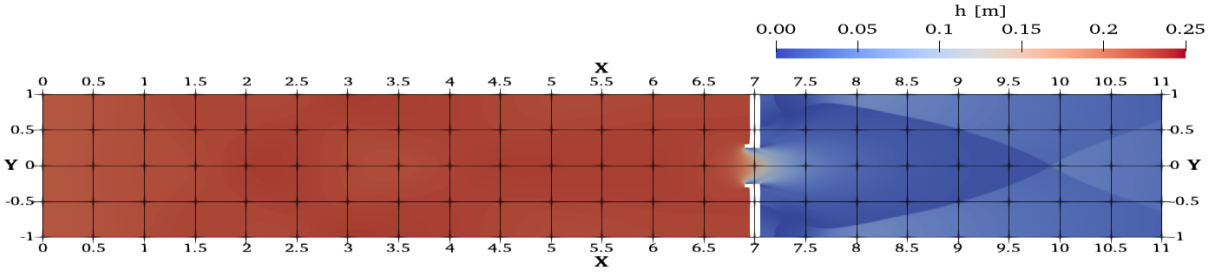

(a) TELEMAC-2D solver

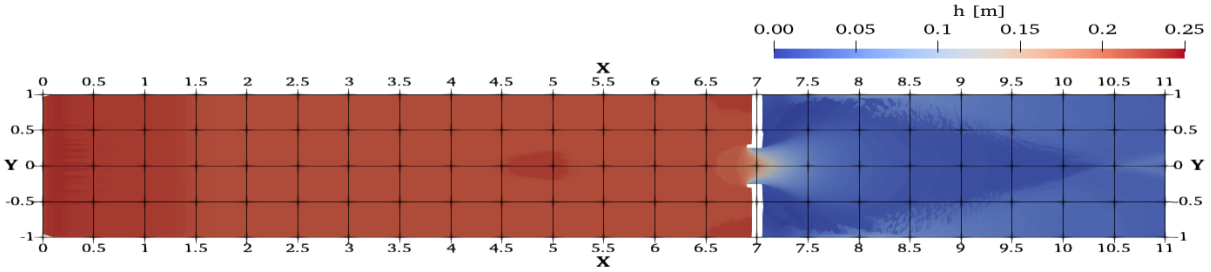

(b) code_saturne solver

Figure 3.8: Water depth comparison between (a) TELEMAC-2D and (b) code_saturne at $t = 5$ s.

An obstacle is then added into the flow, centred in x= 8.65 m and y = 0 m, as illustrated in Figure 3.9.

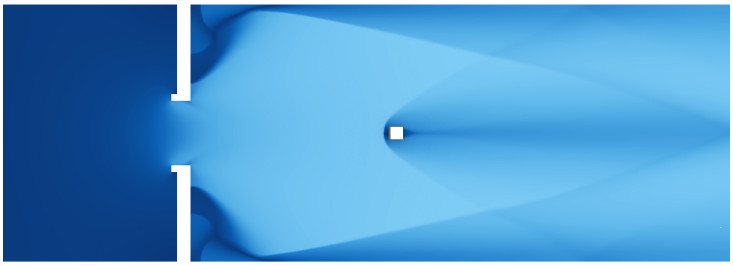

(a) TELEMAC-2D.

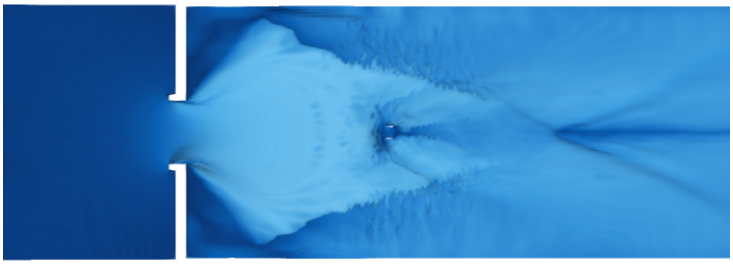

(b) code_saturne with VOF module.

Figure 3.9: Flow visualisation at $t = 10$ s with one obstacle in the flow for solvers (a) TELEMAC-2D and (b) code_saturne ($\alpha \leq 0.5$).

The water depth variation upstream (at position P2) and downstream (at position P3) are shown in Figure 3.10. Results suggest that TELEMAC-2D does not adequately account for its presence, where the water height upstream of the obstacle, as shown in Figure 3.10a, is similar to the one without obstacle. Downstream of it, as seen in Figure 3.10b, the SW approach underestimates strongly the water depth. On the other hand, the RANS approach predicts water depth closer to the experimental results, even if some improvements could be made. Indeed, the 3D post-processing method to retrieve the water height (see Section 3.3.2) may underestimate the position of the free surface when bubbles are trapped beneath

it. This occurs precisely during the impact of the dam-break wave with the obstacle (Figure 3.10a) and after a few moments in the wake zone (Figure 3.10b). Water depth profiles obtained with TELEMAC-2D at different time steps are shown in Figure 3.11. The hydraulic jump is present in the SW model but at a different position. In fact, the shape of the hydraulic jump is thinner than in the experiments and does not reach probe P2, which explains the observed differences in Figure 3.10.

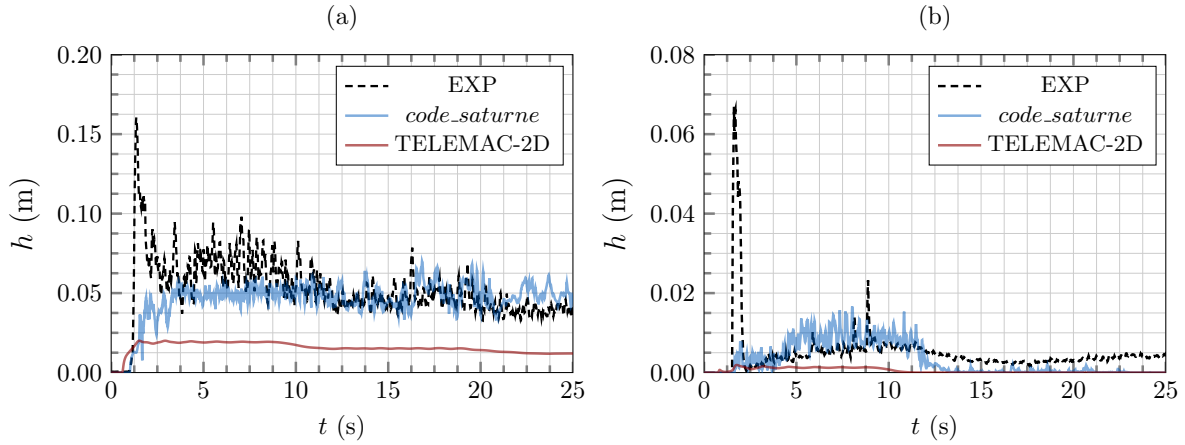

Figure 3.10: Dam-break case with one obstacle: Water depth comparison between experiments, *code_saturne* and TELEMAC-2D simulations at positions: (a) P2, upstream of the obstacle and (b) P3, downstream of the obstacle.

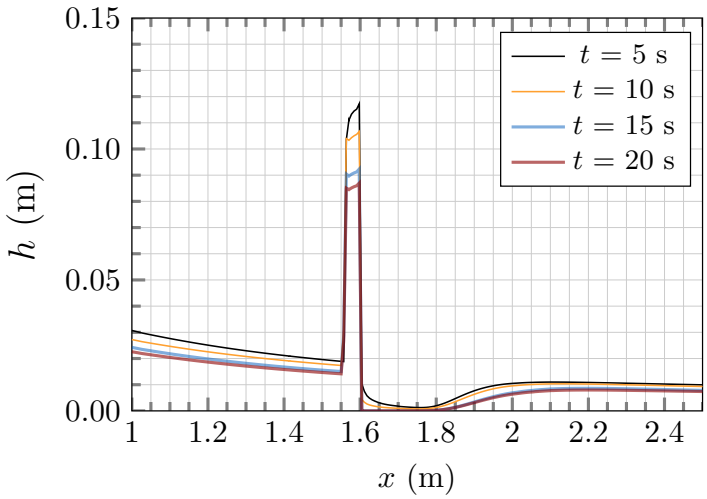

Figure 3.11: Water depth profiles obtained with TELEMAC-2D at four different time-steps.

Figure 3.12 illustrates a slice of the void fraction field during the impact with the obstacle (Figure 3.12a) and later (Figure 3.12b) using code_saturne. During the impact, the dam-break wave is redirected vertically as a water jet and then falls back onto the free surface, trapping air underneath. The trapped air bubble causes the underestimation of the free surface position at this position, as it is post-processed as the sum of the void fraction over the entire column. This effect still occurs later in the experiment (Figure 3.12b) and the complexity of the air-water mixture environment downstream of the obstacle can also leads to inaccurate post-processed water depth measurements.

Remark : The numerical mesh used for the simulations with the presence of obstacles as well as a mesh sensitivity analysis are detailed in Chapter 5.

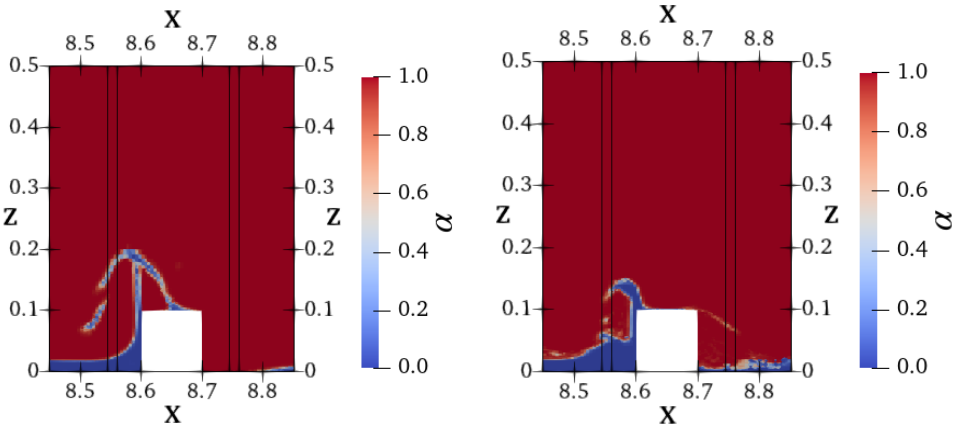

(a) $t = 1.6$ s. **(b)** $t = 10$ s.

Figure 3.12: code_saturne void fraction field (α). Zoom near the obstacle for: (a) $t = 1.6$ s and (b) $t = 10$ s. The black lines centered at $x = 8.55$ m and $x = 8.75$ m corresponds respectively to the position of probes P2 and P3.

Table 3.2 provides performance information for both simulations, highlighting the cost difference between the 2D and 3D approaches. While results showed that the 3D simulation was able to predict the expected phenomena when adding obstacles into the flow path (even if the post-processing method shows some margin for improvement), its computational cost prevents its use for an infinite number of urban forms. Still, 3D simulations can be used to retrieve local information that are not measurable experimentally.

Table 3.2: Computation time comparison between TELEMAC-2D and code_saturne.

	TELEMAC-2D	**code_saturne**
Equations type	SW[2]	RANS[1]
Dimensions	2D	3D
Number of cells	1 372 532	6 134 200
Number of processors	72	420
Total CPU Time for 1s of physical time	21 seconds	43 hours

[1]: Reynolds-Averaged Navier-Stokes
[2]: Shallow Water

SW models are shown to be a good cost-effective alternative to 3D models when reproducing non obstructed dam-break waves. Such approach could be used to perform parametric simulations for the sizing of the experimental setup and to define the hydrodynamic conditions of the experiments. However, some experimental features, such as the vertical displacement of the gate or vertical water-jet during the impact, cannot be simulated with the SW approach, leading to significant differences when simulating the observed flow.

As conclusion, while shallow water models offer computational efficiency and can be highly effective for large-scale applications, their simplifications limit their accuracy in capturing the detailed flow patterns around obstacles. Despite a higher computational demand, 3D approaches appear as a solution to handle this complex flow phenomena and could complete experimental data for a limited number of urban forms. All simulations are performed on EDF high performance computing systems called GAIA and CRONOS.

3.5 ADDITIONAL VALIDATION OF CODE_SATURNE FOR DAM-BREAK FLOW IN AN ENCLOSED DOMAIN

3.5.1 *Case presentation*

To verify the ability of the numerical solver code_saturne to reproduce dam-break scenarios, the numerical reproduction of Kocaman *et al.* (2021) [35] experiments is performed here. The study case has been

selected for several reasons. First, the generated partial dam-break wave resembles current experimental setup with a similar breach opening ratio ($R_b = \frac{W}{breachwidth} = 5$ for Kocaman *et al.* (2021) [35] compared to 4 in the current setup, see Section 3.4). Additionally, the size of the setup is small ($1 \times 0.5 \times 0.2$ m), leading to significantly shorter computational time. Finally, the study provides acoustic wave gauge measurements (sensors similar to that of the current study) and visualisation of the flow propagation for qualitative comparisons.

In the reference paper, the propagation of a partial dam-break wave in an enclosed domain was observed experimentally and compared with both SW and RANS solvers of the industrial software FLOW-3D. Experiments were carried out in a rectangular horizontal channel of 1 meter long, 0.5 meters wide and 0.35 meters high, as sketched in Figure 3.13. The vertical sluice gate opening time is equal to $t_{gate} = 0.04$ s. The upstream water depth h_0 was set to 0.15 m and three different downstream bed scenarios were tested: $h_1 = 0$, 0.015 and 0.030 m. Only the dry bed case scenario is reproduced here. Observations of the dam-break flow were recorded using a video camera with a frequency acquisition of 50 fps and five acoustic wave gauges (one MIC+35/IU/TC upstream of the gate and four MIC+25/IU/TC downstream of the gate) were used to record the water depth variation.

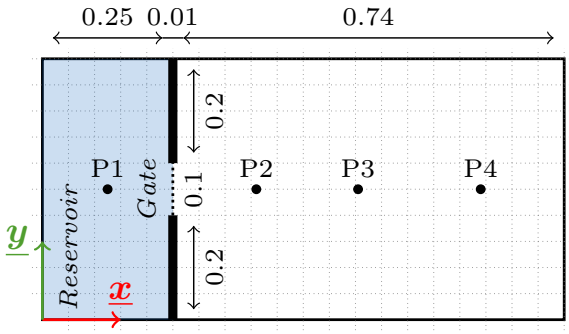

Figure 3.13: Sketch of the experimental setup and associated measurement points from Kocaman *et al.* (2021) [35].

3.5.2 *Numerical model*

code_saturne, presented in Section 3.3.2, is used to perform the numerical simulations. Similarly to the experimental setup size, the computational domain is 1 meter long, 0.5 meters wide and 0.2 meters high. A uniform structured mesh of 6.4 million cells, of size 0.0025 m, is used to perform the simulations. All walls are considered smooth and the top boundary is defined as a symmetry condition. The simulations were run for 10 s with a variable time step Δt to keep the CFL condition under the unity. An initial volume of water of size $0.25 \times 0.5 \times 0.15$ m is defined, corresponding to the initial water depth in the reservoir. Visualisations of the water height at different time steps are illustrated in Figure 3.14.

3.5.3 *Comparisons between experimental and numerical results*

Left columns of Figures 3.15 and 3.16 show the top view from the video camera of the dam-break wave propagation in dry bed condition. After the sudden gate removal, the partial dam-break wave propagates downward, also reflecting on the side walls. After the flow arrival on the end-wall, positive and negative waves are propagated. The right columns of Figures 3.15 and 3.16 show code_saturne's numerical results. A qualitative good agreement between experimental and numerical results is observed, as the wave hits the end wall, the position of the reflected waves and the recirculation zones are correctly captured by the simulation.

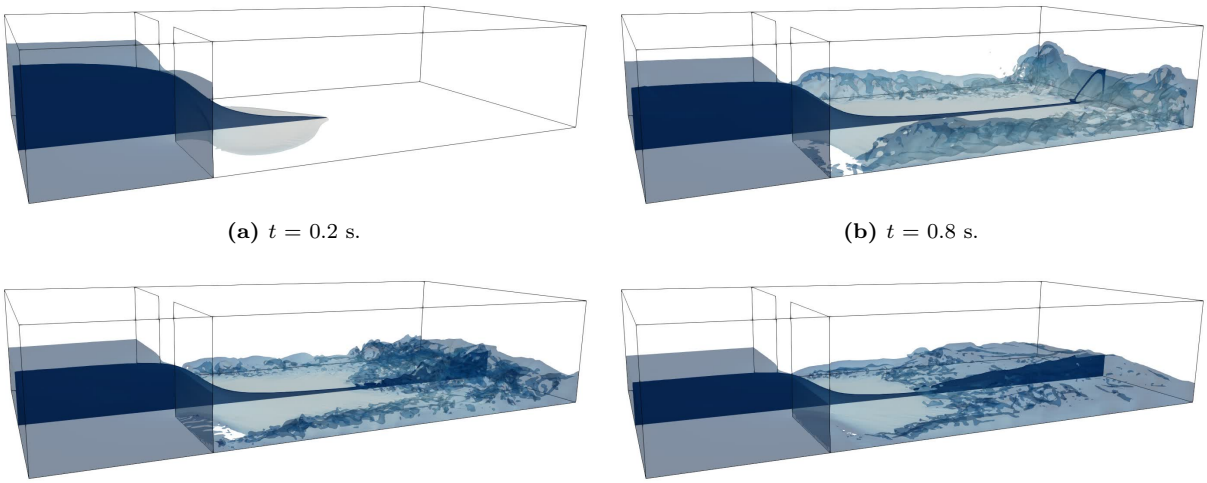

(a) $t = 0.2$ s. **(b)** $t = 0.8$ s.

(c) $t = 1.2$ s. **(d)** $t = 1.8$ s.

Figure 3.14: Water height visualisation at different time steps from code_saturne simulation. Dark blue surface corresponds to $y = 0$ m and $\alpha \leq 0.5$.

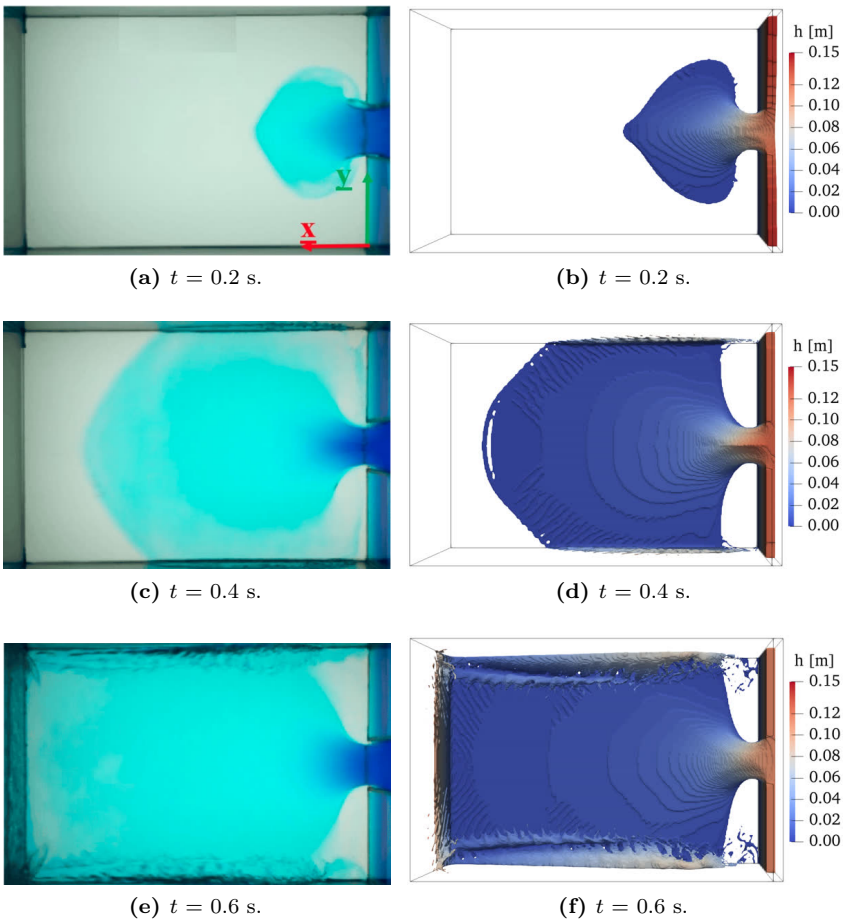

(a) $t = 0.2$ s. **(b)** $t = 0.2$ s.

(c) $t = 0.4$ s. **(d)** $t = 0.4$ s.

(e) $t = 0.6$ s. **(f)** $t = 0.6$ s.

Figure 3.15: Comparison between (left) experimental from Kocaman *et al.* (2021) [35] and (right) water depth field from code_saturne ($\alpha = 0.5$) for $t = [0.2, 0.6]s$.

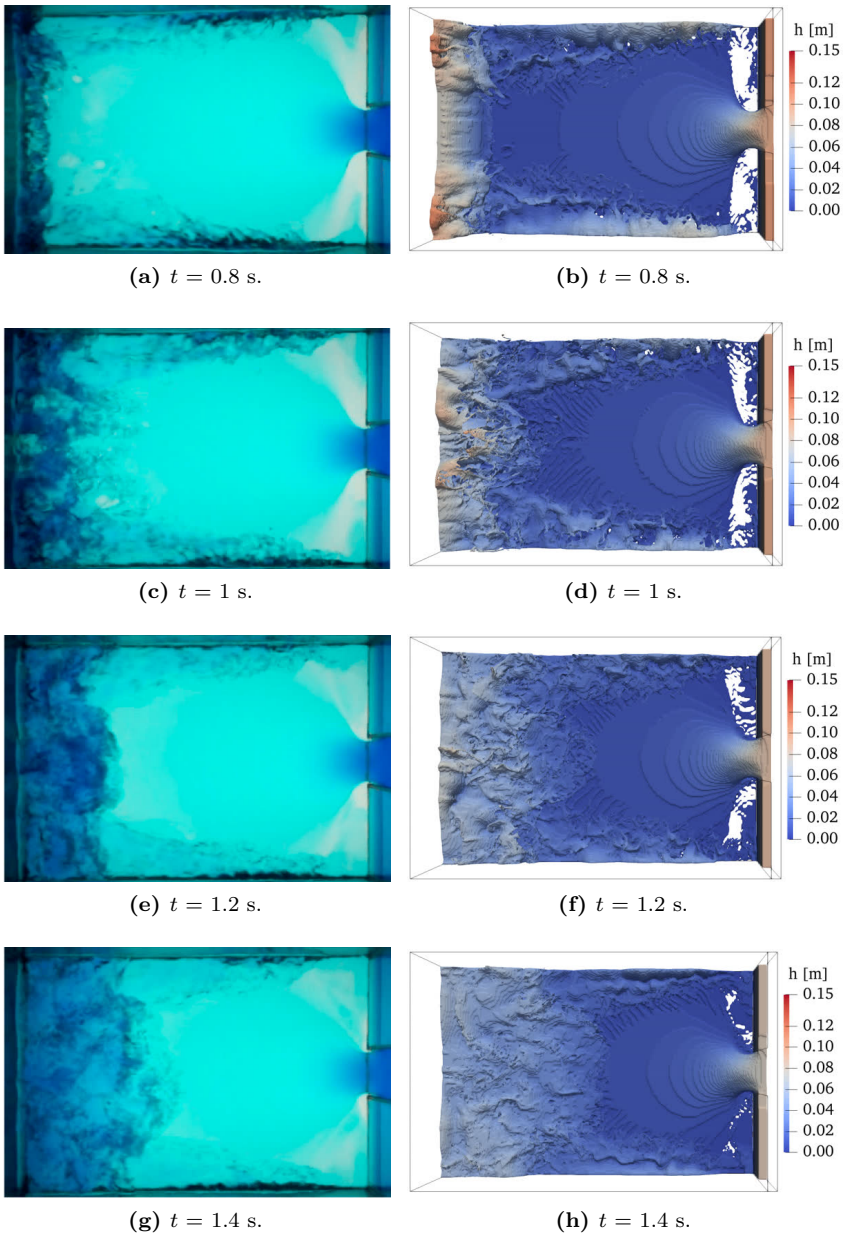

(a) $t = 0.8$ s. **(b)** $t = 0.8$ s.

(c) $t = 1$ s. **(d)** $t = 1$ s.

(e) $t = 1.2$ s. **(f)** $t = 1.2$ s.

(g) $t = 1.4$ s. **(h)** $t = 1.4$ s.

Figure 3.16: Comparison between (left) experimental from Kocaman *et al.* (2021) [35] and (right) water depth field from code_saturne ($\alpha = 0.5$) for $t = [0.8, 1.4]s$.

Figure 3.17 presents good agreement between the experimental and numerical water depth variation at four different positions. First, upstream of the gate (Figure 3.17a), the water depth in the reservoir decreases rapidly after the gate opening. Subsequently, oscillations of the free surface are observable, due to the reflected flow over the end wall.

Note : Kocaman *et al.* (2021) [35] noted that the wave gauge at position P2 led to erroneous water depth measurements between 0-2 seconds after the gate opening. It was explained that the curvature of the flow surface was too high and the acoustic sensors could not perform the measurements accurately.

At position P3 (Figure 3.17c), the arrival time of the wave was correctly captured numerically, as well as the sudden rise in water depth at $t = 2$ s due to the arrival of the reflected wave. Some slight differences in the oscillation amplitudes can be observed and may be due to code_saturne's post-processing method for the water depth. Finally, at position P4 (Figure 3.17d), the wave arrival time and general water depth

were correctly predicted, except at the peak water depth time ($t = 1.25$ s), which in this case, is due to the post-processing method, as highlighted in Section 3.4.

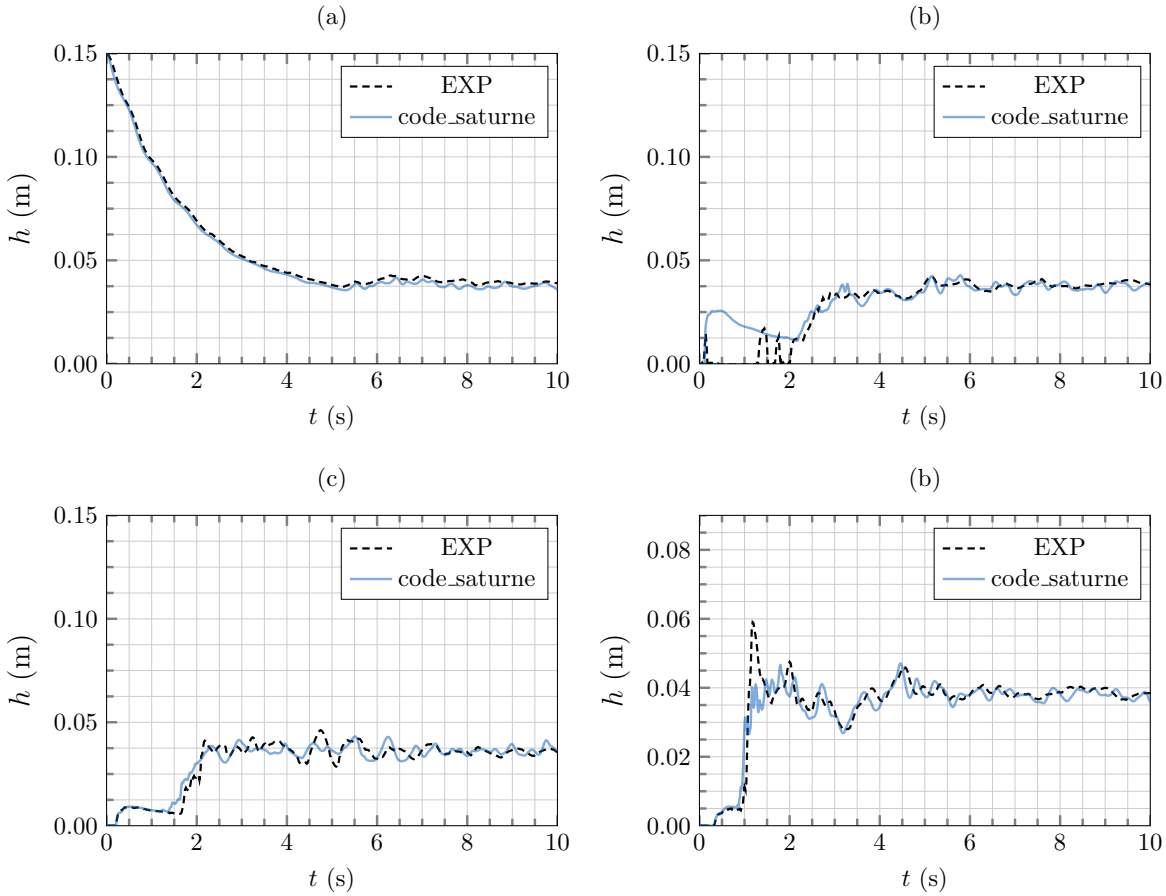

Figure 3.17: Water depth comparison between experimental data from Kocaman *et al.* (2021) [35] and code_saturne at different positions: (a) P1, (b) P2, (c) P3 and (d) P4.

Data from Kocaman *et al.* (2021) [35] was used to access the capability of code_saturne RANS simulation to predict dam-break flow in an enclosed domain with a dry bottom. Results accurately reproduced the dam-break wave and the its reflection against the channel walls.

3.6 CONCLUSION

This chapter provided a general overview of flood models, presented the governing equations and showed first validation results of the two different numerical approaches used in this work to simulate dam-break flow. Two cases were studied: first, both methods were compared to experimental data from this thesis new experimental setup, that will be presented in Chapter 4, followed by the study of the well referenced case of Kocaman *et al.* (2021) [35].

Based on the present comparisons, 3D RANS simulations supplemented with the VOF method appear to be sufficiently accurate in reproducing dam-break flow through idealised urban areas, as the results with and without the presence of obstacles matched both validation data. While 2D SW approaches were unable to account for an obstacle impact on the flow, they may predict the propagation of the dam-break wave without obstacles. Therefore, they can be used for experimental sizing, preliminary parametric studies and time-constrained analysis.

Moreover, results highlighted the importance of numerically accounting for the gate opening and results close to the obstacle (high water height with presence of air bubbles) suggest opportunities for improvement regarding the post-processing method.

For the next simulations, TELEMAC-2D is selected to perform fast and preliminary simulations for the sizing of the experimental setup. On the other hand, code_saturne will be used to perform detailed dam-break simulations with presence of idealised urban areas. The following experimental datasets will also be used for their validation with more complex urban configurations. 3D simulations shall also provide trend confirmation on a larger scale that will be observed experimentally.

4

EXPERIMENTAL SETUP

Summary :
This chapter presents the experimental setup established at EDF Lab Chatou in France, designed to accurately simulate repeatable unsteady dam-break flows through idealised urban areas at a reduced scale. Key aspects such as the sizing of the channel and breach opening, the dam-break flow conditions, and the strategic placement of urban configurations are carefully selected based on the previous literature cases and 2D numerical simulations. The final setup geometry, measurement techniques, and post-processing methods are also outlined. Additionally, the experimental protocol applied during the different measurement campaigns is detailed. Finally, the overall methodology is validated through a comparison with alternative measurement techniques.

Contents

4.1 Introduction **40**
4.2 Sizing of the experimental setup **40**
4.2.1 Sizing of the gate width 40
4.2.2 Selection of the flow conditions 43
4.2.3 Final geometry of the experimental setup 44
4.3 Metrology and calibration **44**
4.3.1 Wave gauge 45
4.3.2 LSPIV analysis 45
4.3.3 Image analysis measurement 46
4.4 Acquisition system **46**
4.5 Repeatability **47**
4.5.1 Setup repeatability 47
4.5.2 Opening of the gate 48
4.6 Experimental protocol **48**
4.7 Post-processing method **50**
4.7.1 LSPIV post-processing 50
4.7.2 IAM post-processing 52
4.8 Validation of the methodology **55**
4.9 Conclusion **56**

4.1 INTRODUCTION

This chapter presents the experimental setup developed during this thesis to study dam-break flow in presence of idealised urban areas. The bench was designed according to the guidelines and reference works listed in Chapter 2. The experiments are performed at EDF Lab Chatou in France.

The chapter is organised as follows: Section 4.2 describes the sizing of the experimental setup. The characteristics of the metrology, acquisition system and setup repeatability are discussed in Sections 4.3, 4.4 and 4.5, respectively. The experimental protocol applied to all measurement campaigns is outlined in Section 4.6 and the different post-processing steps developed in this work are detailed in Section 4.7. Finally, the quality and relevance of the measurement techniques are discussed in Section 4.8.

4.2 SIZING OF THE EXPERIMENTAL SETUP

The original facility used was a rectangular, horizontal wooden channel of 16 m long, 2 m wide and 0.5 m high. The aim of this novel experimental setup is to study a reduced-scale model of unsteady urban flooding and to replicate various idealised suburban districts at a 1/100 scale. The setup's geometry, flow conditions, obstacle sizes and distances from the gate have been carefully selected to define test conditions that result in a turbulent flow with the emergence and submergence of buildings.

To reproduce unsteady flow conditions, the original facility was transformed to create a water tank separated from the remainder of the channel by a watertight sluice gate. The length of the reservoir is defined to contain a volume of water sufficient to allow approximately $t_{acq} = 30$ s of water release. To achieve this, a wall with a thickness of 0.1 m is placed at $x = 7$ m, leading to a [6.95 x 2 x 0.5] m water tank.

4.2.1 *Sizing of the gate width*

For practical and mechanical reasons, the experimental setup was designed with a gate narrower than the channel width. Indeed, this choice was made considering future modifications of the channel, the weight and the time required to open a 2-meter wide gate, the waterproofing of the gate's joint and cost considerations. However, the width of the gate directly impacts the flow behaviour downstream. Indeed, using a narrower gate causes the creation of a hydraulic jump due to the wave reflection on the side wall. Thus, to ensure that the hydraulic jump does not affect the area of interest studied, the sizing of the gate width was selected based on numerical simulation using the SW open-source solver TELEMAC-2D, presented in Chapter 3.

The 2D computational domain used is 14 m long and 2 m wide, as illustrated in Figure 4.1. Two meters at the outlet of the experimental facility are excluded from the numerical model to reduce computational costs. The domain is meshed using uniform-sized triangular cells of 0.007 m, resulting in a mesh composed of approximately 1.3 million cells. As shown in Figure 4.1, the domain is initialised with a constant initial water depth of $h_0 = 0.25$ m in the reservoir (x $<$ 6.975 m) and a dry bed condition downstream of the gate (x $>$ 6.975 m).

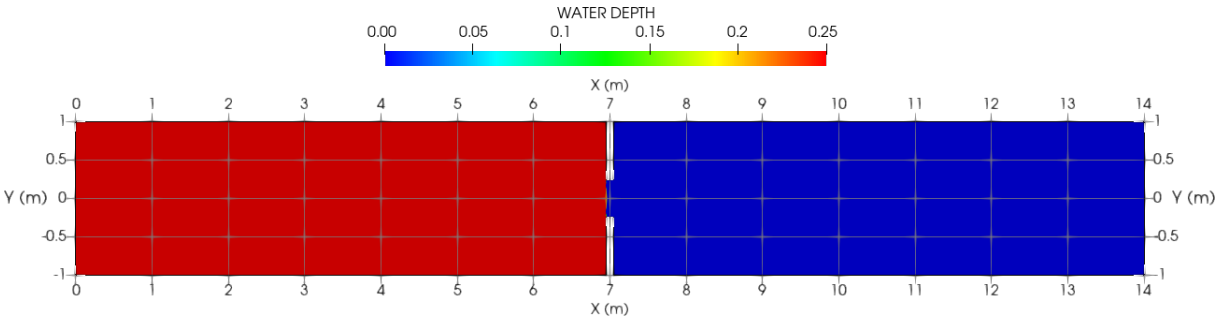

Figure 4.1: 2D computational domain and water depth initial condition for case 50.

All boundaries faces are considered as smooth walls. The Manning's law with the PVC friction coefficient ($n = 0.01$) is applied on the bottom of the domain. The simulation is performed for 10 s using a constant time step of $\Delta t = 0.0025$ s.

To study the impact of the gate size on the flow, four widths values are defined and summarised in Table 4.1. The analysis of the instantaneous water depth field at t = 5 s is compared for all breach width as well as the time evolution of the water depth at three key positions:

- P1 = (4, 0) m, located upstream of the gate, provides an estimation of the tank's emptying speed.
- P2 = (6.5, 0) m, located near the gate in the water tank, offers a good estimation of the impact of the gate width on the flow through the gate.
- P3 = (8.35, 0) m, located downstream of the gate, provides a good estimation of the wave depth.

Table 4.1: Test cases of the gate width study

Case name	50	60	80	100
Gate width (m)	0.5	0.6	0.8	1.0

Figure 4.2 compares all cases at the three defined measurement points. First, the emptying of the reservoir generates oscillations of the free surface (Figure 4.2a and b), leading to variations in the flow rate through the gate that are also observable on Figure 4.3, which is an expected result and was described in Chapter 3. The behaviour of the flow downstream of the gate is directly influenced by the flow rate at the breach; thus, defining the gate width to minimise these oscillations could be beneficial. However, as illustrated in Figure 4.2a and b, the intensity and frequency of the oscillations upstream of the gate are not affected by the gate width variation. Moreover, at position P1 (Figure 4.2a), a gate width increase correlates with an accelerated emptying of the tank. Selecting a narrower gate could benefit longer experiments under consistent flood conditions. Finally, downstream of the gate (Figure 4.2c), the water depth is directly impacted by the gate width. In fact, the water height downstream seems to linearly vary with the gate width: for example, the water depth for case 100 is twice as high as for case 50.

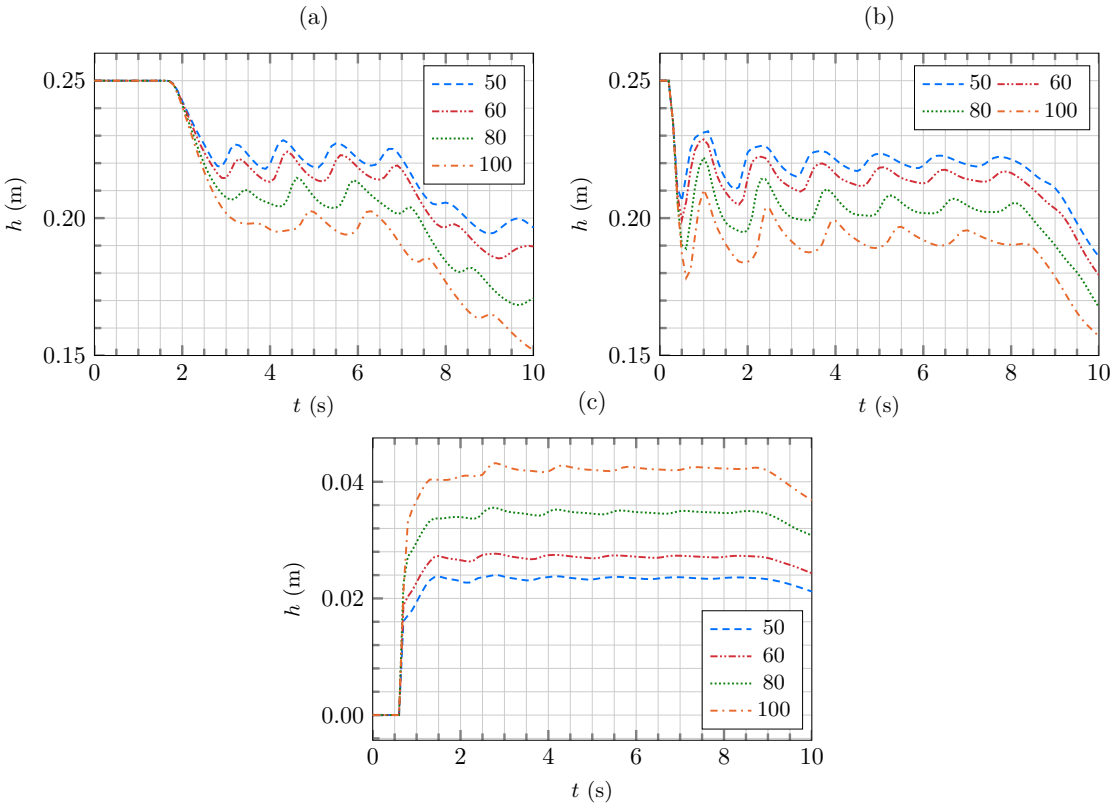

Figure 4.2: Water height time history upstream of the gate at position (a) P1 (4,0) m, (b) P2 (6.5,0) m and, downstream of the gate at position (c) P3 (8.35, 0) m.

Figure 4.3 illustrates, for the different gate widths, the instantaneous water depth field at t = 5 s, following the reunification of two reflection waves. These phenomena occur due to waves reflecting off the side walls at x = 7.8 m, which modify the behaviour of the flow and should not be considered in the current study. To ensure that the reflected waves do not interfere as much as possible with the measurement area, urban configurations must be placed between the gate and the hydraulic jump reunification. Variations in gate width slightly modify the position of the hydraulic jump. Wider gates (Figure 4.3d) tend to reduce the area of interest, while narrower gates (Figure 4.3a) slightly increase it.

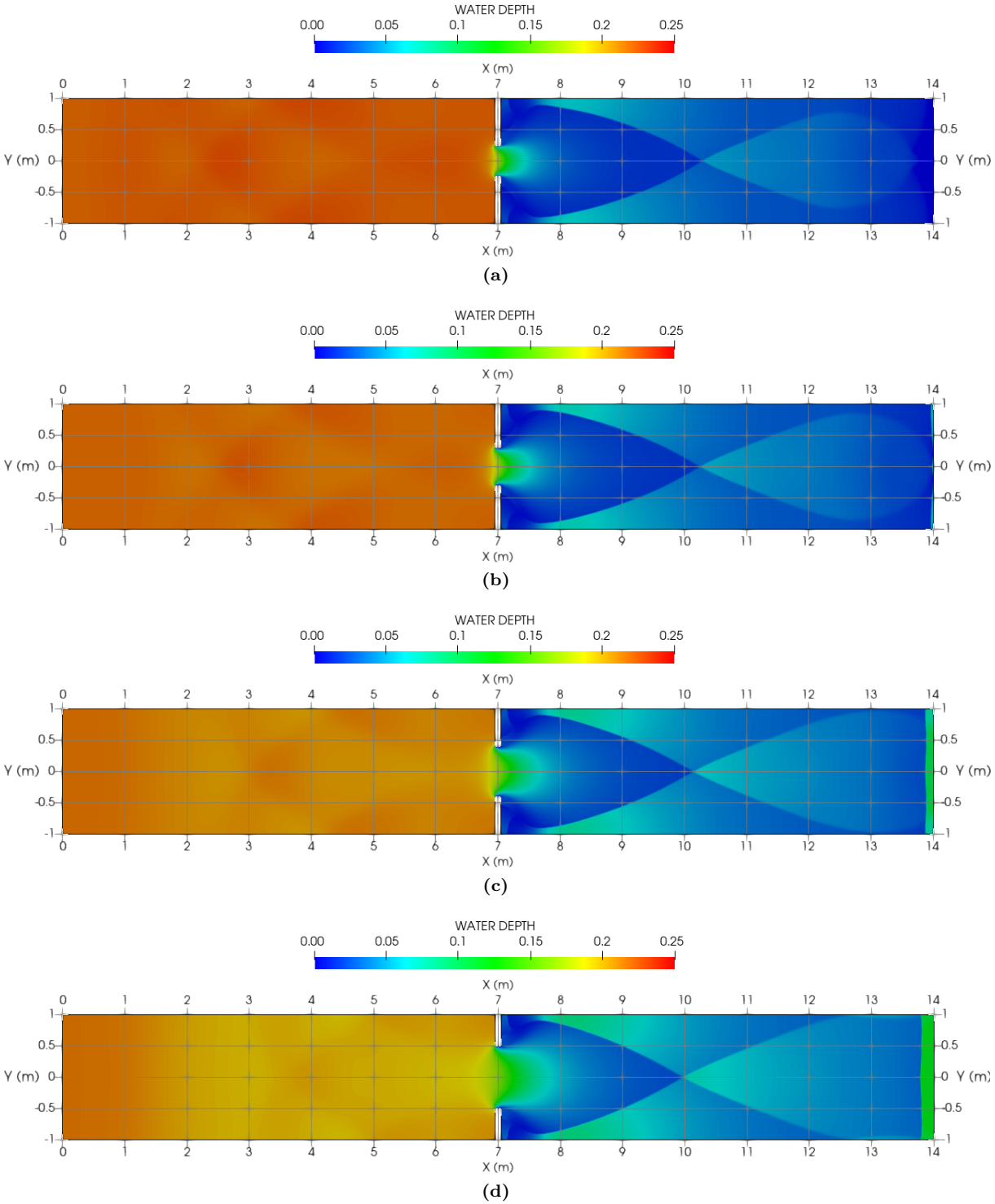

Figure 4.3: Water depth spatial field at t = 5 s for Cases (a) 50, (b) 60, (c) 80 and, (d) 100.

Based on the findings of this study, case 50, a gate width of 50 cm has been selected as the optimal configuration for the final experimental setup. Moreover, based on the water depth spatial field, the obstacles will be placed between x = [8, 9.5] m and y = [-0.5, 0.5] m.

Remark : The position of the urban configurations (and associated sensors) will be adapted between the different measurement campaigns to improve the analysis. All probe locations and names will be detailed at the beginning of each experimental campaign presented in Chapters 5 and 6. Also, the name and geometry of all urban forms studied in the present thesis are summarised in Appendix A.

4.2.2 *Selection of the flow conditions*

Once the geometry of the experimental setup was defined, the flow conditions were carefully selected to achieve a turbulent flow with the emergence and submergence of buildings. The objective was to observe local 3D phenomena near the obstacles, which submerge some of them. In fact, as explained in Chapter 3, in the case of 3D local phenomena, the current methods used to account for urban areas in SW models may not be suitable and require additional datasets for their development. The experimental setup is based on the principles of similarity theory, which states that the ratio between the dominant forces governing the flow should remain consistent in both the model and the prototype. The Froude number is dominant in dam-break flow [129] and is defined as $\mathrm{Fr} = V_c/(gH)^{0.5}$, with V_c the characteristic flow velocity (m/s), g the gravitational acceleration (m/s^2) and H the characteristic water depth (m). To replicate various idealised suburban districts at a 1/100 scale, cubic obstacles of 0.1 m high were selected. To achieve the emergence and submergence of the flow around the obstacles, adjustments were made for the initial water depth and the position of the obstacle in the tank. Accordingly, an idealised urban configuration consisting of 3x3 aligned obstacles was placed in the channel between x = [8.6, 9.1] m and y = [-0.25, 0.25] m and three initial water depths were tested (h_0 = [0.2, 0.25, 0.3] m).

Figure 4.4 illustrates a top view of the flow passing through the idealised urban configuration. Images show that the initial water depth has a significant influence on the flow conditions near the urban configurations. For instance, the first row of obstacles is completely submerged for $h_0 = 0.3$ m (Figure 4.4b) which complicates optical and acoustic measurements in this area (see Section 4.3). Conversely, for $h_0 = 0.2$ m, the water depth around the first row of obstacles is less than 0.1 m, leaving the entire obstacle configuration emerged. Also, some areas around and between the obstacles present very low water heights, preventing some types of measurement techniques. Finally, for $h_0 = 0.25$ m (Figure 4.4a), a thin film of water passes over the first row of obstacles, resulting in mixed emerged/submerged flow conditions, which may be more favourable for measurements. Given these observations, an initial water depth of 0.25 m was chosen for the future experiments. The selected flow conditions led to an estimated Froude number in the obstacle area on the order of magnitude $\mathrm{Fr} > 1$, which was verified spatially using numerical models.

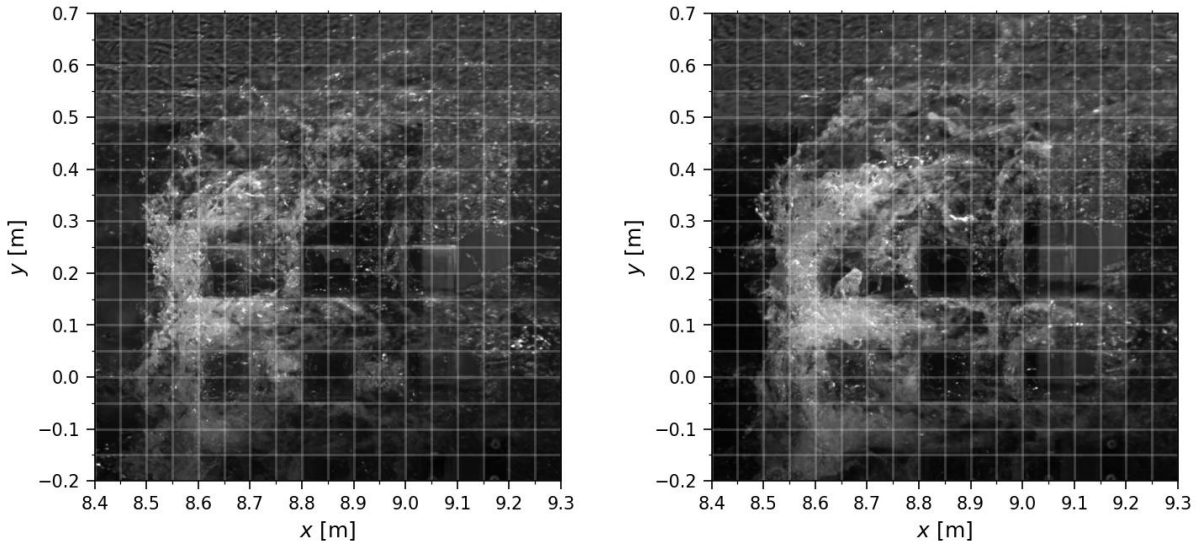

Figure 4.4: Top view of the flow and visual comparison between (a) $h_0 = 0.25$ m and (b) $h_0 = 0.3$ m.

Note : Obstacles are hardly visible as they are all made of transparent PVC. White duct tape will be added to the sides of the obstacles in Chapter 6 for better visualisation.

Note : The maximum vertical size of the gate is 0.31 m, restricting the maximum initial water depth in the reservoir to $h_0 = 0.30$. Otherwise a free surface flow condition at the beginning of the experiment in not ensured.

4.2.3 *Final geometry of the experimental setup*

The final setup geometry, illustrated in Figures 4.5 and 4.6, is 16 m long, 2 m wide and 0.5 m high with a uniform PVC bottom. A 6.95 m reservoir is separated from the remaining of the channel by a 0.5 m wide and 0.31 m high rectangular PVC sluice gate. A pneumatic cylinder is used to ensure repeatability of gate opening. All experiments are realised in dry bed condition. Leaks at the breach are avoided by pressurising the cylinder when filling the tank, adding grease along the gate's guides and using a water hoover between each test.

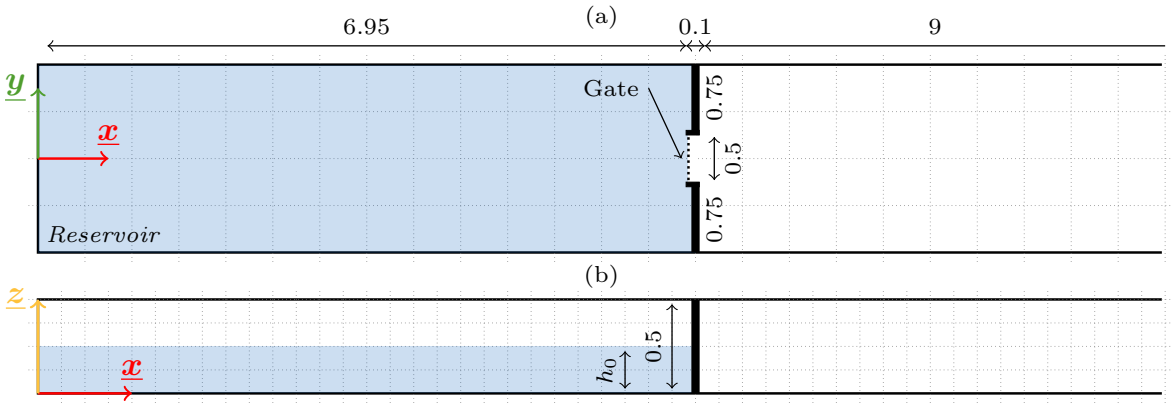

Figure 4.5: Schematic views of the experimental setup, (a) top and (b) side sections [m].

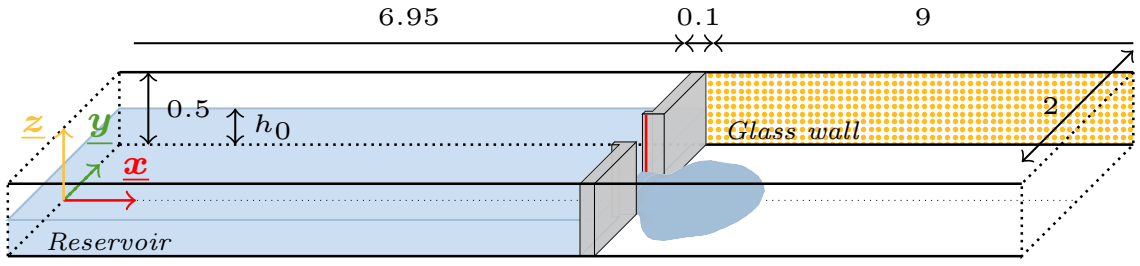

Figure 4.6: Three-dimentional (3D) sketch of the experimental setup [m]. Red line highlight the gate guides at x = 6.925 m.

Note : All urban configurations studied in the manuscript, along with the associated urban parameters and probes, are listed in Appendix A.

4.3 METROLOGY AND CALIBRATION

To characterise the flow, resistive (wave gauge), acoustic (wave gauge) and optical (LSPIV and IAM) measurements are performed and described in this section.

4.3.1 *Wave gauge*

The free surface position is measured with two types of wave gauges (Figure 4.7a). Resistive wave gauges TDH250, with an accuracy of 0.1 mm, are placed upstream of the gate and acoustic gauges Mic+35/IU/TC, with an accuracy of 1 mm, are placed downstream of the gate (Figure 4.7b). This choice has been made given the intrusiveness of the resistive gauge. As presented in Figure 4.7b, the acoustic probes are located in areas of interest such as the obstacles' surroundings.

(a) **(b)**

Figure 4.7: (a) Resistive wave gauge TDH250 placed upstream of the breach and, (b) Acoustic gauges Mic+35/IU/TC placed downstream of the breach.

4.3.2 *LSPIV analysis*

The instantaneous free surface flow velocity around obstacles is retrieved using the Large-Scale Particle Image Velocimetry (LSPIV) method. To do so, a high-velocity laboratory camera (FASTCAM Mini UX50), used with a resolution of 1024x1024 pixels and a recording rate of 250 fps, is placed vertically above the channel (Figure 4.8a). Different types of seeding particles are added to the flow: 2 cm spherical polystyrene, 1.5 cm to 0.5 cm rectangular polystyrene and 1 cm foam spherical particles (Figure 4.9). The different shapes and sizes are used to capture all flow patterns and improve image detection. Some of them are dropped inside the channel before the beginning of the experiment to capture the propagation of the wavefront. Also, in order to optimise LSPIV analysis and given the flow symmetry in the longitudinal direction, the camera is placed to capture only one side of the channel.

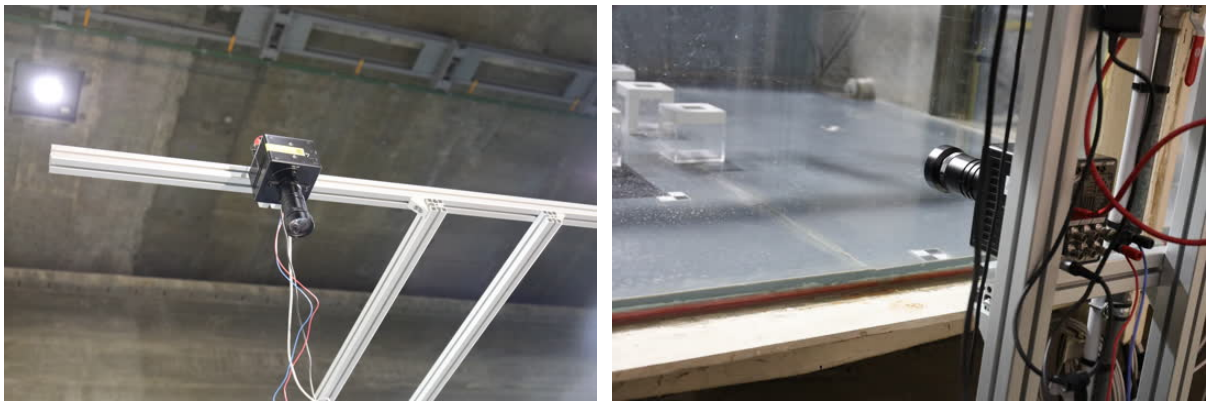

(a) Placed above the channel for the LSPIV analysis.

(b) Placed on the side of the channel for the image analysis measurement.

Figure 4.8: High-velocity laboratory camera (FASTCAM Mini UX50).

4.3.3 *Image analysis measurement*

The position of the free surface is measured, as described in Section 4.3.1, using acoustic wave gauges located near the obstacles. However, the response time of these types of probes is too slow to accurately capture the water height evolution during the collision between the dam-break wave and the obstacle. An image analysis method is thus developed to accurately measure the evolution of the water height during the impact. To do so, a high-velocity laboratory camera (FASTCAM Mini UX50) has been placed on the side of the channel (Figure 4.8b). Note that the acquisition frequency and the resolution of the image were changed between the two experimental campaign and will be provided in the corresponding Chapters 5 and 6.

(a) **(b)**

Figure 4.9: (a) Spherical seeding particles used for the LSPIV analysis, (b) manual addition of the particles to the flow.

4.4 ACQUISITION SYSTEM

All wave gauges sensors are connected to an acquisition card (Measurement Computing USB-1808), visible in Figure 4.10. Then, a program developed with the LabVIEW software is used to record the entire dataset. A schematic diagram of the acquisition software, shown in Figure 4.11, highlights the main functions of the program. More detailed operational information can be found in Appendix B. Also, the software PFV4, developed by Photron, is used to collect the images from the high speed camera and to apply a lens distortion correction. The button used to open the gate starts a synchronised acquisition for all sensors, including the high speed cameras. Thus, in this study, the initial time t = 0 s of the experimental data corresponds to the start of the breach opening. The acquisition frequency of the wave gauges is set to 50 Hz. The acquisition is stopped at t = 25 s due to a reflected wave coming from downstream of the channel caused by a its slow emptying.

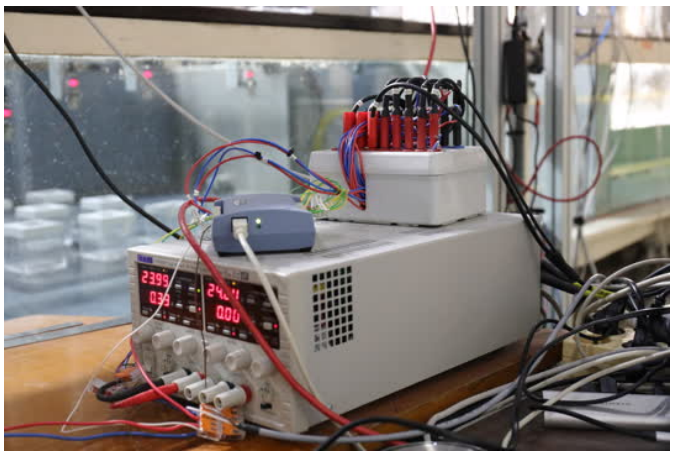

Figure 4.10: Acquisition card and power supply of the water height sensors.

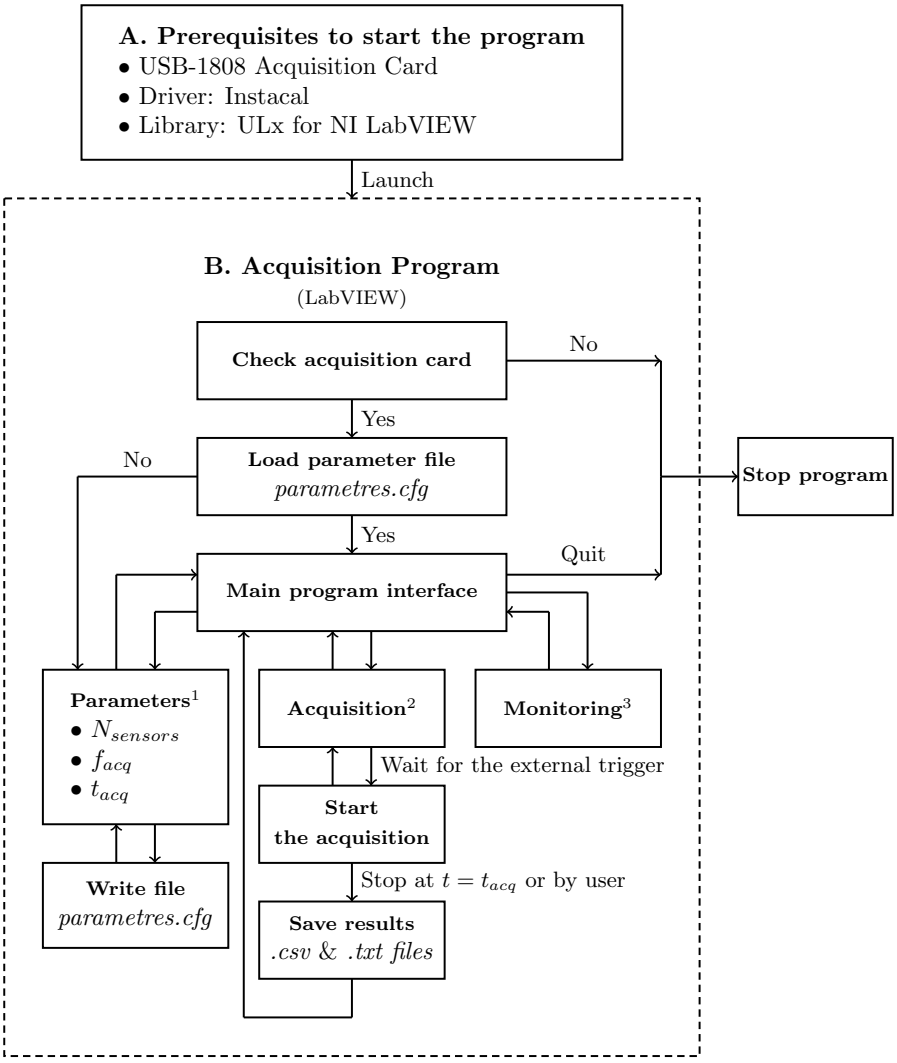

[1]: The parameter entry interface, where users can modify the measurement option. $N_{sensors}$: select the active sensors for the acquisition. f_{acq}: the frequency acquisition. t_{acq}: the measurement duration.
[2]: The acquisition starts when the external trigger occurs, displaying data in real time in the graphical window.
[3]: Display real-time data in a scrolling graph with a history of 1,000 measurements.

Figure 4.11: Schematic diagram of the acquisition software functions.

4.5 REPEATABILITY

4.5.1 *Setup repeatability*

The repeatability of the experimental setup, specifically the gate opening and the initial conditions, is examined without obstacles. To do so, wave gauge values are averaged and compared across 2 to 15 replicates. Since the standard deviation of each probe was less than 1 mm for all tests, the gate opening and initial conditions repeatability are validated. Furthermore, averaging at least three replicates provided a reliable approximation for all tested cases. Figure 4.12 illustrates the variation in water depth and standard deviation for three replicates at two relevant locations: close to and downstream of the gate. Given the demonstrated repeatability, each dataset will involve averaging three replicates.

Note : The repeatability of the wave gauges, in the presence of obstacles, will be examined and presented at the beginning of each experimental campaign (Chapters 5 and 6).

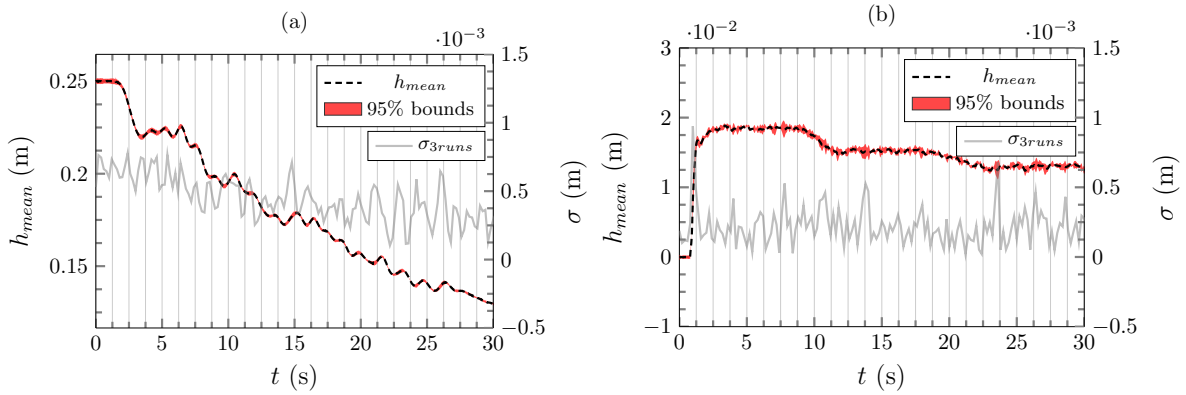

Figure 4.12: Water depth variation, 95% confidence interval and standard deviation for the reference dam-break case, without obstacles, at position (a) (6.5, 0) m and (b) (8.35, 0) m.

4.5.2 *Opening of the gate*

The gate is activated with a pneumatic cylinder connected to an 8 bar pressure network. The pressure in the laboratory network remains constant (daily verification) and the gate's opening time and velocity are obtained through video tracking. Measurements are performed with the reservoir empty and a camera (GoPro HERO10) is placed downstream of the gate in the channel. A target and calibration reference are placed on the gate and the pneumatic cylinder is activated 10 times to record the gate opening. The image processing is conducted using Python's open-source library OpenCV with the TLD tracking framework. The routines compute the gate's opening time, opening size, average opening velocity and the evolution of the opening velocity over time. This information is used to verify the opening repeatability and opening time of the gate for each measurement campaign.

Remark : To improve the opening repeatability and eliminate operator variability, the type of button activating the pneumatic cylinder was changed between two campaigns. Such modification modified the gate's opening time. Therefore, the specific opening time will be provided in each corresponding experimental campaign (Chapters 5 and 6).

4.6 EXPERIMENTAL PROTOCOL

This section describes the detailed step-by-step experimental protocol, ensuring repeatability and accuracy in the experimental procedures.

PREPARATION OF THE EXPERIMENTAL SET-UP

- Set the desired urban configuration inside the channel.
- Apply grease to the sluice gate to prevent leakage at the breach.

PART 1: WATER HEIGHT MEASUREMENTS (3 REPLICATES)

1. Place the acoustic sensors inside the channel.
2. Turn on the power supply for the acoustic sensors (allow approximately 30 minutes for warming up) and for the resistive sensors.
3. Connect the acquisition card and the high-speed camera to the PC.
4. Open the acquisition software (Appendix B) and set, if not already defined in the *parameter.cfg* file, the following parameters: activate 8 channels, acquisition time $t_{acq} = 30$ seconds and the frequency acquisition $f_{acq} = 50$ Hz.
5. Turn on the IAM high-speed camera and open the PFV4 software. Configure the software with the following settings: frame rate = 250 fps, resolution = 1280 x 1024 px and activate (or calibrate, if necessary) the lens distortion correction.

6. Fill the tank (approximately 20 min).
7. Dry the channel using a squeegee and water vacuum to ensure a dry bed condition up to 1 meter downstream of the obstacle configuration. Avoid touching the acoustic sensors during all three replicates to maintain calibration integrity.
8. Stop filling the reservoir once the water level reaches h_0= [0.249-0.251] m.
9. Wait for the reservoir to stabilise (approximately 20 min).
10. Manually measure the water height with a limnimeter (graduated to one-tenth of a millimetre).
11. Launch the acquisition interface on the acquisition software and PFV4. The two software are now waiting for the external trigger to start the data acquisition. Ensure that the acoustic sensors have been on for approximately 30 minutes and the reservoir is stabilised before starting the trial.
12. Initiate the trial by turning the sluice gate opening button, triggering data acquisition.
13. Close the gate once the acquisition is terminated and save the acquired result files and images.
14. Repeat steps 6 to 13 to conduct two replicates.
15. Store the acoustic sensors on the side of the channel.

Note : The acoustic sensors are re-positioned at the beginning and at the end of the water height measurements to avoid interfering with the optical free surface velocity measurements. Therefore, the sensors are calibrated every three replicates. Calibration is performed using solid wedges of 5 cm and 10 cm placed under the sensors. Depending on their vertical position in the channel, they are calibrated across their entire or reduced measurement range using three or four points.

The resistive gauges, which are positioned in the water tank, are calibrated only at the start of the measurement campaign since they are not displaced. The calibration protocol is similar, involving varying water depths in the tank to calibrate the gauges across their entire measurement range. This process involves four calibrations points within a water depth range of 10 to 40 cm.

Then, a linear regression is performed on the results to determine the calibration coefficients for each wave gauge.

PART 2: MEASUREMENT OF FREE SURFACE VELOCITY FIELDS (3 REPLICATES)

1. Turn on the TDH power supply.
2. Connect the acquisition card and the high-speed camera to the PC.
3. Open the acquisition software and set the following parameters: activate N_{TDH} channels, acquisition time t_{acq} = 30 seconds and f_{acq} = 50 Hz.
4. Turn on the LSPIV high-speed camera and open the PFV4 software. Configure the software with the following settings: frame rate = 250 fps, resolution = 1024 x 1024 px and activate (or calibrate, if necessary) the lens distortion correction.
5. Fill the tank (approximately 20 min).
6. Dry the channel using a squeegee and water vacuum to ensure a dry bed condition up to 1 meter downstream of the obstacle configuration.
7. Place the seeding particles in the measurement area around the obstacle configuration, as shown in Figure 4.13a.
8. Stop filling the reservoir once the water level reaches h_0= [0.249-0.251] m.

9. Wait for the reservoir to stabilise (approximately 20 min).
10. Manually measure the water height with a limnimeter (graduated to one-tenth of a millimetre).
11. Launch the acquisition interface on the acquisition software and PFV4. The two software are now waiting for the external trigger to start the data acquisition.
12. Initiate the trial by turning the sluice gate opening button, triggering data acquisition and gradually release the remaining seeding particles downstream of the gate.
13. Close the gate once the acquisition is terminated and save the acquired result files and images.
14. Collect the tracers from the bottom of the channel.
15. Repeat steps 5 to 14 to conduct two replicates.
16. Record an image of the channel bed without tracers used for the background removal step, as shown in Figure 4.13b.

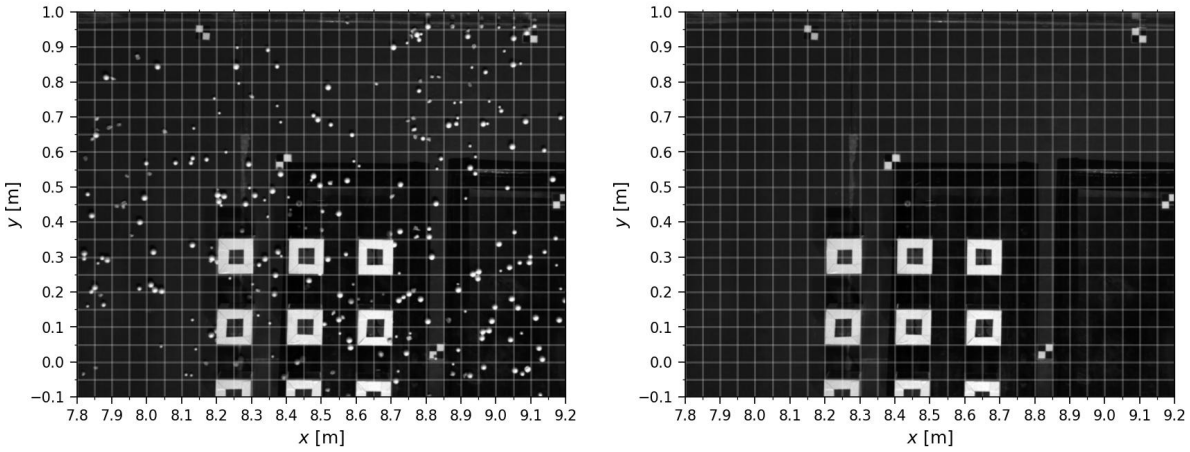

(a) **(b)**

Figure 4.13: (a) Seeding particles placed in the measurement area before the acquisition and, (b) image recorded of the channel bed without seeding particles for the background removal step.

Note : White duct tape has been added to the sides of the obstacles, visible in Figure 4.13, on transparent PVC, creating a visual impression of a hole in the centre. However, all obstacles are watertight cubes of 0.1 m.

4.7 POST-PROCESSING METHOD

The IAM and LSPIV methods were applied to the images acquired with the high-speed laboratory camera. This section details the main post-processing steps.

4.7.1 *LSPIV post-processing*

The recorded image sequences with the high speed camera (Figure 4.14) were analysed with the open-source software Fudaa-LSPIV [130, 131] and the resulting instantaneous velocity field were post-processed with python programming language (Figure 4.15). The Fudaa-LSPIV software analyses a sequence of image by applying the LSPIV method [132]. Several parameters have to be specified such as the Interrogation Area (IA), that defines the size of the area for pattern matching, the Search Area (SA) that defines the scanned zone (i.e. the possible displacement of the pattern) and the filters values. Their values are specified later in Chapters 5 and 6.

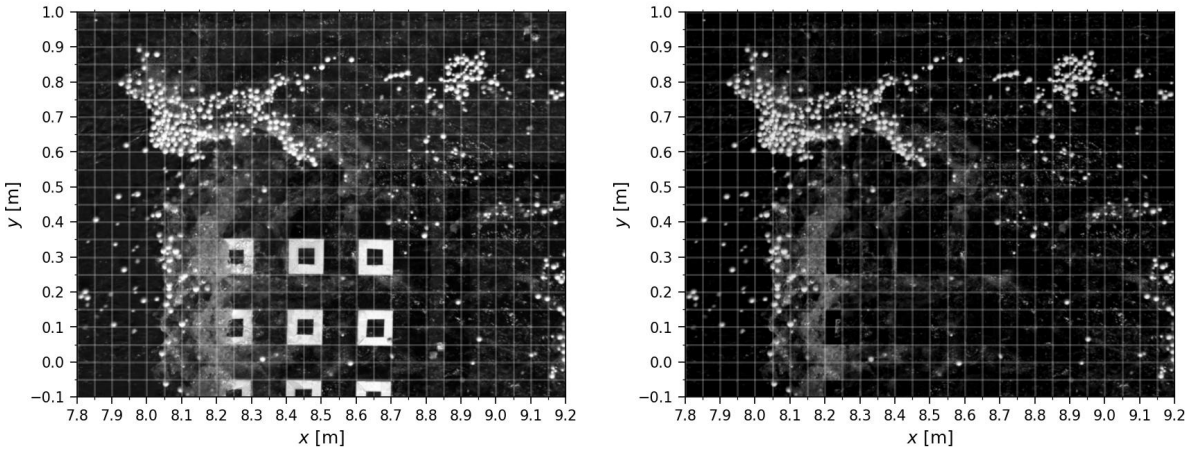

(a) Raw image. **(b)** Background removed image.

Figure 4.14: Illustration of the background removal routine of the LSPIV analysis.

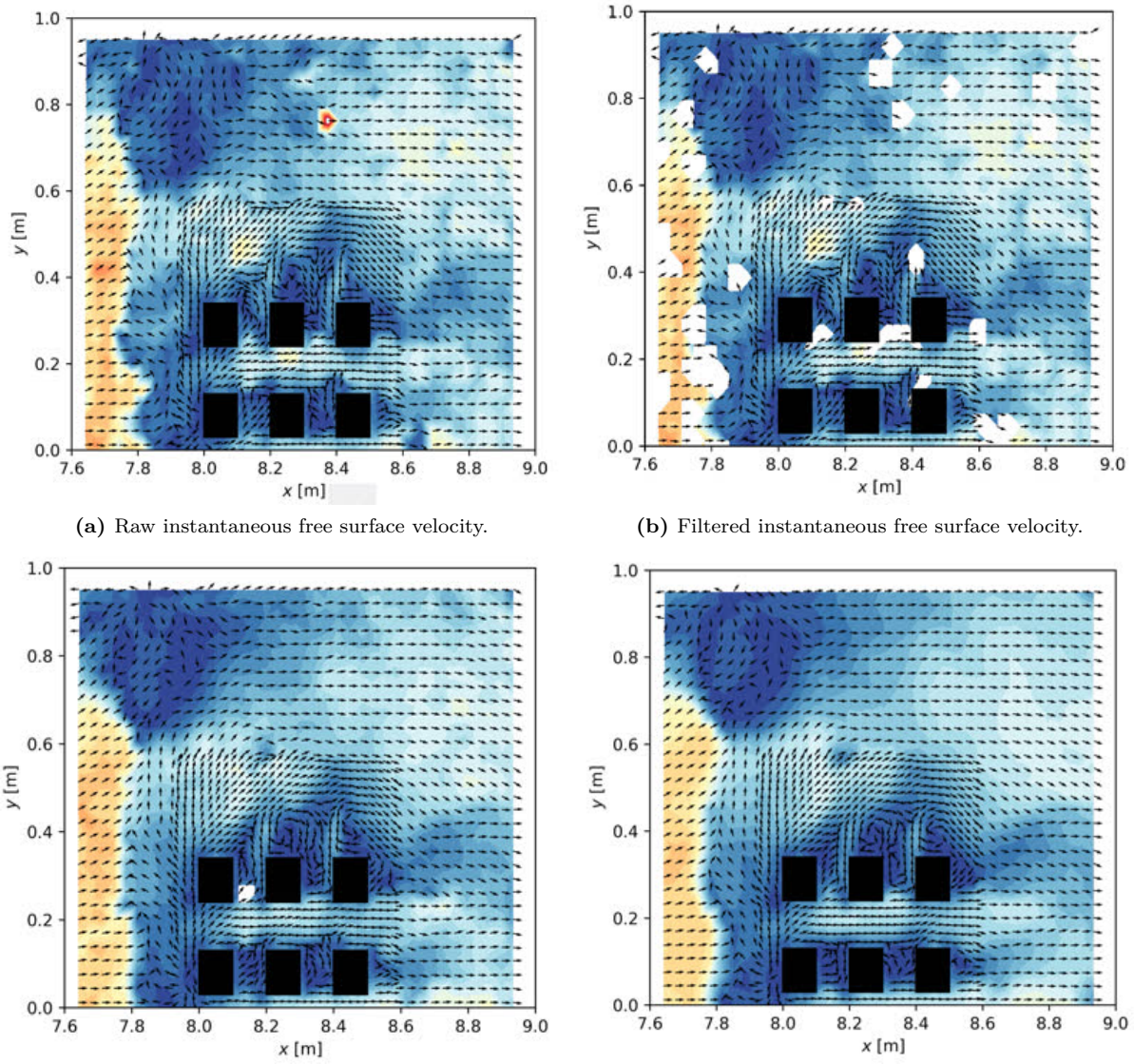

(a) Raw instantaneous free surface velocity. **(b)** Filtered instantaneous free surface velocity.

(c) Averaged velocity field between three replicates. **(d)** Time-averaged velocity field from 25 instantaneous fields ($t_{avg} = 0.1s$).

Figure 4.15: Illustration of the main steps of the LSPIV analysis.

The main post-processing steps of this method are the following:

1. First, a lens distortion correction and background removal routine are applied to the raw images (Figure 4.14).
2. Then a 3D orthorectification of the images is applied based on 10 Ground Reference Points (GRP) obtained by photogrammetry of the channel. The photogrammetry is performed on the software CloudCompare.
3. Next, a velocity analysis of each image is performed on a grid with different refinement zones. Since a LSPIV calculation uses a flat free surface hypothesis, a constant water depth is set to 0.02 m. This value is the mean numerical water depth obtained for a case without obstacles in the measurement zone. At this point, the instantaneous velocity fields are available at each time step (Figure 4.15a).
4. Then, a filter is applied on each instantaneous velocity field, to remove erroneous vectors based on correlation threshold and vector component threshold (Figure 4.15b). A correlation threshold and a median test [133] as a spatial coherency filter is applied to the vector component threshold. The white areas, in Figure 4.15b, correspond to erased erroneous vectors.
5. The next step calculates the average velocity field between the three repetitions for each filtered velocity field (Figure 4.15c).
6. Finally, a variable time-averaged velocity is computed from the previous averaged velocity fields. In Figure 4.15d, t_{avg} is set to 0.1 s, so the velocity field is averaged over 25 instantaneous velocity fields.

4.7.2 *IAM post-processing*

The image analysis is carried out using the NI Vision Development Module of the LabVIEW software. A schematic diagram of the acquisition software, shown in Figure 4.16, highlights the main functions of the program. Detailed operational information about the program is provided in Appendix C and the main post-processing steps are outlined below:

1. First, a lens distortion correction and a background removal routine are applied to the raw images, resulting in Figure 4.17b.
2. A 2D calibration is then performed converting pixel measurements to meters.
3. A binarization process follows, using an adaptive threshold value that is adjusted for each image, as represented in Figure 4.17c.
4. Next, a Region of Interest (ROI) is defined as a vertical line, as illustrated on Figure 4.17d, that can be shifted horizontally to become a rectangle.
5. An edge detection is executed on this line and the highest value is retained as the free surface position (Figure 4.17d). If the ROI is shifted horizontally, the final value for the free surface position is calculated as the mean of all the highest values detected. This approach minimises drop detection and measurement noise.

> **Note** : Figure 4.18 illustrates the principle of the IAM technique for detecting the position of a free surface. Once the images are binarized and the ROI is defined (shown in green in the sketch) for one (on the left) or several (on the right) vertical pixel lines, the software detects the highest transition from white to black (indicated in red on the sketch). The resulting water height corresponds to the position of the detected pixel or the mean of all detected ones.

6. A filtering step is added if drops interfere during the detection of the free surface. The latter eliminates isolated white pixels that correspond to droplets.

Note : The water depth measured with the field of view of the IAM technique is considered to be the water depth corresponding to y = 0 m equivalent to the centre of the channel. An additional camera view could have been used to validate this hypothesis, but this was not formally performed in the present work.

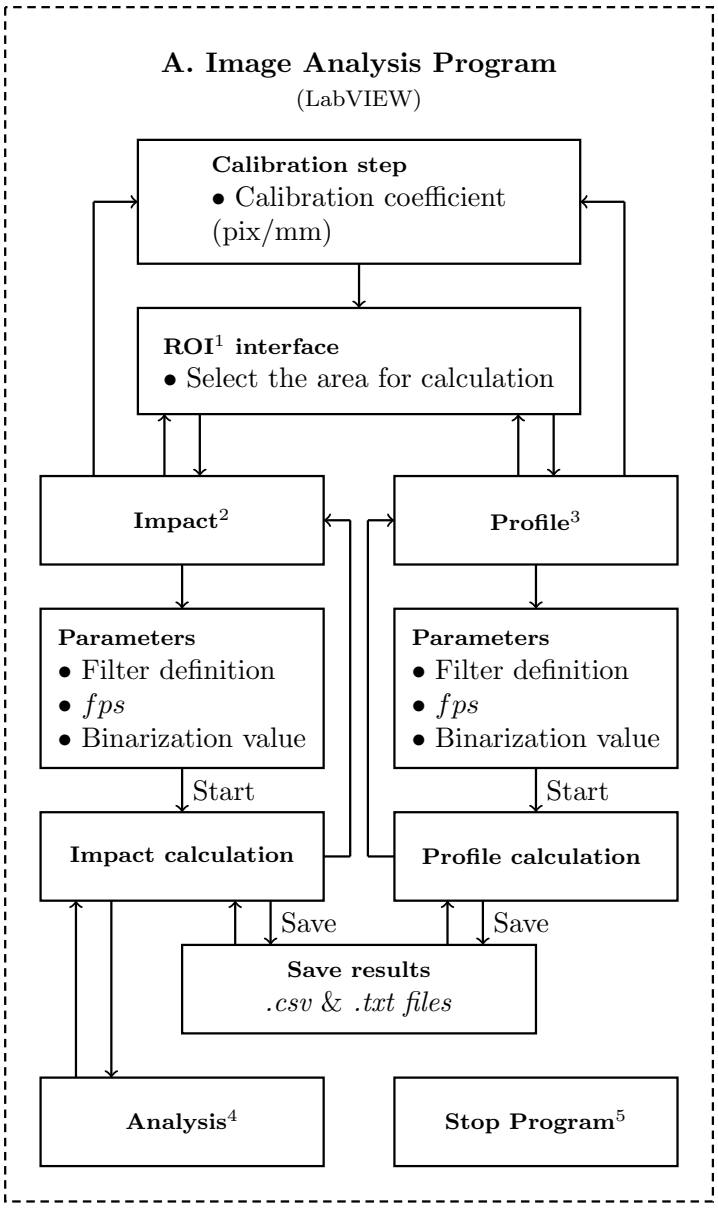

[1]: Region Of Interest (ROI) is a single line or several lines forming an area on which the calculation is performed.
[2]: The objective of the impact analysis is to detect the water depth in the ROI and track its evolution in each image.
[3]: The profile analysis capture the free surface at a specific instant to study the shape of the splash-up area upstream of the obstacles.
[4]: The analysis interface displays each measurement result of the impact analysis and its associated image with the edge detection position.
[5]: Stop program can be reached from 'Calibration step', 'ROI interface', 'Impact' and 'Profile'.

Figure 4.16: Schematic diagram of the Image Analysis Measurement (IAM) software functions.

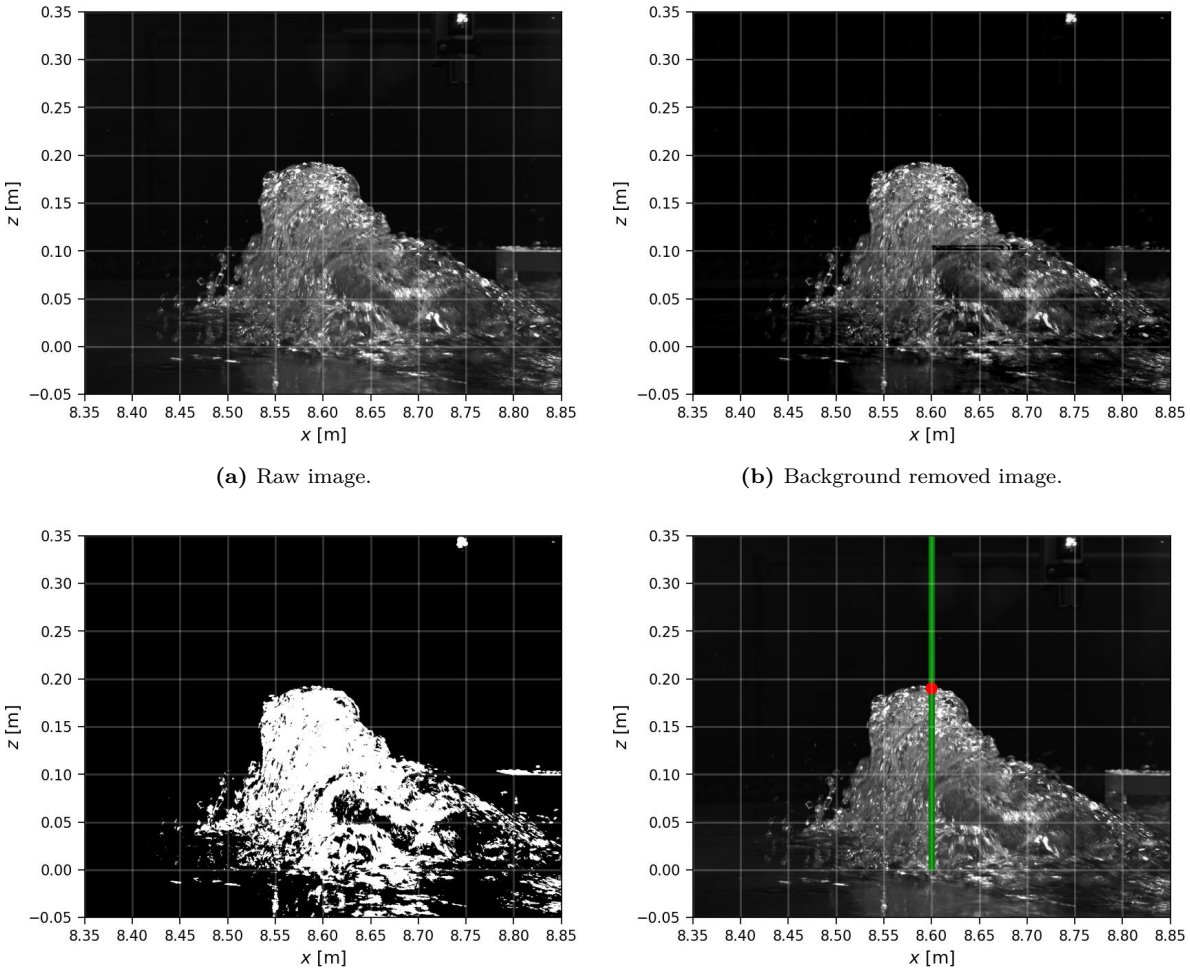

(a) Raw image.

(b) Background removed image.

(c) Binarized image.

(d) Free surface detection. Green line: ROI and red point: edge detection.

Figure 4.17: Illustration of the main steps of water height Image Analysis Measurement (IAM).

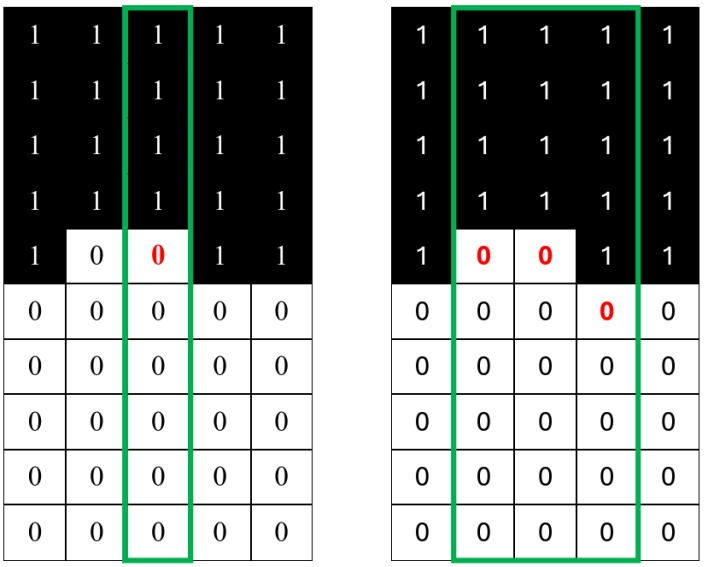

Figure 4.18: Sketch of the principle of the IAM technique for detecting the position on a free surface. Green lines represent the ROI position and red text the detected pixel corresponding to the detected free-surface.

4.8 VALIDATION OF THE METHODOLOGY

It is expected that the combination of various presented measurement techniques to track fast transient flow leads to data that enhances our understanding of the phenomena studied. Table 4.2 lists their respective advantages and disadvantages. In most past laboratory tests, fundamental flow features (such as wave profiles and wavefront motion) were investigated using resistive wave gauges. While these probes, placed upstream of the gate in our study, allow for a high acquisition frequency, their intrusiveness disturbs the flow, particularly in areas with low water depth [129]. Due to these limitations, acoustic wave gauges are sometimes employed for dam-break studies. These probes, placed downstream of the gate in our study, are non-intrusive, but have a lower acquisition frequency and their output data may contain spurious dynamic information, specially during the initial stages of the experiment.

Table 4.2: Advantages and disadvantages of different measurement techniques for fast transient flow.

	Advantages	**Disadvantages**
Water depth		
RWG[1]	Fast acquisition frequency;	Intrusive;
AWG[2]	Non-intrusive;	Low acquisition frequency; Spurious dynamic information; Local flow depth measurement;
IAM	Large area measurement; Fast acquisition frequency; Non-intrusive;	Optical access to the flow;
Velocity		
ADV[3]	Fast acquisition frequency; 3 velocity components;	Intrusive; Local flow velocity;
LSPIV	Large area measurement; Fast acquisition frequency; Non-intrusive;	Free surface velocity field; Optical access to the flow;
PIV[4]	Vertical Velocity field; Large area measurement; Fast acquisition frequency; Non-intrusive;	Complexity of the system, Cost; Optical access to the flow;

[1] RWG: Resistive Wave Gauge;
[2] AWG: Acoustic Wave Gauge;
[3] ADV: Acoustic Doppler Velocimetry;
[4] PIV: Particle Image Velocimetry;

Additionally, acoustic interference can occur if two acoustic wave gauges are placed too close together or to a surface (e.g., obstacle walls), limiting their use. In the present study, to complement acoustic wave gauge measurements, Image Analysis Measurement (IAM) is employed to capture the free surface variation during the impact. This novel measurement technique applied to flash urban floods completes previous acoustic water depth measurements, especially during the initial stages of the experiment when fast transient phenomena occur.

In addition to water depth evolution, the velocity field is a crucial flow variable in dam-break experiments. In general, local flow velocity measurements are performed using Acoustic Doppler Velocimeters (ADV), despite their intrusiveness. However, with the rapid variation of the free surface elevation, interpreting the results from such devices can be challenging [45]. Recently, velocity fields have been retrieved using non-intrusive imaging techniques, such as Large-Scale Particle Image Velocimetry (LSPIV) or Particle Image Velocimetry (PIV). With the development of optical technology, these techniques can achieve high acquisition frequencies and provide valuable insights of the flow evolution. In the present study,

LSPIV measurements are performed to capture free surface velocity. Performing PIV measurements and measuring vertical velocity fields of the flow would require two optical access points, close to the centre of the urban area, which is particularly challenging to implement. Thus, its implementation is beyond the scope of this thesis.

4.9 CONCLUSION

This chapter details the development of a novel experimental setup designed to study unsteady flow in urbanised areas. Established at EDF Lab Chatou, the setup aims to accurately simulate urban flooding on a reduced scale.

The original experimental setup was modified to include a water tank separated by a sluice gate, to generate dam-break flow. A numerical model based on the 2D Shallow Water (SW) equations with TELEMAC-2D is used to determine the setup's geometry. Results indicate that the oscillations of the free surface through the gate are not significantly impacted by the breach width for gates ranging from 0.5 to 1 m wide. Consequently, a 0.5 m wide breach was selected to extend the duration of tank emptying and to optimise gate opening time with a lighter gate. Furthermore, the initial water depth, h_0, is determined based on experimental observations of the flow through a 3x3 aligned obstacle configuration, to achieve both emergence and submergence of the obstacles. The position of the obstacles within the channel is adjusted to ensure that reflected waves do not interfere with the measurement area.

The recent and adapted measurement techniques are deployed to provide a complete water hydrograph. Resistive and acoustic wave gauges are strategically placed upstream and downstream of the breach to measure water depth variations. Additionally, a high-velocity laboratory camera is employed to complete the acoustic gauges measurements during the impact of the submersion wave with the first row of obstacles. Lastly, a LSPIV analysis is performed to obtain the velocity field of the free surface. The repeatability of the setup is demonstrated, with the number of replicates for each measurement type set to three for each configuration. Detailed descriptions of each step of the experimental protocol, applied across all measurement campaign, are provided. Finally, the post-processing steps applied to the images from the two optical techniques are detailed and illustrated.

5

PRELIMINARY EXPERIMENTAL CAMPAIGN: DAM-BREAK FLOW OVER VARIOUS OBSTACLES CONFIGURATIONS

Summary :
This chapter presents the results of the first experimental campaign. The experimental protocol presented in Chapter 4 is also validated through the successful completion of the trials. Four simple obstacle configurations are analysed, focusing on key variables such as water depth variation and the free surface flow velocity within specific regions of interest. A method for quantifying the flow area impacted by the obstacles is also proposed. For validation purposes, the experimental dataset is compared quantitatively and qualitatively with numerical results from the open-source CFD software code_saturne, presented in Chapter 3. Additionally, a mesh and turbulence model sensitivity analysis are performed, justifying a final choice for the future simulations. The main features of the flow are highlighted, and feedback is retained for the design of a second experimental campaign.

Contents

5.1 Introduction **58**
5.2 Methodology **58**
5.2.1 Performed tests and configurations 58
5.2.2 Repeatability 61
5.3 Experimental results **62**
5.3.1 Free surface flow description 62
5.3.2 Investigation of the flow area impacted by the obstacles 65
5.3.3 Water depth description upstream and downstream of the gate 67
5.3.4 Splash-up zone evolution 70
5.4 Numerical methodology **73**
5.5 Numerical validation results **75**
5.5.1 Reproduction of the upstream oscillations 75
5.5.2 Water depth comparison upstream and downstream of the urban area 76
5.5.3 Free surface velocity comparison 78
5.5.4 Turbulence model sensitivity analysis 82
5.5.5 Summary 86
5.6 Conclusion **86**

5.1 INTRODUCTION

In order to validate the geometry and methodology of the experimental setup presented in Chapter 4, a series of dam-break experiments were conducted. The study presented here explores four different obstacle layouts, providing complete water hydrographs within and around these configurations. The main flow features will be highlighted, and the impact of the obstacles on the flow will be quantified.

Additionally, the experiments are reproduced using the open-source Computational Fluid Dynamics (CFD) software, code_saturne. Qualitative and quantitative comparisons are made to evaluate the model's ability to accurately predict the experimental data.

The structure of this chapter is organised as follows: Section 5.2 presents the overall methodology and the urban configurations studied. Experimental results are analysed in Section 5.3 and the numerical setup is presented in section 5.4. code_saturne results are then compared to the experiments in Section 5.5. Finally, Section 5.6 concludes with the findings and provides recommendations for future measurement campaigns.

5.2 METHODOLOGY

The current study methodology is divided into three main steps: (i) conduct dam-break flow experiments impacted by different obstacle configurations, (ii) analyse the experimental results and the impact of the observed obstacle configurations on the flow, and (iii) validate code_saturne using the novel and detailed dataset.

5.2.1 *Performed tests and configurations*

Four independent parameters are used to defined the urban forms and are illustrated in Figure 5.1:

- n_x and n_y: the number of streets along the x and y axis, respectively.
- l_x and l_y: the width of the streets along the x and y axis, respectively.

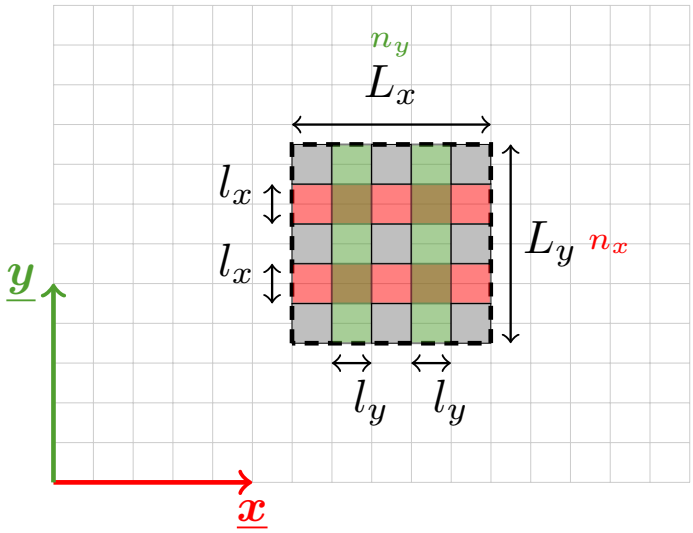

Figure 5.1: Geometry of the urban form $2-10-2-10$ and definition of the parameters characterising urban forms in the manuscript. Grey surfaces represent the position of the obstacles, red surfaces represent the streets along the x axis, and green surfaces represent the streets along the y axis.

The names of the configurations correspond to $n_x - l_x - n_y - l_y$, with each part representing the associated value of the given parameter. Four different configurations of obstacles are studied in this chapter and illustrated in Figure 5.2:

- $0-0-0-0$ is a single cube of size 0.1 m placed in the centre (x = 8.65 m, y = 0 m) of the channel and aligned with the coordinate axes (Figure 5.2a).

- $1-0-1-0$ is equivalent to the previous one but for a cube of size 0.2 m (Figure 5.2b).
- $2-10-2-10$ corresponds to an idealised suburban district of 3×3 aligned obstacles (Figure 5.2c) already studied for steady flow [48, 134]. In this case, cubes of size 0.1 m are all separated by 0.1 m.
- $4-0-4-0$ is a single block of size 0.5 m (Figure 5.2d) equivalent to the area occupied by the $2-10-2-10$ configuration.

To assess the impact of the obstacles on the flow, all configurations are compared to a reference dam-break case with no obstacles, denoted in this work as case '0'. The corresponding parameters of the urban forms are given in Table 5.1.

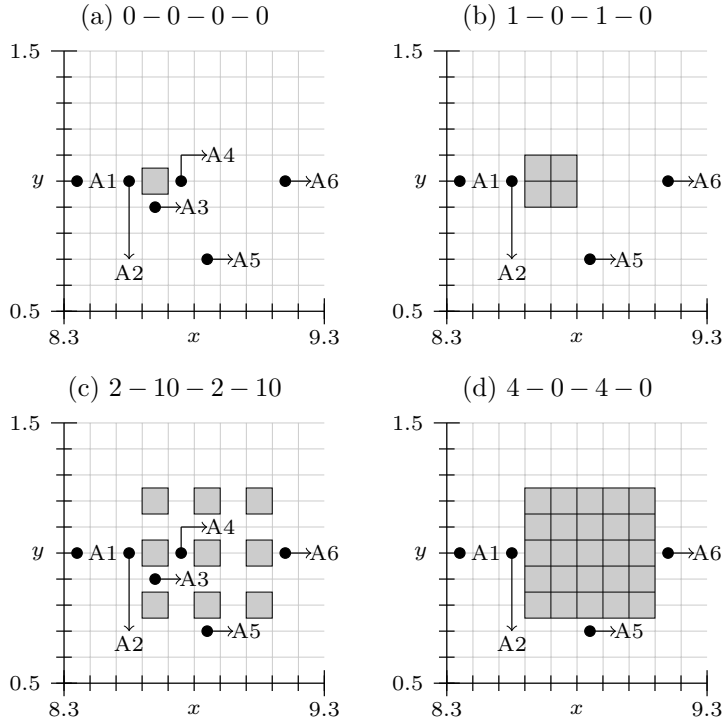

Figure 5.2: Top view of the configurations studied and probes locations, (a) $0-0-0-0$: one single obstacle of length 0.1 m, (b) $1-0-1-0$: one single obstacle of length 0.2 m,(c) $2-10-2-10$: 3x3 aligned obstacles of individual length of 0.1 m and (d) $4-0-4-0$: one single obstacle of length 0.5m.

Table 5.1: Parameters characterising the configurations studied.

Configuration *	**Parameters**					
	n_x	l_x (m)	L_y (m)	n_y	l_y (m)	L_x (m)
0	-	-	-	-	-	-
$0-0-0-0$	0	0	0.1	0	0	0.1
$1-0-1-0$	1	0	0.2	1	0	0.2
$2-10-2-10$	2	0.1	0.5	2	0.1	0.5
$4-0-4-0$	4	0	0.5	4	0	0.5

* Configuration names $n_x - l_x - n_y - l_y$

The four configurations were selected to examine the influence of obstacle size on the flow's blockage effect and validate the experimental protocol. Additionally, the building density effect in the urban area, between configurations $2-10-2-10$ and $4-0-4-0$, was investigated to underscore the influence of modelling streets in large-scale flood study.

The free surface position is measured with two types of wave gauges whose positions are listed in Table 5.2. As illustrated in Figure 5.2 and 5.3, probes are placed in areas of interest such as the obstacles' surroundings. Also, the opening time of the gate, obtained from video tracking, is about $t_{gate} = 0.32$ s ($v_{gate} = 0.78\ m/s$) and is above the recommended value from Lauber *et al.* (1998) [39], $t'_{gate} = 1.25(h_0/g)^{1/2} = 0.2$ s, with g = 9.81 m/s^2 the gravitational acceleration and h_0 the initial reservoir water depth. However, as shown by von Häfen *et al.* (2019) [67], the error in measurements produced by the opening time of the gate decreases while the distance from the gate increases. Since the area of interest is located 1 to 2 m downstream of the gate, this error is considered negligible in the current study. The initial depth for all experiments is h_0 = [0.250 - 0.251] m (± 0.5 mm) and is measured before each experiment using a limnimeter with a scale graduated to one-tenth of a millimetre. Moreover, the parameters used for the LSPIV analysis are summarised in Tables 5.3 and 5.4. The value of each parameter was carefully selected through sensitivity analysis. The parameter values were chosen as a compromise between the computational cost of the LSPIV analysis and the resulting filtered instantaneous field homogeneity. For the sake of brevity, the selection process of the different parameters is not detailed in the manuscript. The calculation on each image is performed on a homogeneous grid of approximately 50 pixels per cell in the x and y directions.

Table 5.2: List of probe types and locations (m).

	Type	**x** (m)	**y** (m)
R1	Resistive	4.00	0.00
R2	Resistive	4.00	0.50
R3	Resistive	6.50	0.00
R4	Resistive	6.50	-0.15
A1	Acoustic	8.35	0.00
A2	Acoustic	8.55	0.00
A3	Acoustic	8.65	-0.10
A4	Acoustic	8.75	0.00
A5	Acoustic	8.85	-0.30
A6	Acoustic	9.15	0.00

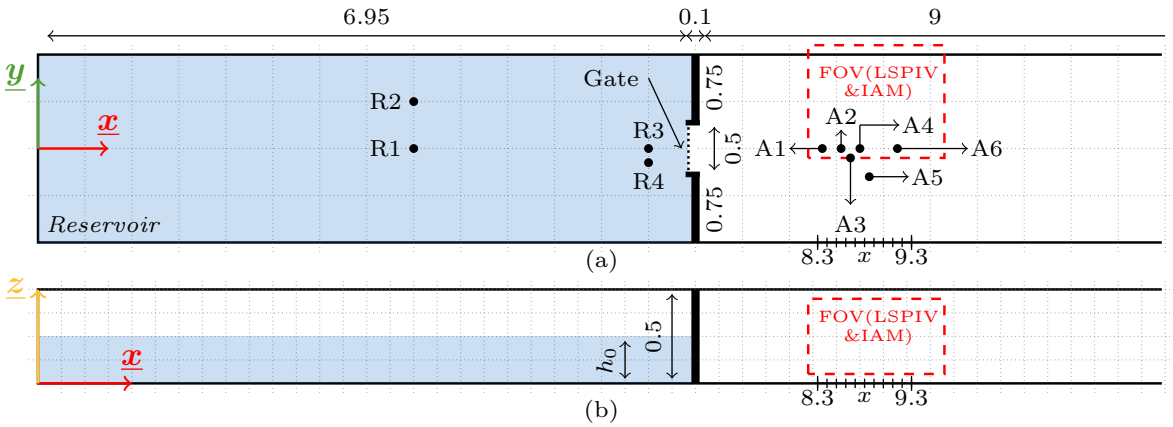

Figure 5.3: Schematic views of the experimental setup, (a) top and (b) side sections. The coordinate system, the probes locations (R1 to R4, A1 to A6) and the Field Of View (FOV) for both Large-Scale Particle Image Velocimetry (LSPIV) and Image Analysis Measurement (IAM) are also illustrated.

Table 5.3: Summary of the parameters used for the LSPIV analysis in Fudaa-LSPIV [130].

Number of frames	Resolution	Water level	IA	SA_{y-}	SA_{y+}	SA_{x-}	SA_{x+}
3850	0.0016 m/pix	0.02 m	30 pix	10 pix	10 pix	5 pix	10 pix

Table 5.4: Summary of the filter parameters used for the LSPIV analysis.

	Correlation threshold	**Median test*** [133]		**Velocity filters**	
		r_0^*	ξ	V_x (m/s)	V_y (m/s)
all cases	0.4	4	0.1 pix	-	-

* r_0^*: Normalised residual threshold, ξ: acceptable fluctuation level

Note : The recommended universal value for the normalised residual threshold r_0^* and the acceptable fluctuation level ξ: $r_0^* > 2$ and $\xi = 0.1$ pix [133].

Finally, an IAM analysis is performed for all cases except for case $4-0-4-0$, as the water jet is out of the FOV. The parameters used for the IAM analysis are available in Table 5.5. The acquisition frequency is set to 100 fps and image resolution to 1280 × 720 pixels. The region of interest is placed 0.05 m upstream of the first row of obstacles equivalent to position A2 for comparison with the acoustic gauges.

Table 5.5: Summary of the parameters used for image analysis measurement program (Appendix C).

	Binarization value	**Calibration** (pix/mm)	**Region Of Interest** Offset[1]	Nb lines[2]	Increment[3]	**Filter**
$0-0-0-0$	Auto	1.62	0.5 m	1	1 pix	Erosion [135]
$1-0-1-0$	Auto	1.56	0.5 m	1	1 pix	Erosion
$2-10-2-10$	Auto	1.69	0.5 m	1	1 pix	Erosion

[1]: Δx between x = 8.6 m and the position of the ROI.
[2]: Number of times the ROI is shifted horizontally from its original position to -x direction.
[3]: Increment between each shifted ROI lines.

Remark : The calibration of the IAM analysis is conducted for each configuration since the cameras were tidied up during the night and thus moved between each studied cases.

5.2.2 *Repeatability*

The repeatability of the experiment was verified for each obstacle configuration. Six experiments (as presented in Chapter 4) were conducted for each case: 3 for acoustic wave gauge measurements and 3 for LSPIV analysis. Resistive probes, placed upstream of the gate, ensured repeatability across all six experiments.

For each configuration, the repeatability of the experiment is verified upstream of the gate and close to the obstacles. Figure 5.4a presents the results for probe R3. Note that the water height upstream of the breach is the average between six experiments for each configuration and verifies the repeatability of flow conditions across all trials. The water height standard deviation has larger values at the beginning of the experiment, with maximum values up to 3mm. Otherwise, the maximum value of the standard deviation is kept below 1 mm. Similarly, Figure 5.4b shows the results for probe A1 as the average of 3 replicates. Downstream of the gate the value of the standard deviation depends on the configuration studied. For cases $0-0-0-0$, $1-0-1-0$ and $2-10-2-10$, the standard deviation is lower than 2 mm except at the wave impact, where it can reach 1 cm for few data points. The raise of the standard deviation compared to case 0 can be explained by the presence of droplets in the measurement zone. For case $4-0-4-0$, the confidence interval is larger, with maximum values reaching 1.5 cm from 1.5 s until the end of the experiment. This can be attributed to the generation of a splash-up upstream of the obstacles, reaching location A1 at = 1.5 s and resulting in a highly unstable free surface. Despite this, the primary oscillations of the free surface remain similar between the three replicates and thus the experiments are considered repeatable.

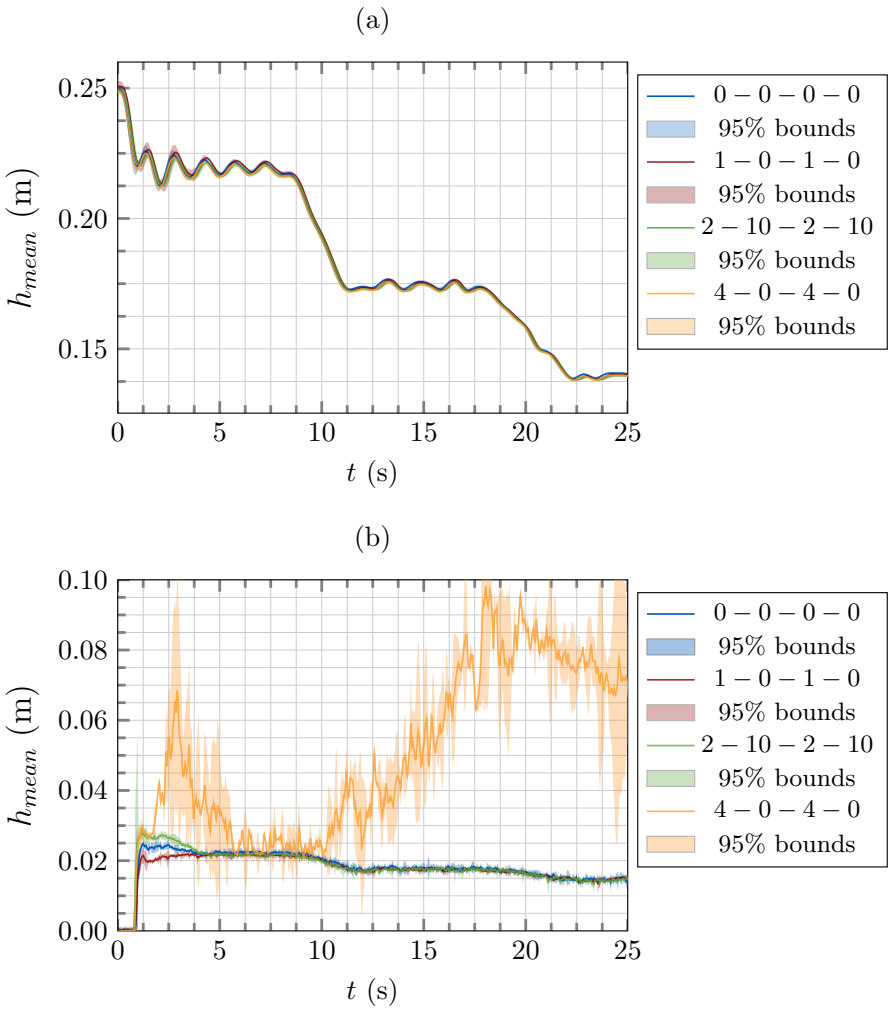

Figure 5.4: Water depth variation for all studied configurations, 95% confidence interval for probes (a) R3 and (b) A1.

5.3 EXPERIMENTAL RESULTS

The flow behaviour of a dam-break wave influenced by various obstacle configurations was investigated through a series of experiments. First, a general description of the flow based on the free surface velocity is given in Section 5.3.1, followed by an analysis of the impacted area around the obstacle configurations in Section 5.3.2. Then, the water depth results at all probes positions are compared between the different configurations in Section 5.3.3. Finally, the evolution of the slash-up upstream of the obstacles is studied in Section 5.3.4.

5.3.1 *Free surface flow description*

After the opening of the gate, the water stored in the tank propagates along the channel as a 3D dam-break wave. After reaching the side walls of the channel at x = 7.8 m, a reflecting wave is generated, forming a hydraulic jump as illustrated by the yellow dashed lines in Figure 5.5. The two symmetric hydraulic jumps reunite downstream of the obstacle configurations and do not interfere with the studied measurement zone. As the water reaches the obstacles, a surge is created, leading to water jets and droplets rising vertically along the z-axis. The surge then transforms into a splash-up of varying height and width as illustrated by the green dashed lines in Figure 5.5 (further splash-up analysis will be made in Section 5.3.4). Moreover, a thin film of water passes over the first row of obstacles, moving downstream of the configurations, where a wake zone (blue dashed lines) with recirculations and lower velocity values is formed.

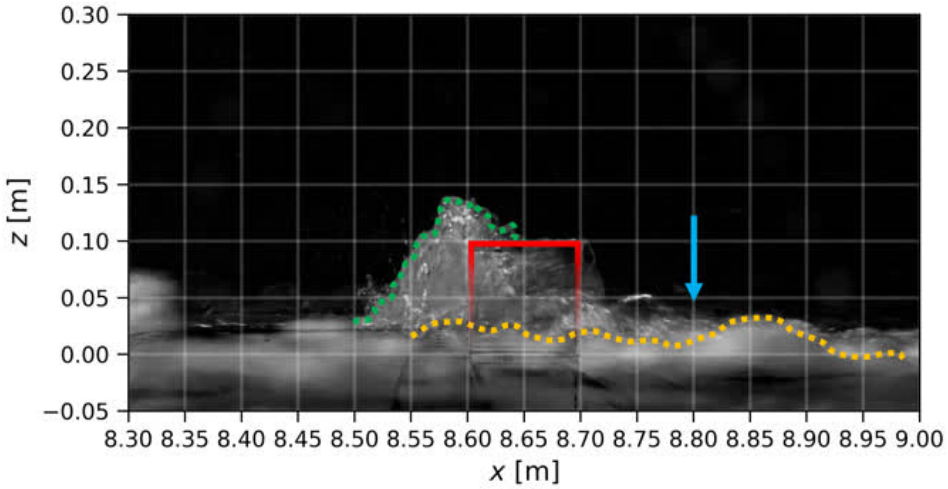

(a) Side view for case $0-0-0-0$.

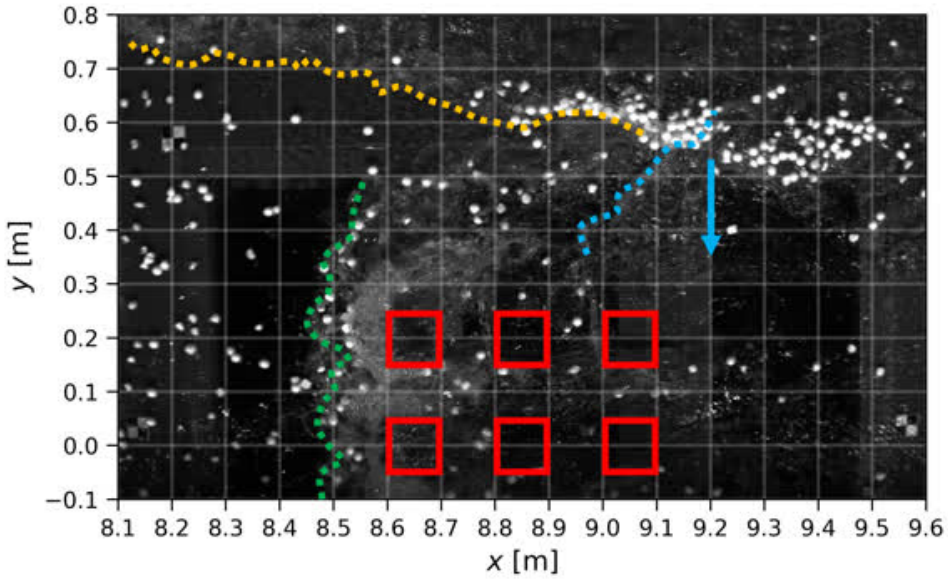

(b) Top view for case $2-10-2-10$.

Figure 5.5: General observation of the flow pattern at t = 15 s. Red lines highlight the presence of obstacles, green dashed lines the presence of a splash-up, blue dashed lines and arrows the presence of a wake zone and yellow dashed lines a reflection zone.

Figure 5.6 describes the evolution of the free surface flow for cases $0-0-0-0$, $2-10-2-10$ and $4-0-4-0$ at t = 4 s, t = 9 s and t = 14 s. The colour map represents the norm of the horizontal free-surface velocity ($\sqrt{V_x^2+V_y^2}$) and the vector field is normalised by the magnitude of the velocity.

Given the LSPIV acquisition frequency of 250 fps and after a sensitivity analysis on the time interval, each velocity field is averaged from 25 instantaneous frames ($\simeq$ 0.1 s). The horizontal velocity field highlights the existence of a splash-up zone in front of the obstacles, generating a low-velocity magnitude zone. Additionally, the flow bypasses the obstacles on both sides leading to the creation of a wake zone downstream of the configurations, whose size varies over time. The overall velocity magnitude decreases over time as the reservoir empties and the flow rate through the gate decreases.

More specifically, three main observations can be made:

- A splash-up zone is created in front of the obstacles. Its width and length are correlated with the width (L_y) and density of the obstacle configurations. Indeed, the size of the splash-up area for case $4-0-4-0$ is greater compared to the other two cases.
- The border of the reflection zone can be observed for all three cases. While its form remains fairly constant for cases $0-0-0-0$ and $2-10-2-10$, the reflection zone is deviated (in terms of velocity direction) by the splash-up for case $4-0-4-0$, creating an additional hydraulic jump with a lower velocity magnitude. This effect intensifies over time until it completely diverts the reflection zone. As time goes on, the splash-up length and width slightly decrease.
- The presence of obstacles creates flow recirculations downstream, forming a wake zone with low velocity magnitudes. Its width seems correlated with the size of the obstacles: larger urban areas result in larger wake zones. For case $2-10-2-10$, recirculations are noticeable downstream of each obstacle. In the central row, recirculations appear symmetrical, whereas in the side rows, water is ejected from the inside to the outside of the configuration.

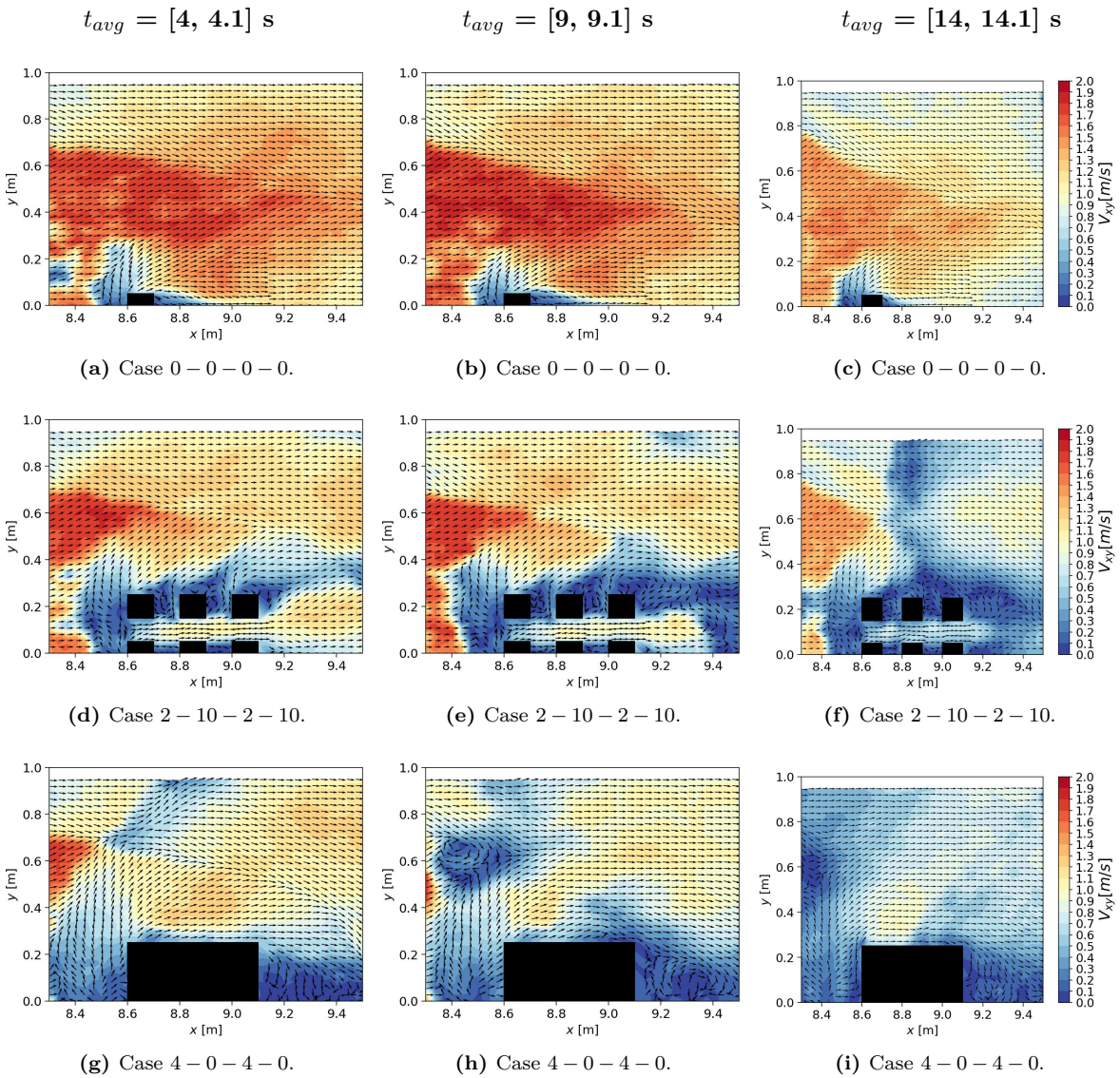

(a) Case $0-0-0-0$. **(b)** Case $0-0-0-0$. **(c)** Case $0-0-0-0$.

(d) Case $2-10-2-10$. **(e)** Case $2-10-2-10$. **(f)** Case $2-10-2-10$.

(g) Case $4-0-4-0$. **(h)** Case $4-0-4-0$. **(i)** Case $4-0-4-0$.

Figure 5.6: Free surface velocity variation for cases $0-0-0-0$, $2-10-2-10$ and $4-0-4-0$ at 3 different time steps. Black surfaces illustrate the obstacles position.

Note : Some areas may be affected by the presence of patterns on the images, such as target GRP points, leading to velocity values tending to zero, as some marks are not completely erased during the background subtraction step. Additionally, some erroneous velocity gradients on the lower-left side of the velocity field are due to highly transparent water and a lack of seeding particles passing through the area during acquisition. These effects are erased in the surroundings of the obstacles where the flow is agitated and foam, hollows and humps appear on the free surface, allowing the LSPIV analysis to accurately track it.

Finally, Tables 5.6 and 5.7 summarise the temporal evolution of the splash-up and wake zone sizes for all studied cases. Note that the different observations described above are confirmed by this quantitative analysis. The delimitation of both areas is defined by a sudden change in terms of velocity direction.

Table 5.6: Evolution of the splash-up size over time.

Case	Parameters		Splash-up					
	L_y (m)	ψ_y	s_x [1]			s_y [2]		
			4 s	9 s	14 s	4 s	9 s	14 s
$0-0-0-0$	0.1	0	0.1	0.1	0.1	0.6	0.4	0.4
$1-0-1-0$	0.2	0	0.15	0.15	0.15	0.6	0.8	0.6
$2-10-2-10$	0.5	0.4	0.15	0.2	0.2	0.9	0.9	0.9
$4-0-4-0$	0.5	0	0.3	0.3	0.3	$\Longleftrightarrow$ [5]	$\Longleftrightarrow$ [5]	$\Longleftrightarrow$ [5]

[1] s_x: Splash-up length along the x-axis.
[2] s_y: Splash-up length along the y-axis.
[5] $\Longleftrightarrow$: Reaching the reflection zone.

Table 5.7: Evolution of the wake zone size over time.

Case	Parameters		Wake zone					
	L_y (m)	ψ_y	w_x [1]			w_y [2]		
			4 s	9 s	14 s	4 s	9 s	14 s
$0-0-0-0$	0.1	0	0.1	0.1	0.05	0.05	0.05	0.05
$1-0-1-0$	0.2	0	0.2	0.2	✗	0.15	0.15	0.3
$2-10-2-10$	0.5	0.4	0.1	✗	✗	0.05	0.8	0.8
$4-0-4-0$	0.5	0	✗	✗	✗	0.4	0.4	0.4

[1] w_x: Wake zone length along the x-axis.
[2] w_y: Wake zone length along the y-axis.
✗: Out of the FOV.

Note : Supplementary data on the free surface velocity fields are available in Appendix D.

5.3.2 *Investigation of the flow area impacted by the obstacles*

To access quantitatively the impact of the obstacles on the flow, each velocity map presented in Figure 5.6 is compared to the velocity map of the reference dam-break (without obstacles), named case 0, at the same time interval. Figure 5.7 presents the relative velocity magnitude variation computed as $|V_{n_x-l_x-n_y-l_y} - V_0|/|V_0| \times 10^2$ [%], with V_0 the velocity magnitude of case 0. As complement, Figure 5.8 and Table 5.8 quantify the flow area impacted by the configurations, by presenting, for each time, the samples weight for different variation intervals (250 000 samples).

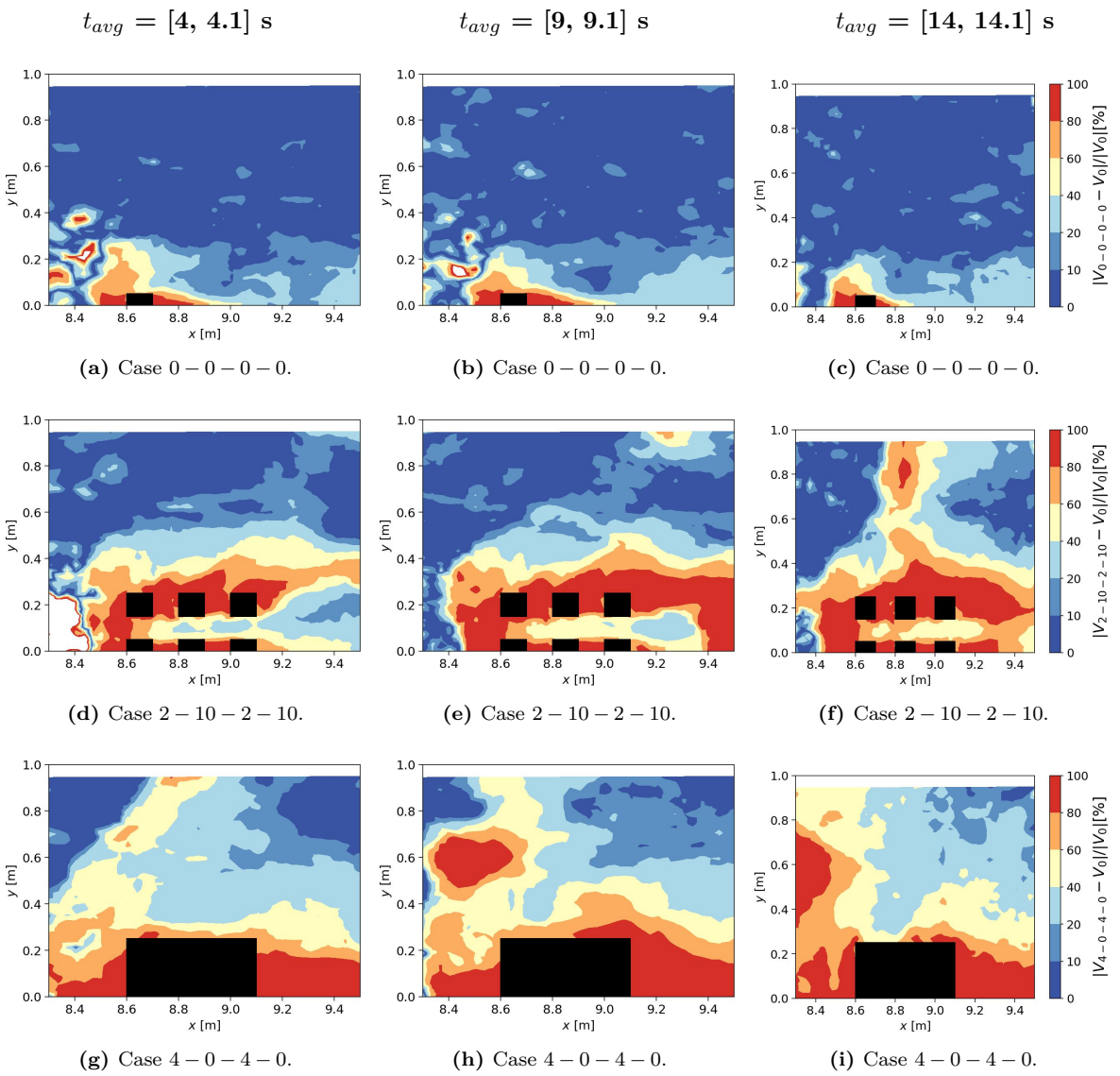

(a) Case $0-0-0-0$. **(b)** Case $0-0-0-0$. **(c)** Case $0-0-0-0$.

(d) Case $2-10-2-10$. **(e)** Case $2-10-2-10$. **(f)** Case $2-10-2-10$.

(g) Case $4-0-4-0$. **(h)** Case $4-0-4-0$. **(i)** Case $4-0-4-0$.

Figure 5.7: Free surface velocity comparison between case 0 and cases $0-0-0-0$, $2-10-2-10$ and $4-0-4-0$ computed as the relative velocity difference $\frac{|V_{n_x-l_x-n_y-l_y}-V_0|}{|V_0|} \times 10^2[\%]$ at 3 different time steps. Black surfaces illustrate the obstacles position.

Remark : Note that points belonging to the interval [100, 200] are considered erroneous as they are situated in the left side of the velocity field, as shown in Figure 5.7, and have been filtered out. Thus, they appear as white space in Figure 5.7.

Results show velocity differences around and downstream of the obstacles (Figure 5.7). Statistical data, summarised in Table 5.8 and Figure 5.8, shows that more than 75% of the samples of case $0-0-0-0$ fall within the variation interval of [0, 20]%, compared to less than 25% of the samples for case $4-0-4-0$ at the three studied time intervals. As expected, the flow is more and more impacted as the size of the obstacle increases, which is quantified by the decrease in the occurrences of velocity variations within the [0, 20]% interval. For instance, case $4-0-4-0$ has around 20% of velocity variation in the range of [80, 100]% for all studied times, compared to values below 5% for case $0-0-0-0$.

The flow in the reflection zone seems less affected by the obstacles, except for the case $4-0-4-0$, where the splash-up meets the reflection wave, highlighting the limitations of studying larger obstacle configurations in the current experimental setup.

Finally, while the obstacles surface are equal between cases $2-10-2-10$ and $4-0-4-0$, adding streets within led to a less impacted flow; this is expected as the blockage effect is less important. This example of analysis appears as a rigorous method to access the impact of obstacles on the flow.

Table 5.8: Interval weight (%) of the velocity variation (%) at 3 different time steps.

Case	Time interval (s)	Interval weight [%]					
		[0, 20]	[20, 40]	[40, 60]	[60, 80]	[80, 100]	[100, 200]
$0-0-0-0$	[4, 4.1]	78.48	10.52	4.38	3.76	2.57	0.30
	[9, 9.1]	78.23	12.39	2.89	2.30	3.07	1.12
	[14, 14.1]	80.64	12.20	2.46	2.02	2.12	0.57
$2-10-2-10$	[4, 4.1]	48.45	15.67	13.17	10.92	11.43	0.34
	[9, 9.1]	45.42	13.76	10.48	11.14	18.33	0.85
	[14, 14.1]	33.11	13.89	13.65	18.44	20.49	0.43
$4-0-4-0$	[4, 4.1]	24.67	26.59	17.5	11.83	19.21	0.20
	[9, 9.1]	24.48	16.96	16.81	14.69	26.04	1.01
	[14, 14.1]	8.00	26.69	21.72	18.15	25.20	0.24

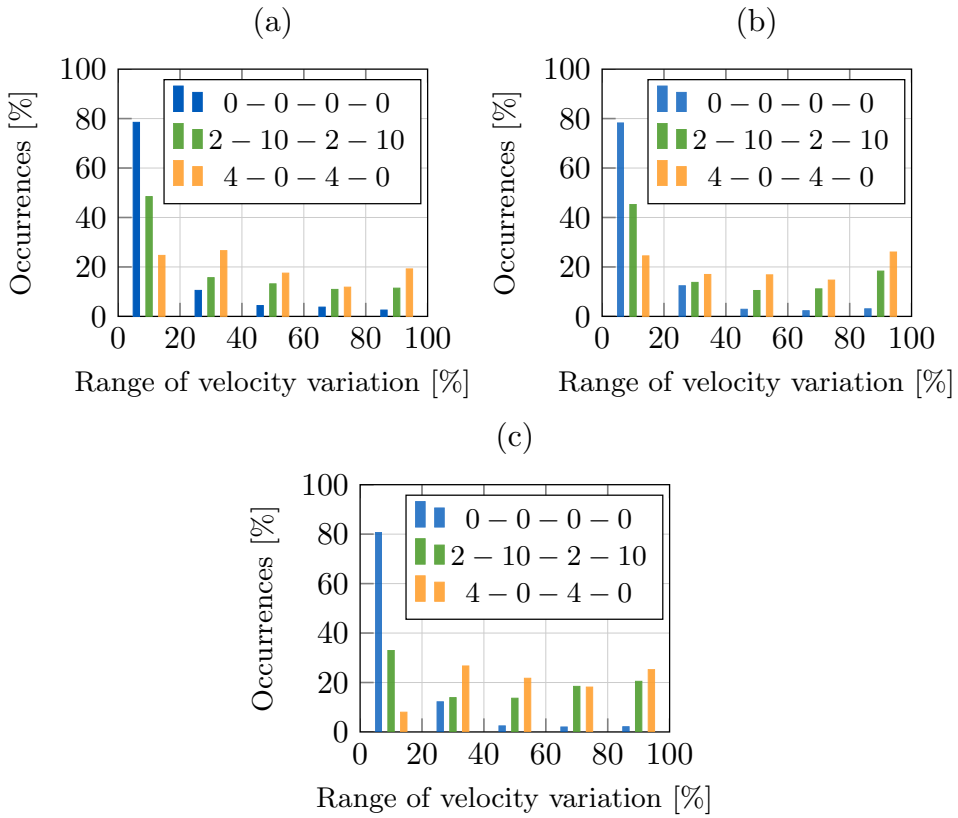

Figure 5.8: Histograms of the relative velocity variation for cases $0-0-0-0$, $2-10-2-10$ and $4-0-4-0$ at (a) t = 4 s, (b) t = 9 s and (c) t = 14 s.

5.3.3 *Water depth description upstream and downstream of the gate*

This section focuses on the evolution of water depth at different positions for the studied configurations. Figures 5.9 and 5.11 compare all cases against case 0, both upstream (positions R1 to R4) and downstream (positions A1 to A6) of the breach. The positions of the acoustic probes around the urban areas along with the corresponding curve colour coding are summarised in Figure 5.10.

The emptying of the reservoir generates oscillations of the free surface that propagate upstream, and lead to variations in the flow rate through the breach. This phenomenon, which has not been extensively documented in previous experimental dam-break studies [64, 73, 82], makes the numerical reproduction of such flows even more challenging. Since the behaviour of the flow downstream of the gate is directly influenced by the breach flow rate, understanding and documenting such phenomenon is important. They seem directly induced by the experimental setup geometry and are similar for all configurations (Figure 5.9). Primary oscillations are observed, resulting from the flow through the gate and the reflecting waves on the reservoir walls. Furthermore, the water height results of the tested configurations and case 0 are similar, indicating that the presence of obstacles downstream do not extend upstream of the gate.

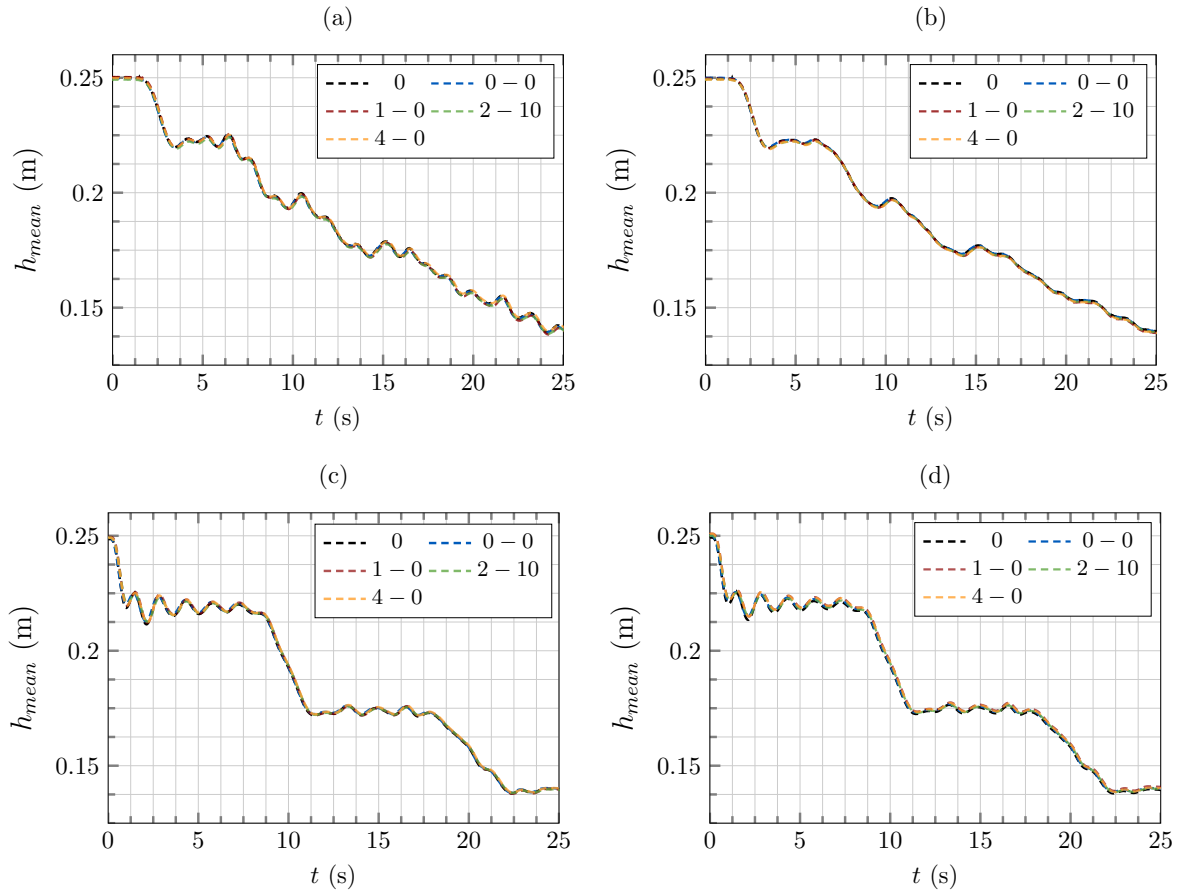

Figure 5.9: Water height time variation at positions (a) R1, (b) R2, (c) R3 and (d) R4 for cases 0, $0-0-0-0$, $1-0-1-0$, $2-10-2-10$ and $4-0-4-0$.

The water depth within and around the configuration are presented in Figure 5.11. Position A2 (Figure 5.11b) is located 0.05 m upstream of the first row of obstacle above the splash-up zone. The water depth is increased in this area and goes through two distinct levels. The first one, for t = [2, 10] s and the other one, for t = [12, 22] s. One possible reason is the nonlinear water depth variation through the breach (Figure 5.9).

Globally, water depths at all measured positions increase when obstacles are added to the flow, except in the wake zone. Additionally, larger obstacles lead to higher water depths. The wake zone, characterised by very low water depth and observable at position A4 for case $0-0-0-0$, is eliminated when surrounded by other obstacles. For instance, the water depth at position A4 is four times higher for case $2-10-2-10$ than for case $0-0-0-0$. The peak visible at the beginning of the experiment ($t \approx 1.5$ s) is induced by water passing over the obstacle (Figure 5.11d). Moreover, the water depth variation along the longitudinal street (position A3) for case $2-10-2-10$ is twice as high as that in the cross street (position A4).

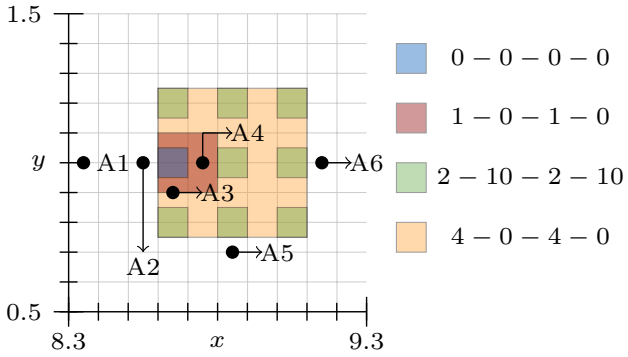

Figure 5.10: Sketch of the positions of probes for cases $0-0-0-0$, $1-0-1-0$, $2-10-2-10$, and $4-0-4-0$, along with the corresponding curve colour coding, are shown.

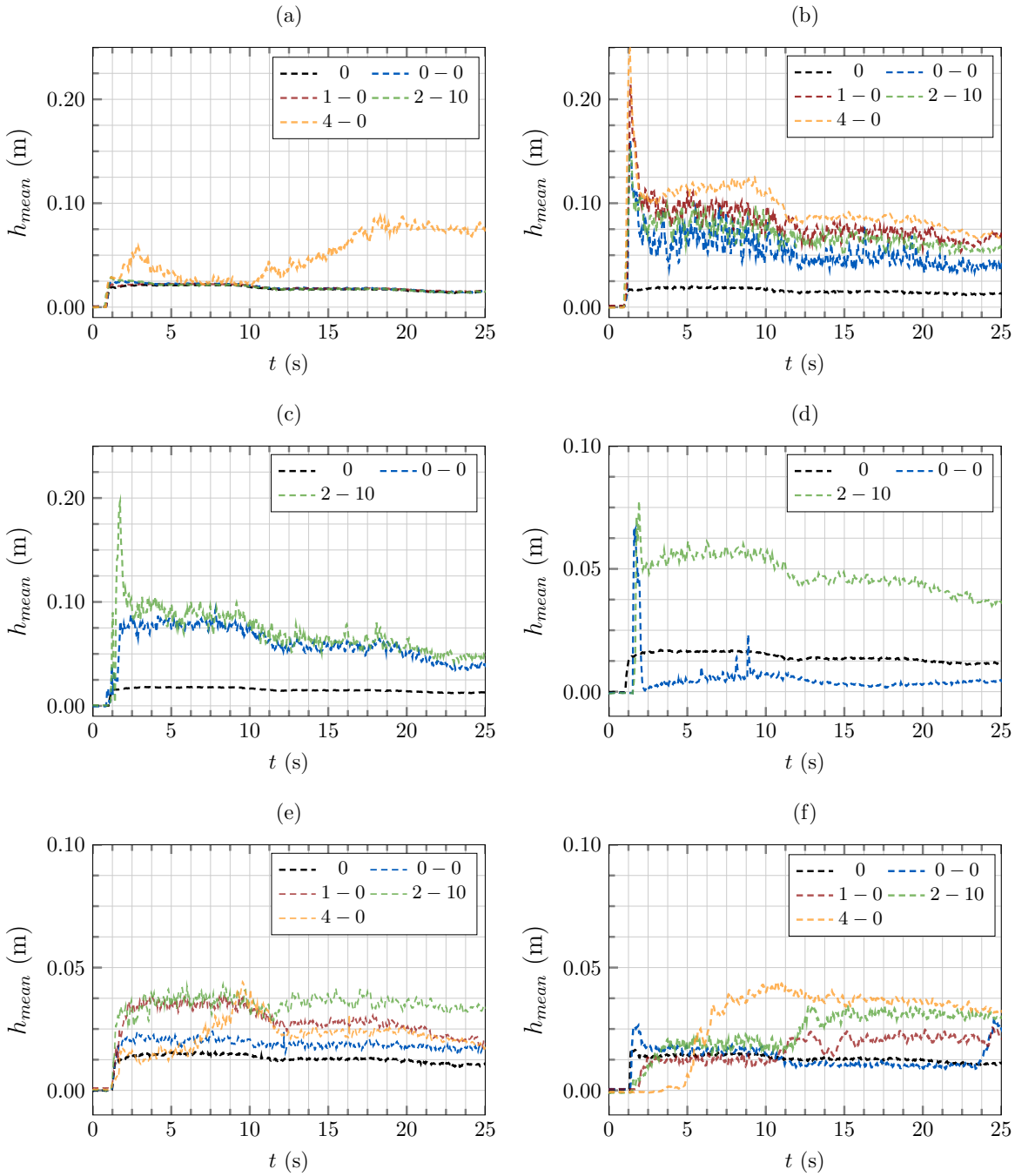

Figure 5.11: Water height time variations downstream of the gate at positions (a) A1, (b) A2, (c) A3, (d) A4, (e) A5 and (f) A6 for cases 0, $0-0-0-0$, $1-0-1-0$, $2-10-2-10$ and $4-0-4-0$.

5.3.4 *Splash-up zone evolution*

Understanding and predicting the evolution of the free surface position in the case of a dam-break passing through various obstacles can be challenging due to its rapid evolution, droplet projections and the heterogeneous air-water mixture. Figures 5.12, 5.13 and 5.14 illustrates, for three cases, the splash-up evolution using Image Analysis Measurements (IAM). Note that IAM is not available for case $4-0-4-0$, as the water-jet was out of the camera field of view.

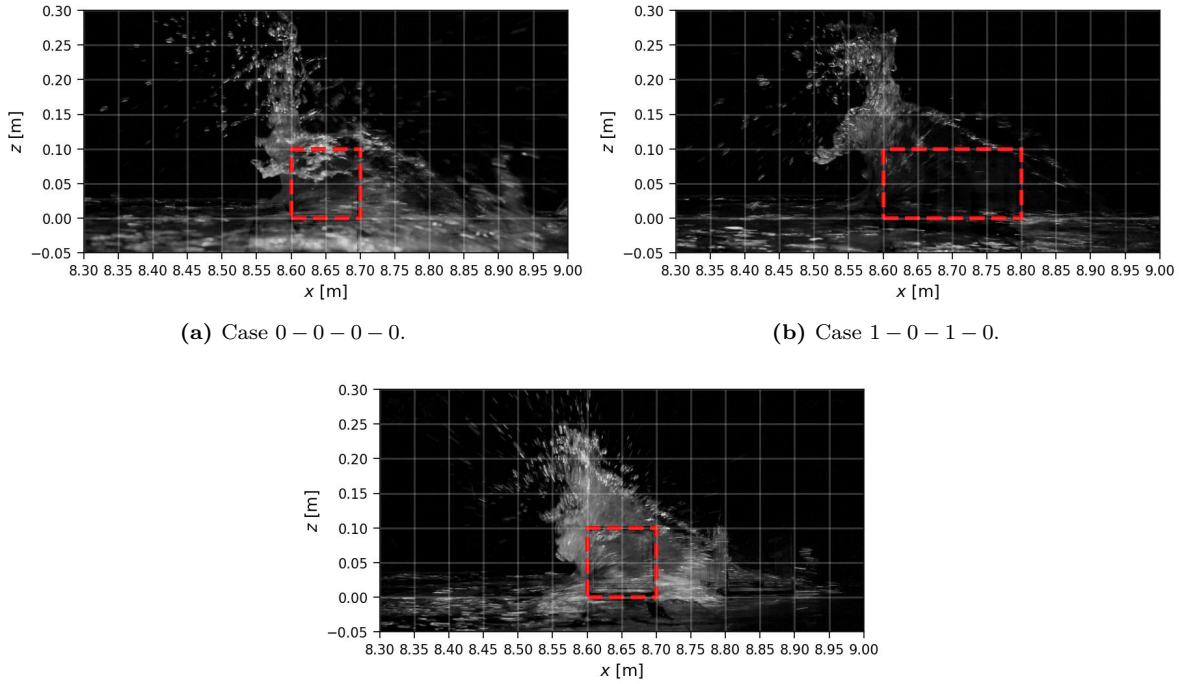

(a) Case $0-0-0-0$.

(b) Case $1-0-1-0$.

(c) Case $2-10-2-10$.

Figure 5.12: Snapshots of the splash-up at $t = 1.25$ s for cases $0-0-0-0$, $1-0-1-0$ and $2-10-2-10$. Red dashed line highlights obstacles edges.

Results illustrates clearly the transient behaviour of the impact process between the dam-break wave and the obstacles. First images (t = 1.25 s in Figure 5.12) illustrates the initial impact where the flow is redirected vertically and visible droplets can be observed. During this stage, the splash-up height can reach values that are challenging to measure with an acoustic wave gauge due to the discontinuity of the free surface and its rapidity. For cases $0-0-0-0$ and $2-10-2-10$, the flow sticks to both sides of the obstacle and creates an additional lateral splash, with a lower water height. For case $1-0-1-0$, at the same time step, the wave front has not yet bypassed the obstacle, so the lateral splash-up is not visible. The splash-up then overturns towards the incoming flow and falls onto the free surface, trapping air and forming a pocket with an air-water mixture in the cavity, as seen in Figure 5.13 at t = 1.75 s. Observations made here are similar to those presented by Tan *et al.* (2023) [136] (2D study on the impact of flow on a wall). As time passes, the splash-up maintains a shape slighty higher than the width of the obstacle, keeping this form until the end of the experiment. This yields a thin film of water passing over the first row of obstacles (Figure 5.14).

The water height variation comparison between IAM and acoustic wave gauge measurements is shown in Figure 5.16 for cases (a) $0-0-0-0$, (b) $1-0-1-0$ and (c) $2-10-2-10$. The IAM indicates that the impact height is more important than the acoustic wave gauge measurements, highlighting the complementarity of both techniques. The maximum water depth for case $0-0-0-0$ is equal to 0.27 m, while for case $2-10-2-10$ it is equal to 0.33 m, representing a 22% increase between the two configurations. Following the impact (t = 2 s), the splash-up height stabilises at a relatively constant level, even-though some small amplitude variations still exist. These effects can be attributed to the high slope of the free surface due to the shape of the splash-up zone, as illustrated in Figure 5.12.

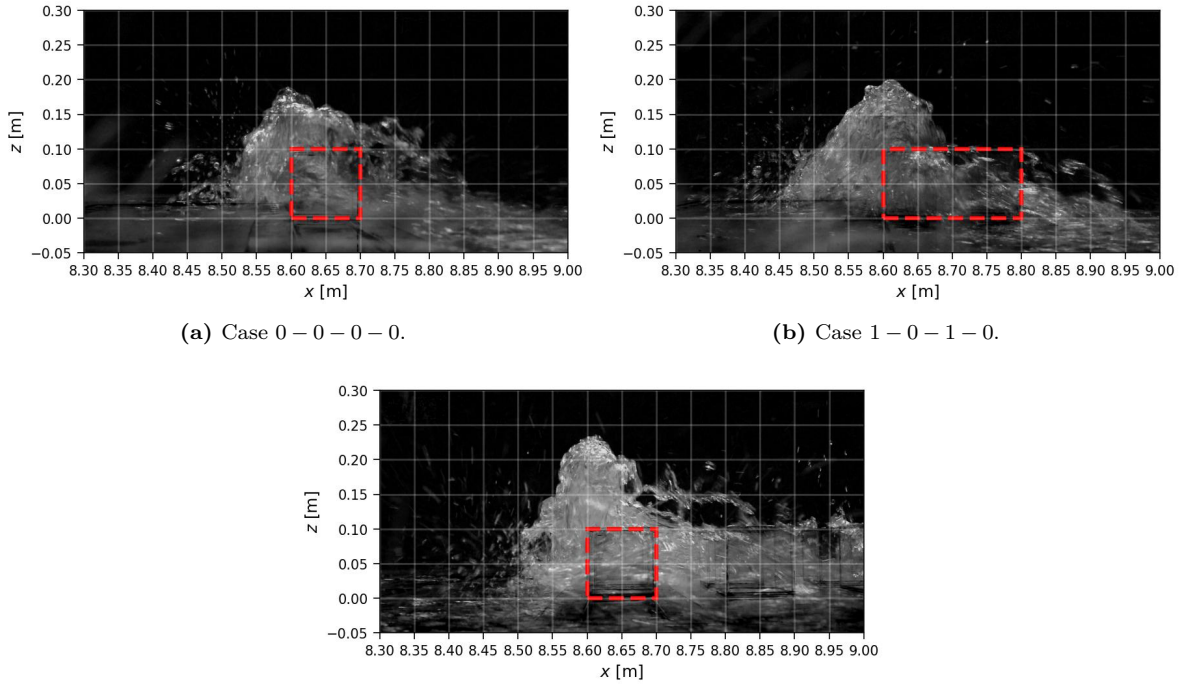

(a) Case $0-0-0-0$.

(b) Case $1-0-1-0$.

(c) Case $2-10-2-10$.

Figure 5.13: Snapshots of the splash-up at $t = 1.75$ s for cases $0-0-0-0$, $1-0-1-0$ and $2-10-2-10$. Red dashed line highlights obstacles edges.

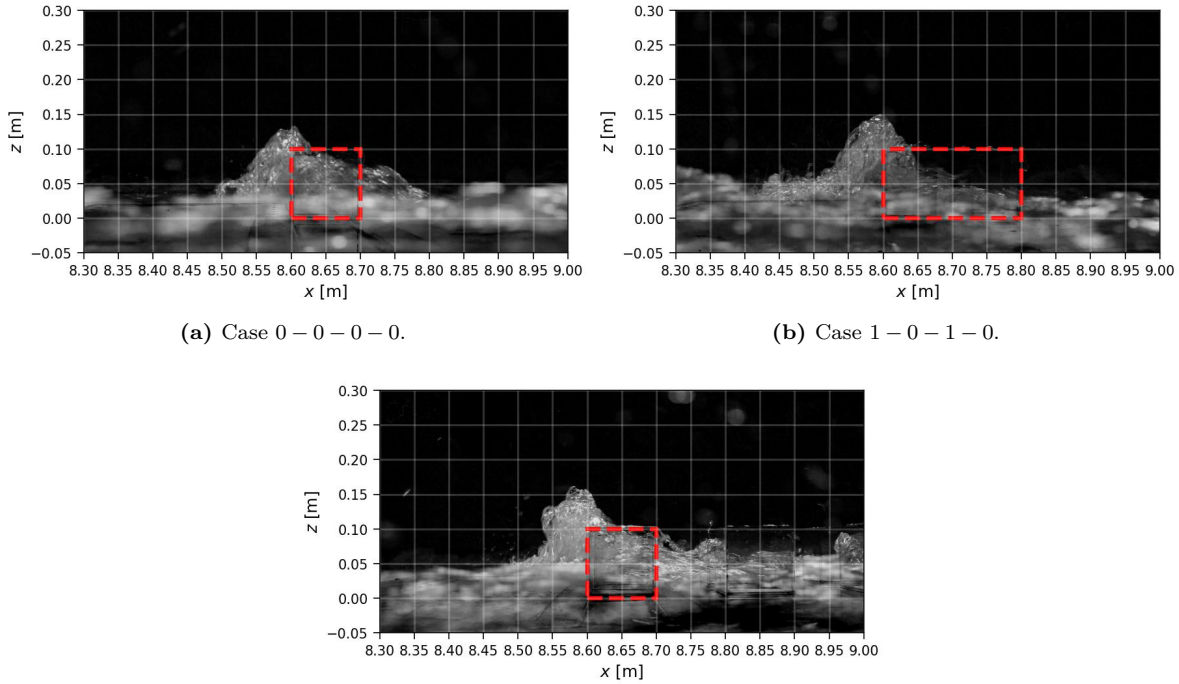

(a) Case $0-0-0-0$.

(b) Case $1-0-1-0$.

(c) Case $2-10-2-10$.

Figure 5.14: Snapshots of the splash-up at $t = 5$ s for cases $0-0-0-0$, $1-0-1-0$ and $2-10-2-10$. Red dashed line highlights obstacles edges.

Note : The principle of the IAM technique for detecting the position of a free surface is detailed in previous Chapter 4. The free-surface detection for case $4-0-4-0$ is illustrated in Figure 5.15 as an example. The ROI parameters are detailed in Table 5.5.

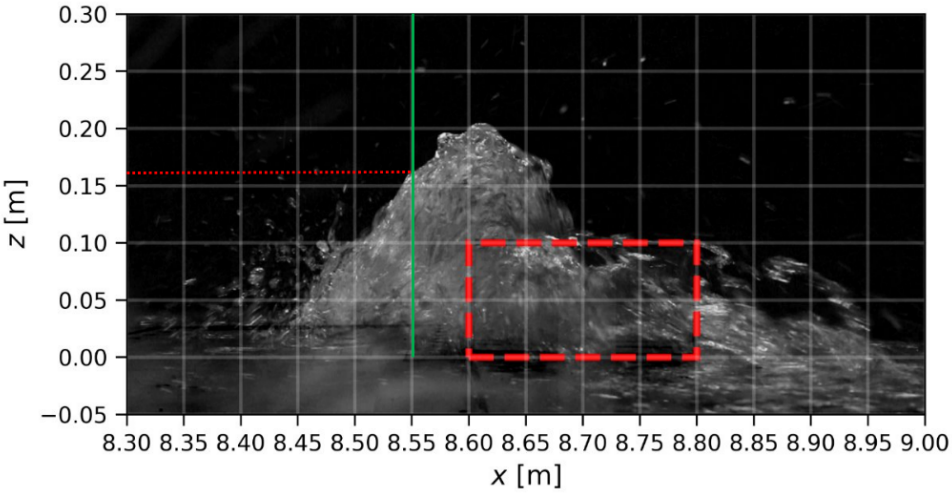

Figure 5.15: Sketch of the free-surface detection using the IAM technique for case $4-0-4-0$ at $t = 1.75$ s. Green lines represent the ROI position (a vertical line of 1 pixel long, see Table 5.5) and red dashed line the resulting elevation z.

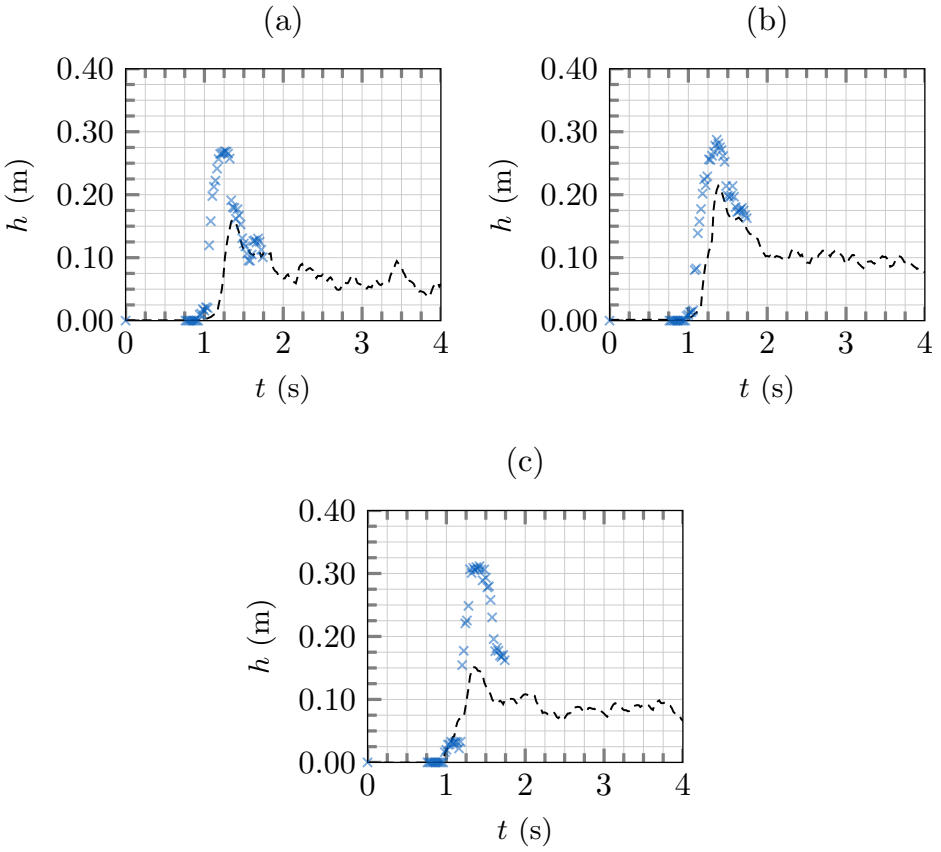

Figure 5.16: Splash-up height comparison at position A2 between wave gauge measurements (black dashed line) and IAM (cross points) for cases (a) $0-0-0-0$, (b) $1-0-1-0$ and (c) $2-10-2-10$.

Applying both methods (acoustic gauge and IAM) to study the splash-up proved useful for capturing detailed information about the phenomena. The complementary information provided by IAM may also be valuable for further numerical comparisons.

Remark : The methodology applied in this preliminary measurement campaign provides a novel and accurate dataset on the flow dynamics in and around urban forms. Nevertheless, improvements are made for future measurement campaigns to enhance data quality. Modifications to the experimental protocol are detailed in Chapter 6.

5.4 NUMERICAL METHODOLOGY

The experiments have been numerically simulated using the CFD open-source solver code_saturne, presented and detailed in Chapter 3. A snapshot of the resulting flow for case $2-10-2-10$ at t = 8 s is showed in Figure 5.17. Each case is run during 25 seconds using an adaptive time step to keep the Courant number under the unity.

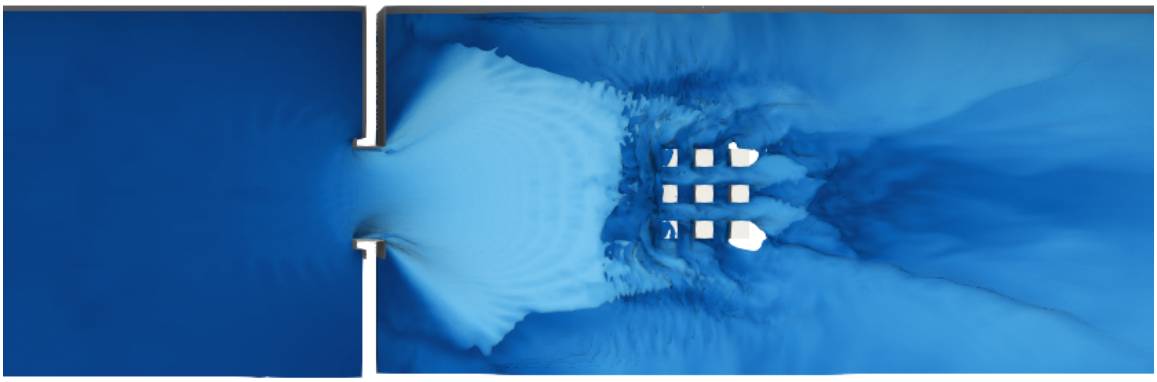

(a) Top view.

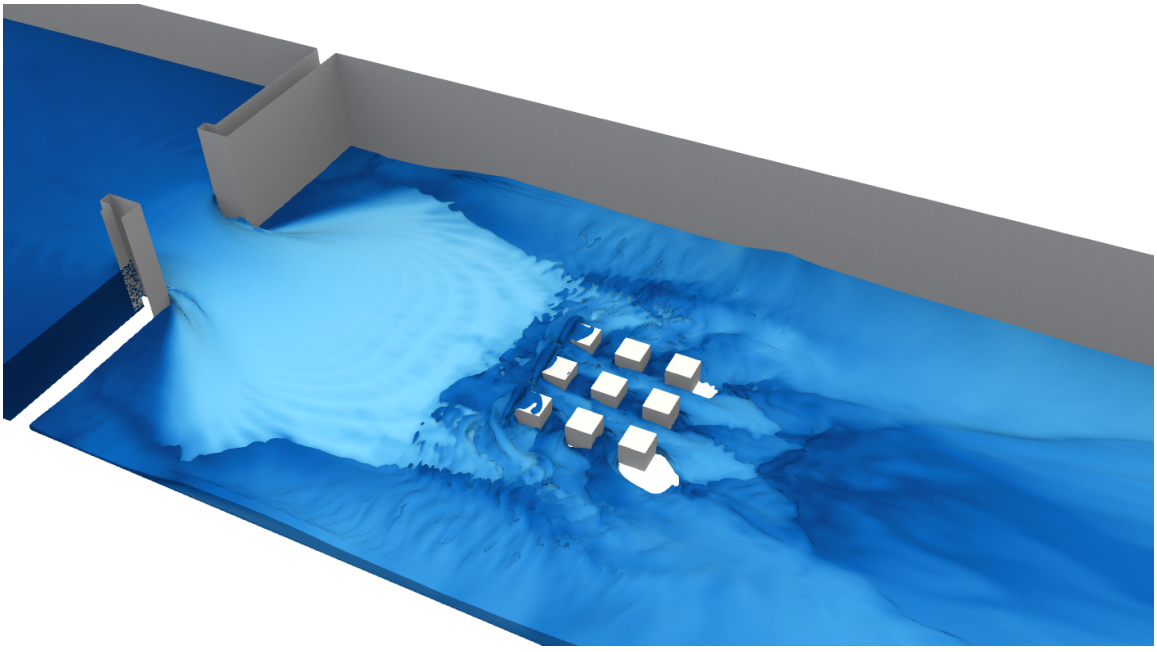

(b) Side view.

Figure 5.17: Case $2-10-2-10$: Snapshots of the simulation at $t = 8$ s. The blue surface represents water cells ($\alpha < 0.5$), and the grey surfaces represent the walls located at y > -0.35 m.

The computational domain used is 12.00 m long, 2 m wide and 0.5 m high and is discretised using hexahedral cells, as illustrated in Figure 5.18. Refinements are made along the z-axis for cells of low height and in the x and y axes in areas of interest, such as the breach surroundings or around the obstacles. For case $2-10-2-10$, a mesh sensitivity analysis was conducted with three different levels of mesh refinement. The initial mesh, composed of 6 million cells (as shown in Figure 5.18), was modified to create two additional meshes: one finer, with cells size halved and one coarser, with cells size doubled.

The comparison of the water height profiles for the three meshes, presented in Figure 5.19, shows few differences between the 48 million and 6 million cells meshes. Moreover, water depth comparisons at positions R3 and A1 in Figure 5.20 confirm that the 6 millions cells mesh is suitable for the upcoming numerical simulations.

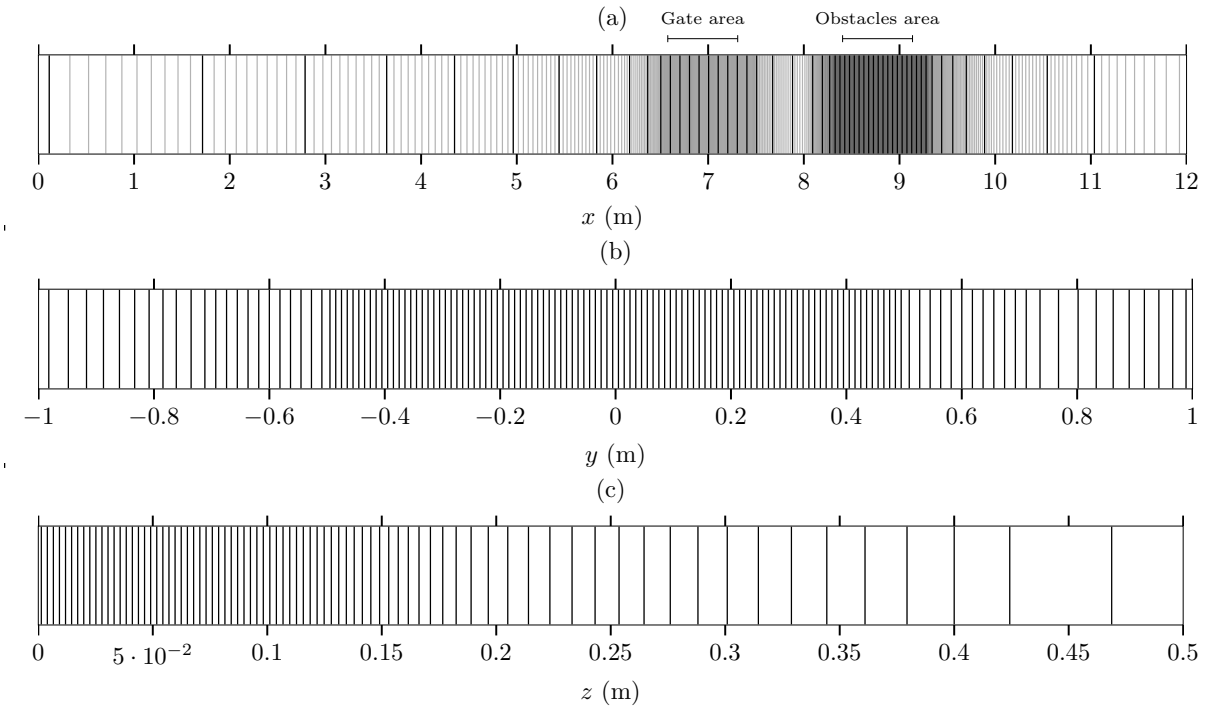

Figure 5.18: Numerical mesh refinement along the (a) x-axis, (b) y-axis and (c) z-axis. Each black line represents the centre of an individual cell, except along the (a) x-axis, where black lines are plotted every 10 cells for enhanced clarity.

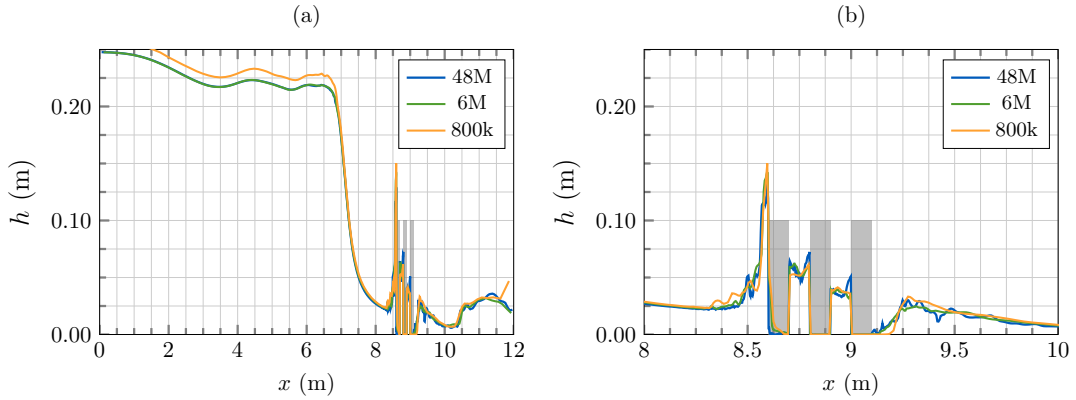

Figure 5.19: Case 2 – 10 – 2 – 10. Mesh sensitivity analysis of the water height profile at y = 0 m for (a) x = [0, 12] m and (b) x = [8, 10] m at t = 4 s. Gray rectangles represent the obstacle positions. 48M: 48 million cells mesh, 6M: 6 million cells mesh and 800K: 800 thousand cells mesh.

Concerning the boundary conditions, the top of the domain is defined as a symmetry and the surface x = 12 m is set as a free outlet. All other boundaries are set as smooth walls. An initial volume of water is defined (7 x 2 x 0.25 m) corresponding to the initial water depth reservoir.

The effect of the gate opening is modelled as a rectangular moving wall with a velocity of 0.78 m/s, as determined from video tracking. The simulations were divided into two parts. The first two seconds ($0 < t < 2$ s), comprising the opening of the gate and the impact of the dam-break wave with the first row of obstacle, were first resolved with a reference time step of $\Delta t = 0.0005$ s. Then, the simulations were restarted ($2 < t < 25$ s) with a reference time step of $\Delta t = 0.001$ s. The simulations times of all five cases are summarised in Table 5.9. A lower reference time step was used at the beginning of the simulation

to ensure computational stability during the impact process, where high velocities can be observed. This value serves as an initial reference for the solver and is then adjusted if needed to keep the CFL under the unity. Once the first two seconds are resolved properly, the rest of the calculation can proceed safely on EDF supercomputers, with the model configuration having been verified.

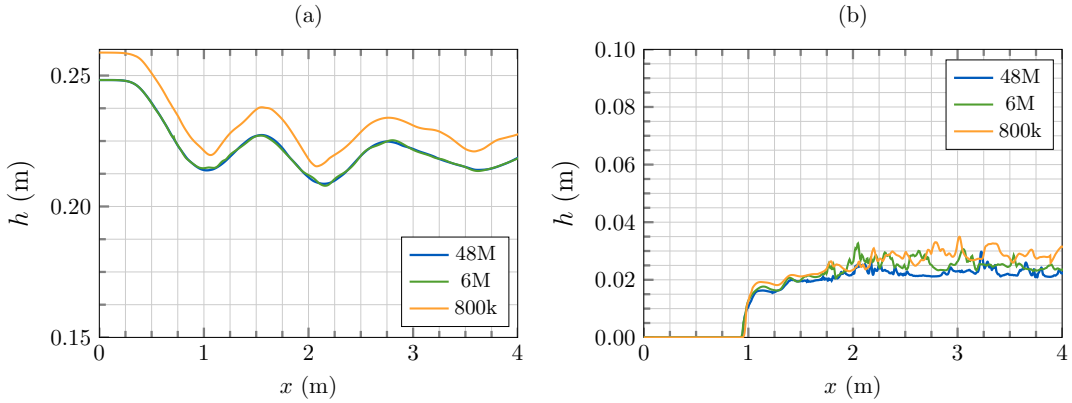

Figure 5.20: Case 2 – 10 – 2 – 10. Mesh sensitivity analysis of the water height variations at positions (a) R3 and (b) A1. 48M: 48 million cells mesh, 6M: 6 million cells mesh and 800K: 800 thousand cells mesh.

Table 5.9: Summary of the computational time for all studied urban forms.

Case	N_{cells}	$[t_{min}, t_{max}]$	Δt_{ref}	Nb proc	Total time	Total CPU time
0	6 141 600	[0, 25] s	0.001 s	420	1.7 hr	707 hr
0 – 0 – 0 – 0	6 134 100	[0, 2] s [2, 25] s	0.0005 s 0.001 s	420	0.4 hr 2.5 hr	157 hr 1080 hr
1 – 0 – 1 – 0	6 112 000	[0, 2] s [2, 25] s	0.0005 s 0.001 s	420	0.4 hr 4.6 hr	164 hr 1930 hr
2 – 10 – 2 – 10	6 075 000	[0, 2] s [2, 25] s	0.0005 s 0.001 s	420	0.35 hr 2.9 hr	149 hr 1247 hr
4 – 0 – 4 – 0	5 956 600	[0, 2] s [2, 25] s	0.0005 s 0.001 s	420	0.39 hr 4.3 hr	167 hr 1826 hr

5.5 NUMERICAL VALIDATION RESULTS

The numerical model is assessed through both qualitative and quantitative comparisons with experimental results across the four studied configurations. The evolution of water height over time is examined at three key locations: R3, situated upstream of the gate; A1, located upstream of the first row of obstacles; and A6, positioned downstream of the configurations. These probe locations aim to validate the numerical model's capability in accurately taking into account the presence of the urban area. The numerical water height is computed using the post-processing method outlined in Chapter 3.

5.5.1 *Reproduction of the upstream oscillations*

Upstream of the gate, one can see the presence of oscillations of the water height (Figure 5.21). As presented in Figure 5.9, these variations are similar for all configurations; hence, only 0 – 0 – 0 – 0 results are presented. Figure 5.21 illustrates a good agreement between experimental and numerical data, showing the ability of code_saturne to reproduce the oscillations inside the reservoir. Accurately reproducing the hydrograph at the gate is fundamental for a high-quality simulation downstream of it. Figure 5.22 illustrates the time variation of the numerical vertical velocity profile through the gate at different positions, highlighting its heterogeneous shape, with larger values close to the ground.

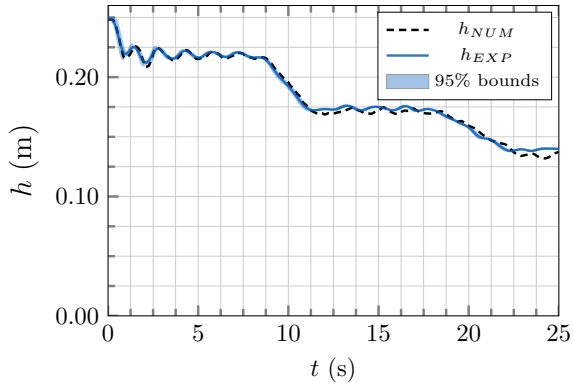

Figure 5.21: Case 0 – 0 – 0 – 0. Water depth variations comparison between experimental and numerical data at position R3.

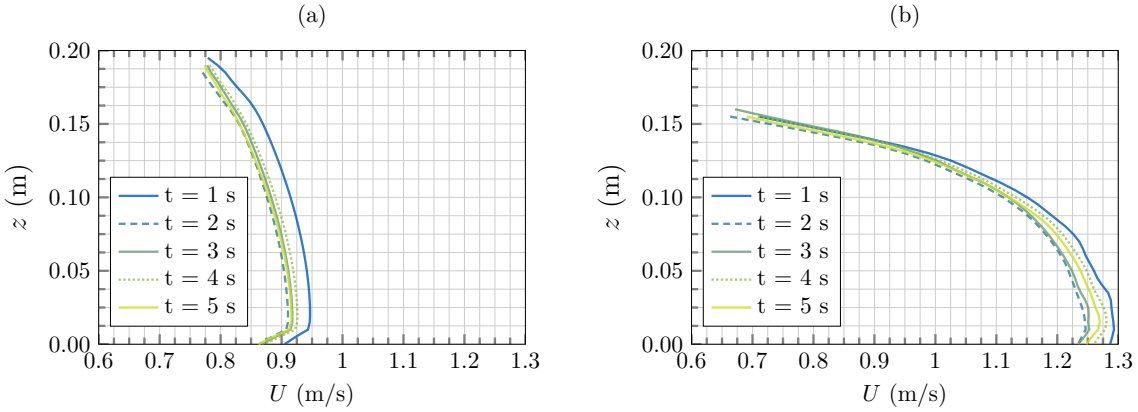

Figure 5.22: Case 0 – 0 – 0 – 0. Vertical velocity profile evolution through the breach (x = -0.075 m) from the numerical model at different positions: (a) y = 0 m (b) y = 0.2 m.

Remark : These effects explain the approach of conducting numerical simulations over the entire tank domain, with a mesh refinement around the gate.

5.5.2 *Water depth comparison upstream and downstream of the urban area*

Figures 5.23 and 5.24 illustrate a comparison of water heights between wave gauge data and the numerical model at positions A1 (upstream of the first row of obstacles) and A6 (downstream of the configurations) for the four studied cases.

For case 0 – 0 – 0 – 0 at position A1 (Figure 5.23a), the water depth is not impacted by the presence of the obstacle and there is a good agreement between experimental and numerical results. The slight decrease in water depth observed at t = 10 s, induced by the variation of the flow rate through the gate (Figure 5.21 and 5.22), is accurately captured by the numerical model. For cases 1 – 0 – 1 – 0 and 2 – 10 – 2 – 10, the numerical model also demonstrates a good ability to replicate the water depth evolution, although some numerical oscillations are observed, which is expected given the post processing method to compute the water height. More difference between experimental and numerical results can be observed for case 4 – 0 – 4 – 0. Here one can see that position A1 belongs to the splash-up zone, causing an 80% increase in the water level at t = 20 s compared to case 0. Despite these differences, the VOF simulation reproduced the splash-up at A1, given the higher water height values.

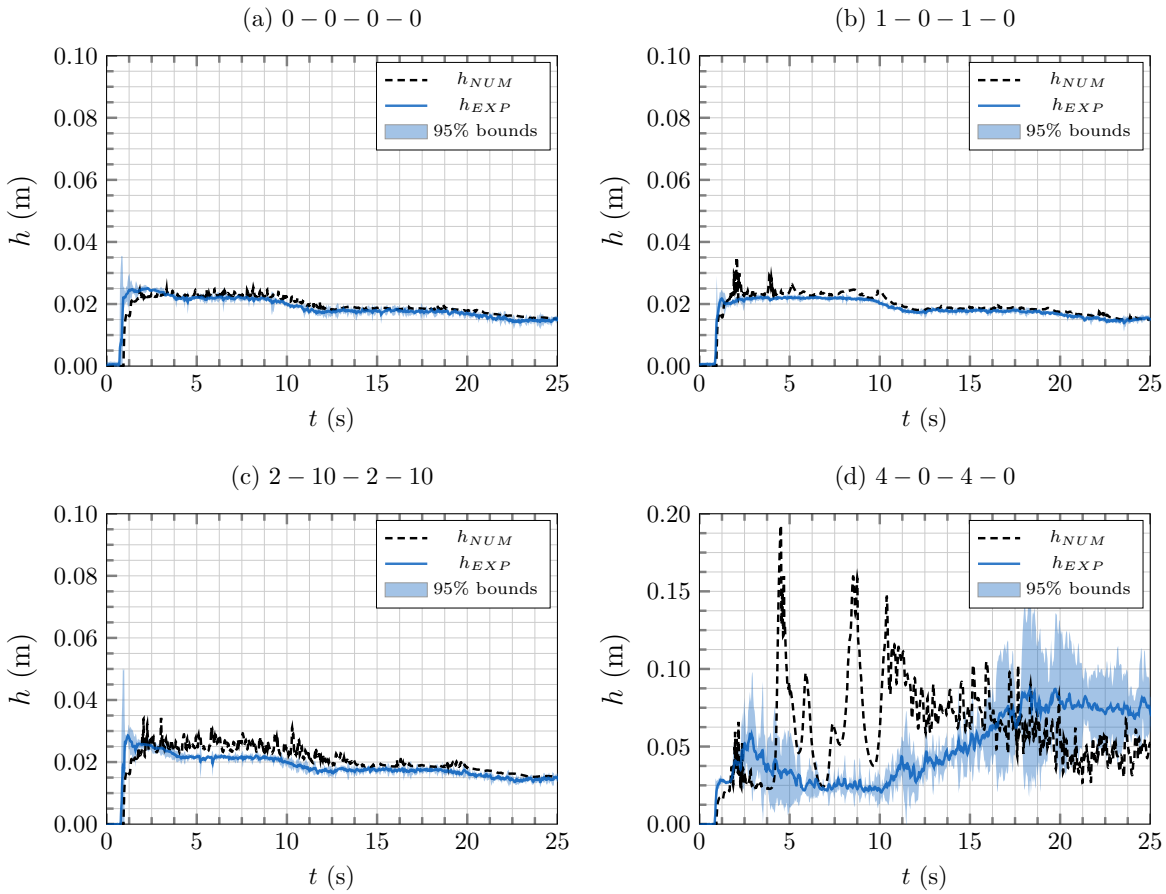

Figure 5.23: Water height comparison at position A1 between wave gauge measurements (black dashed line) and numerical model (blue line) for cases 0 – 0 – 0 – 0, 1 – 0 – 1 – 0, 2 – 10 – 2 – 10 and 4 – 0 – 4 – 0.

Remark : The splash-up zone, characterised by air-water mixture cells, presents challenges for the numerical post-processing method. Further work on the numerical post-processing water height calculation might be of interest.

For probes located downstream of the obstacles, larger differences are observed (Figure 5.24). This can be explained by the presence of hollows and humps due to the obstacle, leading to free surface variations. Initially, for case 0 – 0 – 0 – 0, the numerical simulation underestimates water height for a brief period after the passage of the dam-break wave. Subsequently, the numerical model shows a similar shape compared to experimental data.

Note : The sudden rise in water level at the end of the acquisition for case 0 – 0 – 0 – 0 (Figure 5.24a) is the result of wave reflecting from downstream caused by a too-slow emptying of the channel. The wave arrives faster in the measurement zone for case 0 – 0 – 0 – 0 compared to other study cases due to a lower water depth in this area.

For case 1 – 0 – 1 – 0, the water depth rise at t = 10 s in experiments and occurs 5 s later in the numerical model. However, from that point and until the end of the acquisition, the water depth is correctly predicted. For cases 2 – 10 – 2 – 10 and 4 – 0 – 4 – 0, where position A6 is closer to the obstacles and within the wake zone, a similar tendency is observed, but the numerical model slightly underestimates the water depth. Particularly for 4 – 0 – 4 – 0, the model overestimates the arrival time of the dam-break wave, which can be explained by a more important amount of water that passes over the obstacle. In the experiments, several cubes of 0.1 m were used to build the geometry of case 4 – 0 – 4 – 0. These cubes may not have been completely watertight, which prevented the first water jet from sliding over the obstacle. In fact, an

amount of water was found inside the obstacle after the experiment. In the simulation, the obstacle is modelled as a watertight wall, leading to different estimations of the dam-break wave arrival time with the experimental data.

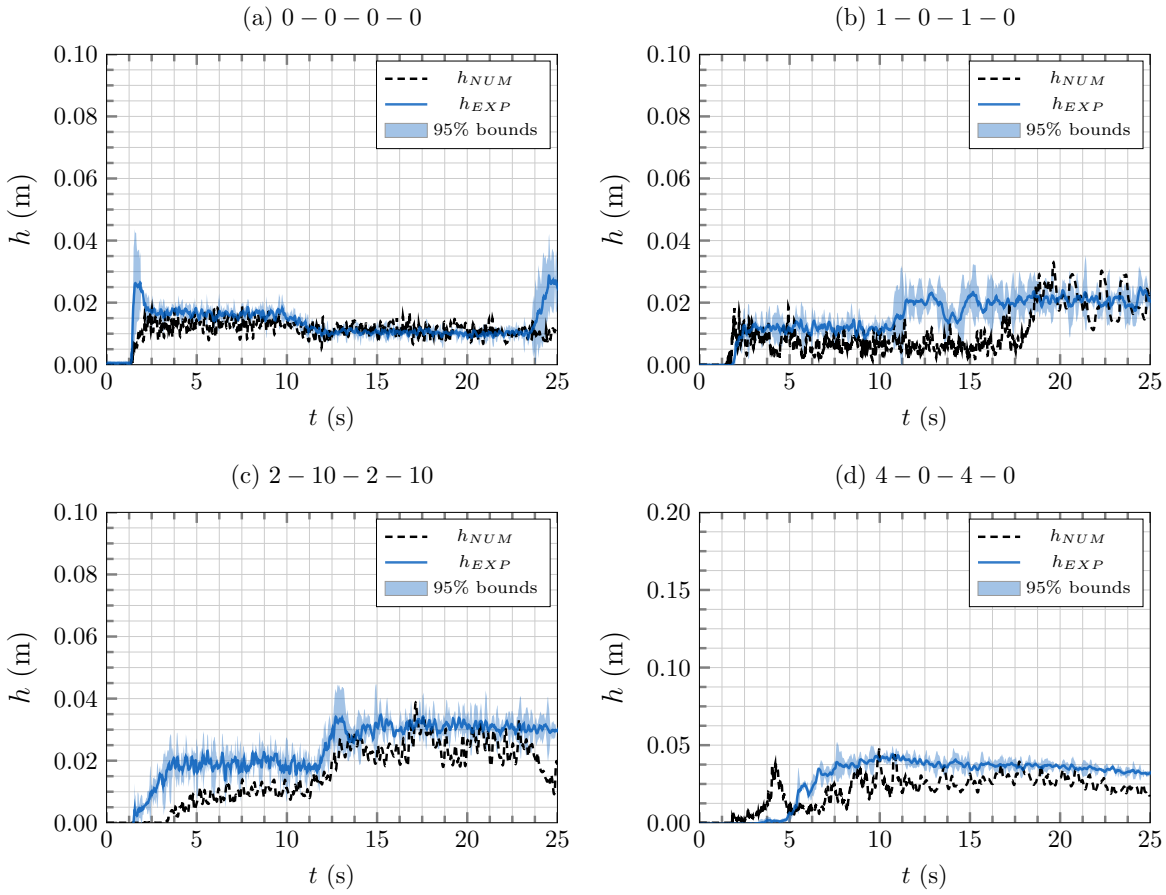

Figure 5.24: Water height comparison at position A6 between wave gauge measurements (black dashed line) and numerical model (blue line) for cases $0-0-0-0$, $1-0-1-0$, $2-10-2-10$ and $4-0-4-0$.

The comparison of water height variations at various key locations, both upstream and downstream of the gate and obstacles, reveals a overall good agreement between the numerical predictions and experimental data. Notably, the model captures the presence of splash-up zones, despite the challenges posed by the air-water mixture environment within these areas. While some deviations are observed during the early stages of certain experiments, the numerical results progressively get closer to predictions over time. As conclusion of the latter quantitative comparison, the numerical model is shown to be a valuable tool for understanding and simulating the dynamics of dam-break waves over various obstacle configurations. It can be used in support of experimental studies to test a larger number of geometric configurations and assess about the influence of complex urban form on the flow variables.

Note : Supplementary water height comparisons at positions A2, A3, A4 and A5 are available in Appendix D.

5.5.3 *Free surface velocity comparison*

Figures 5.25, 5.26 and 5.27 illustrate a comparison of the numerical velocity field around the obstacle configuration with the LSPIV measured field at three different times for cases $0-0-0-0$, $2-10-2-10$ and $4-0-4-0$, respectively.

The surface velocity obtained with the LSPIV analysis is compared to the depth-averaged velocity field from the numerical simulation. In fact, one of the limitations of the VOF method is that the position of

the free surface can be diffused across several cells, making the exact position unknown. This is why we chose to perform comparisons with the depth-averaged velocity rather than the free surface velocity of the numerical model. The validity of such comparisons for unsteady flow has been discussed in Soares-Frazão and Zech (2007) [45] and (2008) [53]. Indeed, velocity profiles under transient flow conditions are complex, as the flow is not yet fully developed and may present complex shapes. However, qualitative comparisons can be made to obtain information about the velocity direction, magnitude and shape around an obstacle (caution is still required for quantitative comparisons).

The experimental velocity field, displayed in the left column of each figure, is averaged over 25 frames ($t_{avg} = 0.1$ s). The numerical post-processing method to compute the velocity is as follows: the velocities of cells having a value of $\alpha \leq 0.5$ (i.e. water cells) are averaged over each column following the z-axis to obtain 2D depth-averaged fields. The numerical velocity fields are thus displayed in the centre of each figure, for different time steps. The colour map represents the norm of the horizontal velocity V_{xy}, calculated as $\sqrt{V_x^2 + V_y^2}$. Finally, the absolute difference between the experimental and numerical velocity magnitudes is displayed in the right column of each figure.

> **Note** : The relative velocity difference cannot be displayed due to low velocity values around the obstacles.

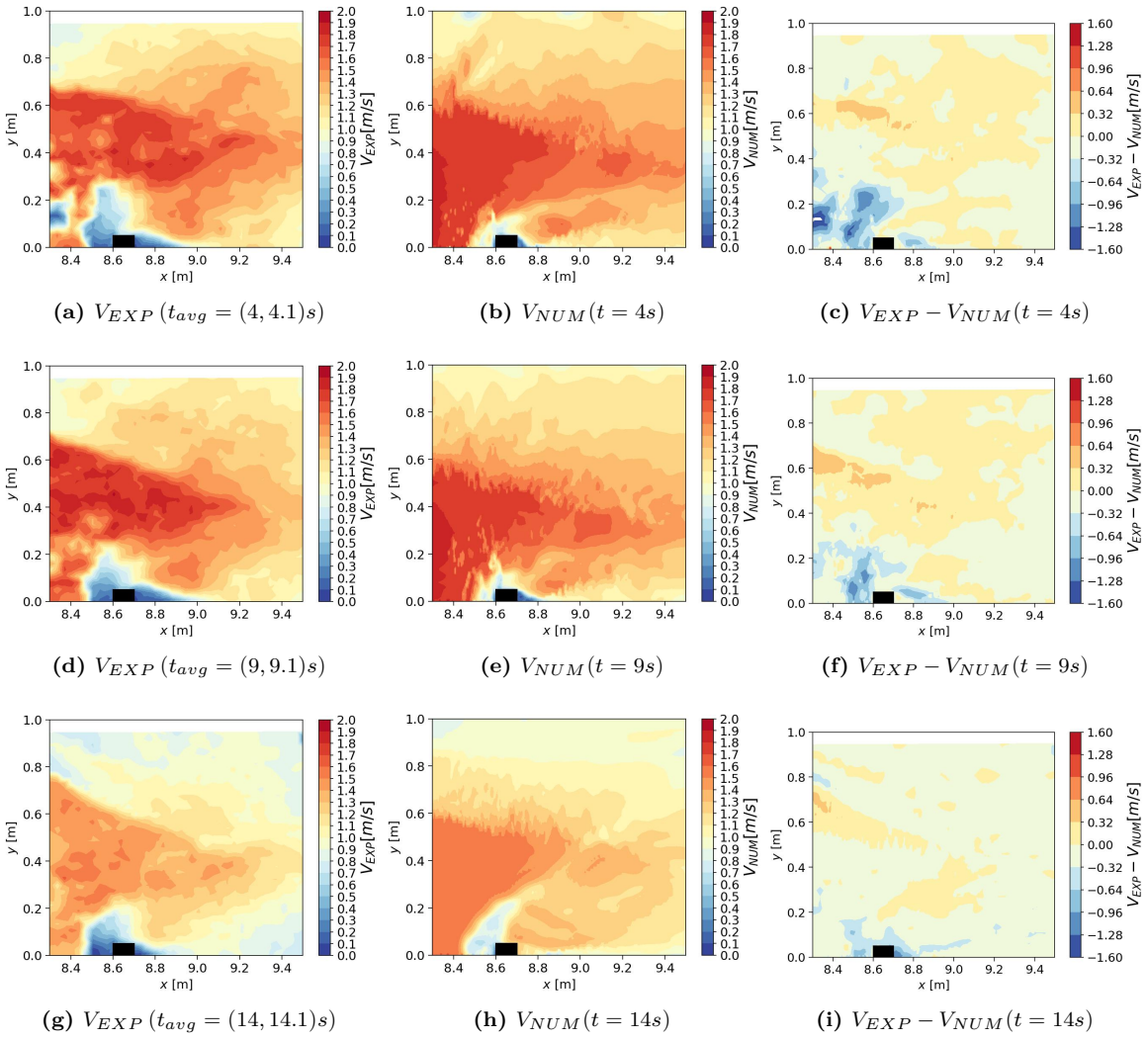

(a) $V_{EXP}\,(t_{avg} = (4, 4.1)s)$ **(b)** $V_{NUM}(t = 4s)$ **(c)** $V_{EXP} - V_{NUM}(t = 4s)$

(d) $V_{EXP}\,(t_{avg} = (9, 9.1)s)$ **(e)** $V_{NUM}(t = 9s)$ **(f)** $V_{EXP} - V_{NUM}(t = 9s)$

(g) $V_{EXP}\,(t_{avg} = (14, 14.1)s)$ **(h)** $V_{NUM}(t = 14s)$ **(i)** $V_{EXP} - V_{NUM}(t = 14s)$

Figure 5.25: Case $0-0-0-0$. Surface velocity field comparison at three different time steps. V_{EXP} represents the horizontal velocity obtained from the LSPIV analysis (Section 5.3.1) and V_{NUM} refers to the vertically averaged horizontal velocity for $\alpha \leq 0.5$. Black surfaces illustrate the obstacles' positions.

For all cases, the specific flow behaviour, such as the splash-up and wake zones or the reflection between the flow and the channel walls is predicted by code_saturne enhanced with the VOF module. Given the experimental and numerical post processing methods, which come with uncertainties, some differences are present, that will be discussed in the next paragraphs.

For case $0-0-0-0$ (Figure 5.25), the differences in most areas of the velocity field are small, ranging between $V_{\mathrm{EXP}} - V_{\mathrm{NUM}} = [-0.32, 0.32]$ m/s. However, three areas show larger differences: the splash-up, the wake zone and the side of the reflection zone. First, downstream of the obstacles, a low velocity area, corresponding to the wake zone is predicted by the numerical model. However the numerical wake zone is shorter and narrower. At $t = 14$ s, the wake zone area decreases in both experiments and simulation. But, the low velocity magnitude close to the obstacle disappears in the numerical simulation, yielding larger differences. Upstream of the obstacles, the splash-up area is visible in the experiments with high velocity gradients. Such phenomena is replicated by the numerical model but in terms of shape the zone is thinner at $t = 4$ s and $t = 9$ s. By $t = 14$ s, the numerical splash-up area extends, adopting its expected shape. The fact that the flow tends toward steady behaviour aligns with the turbulence approach employed. Such observations suggest that numerical simulations are more accurate as the flow approaches a steady state, which is consistent with the turbulence model used.

Case $2-10-2-10$ (Figure 5.26) present similar comparisons as the lengths of the splash-up zone over time are smaller for the numerical simulation; as the time increases, the differences decrease.

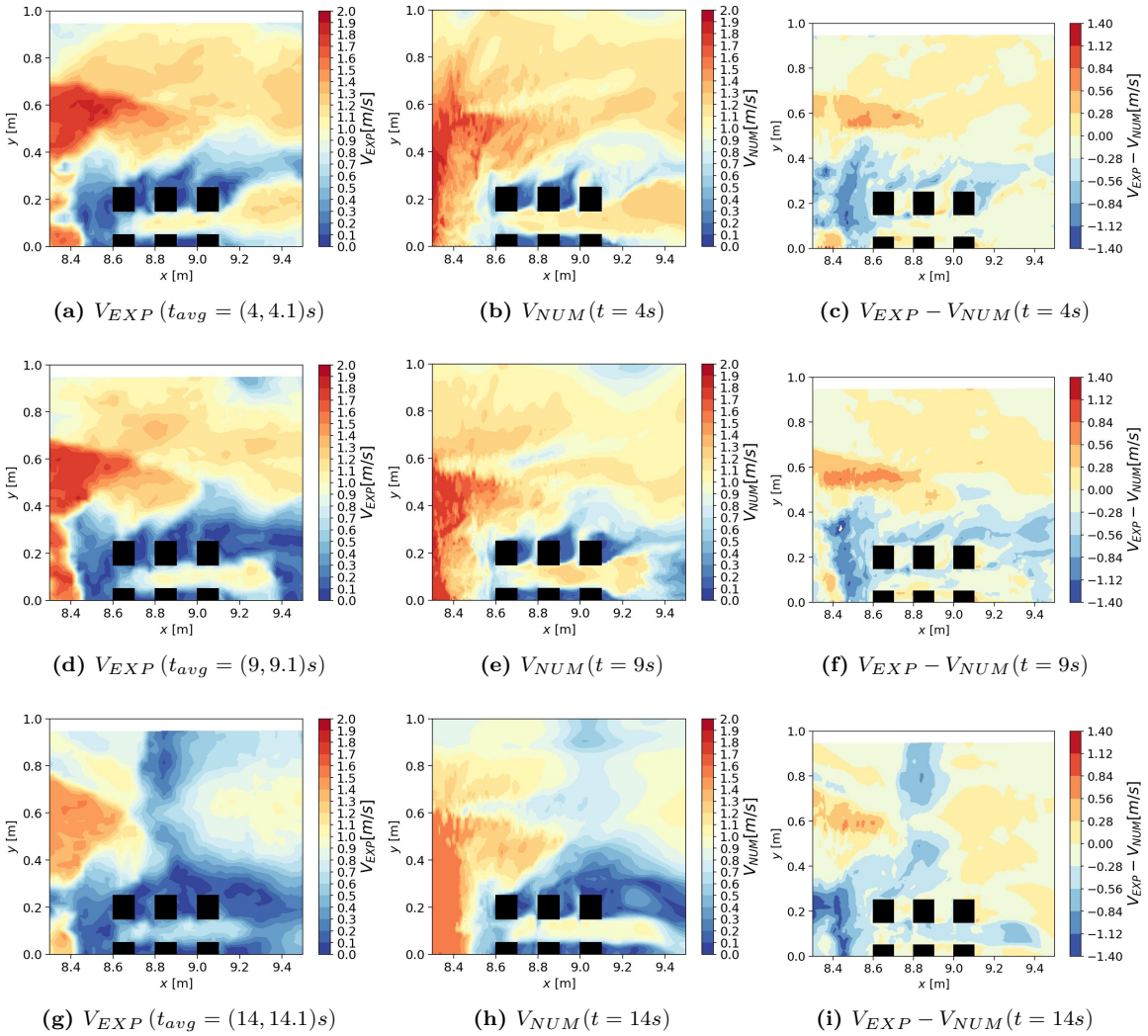

(a) $V_{EXP}\,(t_{avg} = (4, 4.1)s)$ **(b)** $V_{NUM}(t = 4s)$ **(c)** $V_{EXP} - V_{NUM}(t = 4s)$

(d) $V_{EXP}\,(t_{avg} = (9, 9.1)s)$ **(e)** $V_{NUM}(t = 9s)$ **(f)** $V_{EXP} - V_{NUM}(t = 9s)$

(g) $V_{EXP}\,(t_{avg} = (14, 14.1)s)$ **(h)** $V_{NUM}(t = 14s)$ **(i)** $V_{EXP} - V_{NUM}(t = 14s)$

Figure 5.26: Case $2-10-2-10$. Surface velocity field comparison at three different time steps. V_{EXP} represents the horizontal velocity obtained from the LSPIV analysis (Section 5.3.1) and V_{NUM} refers to the vertically averaged horizontal velocity for $\alpha \leq 0.5$. Black surfaces illustrate the obstacles' positions.

However, for case $2-10-2-10$, higher velocities are observed within the streets aligned with the main direction of the flow. Additionally, the flow ejected from the inside to the outside of the configuration was predicted numerically. Downstream of the configurations, the wake zone is better represented; at t = 4 s, the shape and intensity of the velocity field closely match between the two fields. At t = 9 s, a recirculation on the low left side of the images appears in both fields. Finally, the interaction between the splash-up area and the reflection zone at t = 14 s is slightly underestimated, even if a low velocity area is reproduced along the line x = 9 m. This can be explained by the numerical underestimation of the splash-up width.

Remark : Significant differences between the two velocity fields are evident in areas involving vertical displacement of the flow or air-water mixed area (such as the splash-up area and its interaction with the reflection zone) and, consequently, of the tracers during the LSPIV analysis. These vertical displacements affect the final measured velocity. Moreover, air-water mixture pose challenges for 3D VOF models, impacting the vertically averaged numerical velocity. Thus, quantitative comparison should be interpreted with caution, but some interesting features on the flow shapes and interaction with the obstacles can be interpreted.

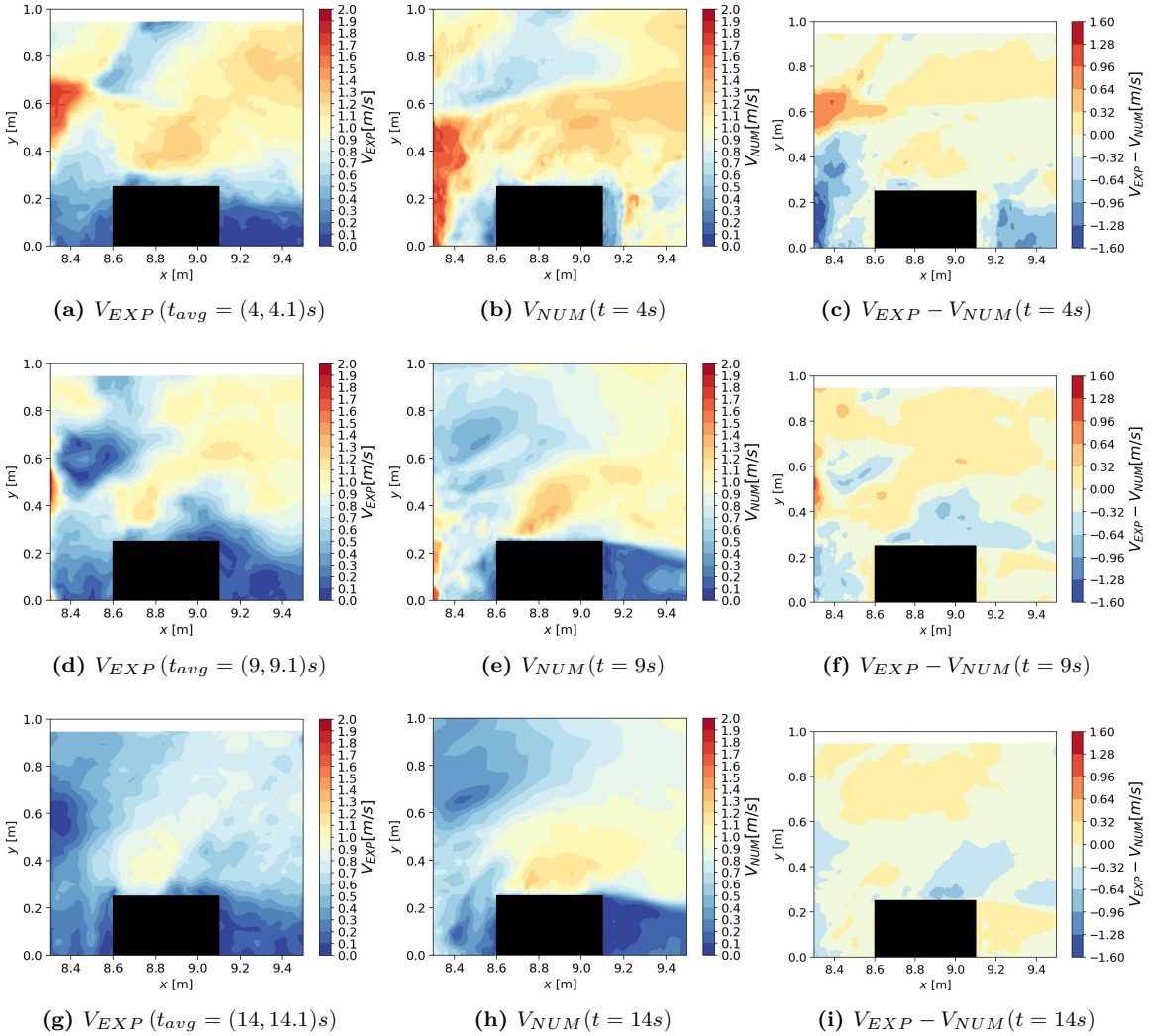

(a) $V_{EXP}\,(t_{avg} = (4, 4.1)s)$ **(b)** $V_{NUM}(t = 4s)$ **(c)** $V_{EXP} - V_{NUM}(t = 4s)$

(d) $V_{EXP}\,(t_{avg} = (9, 9.1)s)$ **(e)** $V_{NUM}(t = 9s)$ **(f)** $V_{EXP} - V_{NUM}(t = 9s)$

(g) $V_{EXP}\,(t_{avg} = (14, 14.1)s)$ **(h)** $V_{NUM}(t = 14s)$ **(i)** $V_{EXP} - V_{NUM}(t = 14s)$

Figure 5.27: Case $2-10-2-10$. Surface velocity field comparison at three different time steps. V_{EXP} represents the horizontal velocity obtained from the LSPIV analysis (Section 5.3.1) and V_{NUM} refers to the vertically averaged horizontal velocity for $\alpha \leq 0.5$. Black surfaces illustrate the obstacles' positions.

The splash-up zone is better reproduced numerically for case $4-0-4-0$ (Figure 5.27). Downstream of the obstacle, the wake zone is only reproduced after some seconds of simulation, as the numerical model over-predicts the velocity deviation around the obstacle. By t = 9 s, this deviation creates an additional

hydraulic jumps, which is captured in the numerical model. This effect intensifies over time and by t = 14 s, it completely diverts the reflection zone, which is also numerically predicted.

The first quantitative (water height) and qualitative (velocity field) comparisons emphasises that CFD can predict the overall behaviour of dam-break flow with presence of idealised urban areas. Indeed, the different zones identified previously in the analysis of the experimental results were predicted with code_saturne. On the other hand, differences have been observed, mostly related with unsteady phenomena, such as an underestimation of the splash-up zone and water height downstream of the obstacles. Again, many factors contributes to these differences, such as numerical choices (time, space schemes, turbulence approach, post-processing method) that may be further investigated.

5.5.4 *Turbulence model sensitivity analysis*

Preceding simulations used the turbulence $k-\epsilon$ model (as detailed in Section 3.3.2), which is the most commonly adopted [35, 112–117] for 3D dam-break cases through complex bottom topography or obstacles configurations. Here, a sensitivity analysis on the different RANS turbulence models is performed for case $2-10-2-10$ to confirm the choice of the numerical model for future urban forms studies. Case $2-10-2-10$ was selected because its geometry is closer to the idealised urban areas that will be studied in the future and involves the most complex flow phenomena, such as 3D recirculations.

The $k-\epsilon$ model is compared with the first-order RANS model $k-\omega\ SST$, the second-order RANS model $R_{ij}-\epsilon\ SSG$ and a case with no specific turbulence treatment. The $k-\omega\ SST$ model is designed to handle near-wall effects and could improve the prediction of phenomena occurring within urban areas. On the other hand, the $R_{ij}-\epsilon\ SSG$ model is more complex, as it solves additional equations for the Reynolds stresses R_{ij}, and is capable of capturing anisotropic effects that occur within urban areas. The computational times of case $2-10-2-10$ with different turbulence models are summarised in Table 5.10.

Table 5.10: Summary of the computational time for case $2-10-2-10$ with different turbulence models.

Case	Total time	Total CPU time on 420 processors
no turbulence	2.6 hr	1090 hr
$k-\omega\ SST$	7.87 hr	3329 hr
$R_{ij}-\epsilon\ SSG$	6.3 hr	2662 hr
$k-\epsilon$	3.3 hr	1396 hr

First, Figure 5.28 shows the variation in water depth upstream and downstream of the urban area for different numerical models and compares them with experimental data. At position A1 (Figure 5.28a), no significant differences are observed; the averaged water depth predicted by all turbulence models is similar. However, at position A6 (Figure 5.28b), the choice of turbulence model clearly impacts the water depth prediction, although all models underestimate the water depth. Without turbulence modelling, there is an almost dry bed area downstream of the obstacle configuration (Figure 5.28b). Between the turbulence models, the $k-\epsilon$ shows the closest agreement with the expected data.

Moreover, the instantaneous numerical depth-averaged velocity fields are compared with the surface velocity fields obtained from LSPIV analysis. The top row of Figures 5.29, 5.30, 5.31 and 5.32 show the instantaneous numerical depth-averaged velocity fields for all turbulence models at three different times. The colour map represents the magnitude of the horizontal velocity V_{xy}, calculated as $\sqrt{V_x^2+V_y^2}$. The absolute difference between the experimental velocity field and the numerical model is displayed in the bottom row of each figure. Also, the relative velocity differences, computed as $\frac{|V_{EXP}-V_{NUM}|}{|V_{EXP}|}[\%]$ are summarised in Table 5.11.

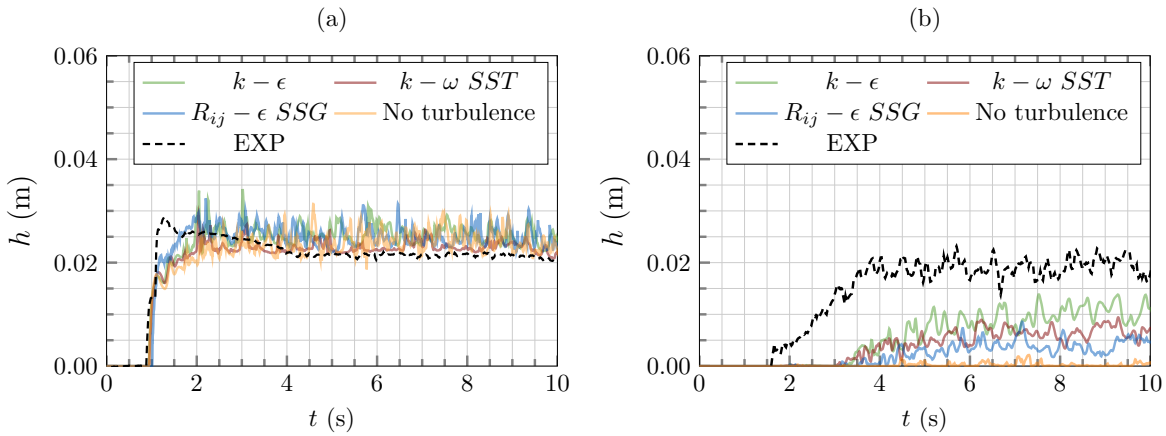

Figure 5.28: Case 2 – 10 – 2 – 10. Water height at positions (a) A1 and (b) A6 between experimental data (black dashed line) and numerical models.

Without a turbulence model (Figure 5.29), the simulation struggles to reproduce the reflection wave on the side walls, resulting in significant absolute relative velocity in this area (x = [8.4, 9.4] m and y = [1.4, 1] m). Additionally, the lateral wake created by the flow passing through the streets along the y-axis (x = [8.6, 9.4] m and y = [0.2, 0.5] m) is not represented in the numerical model, resulting in overestimated velocities. Overall, the computed velocity field differs considerably from the measured one, with around 30% of the relative velocity belonging to the [0, 20] weight interval. Such results emphasises the importance of accounting for turbulence in the dam-break framework.

Indeed, the general characteristics of the flow are reproduced by the three turbulence models. While all three models show a similar distribution of absolute relative velocity across all intervals (Table 5.11), the $k-\epsilon$ model is the closest to the experimental data. Additionally, the computational time for the $k-\epsilon$ model is lower (the pressure solver resolution is slower for the other two models), and it better reproduces water depth variations at position A6. Finally, the $k-\epsilon$ model is the most commonly adopted [35, 112–117] for 3D dam break waves, making it a suitable choice for future numerical studies.

Table 5.11: Case 2 – 10 – 2 – 10. Interval weight (%) of the relative velocity variation (%) between experimental data and numerical model for 3 different turbulence closure models.

Case	**Time step (s)**	**Interval weight [%]**					
		[0, 20]	[20, 40]	[40, 60]	[60, 80]	[80, 100]	[100, 200]
No model	4	29.85	28.57	16.26	10.30	5.47	9.54
	9	35.78	26.11	15.39	6.93	3.79	11.99
	14	24.35	17.62	14.27	12.55	7.90	23.32
$k-\epsilon$	4	61.54	18.32	6.62	3.84	2.81	6.87
	9	57.65	19.29	7.16	4.02	2.97	8.91
	14	50.82	17.21	10.25	5.91	4.03	11.79
$k-\omega$ SST	4	59.29	19.52	6.66	4.17	3.16	7.19
	9	59.05	17.87	6.12	4.14	3.34	9.48
	14	46.11	18.17	10.84	7.15	4.43	13.30
$R_{ij}-\epsilon$ SSG	4	55.14	22.35	6.47	4.25	3.59	8.19
	9	56.95	19.88	6.20	4.38	3.49	9.10
	14	50.63	19.00	9.90	5.58	3.79	11.11

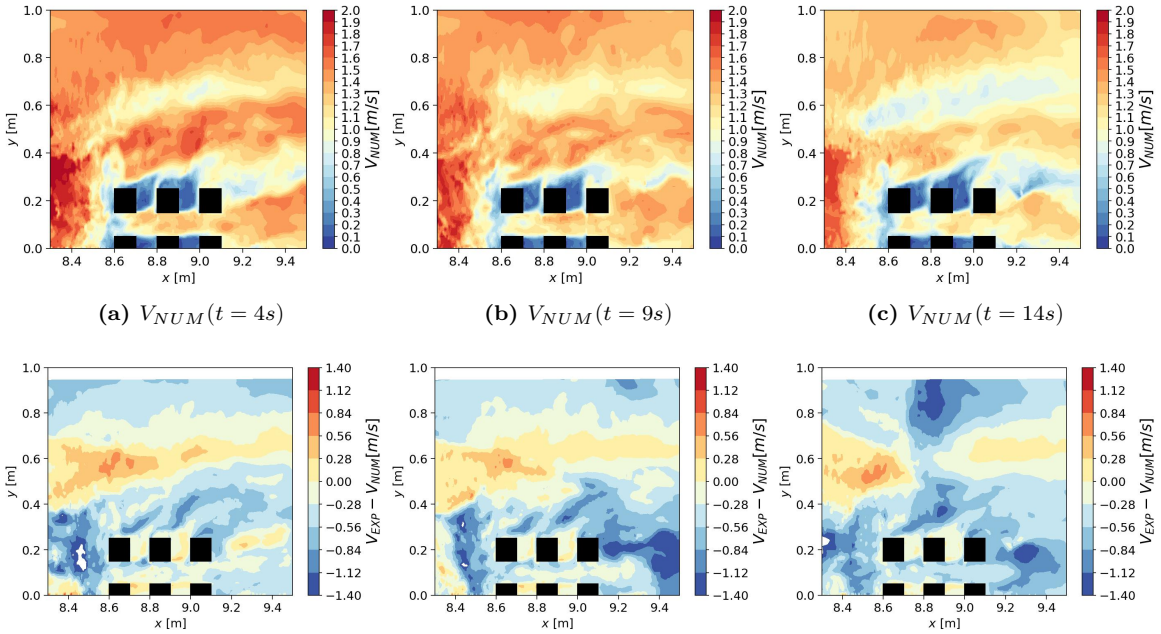

(a) $V_{NUM}(t = 4s)$ **(b)** $V_{NUM}(t = 9s)$ **(c)** $V_{NUM}(t = 14s)$

(d) $V_{EXP} - V_{NUM}(t = 4s)$ **(e)** $V_{EXP} - V_{NUM}(t = 9s)$ **(f)** $V_{EXP} - V_{NUM}(t = 14s)$

Figure 5.29: Case $2 - 10 - 2 - 10$ without turbulence model. Surface velocity field comparison at three different time steps. V_{EXP} represents the horizontal velocity obtained from the LSPIV analysis and V_{NUM} refers to the vertically averaged horizontal velocity for $\alpha \leq 0.5$. Black surfaces illustrate the obstacles' positions.

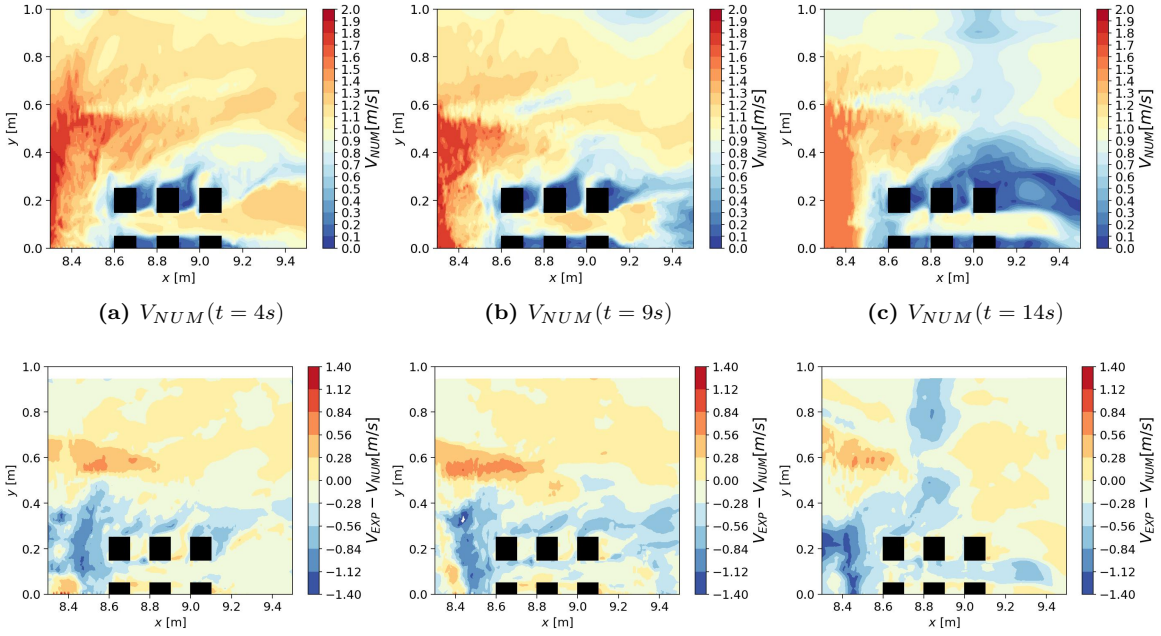

(a) $V_{NUM}(t = 4s)$ **(b)** $V_{NUM}(t = 9s)$ **(c)** $V_{NUM}(t = 14s)$

(d) $V_{EXP} - V_{NUM}(t = 4s)$ **(e)** $V_{EXP} - V_{NUM}(t = 9s)$ **(f)** $V_{EXP} - V_{NUM}(t = 14s)$

Figure 5.30: Case $2 - 10 - 2 - 10$ with $k - \epsilon$ (with linear production) turbulence model. Surface velocity field comparison at three different time steps. V_{EXP} represents the horizontal velocity obtained from the LSPIV analysis and V_{NUM} refers to the vertically averaged horizontal velocity for $\alpha \leq 0.5$. Black surfaces illustrate the obstacles' positions.

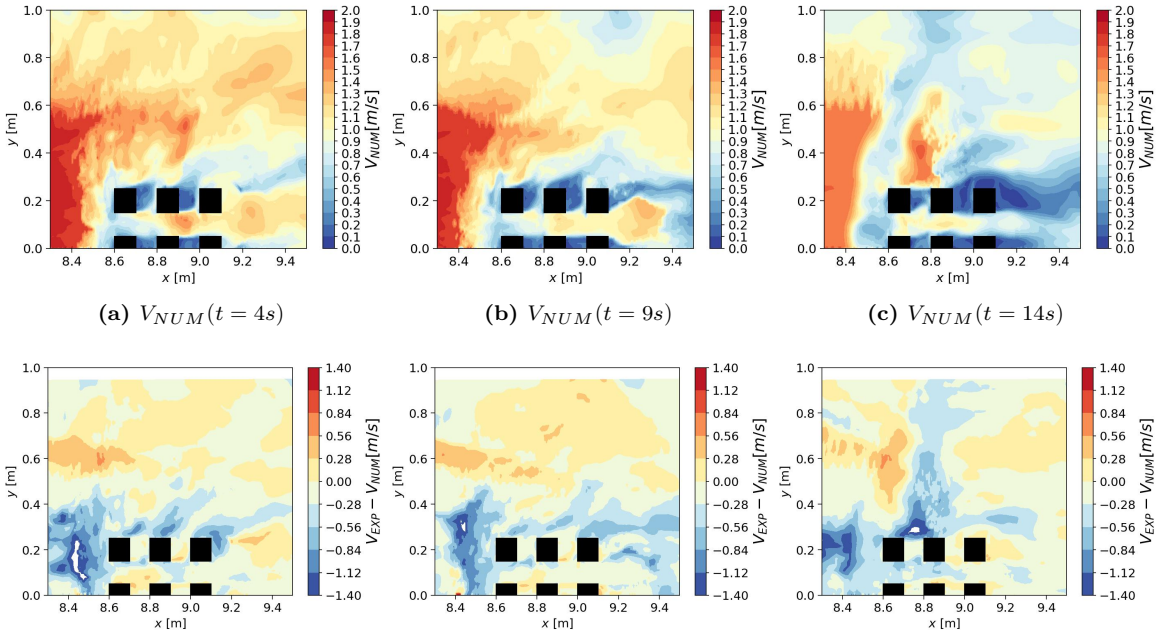

(a) $V_{NUM}(t = 4s)$ **(b)** $V_{NUM}(t = 9s)$ **(c)** $V_{NUM}(t = 14s)$

(d) $V_{EXP} - V_{NUM}(t = 4s)$ **(e)** $V_{EXP} - V_{NUM}(t = 9s)$ **(f)** $V_{EXP} - V_{NUM}(t = 14s)$

Figure 5.31: Case $2-10-2-10$ with $k-\omega$ SST turbulence model. Surface velocity field comparison at three different time steps. V_{EXP} represents the horizontal velocity obtained from the LSPIV analysis and V_{NUM} refers to the vertically averaged horizontal velocity for $\alpha \leq 0.5$. Black surfaces illustrate the obstacles' positions.

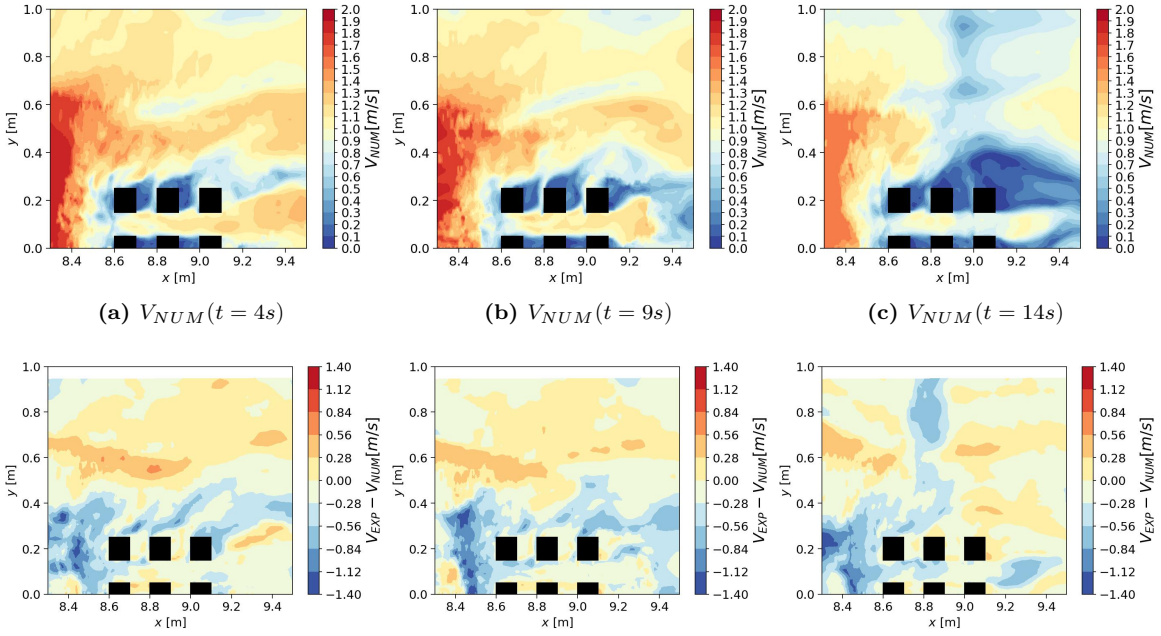

(a) $V_{NUM}(t = 4s)$ **(b)** $V_{NUM}(t = 9s)$ **(c)** $V_{NUM}(t = 14s)$

(d) $V_{EXP} - V_{NUM}(t = 4s)$ **(e)** $V_{EXP} - V_{NUM}(t = 9s)$ **(f)** $V_{EXP} - V_{NUM}(t = 14s)$

Figure 5.32: Case $2-10-2-10$ with $R_{ij}-\epsilon$ SSG turbulence model. Surface velocity field comparison at three different time steps. V_{EXP} represents the horizontal velocity obtained from the LSPIV analysis and V_{NUM} refers to the vertically averaged horizontal velocity for $\alpha \leq 0.5$. Black surfaces illustrate the obstacles' positions.

5.5.5 *Summary*

In this section, code_saturne's capability to accurately replicate the complex transient phenomena induced by the obstacles on the flow is assessed. The numerical results were compared quantitatively and qualitatively with the experimental dataset. The global flow features were correctly reproduced, such as the upstream oscillations and the different wake and splash-up zones. Yet, some limitations of the post-processing method to retrieve the numerical water depth in air-water mixed environments were highlighted. CFD was more accurate when the flow exhibited steady behaviour. Indeed, during the first seconds, the lengths of both the wake and splash-up zones were slightly underestimated. A sensitivity analysis on different turbulence closure models has also been presented, confirming the choice of the $k-\epsilon$ model for the next simulations. Future work should include further comparisons of water depth evolution within the idealised urban configurations. Moreover, the comparison of the numerical depth-averaged velocity field with LSPIV results highlights the model's capacity in accurately reproducing the 3D phenomena around urban areas.

5.6 CONCLUSION

This chapter presented a preliminary experimental study on the propagation of fast transient dam-break waves over four obstacles configurations. The experimental dataset from the preliminary campaign was then used to assess the ability of code_saturne to reproduce the studied phenomena. Numerical results showed promising predictions that shall forecast and complement experimental findings on the influence of urban forms on unsteady urban flooding. Essential physical parameters, such as water height and the horizontal velocity field of the free surface, were investigated within specific regions of interest.

Flow tracking employs recent measurement techniques adapted to the fast physical phenomenon measured. The metrology and experimental methodology deployed on the experimental setup is challenged based on the experimental results of the preliminary study. The accurate and reliable dataset obtained highlights the advantages of combining different techniques to track fast and complex phenomena.

Four obstacle configurations are examined and some interesting features of the flow around the obstacles are observed. The surroundings of the idealised urban area is compared with a reference dam-break case without obstacles.

At last, the main findings from this Chapter are:

- Oscillation waves are observed upstream of the breach for all configurations. This phenomenon leads to variations in the flow rate through the gate, subsequently impacting the flow behaviour downstream of the gate. This is an important condition to take into account for future experimental and numerical studies in order to accurately reproduce the observed dam-break wave. The ability of the 3D numerical model to accurately reproduce the upstream oscillations has been demonstrated by taking into account the vertical displacement of the gate.
- It is evident that the flow downstream of the gate is significantly influenced by the presence of obstacle configuration. Two main observations are made: first, the splash-up in front of the obstacles and second, the position and temporal variation of the wake zone downstream of the obstacles.
- A new methodology for quantitatively studying the impact of obstacles on flow has been proposed.
- IAM measurements complement water depth measurements during the impact process between the dam-break wave and the obstacles, enhancing the data captured by acoustic gauges.
- Results obtained with the VOF module of code_saturne correctly replicate the formation of the splash-up and wake zone around the obstacle configurations. Nevertheless, there is a numerical underestimation of the water height closer to the obstacles. Supplementary sensitivity analysis could be performed on the $k-\epsilon$ turbulence model and its accuracy for shallow dam-break flow cases.

Finally, the next chapter will extend this experimental protocol to new obstacle configurations representative of suburban areas and study the impact of different urban parameters on the flow dynamics at a larger scale.

Thesis Question No. 1:
Can experimental studies contribute to providing accurate and reliable supplementary validation datasets on the influence of urban forms on unsteady flooding?

The first part of the manuscript presented an experimental setup that reproduces the propagation of dam-break flow through various urban layouts. Novel experimental data containing the water height at strategic positions, the unsteady free surface velocity within and around urban configurations were presented, along with an optical measurement technique to record the impact process between the dam-break wave and the first row of obstacles. The complexity of the phenomenon involved underscores the importance of providing such accurate and reliable validation datasets. The experimental setup presented will now be extended to study the influence of urban parameters on the flow.

6

INFLUENCE OF URBAN FORMS ON FAST TRANSIENT FLOW

Summary :
This chapter presents an experimental campaign conducted on 21 idealised urban areas. First, feedback from the preliminary campaign is taken into account and used to modify the experimental protocol. The obtained results analysis is divided into two parts: the effect of the longitudinal streets on the flow and then the effect of the cross streets. Water depth measurements and free surface velocity, related to a reference case, are used to highlight the impact of four urban parameters. Then, the energy head is computed and analysed, mostly downstream of the urban areas, to quantify for this setup the global impact of the urban forms on the flow. Tendencies are observed punctually and guidelines for the representation of urban areas in numerical models are given. Finally, results are compared to past studies, highlighting similarities and novelties brought by the current dataset.

Contents

6.1 Introduction **89**
6.2 Modifications of the experimental protocol **89**
6.3 Repeatability of the experiments **93**
6.4 Urban form parameters **94**
6.5 Influence of the streets in the main direction of the flow **94**
6.5.1 Definition of thirteen urban forms 94
6.5.2 Longitudinal street width impact (l_x) on the flow 95
6.5.3 Longitudinal street number impact (n_x) on the flow 113
6.5.4 Summary 115
6.6 Influence of the streets along the cross section of the flow **117**
6.6.1 Definition of the idealised urban forms 117
6.6.2 Cross streets impact ($n_y = 0$) on the flow 118
6.6.3 Cross streets width and number impact (l_y) on the flow 124
6.6.4 Summary 129
6.7 Comparisons of current experiments with past experimental studies **130**
6.8 Conclusion **132**

6.1 INTRODUCTION

A new experimental campaign is conducted based on the results and feedback obtained from the preliminary experiments discussed in Chapter 5. The validation of the setup design, associated metrology, and post-processing methods were carried out through a series of dam-break flow experiments involving simple obstacle geometries.

Based on the reference work in the literature presented in Chapter 2, this study focuses on the influence of several urban parameters on the flow. To achieve this, urban forms are defined using four different parameters: the number and width of streets parallel and perpendicular to the main direction of the dam-break wave. The previously applied experimental methodology is extended to 21 obstacle configurations representative of suburban areas.

The structure of this chapter is organised as follows: Section 6.2 discusses the changes made to the experimental protocol following the preliminary study. Next, the repeatability of the experiments is presented in Section 6.3, followed by the definition of the urban parameters studied in Section 6.4. The experimental results are then presented, starting with an analysis of the influence of streets along the x-axis in Section 6.5, followed by an analysis of the influence of streets along the y-axis in Section 6.6.

6.2 MODIFICATIONS OF THE EXPERIMENTAL PROTOCOL

Some modifications of the experimental protocol are done for the second campaign, based on the feedback of the previously presented experiments. First, the position of the obstacles in the channel is modified; previously placed at $x = 8.6$ m, they are now placed at $x = 8$ m to minimise the interaction between the urban area and the reflection wave.

OPENING SYSTEM The system used to open the gate is modified since the synchronisation between the gate opening and the trigger in the previous campaign depended on the operator's manual activation. This was done through a change of the controller position (from left to right) which could vary up to 0.1 s. The new system is composed of a dry contact switch, ensuring that the acquisition trigger time is always synchronised. However, this change slightly slowed the opening time of the gate, which is now about $t_{gate} = 0.79$ s ($v_{gate} = 0.31$ m/s).

> **Note** : The opening effect of the gate can be taken into account in the numerical model, as demonstrated in Chapter 5, so a more reliable opening system has been preferred over a faster one.

LSPIV ANALYSIS Some erroneous velocity gradients on the lower-left side of the velocity field were visible in the previous campaign (see Chapter 5 or Appendix D) due to the transparency of the water and the lack of seeding particles. To prevent it, a higher number of seeding particles is used in the present campaign, and a floating line is added through the gate to create patterns on the free surface and reduce its transparency. Specifically, the floating line is positioned in the reservoir before the experiment. Each side of the line is attached to the gate, and once the trial begins, the line passes through the gate and creates patterns on the free surface. The effect of the seeding particles and floating line is illustrated in Figure 6.1. Nevertheless, for case 0, the transparency of the water over the entire measurement zone still led to lower correlation and erroneous velocity gradient. To improve the LSPIV analysis for this case, the velocity field is averaged over 6 experiments (3 LSPIV experiments are performed for all other cases) and a velocity filter is added to the post-processing steps (Table 6.2). The parameters for the LSPIV analysis used in this study are summarised in Tables 6.1 and 6.2. Once again, the value of each parameter was carefully selected through sensitivity analysis. For the sake of brevity, the selection process of the different parameters is not detailed in the manuscript. Since a LSPIV calculation uses a flat free surface hypothesis, a constant water depth is set to 0.025 m for all cases. This value represents the averaged water depth in the measurement zone obtained for case 0 with code_saturne.

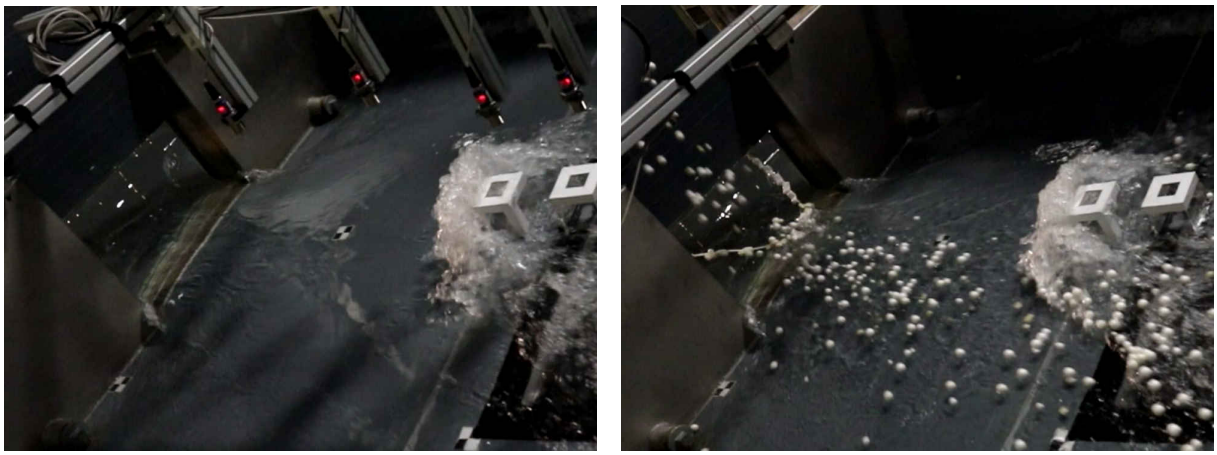

(a) **(b)**

Figure 6.1: Snapshot of the water transparency and free surface patterns during (a) water depth measurements and (b) LSPIV analysis during the urban forms campaign.

Additionally, velocity calculations are now performed on a refined grid around the urban area to obtain detailed velocity information, even for cases with narrower streets. For each case, this homogeneous grid is adjusted to remove grid points located above the obstacles. This results in an identical grid point (if not located above an obstacle) for all studied configurations, making their comparisons easier.

Table 6.1: Summary of the parameters used for the LSPIV analysis in Fudaa-LSPIV [130].

Number of frames	Resolution	Water level	IA	SA_{y-}	SA_{y+}	SA_{x-}	SA_{x+}
4165	0.0016 m/pix	0.02 m	34 pix	5 pix	5 pix	5 pix	10 pix

Table 6.2: Summary of the filter parameters used for the LSPIV analysis.

Cases	**Correlation threshold**	**Median test*** **[133]**		**Velocity filters**	
		r_0^*	ξ	V_x (m/s)	V_y (m/s)
0	0.4	4	0.1 pix	[2.8, 0]	[1.5, -1.5]
21 urban forms	0.4	4	0.1 pix	-	-

* r_0^*: Normalised residual threshold, ξ: acceptable fluctuation level

Note : The recommended universal value for the normalised residual threshold r_0^* and the acceptable fluctuation level ξ are $r_0^* > 2$ and $\xi = 0.1$ pix [133].

IAM ANALYSIS The water jet in the preliminary study for case $4-0-4-0$ was out of the field of view of the camera resolution which is adjusted here to record the entire splash-up height. The resulting image resolution is 1280×1024 pixels and the frequency acquisition is set to 250 fps. Additionally, as shown in Figure 6.2, white duct tape was added to the sides of the obstacles to improve their visibility in the high-speed camera images. The parameters for the IAM analysis used in this study are summarised in Table 6.3. Also, a filter called 'morphological erosion' [135] is used during the analysis on the binarized images to diminish the detection of droplets.

Remark : To ensure a consistent comparison of the free surface height and shape between the different cases, the camera was not moved and the optical parameters were kept constant during the entire experimental campaign.

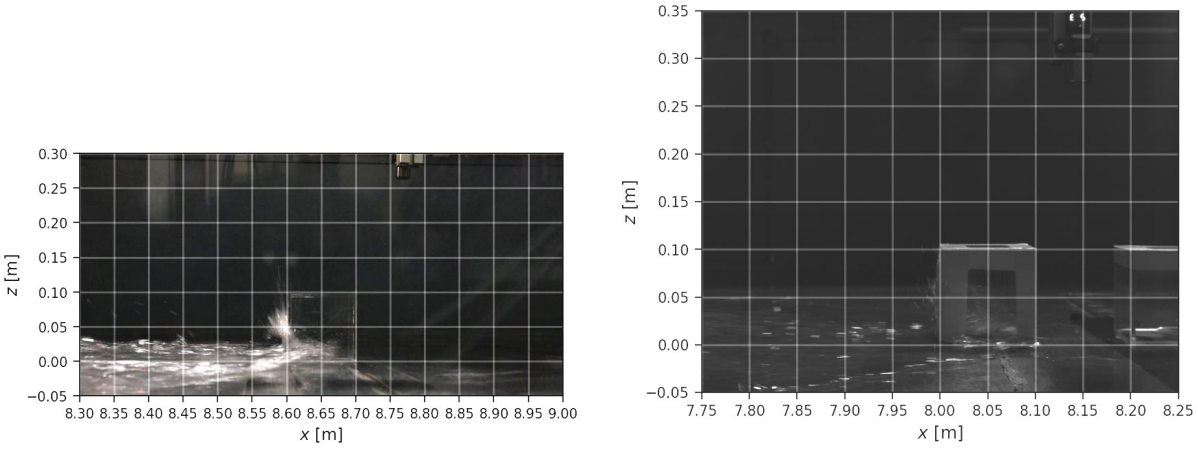

(a) **(b)**

Figure 6.2: IAM high-speed camera resolution from (a) the preliminary study for case $0-0-0-0$ and (b) the actual study for case $0-0-2-10$.

Table 6.3: Summary of the parameters used in the image analysis measurement program (Appendix C).

	Binarization value	**Calibration** (pix/mm)	**Region Of Interest** Offset[1]	Nb lines[2]	Increment[3]	**Filter**
all cases	2.39	0 m	3	1 pix	0 pix	Erosion [135]

[1]: Δx between x = 8 m and the position of the ROI.
[2]: Number of times the ROI is shifted horizontally from its original position to $-x$.
[3]: Increment between each shifted ROI lines.

The initial focus of the camera as well as the calibration of the images and definition of the ROI position were performed on case $0-0-2-10$ (Figure 6.2b). The calibration was performed on the lateral side of the first cube (x = 8 m and z = [0, 0.1] m). Then the ROI was placed on the same side of the cube, as shown in Figure 6.3, starting from x = 0 m at the lower left corner and extending over the entire image height (Δz = 0.35 m). The ROI is placed on the closest face of the central cube and, therefore, is not located at the exact center of the channel (y = 0 m) but at y = -0.05 m. The ROI is shifted 3 times horizontally and the final free surface height is set as the average of the 3 maximum value detected on those lines.

Remark : The ROI position is offset from the centre of the channel and located at y = -0.05 m. As for the camera, the ROI position, calibration parameters, and IAM parameters were kept constant for all cases for comparison purposes. The resulting free surface elevation in the splash-up may be questioned due to the depth of field, but the differences in height and shape between the different urban forms can still be analysed and used for numerical validation. A laser sheet could have been used to highlight a specific profile in the flow, but such improvements are left for future studies.

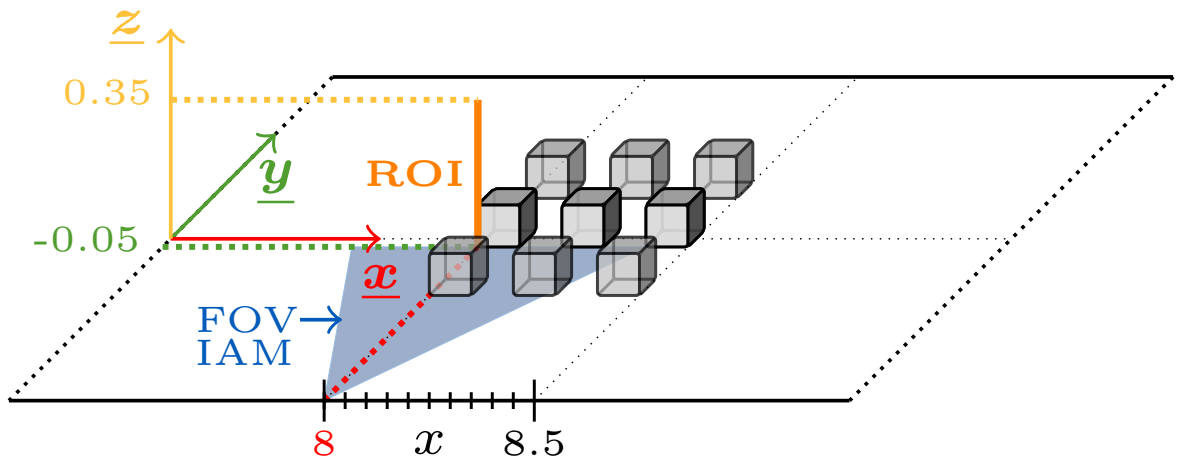

Figure 6.3: 3D schematic view of the position of the Region Of Interest (ROI) used for the IAM analysis. The blue area is an approximation of the Field Of View (FOV) of the IAM camera.

GAUGES POSITION The positions of the water depth gauges have been modified from the preliminary experimental study. Two resistive gauges are placed in the reservoir to ensure the repeatability of the different tests. Six acoustic gauges are placed downstream of the gate along a longitudinal profile as schematised in Figure 6.4. The acoustic gauges are placed upstream, within, and downstream of the urban areas to obtain the temporal and spatial water depth through the urban areas. Gauges positions are listed in Table 6.4.

Note : The locations of the acoustic gauges are defined to ensure that they are within the Field of View (FOV) of the LSPIV and that their positions are compatible with all tested idealised urban forms (i.e., they are not placed above an obstacle). Since they are placed along the same y-axis, the depth profiles will be analysed later.

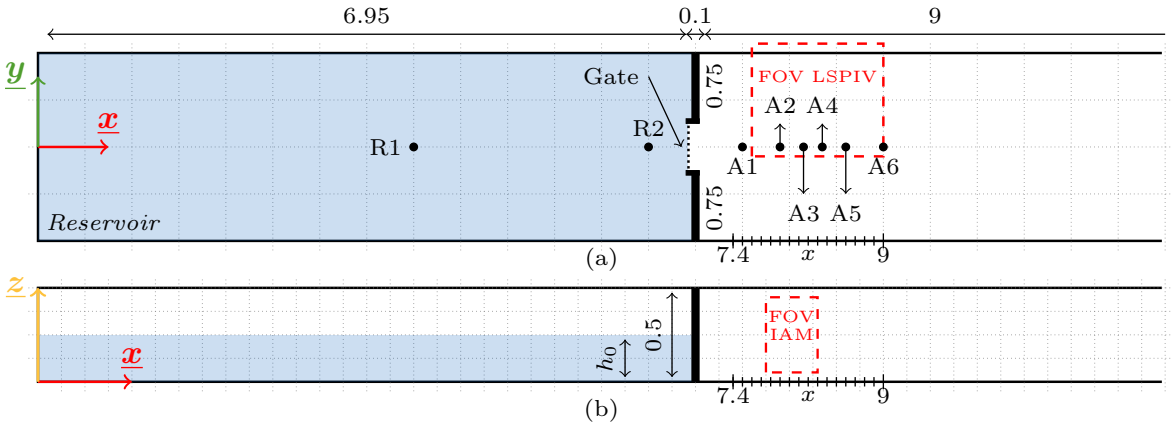

Figure 6.4: Schematic views of the experimental setup, (a) top and (b) side sections. The coordinate system, the probes locations (R1 to R2, A1 to A6) and the Field Of View (FOV) for both Large-Scale Particle Image Velocimetry (LSPIV) and Image Analysis Measurement (IAM) are also illustrated.

Table 6.4: List of probe types and locations (m).

	Type	**x** (m)	**y** (m)
R1	Resistive	4.00	0.00
R2	Resistive	6.50	0.00
A1	Acoustic	7.50	0.00
A2	Acoustic	7.90	0.00
A3	Acoustic	8.15	0.00
A4	Acoustic	8.35	0.00
A5	Acoustic	8.60	0.00
A6	Acoustic	9.00	0.00

6.3 REPEATABILITY OF THE EXPERIMENTS

Twenty-two test cases, 21 urban forms and one case without obstacles, were conducted in this chapter and are summarised in Table 6.5, resulting in a total of 135 experiments. Except for case 0, 6 experiments were done for each case (3 for the LSPIV and 3 for the the water depth). Their repeatability was verified using resistive gauges upstream of the gate (across all 6 experiments) and using acoustic gauges near the gate (across the 3 water depth experiments). Figure 6.5a shows the water depth variation at position R2 for the 135 dam-break flow experiments performed. Note that the initial water depth is set to $h_0 = [0.249 - 0.251]$ m (± 0.5 mm). The filling of the reservoir is stopped using a limnimeter (graduated to one-tenth of a millimetre) as a reference leading to initial water depth differences. Nevertheless, these initial differences do not impact the hydrological conditions of the experiment, such as the tank emptying process or the appearance of oscillation waves in the tank. Figure 6.5b demonstrates the good repeatability of the wave velocity propagation across all 66 water depth measurements downstream of the gate at position A1.

Table 6.5: Number of experiments performed.

Cases	**LSPIV + RG***	**RG + AG****	Total
0	6	3	9
21 urban forms	3	3	21 × 6
			135

*: Resistive Gauges
**: Acoustic Gauges

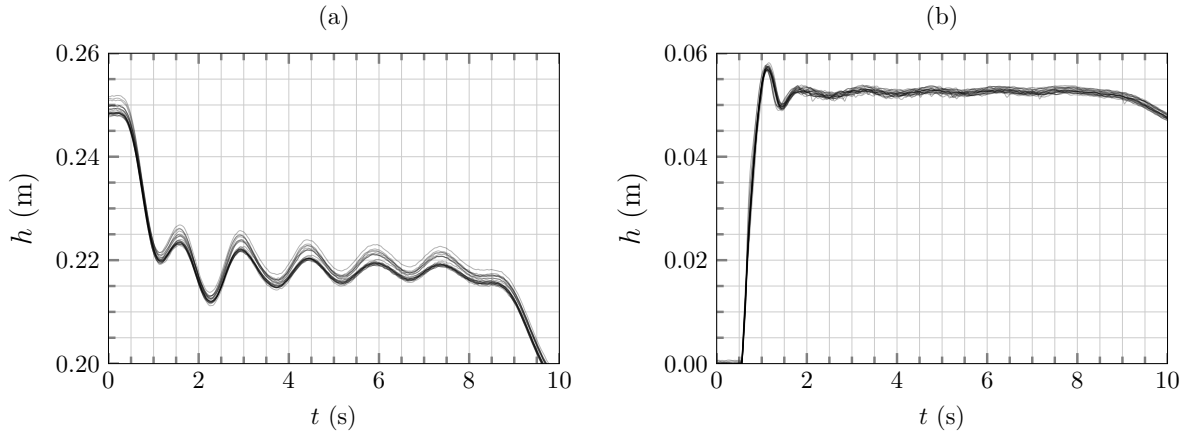

Figure 6.5: Water depth variation for all studied configurations at positions (a) R2 (135 curves) and (b) A1 (66 curves). All curves are plotted with an opacity equal to 0.3 for better readability.

6.4 URBAN FORM PARAMETERS

To study the influence of various urban forms on flood wave propagation, 21 obstacle configurations will be defined based on four independent parameters:

- n_x and n_y: the number of streets along the x and y directions, respectively.
- l_x and l_y: the width of the streets along the x and y directions, respectively.

These parameters are illustrated in Figure 6.6 using the previously studied configuration $2-10-2-10$. The names of the configurations correspond to $n_x - l_x - n_y - l_y$, with each part representing the associated value of the parameter. The obstacles used are cubes with a side length of 0.1 m.

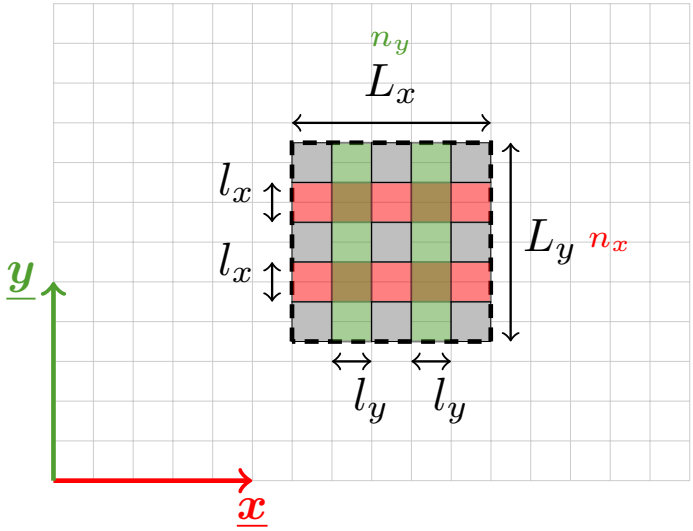

Figure 6.6: Geometry of the urban form $2-10-2-10$ and definition of the parameters characterising urban forms in the manuscript. Grey surfaces represent the positions of the obstacles, red surfaces represent the streets along the x direction, and green surfaces represent the streets along the y direction.

The experimental results are processed using all previously presented measurement techniques and post-processing methods, leading to the acquisition of: (i) the water depth profiles from the wave gauges, (ii) the wave impact and its height using the IAM measurement, (iii) the velocity fields from the LSPIV analysis, and finally (iv) the energy head through the urban area, computed using both water depth and velocity measurements.

6.5 INFLUENCE OF THE STREETS IN THE MAIN DIRECTION OF THE FLOW

The first part of the study analyses the effect of the streets in the main direction of the flow. The first thirteen urban forms studied are presented in Section 6.5.1. Then, the impact of the street width l_x and the number of street n_x are examined in Sections 6.5.2 and 6.5.3, respectively.

6.5.1 *Definition of thirteen urban forms*

As a reminder from Chapter 2, Li et al. (2021) [47] highlighted the influence of one specific urban parameter in the steady flood framework: the conveyance porosity in the main direction of the flow (ψ_y). This parameter is defined as the ratio of the number of streets and their width to the width of the entire urban area (along a given axis). The first part of the current study focuses on the influence on the flow of the following two parameters: the number of streets in the main flow direction (n_x) and their width (l_x).

To do so, the number of streets n_x is varied from 0 to 3. For all n_x values, the associated street width l_x is varied from 0.05 m to 0.2 m. The corresponding parameters of the resulting urban forms are given in Table 6.6 and illustrated in Figures 6.7 and 6.8. The thirteen studied configurations are compared to a dam-break flow with no obstacle, denoted 0.

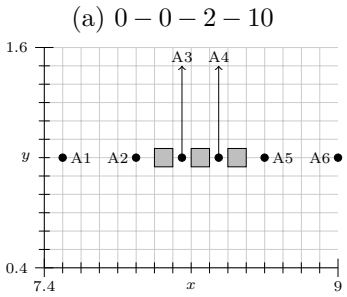

Figure 6.7: Top view of the configuration 0 – 0 – 2 – 10 whitout longitudinal street.

Table 6.6: Parameters characterising urban forms to study the influence of the streets along the x-axis.

Configuration *	**Parameters**					
	n_x	l_x (m)	L_y (m)	n_y	l_y (m)	L_x (m)
0 **	-	-	-	-	-	-
0 – 0 – 2 – 10	0	0	0.10	2	0.1	0.5
1 – 05 – 2 – 10	1	0.05	0.25	2	0.1	0.5
1 – 10 – 2 – 10	1	0.10	0.30	2	0.1	0.5
1 – 15 – 2 – 10	1	0.15	0.35	2	0.1	0.5
1 – 20 – 2 – 10	1	0.20	0.40	2	0.1	0.5
2 – 05 – 2 – 10	2	0.05	0.40	2	0.1	0.5
2 – 10 – 2 – 10 **	2	0.10	0.50	2	0.1	0.5
2 – 15 – 2 – 10	2	0.15	0.60	2	0.1	0.5
2 – 20 – 2 – 10	2	0.20	0.70	2	0.1	0.5
3 – 05 – 2 – 10	3	0.05	0.55	2	0.1	0.5
3 – 10 – 2 – 10	3	0.10	0.70	2	0.1	0.5
3 – 15 – 2 – 10	3	0.15	0.85	2	0.1	0.5
3 – 20 – 2 – 10	3	0.20	1.00	2	0.1	0.5

* Configuration names: $n_x - l_x - n_y - l_y$
**: Case already studied in the preliminary campaign

The acoustic wave gauges are placed within and around the thirteen urban forms, as illustrated in Figures 6.7 and 6.8. Also their position remains constant for all tests. For some cases, they are aligned with the buildings (configurations with $n_x = 0$ or 2) or with a longitudinal street (configurations with $n_x = 1$ or 3). Probes A1 (upstream) and A6 (downstream) are the most distant gauges from the urban area. Probe A1 is mostly used to insure the repeatability of the experiment, since its value remained constant across all studied configurations (Figure 6.5b). Figure 6.9 shows a superposition of all street widths l_x for a given street number n_x and will serve as a configuration memento for future analyses.

6.5.2 *Longitudinal street width impact (l_x) on the flow*

The impact of street width along the x-axis is analysed for configurations with one ($n_x = 1$), two ($n_x = 2$), and three ($n_x = 3$) streets. l_x varies from 0.05 m to 0.20 m, corresponding to half and twice the size of the buildings, respectively.

The water depth variation through the urban area for the different widths is analysed. Figures 6.10, 6.11, and 6.12 illustrate the water depth evolution through the street for cases with $n_x = 1$, $n_x = 3$, and $n_x = 2$, respectively, at all probes positions. All cases are compared to case 0 with no obstacle. Additionally, the water depth profile for cases $n_x = 3$ is described in Figure 6.13 at four time steps.

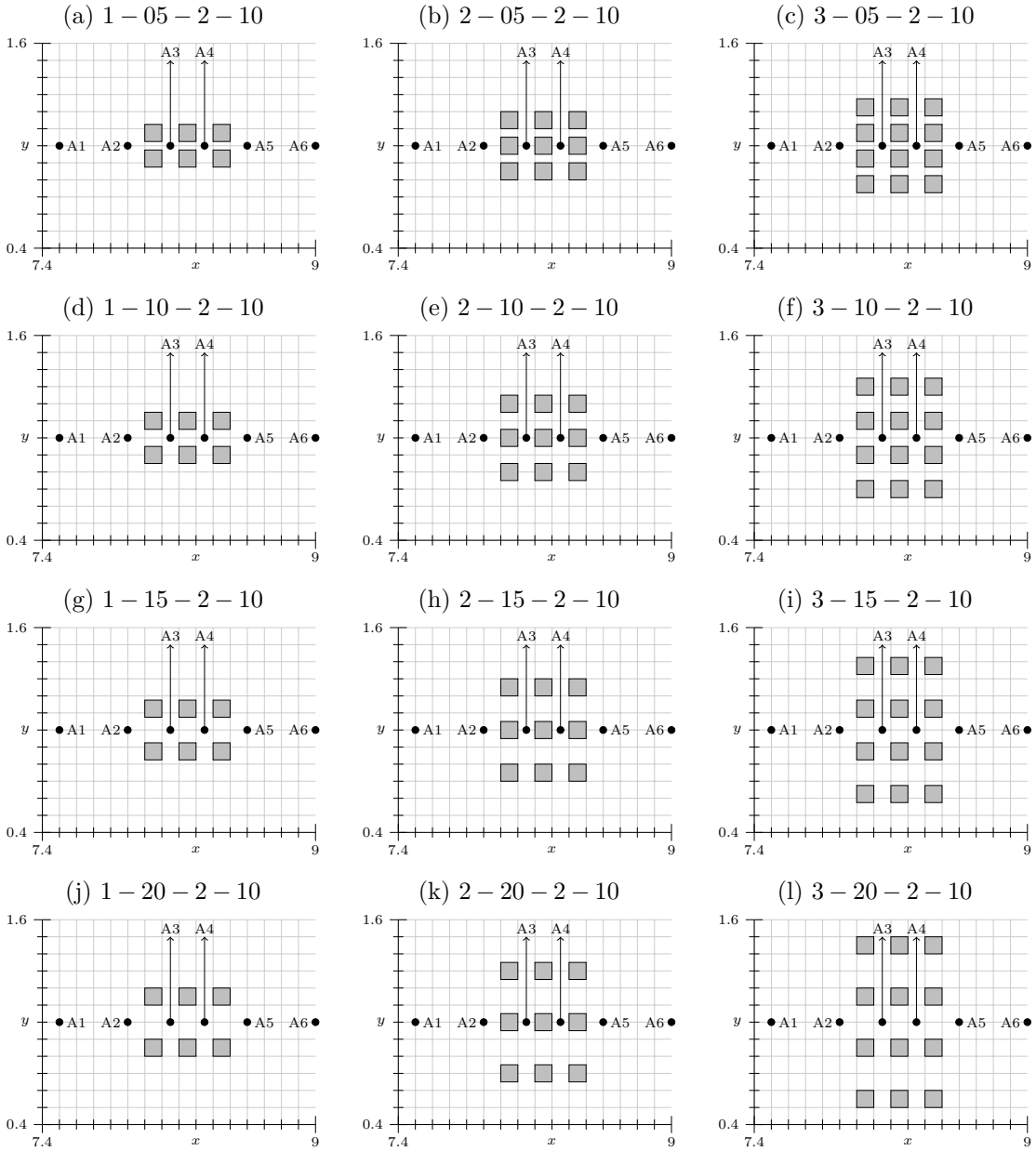

Figure 6.8: Top view of the twelve configurations $n_x - l_x - n_y - l_y$ with three different street number (n_x) and four different street width (l_x).

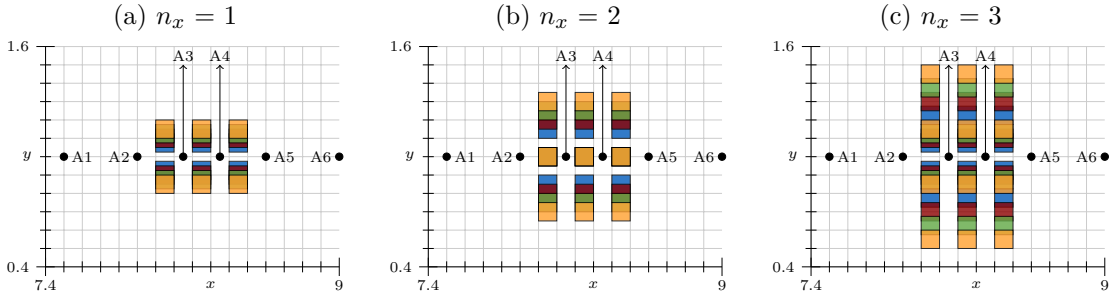

Figure 6.9: Superposition of cases (a) $n_x = 1$, (b) $n_x = 2$ and (c) $n_x = 3$ for all street width l_x.

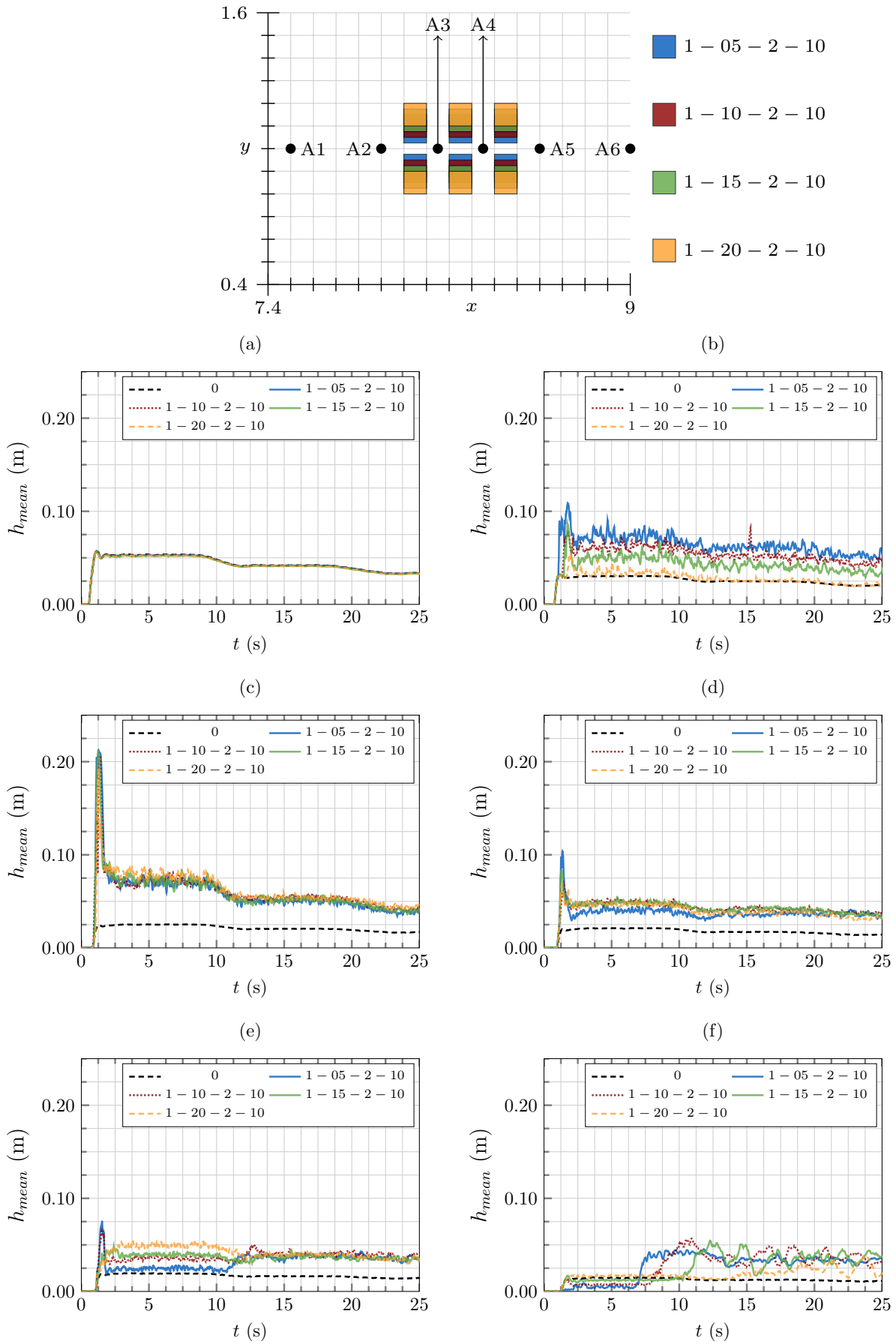

Figure 6.10: Effect of street width l_x on water depth variations for cases with $n_x = 1$ at positions (a) A1, (b) A2, (c) A3, (d) A4, (e) A5 and (f) A6.

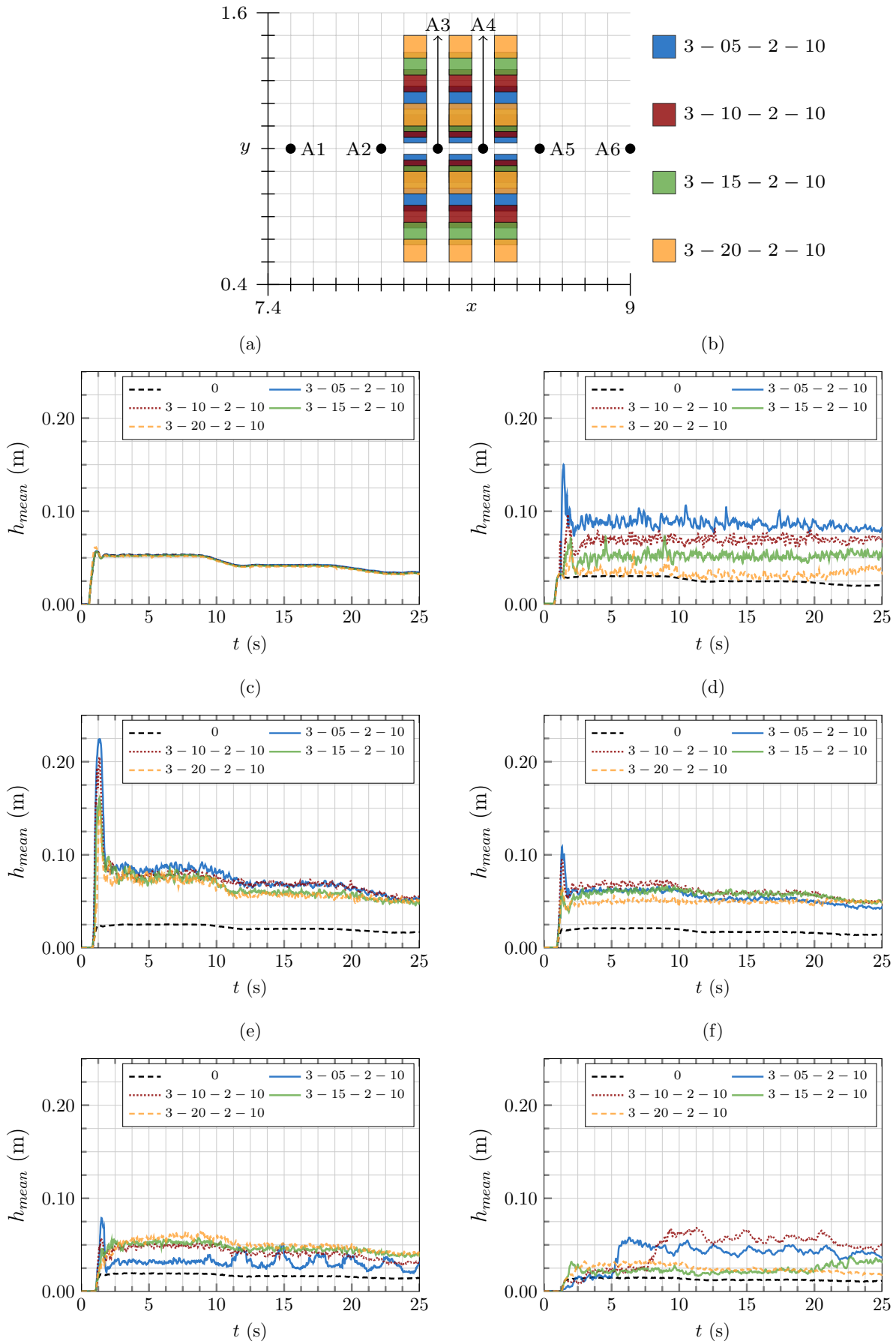

Figure 6.11: Effect of street width l_x on water depth variations for cases with $n_x = 3$ at positions (a) A1, (b) A2, (c) A3, (d) A4, (e) A5 and (f) A6.

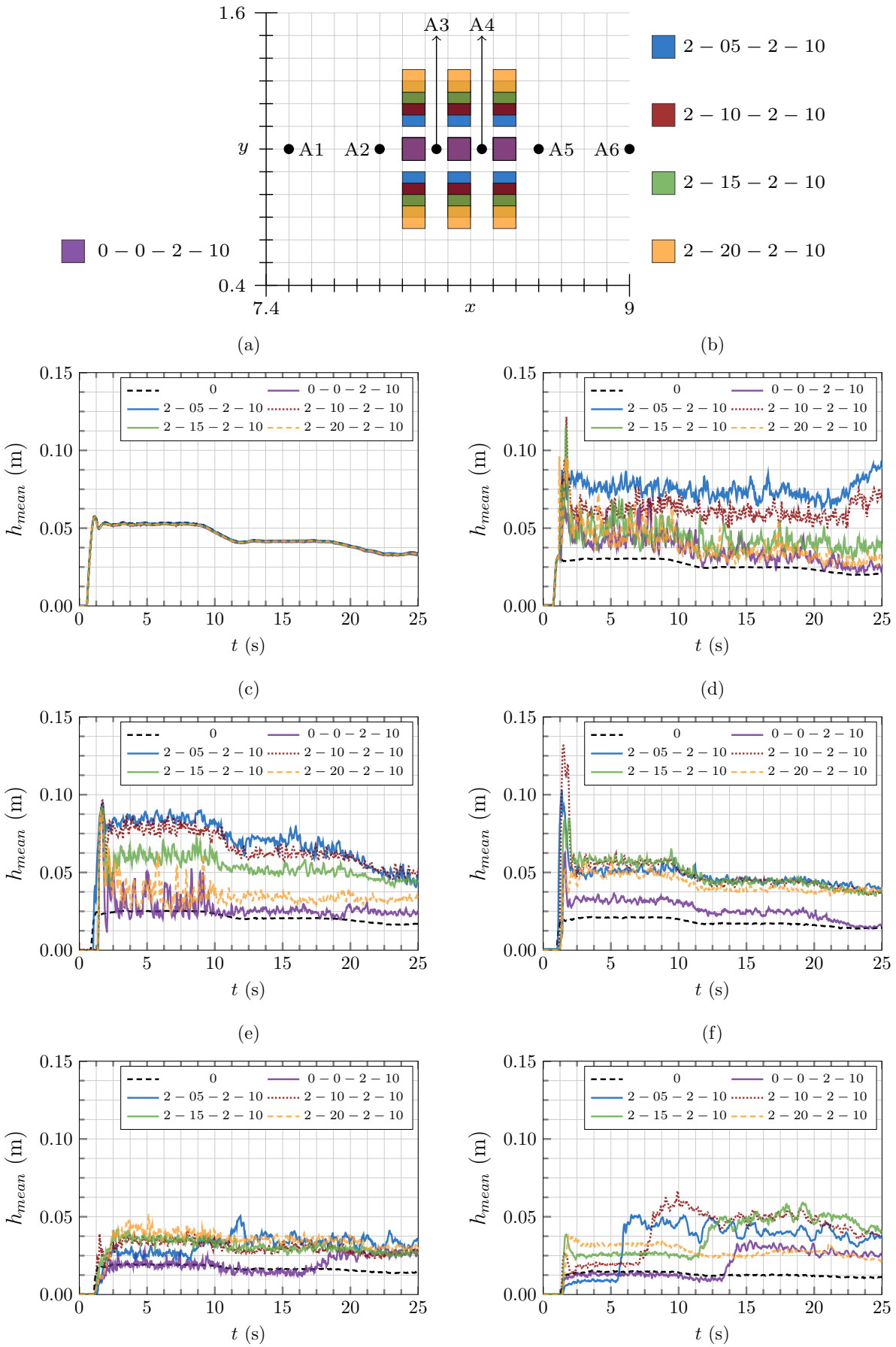

Figure 6.12: Effect of street width l_x on water depth variations for cases with $n_x = 0$ and 2 at positions (a) A1, (b) A2, (c) A3, (d) A4, (e) A5 and (f) A6.

For cases with $n_x = 1$ (Figure 6.10), the sensors are placed in the centre of the longitudinal street with two rows of obstacles on each sides. The results illustrate a correlation between the water depth in the splash-up area and the street width (Figure 6.10b). Indeed, for wider streets, the water depth tends towards case 0, while it is higher for narrower streets. Inside the urban area, no significant impact on the water depth is observed (Figures 6.10c and 6.10d).

On the other hand, narrower streets lead to lower water depth downstream of the urban area (Figure 6.10e). From $t = 12$ s to the end of the acquisition, all street widths have a similar water depth at position A5. While for probes A2 to A5, the presence of urban forms always generates higher water depths related to case 0, probe A6 presents lower height values as the streets become narrower, up to a certain time (Figure 6.10f). Then, the A6 water depth increases and the narrower the street, the earlier this phenomenon appears.

Figure 6.11 shows the water depth evolution along the central street for cases with $n_x = 3$. The same behaviour as for cases with $n_x = 1$ are observed, except that oscillations appear behind the urban area, at position A5, for the narrower street case (Figure 6.11e). Moreover, the water depth for wider streets tends toward case 0 at position A6 and remains constant over time (Figure 6.11f).

The tendencies observed for cases $n_x = 1$ and 3 (Figures 6.10 and 6.11) suggest that smaller streets create a blockage effect on the flow, leading to higher water depth upstream of the urban configurations. Downstream of the urban areas, a hydraulic jump marked by a sudden rise in water depth occurs for some of the configurations studied. The lateral size of the urban form (L_y) and the street width (l_x) influence the appearance of this hydraulic jump and the presence of oscillation waves downstream of the urban area.

Note : For narrower streets, the blockage effect is more pronounced, causing a larger amount of water to bypass the urban forms. Further analysis will be conducted in the next chapter to investigate the influence of the side walls on the hydraulic jump.

Additionally, the water depth profile along $y = 0$ for $n_x = 3$ (Figure 6.13) is analysed at different times. Each point corresponds to an acoustic probe position, extending from A1 on the left to A6 on the right. Grey rectangles represent a row of obstacles. Several tendencies can be observed. First, the splash-up zone height upstream of the urban form seems proportional to the street width, where narrower streets correlate with higher water depth (position A2, for all times). Moreover, the water depth profile tends towards a steady state after 10 s. For wide streets ($l_x = [0.10, 0.15, 0.20]$ m), the water depth reaches its maximum value within the urban configuration and then decreases gradually. Conversely, for narrower streets, the water depth peaks upstream of the obstacles, decreases along the urban area and increases again in A6.

Note : Similar water depth profiles at four time steps (c.f. Figure 6.13) for cases $n_x = 1$ and $n_x = 2$ are available in Appendix E.

Figure 6.13 highlights that studying spatial water height profiles is valuable to better understand the local water depth variations measured by the acoustic gauges (Figure 6.11).

Hereafter, the influence of the street width on the flow for cases with $n_x = 2$ is discussed, where probes A3, A4 and A5 are located behind an obstacle. Figure 6.12 presents the water depth variation for cases with $n_x = 0$ and 2. The main additional tendency that can be observed is a correlation between the water depth behind the first obstacle and the longitudinal street width (Figure 6.12c) which does not occurs in the longitudinal streets (Figures 6.10 and 6.11). Indeed, the narrower the longitudinal street, the higher the water depth behind the first obstacle (position A3). This effect disappears downstream at position A4. At position A6, a hydraulic jump is observed; the narrower the streets, the sooner it reaches A6. Case $2-20-2-10$ is the only configuration without the appearance of a hydraulic jump at position A6, while even case $0-0-2-10$, which has no longitudinal street, exhibits one.

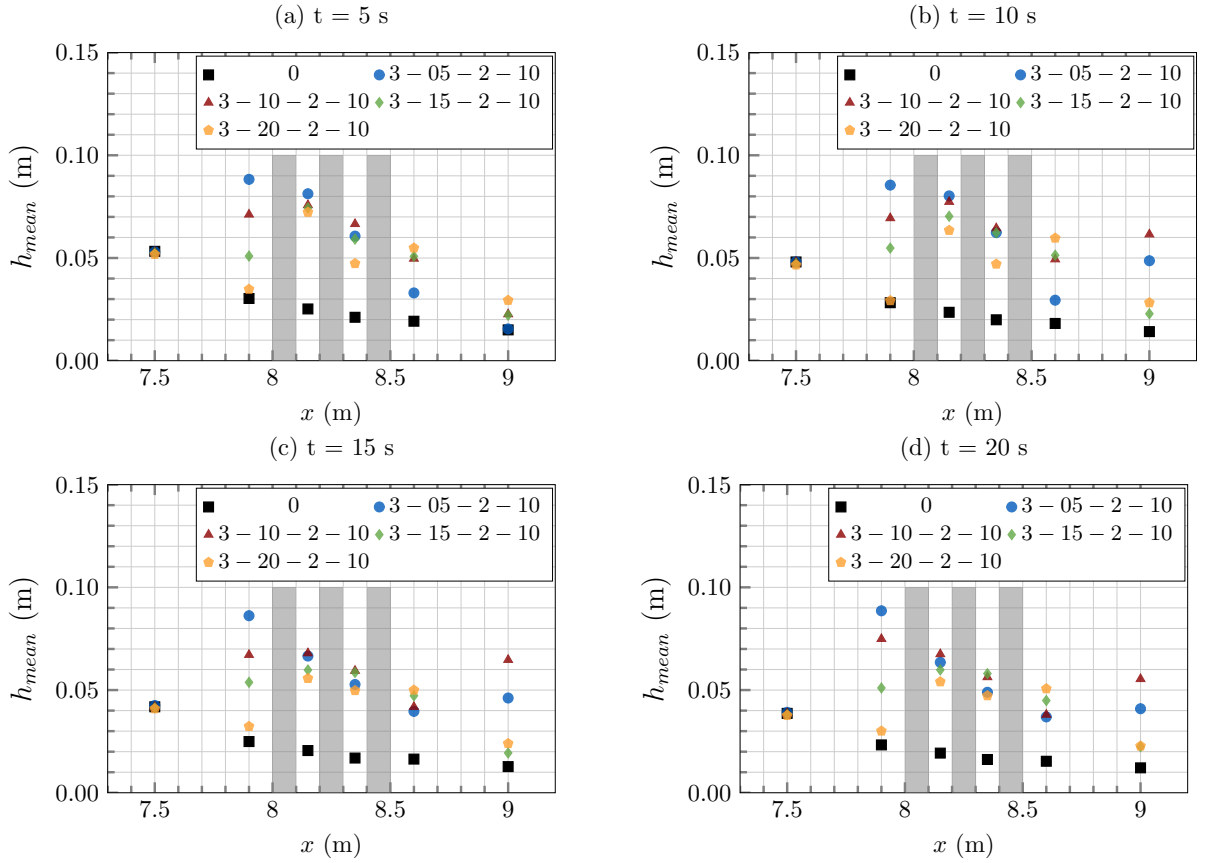

Figure 6.13: Cases $n_x = 3$. Evolution of the water depth profile (y = 0 m) at times (a) t = 5 s, (b) t = 10 s, (c) t = 15 s, and (d) t = 20 s. Grey rectangles represent cubes position.

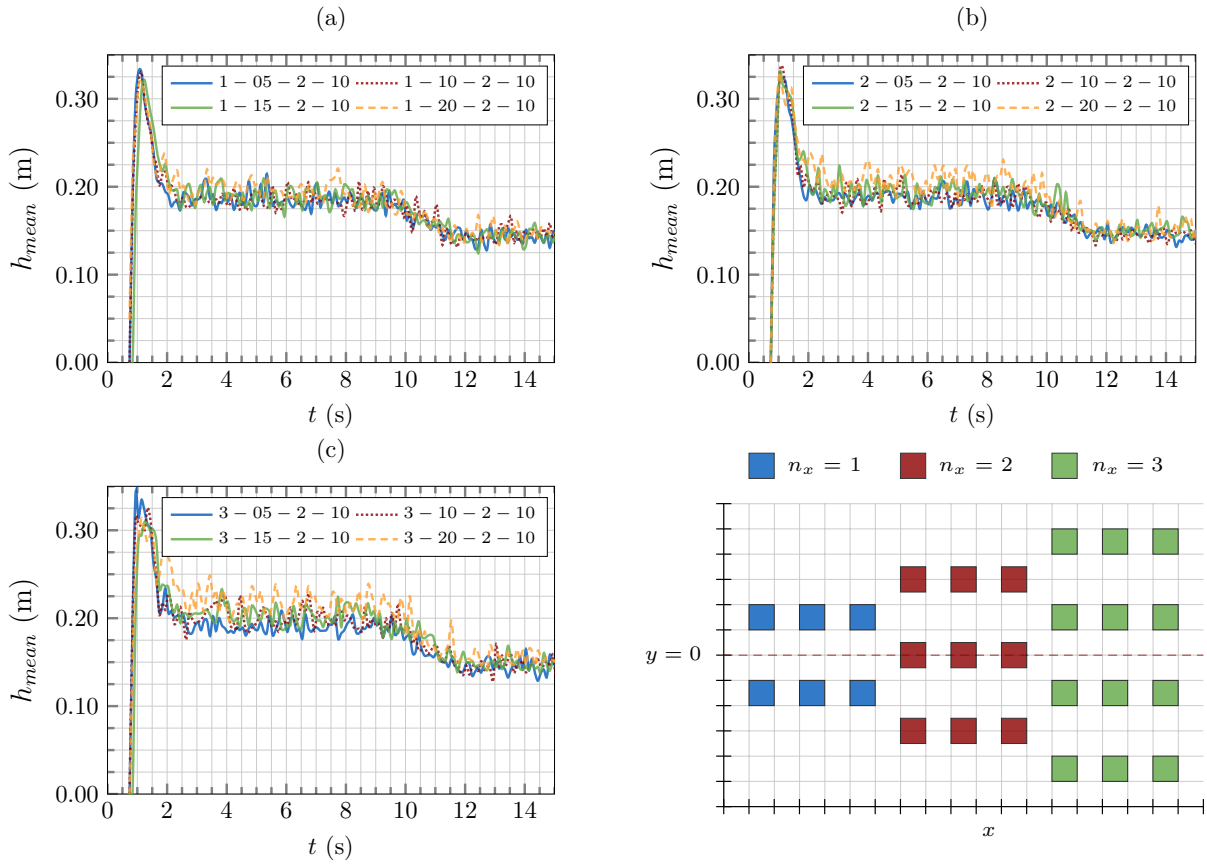

Figure 6.14: Evolution of the water depth at x = 8 and y = -0.05 m from the IAM analysis for cases (a) $n_x = 1$, (b) $n_x = 2$ and (c) $n_x = 3$.

Note : For all cases with $n_x = 0$ and 2, the sensors are placed behind an obstacle rather than along the centre axis of a street, leading to lower heights at all locations compared to other streets number cases.

Acoustic gauge measurements highlighted the influence of street width (l_x) on the water depth at positions A1 and A2, notably on the position of the maximum water depth in the splash-up area.To better quantify this phenomena, an IAM analysis was performed on all cases at x = 8 m (Figure 6.14). Results show that the street width has a low impact on the water depth near the obstacles. The maximum water depth for all cases reaches 0.33 m at t = 1 s, and then the water depth evolves similarly for all cases.

Figure 6.15 shows snapshots at t = 8 s from the IAM camera for all street width cases with $n_x = 2$. Images suggest that the maximum water depth is slightly different between narrow and wide streets, with a maximum water depth for the case with the largest street width. A profile analysis is performed (see Appendix C for more information), consisting of performing ROI detection on a single image and shifting the ROI from its initial position to the end of the image (i.e., the ROI is a vertical line of pixels that shifts to each row of pixels from its initial position to the end of the image). For this analysis, the ROI was placed at x = 8.1 m. The IAM profile process is illustrated in Figure 6.16 on a binary image of case $2-05-2-10$ (Figure 6.15a).

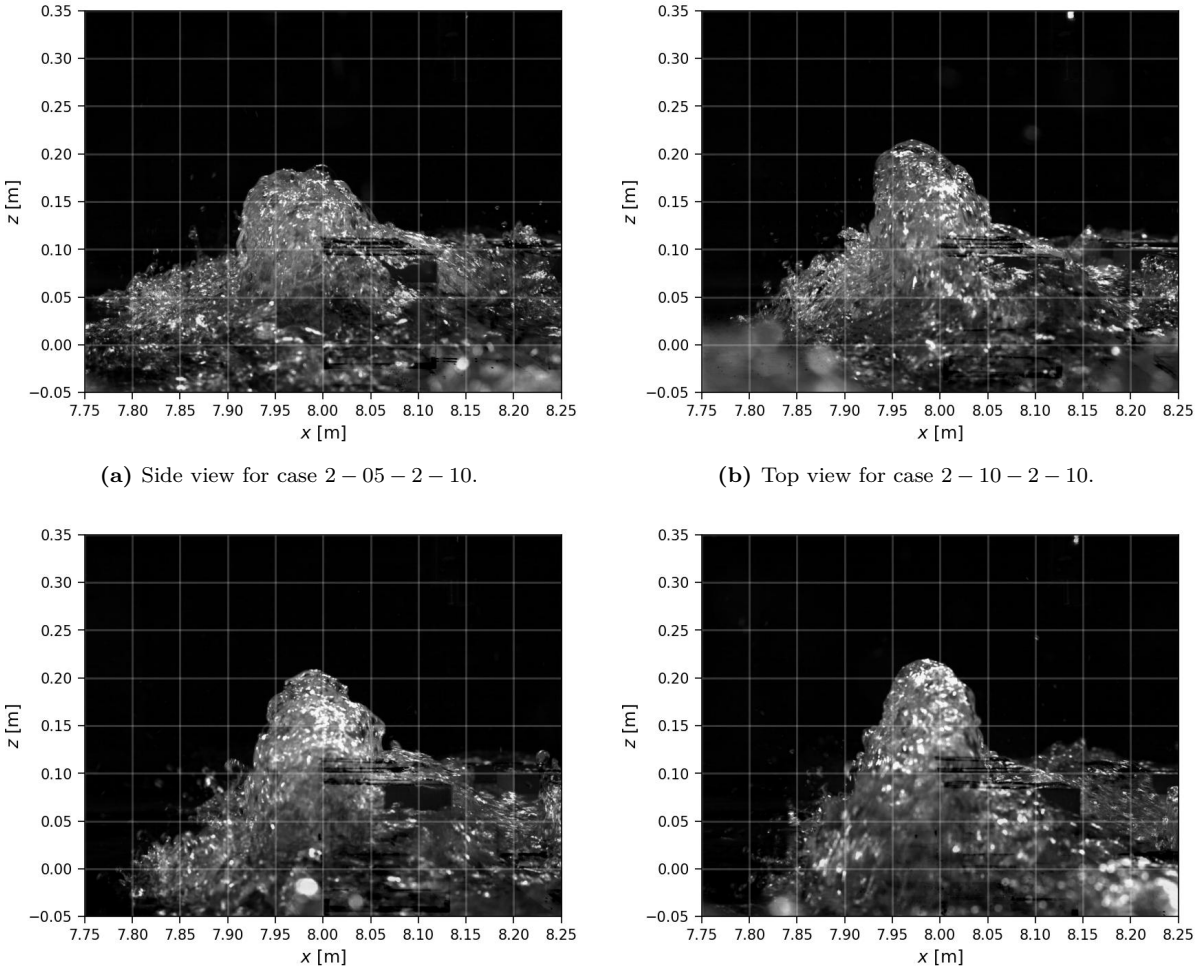

(a) Side view for case $2-05-2-10$.

(b) Top view for case $2-10-2-10$.

(c) Side view for case $2-15-2-10$.

(d) Top view for case $2-20-2-10$.

Figure 6.15: Snapshots from the IAM camera of the splash-up for cases $n_x = 2$ and $l_x = [0.05, 0.20]$ m at $t =$ 8 s.

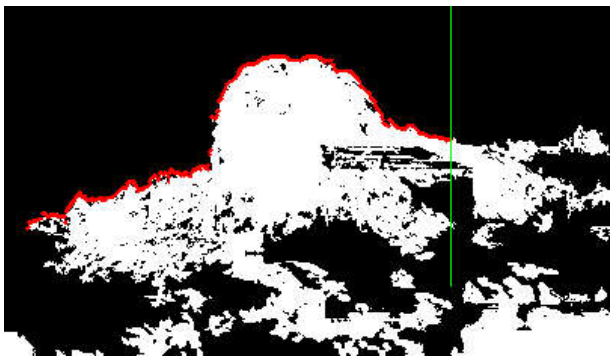

Figure 6.16: Zoomed view of the binarized image during IAM profile detection of image from Figure 6.15a. Green line represents the initial ROI position at x = 8.1 m. Red points represent the free surface position detected for each ROI position.

Figure 6.17 presents the splash-up profiles for all $n_x = 2$ cases. It is observed that wider streets lead to thinner splash-up area. For instance, for case $2-20-2-10$ the splash-up stops at x = 7.85 m, while for case $2-05-2-10$ higher elevation is still observable.

Note : The exact water depth far from the maximum splash-up height (from x = 7.8 m to x = 7.9 m) is difficult to measure due to the depth of field and water transparency. Consequently, cases with thinner splash-up may present water heights close to zero (the transparent water located upstream of the splash-up zone is not visible in the images). The resulting profiles refer to free surface elevations from $z = 0$ the base of the obstacle and do not represent the exact free surface height. Still, this type of analysis allows for the comparison of the splash-up shape for different street widths.

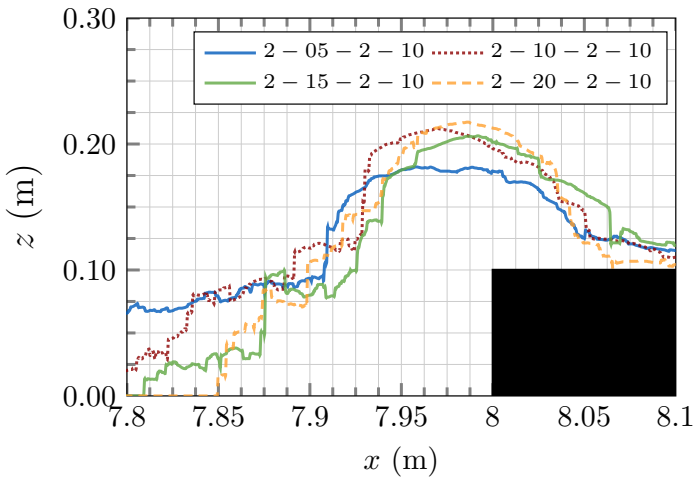

Figure 6.17: Water depth profiles for cases $n_x = 2$ at t = 8s from the IAM analysis of images in Figure 6.15. Black surface represent the cube position.

The free surface velocity field at three different time steps is illustrated in Figures 6.19, 6.20 and 6.21 for cases with $n_x = 1$, 2, and 3, respectively. Black rectangles represent the positions of the cubes. Each figure column corresponds to a given acquisition time. The colour map represents the norm of the horizontal free-surface velocity and the vector field is normalised. Overall, all the macro phenomena observed in the previous experimental campaign are present in all cases. The reflection, splash-up, and wake zone can be identified, along with a hydraulic jump (indicated by a low-velocity zone) downstream of the obstacles for some configurations. The influence of the side walls is clearly visible, and regardless of the urban forms, the shape of the reflection zone tightens over time (Figure 6.18). Additionally, the refined area in the central zone represents the future position of the urban areas, ensuring sufficient information in narrow streets while maintaining similar grid point positions across all studied cases for comparison purposes.

First, all velocity fields share similar features, such as the presence of the reflection zone, which is located in most cases in the upstream right corner of the measured area. The splash-up zone is also visible upstream of the different urban forms, where the dam-break wave is redirected vertically with low velocity values. Then, a wake zone, where the position, size, and intensity are directly controlled by the urban parameters, also appears downstream of the urban forms. In some cases, a hydraulic jump with lower velocity magnitude and higher water depth appears in the wake zone and develops until it reaches the last row of obstacles. Finally, a complex flow path within the obstacle configuration, sometimes interacting with the reflection area is visible.

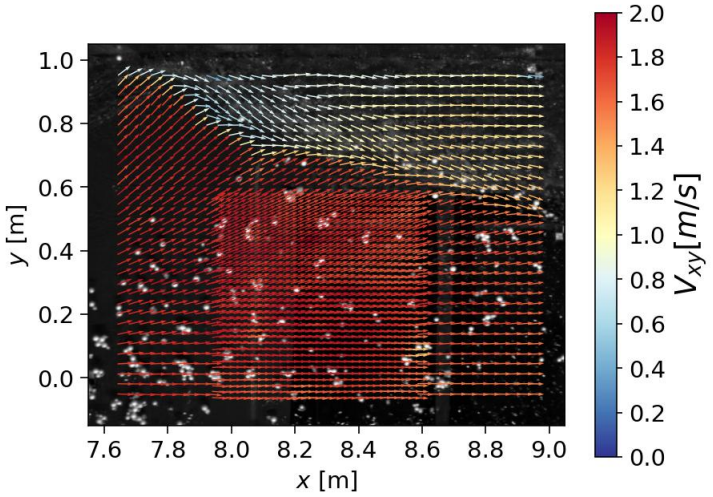

(a) t_{avg} = 6, 6.1 s.

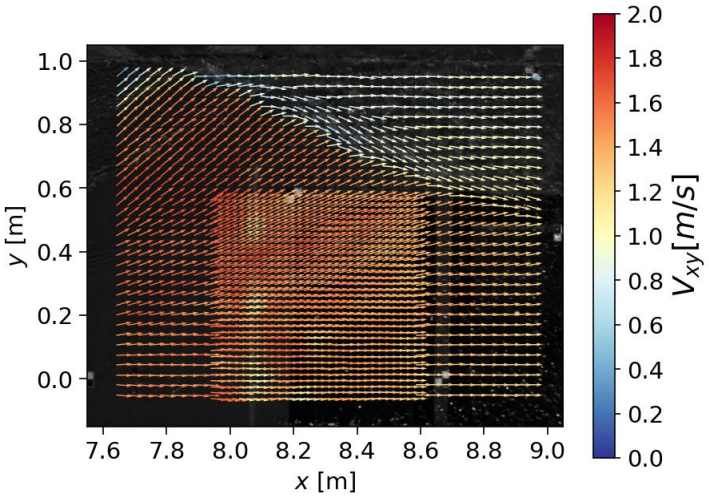

(b) t_{avg} = 16, 16.1 s.

Figure 6.18: Illustration of the reflection zone evolution and side walls influence for case 0 at 2 different times. LSPIV vectors are superposed to background LSPIV camera images.

However, differences within those zones can be discussed, notably with the variation of the number of streets. First, the obstacles blockage effect impacts the splash-up zone size and intensity upstream of the urban form. The flow completely diverts the reflection zone for a higher lateral urban size ($n_x = 3$, Figure 6.21). Moreover, for all cases, configurations with $l_x = 0.05$ or 0.1 m exhibit lower velocity values in the central street, resulting in less flow in the the wake zone. In that cases, the velocity magnitude in the street is not sufficient to prevent an hydraulic jump to reach the urban area (Figures 6.19b and e). Its development process is visible at $x = [8.8, 9]$ m in Figure 6.22.

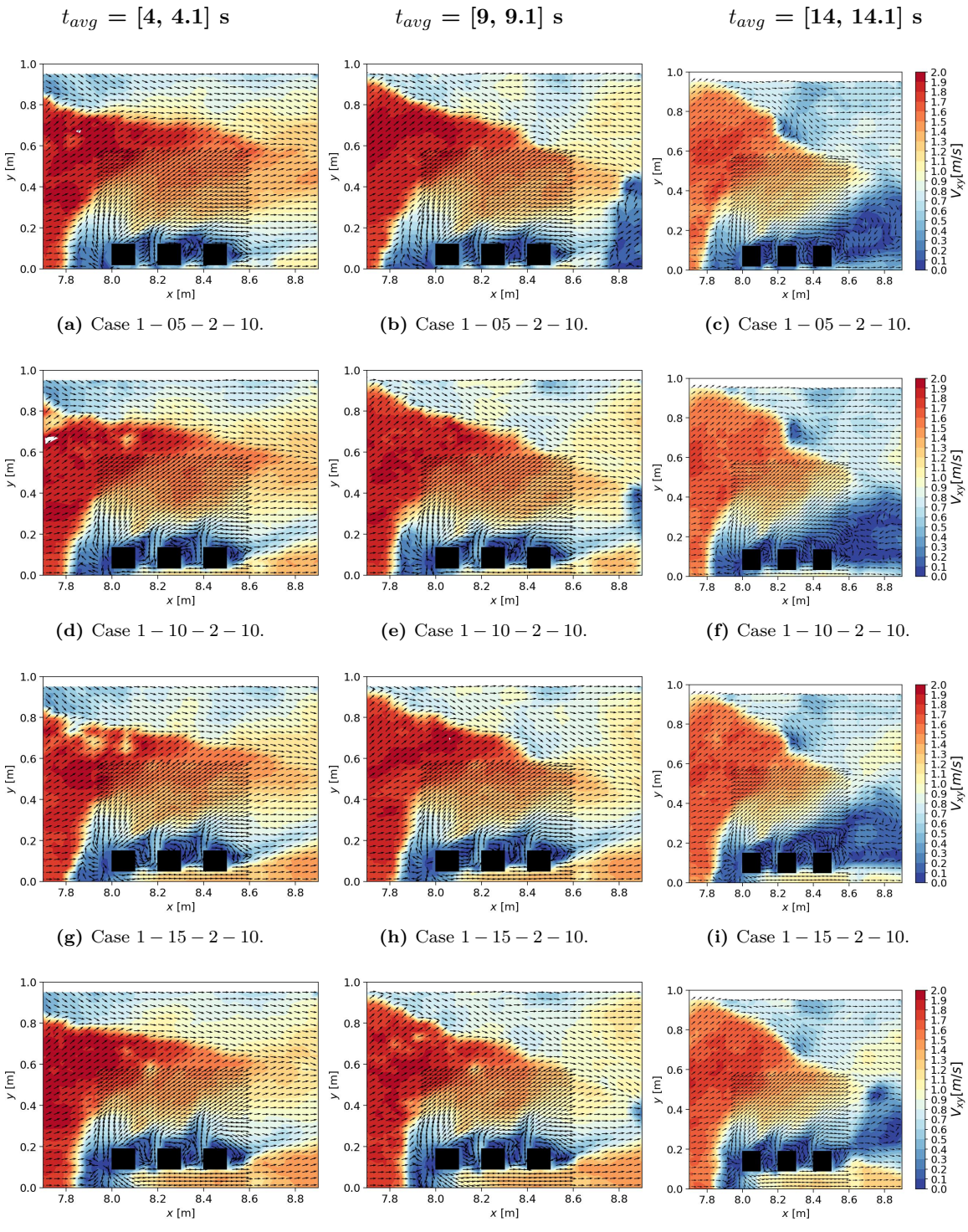

(a) Case $1-05-2-10$. **(b)** Case $1-05-2-10$. **(c)** Case $1-05-2-10$.

(d) Case $1-10-2-10$. **(e)** Case $1-10-2-10$. **(f)** Case $1-10-2-10$.

(g) Case $1-15-2-10$. **(h)** Case $1-15-2-10$. **(i)** Case $1-15-2-10$.

(j) Case $1-20-2-10$. **(k)** Case $1-20-2-10$. **(l)** Case $1-20-2-10$.

Figure 6.19: Free surface velocity variation for cases $n_x = 1$ at 3 different time step. Black surfaces illustrate the obstacles position.

t_{avg} = **[4, 4.1] s** t_{avg} = **[9, 9.1] s** t_{avg} = **[14, 14.1] s**

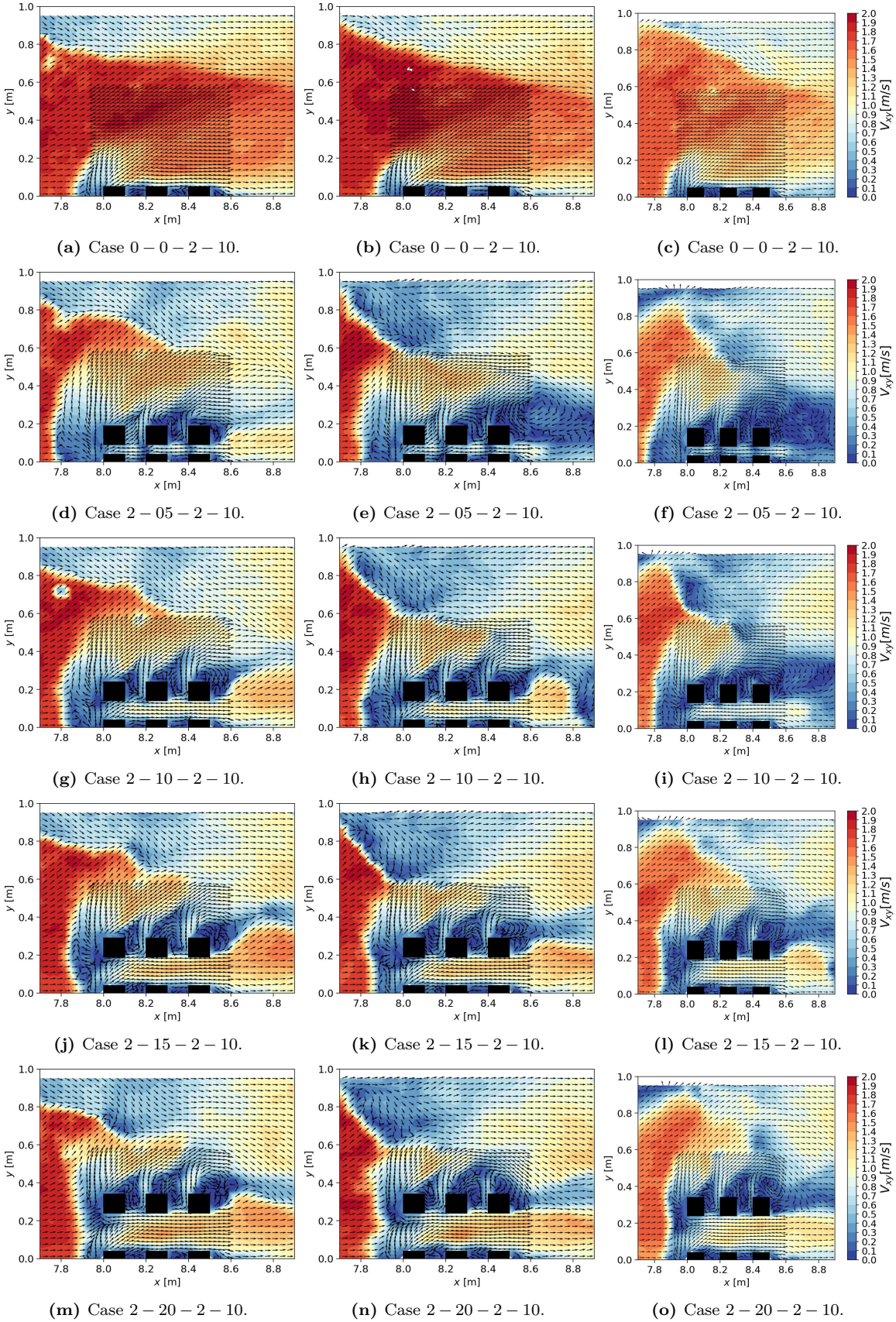

(a) Case $0-0-2-10$. **(b)** Case $0-0-2-10$. **(c)** Case $0-0-2-10$.

(d) Case $2-05-2-10$. **(e)** Case $2-05-2-10$. **(f)** Case $2-05-2-10$.

(g) Case $2-10-2-10$. **(h)** Case $2-10-2-10$. **(i)** Case $2-10-2-10$.

(j) Case $2-15-2-10$. **(k)** Case $2-15-2-10$. **(l)** Case $2-15-2-10$.

(m) Case $2-20-2-10$. **(n)** Case $2-20-2-10$. **(o)** Case $2-20-2-10$.

Figure 6.20: Free surface velocity variation for cases $n_x = 0$ and 2 at 3 different time step. Black surfaces illustrate the obstacles position.

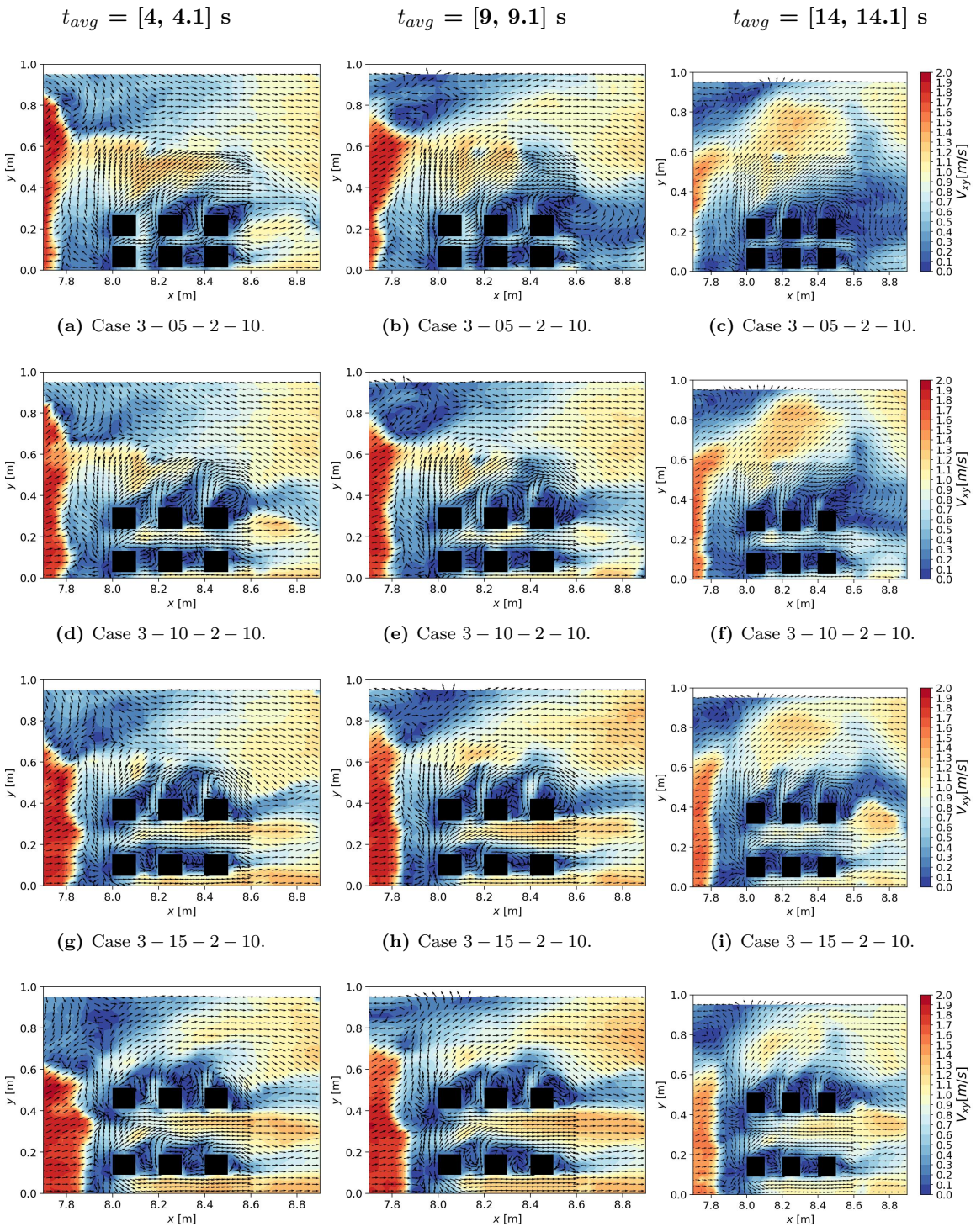

(a) Case $3-05-2-10$. **(b)** Case $3-05-2-10$. **(c)** Case $3-05-2-10$.

(d) Case $3-10-2-10$. **(e)** Case $3-10-2-10$. **(f)** Case $3-10-2-10$.

(g) Case $3-15-2-10$. **(h)** Case $3-15-2-10$. **(i)** Case $3-15-2-10$.

(j) Case $3-20-2-10$. **(k)** Case $3-20-2-10$. **(l)** Case $3-20-2-10$.

Figure 6.21: Free surface velocity variation for cases $n_x = 3$ at 3 different time step. Black surfaces illustrate the obstacles position.

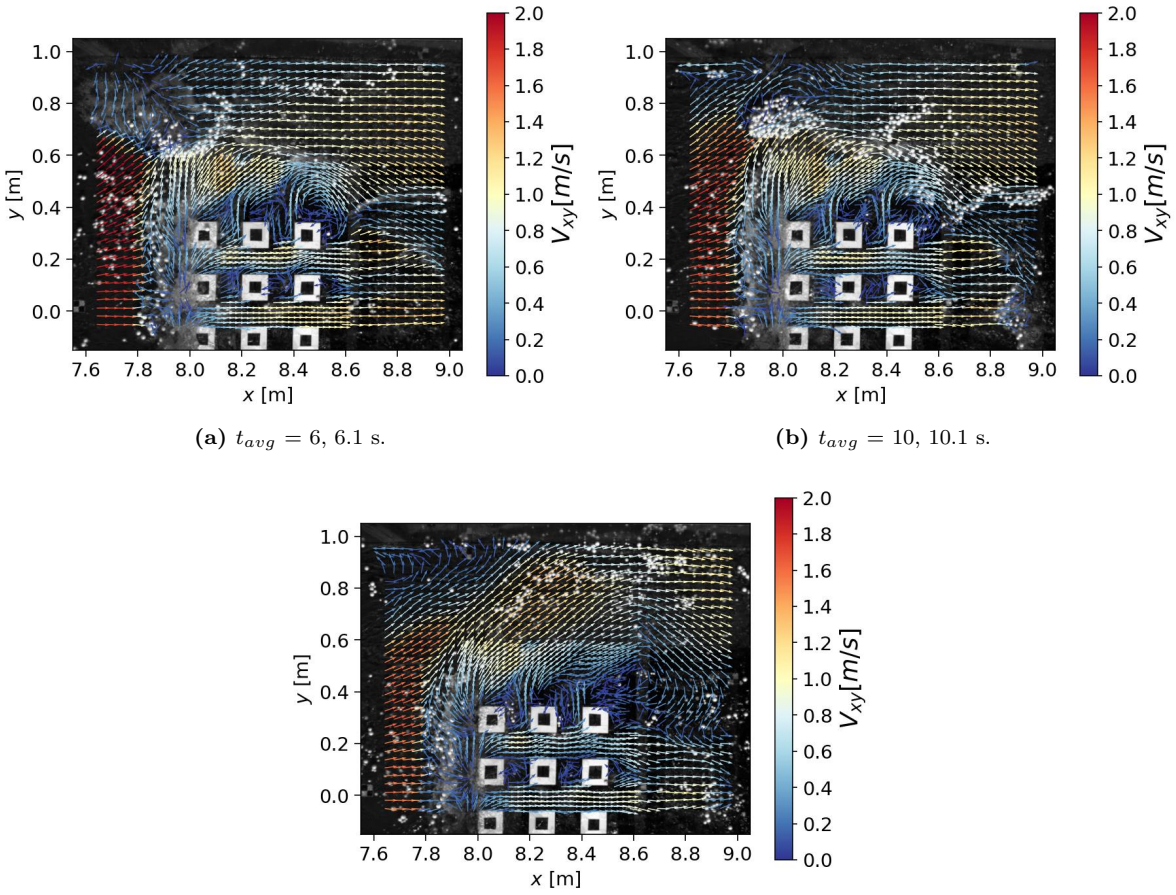

(a) $t_{avg} = 6$, 6.1 s.

(b) $t_{avg} = 10$, 10.1 s.

(c) $t_{avg} = 14$, 14.1 s.

Figure 6.22: Illustration of the hydraulic jump development, visible at $x = [8.8, 9]$ m, for case $3 - 10 - 2 - 10$ at 3 different time step. LSPIV vectors are superposed to background images corresponding from the LSPIV camera at the first time step of the averaged time.

Next, the velocity of the free surface is extracted punctually from the LSPIV analysis at the different probes locations (Figures 6.23 and 6.24). Values are averaged over 0.02 seconds (5 images), corresponding to the acquisition frequency of the water depth probes.

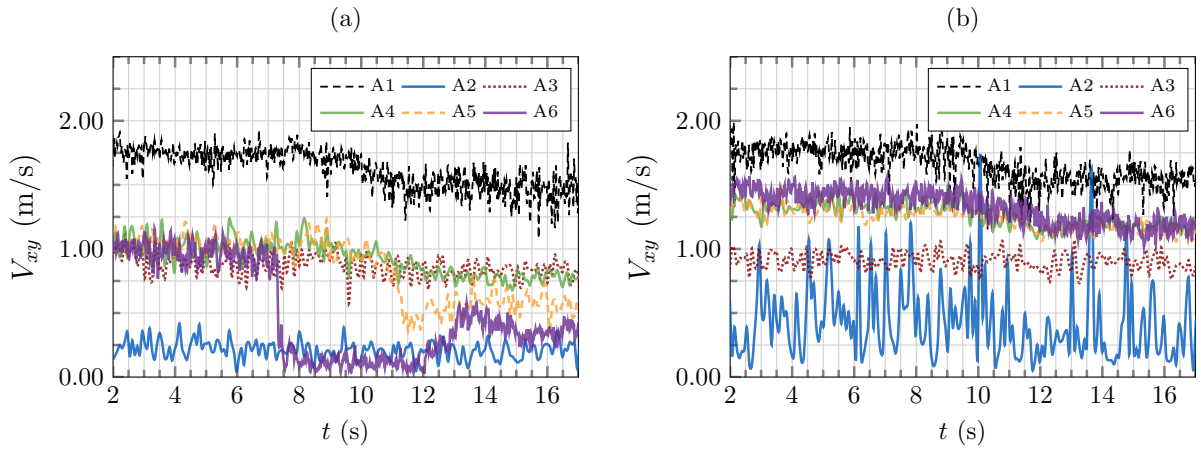

Figure 6.23: Horizontal velocity retrieved from LSPIV at positions A1, A2, A3, A4, A5 and A6 for cases (a) $1 - 05 - 2 - 10$ and (b) $1 - 20 - 2 - 10$.

Overall, the evolution of the free surface velocity for all cases shows a deceleration of the flow between the upstream and downstream positions of the urban areas. The free surface velocity at position A1 is very similar across all cases, confirming that the presence of obstacles do not impact its area. The velocity through the central street is uniform from position A3 to position A6, except for wider streets,

where a deceleration is observed at position A3 (the beginning of the street) and then accelerates. Wider streets also lead to an accelerated flow at the configuration outlet (A6) compared to narrow cases. Finally, the presence of a hydraulic jump is measured at A6 for narrower streets, leading sometimes to velocity oscillations (Figure 6.24a).

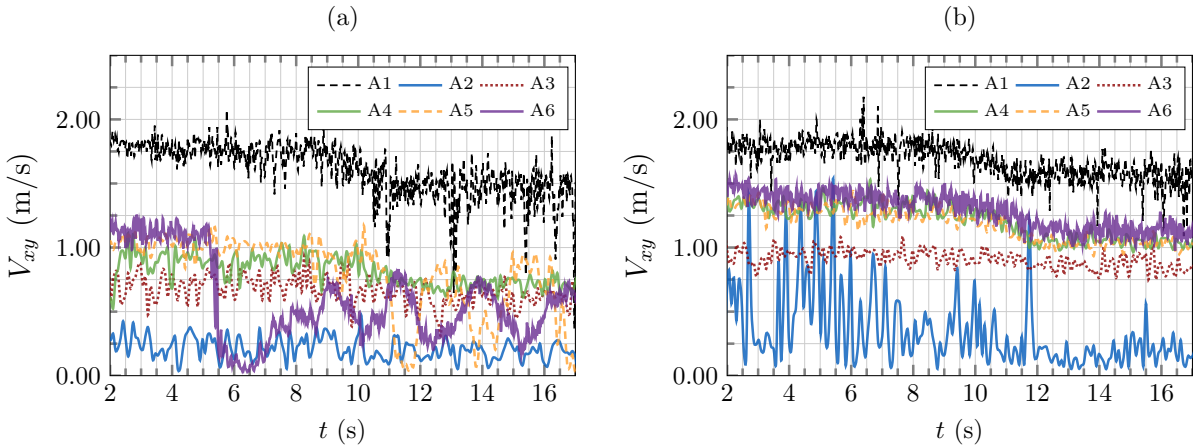

Figure 6.24: Horizontal velocity retrieved from LSPIV at positions A1, A2, A3, A4, A5 and A6 for cases (a) $3-05-2-10$ and (b) $3-20-2-10$.

To better quantify the obstacles impact on the observed flow, the energy head is studied downstream of the urban area. It is defined as

$$E = \frac{V_{xy}^2}{2 \times g} + h. \tag{6.1}$$

V_{xy} $[m/s]$ is the free surface velocity extracted from the LSPIV analysis and averaged over t = 0.02 s, g = 9.81 $[m/s^2]$ is the gravitational acceleration and h $[m]$ the water depth. This quantity is often used in simplified models to compute head losses.

Note : Since the velocity field is averaged here over t_{avg} = 0.02 s (5 instantaneous velocity fields), the resulting energy head for a water column is a time averaged quantity.

The experimental energy head for case 0 (dam-break flow with no obstacles) is illustrated in Figure 6.25 for all probe positions. Measurements show its decrease along the x-axis and also as time passes, which is an expected result in presence of dissipation and variations of the flow rate though the gate.

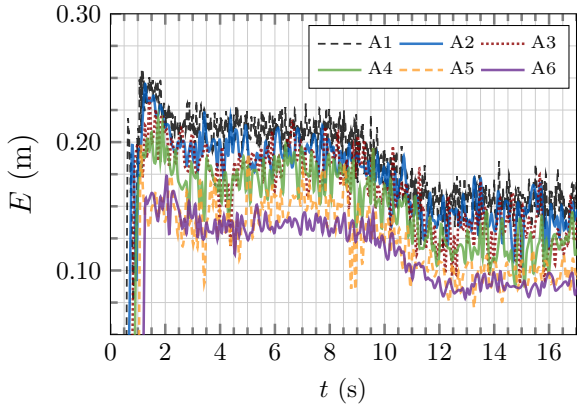

Figure 6.25: Energy head evolution for case 0 at positions A1, A2, A3, A4 , A5 and A6.

Adding obstacles seem not to impact the energy head at position A1 (Figure 6.26). Therefore, to assess the impact of obstacles on the flow, the variation of energy head will be studied only downstream of the urban areas. Variables h', V'_{xy} and E' refer to $\frac{h_{n_x-l_x-n_y-l_y}}{h_0}$, $\frac{V_{xy(n_x-l_x-n_y-l_y)}}{V_{xy(0)}}$ and $\frac{E_{n_x-l_x-n_y-l_y}}{E_0}$, respectively.

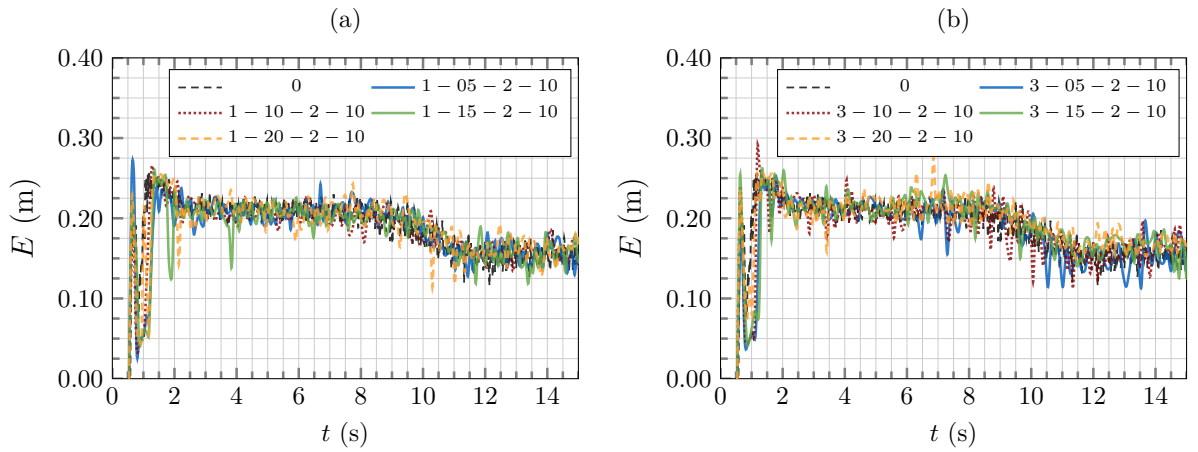

Figure 6.26: Energy head evolution at position A1 for cases (a) $n_x = 1$ and (b) $n_x = 3$.

The ratio between the energy head (E' [-]) at position A6 of all studied cases and case 0 is represented in Figure 6.27.

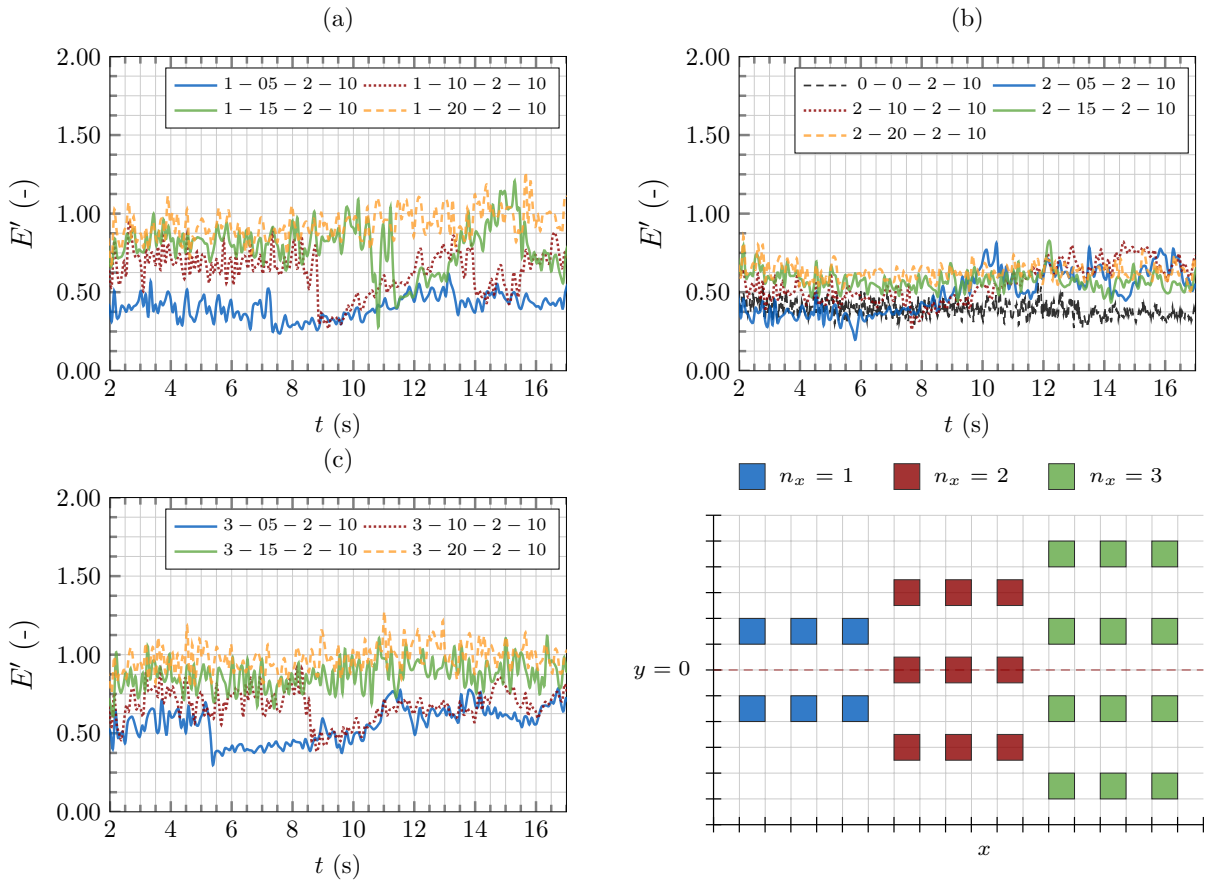

Figure 6.27: Relative urban areas impact for the energy head E' at position A6 related to case 0 for cases (a) $n_x = 1$, (b) $n_x = 2$ and (c) $n_x = 3$.

Results suggest that the variation in energy head is more impacted by the width of the streets when the sensor is located in the centre of an axial street ($n_x = 1$ and 3) rather than when it is aligned with obstacles (cases with $n_x = 2$).

For cases with $n_x = 1$ and 3, the energy head is attenuated by 50% for narrower streets, while no significant attenuation is observed for cases with wider streets. Conversely, for cases with $n_x = 2$, the energy head is attenuated by 50% for all cases and remains constant over time. This attenuation can be explained by the position of sensor A6 behind an obstacle.

Note : The effect of the hydraulic jump on the energy head (for example, case $1-10-2-10$) is not negligible, as variations are observed. To further analyse this phenomenon, 3D numerical simulations could be useful, providing qualitative views of the hydraulic jump arrival.

To better understand the energy head variation across the different configurations, one may represent the relative water depth (h' [-]) and free surface velocity (V' [-]) at the position A6,

$$h' = \frac{h_{n_x - l_x - n_y - l_y}}{h_0}, V' = \frac{V_{xy(n_x - l_x - n_y - l_y)}}{V_{xy(0)}}, \tag{6.2}$$

related to case 0. Results presented in Figures 6.28, 6.29 and 6.30 show that wider streets ($l_x = 0.2$ m) prevented the hydraulic jump from reaching position A6 during the acquisition time. In those cases, the water depth and the horizontal velocity present few variation in time.

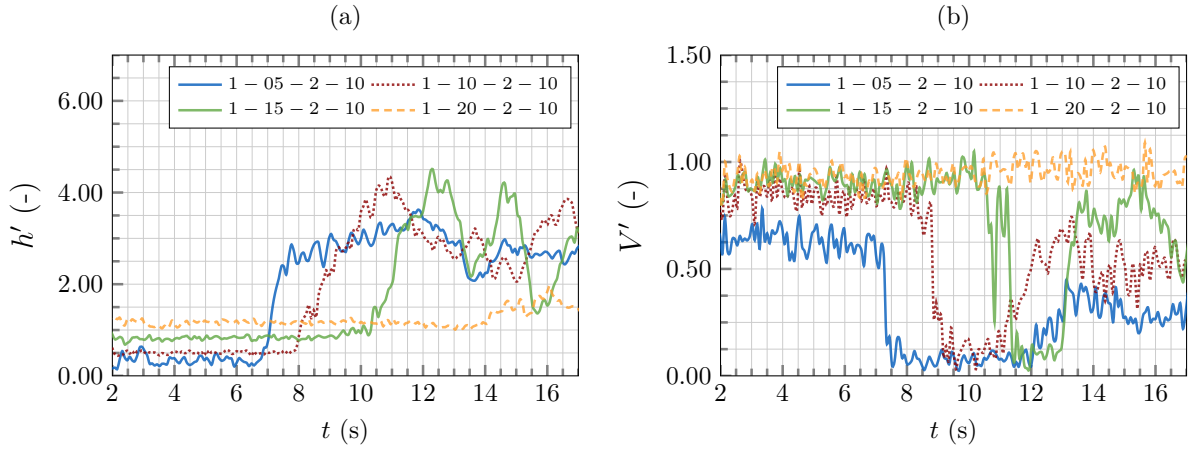

Figure 6.28: Cases $n_x = 1$. Relative urban areas impact for (a) the water depth h' and (b) the free surface velocity V' at position A6 related to case 0.

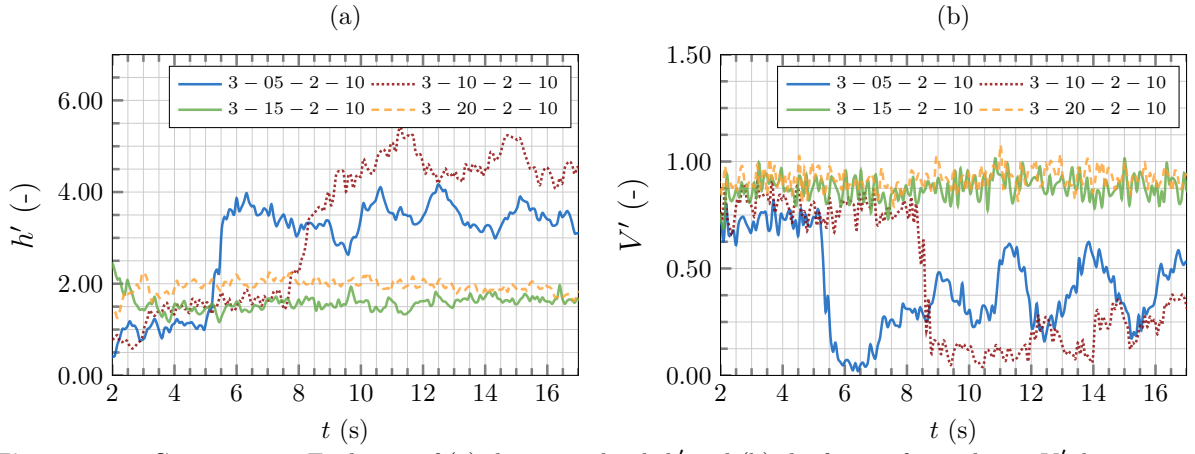

Figure 6.29: Cases $n_x = 3$. Evolution of (a) the water depth h' and (b) the free surface velocity V' downstream of the urban area at position A6.

Additionally, the velocity is reduced by almost 2 when A6 is located behind an obstacle (cases $n_x = 2$). For all cases (except for $l_x = 0.20m$), the narrower the street, the sooner the hydraulic jump arrives at position A6, resulting in an increase in water depth and a decrease in velocity magnitude.

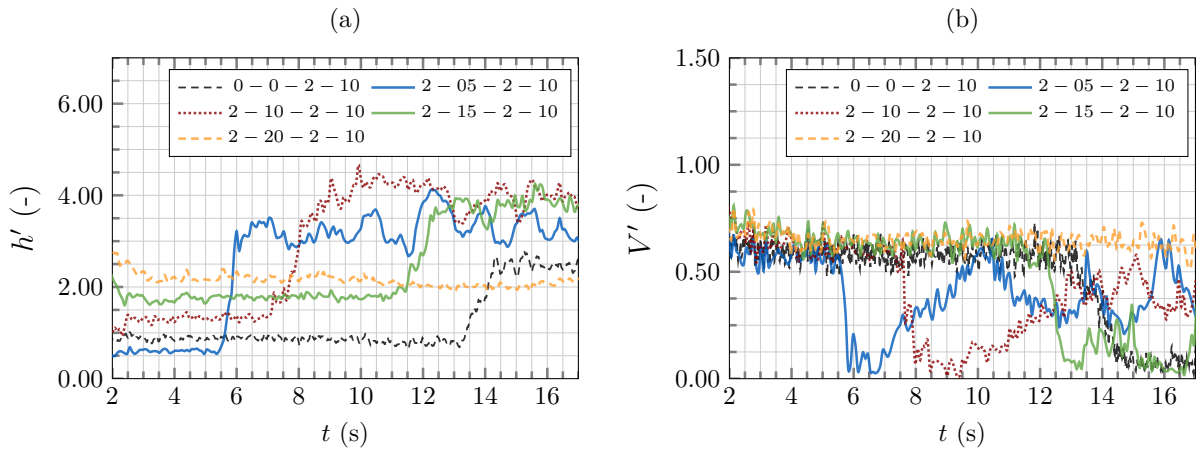

Figure 6.30: Cases $n_x = 2$. Relative urban areas impact for (a) the water depth h' and (b) the free surface velocity V' at position A6 related to case 0.

To complete the last observations, Table 6.7 provides the hydraulic jump arrival time for all cases. Note that no simple relation between this time and the street number is found as for narrower streets ($l_x \leq 0.1$ m), a higher number of streets reduces the arrival, but for wider streets ($l_x \geq 0.15$ m) the opposite is found. The link between the hydraulic jump and the side walls of the experimental setup will be studied in the next chapter. The arrival time estimation could be used as a supplementary physical phenomenon to validate the numerical models. Indeed, a good estimation of such a phenomenon, even if it is induced by the setup geometry, ensures the accurate numerical estimation of the flow rate crossing or being deviated by the urban area.

Table 6.7: Arrival time (s) of the wake zone at position A6 for the studied urban parameters ($n_x - l_x - 2 - 10$).

		n_x		
		1	2	3
l_x	05	7.5	6	5.5
	10	8.5	8	8
	15	11	12	20
	20	✗	✗	✗

✗: $t > t_{acq}$

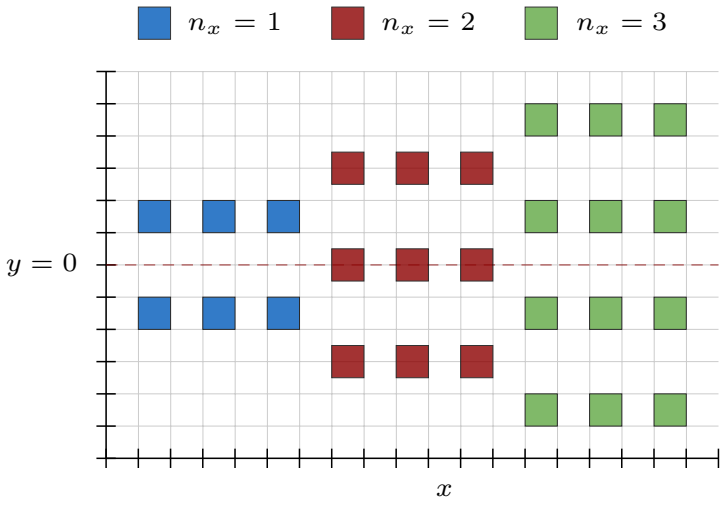

6.5.3 *Longitudinal street number impact (n_x) on the flow*

The previous section demonstrated the influence of street width on the flow both upstream and downstream of the urban area. However, Table 6.7 suggests that the arrival time of the wake zone is also influenced by the number of streets in the main flow direction. Hereafter, the impact of the four street numbers n_x from 0 to 3 on the water height and velocity at position A6 is evaluated (Figure 6.31).

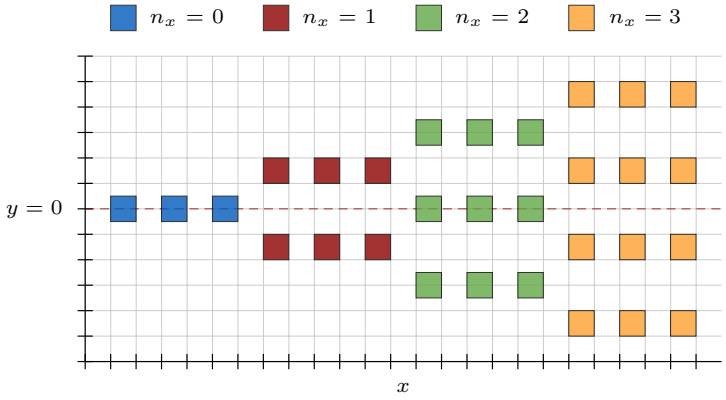

Figure 6.31: Top view of the configurations with $n_x = 0$, 1, 2 and 3 and $l_x = 0.20$ m.

For a given street width (l_x), the number of street (n_x) modifies the lateral urban size (L_y) (see Table 6.8 for a summary of its values).

Table 6.8: Parameter characterising urban forms : the lateral urban size L_y.

L_y		n_x		
		1	2	3
l_x	0.05	0.25	0.40	0.55
	0.10	0.30	0.50	0.70
	0.15	0.35	0.60	0.85
	0.20	0.40	0.70	1.00

First, the impact of the street number on the flow will be studied for two street widths ($l_x = 0.05$ and 0.15 m). Figures 6.32 and 6.33 illustrate the relative water depth (h') and the relative free surface velocity (V') at position A6 related to case 0 for $l_x = 0.05$ m and $l_x = 0.15$ m, respectively.

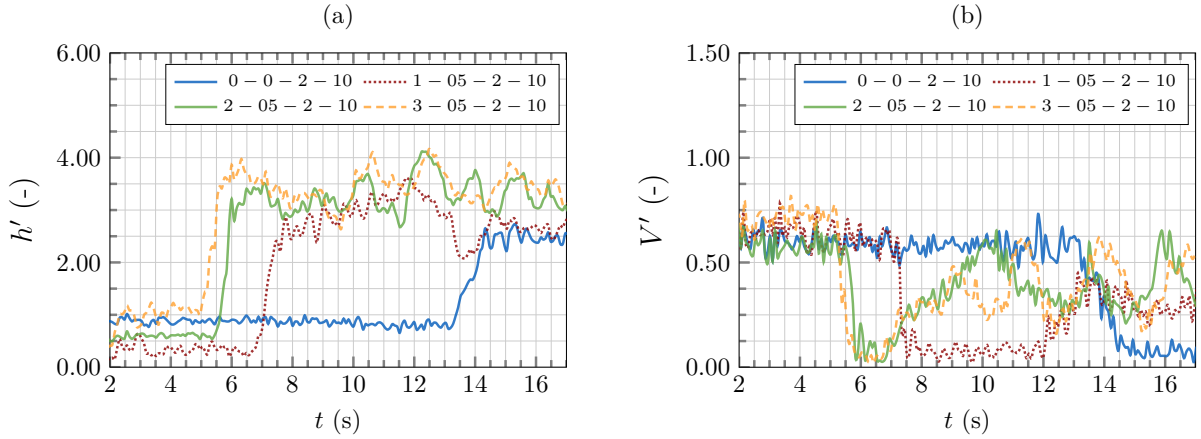

Figure 6.32: Cases $l_x = 0.05$ m. Evolution of (a) the water depth h' and (b) the free surface velocity V' downstream of the urban area at position A6.

As shown in Table 6.7, for narrower streets (Figure 6.32), a higher number of streets leads to an earlier arrival of the hydraulic jump at position A6. On the other hand, the opposite trend is observed for wider streets (Figure 6.33).Additionally, for the case $l_x = 0.05$ m, there seems to be a convergence toward a

minimal time as the number of streets increases (between $t = 4$ and 5 s), which may be related to the blockage effect of wider configurations. Moreover, for narrower streets (Figure 6.32), the water depth and velocity magnitude before the hydraulic jump are independent of the number of streets and their alignment with obstacles or street position. Conversely, for wider streets (Figure 6.33), the alignment of the sensors with the obstacles is visible. For example, the velocity magnitude is offset by 25% between cases $n_x = 1$ and 3 and cases $n_x = 0$ and 2.

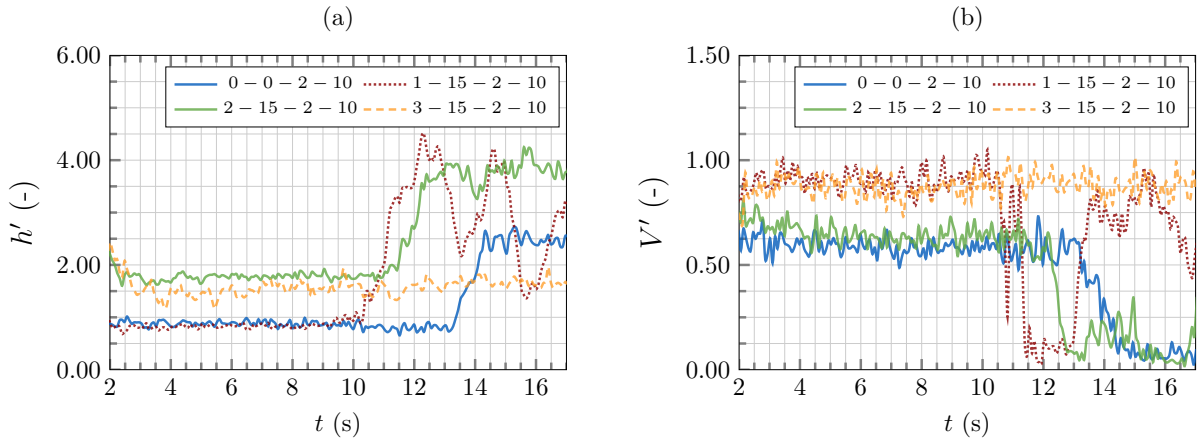

Figure 6.33: Cases $l_x = 0.15$ m. Evolution of (a) the water depth h' and (b) the free surface velocity V' downstream of the urban area at position A6.

Additionally, the water depth profile along $y = 0$ for $l_x = 0.05$ m (Figure 6.34) is represented at different times to highlight its temporal and spatial variation within the urban forms. Each point corresponds to an acoustic probe, ranging from A1 on the left to A6 on the right. Each grey rectangle represents a row of obstacles.

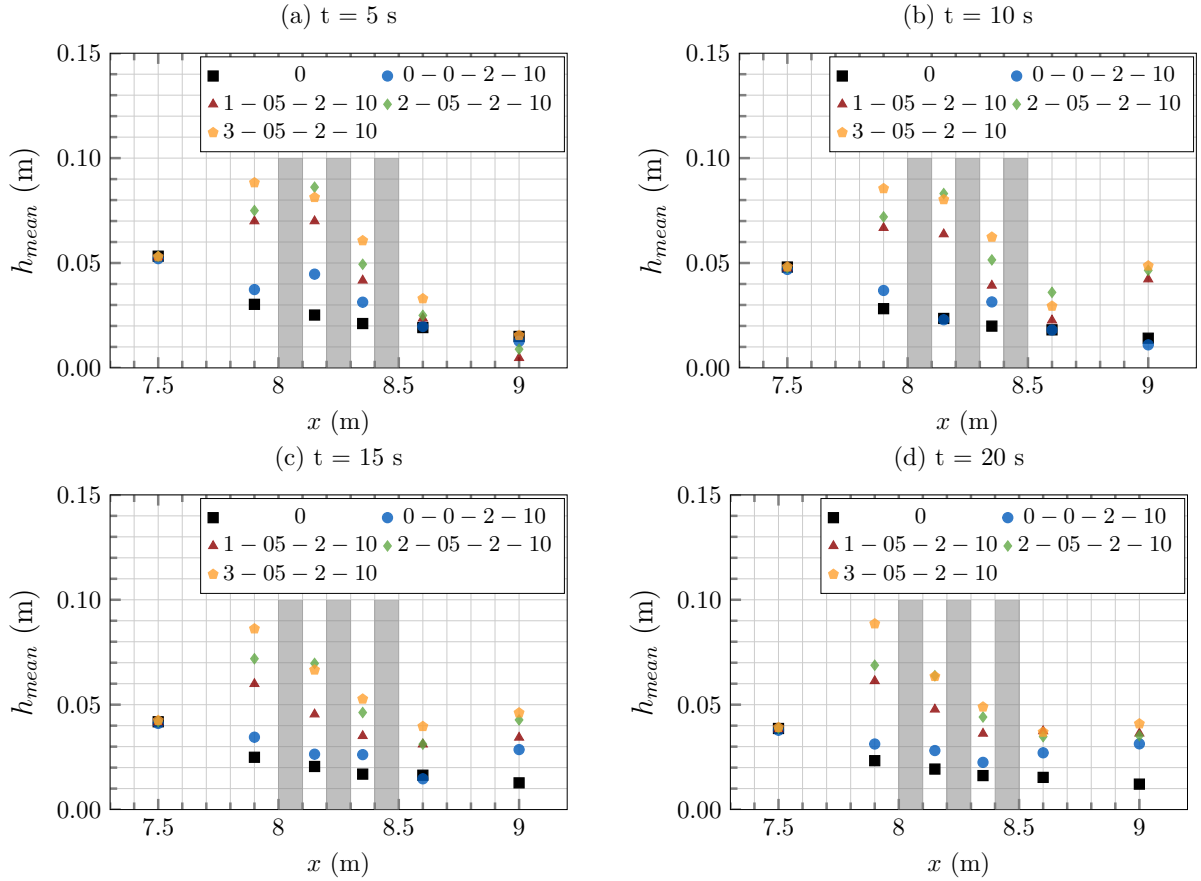

Figure 6.34: Cases $l_x = 0.05$ m. Evolution of the water depth profile (y = 0 m) at times (a) t = 5 s, (b) t = 10 s, (c) t = 15s, and (d) t = 20 s.

After 10 s a steady state seems to be reached, with few water depth variations and similar water depth profiles. As observed previously, the water depth decreases within the urban configuration, before rising again at position A6. A higher number of streets (n_x) leads to higher water depth during the entire experiment. Complementary images from the IAM camera showed that the maximum water depth is located in the surge between positions A2 and A3 (see Figure 6.17).

Note : Similar water depth profiles at four time steps (c.f. Figure 6.34) for cases $l_x = 0.10$, 0.15 and 0.20 m are available in Appendix E. The head loss between A1 and A6 for all configurations is

available in Appendix E.

The relative energy head (E' [-]) related to case 0 is illustrated in Figure 6.35 at position A6, for all studied cases. Attenuation for case $0-0-2-10$ (by 50%) is explained by the location of the probe A6 behind an obstacle. Attenuation on the head value at A6 seems to be sensible to the number of streets only for wider street widths (for instance cases $l_x = 0.15$ and 0.20 m). Still, no tendency can be provided from observations.

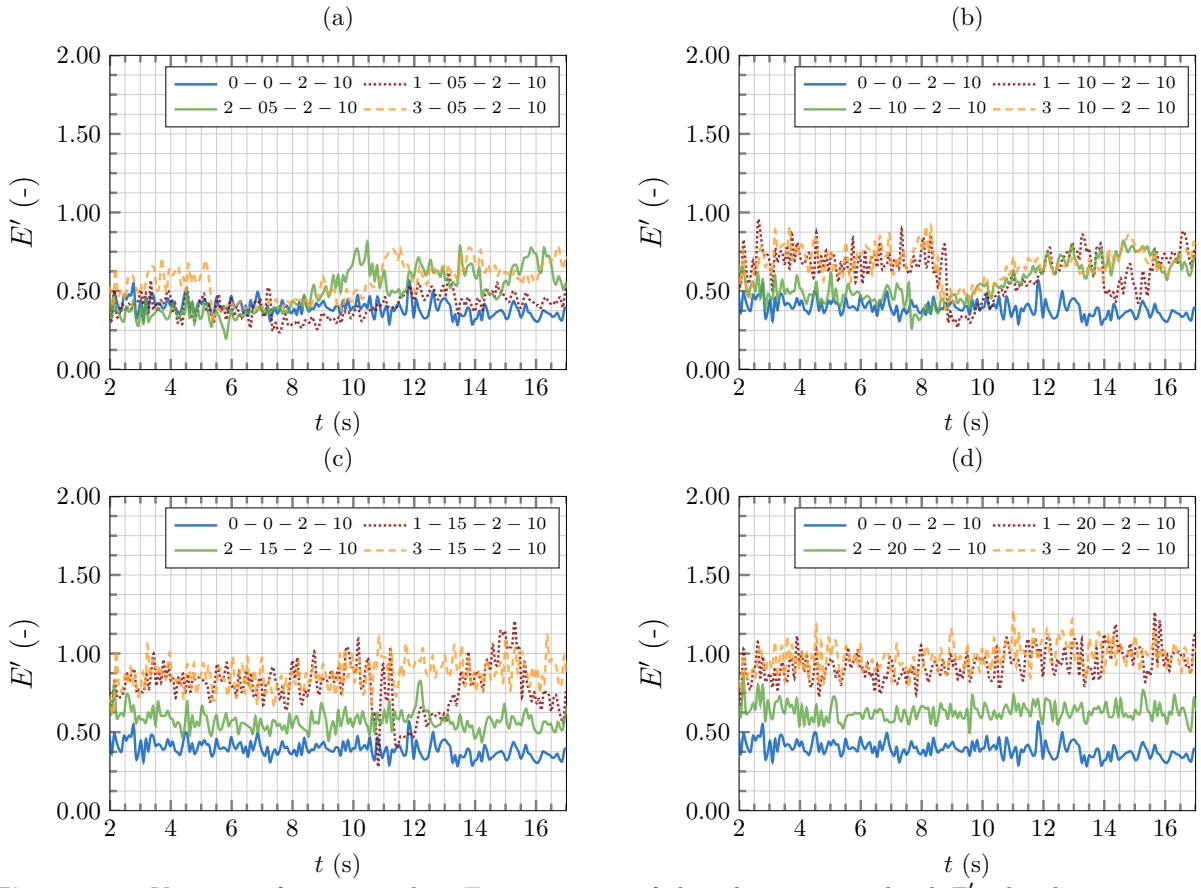

Figure 6.35: Variation of street number. Time variation of the relative energy head E' related to case 0 at position A6 for cases (a) $l_x = 0.05$ m, (b) $l_x = 0.10$ m, (c) $l_x = 0.15$ and (d) $l_x = 0.20$ m.

6.5.4 *Summary*

The impact of two urban parameters on the flow has been studied in this section: the number n_x and the width l_x of the streets along the x-axis. Thirteen urban forms were defined using four street numbers and four street widths. The influence of these parameters on the flow was mainly analysed downstream of the urban area at position A6 (since a very low variation was observed upstream for all cases), focusing on the evolution of the water depth h (m), horizontal velocity V_{xy} (m/s) and energy head E (m). The experimental results at position A6 are summarised in Figure 6.36 for all studied urban parameters.

The main findings regarding the influence of the longitudinal street width l_x and number n_x on the flow are:

- The street width appears to be the most influential parameter, as significant variations were observed in the energy head downstream of the urban area when its value changes.
- Studied urban parameters has no impact on the maximum water depth in the splash-up area but narrower streets lead to longer slash-up areas.
- Wider streets yields to higher flow velocity in longitudinal streets, which prevents the formation of a wake zone downstream. On the other hand, lower velocities in longitudinal narrower street lead to recirculations, creating a blockage effect at the streets outlets.
- Low velocity magnitudes downstream of the urban area allow the growth of a hydraulic jump, which can sometimes extend up to the urban area. Such phenomenon will be numerically characterised in the next chapter.
- The arrival time of the hydraulic jump at position A6 is influenced by both parameters, n_x and l_x, and may result from water accumulation due to the blockage effect of the urban forms and the channel reflection zones.
- Globally, results suggest that wider streets lead to more energy head downstream of the urban area (see Figure 6.36c). This conclusion is made locally, and may be validated at a larger scale by 3D numerical simulations.

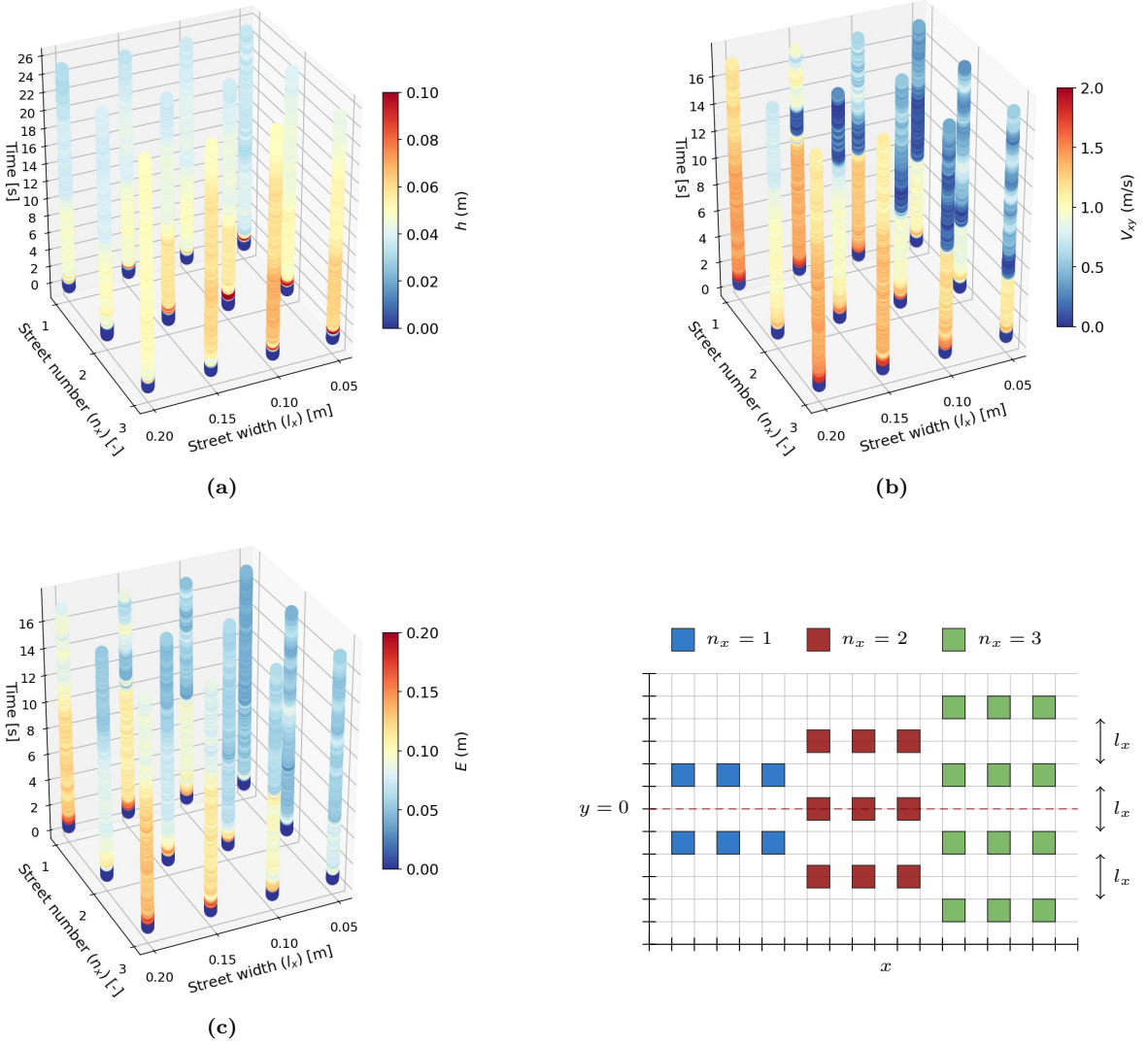

Figure 6.36: Temporal variation at position A6 for (a) water depth h (m), (b) velocity magnitude V_{xy} (m/s) and (c) energy head E (m) for all studied urban parameters.

6.6 INFLUENCE OF THE STREETS ALONG THE CROSS SECTION OF THE FLOW

The second part of the study aims to analyse the effect of streets perpendicular to the main flow direction. Eight additional urban forms are defined and illustrated in Section 6.6.1. Results here will be compared to four previously studied configurations. Section 6.6.2 presents the impact of four urban forms without cross streets on the flow. Then, the effect of different cross street widths and number are studied in Section 6.6.3.

6.6.1 *Definition of the idealised urban forms*

Due to the computational cost of large-scale flood models, urban layouts are often modelled as porous or roughness areas. However, the influence of individual urban parameters on the propagation of urban floods has never been studied and could be used for the simplification of urban areas representation in numerical models. Li *et al.* (2021) [47] highlighted the overwhelming influence of the urban parameters in the main direction of the flow compared to perpendicular direction in steady flood condition. Thus, the impact of cross street parameters will now be quantified for their potential simplifications in future numerical studies.

The impact of the lateral street opening is studied. First, four configurations without cross streets will be studied ($n_y = 0$), followed by four configurations with one cross street whose width varies ($l_y = 0.1$ and 0.3 m). The corresponding parameters of the resulting urban forms are given in Table 6.9. Results will be compared to some previous configurations: $n_x = 3$ and $l_x = [0.05, 0.20]$ m. Figures 6.37 and 6.39 illustrate the new urban forms and the associated positions of the acoustic gauges. Figure 6.38 shows a superposition of cases with $n_x = 3$ and $n_y = 0$ and all street widths l_x.

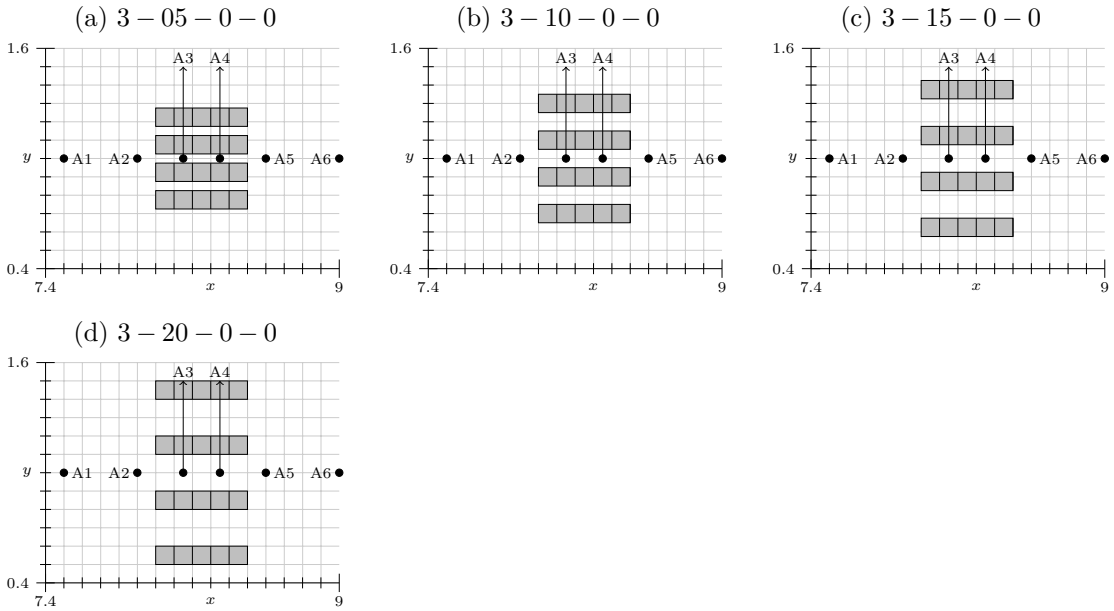

Figure 6.37: Top view of the four configurations without cross street ($n_y = 0$).

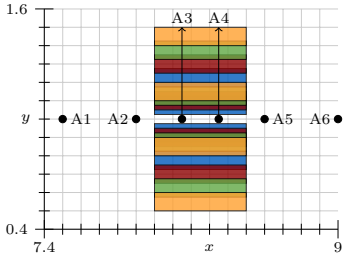

Figure 6.38: Superposition of cases with $n_x = 3$ and $n_y = 0$ for all street width l_x.

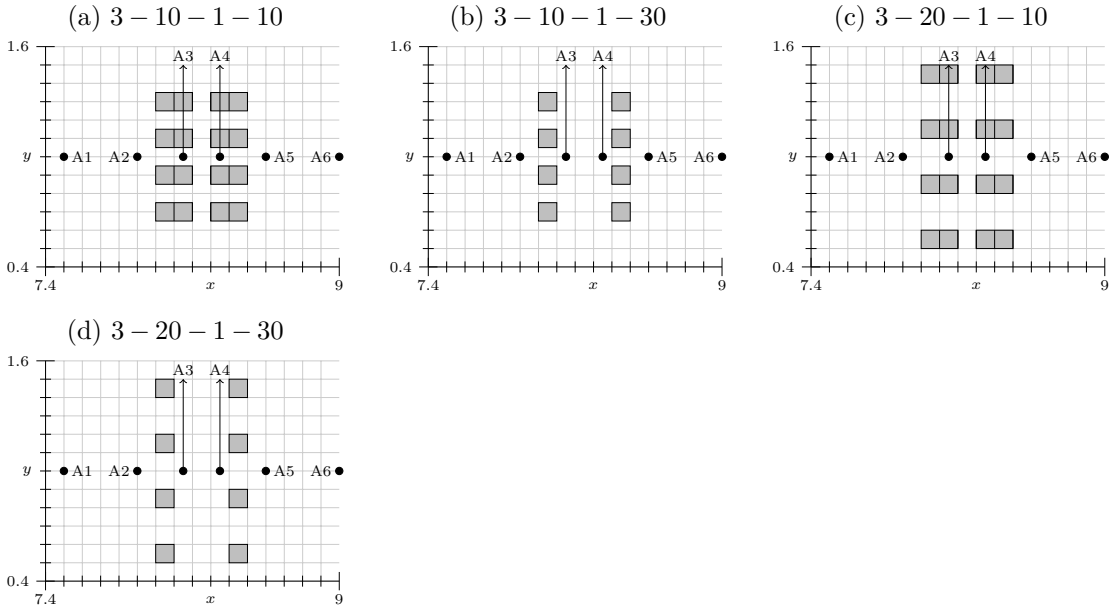

Figure 6.39: Top view of the four configurations with one cross street to study the influence of the streets along the y-axis.

Table 6.9: Parameters characterising urban forms to study the influence of the streets along the y-axis.

Configuration *	**Parameters**					
	n_x	l_x (m)	L_y (m)	n_y	l_y (m)	L_x (m)
3 – 05 – 0 – 0	3	0.05	0.55	0	-	0.5
3 – 10 – 0 – 0	3	0.10	0.70	0	-	0.5
3 – 15 – 0 – 0	3	0.15	0.85	0	-	0.5
3 – 20 – 0 – 0	3	0.20	1.00	0	-	0.5
3 – 10 – 1 – 10	3	0.10	0.70	1	0.1	0.5
3 – 10 – 1 – 30	3	0.10	0.70	1	0.3	0.5
3 – 20 – 1 – 10	3	0.20	1.00	1	0.1	0.5
3 – 20 – 1 – 30	3	0.20	1.00	1	0.3	0.5

∗ Configuration names: $n_x - l_x - n_y - l_y$

6.6.2 *Cross streets impact ($n_y = 0$) on the flow*

Cases with no cross street are studied with the following fixed parameters: $n_x = 3$ and the four previously studied street widths $l_x = [0.05, 0.20]$ m. The resulting urban forms are sketched in Figure 6.37.

The water depth variation over time at the different probes are illustrated in Figure 6.40. Tendencies upstream of the urban area are similar to the previous configurations with cross streets ($n_y = 2$ and $l_y = 0.10$ m). Indeed, no impact on the flow is observed at position A1 (Figure 6.40a) and a clear correlation between the water depth and the street width is visible at position A2 (Figure 6.40b). Similarly, downstream of the urban area, the water height increases with the street width. At position A6, the flow seems less impacted by possible recirculations zones created through the presence of side streets.

Remark : For case 3 – 05 – 0 – 0, the acoustic sensors A3 and A4 were not able to measure the water depth due to the reflection of the signals on the edges of the obstacles.

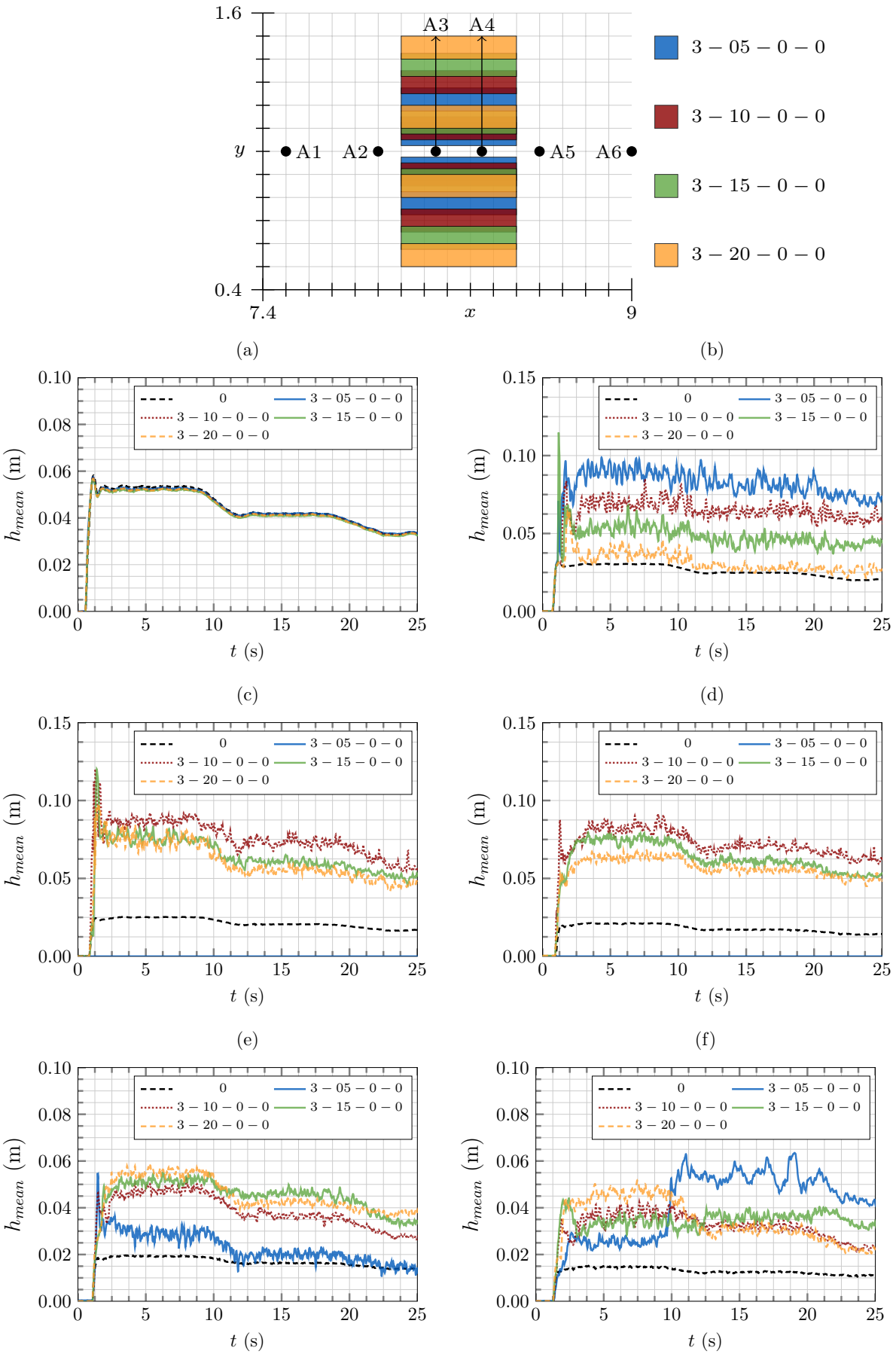

Figure 6.40: Water depth comparison for cases $n_y = 0$ at positions (a) A1, (b) A2, (c) A3, (d) A4, (e) A5 and (f) A6.

The water depth h for cases with and without cross streets ($n_y = 0$ and 2) is compared in Figures 6.41 and 6.42 for cases $l_x = 0.05$ and $l_x = 0.10$ m, respectively. The absence of cross streets delays the arrival time of the wake zone. For narrow streets ($l_x = 0.05$ m), the wake zone arrives at position A6 five seconds later for the case with $n_y = 0$ (Figure 6.41b) and does not reach position A5 (Figure 6.41a). For cases with $l_x = 0.10$ m (Figure 6.42), the wake zone is not observed at all when there are no cross streets.

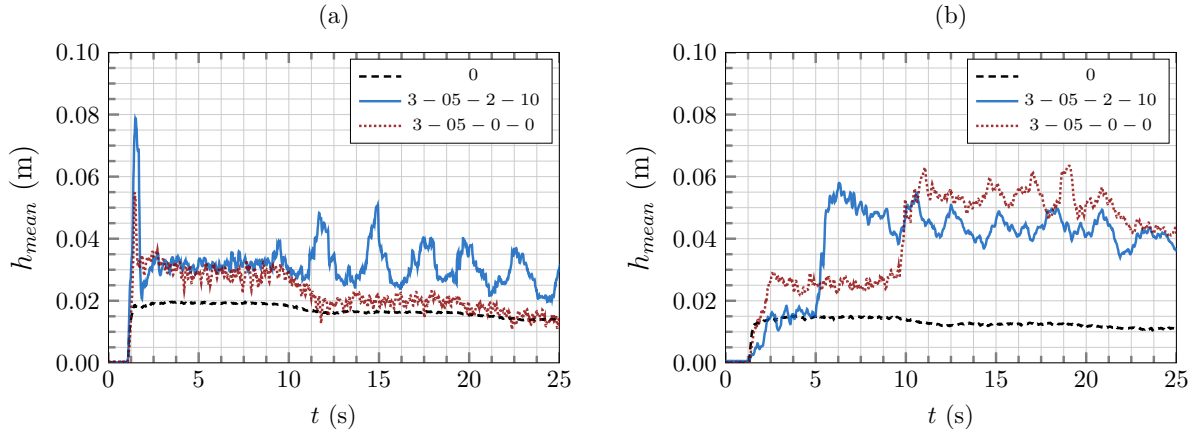

Figure 6.41: Water depth comparison between cases $3-05-2-10$ and $3-05-0-0$ at positions (a) A5 and (b) A6.

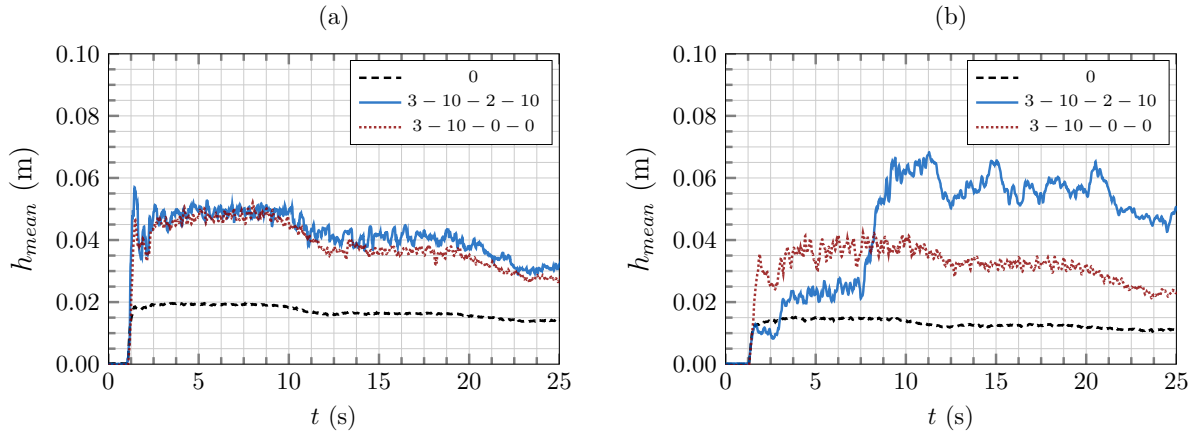

Figure 6.42: Water depth comparison between cases $3-10-2-10$ and $3-10-0-0$ at positions (a) A5 and (b) A6.

> **Note** : Similar water depth comparisons for $l_x = 0.15$ and 0.20 are available in Appendix E.

The relative water depth evolution for cases with cross streets ($n_y = 2$) related to cases without ($n_y = 0$) is compared in Figure 6.43 at position (a) A5 and (b) A6. The water depth downstream of the urban area is not impacted by the presence of cross streets when l_x is high enough to prevent the apparition of the hydraulic jump. For narrower streets, the wake zone apparition is delayed and thus the flow conditions downstream are different between both cases.

The water depth in the splash-up zone at x = 8 m is shown in Figure 6.44. The slash-up is not impacted by the presence of the cross streets and the water height evolution is very similar between the two cases. Overall, the presence of the cross streets does not have an impact upstream of the urban area, as the splash-up shape and height are similar (verified at position A2 and $x = 8$ m).

The free surface velocity along the longitudinal street for all cases related to $n_y = 0$ is illustrated in Figure 6.45. A slight acceleration of the flow along the street is visible for all cases, and except when the hydraulic jump occurs, the velocity magnitude is similar for all cases.

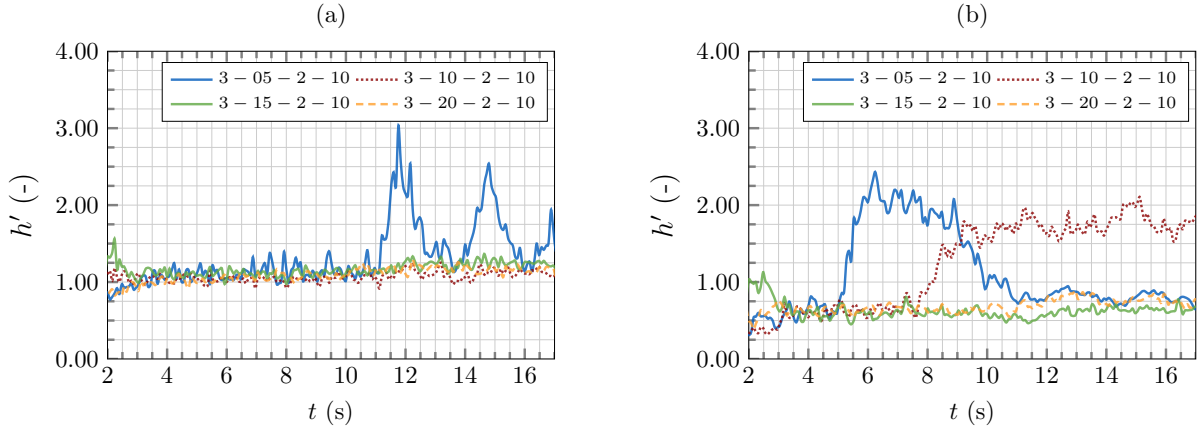

Figure 6.43: Relative water depth h' of cases $n_y = 2$ related to cases with $n_y = 0$ at positions (a) A5 and (b) A6.

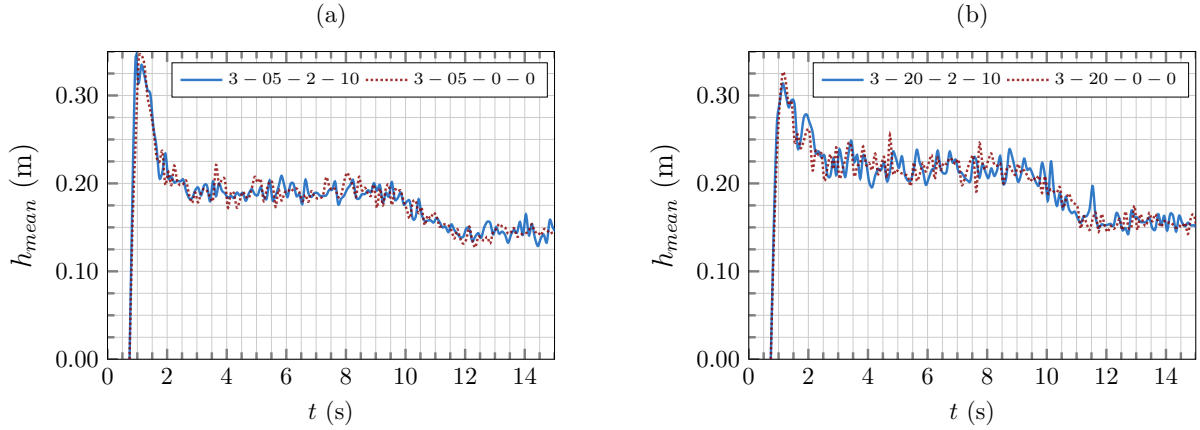

Figure 6.44: Comparison of the water depth at position x = 8 m from the IAM analysis between $n_y = 0$ and 2 for cases (a) $l_x = 0.05$ m and (b) $l_x = 0.20$ m.

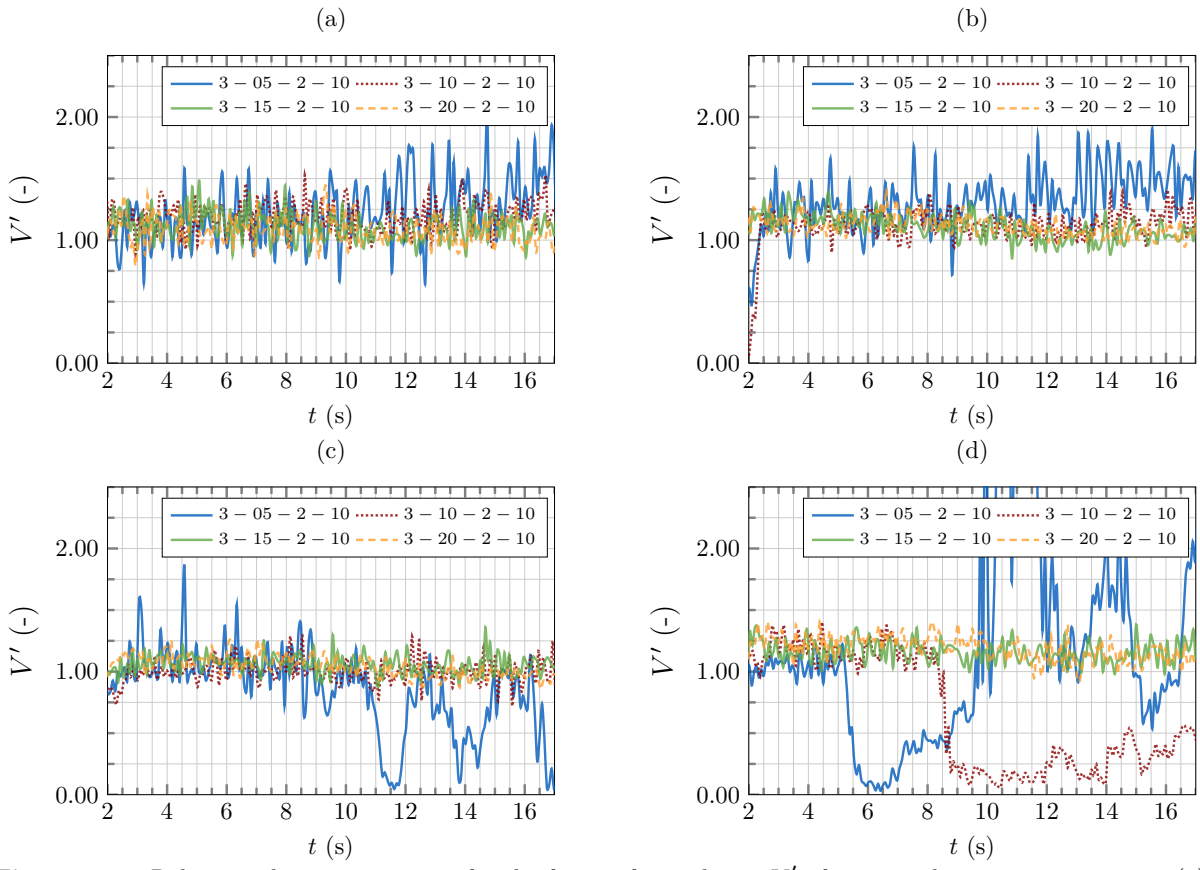

Figure 6.45: Relative urban areas impact for the free surface velocity V' of cases with $n_y = 3$ at positions (a) A3, (b) A4, (c) A5 and (d) A6 related to cases with $n_y = 0$.

Then, the free surface velocity fields for cases with $n_y = 0$ are shown in Figure 6.46 at three different time steps. The main difference in the free surface pattern compared to cases with $n_y = 2$ is the absence of incoming and outgoing flow through the cross streets, which results in all the flow entering the urban area crossing the streets longitudinally without vertical deviation. As a result, smaller recirculations appears downstream of the urban area compared to cases with $n_y = 2$.

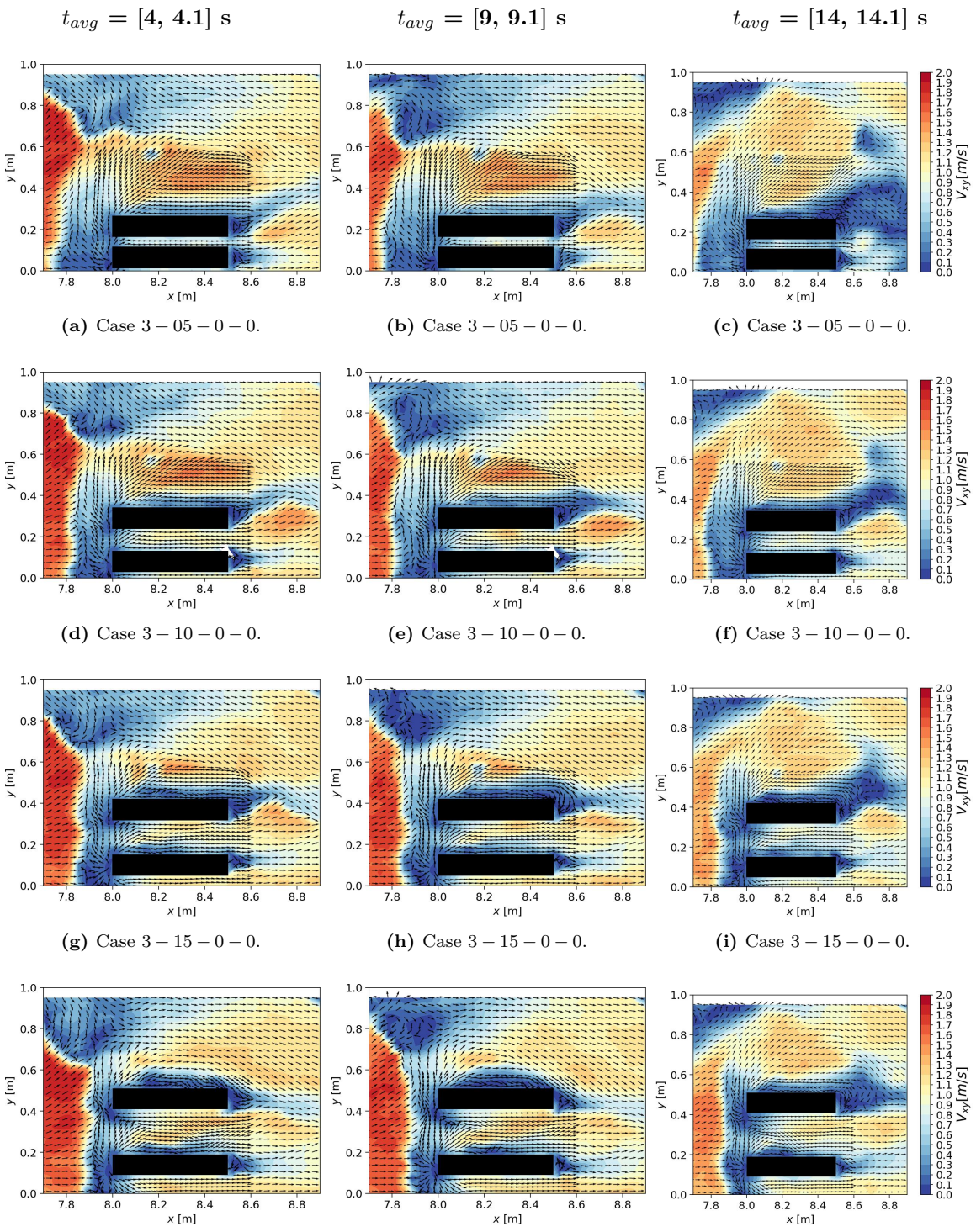

(a) Case 3 – 05 – 0 – 0. **(b)** Case 3 – 05 – 0 – 0. **(c)** Case 3 – 05 – 0 – 0.

(d) Case 3 – 10 – 0 – 0. **(e)** Case 3 – 10 – 0 – 0. **(f)** Case 3 – 10 – 0 – 0.

(g) Case 3 – 15 – 0 – 0. **(h)** Case 3 – 15 – 0 – 0. **(i)** Case 3 – 15 – 0 – 0.

(j) Case 3 – 20 – 0 – 0. **(k)** Case 3 – 20 – 0 – 0. **(l)** Case 3 – 20 – 0 – 0.

Figure 6.46: Free surface velocity variations for cases $n_y = 0$ at 3 different time step. Black surfaces illustrate the obstacles position.

More precisely, Figure 6.47 shows the free surface velocity difference between the cases with $n_y = 2$ and $n_y = 0$. When there are cross streets in the urban area, the flow is decelerated along the sides of the urban area, as well as in some portions of the longitudinal streets. This deceleration is more pronounced at the beginning of the experiment, especially in the longitudinal streets. For larger street widths, the splash-up area is longer, as indicated by the blue lines upstream of them. Overall, the flow is mostly decelerated around the urban area.

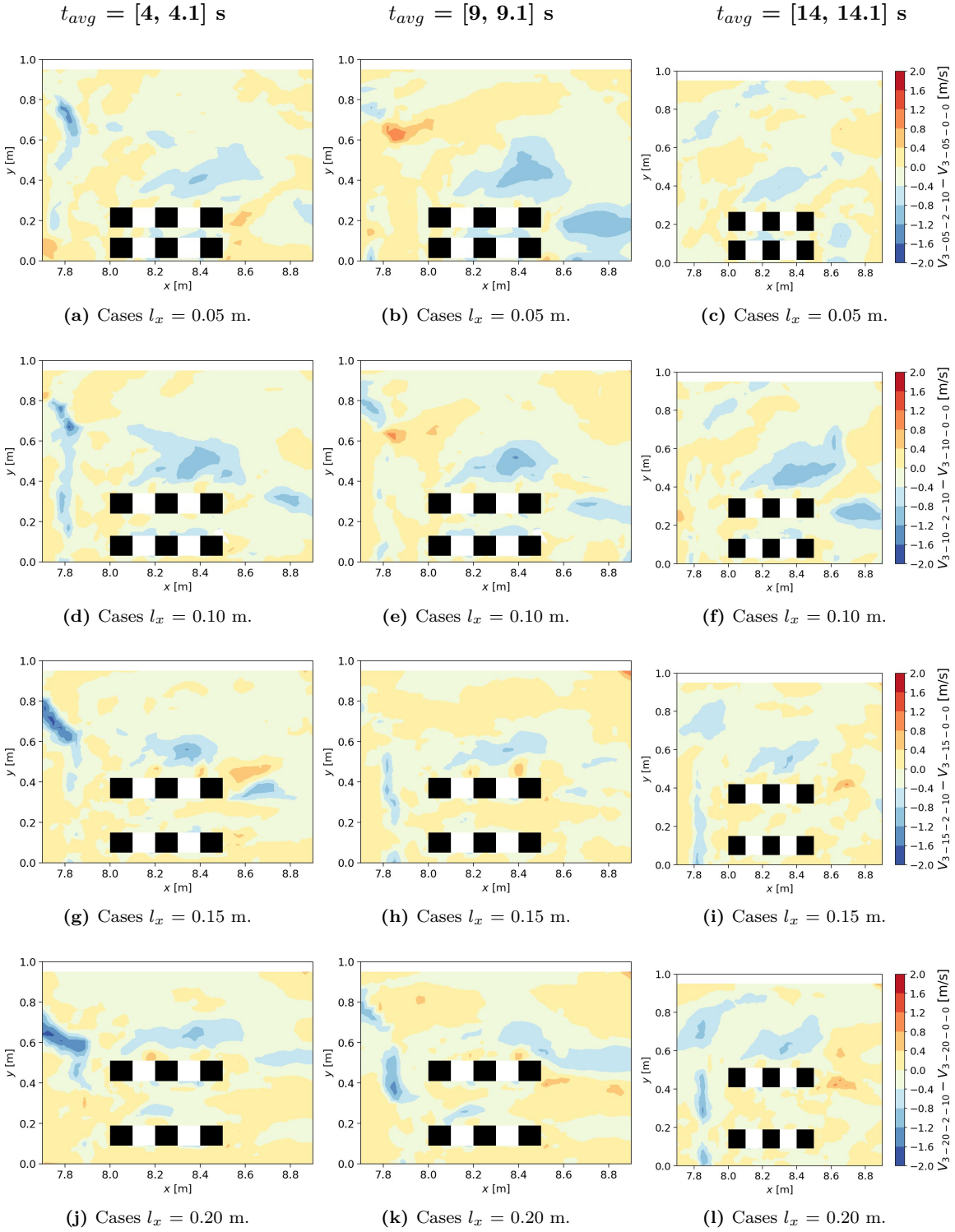

(a) Cases $l_x = 0.05$ m. **(b)** Cases $l_x = 0.05$ m. **(c)** Cases $l_x = 0.05$ m.

(d) Cases $l_x = 0.10$ m. **(e)** Cases $l_x = 0.10$ m. **(f)** Cases $l_x = 0.10$ m.

(g) Cases $l_x = 0.15$ m. **(h)** Cases $l_x = 0.15$ m. **(i)** Cases $l_x = 0.15$ m.

(j) Cases $l_x = 0.20$ m. **(k)** Cases $l_x = 0.20$ m. **(l)** Cases $l_x = 0.20$ m.

Figure 6.47: Free surface velocity comparison between cases $n_y = 2$ and cases $n_y = 0$ at 3 different time step. Black surfaces illustrate the obstacles position for cases $n_y = 2$. White surfaces illustrate the obstacles position for cases $n_y = 0$.

6.6.3 *Cross streets width and number impact (l_y) on the flow*

Finally, the impact of cross streets width and number is analysed for configurations with three longitudinal streets ($n_x = 3$) and two different street width ($l_x = 0.10$ and 0.20 m). Two cross street configurations are added to the study: $n_y = 1$, $l_y = 0.1$ m (cases $3-10-1-10$ and $3-20-1-10$) and $n_y = 1$, $l_y = 0.3$ m (cases $3-10-1-30$ and $3-20-1-30$). The resulting urban forms are sketched in Figure 6.39a, b, c, and d. Those four configurations will be compared to corresponding previously studied cases with and without cross streets ($n_y = 0$ and 2).

Remark : The different cross street parameters were selected to keep the total longitudinal length L_x consistent across all studied cases, ensuring that the positions of the acoustic probes remain the same as in previously studied cases, allowing for direct comparison.

The water depth evolution at all probe positions is shown in Figures 6.48 and 6.49 for cases with $l_x = 0.10$ and $l_x = 0.20$ m, respectively. For all cases, the water depth upstream of the obstacles (positions A1 and A2) remains similar during the acquisition time, although from t = 22 s some divergences appear.

Through the urban area, the effect of cross street parameters is more visible for $l_x = 0.10$ m (Figure 6.48). In these cases, the water depth depends on the cross street opening: higher depths are observed at the beginning of the street (position A3) for smaller cross-street openings, while at the end of the street (position A4), the highest water depths are observed with wider openings. These effects seem to disappear for wider street cases ($l_x = 0.20$ m).

Downstream of the urban area, the hydraulic jump arrives earlier at position A6 for wider cross street openings. This effect highlights once more that the hydraulic jump is linked to the reflection zone and the width of the channel. Wider cross street openings lead to a larger amount of water being deviated in the reflection zone, thus causing the earlier arrival of the hydraulic jump.

Additionally, as observed previously, narrower longitudinal streets also accelerate the arrival time of the wave, so the wake zone in case $3-10-1-30$ reaches position A6 four seconds earlier than in case $3-20-1-30$.

The free surface velocity fields for cases with $n_y = 1$ are shown in Figure 6.50 at three different time steps. The flow pattern indicates that when the lateral street width exceeds the longitudinal street width ($l_y < l_x$), the flow is completely diverted along the y-axis, creating high velocity gradients as most of the flow crosses the longitudinal streets along the y-axis (cases $3-10-1-30$ and $3-20-1-30$). When the streets have the same width ($l_x = l_y$) or when the longitudinal street width is greater than the lateral street width ($l_x > l_y$), the flow direction in the streets remains aligned with the main flow direction (case $3-10-1-10$). When the flow is completely diverted along the y-axis, the outflow from the streets is insufficient to prevent the formation of complex recirculation patterns and hydraulic jump downstream of the urban area, even for wide street parameters (Figure 6.50).

Figure 6.51 shows the free surface velocity difference between the cases with $n_y = 1$ and $n_y = 0$. The deceleration of the flow near wide lateral streets can be observed. For narrower cross streets ($l_y = 0.1$ m), no deceleration is detected along the longitudinal streets, but is observed on the side of the urban area. These patterns highlight the areas affected by the deceleration effect of the cross streets in the urban area.

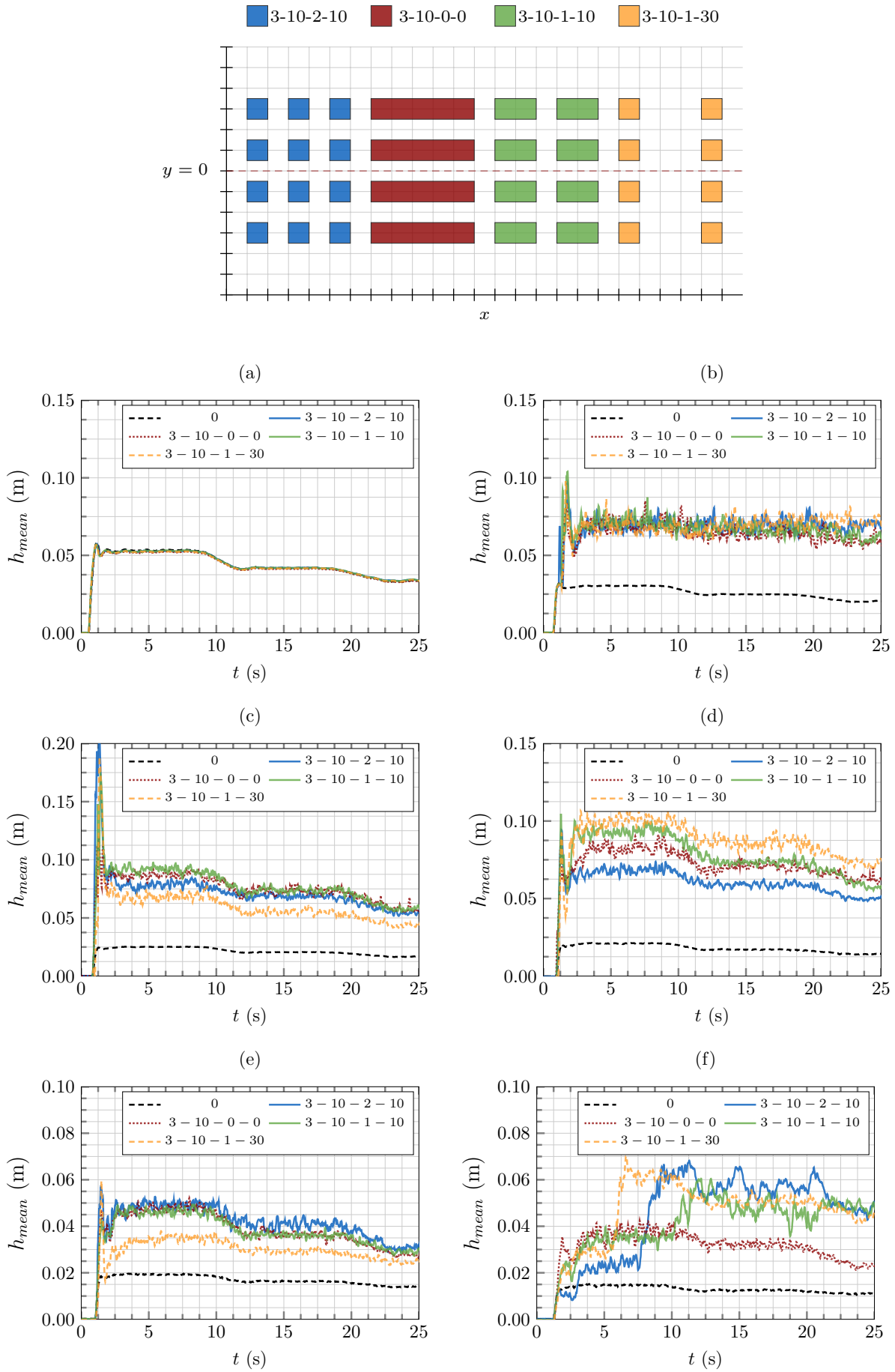

Figure 6.48: Cases $l_x = 0.10$ m. Water depth comparison for four l_y values at position (a) A1, (b) A2, (c) A3, (d) A4, (e) A5 and (f) A6.

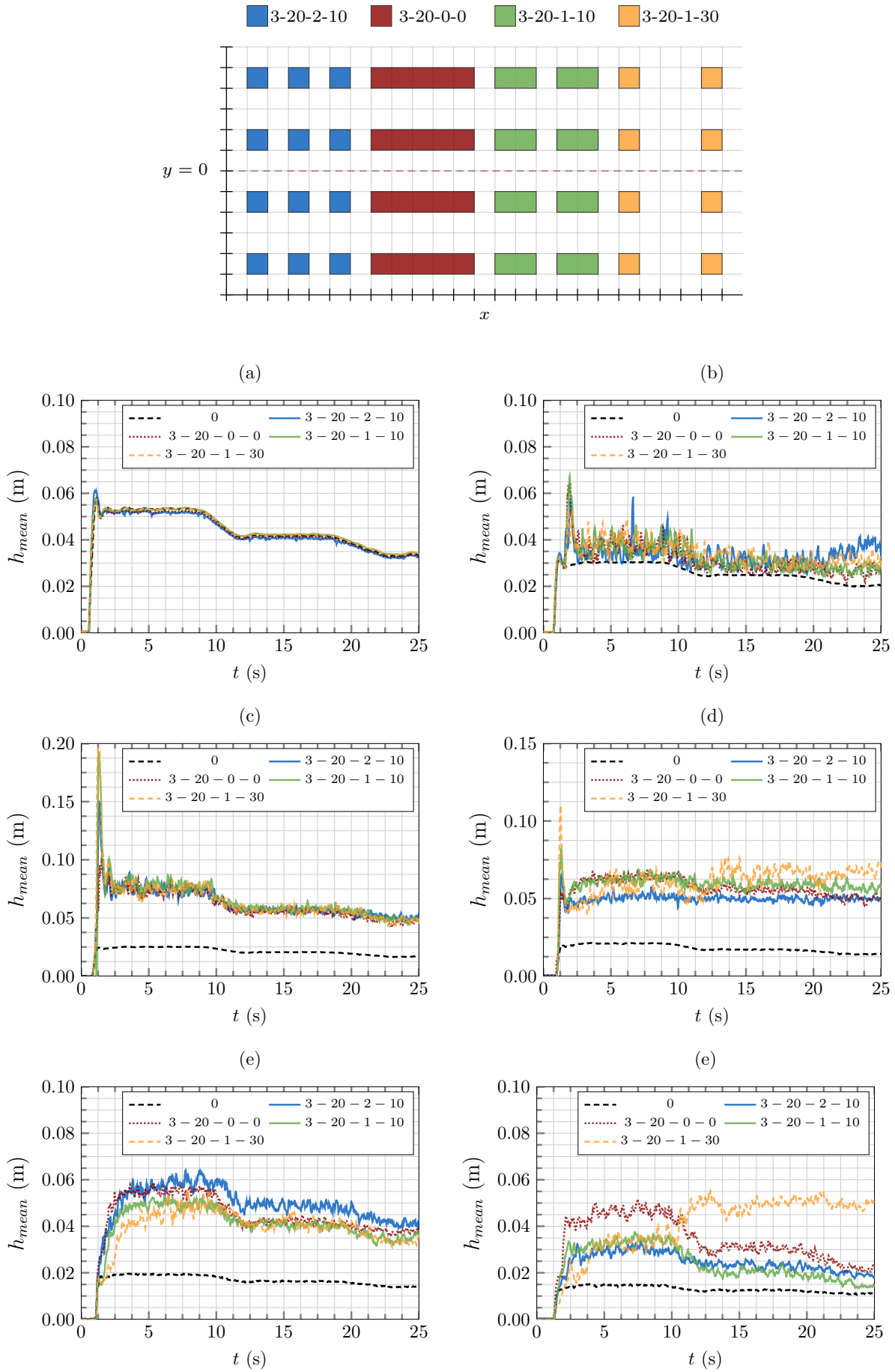

Figure 6.49: Cases $l_x = 0.20$ m. Water depth comparison for four l_y values at position (a) A1, (b) A2, (c) A3, (d) A4, (e) A5 and (f) A6.

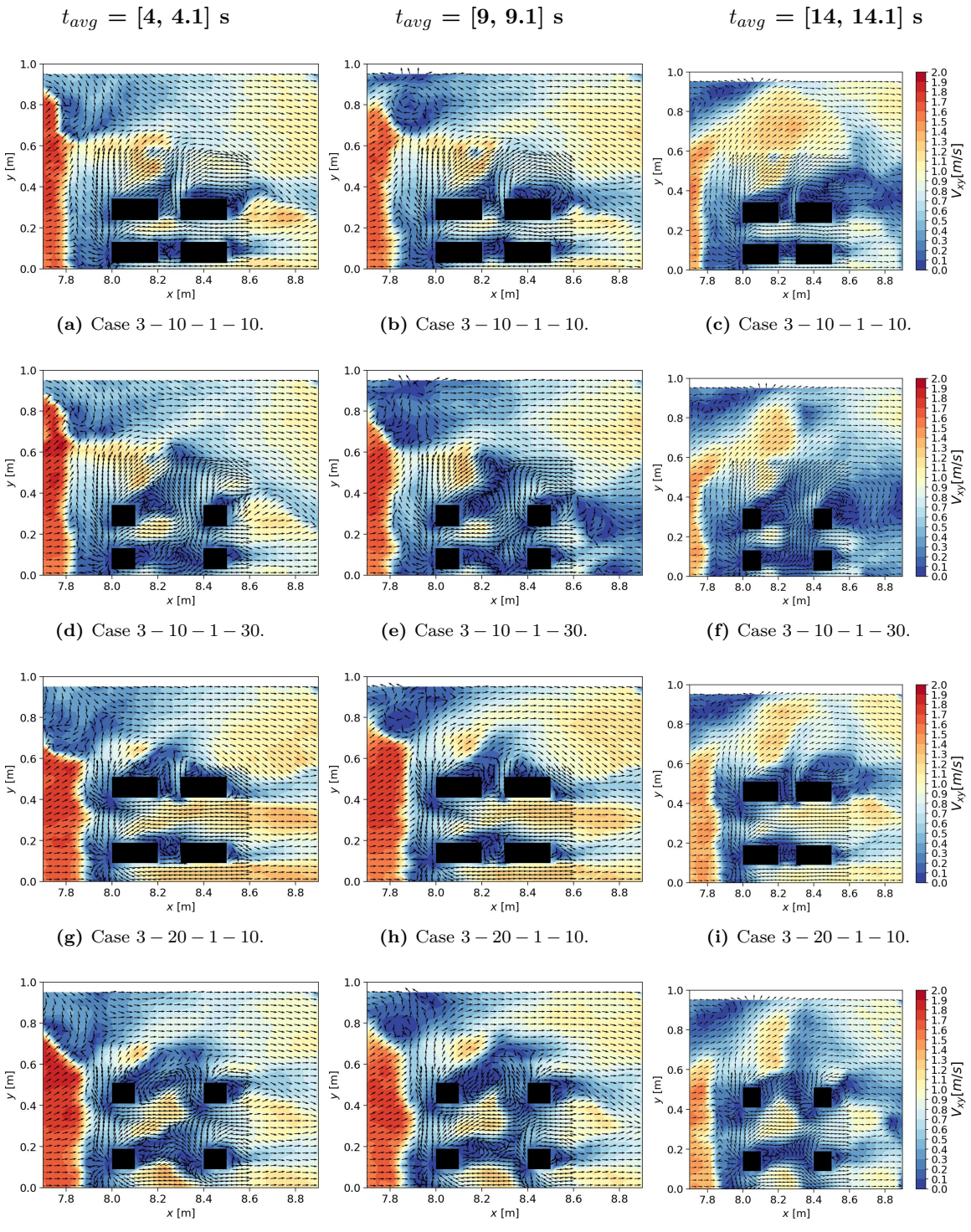

(a) Case $3-10-1-10$. **(b)** Case $3-10-1-10$. **(c)** Case $3-10-1-10$.

(d) Case $3-10-1-30$. **(e)** Case $3-10-1-30$. **(f)** Case $3-10-1-30$.

(g) Case $3-20-1-10$. **(h)** Case $3-20-1-10$. **(i)** Case $3-20-1-10$.

(j) Case $3-20-1-30$. **(k)** Case $3-20-1-30$. **(l)** Case $3-20-1-30$.

Figure 6.50: Free surface velocity variations for cases $n_y = 1$ at different time step. Black surfaces illustrate the obstacles position.

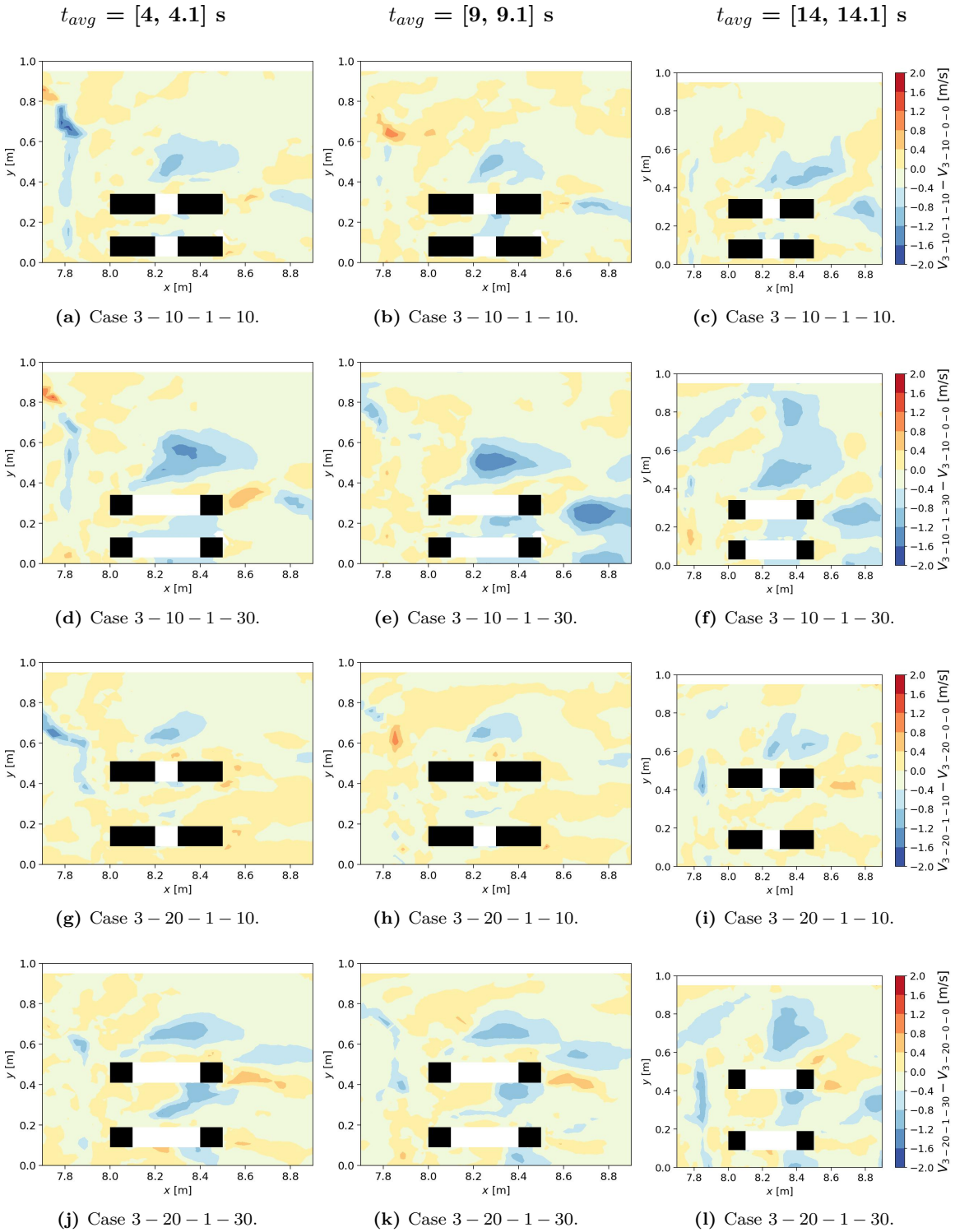

(a) Case $3-10-1-10$. **(b)** Case $3-10-1-10$. **(c)** Case $3-10-1-10$.

(d) Case $3-10-1-30$. **(e)** Case $3-10-1-30$. **(f)** Case $3-10-1-30$.

(g) Case $3-20-1-10$. **(h)** Case $3-20-1-10$. **(i)** Case $3-20-1-10$.

(j) Case $3-20-1-30$. **(k)** Case $3-20-1-30$. **(l)** Case $3-20-1-30$.

Figure 6.51: Free surface velocity comparison between various cross street parameters and case $n_y = 0$ at 3 different time step. Black surfaces illustrate the obstacles position for cases $n_y = 1$. White surfaces illustrate the obstacles position for cases $n_y = 0$.

6.6.4 *Summary*

The impact of cross streets on the flow has been studied in this section. Eight urban forms were defined: four without cross streets and four with one cross streets of two different sizes. Similarly to the previous section, a focus on the evolution of the water depth h (m), the velocity magnitude V_{xy} (m/s) and the energy head E (m) was made. The effects of the cross streets along the longitudinal road from A3 to A6 on the energy head E, related to case $n_y = 0$, are summarised in Figures 6.52 and 6.53, for cases with l_x = 0.10 and 0.20 m, respectively.

At the beginning of the street, no impact of the cross street width and number is visible in the flow (Figure 6.52a and 6.53a). For cross streets wider than longitudinal streets ($l_y > l_x$), a deceleration along the street is then observable (Position A4 to A6). This deceleration is stronger for wider street cases (l_x = 0.20 m, Figure 6.53). Finally, the number of cross streets seems to have a very low impact on the energy head of the flow, since $n_y = 1$ and $n_y = 3$ show similar energy head at all probe positions. This highlights that for $l_x = l_y$, no complete deviation of the flow occurs along the longitudinal streets, and thus no deceleration is observed. Finally, the number of cross streets seems to not have an impact on the downstream energy head.

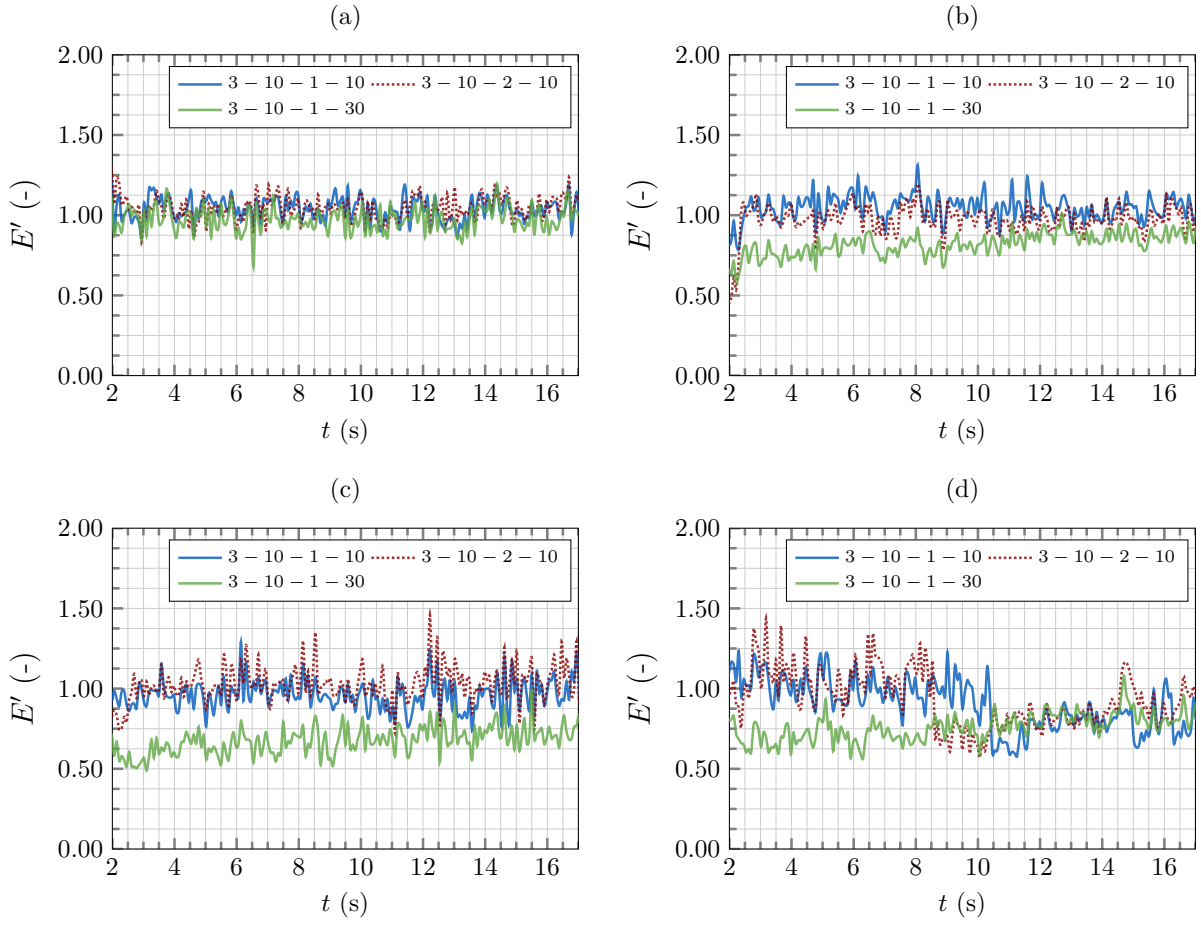

Figure 6.52: Relative cross street impact for the energy head E' at position A6 related to case $n_y = 0$ for cases $n_x = 3$ and $l_x = 0.1$ m at positions (a) A3, (b) A4, (c) A5 and (d) A6.

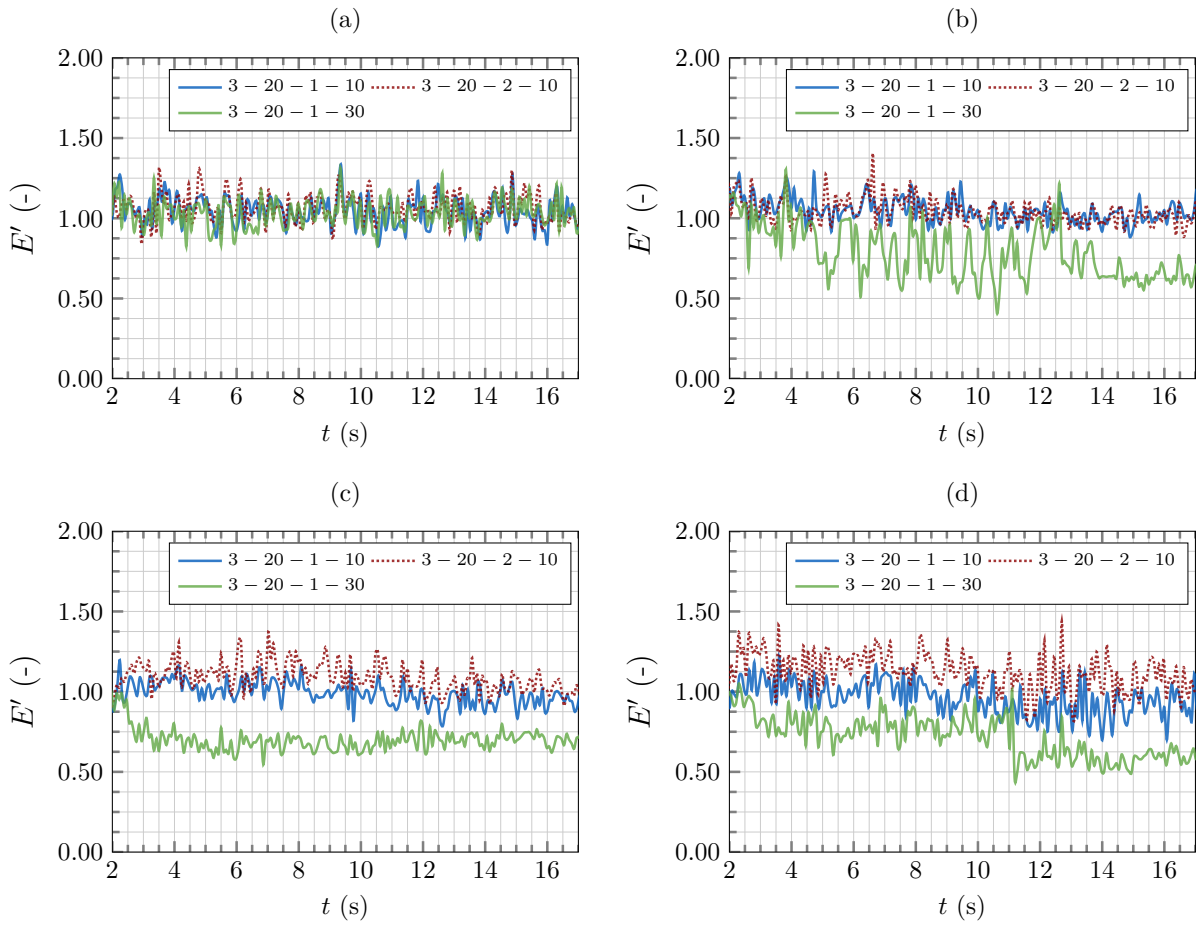

Figure 6.53: Relative cross street impact for the energy head E' at position A6 related to case $n_y = 0$ for cases $n_x = 3$ and $l_x = 0.2$ m at positions (a) A3, (b) A4, (c) A5 and (d) A6.

At last, the main findings regarding the influence of cross street number n_y and width l_y on the flow are:

- Not taking into account cross streets in urban areas leads to an overestimation of the water depth and an underestimation of the velocity magnitude.
- Cross street parameters do not impact the flow upstream of the urban area.
- For cross streets wider than longitudinal streets ($l_y > l_x$), the flow is completely diverted along the y-axis, and the energy head in the longitudinal street is strongly diminished.

Finally, supplementary analysis should be conducted to provide guidelines on the exact influence of the representation of cross streets on the flow. However, it appears that for urban areas with $l_y \leq l_x$, not taking them into account has a low impact on the energy head downstream of the urban area and no impact upstream.

6.7 COMPARISONS OF CURRENT EXPERIMENTS WITH PAST EXPERIMENTAL STUDIES

Past experimental studies, presented in Chapter 2, have already examined flow propagation through urban areas under unsteady conditions. Some of the results obtained with our setup will now be compared to these studies to highlight similarities and the novelty brought by the current dataset.

Globally, all macro-phenomena observed in our campaign were also observed in previous dam-break flow through obstacle configurations. These include the reflection zone (for partial dam-break) [53], the splash-up area upstream [53, 54, 103], and the wake zone downstream [51, 53, 54, 101, 103].

In particular, Soares-Frazão *et al.* (2008) [53] provided water depth profiles along idealised urban layouts with insubmersible obstacles of 4x4 streets with $l_x = l_y = 0.10$ m. The obstacles consist of 0.3 m cubes.

Experimental results provided, among others, water depth profiles at two different time steps: 5 and 10 s. Qualitative comparisons are performed in Figures 6.54 and 6.55 with case $3-05-2-10$. For both cases, the water depth is measured along a central longitudinal street but with a ratio between the longitudinal street and obstacle length slightly different between both cases: 0.5 in current study against 0.33 in Soares-Frazão *et al.* (2008) [53] study.

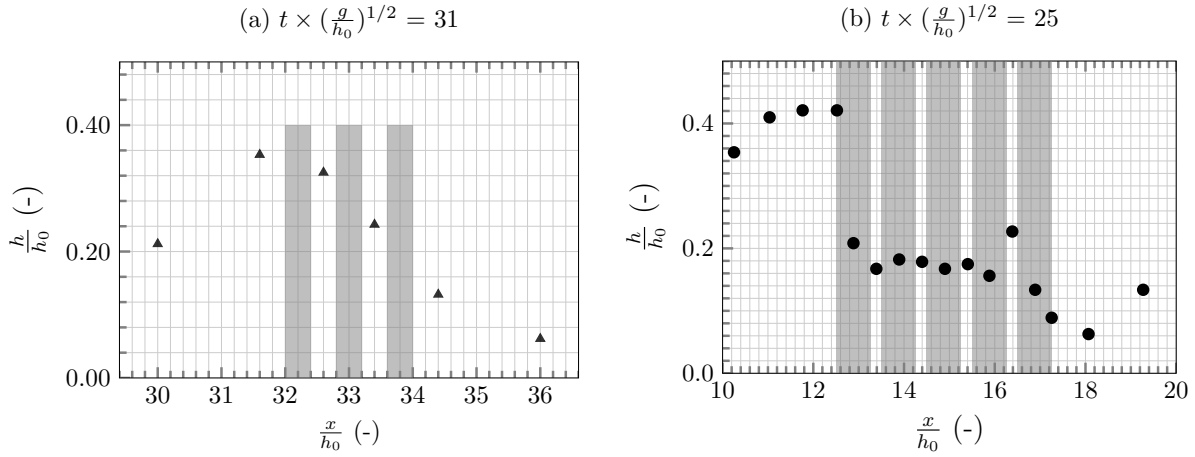

Figure 6.54: Comparison of the free-surface profile $\frac{h}{h_0}$ in central longitudinal street at $t = 5$ s between (a) case $3-05-2-10$ and (b) $4-10-4-10$ from Soares-Frazão *et al.* (2008) [53].

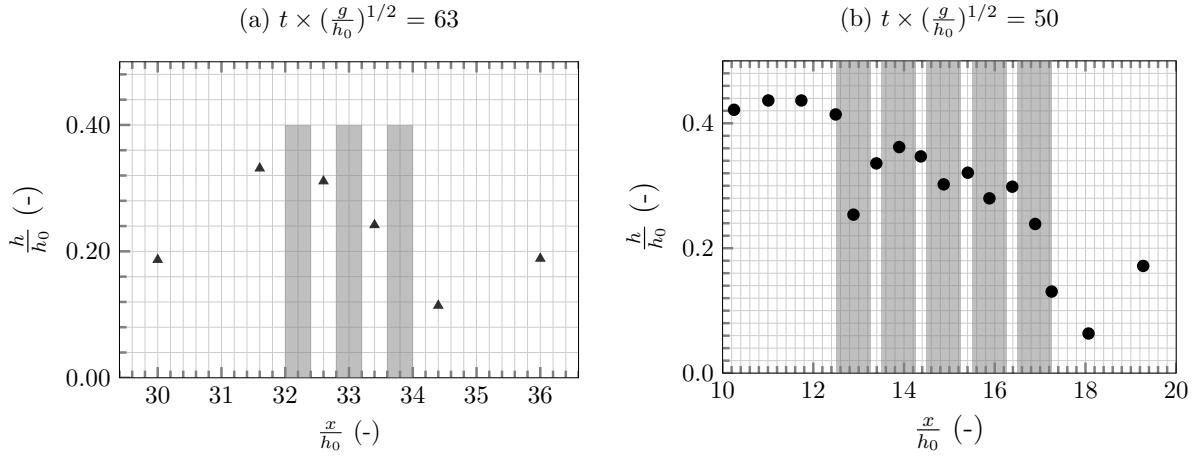

Figure 6.55: Comparison of the free-surface profile $\frac{h}{h_0}$ in central longitudinal street at $t = 10$ s between (a) case $3-05-2-10$ and (b) $4-10-4-10$ from Soares-Frazão *et al.* (2008) [53].

Comparisons of the water depth profiles reveal similarities, even though the time and longitudinal positions are not directly comparable due to the different h_0 values. A higher water depth is observable upstream of the urban area in the splash-up zone, while a lower water depth is visible downstream in the wake zone. The blockage effect difference between both configurations (from the ratio between the longitudinal street and obstacle length) leads to a longer and higher water depth in the splash-up for case $4-10-4-10$, as well as a lower water depth in the urban area at the beginning of the experiment. At $t = 10$ s, Figure 6.55, both water depth profiles have a similar shape with a linear decrease between upstream and downstream of the urban area. Such comparisons show that the blockage effect of the urban forms influences the water depth evolution, especially at the beginning of the experiment, but it tends to reach a similar stationary state.

On the other hand, limitations due to the unsteadiness of the flow combined with the heterogeneous free surface through urban areas lead to some unmeasured phenomena. For example, Szydlowski *et al.* (2006) reported issues in measuring the maximum water depth of the water-jet during impact using hydrostatic sensors. In the current study, we complemented acoustic wave gauge measurements with IAM analysis to obtain the maximum elevation during impact. Results showed that the maximum elevation in the

splash-up was similar for all studied cases. However, this method could be improved by using several cameras to address the depth of field hypothesis.

Moreover, Soares-Frazão *et al.* (2008) [53] performed PTV measurements in the urban area, resulting in velocity direction information along the urban streets. The development of such methods and laboratory cameras in recent years allowed the current study to measure the velocity field in and around urban areas, providing complementary information on the velocity magnitude and pattern as well as its evolution. The next step will be to perform PIV measurements to obtain vertical velocity fields within the urban area.

Additionally, Tomiczek *et al.* (2016) [104] highlighted the complexity of performing ADV measurements in urban areas due to low water levels and breaking-wave turbulence. Thus, LSPIV analysis were performed in the current study that provided information on the free surface velocity, but caution is required when comparing it to depth-averaged numerical results [53].

6.8 CONCLUSION

This chapter presented an experimental dataset of fast transient dam-break waves over twenty-one urban forms. The study focused on the impact of four urban parameters on the flow: the number and width of streets parallel and perpendicular to the main direction of the dam-break wave. Essential physical parameters, such as water height and the horizontal velocity field of the free surface related to reference cases, are investigated within specific regions of interest. The energy head profile along the urban forms is also computed and examined.

The first part of the study focused on the impact of the longitudinal streets on the flow. An analysis on the energy head downstream of the urban area is proposed, gathering the interest quantities in only one variable. Given the measurement technique used to compute the water depth, the energy head is computed punctually downstream of the urban area. A local tendency is observed: the energy head decreases for narrower longitudinal streets, independently of their number. Such information will be verified at a larger scale using 3D numerical simulations in the next chapter.

Additionally, the effect of cross streets is studied, and a low impact on the energy head downstream of the obstacles is observed for widths less than or equal to the longitudinal street width. These preliminary results can guide future research in simplifying the representation of urban forms in numerical models.

Finally, future work aims to numerically reproduce, after validation, some presented cases to complement the experimental dataset and verify observed tendencies at a larger scale. Additionally, simulations will be used to study the origin of the hydraulic jump and conclude on the influence of the setup geometry on the current dataset.

7

MODELLING FAST TRANSIENT FLOW THROUGH VARIOUS URBAN FORMS

Summary :
This chapter performs numerical simulations of six urban forms studied experimentally in Chapter 6. Following a comparison with the experimental results downstream of the urban area for supplementary validation purposes, the local tendencies observed experimentally in Chapter 6 are verified spatially. Following, head loss coefficients related to street size are extracted from the simulations and the origin of the hydraulic jump and its impact on the dataset are analysed.

Contents

7.1 Introduction 134
7.2 Numerical reproduction of selected urban forms with code_saturne 134
7.3 Water depth comparisons with experimental data 136
7.4 Spatialisation of the observed tendencies using 3D simulations 139
7.5 Hydraulic jump investigation and recommendations for future experimental setups . . 146
7.6 Conclusion 149

7.1 INTRODUCTION

This chapter presents the reproduction of previously observed flow (Chapter 6) using the CFD open-source solver code_saturne, described in Chapter 3 and validated against the preliminary campaign dataset in Chapter 5. First, the validation of the numerical approach is performed on six new urban configurations. Then, previously observed tendencies are verified on a larger scale and preliminary results for the head loss coefficient related to urban parameters impact are proposed. Finally, the origin of the hydraulic jump and the influence of the setup geometry on the current dataset is discussed

The structure of this chapter is organised as follows: Section 7.2 presents the configurations studied, the mesh and provide detailed information concerning the simulation times. Then, Section 7.3 compares the results with experimental data at specific locations for validation purposes. Next, numerical results are used to validate tendencies observed with the experimental dataset (Section 7.4). Following, head-loss relations related to the urban areas impact on the flow are proposed. Finally, simulations are performed in Section 7.5 to investigate the origin of the hydraulic jump observed experimentally.

7.2 NUMERICAL REPRODUCTION OF SELECTED URBAN FORMS WITH CODE_SATURNE

Six selected urban forms studied in Chapter 6 are reproduced numerically. More precisely, two cases are studied with $n_x = 1$ ($1-05-2-10$ and $1-20-2-10$, where $l_x = 0.05$ and 0.10 m respectively) and all four cases with $n_x = 3$ ($3-05-2-10$, $3-10-2-10$, $3-15-2-10$ and $3-20-2-10$, where $l_x = 0.05, 0.10, 0.15$ and 0.2 m respectively). Both configurations are reminded in Figure 7.1. These case choices are made to cover both streets' number and width variation for a limited number of simulations.

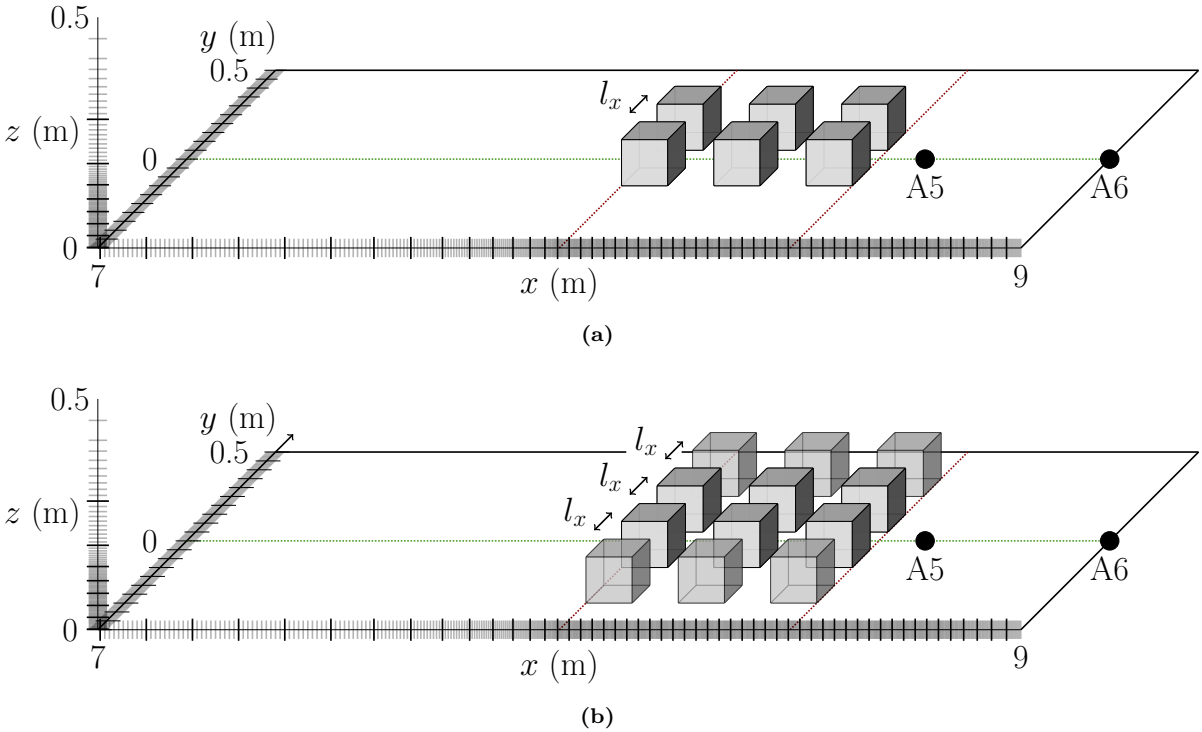

Figure 7.1: Schematic view of the studied configurations with (a) $n_x = 1$ and (b) $n_x = 3$. Each axis grey dash represents the centre of an individual cell, and each black dash is plotted every 10 cells for enhanced clarity. Position of probes A5 and A6 is also illustrated.

Since the positions of the obstacles have been modified compared to the preliminary study, the mesh presented was adapted and refined consequently along the x-axis ($7.5 < x < 8.6$ m). The resulting 9 million cells mesh is schematised in Figure 7.2. The resulting cells sizes in the obstacle area are $\Delta x = 0.0025$ m, $\Delta y = 0.005$ m and $\Delta z = 0.0025$ m. The same initial mesh is used for all configurations before extracting the obstacles.

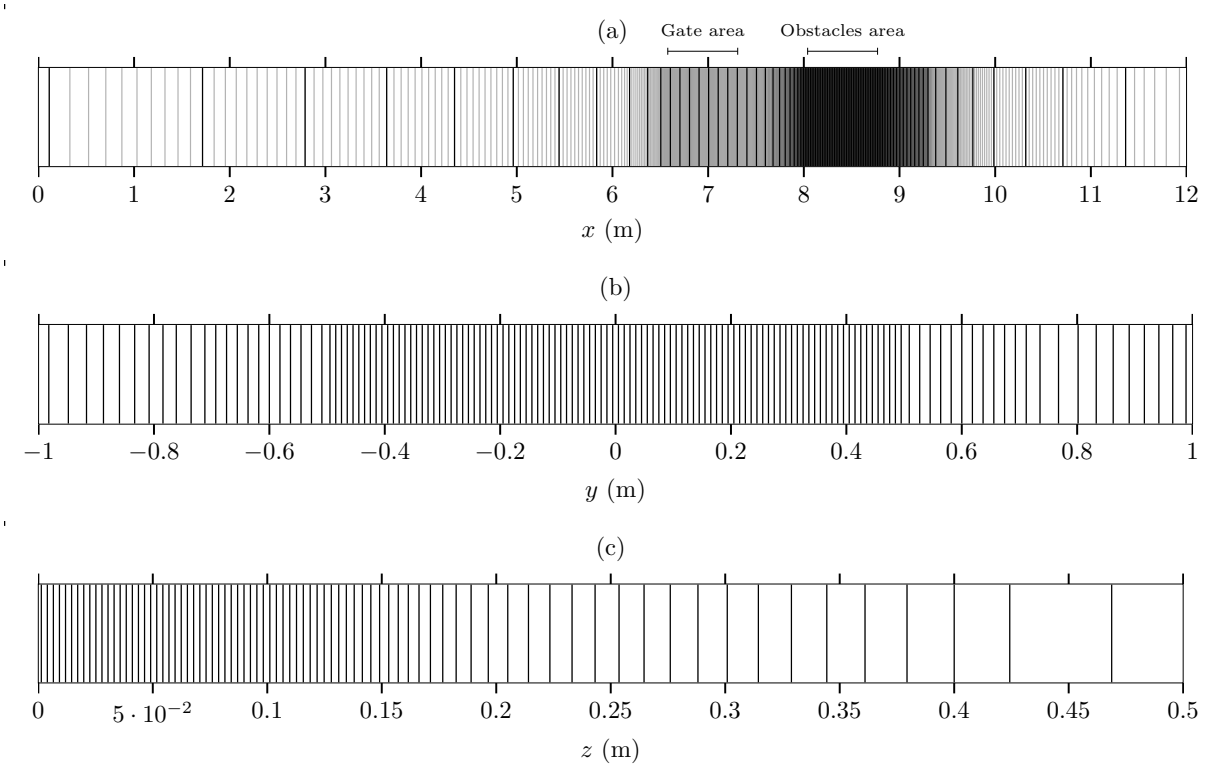

Figure 7.2: Numerical mesh refinement along the (a) x-axis, (b) y-axis and (c) z-axis. Each black line represents the centre of an individual cell, except along the (a) x-axis, where black lines are plotted every 10 cells for enhanced clarity.

Note : The mesh sensitivity study was performed and presented in Chapter 5 and has not been repeated, as the current mesh is more refined compared to the previous one.

The simulations were divided into two parts: the first two seconds ($0 < t < 2$ s), comprising the opening of the gate and the impact of the dam-break wave with the first row of obstacle, are first performed with a reference time step $\Delta t = 5 \cdot 10^{-4}$ s. As the fast transient phenomena happens in the first seconds, this simulations also allows for the control of numerical solution stability. Then, a restart is made until $t = 25$ s with a reference time step $\Delta t = 1 \cdot 10^{-3}$ s. The evolution of the time step, that varies over time to maintain the CFL condition under the unity, is illustrated in Figure 7.3 for case $3 - 10 - 2 - 10$. The computational times of all six cases are summarised in Table 7.1.

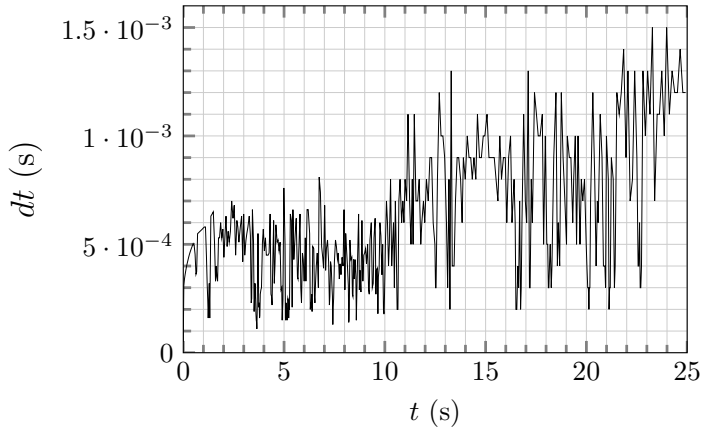

Figure 7.3: Evolution of the time interval for case $3 - 10 - 2 - 10$.

Table 7.1: Summary of the computational time for all studied urban forms.

Case	N_{cells}	$[t_{min}, t_{max}]$	Δt_{ref}	Nb proc	Total time	Total CPU time
$1-05-2-10$	9 462 720	[0, 2] s [2, 25] s	0.0005 s 0.001 s	414	1.2 hr 11 hr	507 hr 4448 hr
$1-20-2-10$	9 462 720	[0, 2] s [2, 25] s	0.0005 s 0.001 s	414	0.9 hr 12 hr	400 hr 4910 hr
$3-05-2-10$	9 373 920	[0, 2] s [2, 25] s	0.0005 s 0.001 s	420	0.9 hr 11.5 hr	359 hr 4809 hr
$3-10-2-10$	9 373 920	[0, 2] s [2, 25] s	0.0005 s 0.001 s	420	0.8 hr 9 hr	341 hr 3923 hr
$3-15-2-10$	9 373 920	[0, 2] s [2, 25] s	0.0005 s 0.001 s	420	0.9 hr 8 hr	400 hr 3460 hr
$3-20-2-10$	9 373 920	[0, 2] s [2, 25] s	0.0005 s 0.001 s	420	0.9 hr 7 hr	381 hr 3073 hr

7.3 WATER DEPTH COMPARISONS WITH EXPERIMENTAL DATA

As first part of the study, the numerical hydraulic variables of interest are studied downstream of the urban area. The water height variation along time is compared with the acoustic water depth measurements at position A5 and A6 for all cases.

Overall, the numerical simulation yields good water depth estimations downstream of the urban areas. The wave arrival time is correctly estimated as well as the water depth evolution along time. Some underestimation of the water depth can be observable, mostly at position A5 (Figure 7.4a, 7.5a, 7.7a). One possible reason is that the numerical water height h_{num} (defined in Chapter 3, equation 3.37) results from a post-processing of the void fraction α. This leads to a downward bias proportional to the volume fraction of air-mixed cells located under the free surface.

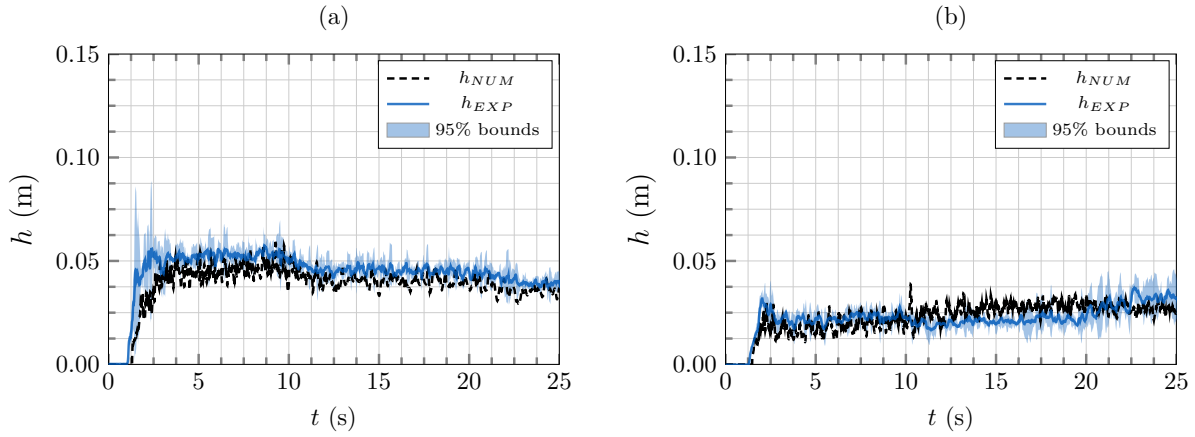

Figure 7.4: Case $3-15-2-10$. Water height comparison downstream of the urban area at positions (a) A5 and (b) A6 between wave gauge measurements (blue line) and the numerical model (black dashed line).

To complete the comparisons, Figure 7.6 illustrates at two different simulation times the void fraction downstream of the obstacles for case $1-20-2-10$. First, air-mixed cells located close to probe A5 ($x = 8.6$ m) are visible, which contribute to the underestimation of the flow water depth. Second, the numerical water height observed for A5 is closer to the expected value (for instance, 5 cm at t = 5 s). Moreover, for case $1-20-2-10$, the hydraulic jump observed in the experiments from t = 15 s, is visible 0.20 m downstream of probe A6 (Figure 7.6b), suggesting an underestimation of its numerical length.

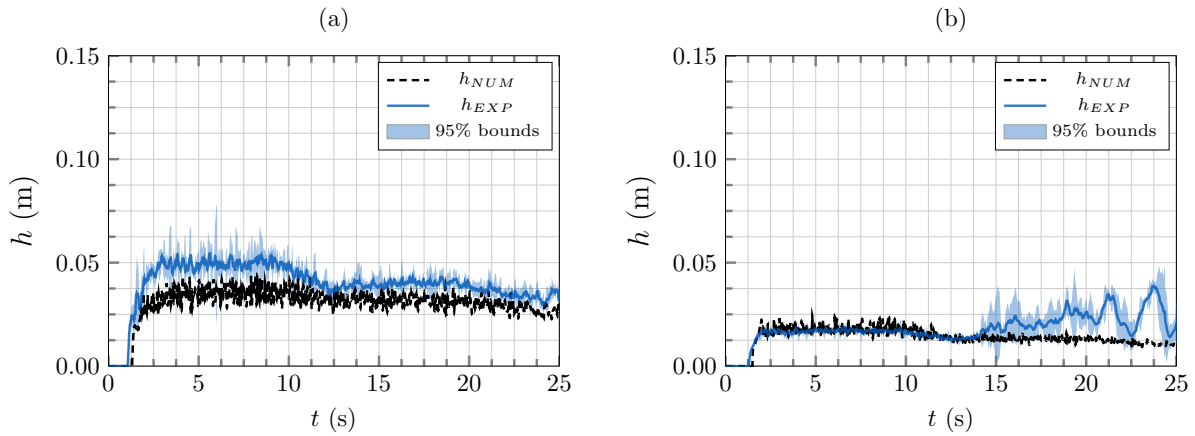

Figure 7.5: Case $1-20-2-10$. Water height comparison downstream of the urban area at positions (a) A5 and (b) A6 between wave gauge measurements (blue line) and the numerical model (black dashed line).

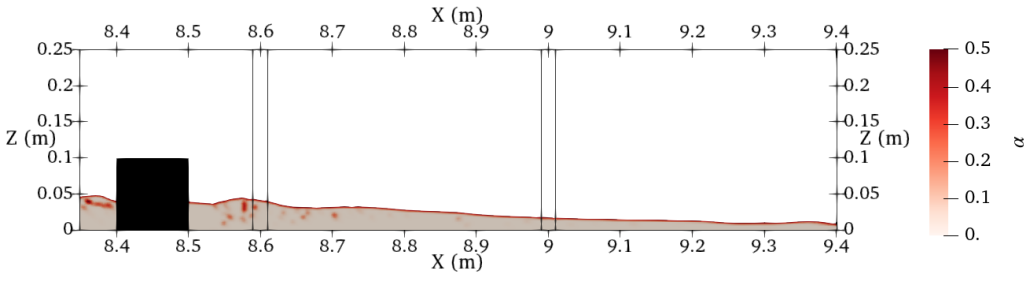

(a) $t = 5$ s

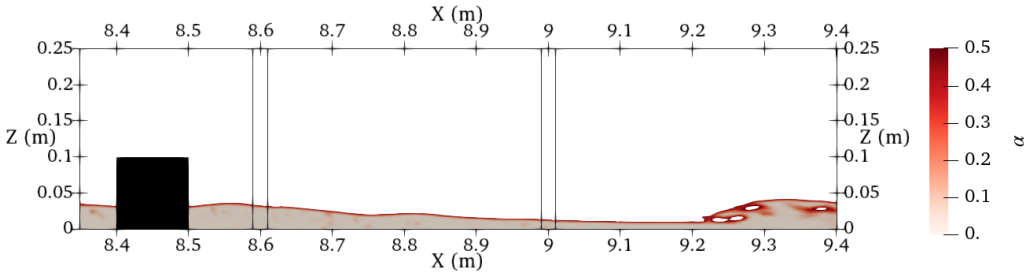

(b) $t = 20$ s

Figure 7.6: Void fraction distribution for case $1-20-2-10$ at (a) $t = 5$ s and (b) $t = 20$ s along $y = 0$. Black lines represents A5 and A6 position.

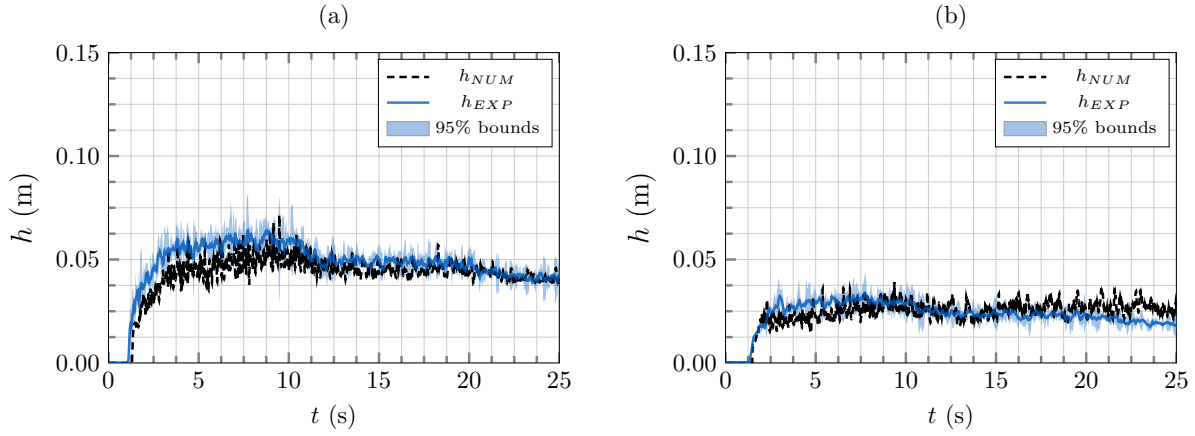

Figure 7.7: Case $3-20-2-10$. Water height comparison downstream of the urban area at positions (a) A5 and (b) A6 between wave gauge measurements (blue line) and the numerical model (black dashed line).

Figures 7.8, 7.10, and 7.11 present the water height comparison for narrower streets. Global observations suggest that the simulation had more difficulty in reproducing smaller water depths located downstream of the configuration. Indeed, the water small depth combined with the presence of air bubbles below the free surface yields to a more important underestimation of the 3D simulation at A5. Still, the general flow variation is predicted by code_saturne. Figure 7.9 suggests a numerical overestimation of the arrival time of the hydraulic jump at A6. However, the jump still arrives slightly later for cases $3-05-2-10$ and $1-05-2-10$. As for wider streets, the simulation of case $3-10-2-10$ was not able to reproduce the hydraulic jump arrival at A6 (Figures 7.11 and 7.12).

Temporal visualisations of a horizontal slice of the dam-break wave along $y = 0$ m are illustrated in Figure 7.13. The evolution of the maximum splash-up water depth and its shape is depicted and shows similarities with snapshots of the flow obtained with the IAM camera. Additionally, the evolution of the wake zone height is shown, with water rising from the outlet of the channel starting at $t = 2$ s and rising to the urban area. This justifies the sudden rise in water depth measurements that can be observed at positions A5 and A6.

From these comparisons, partial conclusions are made: first, simulations performed reasonably well on predicting the dam-break flow below the idealised urban areas. For further numerical investigations, two challenges arise. The first is the prediction of low water heights with presence of air bubbles (observed for narrower streets). The second is the correct prediction of the hydraulic jump arrival time for wider streets. Still, this phenomena appears as a consequence of the interactions between the flow and the channel; it does not prevent the following study on possible obstacle impact on the flow tendencies.

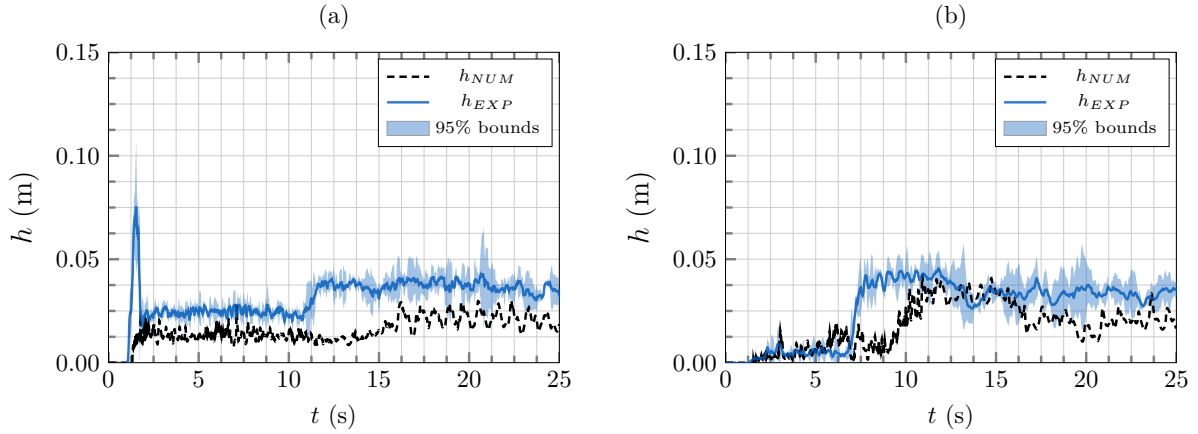

Figure 7.8: Case $1-05-2-10$. Water height comparison downstream of the urban area at positions (a) A5 and (b) A6 between wave gauge measurements (blue line) and numerical model (black dashed line).

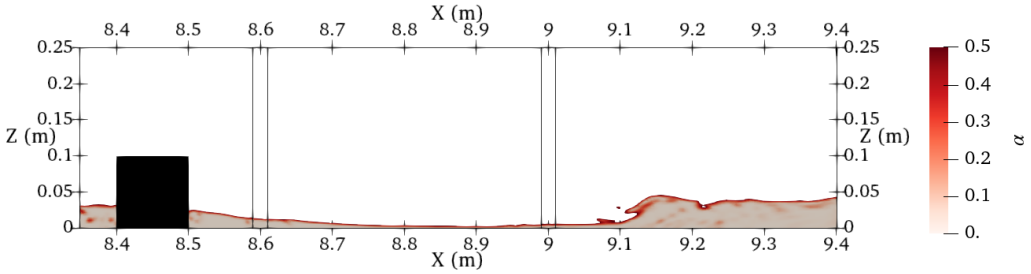

Figure 7.9: Void fraction distribution for case $1-05-2-10$ at $t = 9$ s along $y = 0$. Black lines represents A5 and A6 position.

Remark : The water height comparison at all probe positions for the studied cases are available in Appendix F.

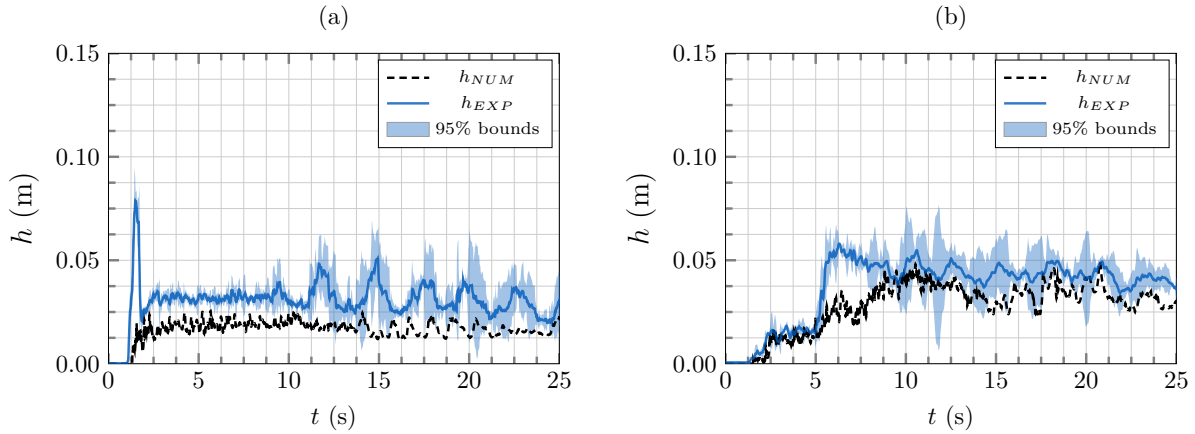

Figure 7.10: Case $3-05-2-10$. Water height comparison downstream of the urban area at positions (a) A5 and (b) A6 between wave gauge measurements (blue line) and numerical model (black dashed line).

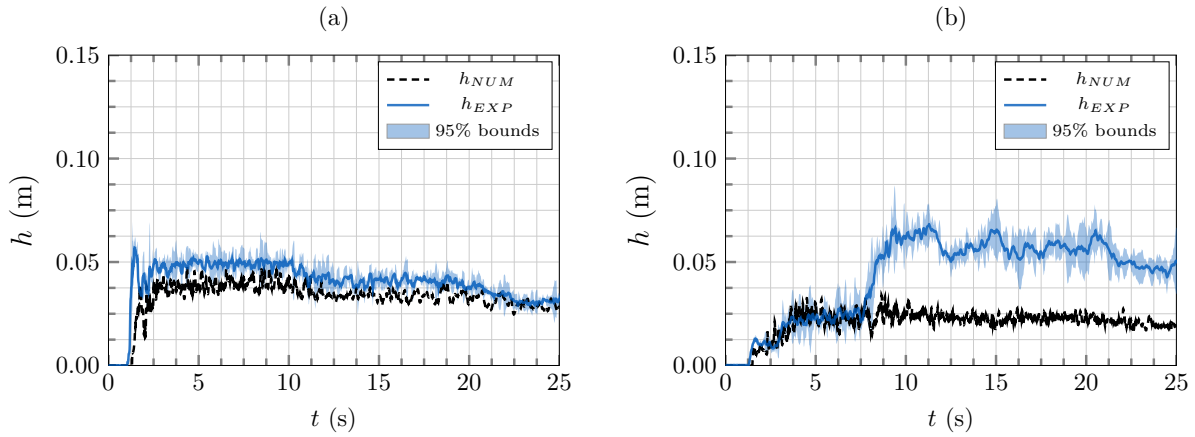

Figure 7.11: Case $3-10-2-10$. Water height comparison downstream of the urban area at positions (a) A5 and (b) A6 between wave gauge measurements (blue line) and numerical model (black dashed line).

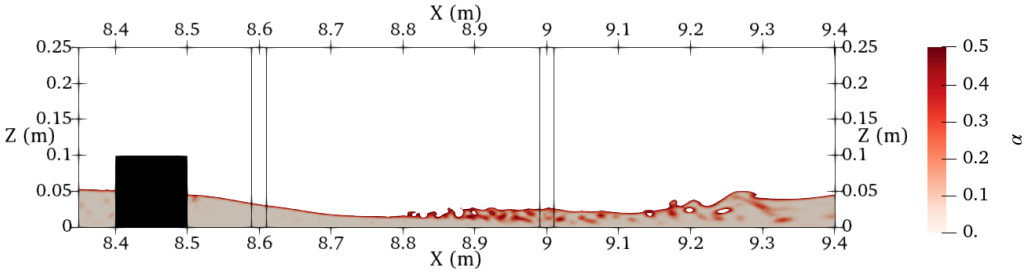

Figure 7.12: Void fraction distribution for case $3-10-2-10$ at $t = 20$ s along $y = 0$. Black lines represents A5 and A6 position.

7.4 SPATIALISATION OF THE OBSERVED TENDENCIES USING 3D SIMULATIONS

Given the validation of the numerical simulation on the experimental dataset downstream of the obstacles, this section focuses on providing additional flow information that cannot be measured. First, the numerical water depth profiles at various time steps will be compared with the experimental data to extend the point measurements. Then, the flow tendencies observed at specific points downstream of the urban areas in Chapter 6 will be verified spatially. This is done through the computation of the energy head variation integrated over a channel section related to different street widths.

Figures 7.14, 7.15, 7.16 and 7.17 compare the water depth profile between experimental and numerical data at four different time steps for cases with $n_x = 3$. For all tests, the numerical results show good agreement with the experimental data. This comparison enhances our understanding of the physical processes involved in a dam-break wave, notably within the several rows of obstacles. The depth profiles through the urban area tend to form a stair-step shape. Downstream of the urban area, the water depth decreases linearly until reaching a minimum value between positions A5 and A6. Afterwards, the water depth rises again.

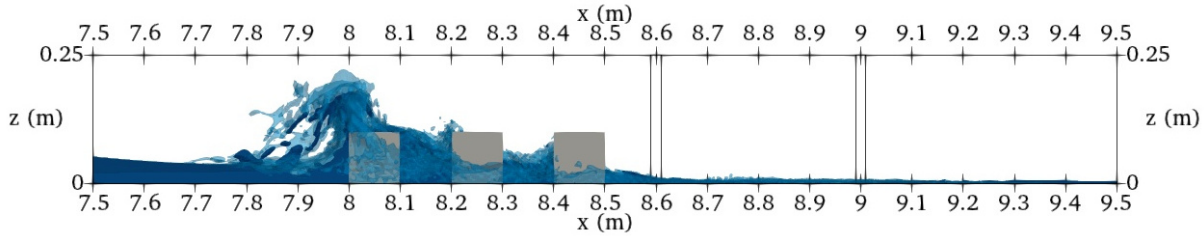

(a) $t = 2$ s

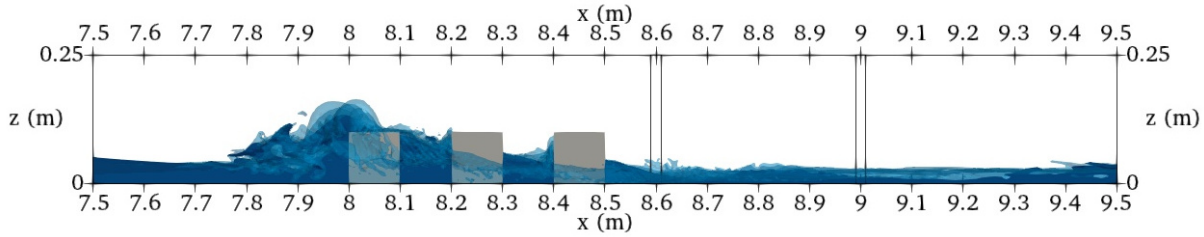

(b) $t = 4$ s

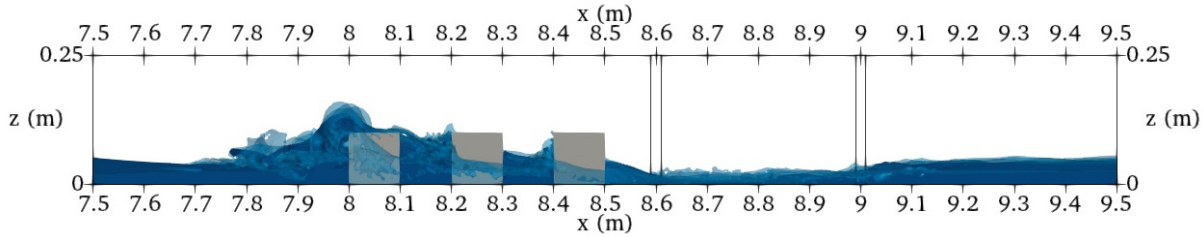

(c) $t = 6$ s

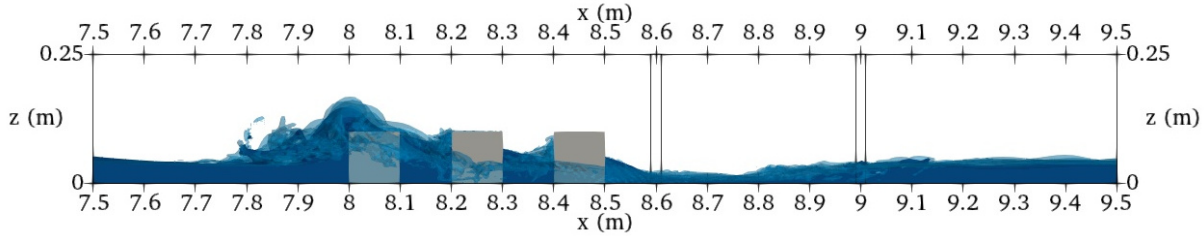

(d) $t = 8$ s

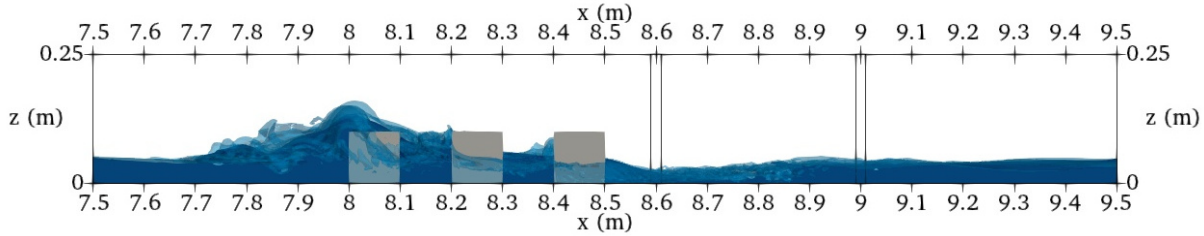

(e) $t = 10$ s

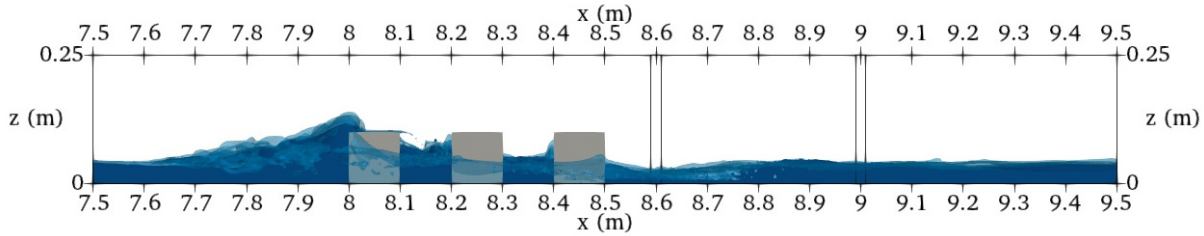

(f) $t = 12$ s

Figure 7.13: Water height visualisation (clear blue) at different time steps for case $3-05-2-10$ (side view). Black lines represents A5 and A6 position. Grey surfaces represents the cube. Dark blue surfaces corresponds to $y = 0$ m and $\alpha \leq 0.5$.

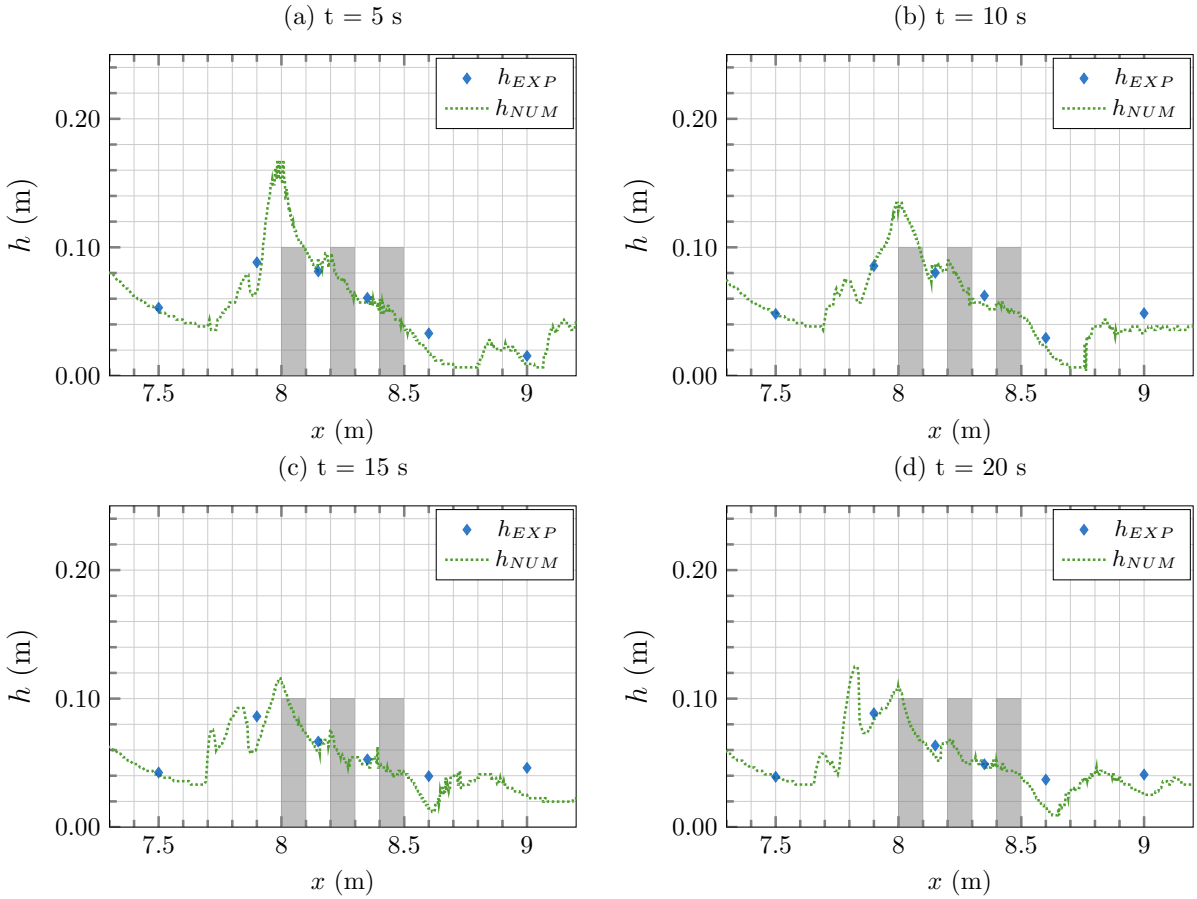

Figure 7.14: Water depth profile for case $3-05-2-10$ at four different time steps.

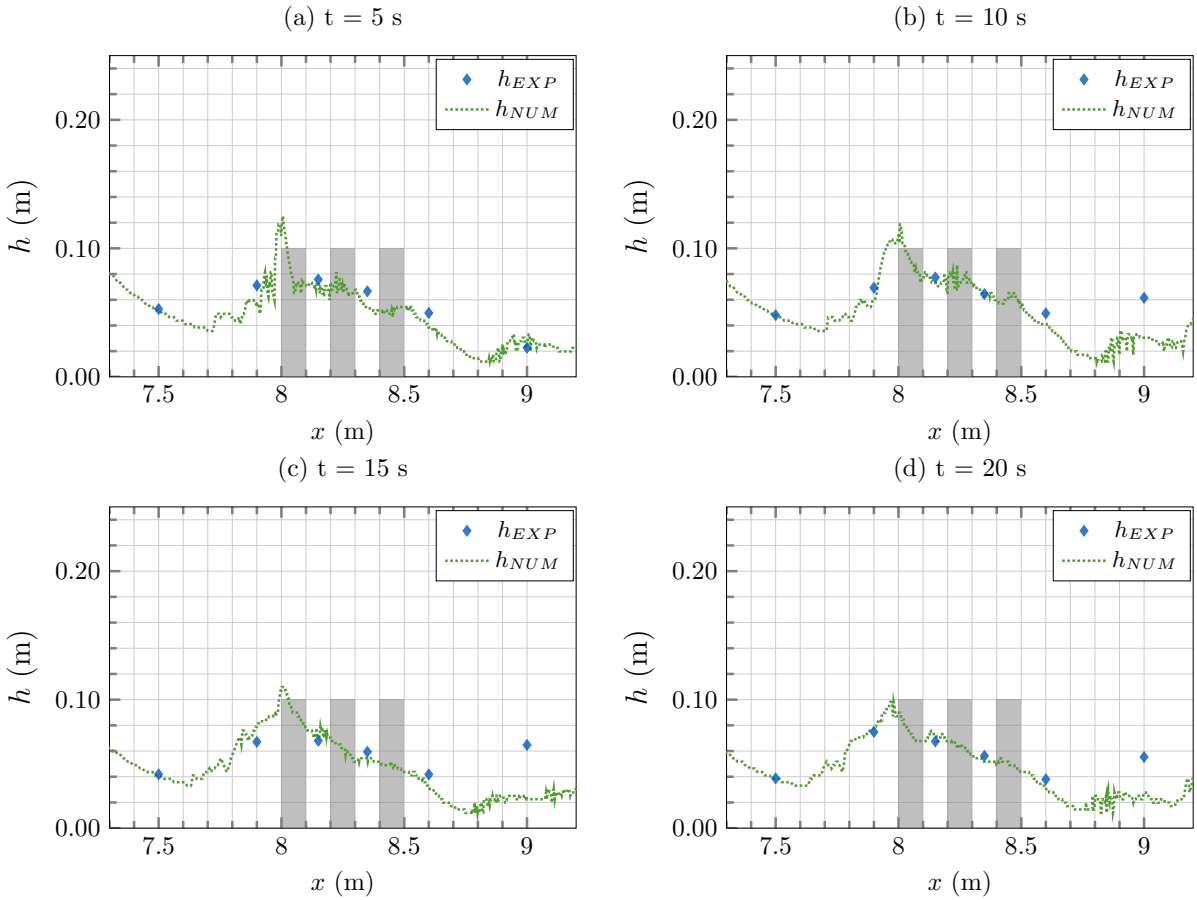

Figure 7.15: Water depth profile for case $3-10-2-10$ at four different time steps.

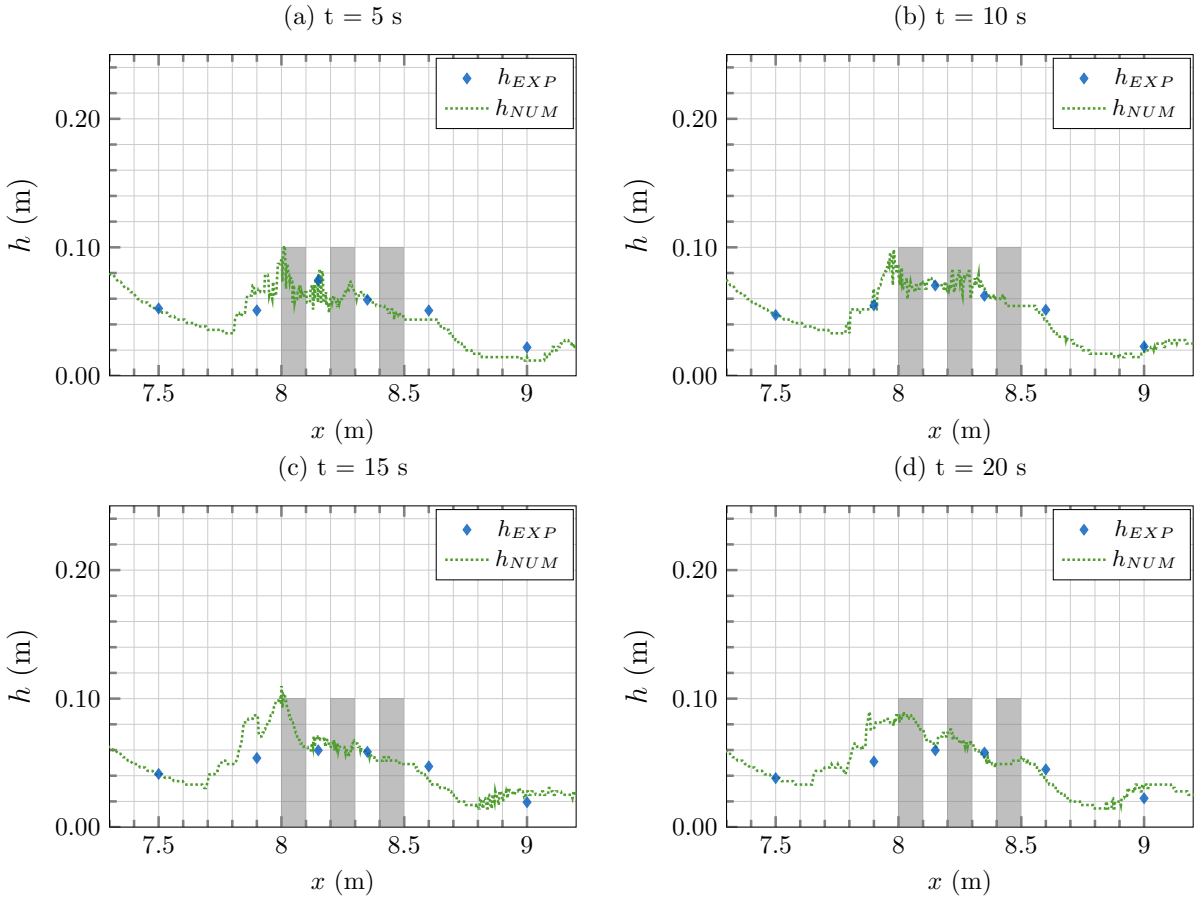

Figure 7.16: Water depth profile for case $3-15-2-10$ at four different time steps.

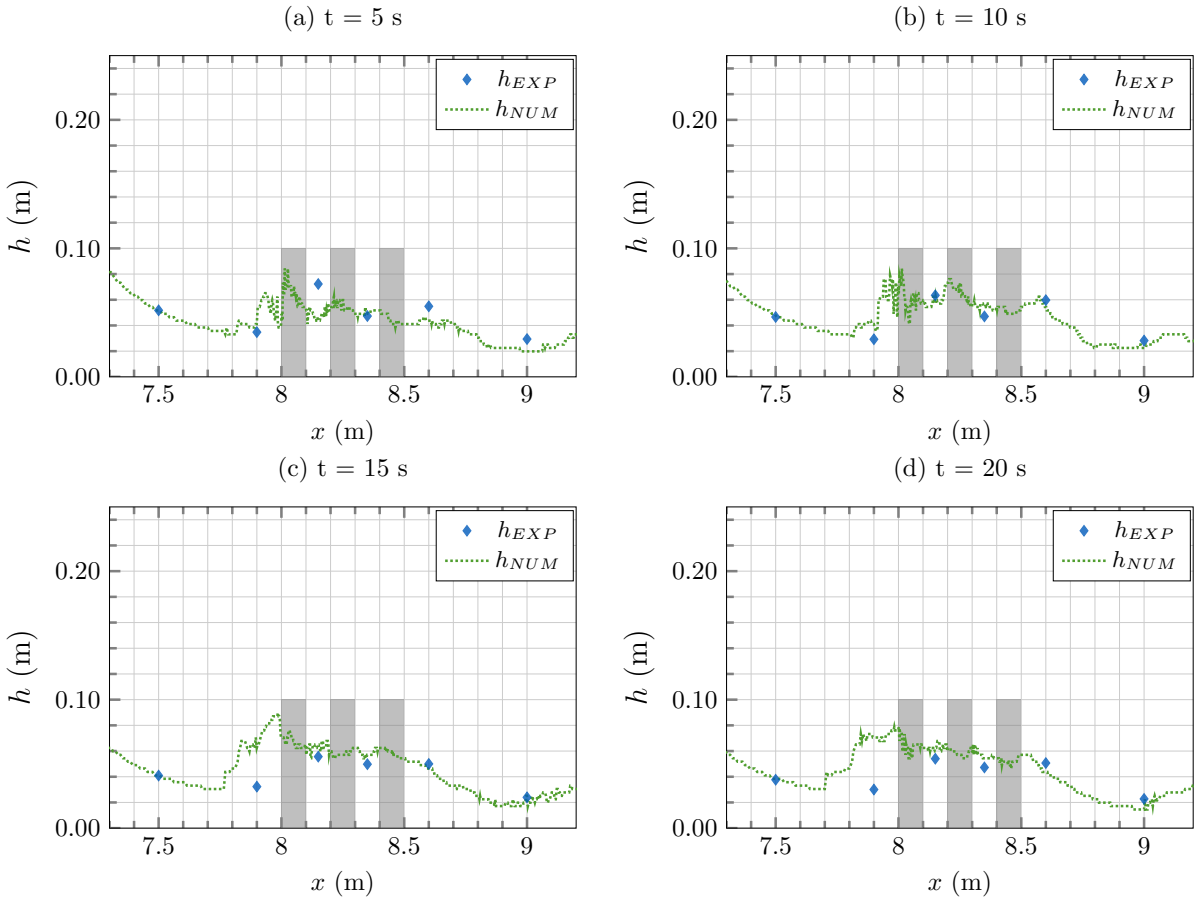

Figure 7.17: Water depth profile for case $3-20-2-10$ at four different time steps.

To quantify the impact of the urban parameters on the flow, the energy head downstream of the urban area was investigated through experiments in Chapter 6. A local tendency was observed at position A6: the energy head increases for wider street widths, independently of the number of streets. The performed 3D simulations are used here to verify this trend through the analysis of energy head profiles at x = 9 m (downstream of the urban area, corresponding to the x coordinate of position A6).

Results are presented in Figures 7.18 and 7.19 at four different times for cases with $n_x = 3$ and two extreme cases with $n_x = 1$ ($l_x = 0.05$ and 0.20 m). The shape of the energy head profile is similar across all time steps. The effects of the reflection wave on the side walls of the channel can be observed. In the central urban zone ($-0.5 < y < 0.5$), the same effect of the street width on the energy head can be observed. As calculated experimentally, narrower streets lead to lower energy heads.

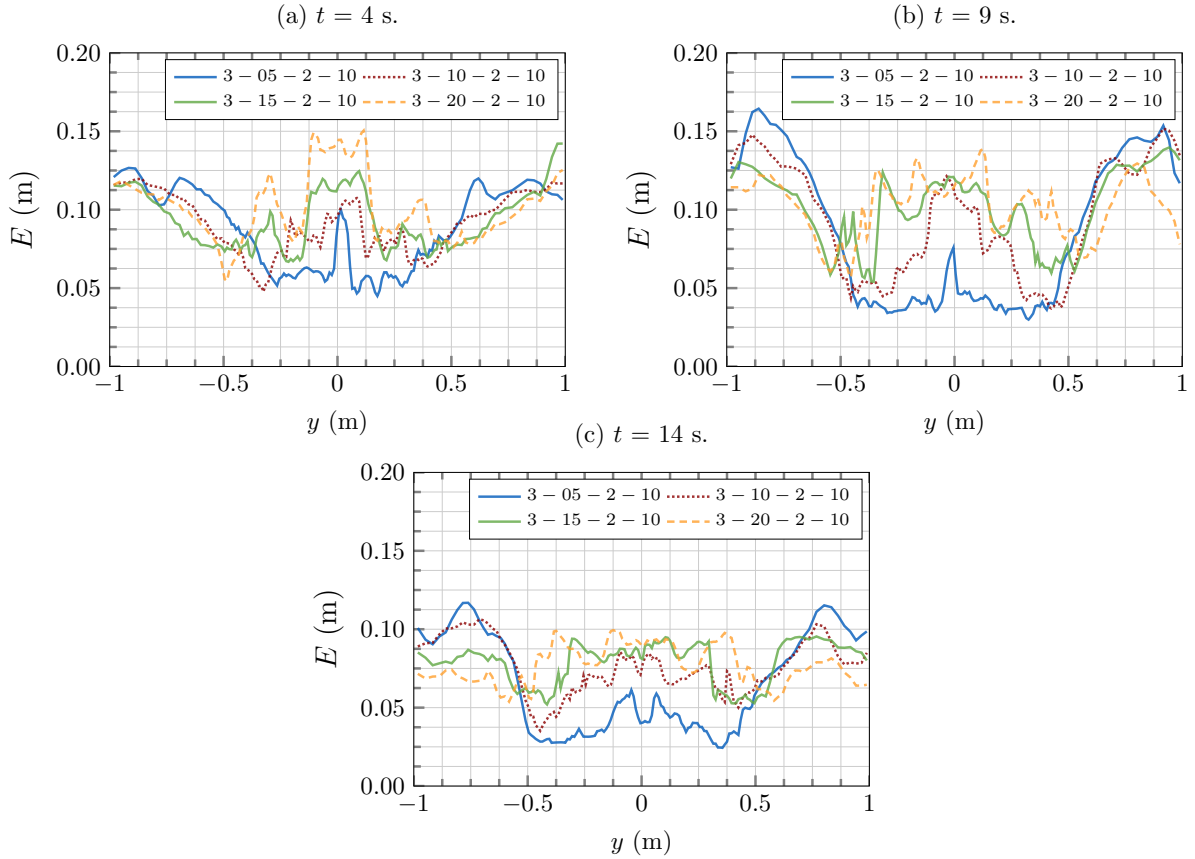

Figure 7.18: Energy head E profiles along $x = 9$ m for cases with $n_x = 3$ at three different time steps.

To better quantify this impact, the energy head is integrated between $-0.5 > y > 0.5$ and compared across the four street width cases. This area was precisely chosen to avoid the effects of the reflection zone close to the walls, phenomena mostly related to the experimental setup. Figure 7.20 presents the section energy head ($\langle E \rangle$) related to the street widths at three coordinates along x. The different positions have been selected to evaluate the influence of the distance from the urban area on the expected head tendency. Two profiles are aligned with positions A5 ($x = 8.6$ m) and A6 ($x = 9$ m) and the third is placed midway between them ($x = 8.8$ m). For all cases, the section energy head increases with street width. This variation confirms local observations performed with the experimental dataset. The different times studied and the distance do not affect the overall head variation.

Figure 7.21 illustrates the impact of the number of streets on the spatially averaged energy head ($\langle E \rangle$) at x = 9 m. Similar to the cases with $n_x = 3$, the section energy head increases with the street width for cases with $n_x = 1$, for all times studied. Light differences are observed here as for narrow streets, the energy head value of case $n_x = 1$ is higher than for 3 streets. The opposite is observed for wider streets.

To conclude on these observations, using CFD to spatialise a local experimental tendency is the first step towards extracting generalisable information about the impact of urban areas on flow.

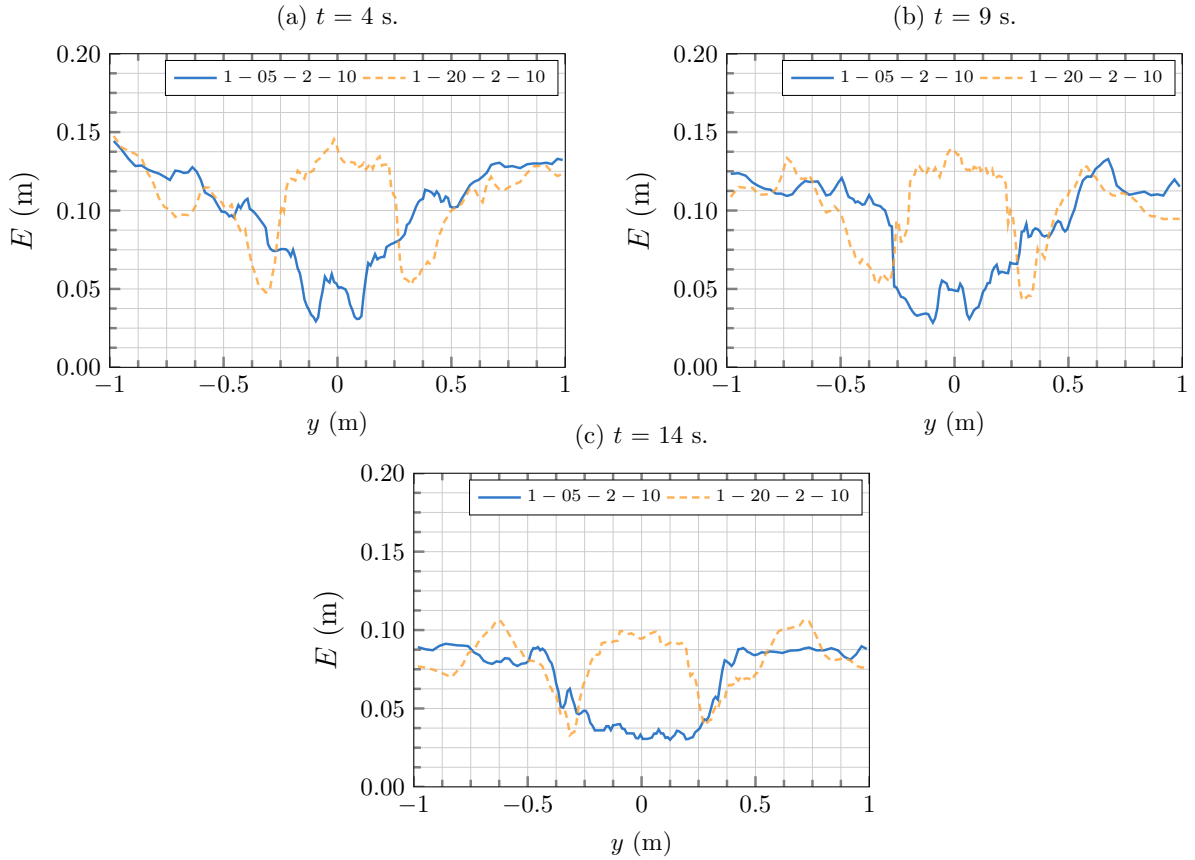

Figure 7.19: Energy head E profiles along $x = 9$ m for cases with $n_x = 1$ at three different time steps.

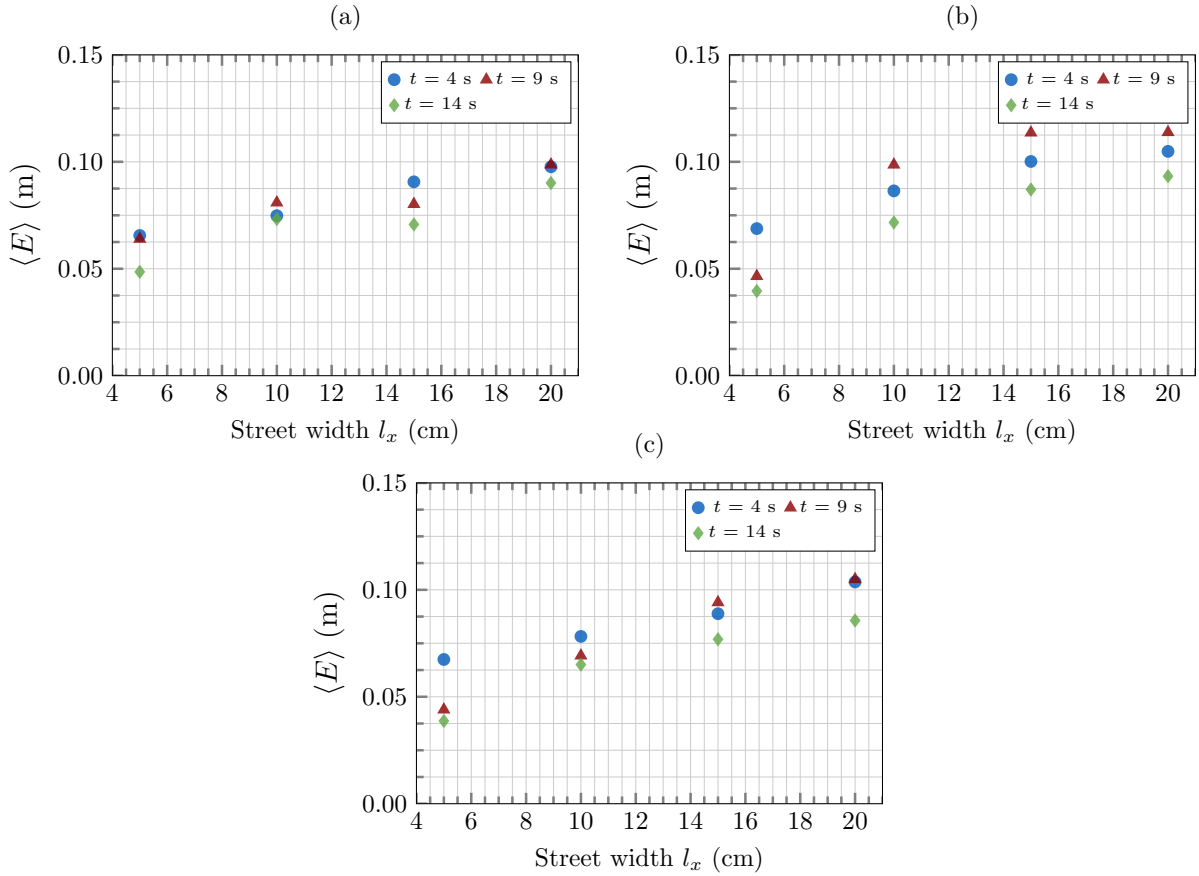

Figure 7.20: Cases $n_x = 3$. Spatially averaged numerical energy head $\langle E \rangle$ between $-0.5 > y > 0.5$ along (a) $x = 8.6$ m, (b) $x = 8.8$ m and (c) $x = 9$ m at three different time steps.

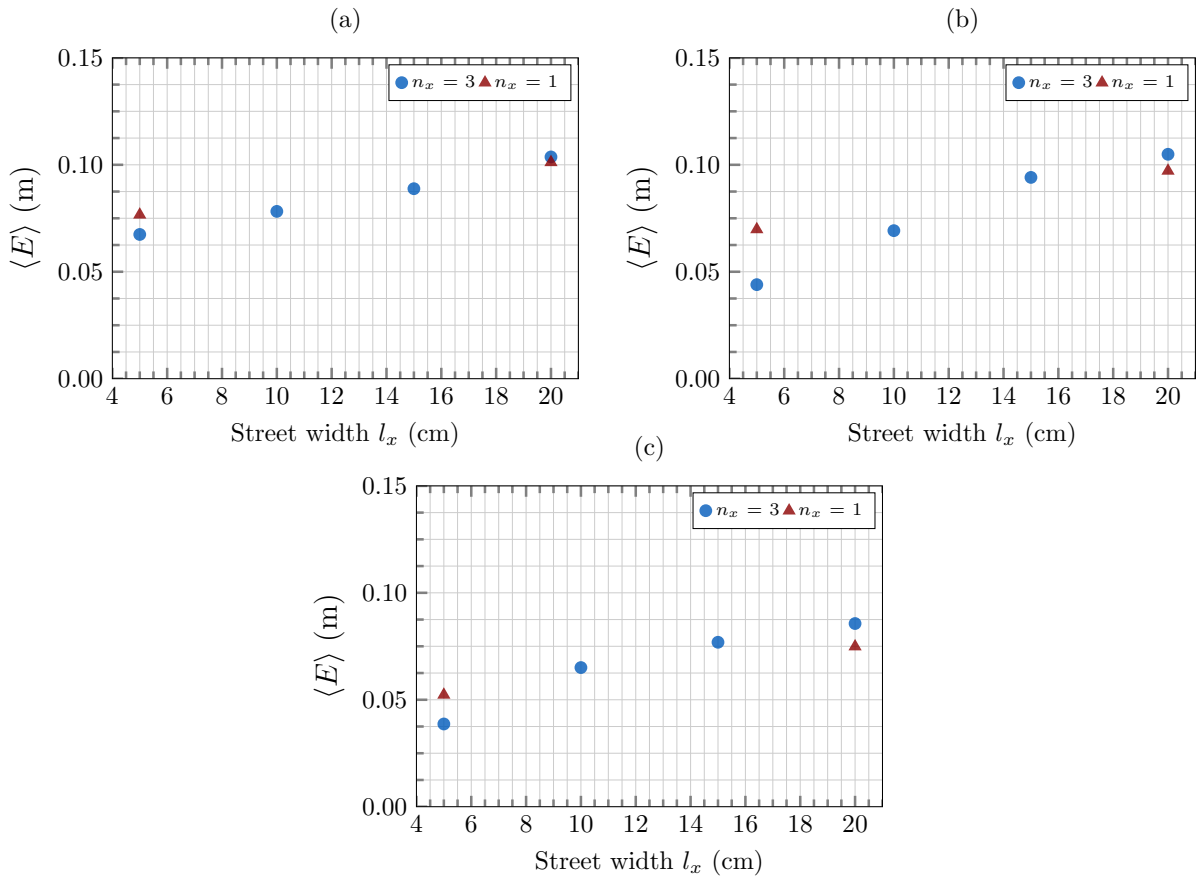

Figure 7.21: Street number impact on the spatially averaged numerical energy head $\langle E \rangle$ between $-0.5 > y > 0.5$ along $x = 9$m at (a) $t = 4$ s, (b) $t = 9$ s and (c) $t = 14$ s.

Thesis Question No. 2:
Are Computational Fluid Dynamics (CFD) models sufficiently mature to reproduce such phenomenon and to provide accurate complementary data on the flow characteristics?

The 3D numerical simulations performed using the open-source solver code_saturne demonstrated good results in reproducing fast transient flow through different obstacle configurations. Due to the complexities associated with measuring transient flows and the limited number of point measurements, CFD appears as an important tool for completing experimental datasets with non-measured or inaccessible hydraulic variables. For example, point-based water depth measurements can be spatialised using numerical data to obtain profiles and enhance our understanding of the complex phenomena. Also, simulations can be used to extend the number of tested configurations, which are experimentally limited due to geometrical and time constraints. Still, some limitations may be highlighted, such as the non negligible computational cost of such simulations. Several areas for improvement may be listed: a better definition of the numerical air-water interface, the reduction of the computational time using the one-fluid VOF technique, and a better estimation of the splash-up and wake extent.

Thesis Question No. 3:
Can one extract generalised trends from various idealised urban layouts and apply them to engineering flood models?

Analysis on the experimental data, combined with numerical simulations appears as a complementary methodology in order to identify possible trends on a given flow topic.

As example in this thesis, the energy head variation related to the urban street widths was first observed experimentally. Given the used metrology, the tendency was only extracted locally, downstream of the configurations. Later, validated numerical simulations allowed for its confirmation, through the study of an integrated head over different sections. To go further, the given tendency shall be translated, if possible, in terms of dimensionless quantities. For instance, Figure 7.22 presents the evolution of the ratio of the section head evaluated at x = 9 m, denoted E_{A6} and the one upstream of the obstacles, at x = 7.5 m, denoted E_{A1}. Excluding results for $t = 14s$, where the presence of the hydraulic jump may interfere, a law for the flow head loss across the obstacle configuration could be proposed. However, due to time constraints, not enough simulations were performed to elaborate a complete 2D model for the head-loss, but such action appears as a promising perspective.

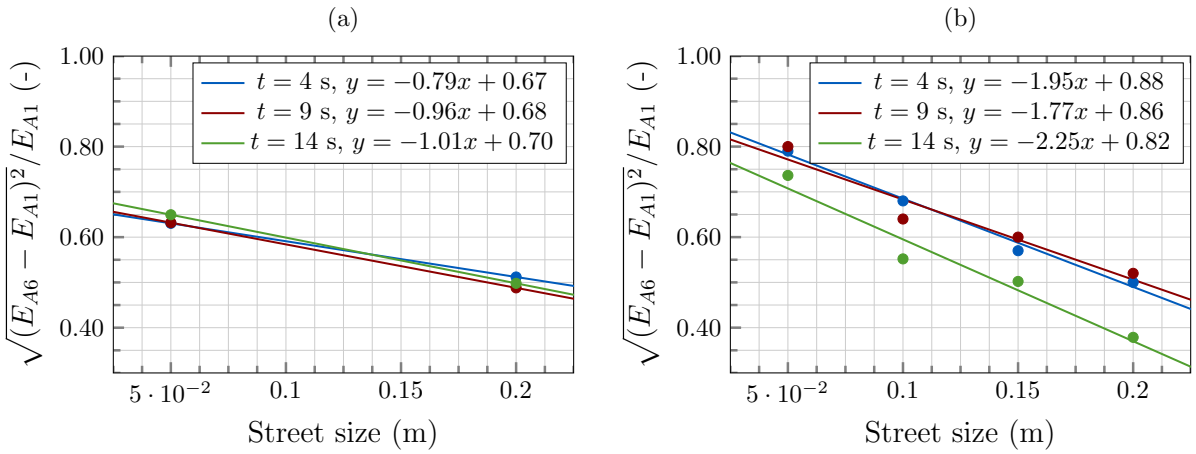

Figure 7.22: Relative difference of the integrated energy head ($\sqrt{(E_{A6} - E_{A1})^2}$ / E_{A1} [-]) over sections A6 and A1 related to the street size for cases (a) $n_x = 1$ and (b) $n_x = 3$.

7.5 HYDRAULIC JUMP INVESTIGATION AND RECOMMENDATIONS FOR FUTURE EXPERIMENTAL SETUPS

Finally, the origin of the hydraulic jump is investigated in this section. Figure 7.23 illustrates the numerical water depth patterns at the area downstream of the obstacles. Three different time steps are studied for both narrow and wide street cases. Due to the higher blockage effect of narrower streets, the flow for case $3-05-2-10$ is strongly diverted to the sides of the urban area. This leads to the formation of a wake zone with a lower water depth downstream. As consequence of the observed deviation, an accumulation of water appears at the end of the channel. This phenomenon grows over time until it completely fills the wake zone. In contrast, it seems to be mitigated in wider street cases, where more important flow cross the urban area.

The growth of the hydraulic jump seems directly influenced by the side walls of the channel and the resulting reflection zone. In the narrow street case, the flow rate passing through the urban area is not sufficient to avoid the water accumulation downstream. To confirm this hypothesis, an additional simulation is performed without side walls. To do so, the domain faces at y = -1 and 1 m, with $x > 7.05$ m, are defined as outlets. Two urban forms with narrower streets, where an hydraulic jump was observed, are modelled: $1-05-2-10$ and $3-05-2-10$.

Figures 7.24 and 7.25 show the water depth variation downstream of the urban area for cases $1-05-2-10$ and $3-05-2-10$, respectively, in the actual experimental setup and with side walls modelled as free outlet. Without side walls, the water accumulation downstream of the obstacles disappears along with the reflection zone.

Figure 7.26 illustrates the water depth patterns downstream of case $1-05-2-10$ with and without side walls. The reflection zone disappears, along with the water accumulation that develops over time. This clearly highlights the undesired effect of the side walls on the presented experiments.

Case $3-05-2-10$. **Case** $3-20-2-10$.

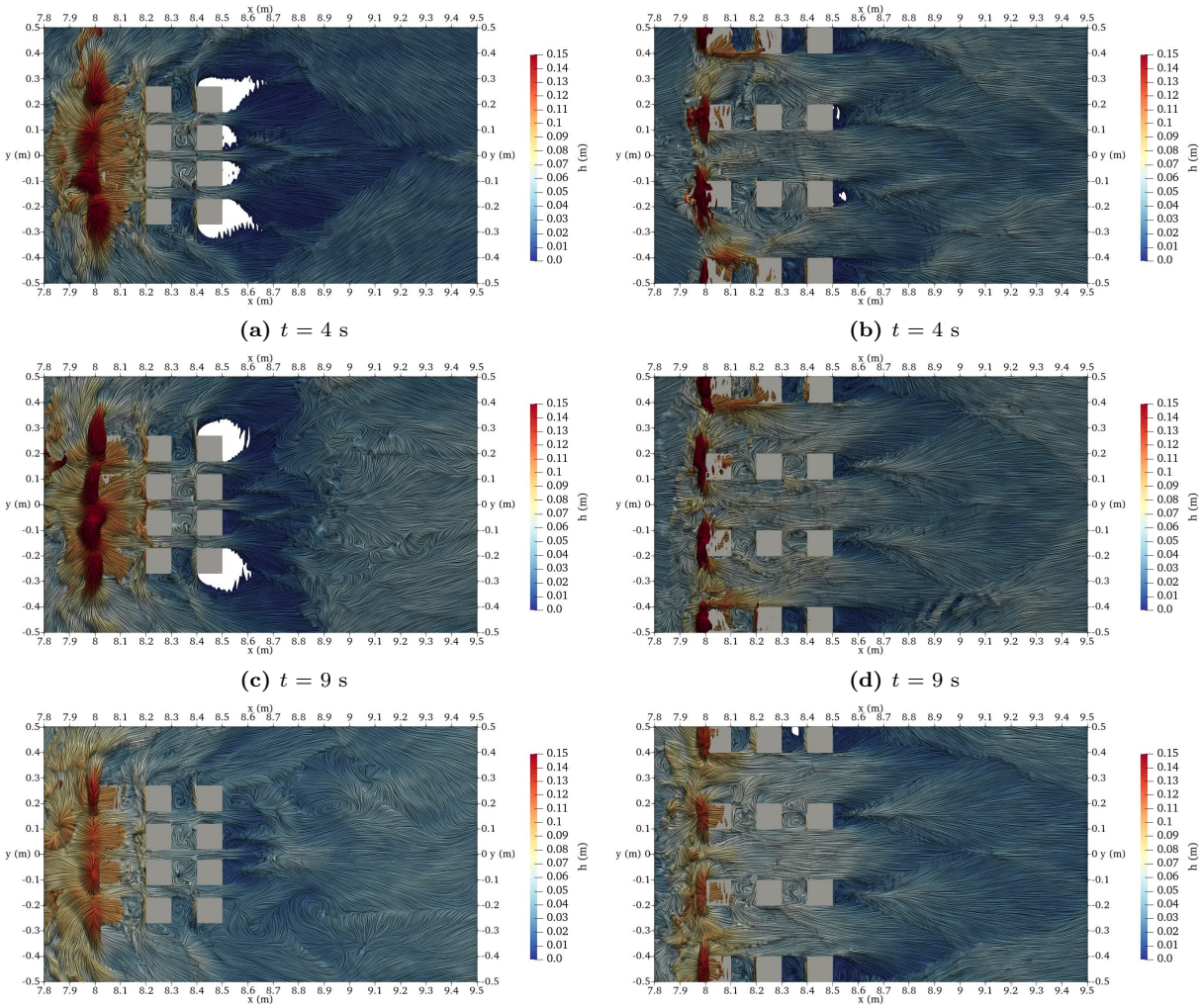

(a) $t = 4$ s **(b)** $t = 4$ s

(c) $t = 9$ s **(d)** $t = 9$ s

(e) $t = 14$ s **(f)** $t = 14$ s

Figure 7.23: Water depth visualisation for cases (left) $3-05-2-10$ and (right) $3-20-2-10$. (Top view) at (a) $t = 4$ s, (b) $t = 9$ s and (c) $t = 14$ s for $\alpha \leq 0.5$.

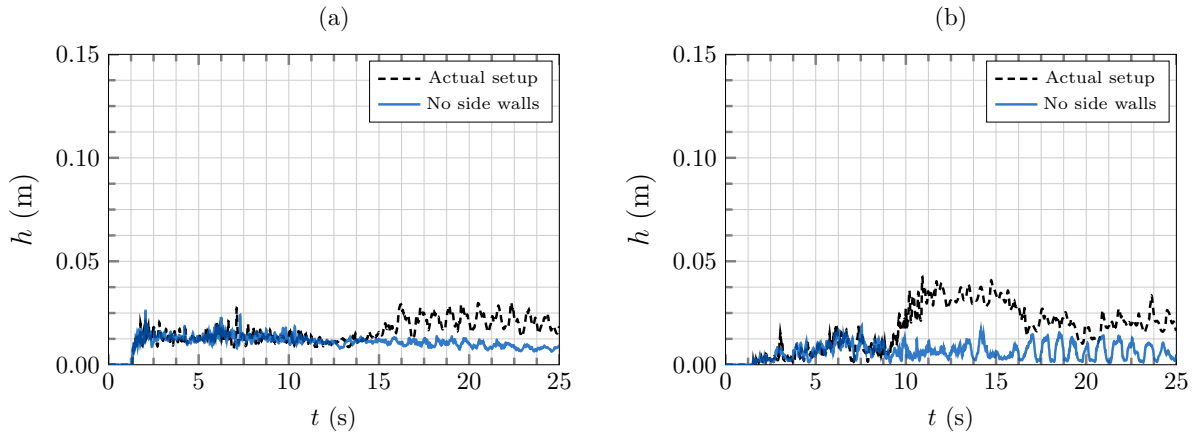

Figure 7.24: Water depth comparison for case $1-05-2-10$ with and without channel side walls at position (a) A5 and (b) A6.

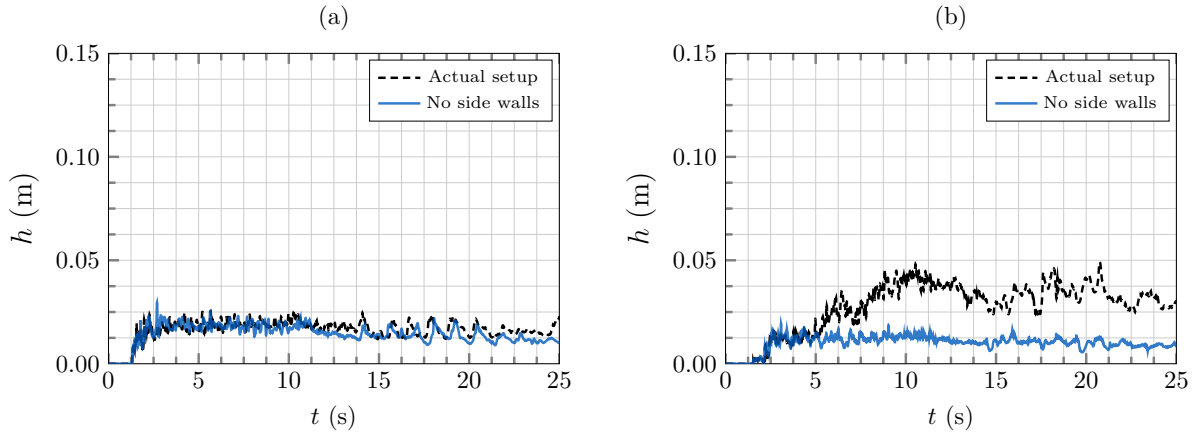

Figure 7.25: Water depth comparison for case $3-05-2-10$ with and without channel side walls at position (a) A5 and (b) A6.

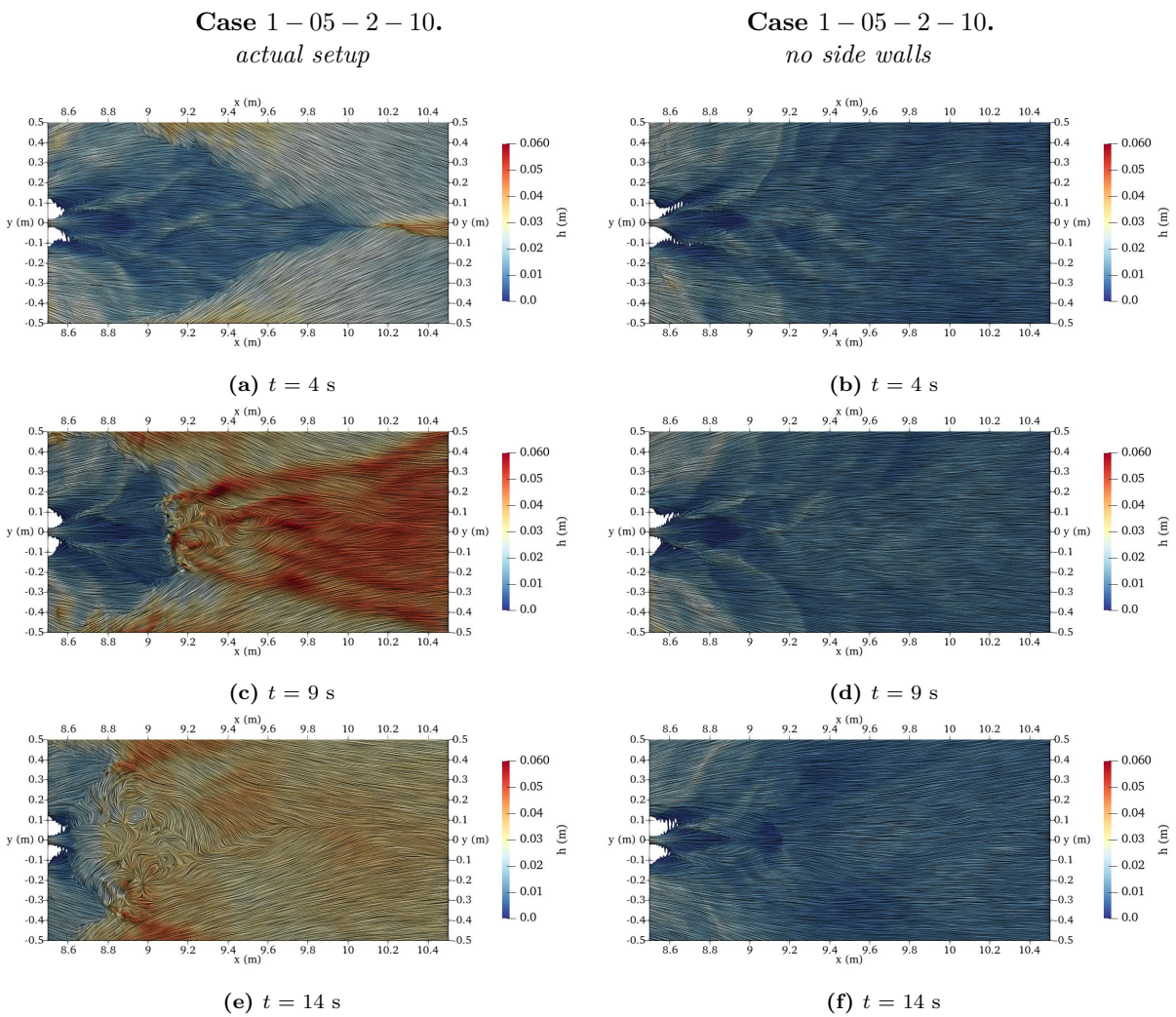

Figure 7.26: Water depth visualisation for case $1-05-2-10$ (top view) at (a) $t = 4$ s, (b) $t = 9$ s and (c) $t = 14$ s for $\alpha \leq 0.5$.

In summary, the hydraulic jump is justified by the setup geometry, and its effect on the hydraulic variables of interest should not be considered in our parametric study. Its presence in some of studied cases could have been prevented by generating a total dam-break wave (as discussed in Chapter 2) or by employing a wider channel. When sizing an experimental setup for studying dam-break flow in an urbanised area, a compromise must be made between having a channel wide enough to add various configurations, a breach size that allows for sufficiently long flow conditions, and a preparation time short enough to perform repetition of the cases. Once validated, numerical models can also complement experimental studies over longer time intervals by preventing the apparition of the hydraulic jumps.

Nevertheless, the numerical reproduction of the hydraulic jump's time of arrival in the wake zone, as it is directly linked to the flow conditions downstream of the urban area, can be useful for validating numerical models as a supplementary physical phenomenon. In this thesis framework, the hydraulic jump affected positions A5 and A6 for few configurations. The impact of urban parameters on the flow can still be assessed before it occurs or as the flow tends towards steady behaviour.

7.6 CONCLUSION

This chapter presented 3D numerical simulations of six experimental studied cases. A focus on the impact of the street width on the energy head downstream of the configuration was made.

Numerical results were first validated through local water depths comparisons downstream of the urban areas, showing a good agreement with the experimental results. Examples of complementary information were provided such as water depth profiles at different time steps and the spatial distribution of the energy head downstream of the urban area. Besides providing continuous flow data, the tendency observed locally in Chapter 6 was confirmed. Indeed, the spatially averaged energy head downstream of the urban areas increases with the street width.

Lastly, the hydraulic jump phenomenon observed both experimentally and numerically was investigated. The models highlighted that the setup geometry is responsible for the apparition of several processes downstream of the obstacles allowing the grow of an hydraulic jump in the measurement. Additional simulations could be performed on the studied cases by adding outlet boundary conditions to avoid the hydraulic jump and analysing the head loss coefficient evolution over longer periods.

8

GENERAL CONCLUSION AND PERSPECTIVES

Contents

8.1 Contributions and findings **151**
8.2 Perspectives **152**
8.2.1 Dam-break flow experiments 152
8.2.2 Numerical aspects 153

The present thesis work, detailed in this manuscript, can be divided in three research axes. The first was to develop an experimental setup to study dam-break flow through different obstacle configurations. The employed setup geometry, measurement techniques and post-processing methods were precisely chosen following a literature review and preliminary 2D numerical simulations to be adapted to fast transient flows. Once the experimental setup methodology and repeatability validated, the influence of urban parameters on the flow was investigated, focusing on different flow quantities of interest downstream of the urban area. Finally, 3D numerical simulations of the tested cases were performed: first, the numerical results were compared to the experimental ones for validation purposes, and then the capability of these models to supplement experimental datasets was demonstrated. Several tendencies regarding the impact of urban parameters on the flow were extracted from the combined experimental and numerical results.

Section 8.1 concludes on the main contributions and findings of the thesis and Section 8.2 highlights possible experimental improvements and provide perspectives for future study.

8.1 CONTRIBUTIONS AND FINDINGS

During the first stage of this work, an experimental setup was developed to reproduce simplified dam-break waves with adapted metrology to measure the fast processes between a flood wave and obstacle configurations. The design choices for the bench were based on a literature review that combined two hydraulic research topics: dam-break waves and steady urban flooding experiments. Additionally, 2D numerical simulations using TELEMAC-2D were employed to determine the breach width and the positioning and sizing of the obstacles. The setup's opening system was designed to enable repeatable breach openings, controlled initial conditions, and synchronised acquisitions across all metrology devices. The associated acquisition program was also developed specifically for these experiments using NI LabVIEW. Furthermore, three measurement techniques were adapted and used to retrieve hydraulic variables of interest. First, Large-Scale Particle Image Velocimetry (LSPIV) was applied to retrieve a new free-surface instantaneous velocity database within and around the urban areas. Additionally, a high-frequency laboratory camera was used to record the impact process between the dam-break wave and the first row of obstacles. A post-processing method was developed using NI LabVIEW to measure the height and the shape of the splash-up. The new program can be reused for future free-surface image detection. Finally, punctual water height measurements were taken upstream of the breach as well as within and around the urban areas. The experimental setup was first tested on simple obstacle geometries for validation, and the preliminary campaign demonstrated its ability to generate accurate and reliable measurements of unsteady phenomena.

Feedback from the first experimental campaign led to some modifications and improvements of the experimental protocol, resulting on a second campaign that focused on the impact of several urban parameters on the flow. A total of 21 urban forms were tested, based on four parameters: the number of streets n_x, n_y and their widths l_x, l_y along the x and y directions respectively. First, to better understand the impact of these parameters on the physical processes involved, snapshots of the water-jet impact, water depth evolution across the urban area, and free-surface patterns were analysed. For example, the temporal evolution of the flow velocity along the longitudinal streets was observed, as well as the different shapes of the splash-up depending on the street size. These observations improve the physical understanding of shallow dam-break flow through various obstacle configurations.

An analysis was then performed on the flow evolution downstream of the urban area, to possibly identify correlations related to the studied urban parameters. This could be useful to support and improve larger scale engineering flood models. To do so, the energy head was calculated at two positions, using water depth measurements combined with free-surface velocity data extracted from the LSPIV fields. Results and discussions suggest that the most influential parameter on the flow is the street width l_x. For instance, the head loss related to the configuration increases for smaller street widths. Another part of the study focused on less influential parameters: the number n_y and the width l_y of the cross streets, to analyse the impact of representing simplified urban areas without cross streets in numerical models. The analysis showed that the cross streets have a low impact on the downstream energy head unless the cross street width l_y is greater than the longitudinal street width l_x. The resulting large dataset is reliable and accurate for modelling validation. From a practical point of view, this parametric study may guide the design of new developments in floodplains. Indeed, the overwhelming influence of street width (l_x) on

the energy head downstream of the configuration sustains further analysis notably on the proposition of simplified laws.

Finally, 3D numerical simulations were performed to reproduce the measured data for a selection of test cases using the Computational Fluid Dynamics (CFD) open-source solver code_saturne, enhanced with the Volume-of-Fluid (VOF) technique. First, the model was validated against simple obstacle geometries from the preliminary experimental study. A mesh and turbulence closure model sensitivity analysis were performed, justifying for the choice of the final numerical parameters. The importance of taking into account the opening system to reproduce the experimental hydraulic conditions was also demonstrated. The VOF technique showed good results when compared to preliminary experimental datasets. Following the second experimental campaign, six configurations from the parametric study were numerically reproduced, focusing on the impact of street width in the main flow direction (l_x). Again, 3D simulations accurately reproduced the flow processes notably downstream of the configurations, zone of interest when studying possible flow correlations related to the urban parameters. Valuable information extracted from the numerical fields were used to complement the experimental observations. For instance, the tendency observed locally was confirmed by analysing the integrated energy head over a section downstream of the urban area. Such analysis highlights the complementarity between both numerical and experimental approaches, where general trends can be extracted and applied as coefficients in large-scale numerical models.

However, some points are left for further investigation and development and are detailed in the next section.

8.2 PERSPECTIVES

The perspectives related to the experimental setup (channel geometry, measurement techniques, etc.) as well as the capacity of the 3D numerical model are addressed in this section.

8.2.1 *Dam-break flow experiments*

Dealing with unsteady phenomenon and performing dam-break flow experiments can be time consuming. This limits the measurement techniques employed and the amount of data that can be collected.

8.2.1.1 *Design of the model*

The set-up geometry (breach width and reservoir size) impacts the experimental results. Performing dam-break flow experiments in large channels, which is necessary when adding obstacles to the flow, leads to longer preparation times (filling the reservoir, drying the bed, collecting the LSPIV particles downstream of the channel, etc.). In this thesis, 30 seconds of experimentation required $\sim$ 1 hour of preparation ($\sim$ 30 minutes to fill the tank and $\sim$ 30 minutes to stabilise the water level in the reservoir, while simultaneously saving the high-speed laboratory camera images for $\sim$ 25 minutes). The preparation time significantly limits the number of repeated trials that can be afforded, which are essential for producing accurate results. During the development of the experimental setup, efforts were made to ensure highly repeatable experiments, resulting in only six repetitions were performed per case allowing a total number of 24 studied urban forms.

The feedback obtained from the different measurement campaigns leads to some recommendations for future experimental setups:

- *Reservoir size and breach width* The size of the reservoir directly impacts the time required for each experiment. Optimising the reservoir size will significantly reduce the preparation time for each trial. The presence of a reflection zone, even when located downstream of the urban area, leads to water accumulation in the channel for higher flow blockage effects, such as narrow streets. The reflection zone constrained the analysis and limited the urban parameters that could be studied (for high L_y, the surge area reaches the reflection zone, while for narrower street l_x, flow accumulation occurs downstream of the urban area). Future experimental setups for unsteady urban studies should, when possible, prevent the formation of a reflection zone too close to the urban forms to avoid its interaction with the measurement area. This would also prevent the formation of a hydraulic jump

when too much water accumulates downstream. Finally, the setup sizing appears as a compromise between a channel sufficiently wide to study the wanted configurations, a breach size allowing for long enough flow conditions and enough space between the wanted configuration and the reflection zones.

- *LSPIV analysis.* LSPIV requires adding a large number of particles to the flow, and patterns on the bed can lead to low-velocity areas if not removed. Particular attention should be given to build the experimental setup with an individual drainage system when possible. This would increase the number of particles used, which would not need to be collected after each LSPIV measurement. Additionally, a uniform bed without screws or joints is preferred to obtain correct LSPIV results.

The number of tested urban parameters remains limited and relatively simple compared to the complexity and variety of possible building forms and road patterns in real urban districts. Further analysis of interest can be mentioned:

- The impact of street width (l_x) for a given lateral urban size (L_y) could provide additional insights into how street width affects flood severity.
- The influence of other urban parameters, such as street angles or the orientation of the urban area relative to the main direction of the flood wave, should be explored. Additionally, conducting similar experiments at a larger horizontal scale would be valuable.
- Performing experiments with larger street widths l_x would enhance and complete the extracted tendencies in this work emphasising its application to engineering flood models.

8.2.1.2 *Measurement challenges related to dam-break flow with presence of idealised urban areas*

Here are some challenges faced when performing measurements on dam-break flow:

- Since a large number of urban forms were tested, a limited number of water depth measurement points were performed. Constructing water height profiles in and around the urban areas with acoustic sensors would have required a large number of replicates. Moreover, the number of acoustic sensors used simultaneously is limited due to acoustic interference. The use of novel water depth measurement techniques, such as laser profilometry or wave radar systems seems promising to cover larger zones of interest [137].
- Although the IAM provided information concerning the splash-up shape and height for the different cases, it remains challenging to precisely perform water depth measurements due to the depth of field. Additional cameras may be used to perform stereoscopic measurements to address this issue in future research.
- While LSPIV measurements provided detailed and accurate instantaneous velocity fields, it is difficult to measure velocity in areas where the flow surface is three-dimensional, such as in the splash-up area. To overcome this, stereoscopic LSPIV techniques could be applied.
- Additionally, vertical velocity fields and recirculations within the urban area would be valuable for validating numerical models and selecting the appropriate turbulence closure model. Such measurements could be performed in the case of a full dam-break without a reflection zone, using the Particle Image Velocimetry (PIV) technique.
- Furthermore, only water depth measurements were taken in the reservoir to validate the hydrodynamic conditions of the experiments. Velocity profiles, acquired using ADCP probes through the breach, would complement the validation dataset.
- Finally, pressure measurements on the first row of buildings could supplement IAM measurements on the splash-up impact on the first row of obstacles.

8.2.2 *Numerical aspects*

From the comparisons between experimental and numerical results, the ability of a 3D numerical model to accurately simulate the flow processes of a dam-break wave through an urban area is confirmed. However, some differences were observed, notably in areas in presence of air bubbles under the free surface,

suggesting potential areas for development related to the numerical post-processing step. Additionally, the computational time for 3D simulations, consequently higher than 2D ones, constrains their use in most engineering applications. The use of new methods, such as the one-fluid VOF, could be of interest to reduce the simulation time. Using numerical results to complement experimental data confirmed local experimental important flow features, highlighting the value of using such approach to supplement experimental datasets if needed. In addition to the studied configurations in this work, 3D numerical results could be used to compute the energy head downstream new sets of urban areas.

Finally, the impact of urban forms on the flow was extracted for a defined set of parameters. The flow energy head downstream of the urban area could be used as a coefficient in large-scale numerical models to more effectively account for the impact of urban areas in engineering flood models. Also, simplified phenomenological models could be implemented in CFD dam-break simulations in presence of obstacles to accelerate their computing time.

APPENDIX

A

SUMMARY OF THE URBAN CONFIGURATIONS STUDIED

For the reader's convenience, the urban configurations studied in this manuscript, along with the associated urban parameters and probes, are summarised in this Appendix. The obstacles used are cubes with a side length of 0.1 m, representing idealised buildings. Larger obstacles are in fact sealed cubes with the same individual dimension (Figure A.2). The configurations, schematised in Figures A.2 and A.3, correspond to idealised suburban districts. Four independent parameters are used to define the urban forms:

- n_x and n_y: the number of streets along the x and y directions, respectively.
- l_x and l_y: the width of the streets along the x and y directions, respectively.

Figure A.1 schematise the parameters on configuration $2-10-2-10$. The corresponding parameters of the urban forms are given in Table A.1. The names of the configurations correspond to $n_x - l_x - n_y - l_y$, with each part representing the associated value of the parameter for each configuration. All studied configurations are compared to a dam break flow with no obstacle, called 0.

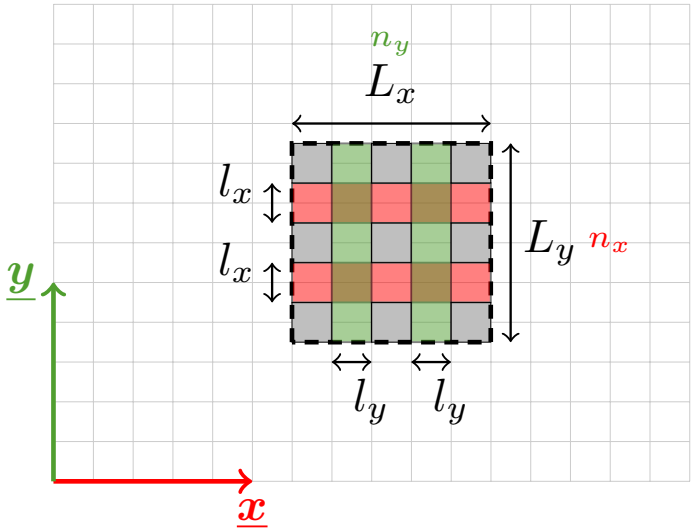

Figure A.1: Geometry of the urban form $2-10-2-10$ and definition of the parameters characterising urban forms in the manuscript.

Table A.1: Parameters characterising urban forms in the manuscript.

Configuration *	**Parameters**					
	n_x	l_x (m)	L_y (m)	n_y	l_y (m)	L_x (m)
0 **	-	-	-	-	-	-
$0-0-0-0$	0	0	0.10	0	0	0.1
$1-0-1-0$	1	0	0.20	1	0	0.2
$4-0-4-0$	4	0	0.50	4	0	0.5
$0-0-2-10$	0	0	0.10	2	0.1	0.5
$1-05-2-10$	1	0.05	0.25	2	0.1	0.5
$1-10-2-10$	1	0.10	0.30	2	0.1	0.5
$1-15-2-10$	1	0.15	0.35	2	0.1	0.5
$1-20-2-10$	1	0.20	0.40	2	0.1	0.5
$2-05-2-10$	2	0.05	0.40	2	0.1	0.5
$2-10-2-10$ **	2	0.10	0.50	2	0.1	0.5
$2-15-2-10$	2	0.15	0.60	2	0.1	0.5
$2-20-2-10$	2	0.20	0.70	2	0.1	0.5
$3-05-2-10$	3	0.05	0.55	2	0.1	0.5
$3-10-2-10$	3	0.10	0.70	2	0.1	0.5
$3-15-2-10$	3	0.15	0.85	2	0.1	0.5
$3-20-2-10$	3	0.20	1.00	2	0.1	0.5
$3-05-0-0$	3	0.05	0.55	0	-	0.5
$3-10-0-0$	3	0.10	0.70	0	-	0.5
$3-15-0-0$	3	0.15	0.85	0	-	0.5
$3-20-0-0$	3	0.20	1.00	0	-	0.5
$3-10-1-10$	3	0.10	0.70	1	0.1	0.5
$3-10-1-30$	3	0.10	0.70	1	0.3	0.5
$3-20-1-10$	3	0.20	1.00	1	0.1	0.5
$3-20-1-30$	3	0.20	1.00	1	0.3	0.5

$*$ Configuration names: $n_x - l_x - n_y - l_y$
$**$: Studied twice at different positions.

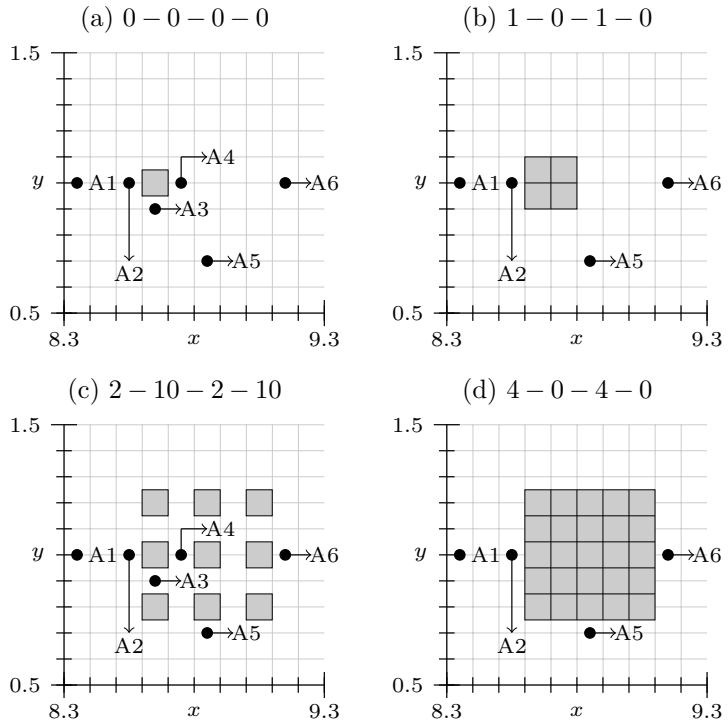

Figure A.2: Top view of the configurations studied and probes locations in Chapter 5.

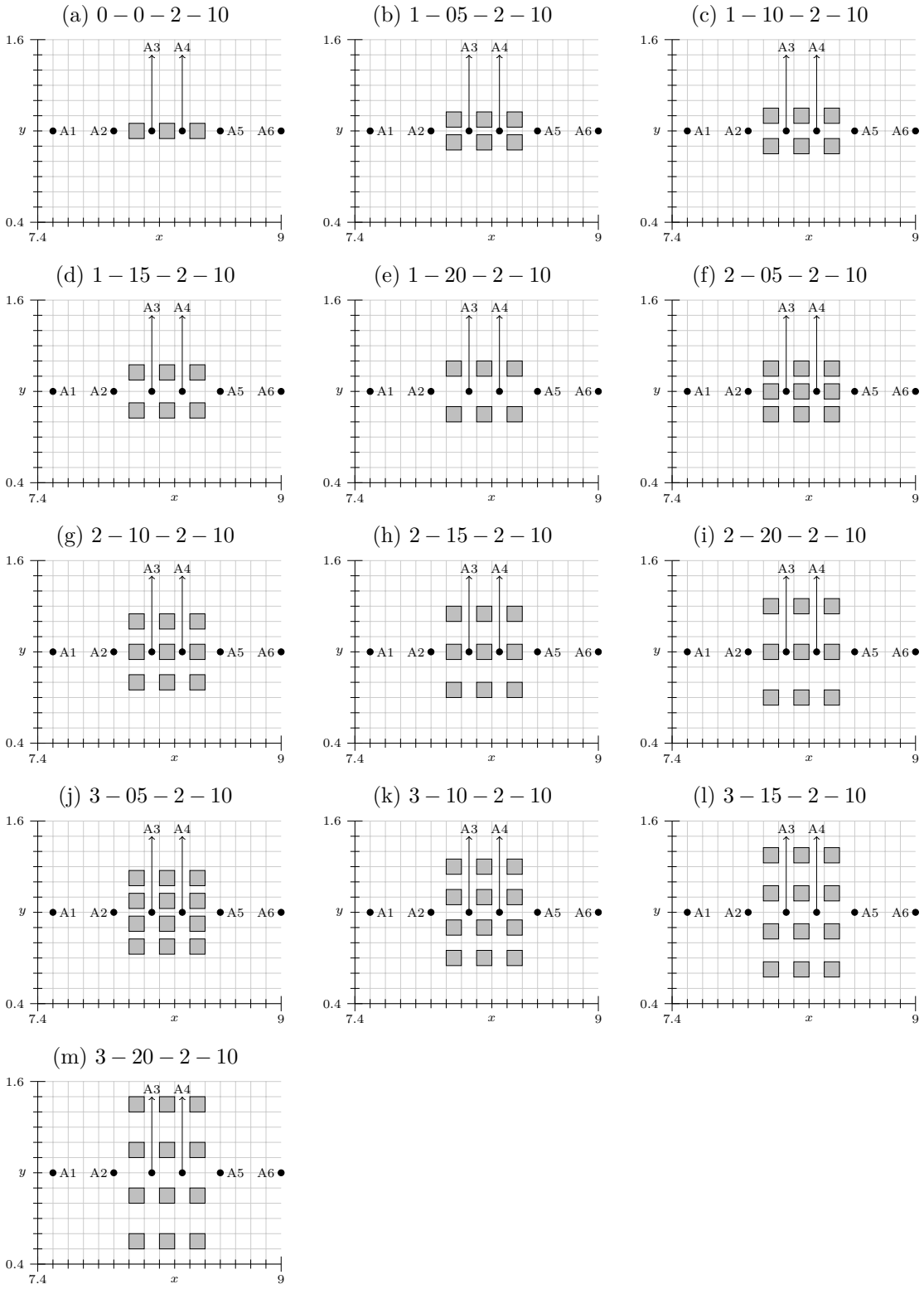

Figure A.3: Top view of the configurations with various longitudinal street number/width and probes locations studied in Chapter 6.

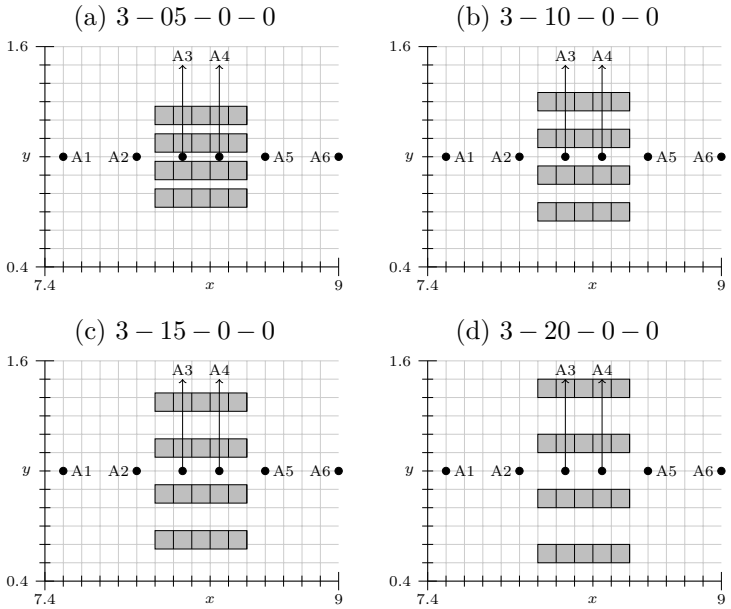

Figure A.4: Top view of the configurations with no lateral streets and probes locations studied in Chapter 6.

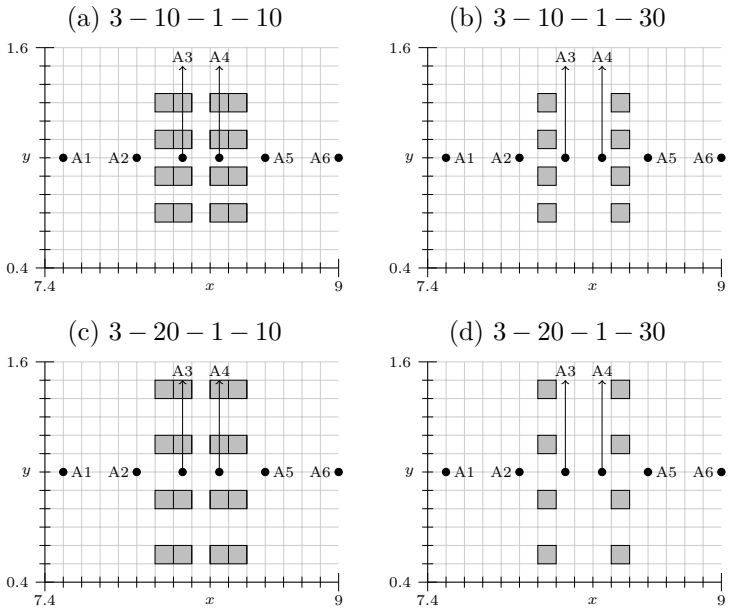

Figure A.5: Top view of the configurations with various lateral street width and probes locations studied in Chapter 6.

B

DETAILS ABOUT THE ACQUISITION PROGRAM

The acquisition program acquires signals from wave gauges using a USB-1808 acquisition card (Measurement Computing). This measurement device is equipped with eight 18-bit analog-to-digital converters, enabling it to simultaneously acquire up to 200,000 samples from the eight available inputs. Implementing it in a Windows 10 environment requires installing a driver called *Instacal*. Access to the various functions of this driver from LabVIEW is provided by the *Ulx for NI LabVIEW* library.
The LabVIEW program's architecture is based on a state machine. When the program is started, a test is conducted to check for the presence of the acquisition card. If this test fails, the program stops. Then, and if the acquisition card is recognised, the program load a file named *parametres.cfg* (see example below) located in the program's current directory. This file contains the measurement parameters used during the previous acquisition.

Example file *parametres.cfg*:
Id Carte=Dev1/;
Fe=50,0;
Durée=25,0;
Trigger=Front Descendant;
Axe Y=Millimètres;
AI0=1;TDH;X0=4,0;Y0=0,00;Z0=500,0;a0=0,0228;b0=0,2128;
AI1=1;TDH;X1=4,0;Y1=0,50;Z1=500,0;a1=0,0228;b1=0,2228;
AI2=1;TDH;X2=6,50;Y2=0,00;Z2=500,0;a2=0,0228;b2=0,2328;
AI3=1;TDH;X3=6,50;Y3=0,15;Z3=500,0;a3=0,0228;b3=0,2428;
AI4=0;Mic 35;X4=8,35;Y4=0,00;Z4=500,0;a4=0,0228;b4=0,2528;
AI5=0;Mic 35;X5=8,55;Y5=0,00,0;Z5=500,0;a5=0,0228;b5=0,2628;
AI6=0;Mic 35;X6=8,65;Y6=0,30,0;Z6=500,0;a6=0,0228;b6=0,2728;
AI7=0;Mic 35;X7=8,75;Y7=0,00;Z7=500,0;a7=0,0228;b7=0,2828;

Successfully loading the *parameter.cfg* file initiates the acquisition interface (Figure B.1a). Except in monitoring mode (Figure B.1d), the beginning of the acquisition is in all cases conditioned by an external trigger signal (either a rising or falling edge). If the loading of the *parametres.cfg* file fails, the parameter entry interface is displayed (Figure B.1c).
Figure B.1a displays the main interface of the program. The commands are located at the bottom of the window and are detailed below:

- '**Acquisition**' navigates to the acquisition interface shown in Figure B.1b. All control buttons at the bottom of the interface become inactive, and the graphical window is scaled in the Y-axis according to the sensor with the greatest measurement range. The X-axis corresponds to the maximum measurement time defined in the *parametres.cfg* file. At the top right of this window, the sensors involved in the current acquisition are listed. A new command button named '*Stop*' appears, along with an indicator named '*Acq On*'. The latter is activated when the external trigger occurs, displaying data in real time in the graphical window. '*Stop*' can be used to interrupt the acquisition before the measurement time ends. If '*Stop*' is pressed before the external trigger occurs, the acquisition sequence is cancelled, and the interface returns to the main interface of the program (Figure B.1a).

- '**Monitoring**' opens the interface shown in Figure B.1d. This interface is designed to validate the measurement chain and ensure that sensors are functioning correctly by displaying real-time data in a scrolling graph with a history of 1,000 measurements. All parameters match those defined in the *parametres.cfg* file, except for the trigger mechanism, which is purely software-based. Pressing

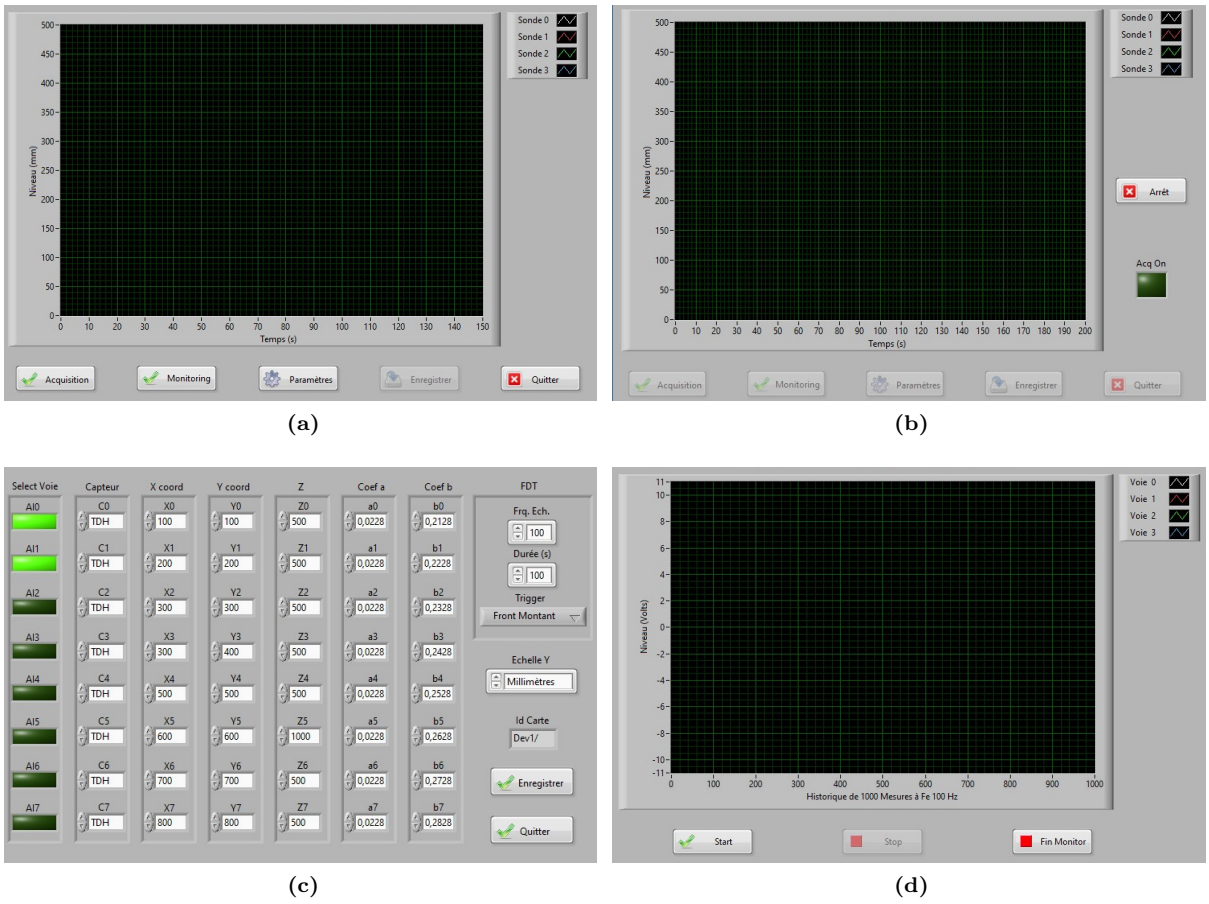

(a) **(b)**

(c) **(d)**

Figure B.1: Illustration of the graphical interface of the acquisition program.

the '*Start*' button initiates the data display. While the measurements are in progress, the '*Stop*' button is used to interrupt the display. Finally, '*Fin Monitor*' returns to the main interface (Figure B.1a).

- '**Paramètres**' accesses the parameter entry interface, as displayed in Figure B.1c, where users can modify the *parametres.cfg* file and adjust the measurement conditions. Within this interface, it's possible to specify whether a sensor is active ('*Select Voie*'), as well as to set the sensor type ('*Capteur*'), its coordinates in the channel ('*X coord*', '*Y coord*'), its measurement range ('*Z*'), and calibration coefficient ('*Coef a*', '*Coef b*'). The '*Echelle Y*' option also determines whether the data is plotted and saved in millimeters (by applying the two calibration coefficients) or in voltage. Additionally, users can define the sampling frequency ('*Frq. Ech.*'), measurement duration ('Durée (s)'), and the external trigger edge ('Trigger'). '*Enregistrer*' saves the changes to the *parametres.cfg* file, and '*Quitter*' returns to the main program interface (Figure B.1a).
- '**Quitter**' exits the program.

Thus, when a series of measurements has been either completed or cancelled, the program reverts to the main interface as shown in Figure B.1a. If any measurements were successfully carried out, the '*Save*' button is enabled, allowing data to be saved in a *result.txt* file (see example below), which includes both the measurement parameters and results. For convenience in post-processing, a second file *result.csv* is also generated, containing only the measurement results.

Example file *result.csv*:
Temps(s),V0(Volts),V1(Volts),V2(Volts),V3(Volts),V4(Volts),V5(Volts),V6(Volts),V7(Volts)
0.000000,-2.716342,-0.362512,1.737258,1.925094,9.649810,8.278955,7.771522,9.832458
0.020000,-2.713290,-0.360605,1.739394,1.928375,9.659347,8.279489,7.776862,9.832534
0.040000,-2.711917,-0.358163,1.740233,1.928833,9.660033,8.275979,7.789145,9.831389
(...)

Example file *result.txt*:
Date: 24/05/2023
Heure: 18:04
Fe: 50,0
Nb Pts: 1522
Durée: 30,4
Nb V: 8
Unité: Volts
Trig.: Front descendant

Voie Capteur X Y Z Coef a Coef b

0 TDH 4,0 0,1 500 0,0228 0,2128
1 TDH 4,0 0,5 500 0,0228 0,2228
2 TDH 6,5 0,1 20 0,0166 0,2328
3 TDH 6,5 -0,1 20 0,0165 0,0655
4 Mic 35 8,3 0,1 500 0,0228 0,0653
5 Mic 35 8,6 0,1 20 0,0167 0,0638
6 Mic 35 8,8 -0,3 500 0,0228 0,2728
7 Mic 35 9,0 0,1 500 0,0228 0,2828

V0(Volts) V1(Volts) V2(Volts) V3(Volts) V4(Volts) V5(Volts) V6(Volts) V7(Volts)

-2,716342 -0,362512 1,737258 1,925094 9,649810 8,278955 7,771522 9,832458
-2,713290 -0,360605 1,739394 1,928375 9,659347 8,279489 7,776862 9,832534
-2,711917 -0,358163 1,740233 1,928833 9,660033 8,275979 7,789145 9,831389
(...)

C

DETAILS ABOUT THE IMAGE ANALYSIS MEASUREMENT PROGRAM

The Image Analysis Measurement program processes the water depth variation in the splash-up area during the impact process and conducts free surface detection profiles from a series of images captured with a high-speed camera. Prior image calibration (pixels/mm) is required to determine the water depth. A series of command buttons are placed at the bottom of the user interface ('*Calibration*', '*ROI*', '*Impact*', '*Analyse*', '*Profil*', etc.) to launch the execution of various actions. Upon starting the program, the only active button is '*Quit*', which closes the program. The program architecture is also based on a state machine.

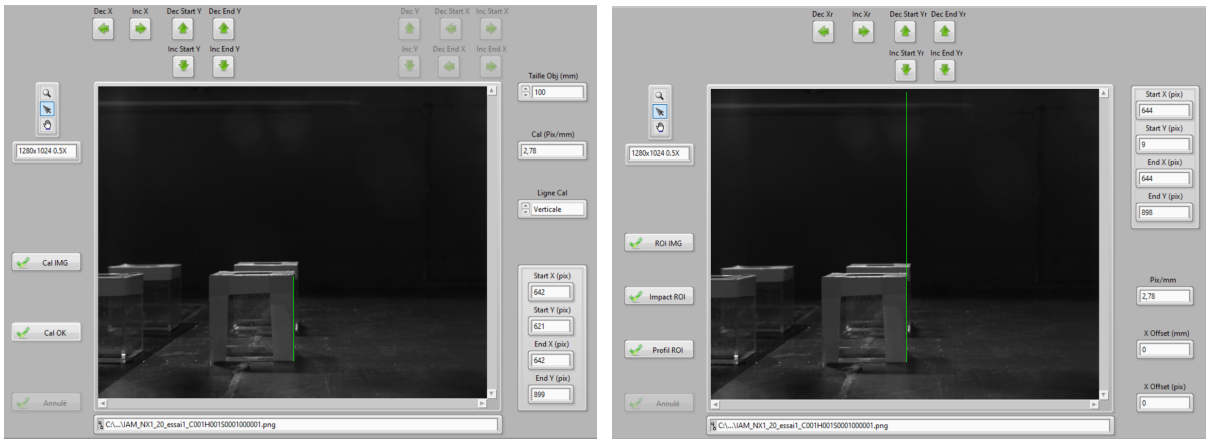

(a) **(b)**

Figure C.1: Illustration of the calibration and ROI definition steps of the Image Analysis Measurement (IAM) program.

When starting the program, a calibration step is required, so the calibration interface is opened, as shown in Figure C.1a. The '*Cal IMG*' button loads the chosen image for calibration. The image then appears, and the file path is displayed in the indicator located below it. On the left side of the image, there are three tools for manipulating it: The arrow tool, active by default, allows for moving and resizing the green line used to define the calibration line. This calibration segment must be placed on an object with known dimensions, such as the side of the cube placed in the center of the channel. Additionally, the magnifying glass tool, located above the arrow tool, enables zooming in on the image. The hand tool, located under the arrow tool, allows for moving the image when it is larger than the window. Below these tools, an indicator displays the original image size and the level of zoom applied. The image manipulation tools and the size and zoom level indicator are features present in all user interfaces of the program.

On the right side of the image, the size of the reference object ('*Obj Size*' (mm)), with a default value of 100 mm, is specified. '*Cal (pix/mm)*' displays the calibration resulting value. The calibration line, which can be oriented vertically or horizontally, is defined by four coordinates ('*Start X (mm)*', '*Start Y (mm)*', '*End X (mm)*', and '*End Y (mm)*'). These coordinates, along with the calibration results, are continuously updated. The green line can be manipulated with the mouse and will remain strictly vertical or horizontal upon releasing the left mouse button. For more precise positioning, the upper keys can be used to move the line right or left, and adjust the coordinates of the end points of the line independently. The calibration is assumed to be identical on the X and Y axes. Once the calibration is complete, pressing '*Cal OK*' validates the operation and launches the ROI definition interface.

The Region Of Interest (ROI) definition interface is shown in Figure C.1b. The ROI is a single line or several lines forming an area on which the calculation is performed. The process is analogous to that described in the previous step. '*ROI IMG*' selects the image used to define the ROI. This green line can be manipulated with the mouse. More precise positioning can be achieved using the upper keys. The ROI coordinates are displayed on the indicators to the right of the image and will be used for all subsequent manipulations. 'X Offset (mm)' and 'X Offset (pix)' represent the offset between the current ROI line and the previously defined calibration line. Once the ROI is defined, two types of measurements can be conducted via '*Impact ROI*' or '*Profil ROI*'.

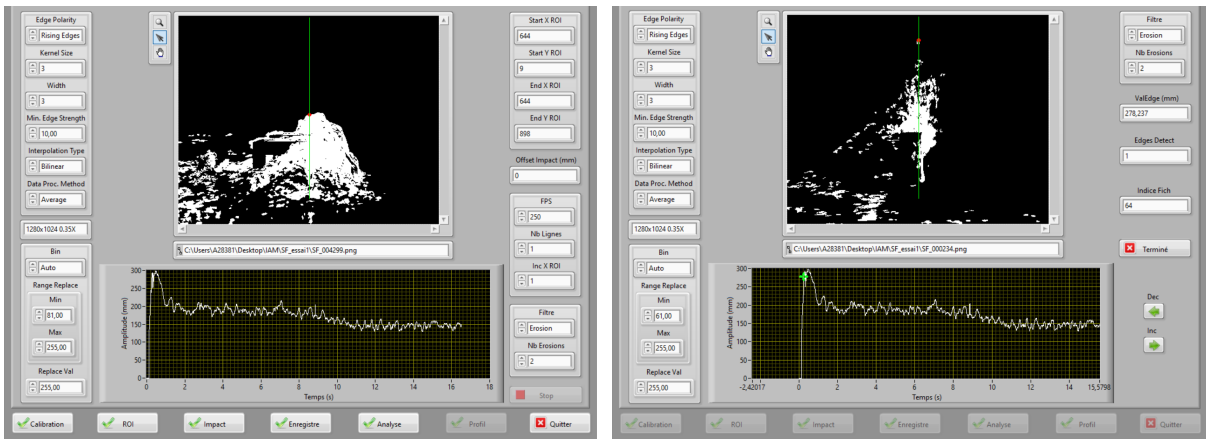

(a) **(b)**

Figure C.2: Example of impact measurement using the Image Analysis Measurement (IAM) program.

IMPACT MEASUREMENTS When the '*Impact ROI*' button is activated, the interface shown in Figure C.2 is displayed. The objective of this analysis is to detect the water depth in the ROI and its evolution in each image captured with a high-speed camera. The layout of the window is quite similar to the previous steps, featuring the image manipulation tool and the file path indicator. The lower graph shows the measurement results. The Y-axis represents the distance in millimeters measured on the ROI line between the highest detected fronts and the lowest coordinate of the ROI. The X-axis indicates the time in seconds, calculated based on the camera's Frames Per Second (FPS) acquisition rate.
On the left, controls such as '*Edge Polarity*' and '*Kernel Size*' allow for modifications of the front detection module settings. The indicator below displays the image resolution and zoom level within the image window. At the bottom, the controls define the image binarization with three options: '*Auto*', which automatically adjusts the value to the optimal level for each image (by default). '*Manual*' allows the operator to fix and define the '*Range Replace*' value. Finally, '*None*' cancels the binarization step.
Additionally, on the right, the ROI coordinates and the offset between the calibration line and the ROI are indicated. Also, '*FPS*', set to a default value of 250, represents the number of frames per second captured by the camera. '*Nb Lignes*' allows averaging the measurements by moving the ROI line horizontally by '*Inc X ROI*' pixels between each measurement. The final value for the free surface position is calculated as the mean of all the highest values detected. '*Filtre*', with the 'Erosion' option selected, removes small artifacts (such as droplets) from the image using an erosion image processing method. The '*Nb Erosions*' parameter can be increased to eliminate larger artifacts.

The measurement is performed by activating the '*Impact*' control button in the lower banner. A file dialog box is launched for selecting the directory containing the images to be processed. The '*Stop*' button allows for the interruption of an ongoing measurement. Figure C.2 shows the results of an impact measurement. Any action on '*Calibration*', '*ROI*', '*Impact*', or '*Quit*' open a dialog box if the results have not been saved. In this dialog, 'Save' performs the operation and validates the page change, while 'Delete' validates the page change without saving. Saving the results produces two files: a '*result.txt*' file that contains a header with all the measurement parameters followed by the actual results (see example below), and a 'result.csv' file, which contains only the measurement results.

Then, if the '*Analyse*' button is activated, the interface shown in Figure Figure C.2b is displayed. This interface analyses the previous results of impact measurements, and each point on the graph and its

associated image with the edge detection position can be displayed. On the left, the processing parameters are identical to those previously described. The image displayed is the one corresponding to the green cross located on the water height curve of the lower graph. This cursor can be moved along the curve using the mouse, or more precisely, pixel by pixel using the side keys. The corresponding image then appears, and its path is indicated in the indicator located below. On the right of the image, '*Filter*', as previously mentioned, allows for a filtering operation on the image using an erosion method. '*Val Edge*' represents the height of the detected front and corresponds to the distance between the detected position on the ROI line and the lower coordinate of the line. '*Edges Detect*' indicates the number of detected fronts, and '*Image File Index*' shows the position of the image file represented in the directory. Any modification to the front detection parameters, binarization values, or image filtering parameters leads to a new calculation on the displayed image, facilitating the optimisation of these parameters.

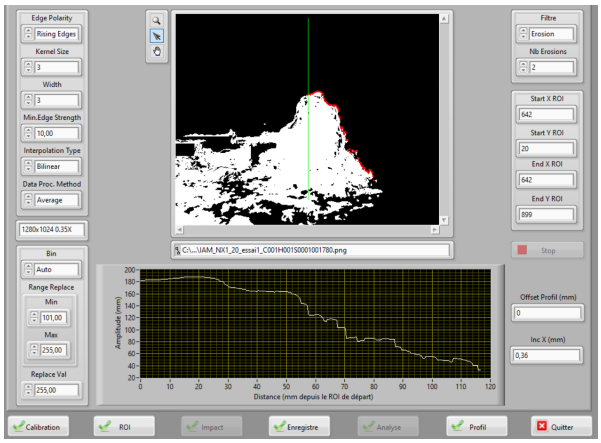

Figure C.3: Example of profile detection using the Image Analysis Measurement (IAM) program.

FREE SURFACE PROFILES DETECTION When the '*Profil ROI*' button is activated, Figure C.1b, the interface dedicated to profile measurements, as shown in Figure C.3, is displayed. The objective of this analysis is to capture the free surface profile at a specific instant to study the shape of the splash-up area upstream of the obstacles. To achieve this, edge detection is performed on a region of the image by horizontally moving the ROI from its initial position to the end of the image. The processing parameters, located to the left of the image, are identical to those used and presented previously for the impact measurements. In the lower graph representing the analysis results, the Y-axis indicates the height measured in millimetres along the ROI line. The X-axis represents the distance calculated from the initial horizontal position of the ROI. To the right of the image, the filtering operation can be activated, and indicators for the ROI position are displayed. '*Offset Profile (mm)*' indicates the offset between the calibration line and the initial position of the ROI. '*Inc X(mm)*' indicates the resolution on the X-axis of the lower graph and the value depends on the calibration step.

When the processing parameters are correct, the measurement is initiated by activating the '*Profile*' command button in the lower banner. After selecting the file (a single image) to be processed in the dialog box, the measurement is performed. Figure C.3 displays a measurement profile result from the upstream side of the obstacle to the end of the splash-up area. In the image, each edge found, resulting from the horizontal displacement of the ROI, is highlighted with a red dot. The resulting profile is plotted in the lower graph. At the end of the measurement, which occurs when the ROI reaches the right edge of the image or by activating the '*Stop*' command, the '*Save*' button becomes active in the lower banner. Saving the results produces two files (see example below) similar to those from the impact measurement analysis.

Example file *result.csv*:
Temps(s),Hauteur (mm)
0.000000,0.000000
0.004000,0.000000
0.008000,0.000000
(...)

Example file *result.txt*:
Fichier Calibration : C:\1.png
Fichier ROI : C:\1.png
Répertoire Fichiers Impact : C:\SF_essai1

Calibration (pix/mm) : 2,780
Taille Objet (mm) : 100,000
Ligne Calibration : Verticale

Start X Cal (pix) : 644
Start Y Cal (pix) : 620
End X Cal (pix) : 644
End Y Cal (pix) : 898

Start X ROI (pix) : 644
Start Y ROI (pix) : 9
End X ROI (pix) : 644
End Y ROI (pix) : 898

Offset Impact (mm) : 0,000

Edge Polarity : Rising Edges
Kernel Size : 3
Width : 3
Minimum Edge Strength : 10,000
Interpolation Type : Bilinear
Data Processing Method : Average

FPS : 250,000
Nb Lignes : 1
Inc X (pix) : 1

Binarisation : Auto
Replace Min : 75,000
Replace Max : 255,000
Replace Val : 255,000

Filtrage : Erosion
Nombre d'érosions : 2

Temps (s) Hauteur (mm)
0,000000 0,000000
0,004000 0,000000
0,008000 0,000000
(...)

D

SUPPLEMENTARY DATA FROM CHAPTER 5

This appendix contains supplementary experimental results from the preliminary study presented in Chapter 5.

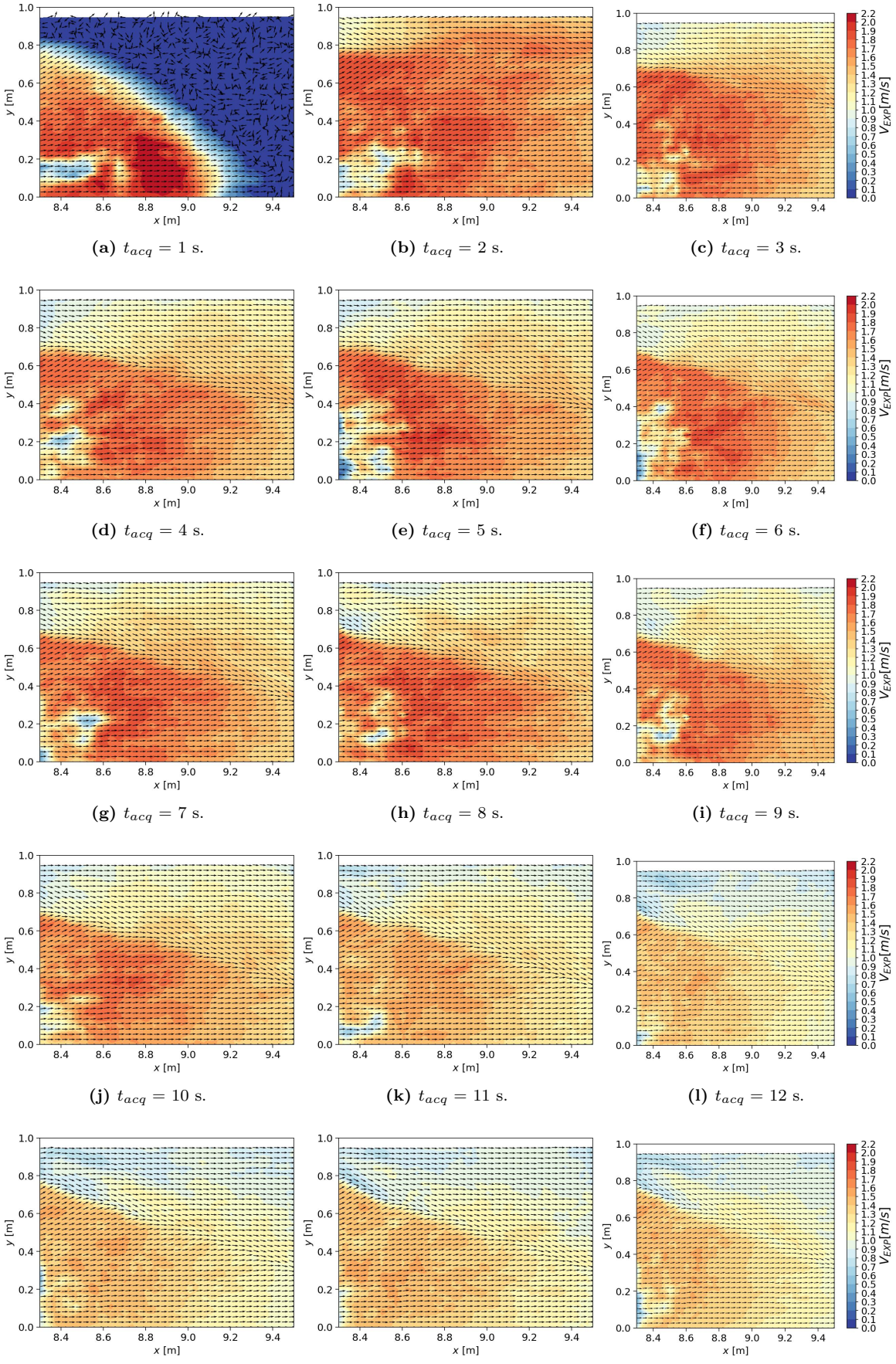

(a) $t_{acq} = 1$ s. **(b)** $t_{acq} = 2$ s. **(c)** $t_{acq} = 3$ s.

(d) $t_{acq} = 4$ s. **(e)** $t_{acq} = 5$ s. **(f)** $t_{acq} = 6$ s.

(g) $t_{acq} = 7$ s. **(h)** $t_{acq} = 8$ s. **(i)** $t_{acq} = 9$ s.

(j) $t_{acq} = 10$ s. **(k)** $t_{acq} = 11$ s. **(l)** $t_{acq} = 12$ s.

(m) $t_{acq} = 13$ s. **(n)** $t_{acq} = 14$ s. **(o)** $t_{acq} = 14.2$ s.

Figure D.1: Free surface velocity evolution for case 0. Black surfaces illustrate the obstacles position.

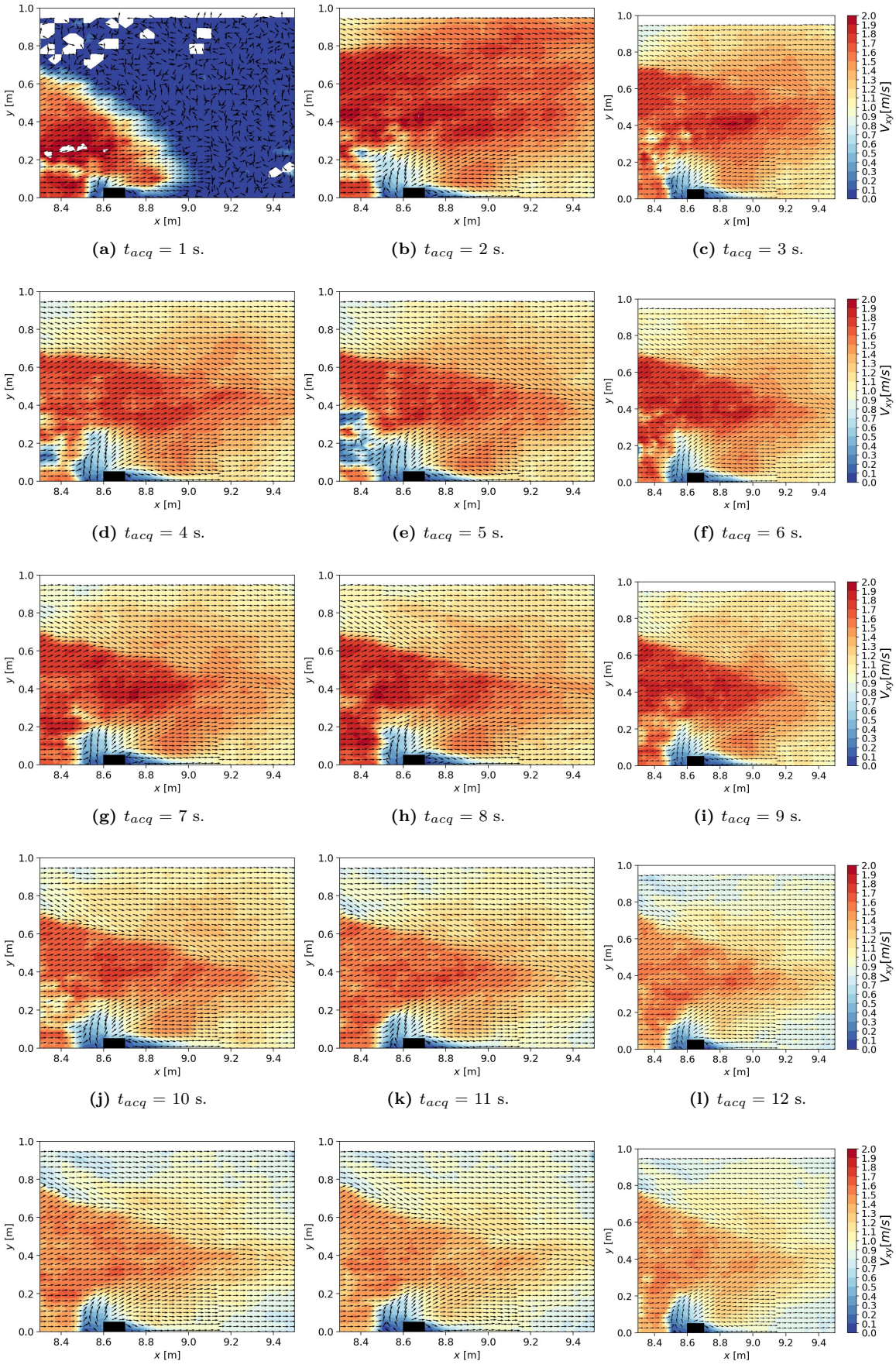

(a) $t_{acq} = 1$ s. **(b)** $t_{acq} = 2$ s. **(c)** $t_{acq} = 3$ s.

(d) $t_{acq} = 4$ s. **(e)** $t_{acq} = 5$ s. **(f)** $t_{acq} = 6$ s.

(g) $t_{acq} = 7$ s. **(h)** $t_{acq} = 8$ s. **(i)** $t_{acq} = 9$ s.

(j) $t_{acq} = 10$ s. **(k)** $t_{acq} = 11$ s. **(l)** $t_{acq} = 12$ s.

(m) $t_{acq} = 13$ s. **(n)** $t_{acq} = 14$ s. **(o)** $t_{acq} = 14.2$ s.

Figure D.2: Free surface velocity evolution for case $0-0-0-0$. Black surfaces illustrate the obstacles position.

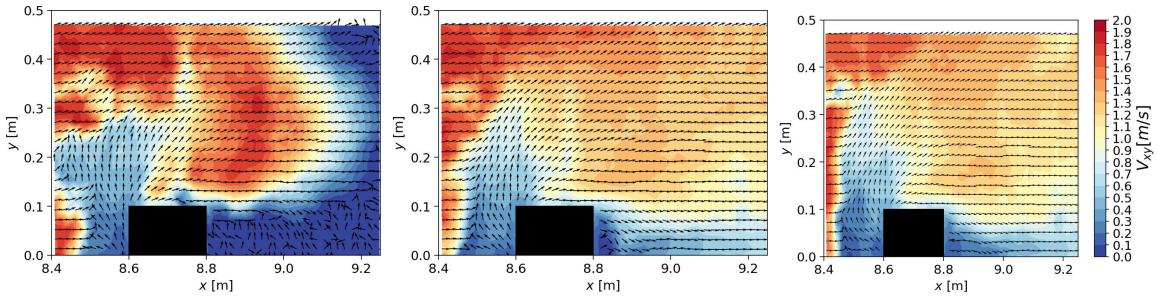

(a) $t_{acq} = 1$ s. **(b)** $t_{acq} = 2$ s. **(c)** $t_{acq} = 3$ s.

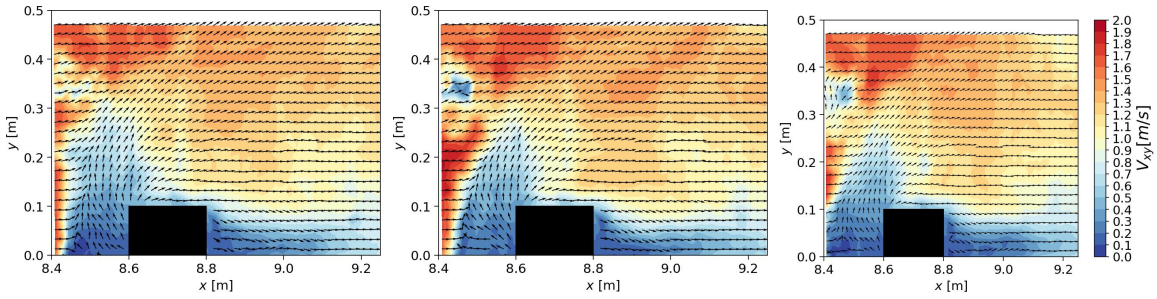

(d) $t_{acq} = 4$ s. **(e)** $t_{acq} = 5$ s. **(f)** $t_{acq} = 6$ s.

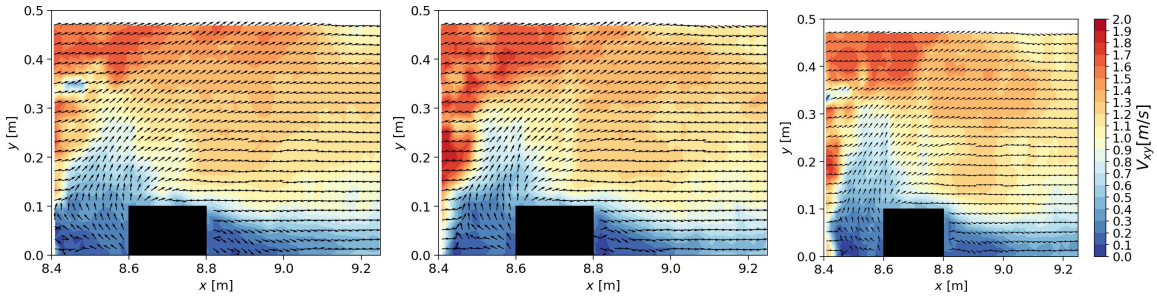

(g) $t_{acq} = 7$ s. **(h)** $t_{acq} = 8$ s. **(i)** $t_{acq} = 9$ s.

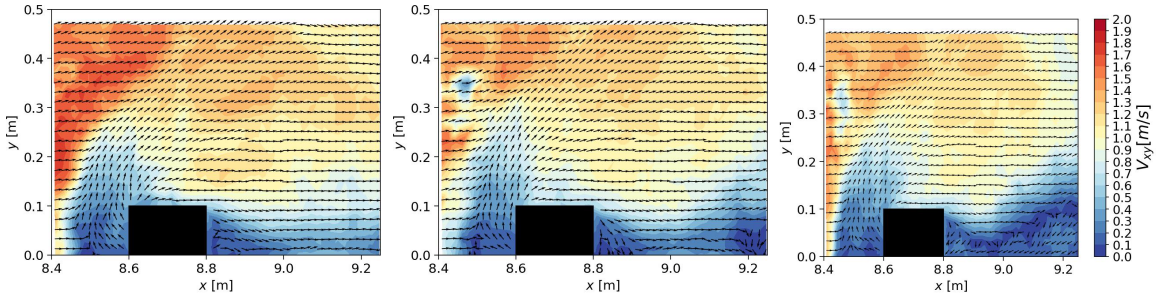

(j) $t_{acq} = 10$ s. **(k)** $t_{acq} = 11$ s. **(l)** $t_{acq} = 12$ s.

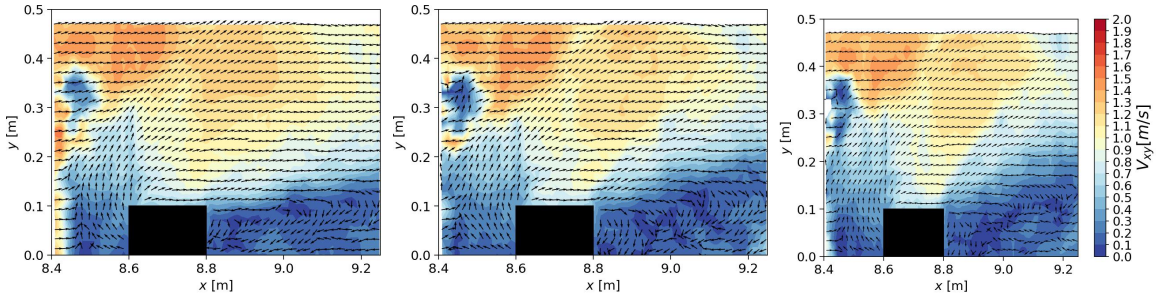

(m) $t_{acq} = 13$ s. **(n)** $t_{acq} = 14$ s. **(o)** $t_{acq} = 14.2$ s.

Figure D.3: Free surface velocity evolution for case $1-0-1-0$. Black surfaces illustrate the obstacles position.

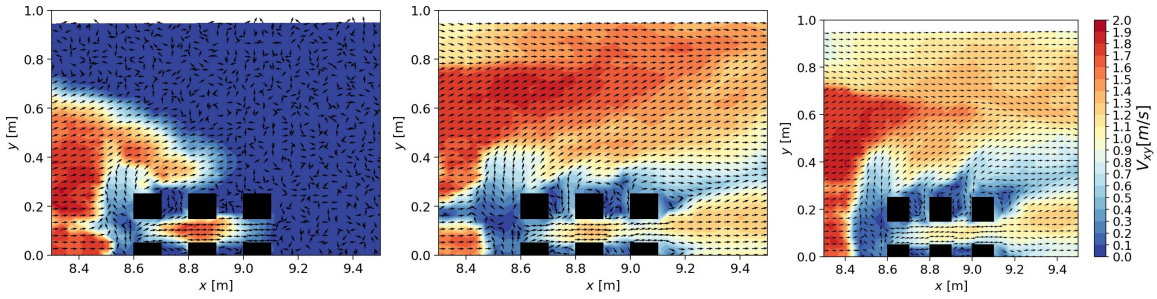

(a) $t_{acq} = 1$ s. **(b)** $t_{acq} = 2$ s. **(c)** $t_{acq} = 3$ s.

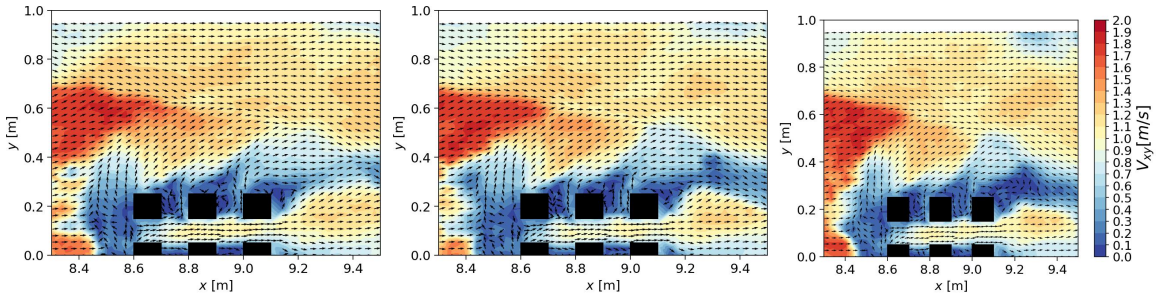

(d) $t_{acq} = 4$ s. **(e)** $t_{acq} = 5$ s. **(f)** $t_{acq} = 6$ s.

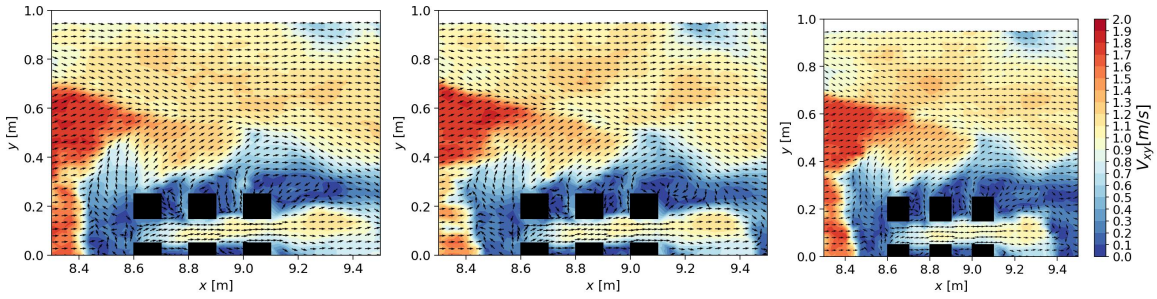

(g) $t_{acq} = 7$ s. **(h)** $t_{acq} = 8$ s. **(i)** $t_{acq} = 9$ s.

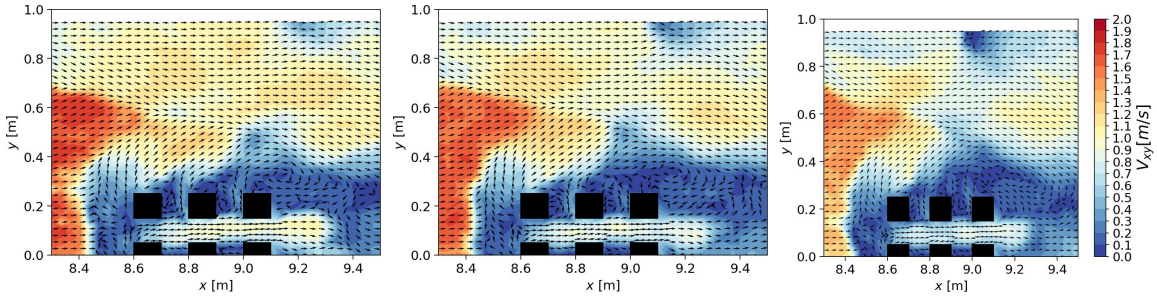

(j) $t_{acq} = 10$ s. **(k)** $t_{acq} = 11$ s. **(l)** $t_{acq} = 12$ s.

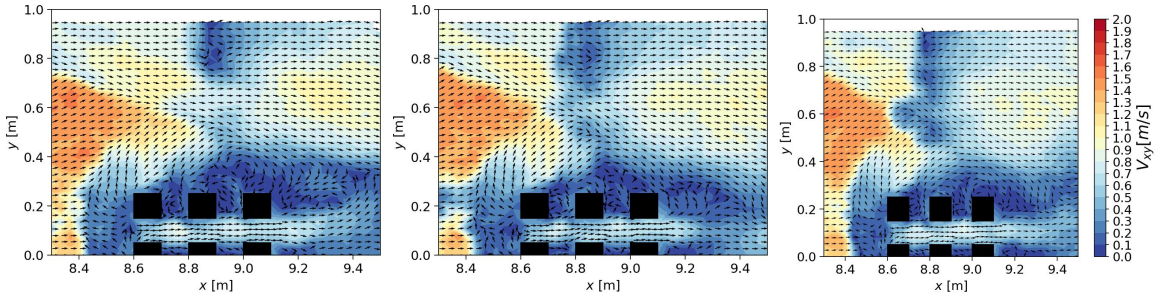

(m) $t_{acq} = 13$ s. **(n)** $t_{acq} = 14$ s. **(o)** $t_{acq} = 14.2$ s.

Figure D.4: Free surface velocity evolution for case $2-10-2-10$. Black surfaces illustrate the obstacles position.

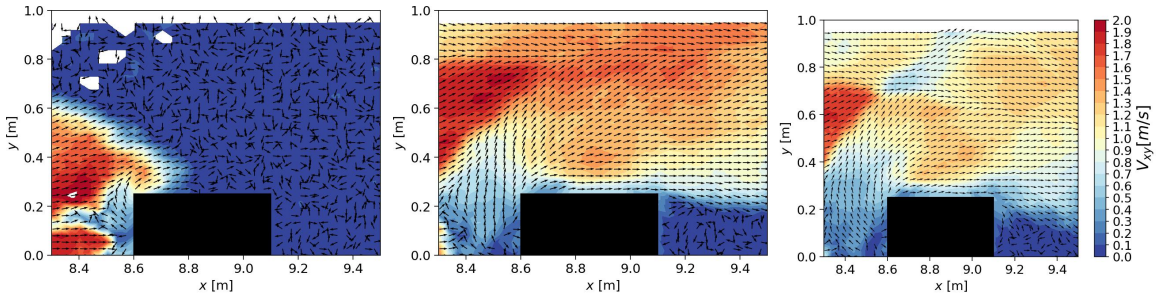

(a) $t_{acq} = 1$ s. **(b)** $t_{acq} = 2$ s. **(c)** $t_{acq} = 3$ s.

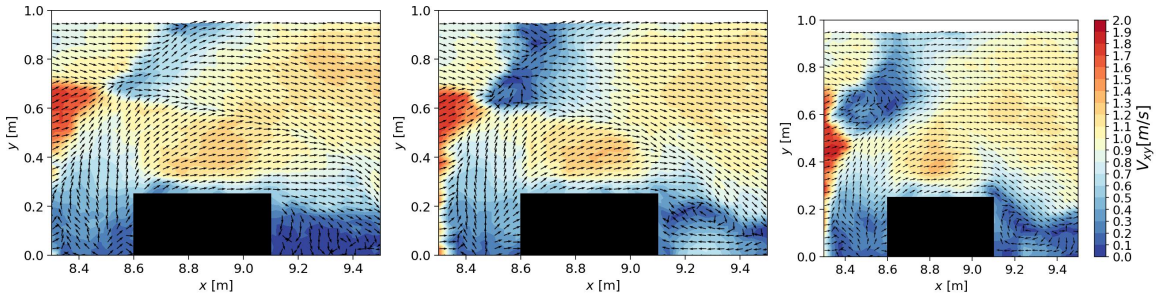

(d) $t_{acq} = 4$ s. **(e)** $t_{acq} = 5$ s. **(f)** $t_{acq} = 6$ s.

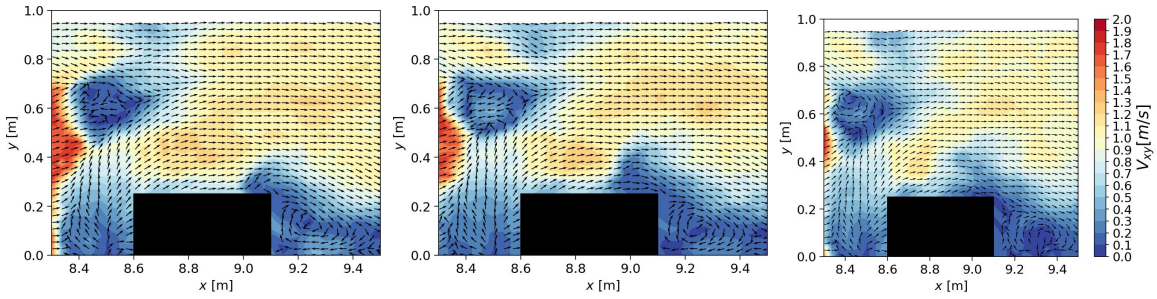

(g) $t_{acq} = 7$ s. **(h)** $t_{acq} = 8$ s. **(i)** $t_{acq} = 9$ s.

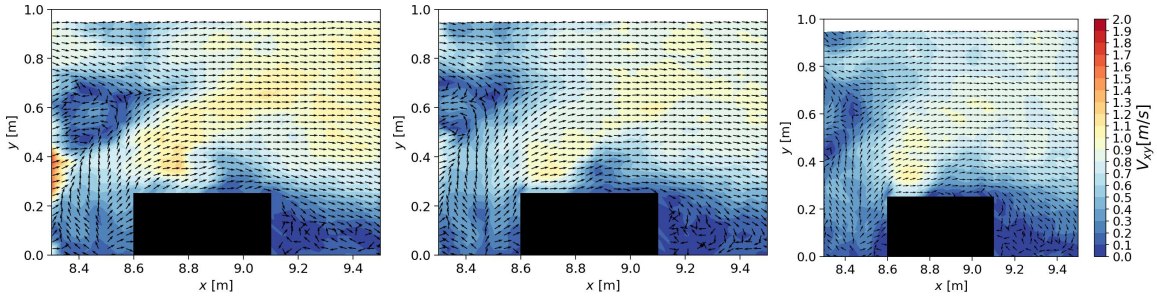

(j) $t_{acq} = 10$ s. **(k)** $t_{acq} = 11$ s. **(l)** $t_{acq} = 12$ s.

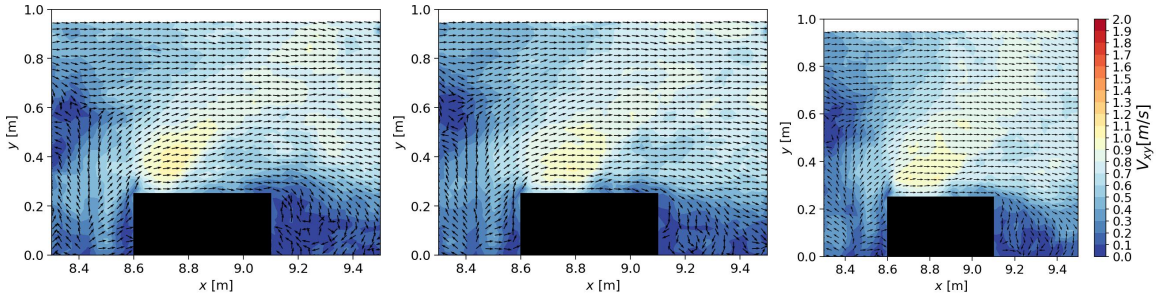

(m) $t_{acq} = 13$ s. **(n)** $t_{acq} = 14$ s. **(o)** $t_{acq} = 14.2$ s.

Figure D.5: Free surface velocity evolution for case $4-0-4-0$. Black surfaces illustrate the obstacles position.

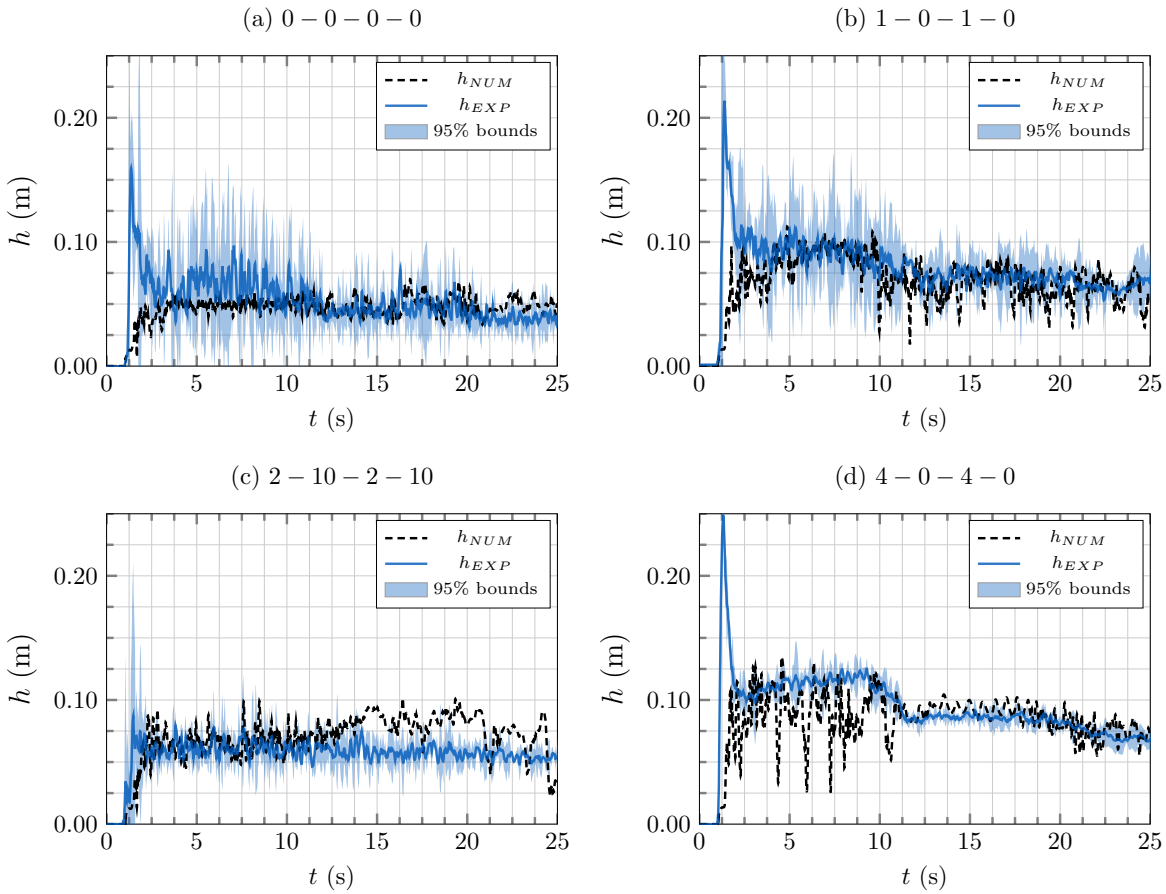

Figure D.6: Water height comparison at position A2 between wave gauge measurements (black dashed line) and numerical model (blue line) for cases $0-0-0-0$, $1-0-1-0$, $2-10-2-10$ and $4-0-4-0$.

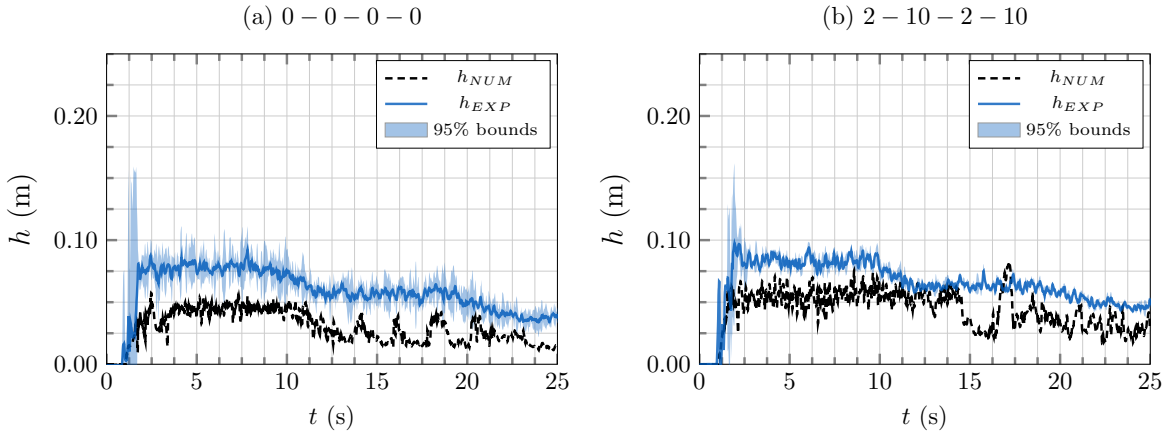

Figure D.7: Water height comparison at position A3 between wave gauge measurements (black dashed line) and numerical model (blue line) for cases $0-0-0-0$ and $2-10-2-10$.

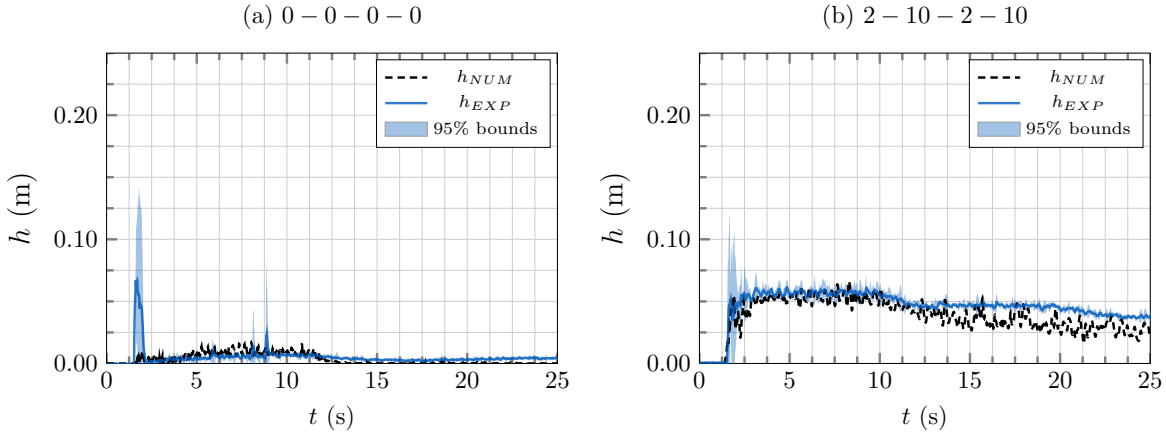

Figure D.8: Water height comparison at position A4 between wave gauge measurements (black dashed line) and numerical model (blue line) for cases $0-0-0-0$ and $2-10-2-10$.

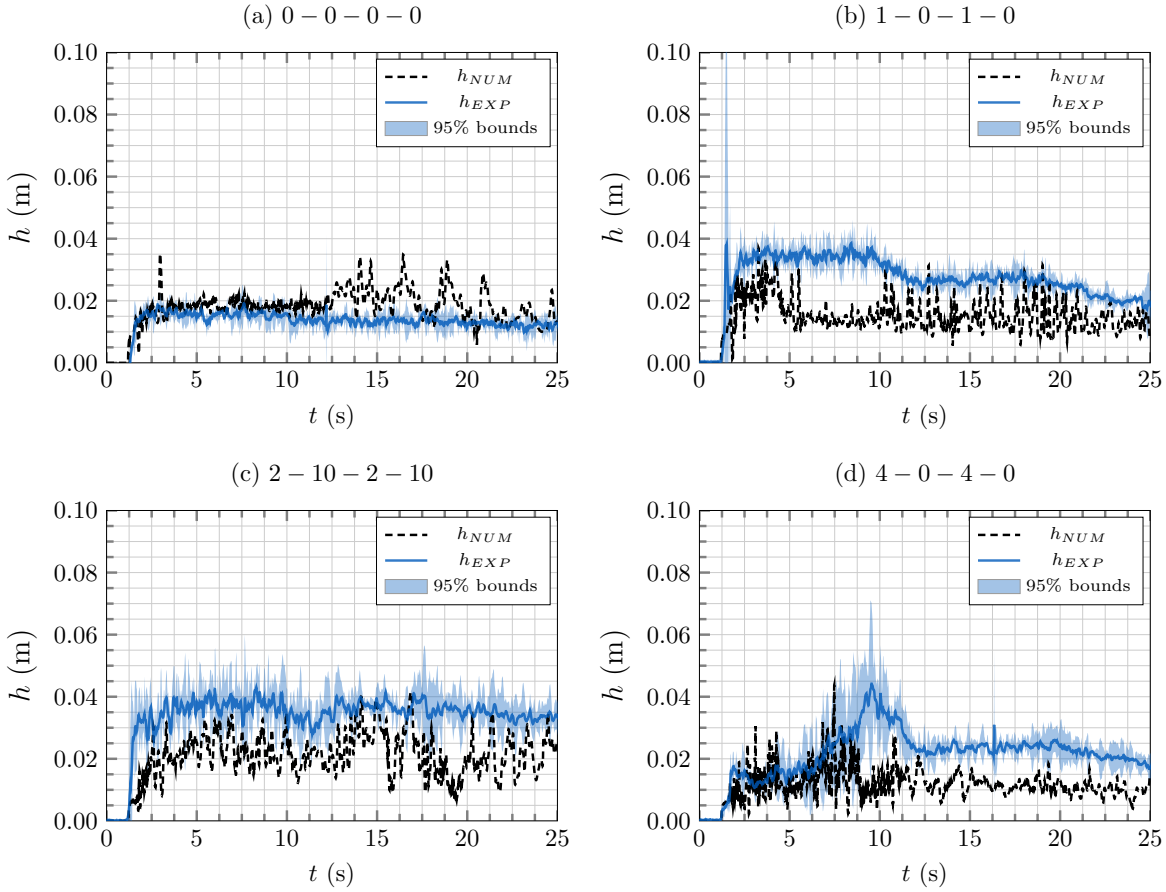

Figure D.9: Water height comparison at position A5 between wave gauge measurements (black dashed line) and numerical model (blue line) for cases $0-0-0-0$, $1-0-1-0$, $2-10-2-10$ and $4-0-4-0$.

E

SUPPLEMENTARY DATA FROM CHAPTER 6

This appendix contains supplementary experimental results from the urban form study presented in Chapter 6.

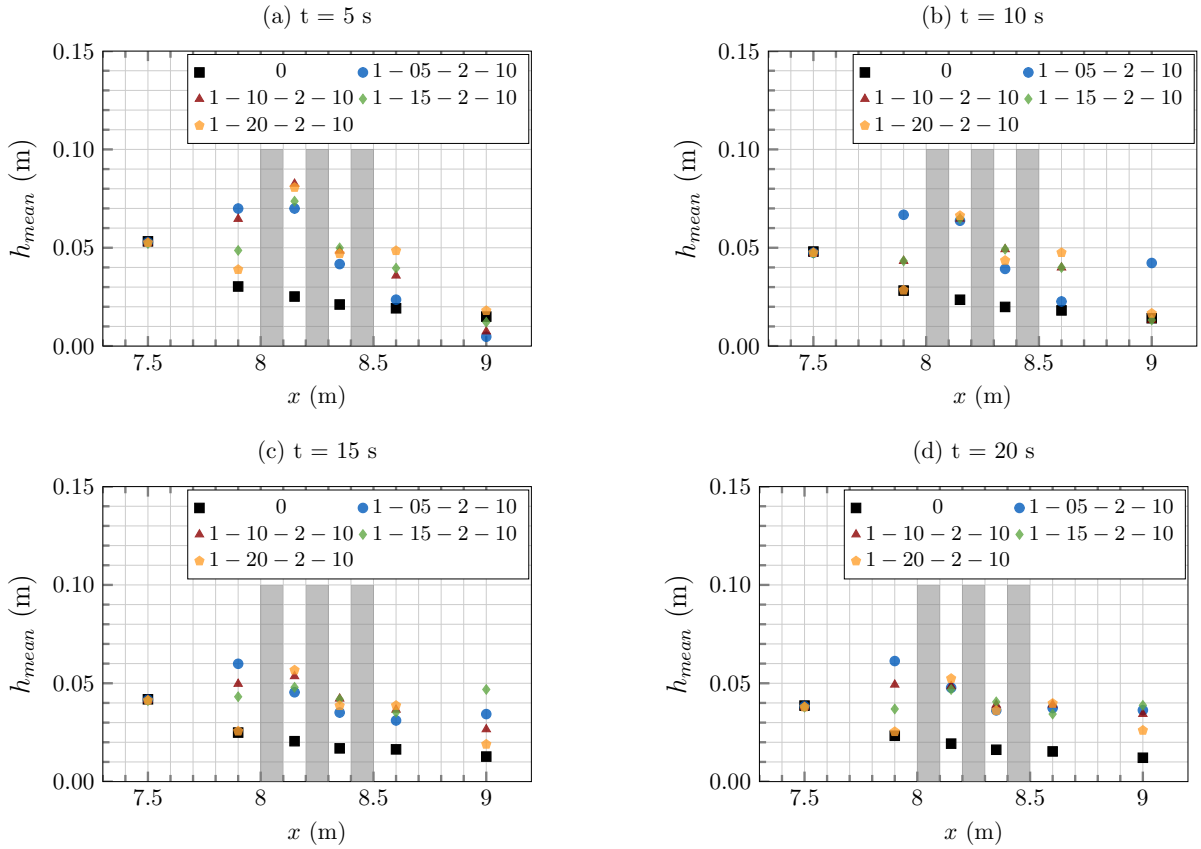

Figure E.1: Cases $n_x = 1$. Evolution of the water depth profile (y = 0 m) at times (a) t = 5 s, (b) t = 10 s, (c) t = 15 s, and (d) t = 20 s. Grey rectangles represent cubes position.

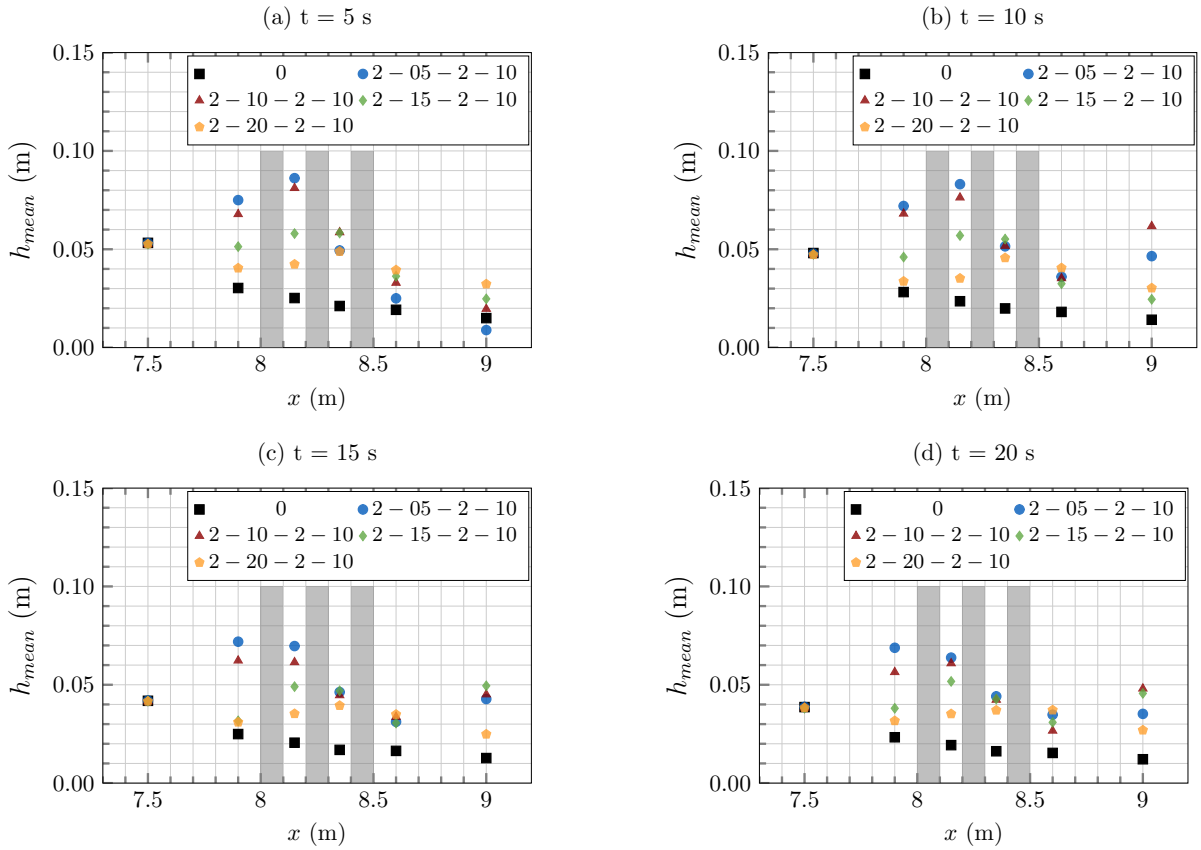

Figure E.2: Cases $n_x = 2$. Evolution of the water depth profile (y = 0 m) at times (a) t = 5 s, (b) t = 10 s, (c) t = 15 s, and (d) t = 20 s. Grey rectangles represent cubes position.

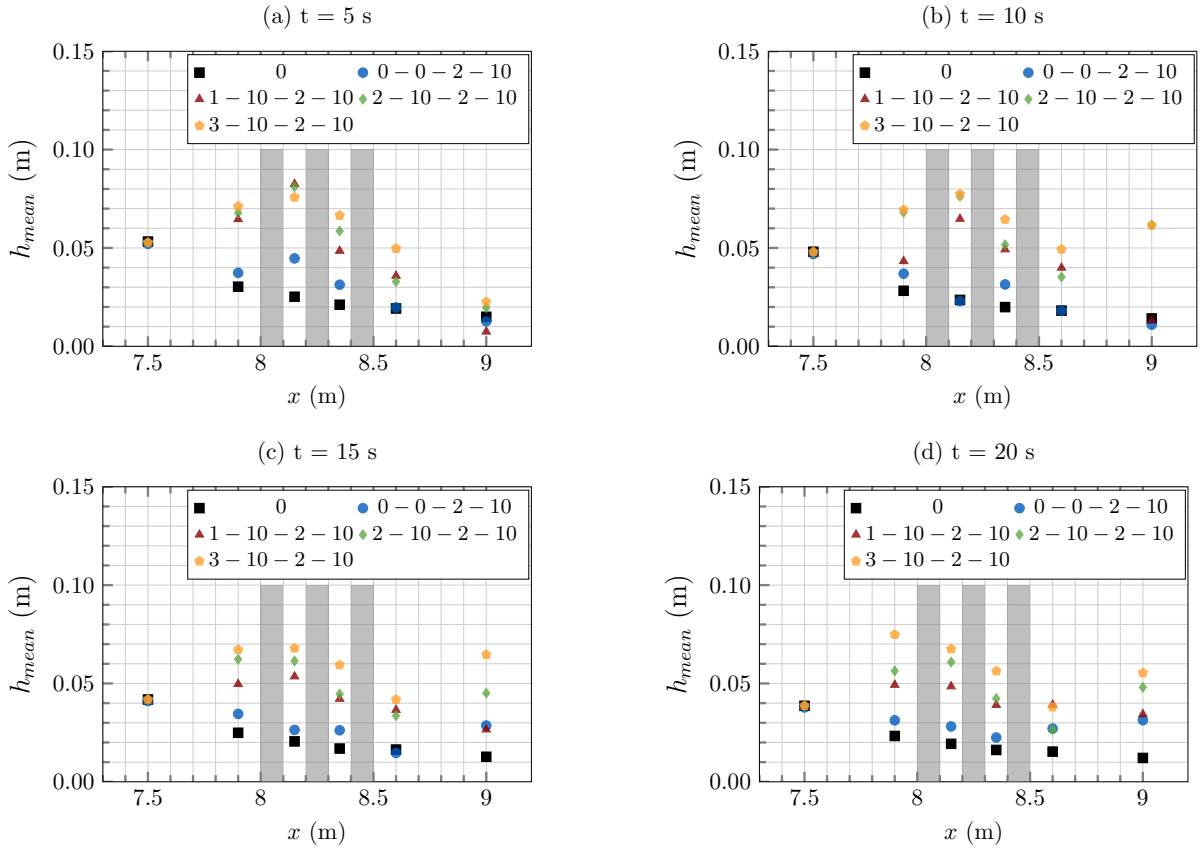

Figure E.3: Cases $l_y = 0.10$ m. Evolution of the water depth profile (y = 0 m) at times (a) t = 5 s, (b) t = 10 s, (c) t = 15s, and (d) t = 20 s.

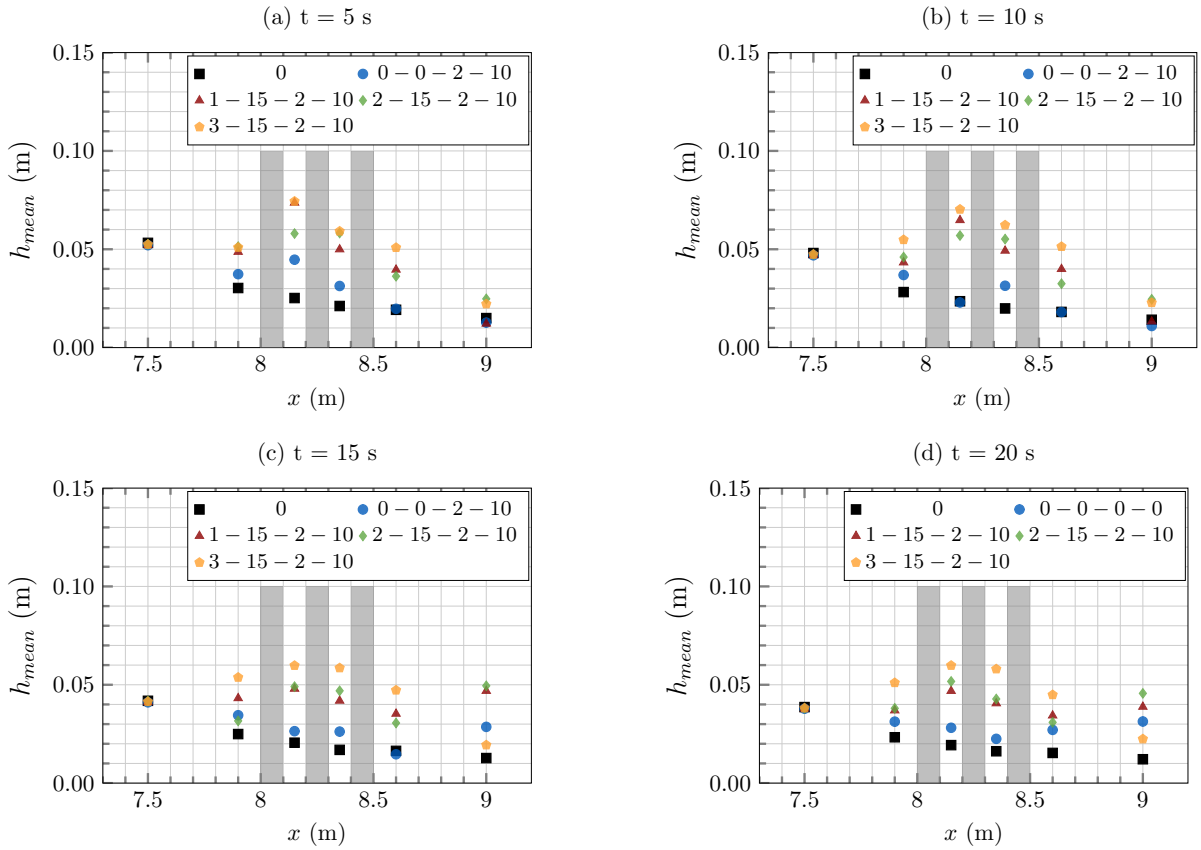

Figure E.4: Cases l_y = 0.15 m. Evolution of the water depth profile (y = 0 m) at times (a) t = 5 s, (b) t = 10 s, (c) t = 15s, and (d) t = 20 s.

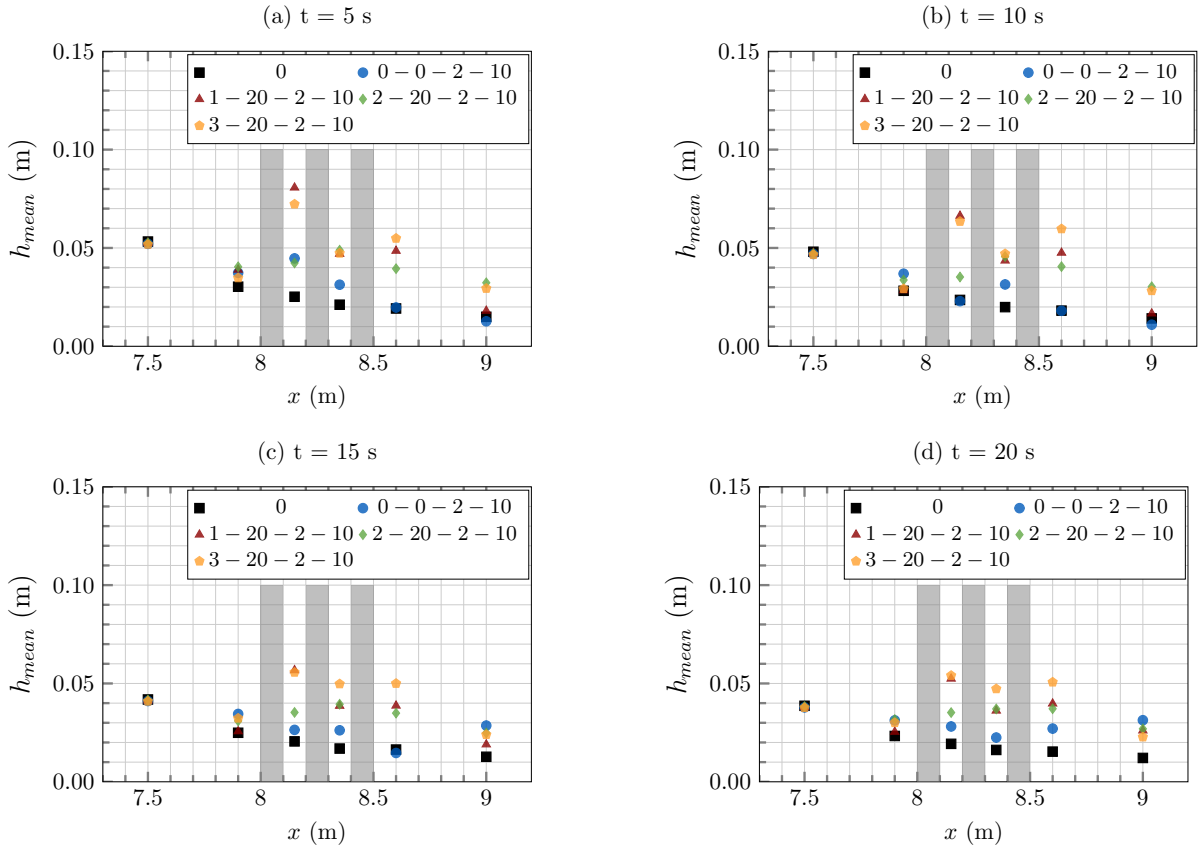

Figure E.5: Cases l_y = 0.20 m. Evolution of the water depth profile (y = 0 m) at times (a) t = 5 s, (b) t = 10 s, (c) t = 15s, and (d) t = 20 s.

Snapshots of the jet induced by the impact of the dam-break wave on the urban area at t = 1.1 s are shown in Figures E.6 and E.7 for cases with $l_x = 0.05$ m and $l_x = 0.20$ m, respectively.

The snapshots illustrate the effect of the number of streets on the splash-up height and shape. Additionally, Figure E.8a shows that the number of streets does not impact the splash up maximum water height. However, some differences are visible afterwards for cases with wider streets (Figure E.8b), which is expected as larger urban areas (L_y) leads to longer splash-up (the mass of water is distributed over a longer area).

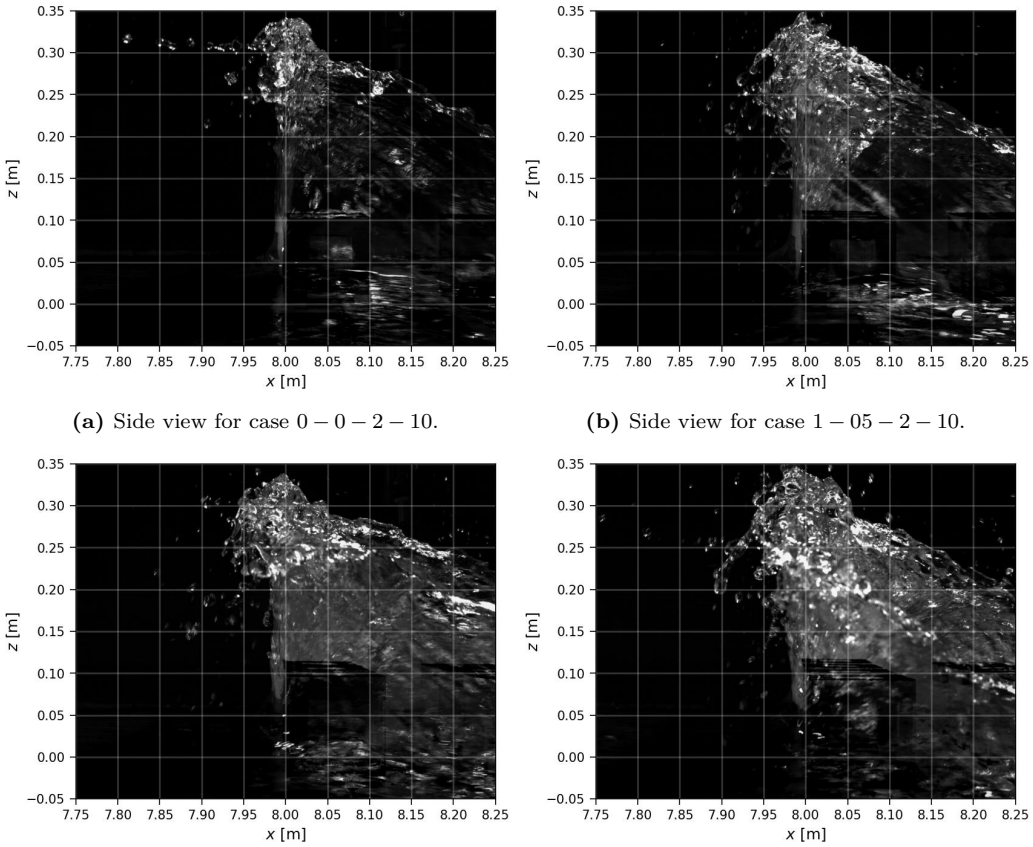

(a) Side view for case $0-0-2-10$.

(b) Side view for case $1-05-2-10$.

(c) Side view for case $2-05-2-10$.

(d) Side view for case $3-05-2-10$.

Figure E.6: Images of the water jet at t = 1.1 s for cases $l_x = 0.05$ (b, c, d).

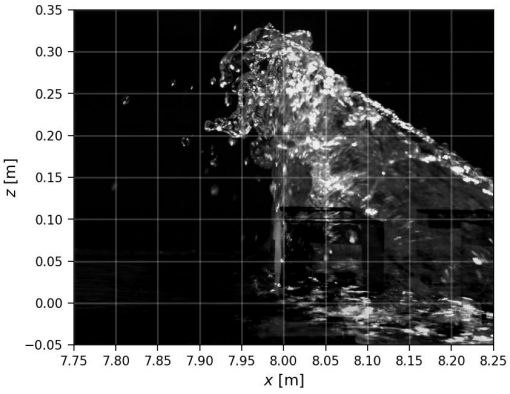

(a) Side view for case $1-20-2-10$.

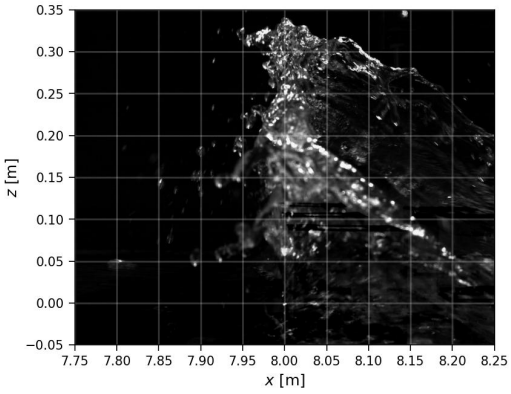

(b) Side view for case $2-20-2-10$.

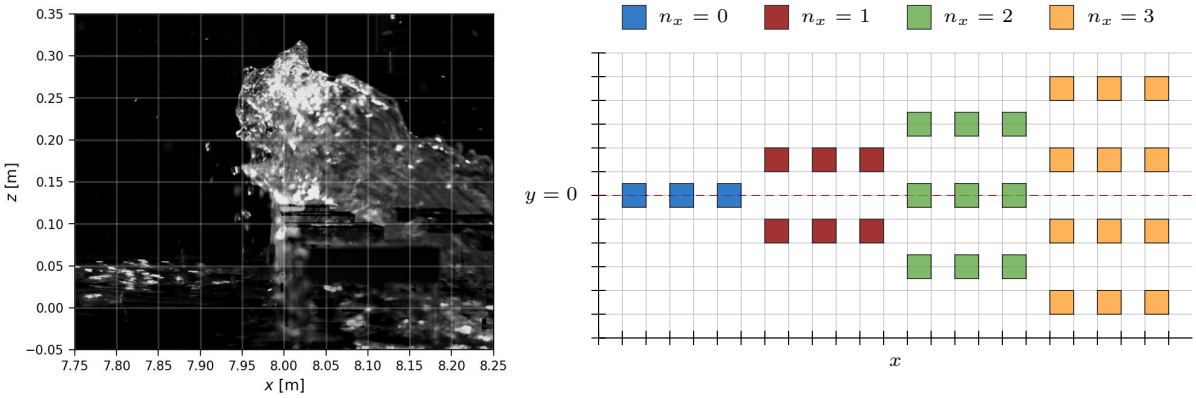

(c) Side view for case $3-20-2-10$.

Figure E.7: Images of the water jet at t = 1.1 s for cases $l_x = 0.20$.

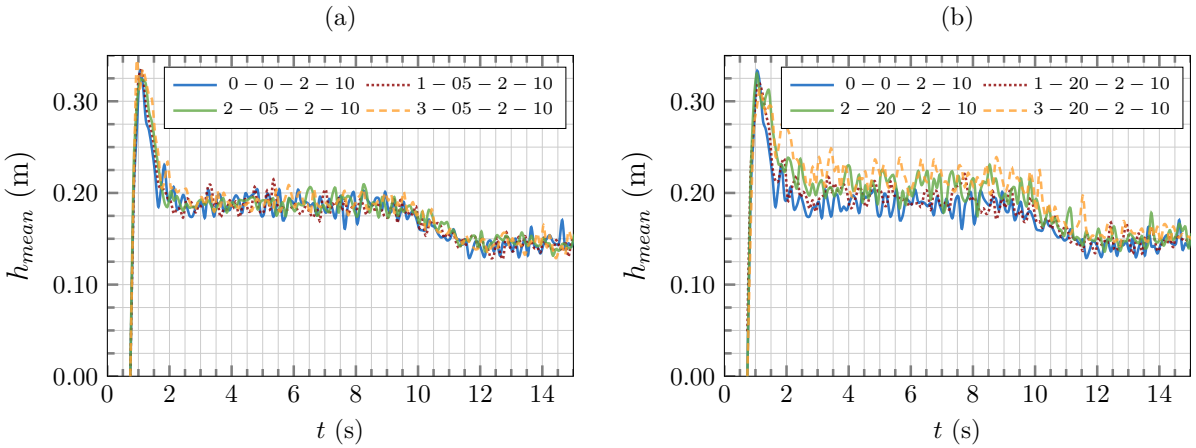

Figure E.8: Evolution of the water depth at x = y = 8 m from the IAM analysis for cases (a) $l_x = 0.05$ m and (b) $l_x = 0.20$ m.

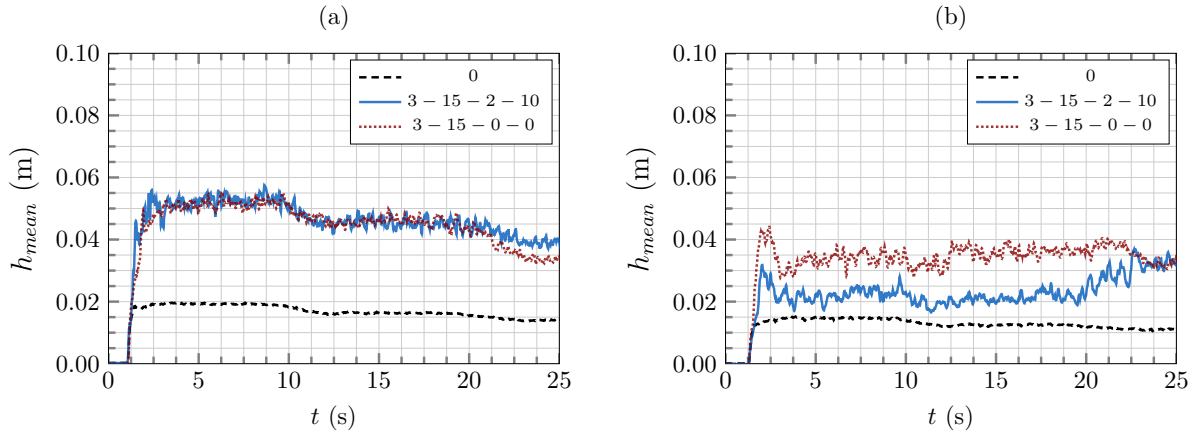

Figure E.9: Water depth comparison between cases 3 – 15 – 2 – 10 and 3 – 15 – 0 – 0 at positions (a) A5 and (b) A6.

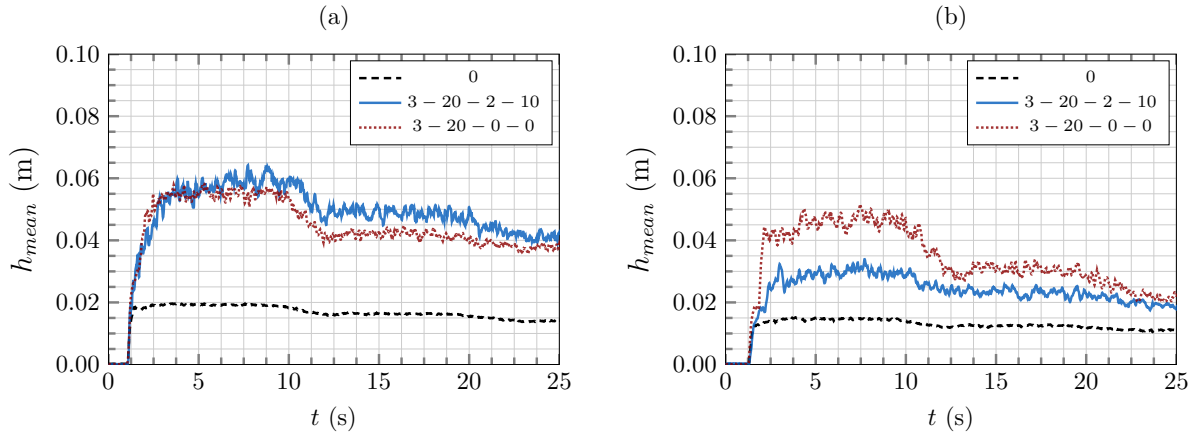

Figure E.10: Water depth comparison between cases 3 – 20 – 2 – 10 and 3 – 20 – 0 – 0 at positions (a) A5 and (b) A6.

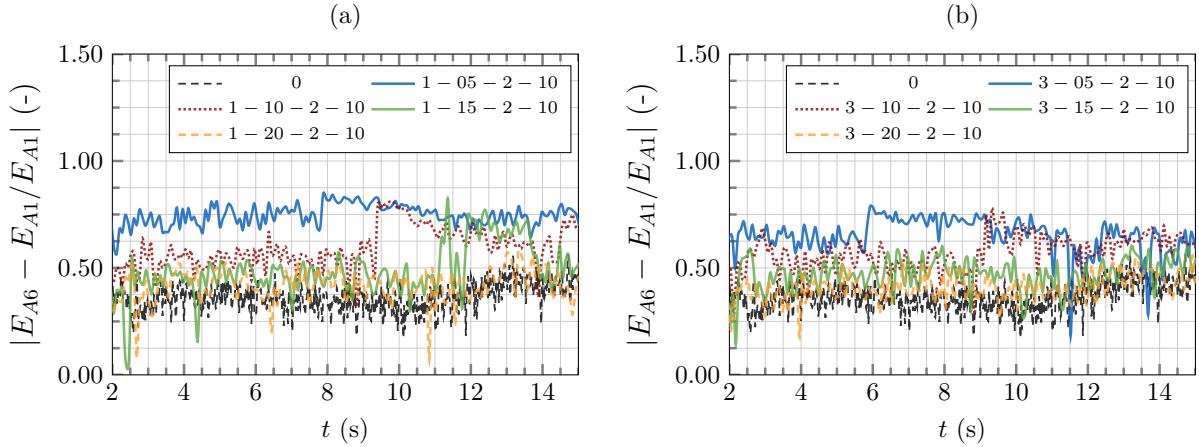

Figure E.11: Evolution of the head loss calculated between position A1 and A6 for cases (a) $n_x = 1$ and (b) $n_x = 3$.

F

SUPPLEMENTARY DATA FROM CHAPTER 7

This appendix contains supplementary results from the numerical study presented in Chapter 7.

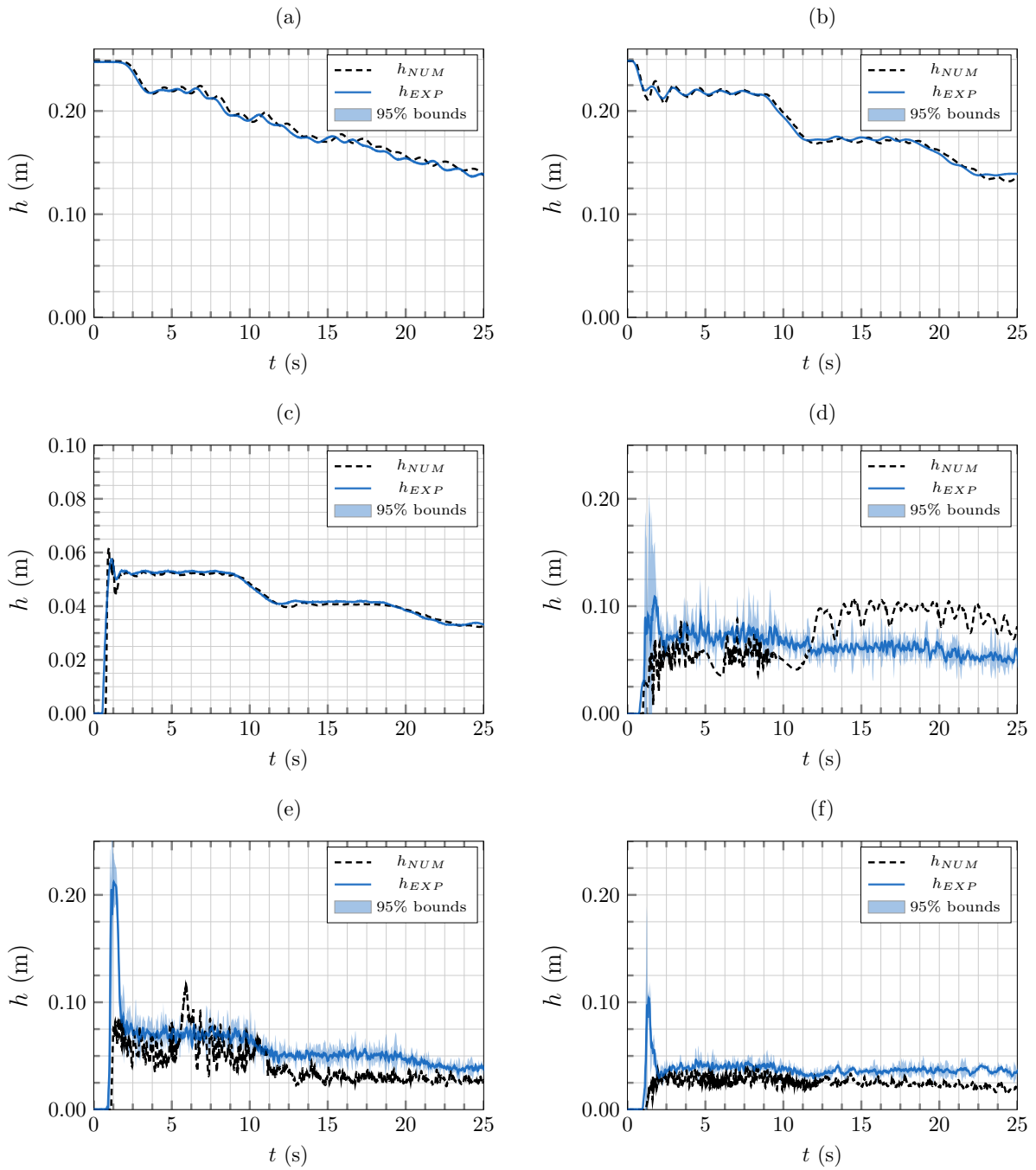

Figure F.1: Case $1-05-2-10$. Water height comparison at positions (a) R1, (b) R2, (c) A1, (d) A2, (e) A3 and (f) A4 between wave gauge measurements (blue line) and numerical model (black dashed line).

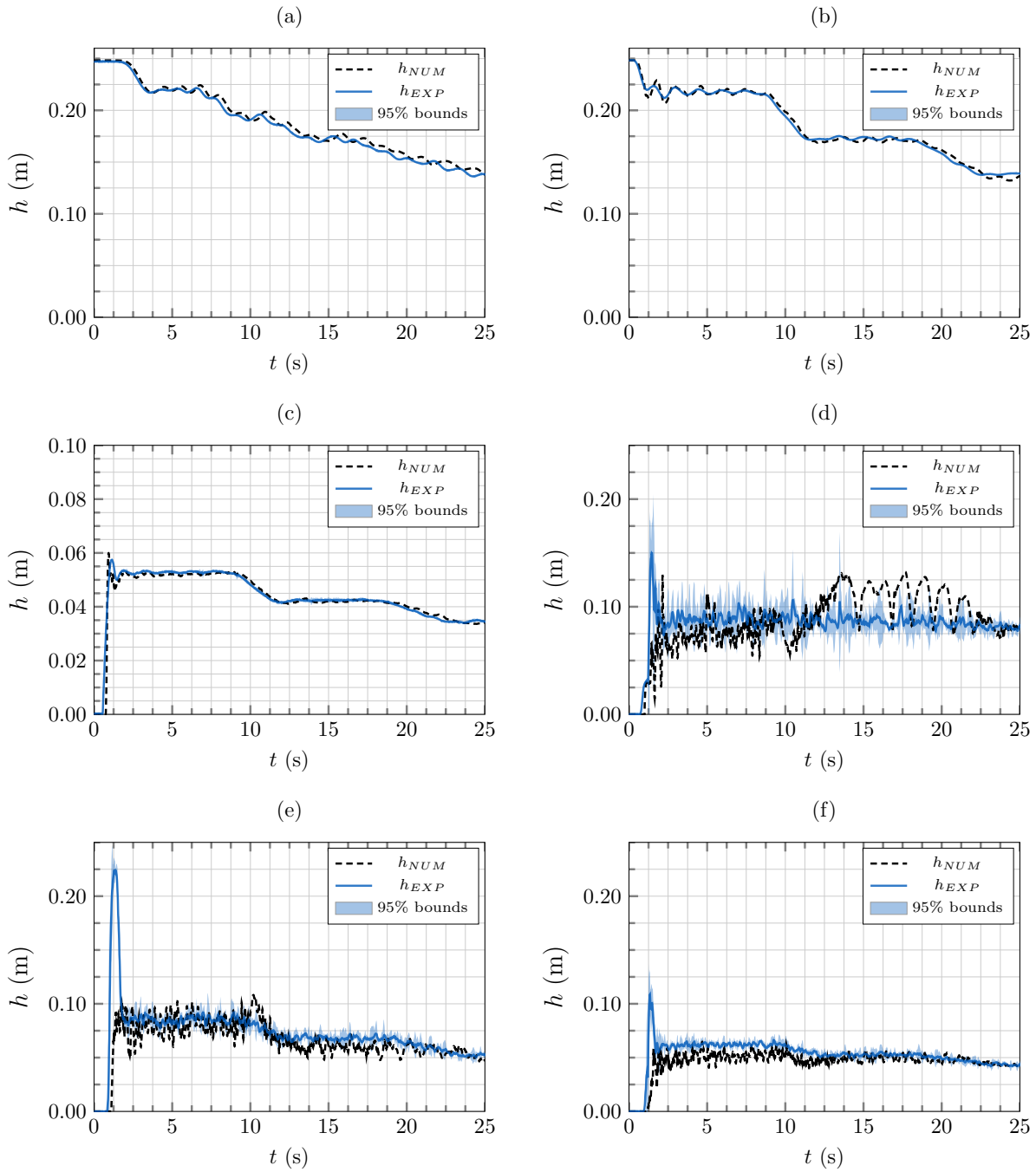

Figure F.2: Case $3-05-2-10$. Water height comparison at positions (a) R1, (b) R2, (c) A1, (d) A2, (e) A3 and (f) A4 between wave gauge measurements (blue line) and numerical model (black dashed line).

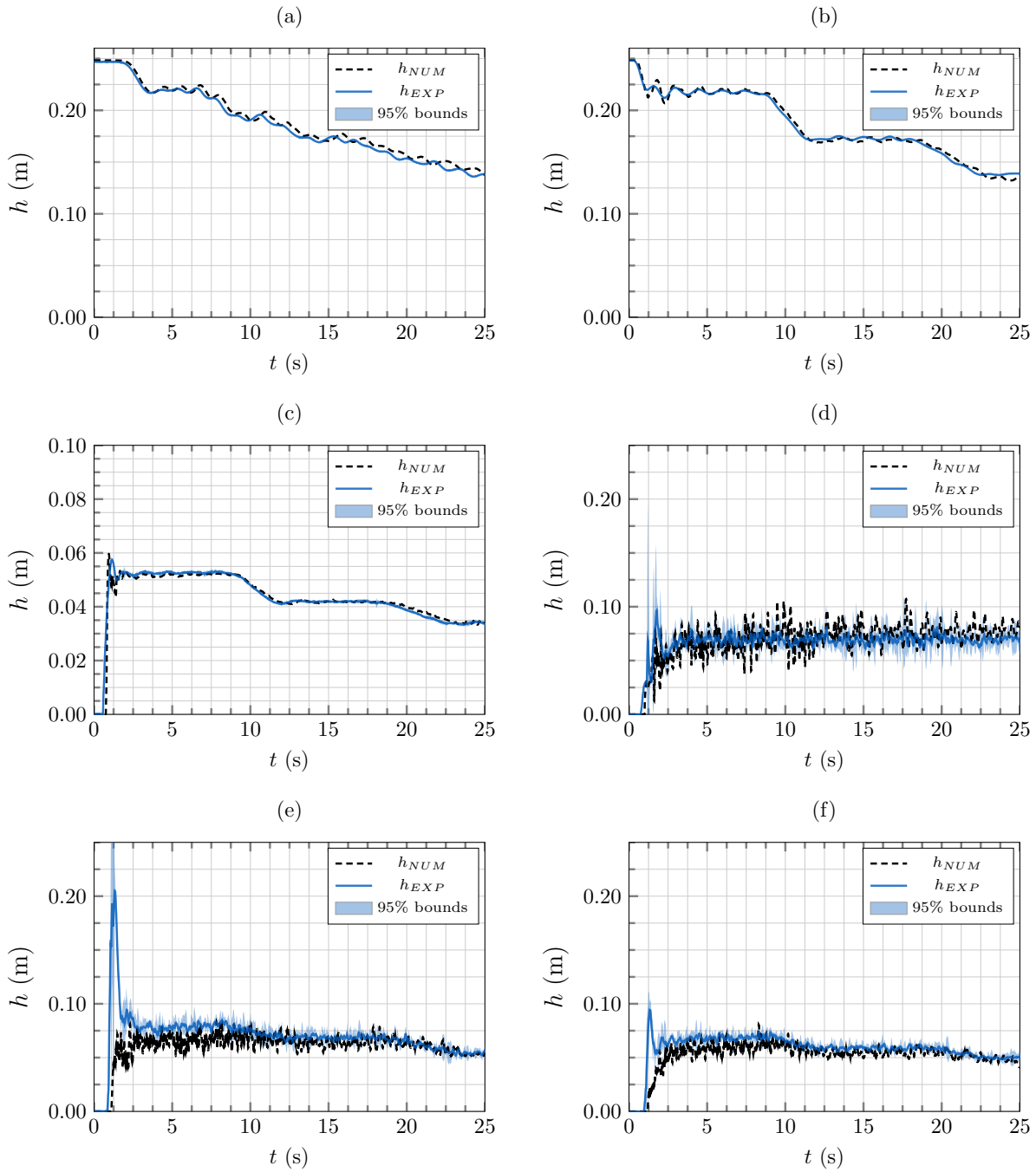

Figure F.3: Case $3-10-2-10$. Water height comparison at positions (a) R1, (b) R2, (c) A1, (d) A2, (e) A3 and (f) A4 between wave gauge measurements (blue line) and numerical model (black dashed line).

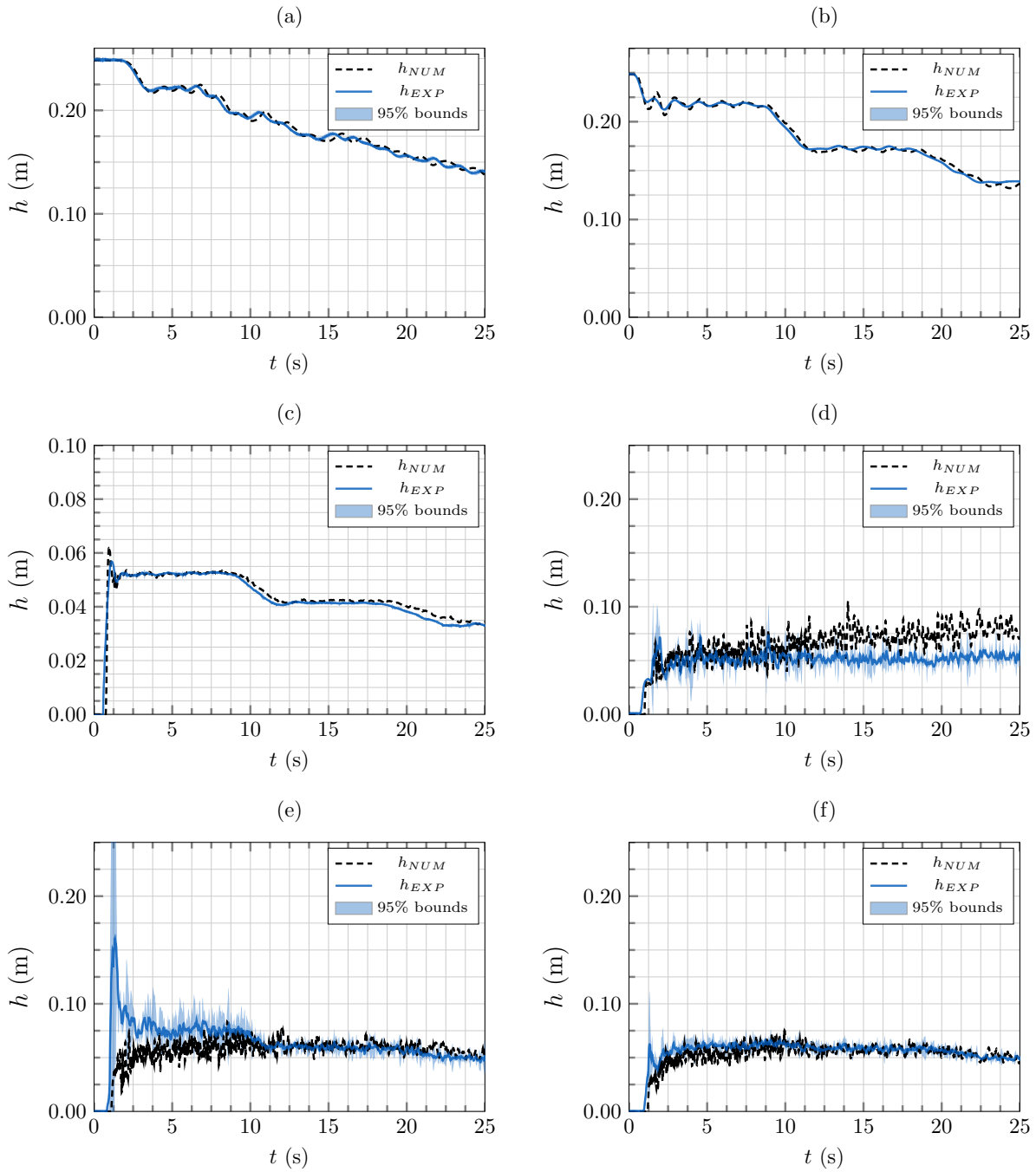

Figure F.4: Case $3-15-2-10$. Water height comparison at positions (a) R1, (b) R2, (c) A1, (d) A2, (e) A3 and (f) A4 between wave gauge measurements (blue line) and numerical model (black dashed line).

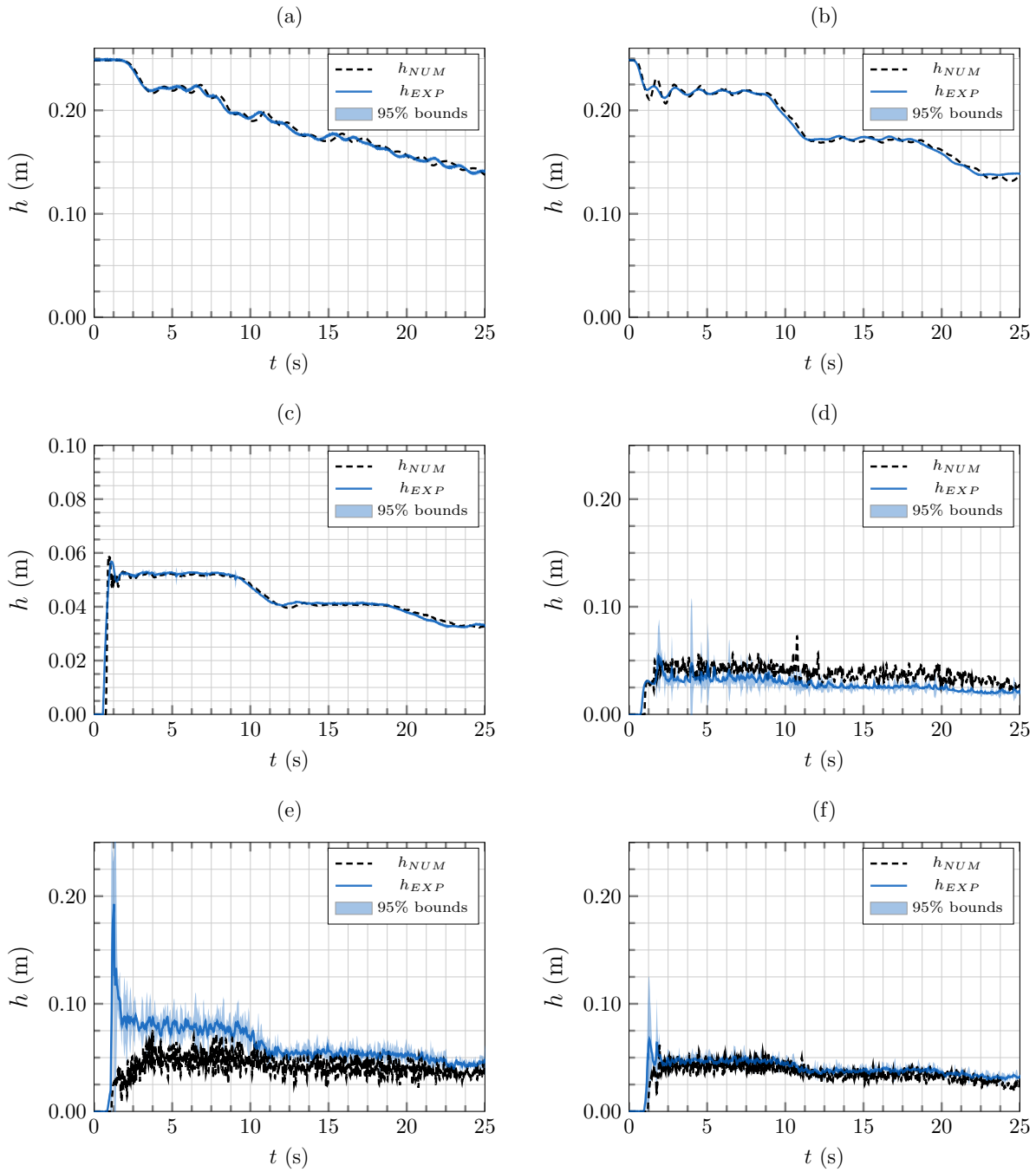

Figure F.5: Case $1-20-2-10$. Water height comparison at positions (a) R1, (b) R2, (c) A1, (d) A2, (e) A3 and (f) A4 between wave gauge measurements (blue line) and numerical model (black dashed line).

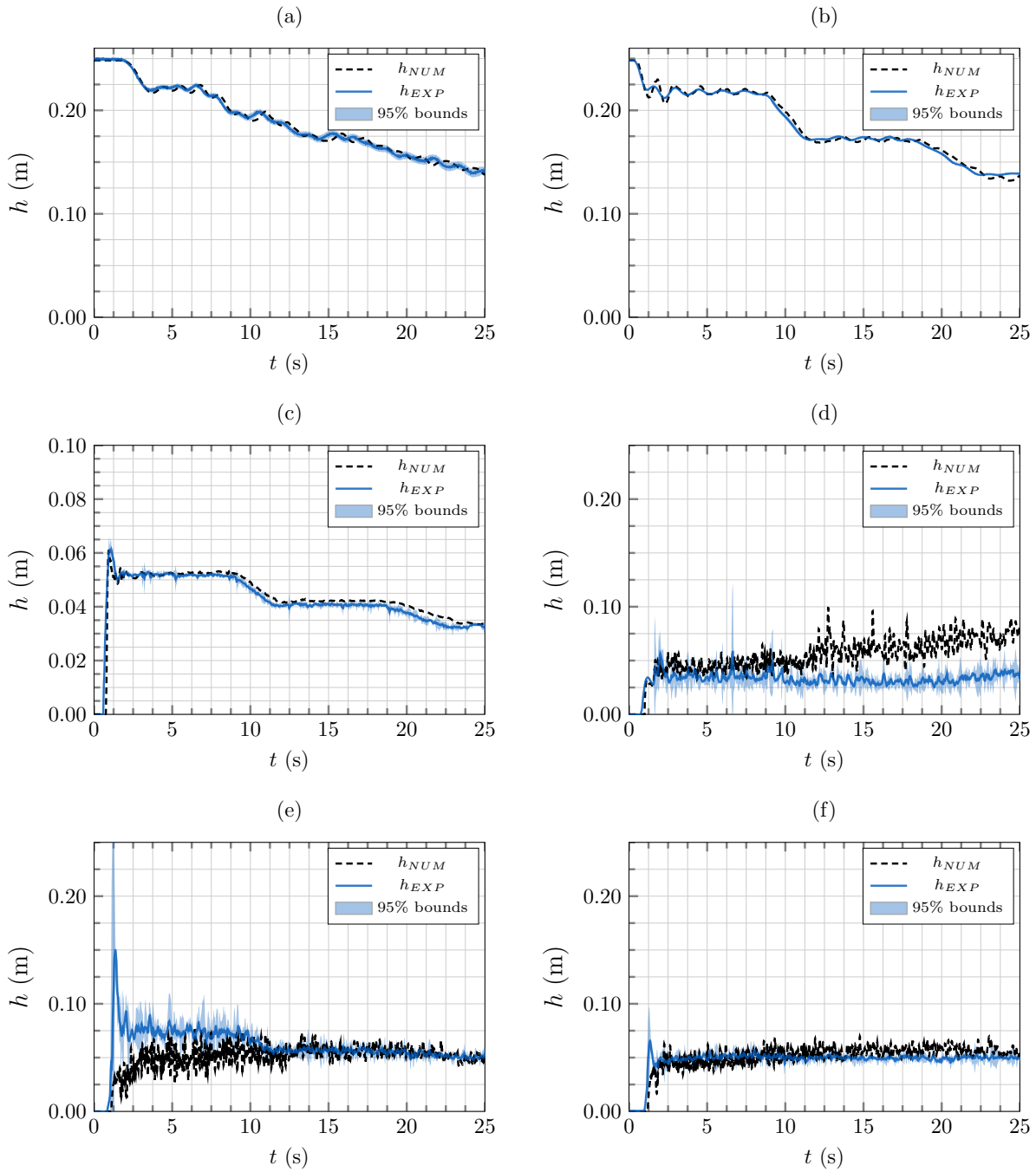

Figure F.6: Case $3-20-2-10$. Water height comparison at positions (a) R1, (b) R2, (c) A1, (d) A2, (e) A3 and (f) A4 between wave gauge measurements (blue line) and numerical model (black dashed line).

BIBLIOGRAPHY

[1] Francesca Aureli, Andrea Maranzoni, and Gabriella Petaccia. "Review of Historical Dam-Break Events and Laboratory Tests on Real Topography for the Validation of Numerical Models". en. In: *Water* 13.14 (July 2021), p. 1968. ISSN: 2073-4441. DOI: 10.3390/w13141968.

[2] Emmanouil Psomiadis, Lefteris Tomanis, Antonis Kavvadias, Konstantinos X. Soulis, Nikos Charizopoulos, and Spyros Michas. "Potential Dam Breach Analysis and Flood Wave Risk Assessment Using HEC-RAS and Remote Sensing Data: A Multicriteria Approach". en. In: *Water* 13.3 (Jan. 2021), p. 364. ISSN: 2073-4441. DOI: 10.3390/w13030364.

[3] Wei Ge, Yutie Jiao, Heqiang Sun, Zongkun Li, Hexiang Zhang, Yan Zheng, Xinyan Guo, Zhaosheng Zhang, and P.H.A.J.M. van Gelder. "A Method for Fast Evaluation of Potential Consequences of Dam Breach". en. In: *Water* 11.11 (Oct. 2019), p. 2224. ISSN: 2073-4441. DOI: 10.3390/w11112224.

[4] Jian Mao, Shandong Wang, Jianhua Ni, Changbai Xi, and Jiechen Wang. "Management System for Dam-Break Hazard Mapping in a Complex Basin Environment". en. In: *ISPRS International Journal of Geo-Information* 6.6 (June 2017), p. 162. ISSN: 2220-9964. DOI: 10.3390/ijgi6060162.

[5] Javier Fluixá-Sanmartín, Luis Altarejos-García, Adrián Morales-Torres, and Ignacio Escuder-Bueno. "Climate change impacts on dam safety". In: *Natural Hazards and Earth System Sciences* 18.9 (2018), pp. 2471–2488.

[6] Sudha Yerramilli. "Potential impact of climate changes on the inundation risk levels in a dam break scenario". In: *ISPRS international journal of geo-information* 2.1 (2013), pp. 110–134.

[7] Yue Zhang, Ying Wang, Yu Chen, Yingjun Xu, Guoming Zhang, Qigen Lin, and Rihong Luo. "Projection of changes in flash flood occurrence under climate change at tourist attractions". In: *Journal of Hydrology* 595 (2021), p. 126039. ISSN: 0022-1694. DOI: https://doi.org/10.1016/j.jhydrol.2021.126039.

[8] S. Hettiarachchi, C. Wasko, and A. Sharma. "Increase in flood risk resulting from climate change in a developed urban watershed - the role of storm temporal patterns". In: *Hydrology and Earth System Sciences* 22.3 (2018), pp. 2041–2056. DOI: 10.5194/hess-22-2041-2018.

[9] Jascha Lehmann, Dim Coumou, and Katja Frieler. "Increased record-breaking precipitation events under global warming". In: *Climatic Change* 132 (Aug. 2015). DOI: 10.1007/s10584-015-1466-3.

[10] K. Jenkins, S. Surminski, J. Hall, and F. Crick. "Assessing surface water flood risk and management strategies under future climate change: Insights from an Agent-Based Model". In: *Science of The Total Environment* 595 (2017), pp. 159–168. ISSN: 0048-9697. DOI: https://doi.org/10.1016/j.scitotenv.2017.03.242.

[11] Yukiko Hirabayashi, Roobavannan Mahendran, Sujan Koirala, Lisako Konoshima, Dai Yamazaki, Satoshi Watanabe, Hyungjun Kim, and Shinjiro Kanae. "Global flood risk under climate change". In: *Nature climate change* 3.9 (2013), pp. 816–821.

[12] Nigel W Arnell and Simon N Gosling. "The impacts of climate change on river flood risk at the global scale". In: *Climatic Change* 134 (2016), pp. 387–401.

[13] Wu Qin, Hong-mei Xu, Min Liu, Lüliu Liu, Chan Xiao, Iman Mallakpour, Matin Rahnamay Naeini, Kuolin Hsu, and Soroosh Sorooshian. "Projected impacts of climate change on major dams in the Upper Yangtze River Basin". In: *Climatic Change* 170 (Jan. 2022). DOI: 10.1007/s10584-021-03303-w.

[14] Yangbo Chen, Haolan Zhou, Hui Zhang, Guoming Du, and Jinhui Zhou. "Urban flood risk warning under rapid urbanization". In: *Environmental Research* 139 (2015). Environmental Research on Hydrology and Water Resources, pp. 3–10. ISSN: 0013-9351. DOI: https://doi.org/10.1016/j.envres.2015.02.028.

[15] Wei Li, Zongkun Li, Wei Ge, and Sai Wu. "Risk Evaluation Model of Life Loss Caused by Dam-break Flood and Its Application". en. In: *Water* 11.7 (June 2019), p. 1359. ISSN: 2073-4441. DOI: 10.3390/w11071359.

[16] EPTB Fleuve Hérault. *Fleuve Hérault*. https://fleuve-herault.fr/le-bassin-versant/enjeux-et-problematiques/risque-inondation. Accessed on August 5, 2024. 2024.

[17] Frank Jordans. *The Associated Press*. https://apnews.com/article/europe-environment-and-nature-germany-floods-44498a9899e1a75929f8de9e3df07874. Accessed on August 5, 2024. 2021.

[18] Diego Fernández-Nóvoa, José González-Cao, and Orlando García-Feal. "Enhancing Flood Risk Management: A Comprehensive Review on Flood Early Warning Systems with Emphasis on Numerical Modeling". In: *Water* 16.10 (2024). ISSN: 2073-4441. DOI: 10.3390/w16101408.

[19] Andrea Maranzoni and Massimo Tomirotti. "Three-Dimensional Numerical Modelling of Real-Field Dam-Break Flows: Review and Recent Advances". In: *Water* 15 (Aug. 2023), p. 3130. DOI: 10.3390/w15173130.

[20] P García-Navarro, J Murillo, J Fernández-Pato, I Echeverribar, and M Morales-Hernández. "The shallow water equations and their application to realistic cases". en. In: *Environ. Fluid Mech. (Dordr.)* 19.5 (Oct. 2019), pp. 1235–1252.

[21] M.S. Horritt and P.D. Bates. "Evaluation of 1D and 2D numerical models for predicting river flood inundation". In: *Journal of Hydrology* 268.1 (2002), pp. 87–99. ISSN: 0022-1694. DOI: https://doi.org/10.1016/S0022-1694(02)00121-X.

[22] Zhu Liu, Venkatesh Merwade, and Keighobad Jafarzadegan. "Investigating the role of model structure and surface roughness in generating flood inundation extents using 1D and 2D hydraulic models". In: *Journal of Flood Risk Management* 12 (Mar. 2018), e12347. DOI: 10.1111/jfr3.12347.

[23] Venkatesh Merwade, Francisco Olivera, Mazdak Arabi, and Scott Edleman. "Uncertainty in Flood Inundation Mapping: Current Issues and Future Directions". In: *Journal of Hydrologic Engineering - J HYDROL ENG* 13 (July 2008). DOI: 10.1061/(ASCE)1084-0699(2008)13:7(608).

[24] Emrah Yalcin. "Assessing the impact of topography and land cover data resolutions on two-dimensional HEC-RAS hydrodynamic model simulations for urban flood hazard analysis". In: *Natural Hazards* 101 (Apr. 2020). DOI: 10.1007/s11069-020-03906-z.

[25] Emmanuel Mignot, Xuefang Li, and Benjamin Dewals. "Experimental modelling of urban flooding: A review". en. In: *Journal of Hydrology* 568 (Jan. 2019), pp. 334–342. ISSN: 00221694. DOI: 10.1016/j.jhydrol.2018.11.001.

[26] Kaihua Guo, Mingfu Guan, and Dapeng Yu. "Urban surface water flood modelling – a comprehensive review of current models and future challenges". en. In: *Hydrology and Earth System Sciences* 25.5 (May 2021), pp. 2843–2860. ISSN: 1607-7938. DOI: 10.5194/hess-25-2843-2021.

[27] Yun Xing, Qiuhua Liang, Gang Wang, Xiaodong Ming, and Xilin Xia. "City-scale hydrodynamic modelling of urban flash floods: the issues of scale and resolution". In: *Natural Hazards* 96 (Mar. 2019). DOI: 10.1007/s11069-018-3553-z.

[28] Qiuhua Liang and Luke S. Smith. "A high-performance integrated hydrodynamic modelling system for urban flood simulations". In: *Journal of Hydroinformatics* 17.4 (Jan. 2015), pp. 518–533. ISSN: 1464-7141. DOI: 10.2166/hydro.2015.029. eprint: https://iwaponline.com/jh/article-pdf/17/4/518/388647/jh0170518.pdf.

[29] J. Teng, A.J. Jakeman, J. Vaze, Barry Croke, D. Dutta, and S. Kim. "Flood inundation modelling: A review of methods, recent advances and uncertainty analysis". In: 90 (Apr. 2017), pp. 201–216. DOI: 10.1016/j.envsoft.2017.01.006.

[30] X. Li, S. Erpicum, M. Bruwier, E. Mignot, P. Finaud-Guyot, P. Archambeau, M. Pirotton, and B. Dewals. "Technical note: Laboratory modelling of urban flooding: strengths and challenges of distorted scale models". In: *Hydrology and Earth System Sciences* 23.3 (2019), pp. 1567–1580. DOI: 10.5194/hess-23-1567-2019.

[31] DW team. *DW*. https://www.dw.com/en/libya-more-than-2000-dead-after-catastrophic-floods/a-66786792. Accessed on August 5, 2024. 2023.

[32] Francesca Aureli, Andrea Maranzoni, Gabriella Petaccia, and Sandra Soares-Frazão. "Review of Experimental Investigations of Dam-Break Flows over Fixed Bottom". en. In: *Water* 15.6 (Mar. 2023), p. 1229. ISSN: 2073-4441. DOI: 10.3390/w15061229.

[33] Faroogh Garoosi, Andrea Nicole Mellado-Cusicahua, Maryam Shademani, and Ahmad Shakibaeinia. "Experimental and numerical investigations of dam break flow over dry and wet beds". en. In: *International Journal of Mechanical Sciences* 215 (Feb. 2022), p. 106946. ISSN: 00207403. DOI: 10.1016/j.ijmecsci.2021.106946.

[34] Shaolin Yang, Wanli Yang, Chuanjiang Zhang, Shunquan Qin, Kai Wei, and Jiarui Zhang. "Experimental and numerical study on the evolution of wave front profile of dam-break waves". en. In: *Ocean Engineering* 247 (Mar. 2022), p. 110681. ISSN: 00298018. DOI: 10.1016/j.oceaneng.2022.110681.

[35] Selahattin Kocaman, Stefania Evangelista, Hasan Guzel, Kaan Dal, Ada Yilmaz, and Giacomo Viccione. "Experimental and Numerical Investigation of 3D Dam-Break Wave Propagation in an Enclosed Domain with Dry and Wet Bottom". In: *Applied Sciences* 11.5638 (2021), pp. 1–21. DOI: https://doi.org/10.3390/app11125638.

[36] Mattias Melis. "Dam-break wave propagation on a rough surface: Experimental and numerical study". English. PhD thesis. Falcolta di Ingeneria, 2018.

[37] Atabak Feizi Khankandi, Ahmad Tahershamsi, and Sandra Soares-Frazão. "Experimental investigation of reservoir geometry effect on dam-break flow". en. In: *Journal of Hydraulic Research* 50.4 (Aug. 2012), pp. 376–387. ISSN: 0022-1686, 1814-2079. DOI: 10.1080/00221686.2012.690974.

[38] V. I. Bukreev. "On the Water Depth in the Breach during a Partial Dam Break". en. In: *Fluid Dynamics* 40.5 (Sept. 2005), pp. 769–776. ISSN: 0015-4628, 1573-8507. DOI: 10.1007/s10697-005-0114-4.

[39] Guido Lauber and Willi H. Hager. "Experiments to dambreak wave: Horizontal channel". en. In: *Journal of Hydraulic Research* 36.3 (May 1998), pp. 291–307. ISSN: 0022-1686, 1814-2079. DOI: 10.1080/00221689809498620.

[40] P. K. Stansby, A. Chegini, and T. C. D. Barnes. "The initial stages of dam-break flow". en. In: *Journal of Fluid Mechanics* 374 (Nov. 1998), pp. 407–424. ISSN: 0022-1120, 1469-7645. DOI: 10.1017/S0022112098001918.

[41] R.F. Dressler. "Hydraulic resistance effect upon the dam-break functions". en. In: *Journal of Research of the National Bureau of Standards* 49.3 (Sept. 1952), p. 217. ISSN: 0091-0635. DOI: 10.6028/jres.049.021.

[42] Selahattin Kocaman, Stefania Evangelista, Giacomo Viccione, and Hasan Güzel. "Experimental and Numerical Analysis of 3D Dam-Break Waves in an Enclosed Domain with a Single Oriented Obstacle". en. In: *Environmental Sciences Proceedings* 2.1 (Aug. 2020), p. 35. ISSN: 2673-4931. DOI: 10.3390/environsciproc2020002035.

[43] Lu Liu, Jian Sun, Binliang Lin, and Lingwei Lu. "Building performance in dam-break flow – an experimental study". en. In: *Urban Water Journal* 15.3 (Mar. 2018), pp. 251–258. ISSN: 1573-062X, 1744-9006. DOI: 10.1080/1573062X.2018.1433862.

[44] Francesca Aureli, Susanna Dazzi, Andrea Maranzoni, Paolo Mignosa, and Renato Vacondio. "Experimental and numerical evaluation of the force due to the impact of a dam-break wave on a structure". en. In: *Advances in Water Resources* 76 (Feb. 2015), pp. 29–42. ISSN: 03091708. DOI: 10.1016/j.advwatres.2014.11.009.

[45] S. Soares-Frazão and Y. Zech. "Experimental study of dam-break flow against an isolated obstacle". en. In: *Journal of Hydraulic Research* 45.sup1 (Dec. 2007), pp. 27–36. ISSN: 0022-1686, 1814-2079. DOI: 10.1080/00221686.2007.9521830.

[46] Francesca Aureli, Andrea Maranzoni, Paolo Mignosa, and Chiara Ziveri. "Dam-Break Flows: Acquisition of Experimental Data through an Imaging Technique and 2D Numerical Modeling". en. In: *Journal of Hydraulic Engineering* 134.8 (Aug. 2008), pp. 1089–1101. ISSN: 0733-9429, 1943-7900. DOI: 10.1061/(ASCE)0733-9429(2008)134:8(1089).

[47] Xuefang Li, Sébastien Erpicum, Emmanuel Mignot, Pierre Archambeau, Michel Pirotton, and Benjamin Dewals. "Influence of urban forms on long-duration urban flooding: Laboratory experiments and computational analysis". In: *Journal of Hydrology* 603 (2021), p. 127034. ISSN: 0022-1694. DOI: https://doi.org/10.1016/j.jhydrol.2021.127034.

[48] Augustin Doumic, Frédérique Larrarte, Radjae Rtimi, and Nicole Goutal. "Investigation of the hydraulics in flooded housing estate". English. In: *SimHydro*. 2021, p. 9.

[49] Marina Oukacine, Sébastien Proust, Frédérique Larrarte, and Nicole Goutal. "Experimental flows through an array of emerged or slightly submerged square cylinders over a rough bed". en. In: *Scientific Data* 8.1 (Jan. 2021), p. 6. ISSN: 2052-4463. DOI: 10.1038/s41597-020-00791-w.

[50] Mirjana Velickovic, Yves Zech, and Sandra Soares-Frazão. "Steady-flow experiments in urban areas and anisotropic porosity model". en. In: *Journal of Hydraulic Research* 55.1 (Jan. 2017), pp. 85–100. ISSN: 0022-1686, 1814-2079. DOI: 10.1080/00221686.2016.1238013.

[51] Qi Zhou, Wangyang Yu, Albert S. Chen, Chunbo Jiang, and Guangtao Fu. "Experimental Assessment of Building Blockage Effects in a Simplified Urban District". en. In: *Procedia Engineering* 154 (2016), pp. 844–852. ISSN: 18777058. DOI: 10.1016/j.proeng.2016.07.448.

[52] Chen-Jia Huang, Ming-Hsi Hsu, Wei-Hsien Teng, and Yen-Hsiang Wang. "The Impact of Building Coverage in the Metropolitan Area on the Flow Calculation". en. In: *Water* 6.8 (Aug. 2014), pp. 2449–2466. ISSN: 2073-4441. DOI: 10.3390/w6082449.

[53] Sandra Soares-Frazão and Yves Zech. "Dam-break flow through an idealised city". en. In: *Journal of Hydraulic Research* 46.5 (Sept. 2008), pp. 648–658. ISSN: 0022-1686, 1814-2079. DOI: 10.3826/jhr.2008.3164.

[54] Guido Testa, David Zuccalà, Francisco Alcrudo, Jontan Mulet, and Sandra Soares-Frazão. "Flash flood flow experiment in a simplified urban district". en. In: *Journal of Hydraulic Research* 45.sup1 (Dec. 2007), pp. 37–44. ISSN: 0022-1686, 1814-2079. DOI: 10.1080/00221686.2007.9521831.

[55] Byunghyun Kim, Brett F. Sanders, James S. Famiglietti, and Vincent Guinot. "Urban flood modeling with porous shallow-water equations: A case study of model errors in the presence of anisotropic porosity". en. In: *Journal of Hydrology* 523 (Apr. 2015), pp. 680–692. ISSN: 00221694. DOI: 10.1016/j.jhydrol.2015.01.059.

[56] Muhammad Syahril Badri Kusuma. "Experimental Model of Dam Break Flow around several Blockages Configurations". In: *International Journal of GEOMATE* 16.58 (June 2019). ISSN: 21862982, 21862990. DOI: 10.21660/2019.58.97684.

[57] ASN (Autorité de Sûreté Nucléaire). *Protection of Basic Nuclear Installations Against External Flooding*. Tech. rep. https://www.french-nuclear-safety.fr/asn-regulates/asn-guides/asn-guide-no.-13, 2013.

[58] R. Dressler. "Comparison of Theories and Experiments for the Hydraulic Dam-Break Wave". In: *Proceedings of the International Association of Scientific Hydrology, Assemblée Générale*. Vol. 3. Rome, Italy, Sept. 1954, pp. 319–328.

[59] E.K. Trifonov. "Experimental Investigation of Positive Wave's Propagation along Dry Bottom". In: *Sci. Research Inst. Hydrotechnics Trans.* 10 (1933). (In Russian), pp. 169–188.

[60] L. Levin. "Mouvement Non Permanent sur les Cours d'Eau à la Suite de Rupture de Barrage [Unsteady River Flow Caused by a Dam-Break]". In: *Rev. Gén. Hydr.* 18 (1952). (In French), pp. 297–315.

[61] A. Ritter. "Die Fortpflanzung der Wasserwellen [Propagation of Water Waves]". In: *Z. Ver. Dtsch. Ing.* 36 (1892). (In German), pp. 947–954.

[62] J.J. Stoker. *Water Waves: The Mathematical Theory with Applications*. New York, NY, USA: Wiley, 1957.

[63] Chen Yang, Binliang Lin, Chunbo Jiang, and Ying Liu. "Predicting near-field dam-break flow and impact force using a 3D model". In: *Journal of Hydraulic Research* 48.6 (Dec. 2010). Publisher: Taylor & Francis _eprint: https://doi.org/10.1080/00221686.2010.531099, pp. 784–792. ISSN: 0022-1686. DOI: 10.1080/00221686.2010.531099.

[64] Hatice Ozmen-Cagatay, Evren Turhan, and Selahattin Kocaman. "An experimental investigation of dam-break induced flood waves for different density fluids". en. In: *Ocean Engineering* 243 (Jan. 2022), p. 110227. ISSN: 00298018. DOI: 10.1016/j.oceaneng.2021.110227.

[65] Mattia Melis, Davide Poggi, Giovanni Fasanella Oscar Domenico, Silvia Cordero, and Gabriel G. Katul. "Resistance to Flow on a Sloping Channel Covered by Dense Vegetation following a Dam Break". en. In: *Water Resources Research* 55.2 (Feb. 2019), pp. 1040–1058. ISSN: 0043-1397, 1944-7973. DOI: 10.1029/2018WR023889.

[66] Silvia Cordero, Andrea Cagninei, and Davide Poggi. “Dam-break on an idealised hill side: Preliminary results of a physical model”. en. In: *E3S Web of Conferences* 40 (2018). Publisher: EDP Sciences, p. 05002. ISSN: 2267-1242. DOI: 10.1051/e3sconf/20184005002.

[67] H. von Häfen, N. Goseberg, J. Stolle, and I. Nistor. “Gate-Opening Criteria for Generating Dam-Break Waves”. en. In: *Journal of Hydraulic Engineering* 145.3 (Mar. 2019), p. 04019002. ISSN: 0733-9429, 1943-7900. DOI: 10.1061/(ASCE)HY.1943-7900.0001567.

[68] Peter Nielsen, Beibei Xu, Davide Wüthrich, and Shaotong Zhang. “Friction effects on quasi-steady dam-break wave propagation on horizontal beds”. fr. In: *Journal of Fluid Mechanics* 939 (May 2022), A21. ISSN: 0022-1120, 1469-7645. DOI: 10.1017/jfm.2022.182.

[69] Beibei Xu, Shaotong Zhang, Peter Nielsen, and Davide Wüthrich. “Measurements of bed shear stresses near the tip of dam-break waves on a rough bed”. en. In: *Experiments in Fluids* 62.3 (Mar. 2021), p. 49. ISSN: 1432-1114. DOI: 10.1007/s00348-021-03152-4.

[70] R. Aleixo, S. Soares-Frazão, and Y. Zech. “Velocity-field measurements in a dam-break flow using a PTV Voronoï imaging technique”. en. In: *Experiments in Fluids* 50.6 (June 2011), pp. 1633–1649. ISSN: 0723-4864, 1432-1114. DOI: 10.1007/s00348-010-1021-y.

[71] Hiroshi Takagi and Fumitaka Furukawa. “Stochastic Uncertainty in a Dam-Break Experiment with Varying Gate Speeds”. en. In: *Journal of Marine Science and Engineering* 9.1 (Jan. 2021), p. 67. ISSN: 2077-1312. DOI: 10.3390/jmse9010067.

[72] Lindsey Ann LaRocque, Jasim Imran, and M. Hanif Chaudhry. “Experimental and Numerical Investigations of Two-Dimensional Dam-Break Flows”. en. In: *Journal of Hydraulic Engineering* 139.6 (June 2013), pp. 569–579. ISSN: 0733-9429, 1943-7900. DOI: 10.1061/(ASCE)HY.1943-7900.0000705.

[73] Farhad Hooshyaripor, Ahmad Tahershamsi, and Sahand Razi. “Dam break flood wave under different reservoir’s capacities and lengths”. en. In: *Sādhanā* 42.9 (Sept. 2017), pp. 1557–1569. ISSN: 0256-2499, 0973-7677. DOI: 10.1007/s12046-017-0693-x.

[74] Bo Wang, Jianmin Zhang, Yunliang Chen, Yong Peng, Xin Liu, and Wenjun Liu. “Comparison of measured dam-break flood waves in triangular and rectangular channels”. en. In: *Journal of Hydrology* 575 (Aug. 2019), pp. 690–703. ISSN: 00221694. DOI: 10.1016/j.jhydrol.2019.05.081.

[75] Fengjie Zhang, Bo Wang, and Yakun Guo. “Experimental study of the dam-break waves in triangular channels with a sloped wet bed”. In: *Ocean Engineering* 255 (July 2022), p. 111399. ISSN: 0029-8018. DOI: 10.1016/j.oceaneng.2022.111399.

[76] Bo Wang, Fengjie Zhang, Xin Liu, Yakun Guo, Jianmin Zhang, and Yong Peng. “Approximate Analytical Solution and Laboratory Experiments for Dam-Break Wave Tip Region in Triangular Channels”. EN. In: *Journal of Hydraulic Engineering* 147.10 (Oct. 2021). Publisher: American Society of Civil Engineers, p. 06021015. ISSN: 1943-7900. DOI: 10.1061/(ASCE)HY.1943-7900.0001928.

[77] G. Lauber and W. H. Hager. “Experiments to dambreak wave: Sloping channel”. en. In: *Journal of Hydraulic Research* 36.5 (Sept. 1998), pp. 761–773. ISSN: 0022-1686, 1814-2079. DOI: 10.1080/00221689809498601.

[78] Hui Liu, Haijiang Liu, Liheng Guo, and Senxun Lu. “Experimental study on the dam-break hydrographs at the gate location”. en. In: *Journal of Ocean University of China* 16.4 (Aug. 2017), pp. 697–702. ISSN: 1672-5182, 1993-5021. DOI: 10.1007/s11802-017-3470-x.

[79] Wenjun Liu, Bo Wang, Yunliang Chen, Chao Wu, and Xin Liu. “Assessing the Analytical Solution of One-Dimensional Gravity Wave Model Equations Using Dam-Break Experimental Measurements”. en. In: *Water* 10.9 (Sept. 2018), p. 1261. ISSN: 2073-4441. DOI: 10.3390/w10091261.

[80] Jacob Stolle, Behnaz Ghodoosipour, Caren Derschum, Ioan Nistor, Emil Petriu, and Nils Goseberg. “Swing gate generated dam-break waves”. en. In: *Journal of Hydraulic Research* 57.5 (Sept. 2019), pp. 675–687. ISSN: 0022-1686, 1814-2079. DOI: 10.1080/00221686.2018.1489901.

[81] Bo Wang, Wenjun Liu, Wei Wang, Jianmin Zhang, Yunliang Chen, Yong Peng, Xin Liu, and Sha Yang. “Experimental and numerical investigations of similarity for dam-break flows on wet bed”. en. In: *Journal of Hydrology* 583 (Apr. 2020), p. 124598. ISSN: 00221694. DOI: 10.1016/j.jhydrol.2020.124598.

[82] Lélis Espartel and Rafael Manica. “Experiments on initial stages of development of dam-break waves”. In: *RBRH* 26 (2021), e6. ISSN: 2318-0331, 1414-381X. DOI: 10.1590/2318-0331.262120200106.

[83] Le-Quyen Nguyen-Thi, Viet-Dung Nguyen, Xavier Pierens, and Patrice Coorevits. “An experimental and numerical study of the influence of viscosity on the behavior of dam-break flow”. en. In: *Theoretical and Computational Fluid Dynamics* 35.3 (June 2021), pp. 345–362. ISSN: 1432-2250. DOI: 10.1007/s00162-021-00562-2.

[84] Davide Wüthrich. “Extreme Hydrodynamic impact onto buildings”. PhD thesis. École Polytechnique Fédérale de Lausanne, Mar. 2018, p. 267. DOI: 10.5075/epfl-thesis-8116.

[85] R. Aleixo, Sandra Soares-Frazão, and Yves Zech. “Before the dam breaks: Analysis of the flow behind a downward moving gate”. In: June 2016, pp. 436–442. DOI: 10.1201/9781315644479-71.

[86] Sandra Soares-Frazão. “Review of imaging-based measurement techniques for free surface flows involving sediment transport and morphological changes”. In: *Journal of Hydroinformatics* 22 (June 2020). DOI: 10.2166/hydro.2020.026.

[87] Guillaume Gomit, Ludovic Chatellier, and Laurent David. “Free-surface flow measurements by non-intrusive methods: a survey”. In: *Experiments in Fluids* 63 (May 2022). DOI: 10.1007/s00348-022-03450-5.

[88] Jie Liu and Hong Xiao. “Experimental investigation of flood hydrograph induced by landslide dam breach based on transient surface velocity measurement”. In: *Arabian Journal of Geosciences* 15.18 (2022), p. 1520.

[89] Elisa Beteille, Frédérique Larrarte, Sébastien Boyaval, and Eric Demay. “Providing Validation Data for Numerical Codes Dealing with Unsteady Urban Flooding”. In: *Proceedings of the 40th IAHR World Congress*. Vienna, Austria, 2023, pp. 1456–1464. DOI: 10.3850/978-90-833476-1-5_iahr40wc-p0127-cd.

[90] Elisa Beteille, Frédérique Larrarte, Sebastien Boyaval, Eric Demay, and Minh-Hoang Le. “Dam-break flow over various obstacles configurations”. In: *Journal of Hydraulic Research* (2025). DOI: 10.1080/00221686.2025.2460020.

[91] Ting Tan, Yuxiang Ma, Jie Zhang, Xuyang Niu, and Kuang-An Chang. “Experimental study on flow kinematics of dam-break induced surge impacting onto a vertical wall”. In: *Physics of Fluids* 35.2 (Feb. 2023), p. 025127. ISSN: 1070-6631. DOI: 10.1063/5.0137475. eprint: https://pubs.aip.org/aip/pof/article-pdf/doi/10.1063/5.0137475/16677595/025127_1_online.pdf.

[92] Wenang Xie and Takenori Shimozono. “Water surge impingement onto a vertical wall: A new self-similarity solution for impact pressure”. In: *Physics of Fluids* 34.7 (July 2022), p. 076607. ISSN: 1070-6631. DOI: 10.1063/5.0100468. eprint: https://pubs.aip.org/aip/pof/article-pdf/doi/10.1063/5.0100468/16733932/076607_1_online.pdf.

[93] Zijing Huo and Haijiang Liu. “Experimental study of the surge- and bore-induced impact pressure on a vertical wall and its foundation”. In: *Physics of Fluids* 35.1 (Jan. 2023), p. 016602. ISSN: 1070-6631. DOI: 10.1063/5.0128668. eprint: https://pubs.aip.org/aip/pof/article-pdf/doi/10.1063/5.0128668/16674226/016602_1_online.pdf.

[94] Abdullah Demir, Ali Ersin Dincer, Zafer Bozkuş, and Arris S. Tijsseling. “Numerical and experimental investigation of damping in a dam-break problem with fluid-structure interaction”. In: *JOURNAL OF ZHEJIANG UNIVERSITY-SCIENCE A* (2019), 258–271.

[95] Kangping Liao, Changhong Hu, and Makoto Sueyoshi. “Free surface flow impacting on an elastic structure: Experiment versus numerical simulation”. In: *Applied Ocean Research* 50 (Mar. 2015). DOI: 10.1016/j.apor.2015.02.002.

[96] Lin Jing-Hua, Yi-Wei Chang, and Guan-Yu Chen. “Boulder Transportation on the Flat Bed by Dam Break”. In: *Journal of Earthquake and Tsunami* 16 (July 2022). DOI: 10.1142/S1793431122410020.

[97] Shaolin Yang, Zhiqiang Tan, Wanli Yang, Hasan Imani, Danqing Song, Jun Luo, and Jiarui Zhang. “Experimental study on hydrodynamic interaction between dam-break waves and circular pier”. In: *Ocean Engineering* 266 (2022), p. 113093. ISSN: 0029-8018. DOI: https://doi.org/10.1016/j.oceaneng.2022.113093.

[98] Shengzhe Wang, Maria Garlock, Luc Deike, and Branko Glisic. “Feasibility of Kinetic Umbrellas as Deployable Flood Barriers during Landfalling Hurricanes”. In: *Journal of Structural Engineering* 148.5 (2022), p. 04022047. DOI: 10.1061/(ASCE)ST.1943-541X.0003295. eprint: https://ascelibrary.org/doi/pdf/10.1061/%28ASCE%29ST.1943-541X.0003295.

[99] Shilong Liu, Ioan Nistor, Abdolmajid Mohammadian, and Amir H. Azimi. "Experimental Investigation on the Impact of Dam-Break Induced Surges on a Vertical Wall". In: *Fluids* 7.8 (2022). ISSN: 2311-5521. DOI: 10.3390/fluids7080258.

[100] Qi Fang, Shuguang Liu, Guihui Zhong, Jiyu Liang, and Yiwei Zhen. "Experimental Investigation of Extreme Flood Loading on Buildings Considering the Shadowing Effect of the Front Building". In: *Journal of Hydraulic Engineering* 148.6 (2022), p. 04022007. DOI: 10.1061/(ASCE)HY.1943-7900.0001986. eprint: https://ascelibrary.org/doi/pdf/10.1061/%28ASCE%29HY.1943-7900.0001986.

[101] S. V. Norin, V. V. Belikov, and A. I. Aleksyuk. "Simulating Flood Waves in Residential Areas". en. In: *Power Technology and Engineering* 51.1 (May 2017), pp. 52–57. ISSN: 1570-145X, 1570-1468. DOI: 10.1007/s10749-017-0782-3.

[102] Chartchay Chumchan and Phadungsak Rattanadecho. "Experimental and numerical investigation of dam break flow propagation passed through complex obstacles using LES model based on FVM and LBM." In: *Songklanakarin Journal of Science & Technology* 42.3 (2020).

[103] Michal Szydłowski and Bernard Stanislaw Twaróg. "Numerical Investigation of Flooding of Real-Topography Developed Areas Following River Embankment Failure". In: *Task Quaterly* 10.3 (2006), pp. 321–338.

[104] Tori Tomiczek, Adi Prasetyo, Nobuhito Mori, Tomohiro Yasuda, and Andrew Kennedy. "Physical modelling of tsunami onshore propagation, peak pressures, and shielding effects in an urban building array". en. In: *Coastal Engineering* 117 (Nov. 2016), pp. 97–112. ISSN: 03783839. DOI: 10.1016/j.coastaleng.2016.07.003.

[105] Marina Oukacine. "Etude expérimentale et numérique des écoulements à surface libre en présence d'obstacles émergés et faiblement submergés". Français. Thèse. Université Paris-Est, 2019.

[106] H. de Moel, J. van Alphen, and J. C. J. H. Aerts. "Flood maps in Europe: methods, availability and use". In: *Natural Hazards and Earth System Sciences* 9.2 (2009), pp. 289–301. DOI: 10.5194/nhess-9-289-2009.

[107] Kun Wang, Peng Yang, Guangming Yu, Chao Yang, and Liyi Zhu. "3D Numerical Modelling of Tailings Dam Breach Run Out Flow over Complex Terrain: A Multidisciplinary Procedure". In: *Water* 12.9 (2020). ISSN: 2073-4441. DOI: 10.3390/w12092538.

[108] Hong-Xin Chen, Jin Li, Shi-Jin Feng, Hong-Yu Gao, and Dong-Mei Zhang. "Simulation of interactions between debris flow and check dams on three-dimensional terrain". In: *Engineering Geology* 251 (2019), pp. 48–62. ISSN: 0013-7952. DOI: https://doi.org/10.1016/j.enggeo.2019.02.001.

[109] Yu Zhuang, Kaiping Jin, Qian-gong Cheng, Aiguo Xing, and Hao Luo. "Experimental and numerical investigations of a catastrophic tailings dam break in Daye, Hubei, China". In: *Bulletin of Engineering Geology and the Environment* 81 (Jan. 2022). DOI: 10.1007/s10064-021-02491-0.

[110] Sauro Manenti Andrea Amicarelli and Marco Paggi. "SPH Modelling of Dam-break Floods, with Damage Assessment to Electrical Substations". In: *International Journal of Computational Fluid Dynamics* 35.1-2 (2021), pp. 3–21. DOI: 10.1080/10618562.2020.1811240. eprint: https://doi.org/10.1080/10618562.2020.1811240.

[111] Zhangping Wei, Robert A. Dalrymple, Alexis Hérault, Giuseppe Bilotta, Eugenio Rustico, and Harry Yeh. "SPH modeling of dynamic impact of tsunami bore on bridge piers". en. In: *Coastal Engineering* 104 (Oct. 2015), pp. 26–42. ISSN: 03783839. DOI: 10.1016/j.coastaleng.2015.06.008.

[112] Daniel Horna Munoz and George Constantinescu. "3-D dam break flow simulations in simplified and complex domains". In: *Advances in Water Resources* 137 (2020), p. 103510. ISSN: 0309-1708. DOI: https://doi.org/10.1016/j.advwatres.2020.103510.

[113] Chiara Biscarini, Silvia Di Francesco, Elena Ridolfi, and Piergiorgio Manciola. "On the Simulation of Floods in a Narrow Bending Valley: The Malpasset Dam Break Case Study". In: *Water* 8.11 (2016). ISSN: 2073-4441. DOI: 10.3390/w8110545.

[114] Xiaoling Wang, Chen Wenlong, Zhengyin Zhou, Yushan Zhu, Wang Cheng, and Zhen Liu. "Three-dimensional flood routing of a dam break based on a high-precision digital model of a dense urban area". In: *Natural Hazards* 86 (Apr. 2017). DOI: 10.1007/s11069-016-2734-x.

[115] Zhengyin Zhou, Xiaoling Wang, Ruirui Sun, Xuefei Ao, Xiaopei Sun, and Mingrui Song. "Study of the comprehensive risk analysis of dam-break flooding based on the numerical simulation of flood routing. Part II: Model application and results". In: *Natural Hazards* 72 (June 2014), pp. 675–700. DOI: 10.1007/s11069-013-1029-8.

[116] A. Zhainakov and Abdikerim Kurbanaliev. "Verification of the open package OpenFOAM on dam break problems". In: *Thermophysics and Aeromechanics* 20 (Nov. 2013). DOI: 10.1134/S0869864313040082.

[117] Amanbek Jainakov, Abdikerim Kurbanaliev, and Maralbek Oskonbaev. "Large-Scale Modeling of Dam Break Induced Flows". In: *Dam Engineering*. Ed. by Hasan Tosun. Rijeka: IntechOpen, 2018. Chap. 4. DOI: 10.5772/intechopen.78648.

[118] *Open TELEMAC-MASCARET website*. http://www.opentelemac.org/.

[119] *code_saturne website*. https://www.code-saturne.org/.

[120] M. de Saint Venant. "Théorie du mouvement non-permanent des eaux, avec application aux crues des rivières et à l'introduction des marées dans leur lit". In: *C. R. Acad. Sc. Paris* 73 (1871), pp. 147–154.

[121] J.M. Hervouet. *Hydrodynamique des écoulements à surface libre: modélisation numérique avec la méthode des éléments finis*. Presses de l'école nationale des Ponts et Chaussées, 2003. ISBN: 9782859783792.

[122] Frédéric Archambeau, Namane Méchitoua, and Marc Sakiz. "Code Saturne: A Finite Volume Code for the computation of turbulent incompressible flows - Industrial Applications". In: *International Journal on Finite Volumes* 1.1 (Feb. 2004). Publisher: Institut de Mathématiques de Marseille, AMU, http://www.latp.univ–mrs.fr/IJFV/spip.php?article3.

[123] Suraj S Deshpande, Lakshman Anumolu, and Mario F Trujillo. "Evaluating the performance of the two-phase flow solver interFoam". In: *Computational Science & Discovery* 5.1 (Nov. 2012), p. 014016. ISSN: 1749-4699. DOI: 10.1088/1749-4699/5/1/014016.

[124] Frédéric Archambeau, Namane Méchitoua, and Marc Sakiz. "Code Saturne: A Finite Volume Code for the computation of turbulent incompressible flows - Industrial Applications". In: *International Journal on Finite Volumes* 1.1 (Feb. 2004), http://www.latp.univ–mrs.fr/IJFV/spip.php?article3.

[125] K. C. Karki and S. V. Patankar. "Pressure based calculation procedure for viscous flows at all speedsin arbitrary configurations". In: *AIAA Journal* 27.9 (1989), pp. 1167–1174. DOI: 10.2514/3.10242. eprint: https://doi.org/10.2514/3.10242.

[126] V. Guimet and D. Laurence. "A LINEARISED TURBULENT PRODUCTION IN THE k-e MODEL FOR ENGINEERING APPLICATIONS". In: *Engineering Turbulence Modelling and Experiments 5*. Ed. by W. RODI and N. FUEYO. Oxford: Elsevier Science Ltd, 2002, pp. 157–166. ISBN: 978-0-08-044114-6. DOI: https://doi.org/10.1016/B978-008044114-6/50014-4.

[127] code_saturne development team. *code_saturne 8.0 Theory Guide*. Tech. rep. 2023.

[128] Josh Davidson, Marie Cathelain, Louise Guillemet, Thilbault Le Huec, and John Ringwood. "Implementation of an openfoam numerical wave tank for wave energy experiments". In: *Proceedings of the 11th European wave and tidal energy conference*. European Wave and Tidal Energy Conference 2015. 2015.

[129] S. Soares-Frazão. "Experiments of dam-break wave over a triangular bottom sill". en. In: *Journal of Hydraulic Research* 45.sup1 (Dec. 2007), pp. 19–26. ISSN: 0022-1686, 1814-2079. DOI: 10.1080/00221686.2007.9521829.

[130] Magali Jodeau, Alexandre Hauet, Jérôme Le Coz, Jean-Baptiste Faure, and Guillaume Bodart. *Fudaa-LSPIV User Manual (v 1.9.2)*. Tech. rep. Dec. 2022.

[131] J Le Coz, M Jodeau, A Hauet, B Marchand, and R Le Boursicaud. "Image-based velocity and discharge measurements in field and laboratory river engineering studies using the free Fudaa-LSPIV software". en. In: *River Flow 2014*. Ed. by Anton Schleiss, Giovanni de Cesare, Mario Franca, and Michael Pfister. CRC Press, Aug. 2014, pp. 1961–1967. ISBN: 978-1-138-02674-2 978-1-4987-0442-7. DOI: 10.1201/b17133-262.

[132] G. Bodart, J. Le Coz, M. Jodeau, and A. Hauet. "Quantifying and Reducing the Operator Effect in LSPIV Discharge Measurements". In: *Water Resources Research* 60.2 (Feb. 2024), e2023WR034740. DOI: 10.1029/2023WR034740.

[133] Jerry Westerweel and Fulvio Scarano. "Universal outlier detection for PIV data". en. In: *Experiments in Fluids* 39.6 (Dec. 2005), pp. 1096–1100. ISSN: 0723-4864, 1432-1114. DOI: 10.1007/s00348-005-0016-6.

[134] Frédérique Larrarte, Nicole Goutal, and Augustin Doumic. "Floods in housing estate: some experimental data". en. In: *Proceedings of the 39th IAHR World Congress*. International Association for Hydro-Environment Engineering and Research (IAHR), 2022, pp. 6981–6986. ISBN: 978-90-832612-1-8. DOI: 10.3850/IAHR-39WC252171192022577.

[135] Megha Goyal. "Morphological image processing". In: *IJCST* 2.4 (2011), p. 59.

[136] Ting Tan, Yuxiang Ma, Jie Zhang, Xuyang Niu, and Kuang-An Chang. "Experimental study on flow kinematics of dam-break induced surge impacting onto a vertical wall". en. In: *Physics of Fluids* 35.2 (Feb. 2023), p. 025127. ISSN: 1070-6631, 1089-7666. DOI: 10.1063/5.0137475.

[137] P. García-Navarro R. Meurice S. Martínez-Aranda and S. Soares-Frazão. "Laser profilometry to measure the bed evolution in a dam-break flow". In: *Journal of Hydraulic Research* 60.5 (2022), pp. 725–737. DOI: 10.1080/00221686.2022.2059584. eprint: https://doi.org/10.1080/00221686.2022.2059584.